

# Fluid Power and Motion Control

FPMC 2012



Dr D N Johnston  
**and** Professor A R Plummer  
**Editors**



# **Fluid Power and Motion Control**





# **Fluid Power and Motion Control**

(FPMC 2012)

*Edited by*

**Dr D N Johnston**

Symposium Organiser

**Professor Andrew Plummer**

Director

*Centre for Power Transmission and Motion Control  
University of Bath, UK*

Copyright © With The Centre for Power Transmission and Motion Control.

***British Library Cataloguing in Publication Data***

A catalogue record for this book is available from the British Library

All rights reserved. No part of this publication or the information contained herein may be reproduced, stored in a retrieval system, or transmitted in any form or by any means, electronic, mechanical, by photocopying, recording otherwise, without written prior permission from the publisher. Although all care is taken to ensure the integrity and quality of this publication and the information herein, no responsibility is assumed by the publishers nor the author for any damage to property or persons as a result of operation or use of this publication and/or information contained herein.

Printed by:

**Harness Publicity Ltd**

13 Winstanley Way, Basildon, Essex SS14 3BP, United Kingdom

Tel: +44 (0) 1268 533121

Fax: +44 (0) 1268 286879

[www.harnesspublicity.com](http://www.harnesspublicity.com)

email: [enquiries@harnesspublicity.com](mailto:enquiries@harnesspublicity.com)

ISBN 978-0-86197-187-9

Printed in Great Britain

Front cover picture: Pulteney Bridge and Weir, Bath

Back cover picture: Shield tunneling machine

# Preface

The Fluid Power and Motion Control Symposium took place on 12-14 September 2012. It was the 24th in the series of Symposia held at the University of Bath, and was co-organised by the American Society of Mechanical Engineers (ASME). It was co-sponsored by the Network of Fluid Power Centres in Europe (FPCE). The Symposium was truly international, with authors from 12 countries. 41 fully refereed papers were presented, reflecting the latest advances in hydraulic and pneumatic fluid power and focusing on topics such as energy efficiency, advanced control, and modern applications such as renewable energy generation. A Keynote speech was presented by Professor Jan-Ove Palmberg, entitled “Fluid Power under Pressure”. The event included a gala dinner at the Bath Spa Hotel, Bath, during which one of the world’s most prestigious fluid power awards was presented, the Koski Medal.

Since 2009, the FPMC Symposia have alternated each year between Bath and the USA, and have taken place in Hollywood (2009) and Washington DC (2011). We are honoured that ASME is collaborating with us in this venture, and look forward to a long and fruitful partnership. In 2013 the event will take place at Stanford University, California.

Without the continued support and enthusiasm of authors, reviewers, delegates and staff, it would not be possible to sustain such a long-running and successful series of events. Heartfelt thanks are due to all who have contributed. Special thanks are due to Gillian Elsworth for her considerable effort in compiling the material for this book, and for organizing and ensuring the smooth running of the event. We are also grateful for the support from Harness Publicity Ltd.

Professor A R Plummer, Director  
Dr D N Johnston, Symposium Organiser  
Centre for Power Transmission and Motion Control  
Bath, September 2012



The Centre for  
Power Transmission  
and Motion Control



# Contents

Preface

iv

## **Pumps and motors**

A novel approach to predict the cylinder block / valve plate interface performance in swash plate type axial piston machines <i>Marco Zecchi, Prof.Dr.-Ing. Monika Ivantysynova</i>	13
Optimal Design of Gears and Lateral Bushes of External Gear Machines <i>Ram Sudarsan Devendran, Andrea Vacca</i>	29
Friction measurement of plunger bushing contact in fuel injection pumps <i>Sebastian Drumm, Stefan Heitzig, Hubertus Murrenhoff</i>	51
Geometric Features of Gerotor Pumps Analytic vs Cad Methods <i>Gianluca Carconi, Cristian D’Arcano, Nicola Nervegna, Massimo Rundo</i>	59

## **Efficient Fluid Power**

Thermal Insulation in Enhancing Performance Characteristics of Hydraulic Accumulator <i>J. Juhala, J. Kajaste, M. Pietola</i>	81
Energy-efficient electrohydraulic compact drives for low power applications <i>Dipl.-Ing. Sebastian Michel, Professor Dr.-Ing. Jürgen Weber</i>	93
Optimizing Hydraulic Energy Recovery System of Reach Truck <i>H. Hänninen, J. Kajaste, M. Pietola</i>	109
Minimizing the Power Dissipation in the Piston-Cylinder Gap Using a Barrel-Shaped Piston <i>Kim A. Stelson, Feng Wang</i>	123

## **Digital Hydraulics**

- Digital Hydraulic Pressure Relief Function 137  
*M. Ketonen, M. Huova, M. Heikkilä, M. Linjama, P. Boström, M. Waldén*
- Analysis of Dynamic Properties of a Fast Switching On-Off Valve for Digital Displacement Pumps 151  
*Daniel B. Rømer, Per Johansen, Henrik C. Pedersen, Torben O. Andersen*
- Active control of pressure pulsation in a switched inertance hydraulic system using a rectangular-wave reference signal 165  
*Min Pan, Nigel Johnston, Andrew Hillis*

## **Control I**

- A Sliding Mode Controller Based on the Interacting Multiple Model Strategy 181  
*M. A. El Sayed, S. A. Gadsden, S. R. Habibi*
- Hydraulic servoactuator for adaptive force control of fast trains pantographs 195  
*Davide Ferrara, Giovanni Jacazio, Andrea Mornacchi, Stefano Pastorelli, Massimo Sorli*
- Issues of sensor noise, bandwidth and sampling time in PID pressure control 213  
*Matthias Liermann*
- Overshoot and steady-state error of hydraulic press driven by DCV-positioned pump-controlled asymmetric cylinder 227  
*Jianfeng Tao, Haiyan Yang, Guofang Gong, Chengliang Liu*

## **Pneumatics I**

- A Pneumatic Position Servo Based on On/Off Valve Actuated Muscle Actuators in Opposing Pair Configuration 243  
*Ville Jouppila, Asko Ellman*
- Implementation and Analysis of a Pneumatic Pipe Model 259  
*Jan Elvers, Hubertus Murrenhoff*
- Investigation on the Efficiency of Pneumatic System Using Air Power 271  
*Toshiharu Kagawa, Maolin Cai, Xin Li*
- Sliding Mode Control of an MRI-Compatible Pneumatically Actuated Robot 283  
*David B. Comber, Diana Cardona, Robert J. Webster, III, Eric J. Barth*

## **Control II**

- A Combined Multiple Inner Loop Control Strategy for an Electro-Hydraulic Actuator 297  
*Mohammed A. El Sayed, Saeid Habibi*
- The Fractional Order PID Control of Hydraulic Position System Based on Internet 321  
*Shi Guanglin, Wang Ruigang, Xu Zhenyin*
- Deterministic Control Strategy for a Hybrid Hydraulic System with Intermediate Pressure Line 333  
*Dipl.-Ing. Peter Dengler, Prof. Dr.-Ing. Marcus Geimer,  
Dipl.-Ing. René von Dombrowski*
- Proportional control system design and probability of stability for a pilot operated proportional valve with parametric uncertainty 347  
*Richard Carpenter, Roger Fales*

## **Control and Modelling**

- Optimizing Dynamic Properties of Hydraulic Actuator for Hardware-in-the- Loop Damper Testing 365  
*T. Saarikoski, J. Kajaste, M. Pietola*
- Dynamic Modelling of a Linear Friction Welding Machine actuation system 379  
*D.T. Williams, P. Wilson, A. R. Plummer*
- Multivariable Backstepping Controls of a High Bandwidth Electro-hydraulic Actuator 397  
*Yaozhong Xu, Lilia Sidhom, Eric Bideaux, Mohamed Smaoui*
- Analysis of Two Typical Thrust Electro-hydraulic Control Systems for Shield Tunneling Machine 411  
*Weiqiang Wu, Guofang Gong, Hu Shi*

## **Modelling and Simulation**

System Modelling and Bulk Modulus Estimation of an Electrohydrostatic Actuator	423
<i>Y. Song, S. A. Gadsden, S. A. El Delbari, S. R. Habibi</i>	
Modeling of a Proportional Valve by MCMC Method	439
<i>Junhong Liu, Huapeng Wu, Heikki Handroos, Heikki Haario</i>	
Steady and Unsteady Flow Force acting on a Spool Valve	451
<i>Kazuhiro Tanaka, Keitaro Kamata, Kouki Tomioka, Takeshi Yamaguchi</i>	
Effective Bulk Modulus Model Verification for the Mixture of Air/Gas and Oil	467
<i>H.Gholizadeh, D. Bitner, R.Burton, G.Schoenau</i>	

## **Automotive and Aerospace Application**

Optimal Sizing of Pipe Networks in Aircraft Hydraulic System Preliminary Design	489
<i>C. Dunker, F. Thielecke, T. Homann</i>	
Coupling Displacement Controlled Actuation with Power Split Transmissions in Hydraulic Hybrid Systems for Off-Highway Vehicles	505
<i>Michael Sprengel, Dr. Monika Ivantysynova</i>	
Fault-tolerant steer-by-wire valve for agricultural tractors based on independent metering with on/off valves	519
<i>Dipl.-Ing. David Schmitz, Prof. Dr.-Ing. Marcus Geimer</i>	
Generation of power transmission architectures for redundant actuators	537
<i>Amine Fraj, Jean-Charles Mare, Marc Budinger</i>	



## **Renewable Energy**

- Design and Control of Full Scale Wave Energy Simulator System 551  
*Henrik C. Pedersen, Anders H. Hansen, Rico H. Hansen1, Torben O. Andersen, Michael M. Bech*
- Determining Required Valve Performance for Discrete Control of PTO Cylinders for Wave Energy 565  
*Rico H. Hansen, Torben O. Andersen and Henrik C. Pedersen*
- Wind turbines with variable hydraulic transmissions and electrically excited synchronous generators directly connected to the grid 579  
*Peter Chapple, Michael Niss, Knud Erik Thomsen*

## **Pneumatics II**

- Design of a Figure-Eight free-liquid-piston engine compressor for compact robot power 595  
*Mark E Hofacker, Mengze Sun, Eric J Barth*
- Test rig and Simulation Software for Performance Comparison of Pneumatic Servo Controllers Given three Actuator Setups and five Circuit Configurations of Control Valve 609  
*Ramhuzaini Abd. Rahman, Nariman Sepehri*
- Development of a Low Noise Pressure Reducing Valve for High Pressure Hydrogen Using a Radial Slit Structure 623  
*Chongho Youn, Yoshinari Nakamura, Toshiharu Kagawa*

# **Pumps and Motors**



# **A novel approach to predict the cylinder block / valve plate interface performance in swash plate type axial piston machines**

**Marco Zecchi, Prof.Dr.-Ing. Monika Ivantysynova**

Maha Fluid Power Research Center, Purdue University

1500 Kepner Dr, Lafayette IN, 47905, USA

## **1 ABSTRACT**

This paper focuses on the cylinder block/valve plate interface of swash plate type axial piston machines. The prediction of the film thickness is the crucial point to determine the interface performance in terms of viscous friction and leakage flow.

The authors recently developed a fluid structure interaction model for the cylinder block/valve plate interface, where the precise estimations of thermal and elasto-hydrodynamic effects are fully coupled together, in order to have an accurate description of the fluid film thickness as a function of the main operative parameters. A similar model was developed by Pelosi and Ivantysynova (2010-2012) also for the piston/cylinder interface; the goal of this work is to study the interaction between the two interfaces in terms of forces exchange.

In particular, a simplified analytical method for the calculation of the external forces transferred from the piston-slipper assembly to the cylinder block/valve plate interface is compared to a more advanced approach, where the cylinder block is loaded directly with the pressure field between pistons and cylinders bore, calculated through the fluid structure model for the piston/cylinder interface. The differences between the two calculation methods are presented in terms of steady state valve plate surface temperature predictions. An absolute benchmark of the two different approaches is also determined by direct comparison of the predicted temperature fields with measurements.

## **2 INTRODUCTION**

The design of the rotating group represents one of the most critical aspects in pump design. The design of the lubricating interfaces is the key to the design of the rotating group. The cross section of Figure 1 illustrates the three main lubricating interfaces of axial piston pump. Each interface has to fulfill in the same time a sealing and a bearing function and therefore needs to be optimized with regards to opposite requirements. In order to limit the leakage flow, the interface should provide a very thin lubricating film; on the other hand this would dramatically

increase the energy dissipated by viscous friction. Moreover, the lubricating film is responsible of the load carrying ability of the interface: to minimize possible conditions of mixed lubrication, with a consequent extensive wearing of the solid parts, an adequate film thickness should always be present as a reaction to the external loads.

## 2.1 Cylinder block / valve plate interface

This paper focuses on the cylinder block/valve plate interface. At any instant of time the lubricating film has to carry a complex set of external loads acting on the cylinder block. The main load is determined by the pressurized fluid in the displacement chambers: in addition to the axial force  $F_{DB}$ , since the high pressure region is limited to just half of the cylinder block (positive  $x$ - $y$  semi-plane in Figure 1), a bending moment in the  $y$  direction is generated. A second load acting directly to the cylinder block body derives from the action of a spring, which generates a constant axial thrust  $F_S$  in the negative  $z$  direction. The cylinder block also exchanges forces with the pistons; these forces however are not directly applied to the cylinder block but are transferred to it through the lubricating film between pistons and cylinders bore. The resultant of these force,  $F_R$  is responsible of a bending moment mainly in the  $x$  direction, while the friction force  $F_{TB}$  contributes also to the axial load.

The described forces and moments are time dependent and they determine a complex dynamic load condition over one shaft revolution; Figure 2 shows an example of external loads for a 100 cc unit, calculated at 3000 rpm, maximum swash plate angle and 300 bar differential pressure.

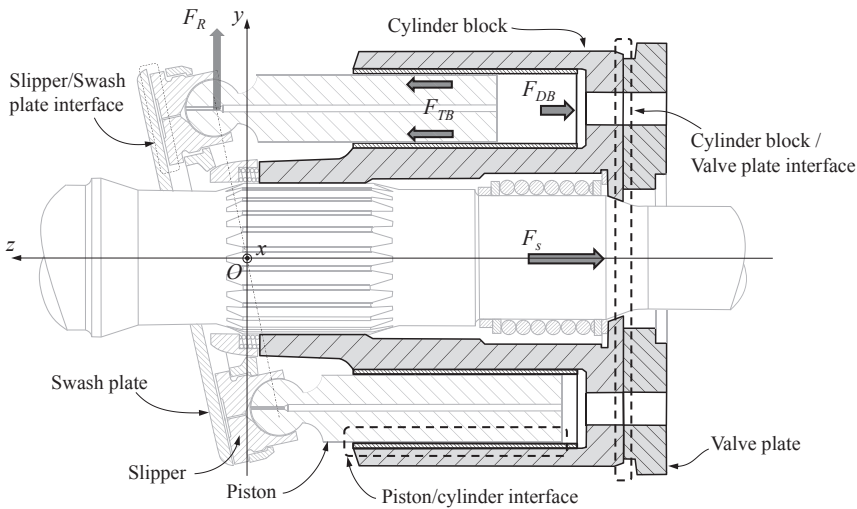


**Figure 1: Rotating kit cross section for a swash plate type axial piston machine. The three lubricating interfaces and the external loads acting on the cylinder block are indicated**

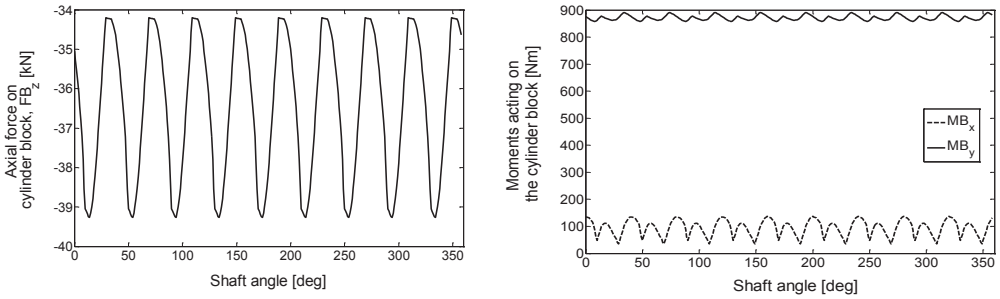


**Figure 2: Axial forces and moments acting on the cylinder block over one shaft revolution**

The external loads need to be balanced by the pressure field generated in the fluid film in order to limit mixed friction and wear (condition of full film lubrication). The pressure field has two components: hydrostatic and hydrodynamic. The first is determined by diffusion of pressure from the boundaries (displacement chambers, ports and case areas) and it can change just if the boundary changes. The second component is instead associated with the relative motion of the cylinder block with respect to the valve plate, both macroscopic (cylinder block rotation) and microscopic (cylinder block micro motion) and is fundamental to allow dynamic loads to be balanced at any instant of time.

The hydrodynamic pressure field is strongly affected by the lubricating film geometry. Since both the cylinder block and valve plate & end case assembly are usually subjected to high pressure loads, their elastic deformations are of the same order of magnitude of the film thickness itself and consequently they affect directly the hydrodynamic pressure reaction. On the other hand, the fluid flow in the gap dissipates energy and consequently heats the boundary solids. This temperature increment is an additional load for the boundary solids and is responsible of a further elastic deflection, which can be even more important of the pressure deformation. Recent research results [13,14] and [20] have shown that these effects are definitely not negligible and need to be considered to model this interface.

## 2.2 Previous research

The cylinder block / valve plate interface has been subject of many studies in the last 40 years. Experimental investigation of the clearance and its modification as regard to oil properties, operative conditions and geometric details were carried out by [1], [10,11], [18]. In all these works the experimental apparatus were not able to measure directly the film thickness, but rather to capture the relative position of the block with respect to the valve plate in one or more points. Other important experimental investigation is reported in [12], with focus on the thermal behavior of the rotating kit.

Analytical models were developed by [2], [5], [6], [8], [9], [16,17]. The limited computation power of the past years forced the authors to introduce strong simplifications in the solution of the fluid flow. These models were able to provide just general information on the interface performance, or basic guidelines to support the design process.

For this reason, the growing need in computational tool to aid the design process, combined with the exponential improvement in computer speed of the last ten years, led the researchers to the development of more advanced CFD based models. In these models new phenomena

such as micro-motion, elasto-hydrodynamic lubrication, non-isothermal flow and heat exchange with boundary solids could be introduced. In particular [15] represented the first attempt of predicting the film thickness based on the balance of the external forces acting on the cylinder block through the calculation of the hydrodynamic pressure field in the gap. Unfortunately this model has revealed to be poor: the simulations were not able to determine a stable lubricating film between the cylinder block and the valve plate for any operating condition. Clearly, some important phenomenon involved in the lubrication mechanism was missing.

Successive developments in the interface modeling moved towards the elasto-hydrodynamic lubrication direction, as in [3] and [4], since also experimental evidence underlined the importance of these effects: Bergada, and Davies [1] measured the relative position of the cylinder block through three inductive position transducers located on the valve plate periphery and concluded that for some operating conditions the calculation of the film thickness assuming the bodies to be completely rigid leads to negative values. The model of Huang introduced for the first time the elastic deformation of the cylinder block due to pressure loads through a coupling of the pre-existing model [15] and the commercial code ANSYS. The introduction of this effect solved the stability problems encountered with the rigid approach.

Some years later, Jouini and Ivantysynova [7] introduced thermal capabilities in the model described in [4]. The temperature of the surfaces bounding the gap were calculated taking into consideration heat fluxes due to energy dissipation, accounting in a simplified way for the heat transfer through solid parts (cylinder block and valve plate) to the pump case and ambience. Jouini and Ivantysynova compared their simulation results with surface temperature measurements conducted on a 100cc swash plate type axial piston pump. The simulation results captured the main trend; however the authors concluded that a more precise model was still necessary before this method could be introduced into practical computational pump design.

In [20] Zecchi and Ivantysynova presented a fully coupled, elasto-hydrodynamic and thermal model for the cylinder block valve plate interface. For the first time, in this new model the precise estimations of thermal and elasto-hydrodynamic effects were fully coupled together, providing an accurate description of the fluid film thickness as a function of the main operative parameters. Temperatures predicted in simulation matched the measured temperatures on the valve plate surfaces for different operating conditions.

In the work presented in this paper the aforementioned simulation model was coupled with a similar model for the piston/cylinder interface developed by Pelosi and Ivantysynova [13,14], to study the effect of the interaction between the two interfaces in terms of loads transferred from the piston slipper-assembly to the cylinder block body. A simplified analytical method to calculate the external loads on the cylinder block is compared with a more advanced method based on the direct exchange of information between the two fluid-structure interaction models.

### 3 SIMULATION MODEL DESCRIPTION

An overview of the overall simulation model used in this work is represented in Figure 3. The two fluid structure interaction models face exactly the same type of problems and therefore, the solution structure is the same for both.

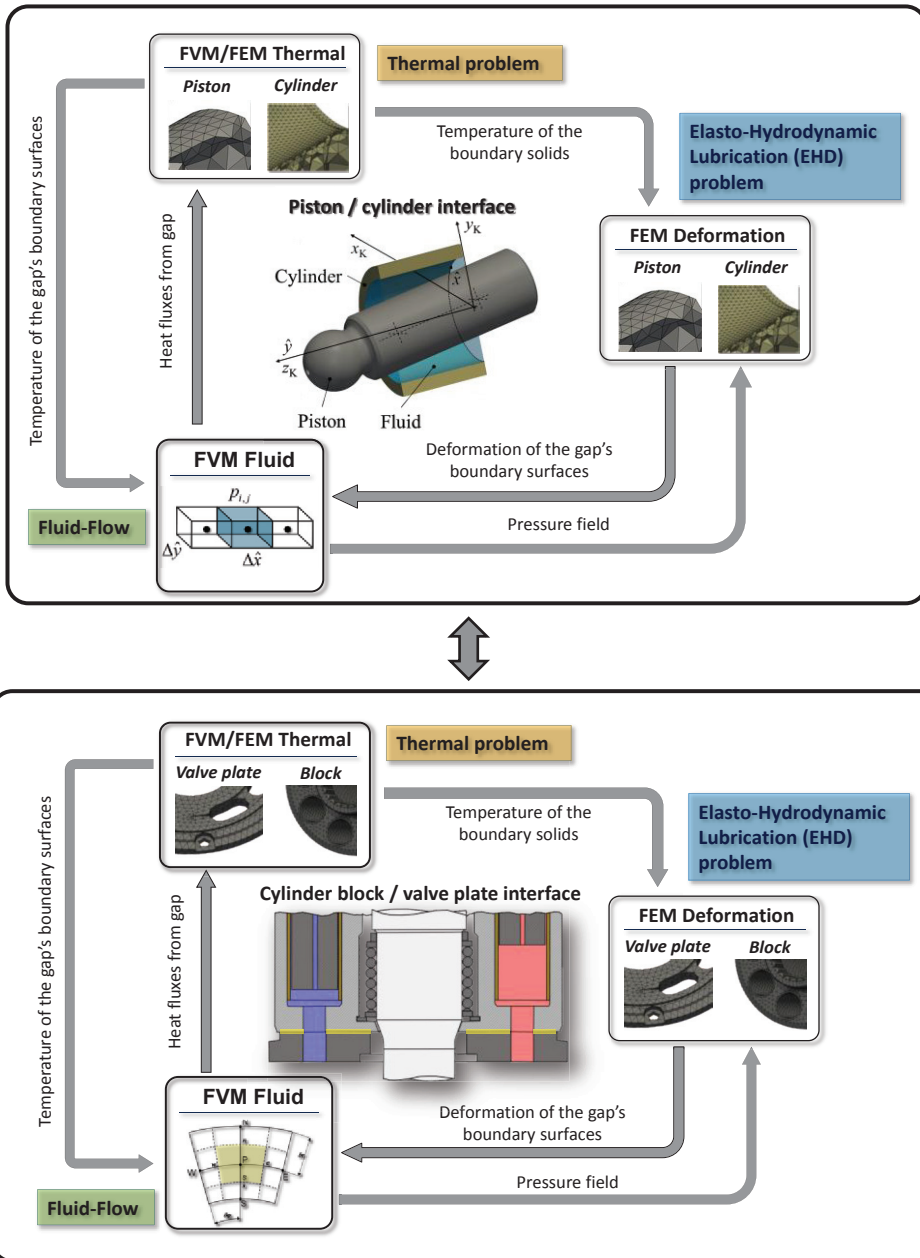


Figure 3: Overview of the simulation model

Three main modules, coupled together, accounts for all the main physical phenomena in the lubricating interfaces. The first module (FVM Fluid) solves the Reynolds and the Energy equations using the Finite volume method, describing the non-isothermal fluid flow in the lubricating gap. Different numeric techniques were developed to optimize the solution according with



the geometric features of each interface: the geometric multigrid method was used for the piston/cylinder interface whereas the preconditioned bi-conjugate gradient stabilized method was addressed to the cylinder block valve plate interface. The pressure field in the lubricant is calculated as a dynamic reaction to the oscillating external loads: at every instant of time a multi-dimensional root finding algorithm iteratively changes the squeeze motion of the cylinder block and pistons until the parts reach the equilibrium. Integration in time of the squeeze motion fields determines the instantaneous parts position. A precise estimation of the fluid viscosity is fundamental to achieve reliable prediction of the interface's load carrying ability, leakages and torque losses. In the developed model, an empirical correlation is used to determine the viscosity as a function of pressure and temperature.

From the knowledge of the pressure field, the elastic deformations of pistons, bushings, cylinder block, valve plate and end case assembly are calculated using an in house FEM solver (FEM deformation module). The relative deformations of the gap boundary surfaces are extracted and used to correct the film thickness in the fluid flow module. Pressure and deformation mutually influence each other and therefore a converged solution can be achieved only by solving a fluid structure interaction problem or, more precisely, an elasto-hydrodynamic lubrication problem. A partitioned fluid structure interaction scheme was developed for both the interfaces.

Also the heat transfer is characterized by an interaction between the lubricating interface and the boundary solids. In the solution of the Energy equation the surface temperatures of the gap's boundary solids are important boundary conditions that strongly affect the calculated temperature field. On the other hand, the energy dissipated in the fluid film generates heat fluxes towards these boundary solids. Using these fluxes as boundary conditions, the pistons, bushings, cylinders block, valve plate and end case temperature fields are calculated through an unstructured finite volume solver, specifically developed for this purpose. From the knowledge of these temperature fields, the thermal loads are estimated and the corresponding thermal expansions are calculated with the FEM solver (FVM/FEM thermal module). Since the thermal problem is assumed to be "quasi-stationary" the thermal analysis is carried out just once per revolution. As for the elastic deformation due to pressure, the deflections deriving from the thermal expansion affect the fluid film thickness with substantial modification of the lubrication behavior. This second interaction between lubricating interface and boundary solids represents the thermal problem.

Both the simulation models are particularly complicated and a thorough description of all the three modules clearly lies outside the purpose of this paper. Details about the implementation and the model validation can be found in [13,14] and [19,20] and will be further addressed to future publications.

#### **4 CALCULATION OF THE EXTERNAL FORCES ACTING ON THE CYLINDER BLOCK**

The load condition of the cylinder block was briefly described in section 2.1, where it was anticipated that the entire set of loads can be represented by a system composed of one axial force  $FB_z$  and two moments in  $x$  and  $y$  direction,  $MB_x$  and  $MB_y$  respectively (Figure 2). This system is determined by two separate contributions

1. direct loads on the cylinder block (pressure in the displacement chamber and spring action) ;
2. loads transferred to the cylinder block from the piston-slipper assembly.

The direct loads on the block are relatively easy to calculate, as shown in Equation (1).

$$\begin{aligned}
 FB_z &= F_S + \sum_{i=1}^z F_{DBzi} = F_S + \sum_{i=1}^z p_{DCi} A_{DCi} \\
 MB_x &= \sum_{i=1}^z y_{DBi} F_{DBzi} = \sum_{i=1}^z y_{DBi} p_{DCi} A_{DCi} \\
 MB_y &= -\sum_{i=1}^z x_{DBi} F_{DBzi} = -\sum_{i=1}^z x_{DBi} p_{DCi} A_{DCi}
 \end{aligned} \tag{1}$$

In Equation (1)  $F_S$  is the spring force and  $F_{DBz}$  the axial pressure force, given by the product of the displacement chamber pressure  $p_{DC}$  and the displacement chamber area  $A_{DC}$ . The summation in Equation (1) goes through all the  $z$  pistons.

The calculation of the loads associated with the piston-slipper assembly is a more delicate subject and is presented in the following sections.

#### 4.1 Forces acting on the piston/slipper assembly

Figure 4 shows schematically the loads acting on the piston/slipper assembly. The entire set of loads can be described by three main forces:

- Reaction force of the swash plate,  $F_{SK}$
- Centrifugal force,  $F_{\omega K}$
- Friction force between slipper and swashplate,  $F_{TK}$

The sum of these three forces gives the total load acting on the piston-slipper assembly,  $F_R$ .

The force  $F_{SK}$  is calculated from the total axial force on the piston  $F_{AK}$  as follows

$$F_{SK} = -\frac{F_{AK}}{\cos \beta} = -\frac{F_{DK} + F_{aK} + F_{TK}}{\cos \beta} \tag{2}$$

The total axial load in Equation (2) is determined by the pressure in the displacement chamber  $F_{DK}$ , the inertia force  $F_{aK}$  and the resultant friction force produced in the piston guide,  $F_{TK}$ . The direction of  $F_{SK}$  is normal to the swash plate surface; therefore it always has a  $y$  and a  $z$  component:

$$\begin{aligned}
 F_{SKy} &= F_{AK} \tan \beta \\
 F_{SKz} &= -F_{AK}
 \end{aligned} \tag{3}$$

With reference to Figure 4, the origin of the swash plate reaction force is the point  $K$ , which coordinates can be calculated as in Equation (4).

$$\begin{aligned}
x_K &= R \sin \varphi \\
y_K &= R \cos \varphi \\
z_K &= z_{K0} - R \tan \beta (1 - \cos \varphi)
\end{aligned} \tag{4}$$

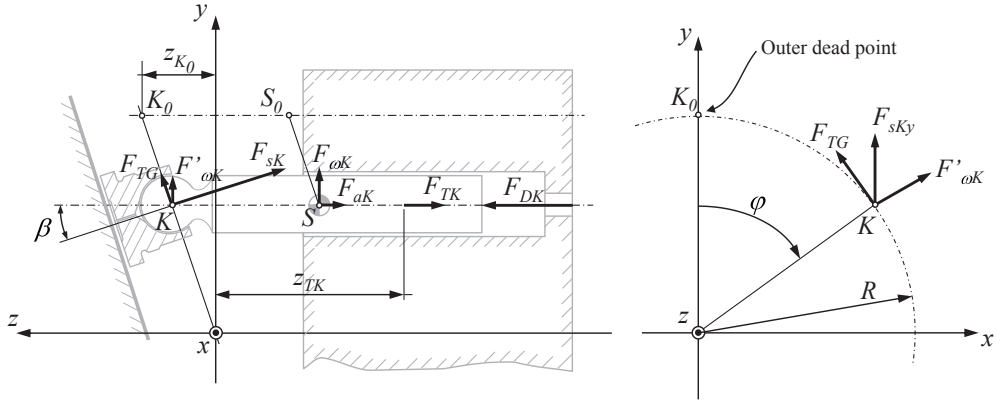


**Figure 4: Forces acting on the piston/slipper assembly that are transferred to the cylinder block**

The centrifugal force acts always in the radial direction; therefore has components just in the  $x$ - $y$  plane and it can be described as in Equation (5)

$$\begin{aligned}
F_{\omega Kx} &= m_{KG} R \omega^2 \sin \varphi \\
F_{\omega Ky} &= m_{KG} R \omega^2 \cos \varphi
\end{aligned} \tag{5}$$

Where  $m_{KG}$  is the mass of the piston-slipper assembly and  $\omega$  is the machine angular speed. The centrifugal force is applied in the center of mass of the assembly; however, in order to calculate the total force, the centrifugal force is transformed into an equivalent load  $F'_{\omega K}$  applied at the point  $K$ , as described in [5]. Also the volume of fluid in the displacement chamber determines a centrifugal force on the cylinder block; however the mass of this volume is about one order of magnitude smaller than  $m_{KG}$  and therefore it can be neglected in Equation (5).

The friction force  $F_{TG}$  produced in the sliding surface of the slipper during its motion on the swash plate is assumed to be applied on point  $K$  as well and has always components just in the  $x$ - $y$  plane, as indicated in Equation (6).

$$\begin{aligned}
F_{TGx} &= -F_{TG} \cos \varphi \\
F_{Tgy} &= F_{TG} \sin \varphi
\end{aligned} \tag{6}$$

The resultant force  $F_R$  acts on the piston-slipper assembly at point  $K$ , perpendicularly to the cylinder bore axis and its magnitude is determined by the vector addition of the forces  $F_{SKy}$ ,  $F'_{\omega K}$  and  $F_{TG}$  as in Equation (7).

$$F_R = \sqrt{(F_{SKy} + F'_{oKy} + F_{TGy})^2 + (F'_{oKx} + F_{TGx})^2} \quad (7)$$

Under the hypothesis of full film lubrication, the load determined by  $F_R$  has to be borne by the film of lubricant present between piston and cylinder. Therefore  $F_R$  does not represent an actual external load on the cylinder block body: the external load on the cylinder block is indeed represented by the pressure field in the gap.

## 4.2 Simplified analytical approach

In all the previous works [4], [7], [15], [19] the loads from the piston slipper assembly were transferred to the cylinder block using a simplified analytical approach, assuming that the force  $F_R$  was directly applied to the cylinder block body at the point  $K$  in Figure 4, as described in [5].

In this condition, the axial force and the moments deriving from the piston-slipper assembly (to be summed to Equation (1)), are expressed by Equation (8).

$$\begin{aligned} FB_z &= F_{TB} \\ MB_x &= -\sum_{i=1}^z z_A F_{Ryi} + \sum_{i=1}^z y_{TBi} F_{TBi} \\ MB_y &= \sum_{i=1}^z z_A F_{Rxi} - \sum_{i=1}^z x_{TBi} F_{TBi} \end{aligned} \quad (8)$$

The two moments in Equation (8) do not represent a precise estimation of the actual loads on the cylinder block because the pistons are not rigidly attached to it and therefore the force  $F_R$  cannot be assumed to be applied at point  $K$  for the purpose of calculating the loads transferred from the piston-slipper assembly to the cylinder block body.

The second problem is represented by the resultant friction force on the cylinder block  $F_{TB} = -F_{TK}$  and its point of application. Simplified analytical methods based on the assumption of a constant gap throughout the piston guide or experimental correlations can be found for example in [5]. However, as shown in [13], a precise estimation of  $F_{TK}$  can be achieved only through a fluid structure interaction analysis.

## 4.3 Advanced calculation method

The new calculation method proposed in this work determines the load on the cylinder block generated by the piston-slipper assembly through the pressure field in the gap between piston and cylinder, calculated coupling the two fluid structure interaction model for the piston/cylinder and cylinder block/valve plate interfaces.

Through an unwrapped representation, Figure 5 illustrates the pressure field between piston and cylinder calculated with the piston/cylinder fluid structure interaction model for a shaft angle  $\varphi = 0^\circ$ . In Figure 5  $z_K$  is the direction of the gap length and  $\phi_K$  the angle defining the circumferential position.

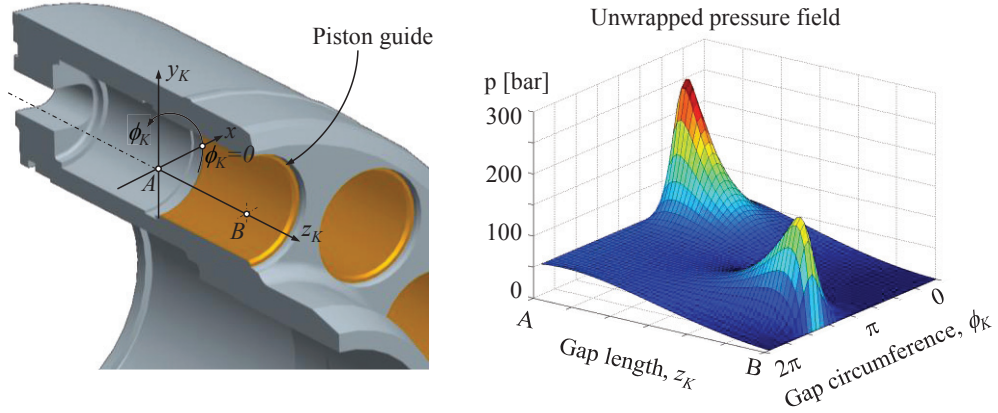


**Figure 5: pressure field in the lubricating film between piston and cylinder, unwrapped representation**

With reference to the  $x_K$ - $y_K$  reference system in Figure 5, the loads associated with the pressure field can be calculated as indicated in Equation (9).

$$\begin{cases}
 F_{fKx} = \int_{gap} dF_{fKx} = \int_{gap} (pda) \cos \phi \cong \sum_{i,j,k} p_{ijk} \delta a \cos \phi_{ik} \\
 F_{fKy} = \int_{gap} dF_{fKy} = \int_{gap} (pda) \sin \phi \cong \sum_{i,j,k} p_{ijk} \delta a \sin \phi_{ik} \\
 M_{fKx} = \int_{gap} dF_{fKy} z = \int_{gap} z(pda) \sin \phi \cong \sum_{i,j,k} p_{ijk} \delta a \sin \phi_{ik} z_k \\
 M_{fKy} = - \int_{gap} dF_{fKx} z = - \int_{gap} z(pda) \cos \phi \cong - \sum_{i,j,k} p_{ijk} \delta a \cos \phi_{ik} z_k
 \end{cases} \quad (9)$$

Since the pressure field is solved numerically on a discretized grid, the integrals are approximated with summations. The system of two forces and two moments in Equation (9),  $\{F_{fKx}, F_{fKy}, M_{fKx}, M_{fKy}\}$ , is transformed into an equivalent system composed of four forces applied in the two points A and B,  $\{F_{fAx}, F_{fAy}, F_{fBx}, F_{fBy}\}$ , as shown in Figure 6.

The system of forces  $\{F_{fAx}, F_{fAy}, F_{fBx}, F_{fBy}\}$  determines two moments on the cylinder block body, as shown in Equation (10).

$$\begin{aligned}
 M_{Bx} &= -z_A (F_{Ay} \cos \phi - F_{Ax} \sin \phi) - z_B (F_{By} \cos \phi - F_{Bx} \sin \phi) \\
 M_{By} &= z_A (F_{Ay} \sin \phi + F_{Ax} \cos \phi) + z_B (F_{By} \sin \phi + F_{Bx} \cos \phi)
 \end{aligned} \quad (10)$$

The two moments are calculated with respect the point O in Figure 6 (also shown in Figure 1), which is the reference point use to calculate all the external loads on the cylinder block, being the point where the reaction moments of the splined shaft is assumed to be zero.

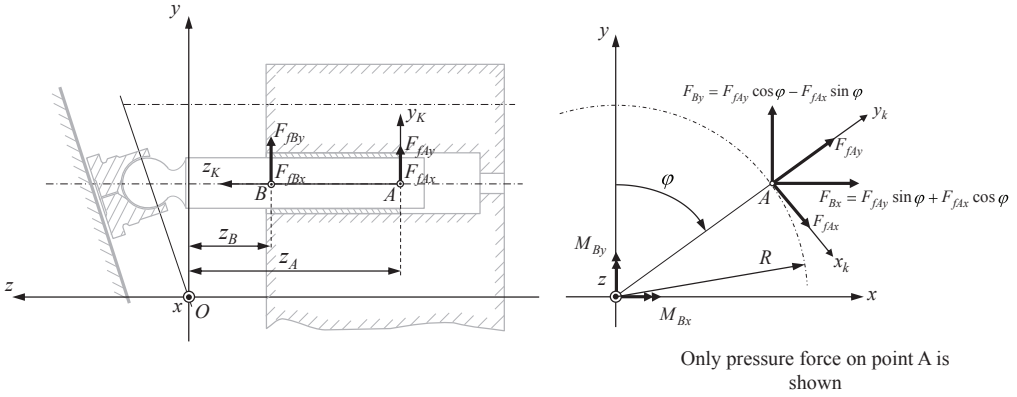


**Figure 6: Loads on cylinder block from the pressure field in the gap between piston and cylinder**

Also the resultant friction force  $F_{TK}$  and its point of application  $(x_{TB}, y_{TB}, z_{TB})$  are calculated through the piston/cylinder fluid structure interaction model and fed into the cylinder block/valve plate fluid structure interaction model.

The total external loads on the cylinder block valve plate interface can be finally expressed as illustrated in Equation (11).

$$\begin{aligned}
 FB_z &= F_S + \sum_{i=1}^z F_{DBzi} + \sum_{i=1}^z F_{TBi} \\
 MB_x &= \sum_{i=1}^z y_{DBi} F_{DBzi} - z_A (F_{Ay} \cos \varphi - F_{Ax} \sin \varphi) - z_B (F_{By} \cos \varphi - F_{Bx} \sin \varphi) + \sum_{i=1}^z y_{TBi} F_{TBi} \\
 MB_y &= -\sum_{i=1}^z x_{DBi} F_{DBzi} + z_A (F_{Ay} \sin \varphi + F_{Ax} \cos \varphi) + z_B (F_{By} \sin \varphi + F_{Bx} \cos \varphi) - \sum_{i=1}^z x_{TBi} F_{TBi}
 \end{aligned} \quad (11)$$

In conclusion, in order to calculate the total external loads on the cylinder block expressed by Equation (11), the piston/cylinder feeds into the cylinder block valve plate model the following input:

- A system of four forces  $\{F_{fAx}, F_{fAy}, F_{fBx}, F_{fBy}\}$  deriving from the solution of the elasto-hydrodynamic pressure field in the gap between piston and cylinder
- The position of point A and B in Figure 6 (in some design A and B may not be fixed during the piston stroke);
- The resultant friction force  $F_{TB}$  and its point of application in the x-y plane,  $(x_{TR}, y_{TR})$

Clearly, this set information need to be provided at any angular position of the shaft, for all the z pistons.

## 5 RESULTS

Figure 7(a) shows the measured valve plate temperature field for a 100 cc swash plate unit at 3000 rpm, 300 bar differential pressure and maximum displacement angle. The surface temperature was measured through 28 thermocouples installed just underneath the valve plate surface; the temperature field was then derived by interpolation of the measured data. Figure 7(b) illustrates the average film thickness and the solid bodies' deflections predicted by the simulation model for the same operating condition. The lubricating film and the deformations due to pressure and temperature loads are scaled 1000 times only in axial direction.

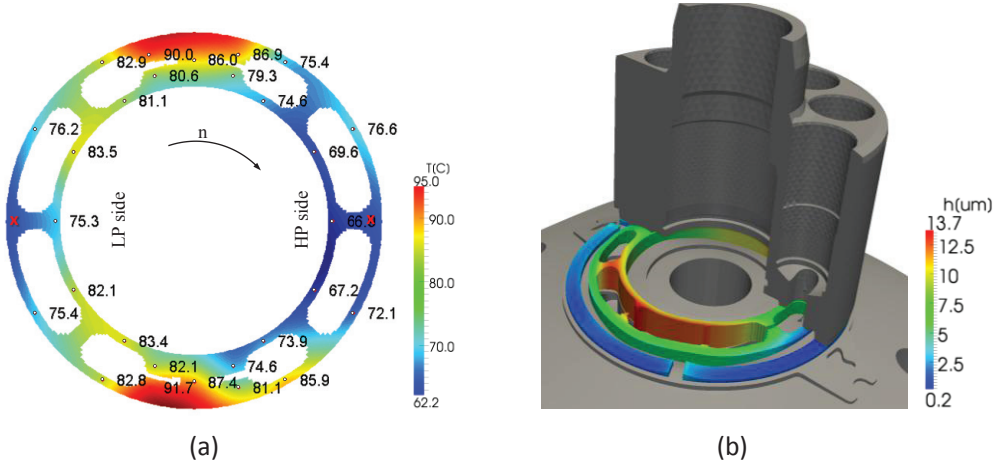


**Figure 7: (a) measured valve plate surface temperature field from [7]; (b) simulation model prediction of film thickness and solid bodies' deflections (scaled 1000 times only in axial direction).**

For the same operating condition, Figure 8 shows a comparison of the simulated valve plate surface temperature obtained by the two external force calculation methods described in section 4.2 and 4.3. The two temperature fields look similar, being the deformations due to pressure and temperature and the heat transfer from the gaps to the solid bodies the main phenomena affecting the film thickness, as shown in Figure 7(b) and thoroughly explained in [20]. However, especially at critical operating condition, the external forces on the cylinder block deriving from the piston-slipper assembly have a non-negligible impact on the film thickness prediction and therefore on the final valve plate surface temperature. In particular, the main difference between the two temperature fields in Figure 8 is in the proximity of the points S and N.

The simplified external force calculation method determines a wide region at high temperature around point N, whereas the temperature becomes quite lower near point S. With the advanced calculation method the situation is opposite. The region surrounding the point S is the one at higher temperature while the smaller area close to point N is characterized by a lower temperature. Comparing Figure 8 with Figure 7 it turns out that the advanced method for the calculation of the external forces transferred from the piston-slipper assembly to the cylinder block predicts a result that is closer to the measurement.

The reason of this fact is in Figure 9, where the moments  $M_{Bx}$  loading the block are represented for the two calculation methods. The moment calculated with Equation (11) (Figure 9-a) is always positive having an average value of 94 Nm. On the other hand, the moment computed following the simplified methodology described by Equation (8) (Figure 9-b) oscillates around the average value of 14 Nm, jumping from positive to negative values.

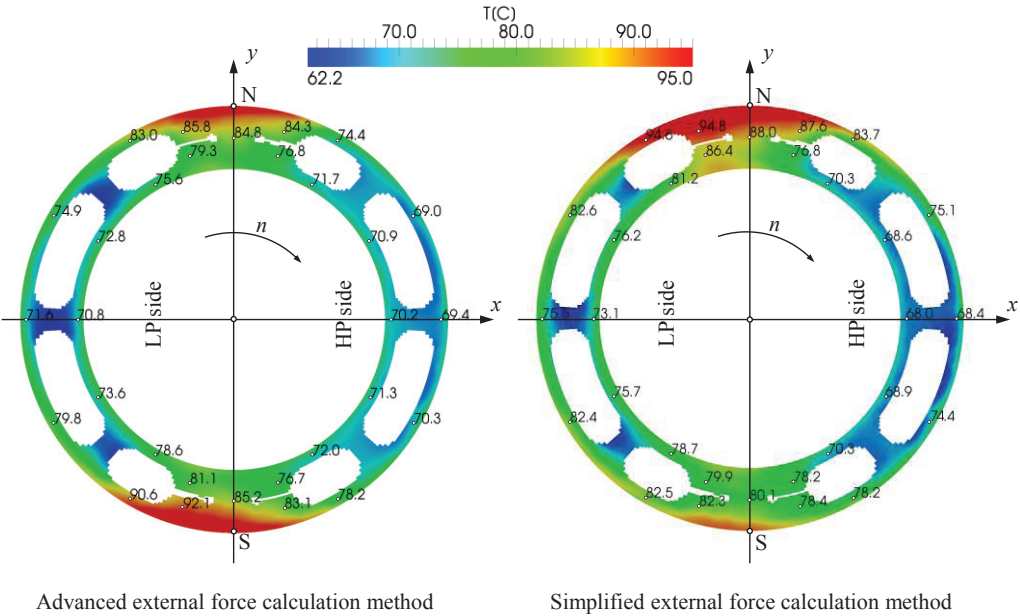


Figure 8: comparison between the two force calculation methods in terms of valve plate surface temperature

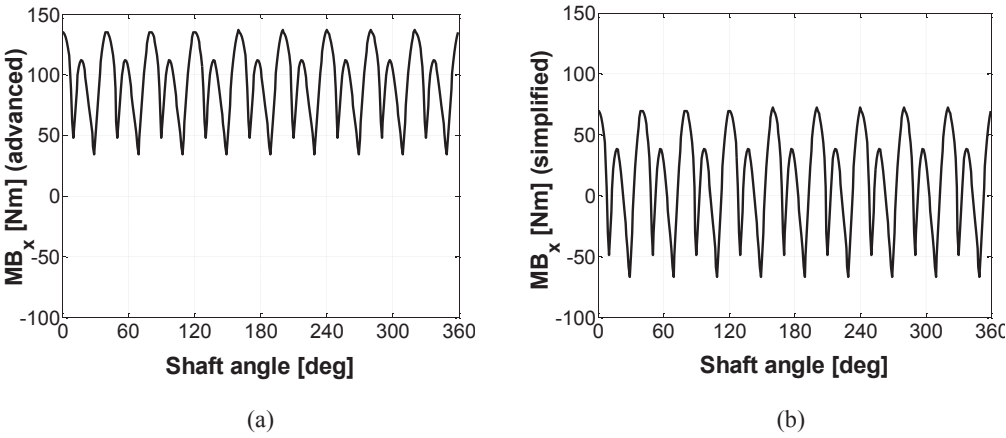


Figure 9: MBx moments; (a) calculated with Equation (8), (b) calculated with Equation (11).



This means that with the advanced calculation method the block is constantly pushed towards point S by the loads transferred by the piston-slipper assembly, because  $M_{Bx}$  is always positive. The film thickness will be therefore lower around the point S, to generate the proper hydrodynamic reaction and carry the load. The effect of the viscous friction in the fluid flow generates higher energy dissipation which is what determines the higher temperature.

With the simplified approach, the block is pushed alternatively towards point N and S with a lower intensity, being  $M_{Bx}$  an oscillating function with variable sign. In this case, the external moment does not determine a constant region of lower film thickness over point S or N and the gap shape is mainly determined by the thermal deflection and the hydrodynamic pre deformation of the solid bodies, as shown in [20].

## 6 CONCLUSION

In this work the interaction between cylinder block/valve plate interface and piston/cylinder interface was studied in terms of forces exchange. The study was carried out coupling two fluid structure interaction models, where the elasto-hydrodynamic lubrication problem solution was coupled with the complete thermal analysis of the rotating kit.

A simplified analytical method for the calculation of the external forces transferred from the piston-slipper assembly to the cylinder block/valve plate interface was compared to a more advanced approach, where the cylinder block is loaded directly with the pressure field between pistons and cylinders bore, calculated through the fluid structure model for the piston/cylinder interface.

Both the models showed a good prediction of the valve plate surface temperature respect the measured data. However, the force calculation method based on the direct coupling of the cylinder block /valve plate and the piston/cylinder interfaces fluid structure interaction models demonstrated a higher precision. On the other hand, the simplified analytical method can be assumed as a reasonable approximation when precise information about the pressure field between piston and cylinder bore is not available, especially for moderate operative condition, where the interaction between the two interfaces is limited.

## 7 REFERENCES

- [1] **Bergada, J.M. and Davies, D.L.** 2011. The effect of oil pressure and temperature on barrel film thickness and barrel dynamics of an axial piston pump. *Meccanica* DOI 10.1007/s11012-011-9472-7
- [2] **Bergada, J. M., Watton, J. and Kumar, S.** 2008. Pressure, Flow, Force, and Torque Between the Barrel and Port Plate in an Axial Piston Pump. *Journal of Dynamic Systems, Measurement, and Control* JANUARY 2008, Vol. 130 / 011011-1
- [3] **Deeken, M.** 2003 Simulation of the tribological contacts in an axial piston machine. *O + P Ölhdraulik und Pneumatik* Vol 47 (2003) Nr. 11- 12

- [4] **Huang, C. and Ivantysynova, M.** 2003. A new approach to predict the load carrying ability of the gap between valve plate and cylinder block. *Proceedings of the Bath Workshop on Power transmission and Motion Control PTMC 2003, Bath, UK*, pp. 225 – 239
- [5] **Ivantysyn, J. and Ivantysynova, M.** 2001. *Hydrostatic Pumps and Motors, Principles, Designs, Performance, Modeling, Analysis, Control and Testing*. New Delhi. Academia Books International, ISBN -81-85522-16-2.
- [6] **Jacazio, G. and Vatta, F.** 1981. The block-lift in axial piston hydraulic motors. *Proceedings of the The ASME/ASCE Bioengineering, Fluids Engineering and Applied Mechanics Conference, Boulder, Colorado, USA, June 22–24, 1981* pp. 1–7.
- [7] **Jouini, N. and Ivantysynova, M.** 2008. Valve plate surface temperature prediction in axial piston machines. *Proceedings of the 5th FPNI PhD symposium, Cracow, Poland*, pp 95–110
- [8] **Matsumoto K. and Ikeya M.** 1991. Friction and leakage characteristics between the valve plate and cylinder for starting and low speed conditions in a swashplate type axial piston motor. *Transactions of the Japan Society of Mechanical Engineers - Part C 57*, pp. 2023–2028
- [9] **Manring ND.** 2000. Tipping the cylinder block of an axial piston swash-plate type hydrostatic machine. *Journal of Dynamic Systems Measurements and Control*, 122 pp. 216–221.
- [10] **Kim, J.K. and Jung, J.Y.** 2003. Measurement of fluid film thickness on the valve plate in oil hydraulic axial piston pumps (Part I - bearing pad effects). *KSME Int. Journal*, Vol. 17 No. 2, pp. 246-253
- [11] **Kim, J.K., Kim, H.E. and Oh, S.H.** 2005. Measurement of fluid film thickness on the valve plate in oil hydraulic axial piston pumps (Part II- spherical design effects). *Journal of Mechanical Science and Technology*, Vol. 19 No. 2, pp 655-663
- [12] **Olems, L.** 2000. Investigations of the Temperature Behavior of the Piston Cylinder Assembly in Axial Piston Pumps. *International Journal of Fluid Power*, Vol. 1 (2000), No.1, pp. 27-38.
- [13] **Pelosi, M. and Ivantysynova, M.** 2011. The Influence of Pressure and Thermal Deformation on the Piston/Cylinder Interface Film Thickness. *Proceedings of the 52nd National Conference on Fluid Power 2011, NCFP III-9.3*
- [14] **Pelosi, M. and Ivantysynova, M.** 2011. Surface Deformation Enables High Pressure Operation of Axial Piston Pumps. *ASME/Bath Symposium on Fluid Power and Motion Control, Arlington, VI, USA*.
- [15] **Wieczorek, U. and Ivantysynova, M.** 2002. Computer Aided Optimization of Bearing and Sealing Gaps in Hydrostatic Machines - The Simulation Tool CASPAR. *International Journal of Fluid Power*, Vol. 3 (2002), No.1, pp. 7-20

- [16] **Yamaguchi A, Sekine H, Shimizu S, and Ishida S.** 1987 Bearing/seal characteristics of the Oil film between a valve plate and a cylinder block of axial pumps. *JHPS* 18(7):543–550
- [17] **Yamaguchi A.** 1987. Formation of a fluid film between a valve plate and a cylinder block of piston pumps and motors (2nd report, a valve plate with hydrostatic pads). *JSME* 30(259), pp. 87–92
- [18] **Yamaguchi A.** 1990. Bearing/seal characteristics of the film between a valve plate and a cylinder block of axial piston pumps: Effects of fluid types and theoretical discussion. *Journal of Fluid Control* 20(4), pp. 7–29
- [19] **Zecchi, M. and Ivantysynova, M.** 2011. A Novel Fluid Structure Interaction Model for the cylinder block / valve plate interface of axial piston machines. *Proceedings of the IFPE 2011, Las Vegas, NV, USA.*
- [20] **Zecchi, M. and Ivantysynova, M.** 2012. Cylinder block / valve plate interface – a novel approach to predict thermal surface loads. *Proceedings of the 8th IFK, Dresden, Germany*

# Optimal Design of Gears and Lateral Bushes of External Gear Machines

**Ram Sudarsan Devendran, Andrea Vacca**

Maha Fluid Power Research Center, Purdue University, West Lafayette, IN, USA

## ABSTRACT

The aim of this paper is to propose a novel methodology for identifying the optimal design of external spur gear machines for high pressure hydraulic applications. Due to the existence of complex inter-dependencies between design parameters and the unit performance, presently the design of these machines is extensively based on empirical procedures, with limited recourse to simulations. In this research the problem of optimizing the volumetric performance, minimizing internal cavitation, pressure peaks and noise emissions has been addressed by means of a multi-objective optimization algorithm that optimize the most important components of the external gear machines: the gears and the lateral bushes. The simulation tool HYGESim (HYdraulic GEAr machines Simulator) which has been developed and validated by the authors' research group, was used for accurately predicting the performance of the unit. The paper describes the optimization problem in terms of design variables, constraints and objective functions that permits the determination of feasible designs that optimizes the performance of the unit. Although the paper considers the case of a particular pump, the developed procedure can be generalized for any external gear machine. The results section of the paper focuses not only on the description of the optimal design, but also on the potential of the procedure for studying the various relationships between the design variables and the machine performance.

**Keywords:** External gear pump and motor, Optimal design, Quieter pump and motors, Genetic Algorithm, Efficiency of external gear machines.

## 1. INTRODUCTION

External gear machines are one of the most extensively used machines in industrial and mobile fluid power applications like construction and earthmoving machines, hydraulic press and forming machines, etc. The key to success of these machines can be represented by their reliability, ease of manufacturing and low cost. In fact, in external gear machines design, all the major functions of positive displacement units are essentially accomplished by three elements: the gears, the lateral bushes and the case (figure 1.A). The principle of operation of gear units is very simple: the fluid is transferred from the inlet to the outlet through the periphery formed by the gear and the casing and the displacing action is achieved by the meshing process of the gears (figure 1.B).

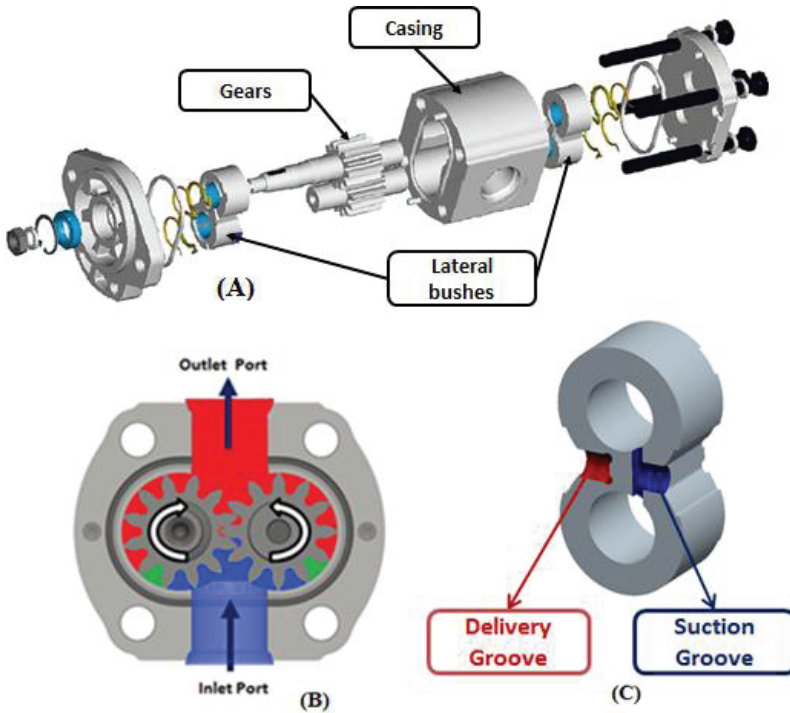


**Figure 1: (A) Different parts of a gear pump. (B) Grooves machined on a bearing block. (C) Displacing action of a gear pump**

The lateral bushes seal the displacement chambers and usually have grooves (figure 1.C) which help in avoiding the tooth space volumes being isolated by contact points during the meshing process. Hence, these grooves aid in optimizing the timing of the connection between the displacement chambers (tooth space volumes) and the inlet and outlet ports, thereby avoiding internal pressure peaks and cavitation.

Despite their simple principle of operation, the design analysis of external gear units is a complex problem that has to consider the complicated relations between the pure mechanical requirements for gears (their design has to guarantee smooth operation with optimal transmission of forces) and the hydraulic requirements (low pressure pulsations, limited pressure peak and optimal volumetric performance). For this reason, the analysis of the features of operation of external gear machines is a research topic that has captivated the interest of researchers for decades. Various simulation models have been developed to study particular aspects of operation [such as 1-4], and more recently models capable of simulating the entire unit have been developed. Representative of this effort is the simulation tool HYGESim (HYdraulic GEAr machines Simulator), developed by the authors' research group [5-7].

Thanks to the possibility of automating the simulation on the basis of CAD drawings of the machines, HYGESim can be utilized within an exclusive optimization procedure aimed at identifying the optimal design of the unit. The use of wide range of simulation tools combined with a multi-objective optimization procedure permits to overcome the limitations of simplified optimizations that neglect the mutual interaction between design

parameters. For example, in [8], considerations about the optimal design of gears are made neglecting the important effects of the lateral grooves on the timing of the connections. In [9] the nonlinear equations which govern the instantaneous flow areas connecting the tooth space volumes and the suction/delivery grooves have been used to just minimize the pressure overshoots while noise emissions due to the delivery flow pulsations have not been considered. In [10,11], HYGESim was utilized for the first time for optimization purposes, considering the design of the grooves of the lateral pressure plates of a particular pump, considering a fixed gear profile. From this work, it is clear that the recesses (suction, delivery and backflow) machined on the bearing block have a strong influence on the operation of the machine and even a small modification of their geometry can significantly affect the unit performance. However, very few studies [8] have analyzed the influence of the gear profile on the flow oscillations at the outlet of the machine.

In this work, the ambitious target of optimizing the “complete” design of external gear machines is addressed for the case of a pump. The term “complete” in this case refers to the key elements of the unit: the gear and the lateral bushes. To accomplish this goal, it is assumed that the gear profile follows the conventional involute geometry and all the geometrical and manufacturing requirements pertaining to involute gears have been considered. Moreover, to evaluate the hydraulic performance of each particular gear profile, the optimal design of the lateral plates has to be identified.

The following sections illustrate how this optimization problem can be formulated and solved considering a multi-objective optimization procedure. Several considerations about the effects of the design parameters on pump performance will be made on the basis of the results of the developed procedure, and the identification of the optimal design will be made on the basis of the operating requirements.

## 2. HYGESIM SIMULATION TOOL

HYGESim is a multi-domain simulation tool created to simulate external gear machines. It allows simulations in LMS.AMESIM<sup>®</sup> platform to simulate complete hydraulic systems and it consists of several parts (figure. 2): a) Geometrical Model, b) a lumped parameter

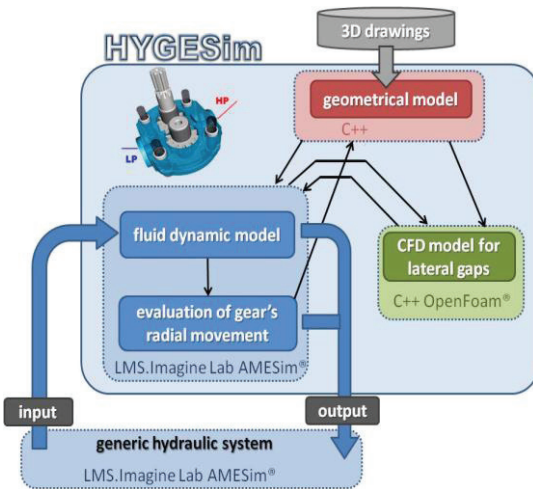
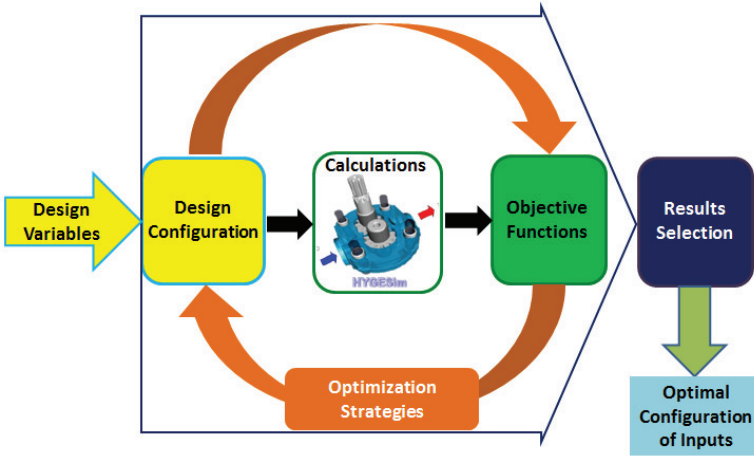


Figure 2: HYGESim Architecture

fluid dynamic model for the study of the main flow through the unit, c) a mechanical model to study the radial balance of the gears considering the micro motions of their axis d) a fluid structure interaction model to study the lubricating gap between gear and lateral bushes and the axial balance of the machine. Details on the main fluid dynamic model of HYGESim are reported in [7], while the fluid structure interaction model and the axial balance module are described in [12,13]. Experimental validation has also been provided in the mentioned works.

### 3. OPTIMIZATION PROBLEM

Optimization is the process by which a best design is identified from a set of several alternatives. In simple words, the process can be defined as the generation of several designs that meet the target performance defined by the objective functions. Necessarily, the ranges of variation of the design variables are restricted by constraints which govern the feasible design space. Figure 3, depicts a schematic of the optimization workflow. For a particular combination of design variables (gears and grooves), HYGESim is used to evaluate the objective functions. Several designs will be generated using optimization strategies and an optimal configuration of the inputs is selected from the entire set of designs analyzed.



**Figure 3: Optimization workflow**

As depicted in figure 4, in the primary level the gear geometry is defined and verified if the particular geometry falls within the feasible design space. Since the design of the lateral bushes greatly depends on the particular gear design under consideration, for every gear generated, multiple lateral bush designs are analyzed to identify the best design. For this purpose an inner/secondary level for lateral bush design has been implemented. Following the successful generation of gears the algorithm moves to the secondary level for designing the lateral bushes based on the particular gear geometry. The particular design configuration is analyzed using HYGESim to evaluate the objective functions. The secondary level continues to perform sufficient number of iterations until an optimum design of the bearing block is determined. The objective functions for this particular combination of the gear and the bearing block is passed on to the primary level for further evaluation of gear profiles. In this way, all the gear designs are compared considering the best lateral bush design in each case. Hence the optimal design of the pump can be determined.



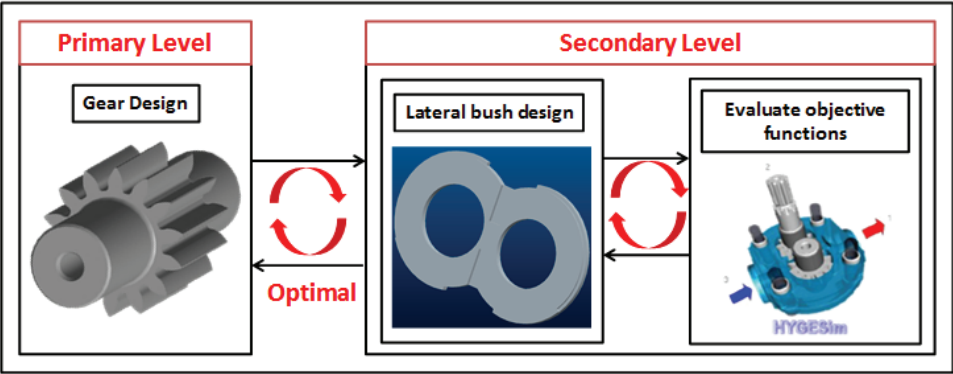


Figure 4: Implementation of different levels for the determining the optimal design

In the following sub-sections the design variables, objective functions and the constraints which form the design space for the optimization problem are discussed in detail.

3.1. Objective Functions

In this research, the performance of the unit is evaluated based on four important features: the delivery flow ripple (representing the tendency of noise emissions), internal pressure peaks, localized cavitation and volumetric efficiency. The performance usually depends broadly on the operating conditions (shaft speed and the outlet pressure).

3.1.1. Minimize Delivery Flow Ripple ( $OF_1$ )

The fluctuation of the flow at the delivery is one of the major contributions to the fluid borne noise[14]. According to the procedure discussed in [15], the pulsations of the delivery flow can be calculated in terms of delivery pressure propagation in a particular system at the delivery of the pump. These pressure oscillations can be quantified as the total energy possessed by the signal. In [10, 15] an accurate estimation of energy of the signal,  $OF_1$  has been expressed as the sum of squares of the amplitude corresponding to the different frequencies obtained from the FFT of the pressure ripple signal (figure 5).

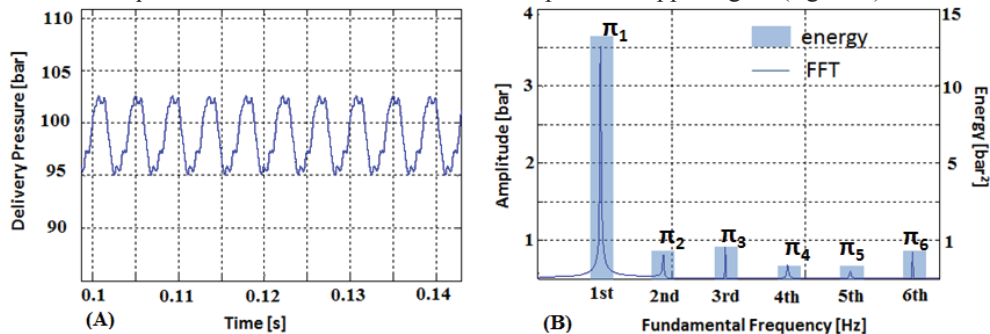


Figure 5: (A) Pressure ripple in time domain (B) FFT of pressure ripple and Bar chart of energy corresponding to each fundamental frequency



The expression for  $OF_1$  is given by,

$$OF_1 = \sum_{k=1}^N \pi_k \quad (1)$$

Where,

$$\pi_k = \sum_{f_k - \Delta f}^{f_k + \Delta f} P(f_k)^2 \quad (2)$$

where  $N$  is the number of fundamental frequencies of interest,  $P(f)$  is the total energy of the waveform's Fourier Transform (figure 4(B)),  $\Delta f$  an opportune frequency interval and  $k$  is the index of each fundamental frequency, given by the shaft speed and the number of teeth.

### 3.1.2. Minimize Internal Pressure Overshoots ( $OF_2$ )

During the meshing process of the gears, a certain amount of fluid is trapped between the points of contact between the two gears. During the initial phase of the meshing process this volume decreases and hence the pressure of the trapped fluid shoots to a very high value. This phenomenon has been highlighted in figure 6 below where the pressure in the tooth space volume (TSV) of the gear reaches a high value. An estimate of this  $OF$  [10] is expressed as a non-dimensional number given by eq. (3).

$$OF_2 = \frac{P_{TSV,peak} - P_{D,avg}}{P_{D,avg}} \quad (3)$$

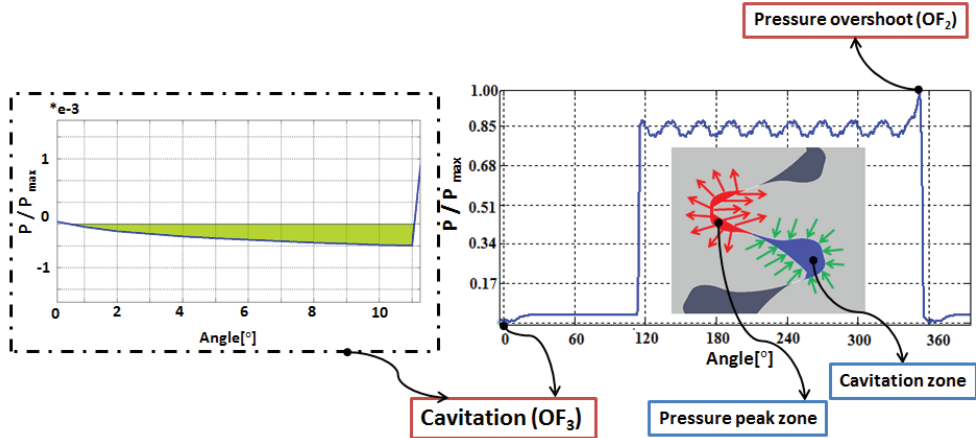


Figure 6: Pressure in the TSV, detail of  $OF_2$  and  $OF_3$

### 3.1.3. Minimize Localized Cavitation ( $OF_3$ )

During the latter phase of the meshing process, when the TSV increases, the pressure in the TSV reaches a value below the saturation pressure of the fluid hence localized cavitation due to air release occurs. The simulation tool HYGESim is equipped with a model for the evaluation of fluid properties which predicts the density and bulk modulus of the fluid as a function of the pressure in the TSV [16, 17]. Hence, cavitation effects are being taken care of when the TSV pressure drops below the saturation pressure [16]. An estimate of  $OF_3$  is calculated based on the area of the curve which lies under the saturation pressure of the

working fluid under consideration. The expression used for the calculation [10] of  $OF_3$  is given by eq. (4) below.

$$OF_3 = \int P_{TSV} d\theta \quad (4)$$

#### 3.1.4. Maximize Volumetric Efficiency ( $OF_4$ )

The volumetric performance of the unit has to be maximized in the optimal design. In external gear machines, volumetric losses are caused by lateral leakages (in the gap between the gear side face and the thrust face of bushes), radial leakages (between the gear tip and the casing) and by backflows in the meshing process. While backflows and radial leakages are accurately evaluated, this work simplifies the evaluation of lateral leakages by assuming a constant gap height. This assumption is made according to axial balance evaluations previously performed by the authors' research group [12, 13, 18]: a reasonable value of equivalent constant gap height corresponding to a well axially balanced machine is considered, although the axial balance problem is not considered in this research. More details concerning the radial leakages evaluation can be found [12], while [13, 18] reports details about the evaluation of the axial leakages.

The expression for  $OF_4$  is given by eq. (5) shown below.

$$OF_4 = \eta_v = \frac{Q_{avg}}{n \cdot V_d} \quad (5)$$

## 3.2. Design Variables

In this section the design variables of the optimization problem, for the gears and the lateral bushes are described separately. The manufacturing process for the gears such as hobbing is taken into consideration for accurately defining the shape of the gears. The major design variables which define the shape of the particular spur gear profile are summarized in table 1 below.

**Table 1: Design variables pertaining to gear profile**

Symbol	Description	Unit	Range	
			min	max
$m$	<i>Normal module</i>	mm	1.00	3.20
$z$	<i>Number of teeth</i>	-	9	26
$h_{ap}$	<i>Addendum coefficient</i>	-	0.50	1.47
$h_{fp}$	<i>Dedendum coefficient</i>	-	0.50	1.47
$\rho_{fp}$	<i>Fillet radius coefficient</i>	-	0.17	0.60
$\alpha$	<i>Pressure Angle</i>	°	14.0	29.0

The parameters described in table 1 allows the description of the proper profile of the gear cutter which should be used for obtaining the desired gear profile. It is also assumed that a standard rack type cutter with a normal pressure angle of  $20^\circ$  is used for the manufacturing of the gears [19]. The different parameters for gears which can be calculated based on the design variables are shown in the figure 7 below.

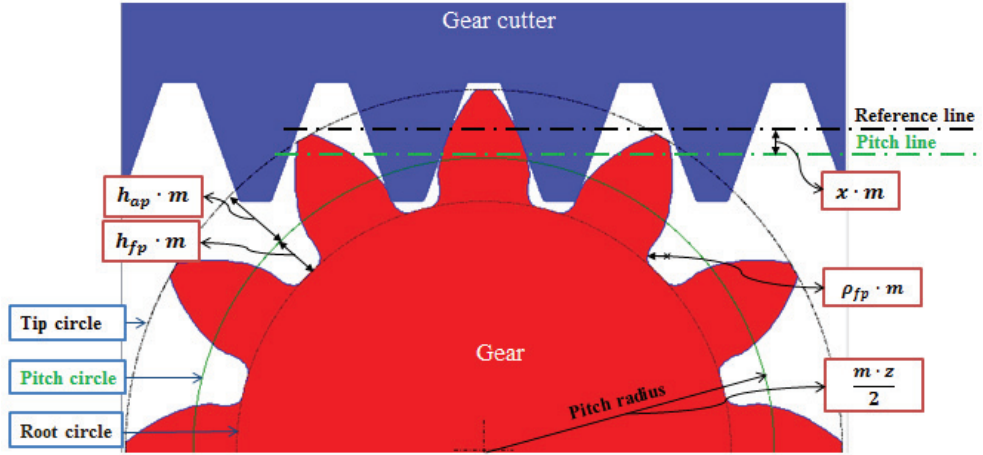


**Figure 7: Design variables governing the gear profile**

All the parameters described in table 1 form the inputs for the primary optimization of the gears. As concerns the grooves on the lateral bushes, this research considers the simplified rectangular design shown in figure 8. It is assumed that the dimension,  $H$ , as shown in figure 8 is a constant. This limits the sub-optimization problem of finding the optimal lateral bush set for a given gear profile to two input parameters, as shown in figure 8. This simplification does not affect the efficacy of the procedure: more complex groove profiles (like the ones considered in [7,20,21]) allow for a better performance on wide range of operating speeds and pressures, but not for the case of a single and fixed point of operation, as considered in this paper (see section 4). Once the best design for the gear is identified with the defined procedure, the optimization of different groove profiles can be performed separately, for example following the procedure already described in [10]. The calculation of  $D$ ,  $S$  and  $H$  are explained in section 3.3.4.

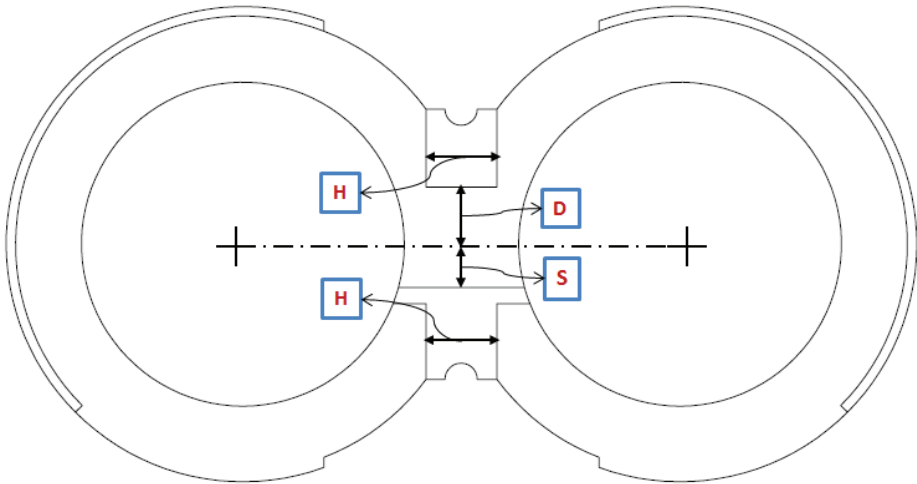


**Figure 8: Design variables governing the groove profiles**

### 3.3. Constraints

Due to the wide range of variability of the values of the design variables, designs of gears and bushes which are unfeasible or impractical could be generated by the optimization algorithm. To eliminate such designs, several constraints were identified to define the feasible design space. As already stated, in this work only gears with involute profiles are taken into consideration. The various constraints pertaining to the gear profile have been broadly classified into three different categories as: meshing constraints, manufacturing constraints and geometrical constraints.

#### 3.3.1 Meshing constraints

Meshing constraints enable a pair of spur gears to be matched in such a way that there is smooth operation of the pump when the gears are meshing. Three different constraints which fall in this category are described below.

*Contact ratio* constraint ensures that there is a smooth and continuous power transmission between the two gears. This constraint ensures that there is at least one pair of teeth which is always in contact with each other during the rotation of the gears.

*Interference* is the phenomenon by which the involute portion of one gear digs into the flank of the other member of the pair. Thus resulting in the removal of involute portions of the gear near the base circle and hence weakening the teeth. Figure 9 depicts interference between two gears clearing showing that considerable portion of one gear is below the base circle of the other.

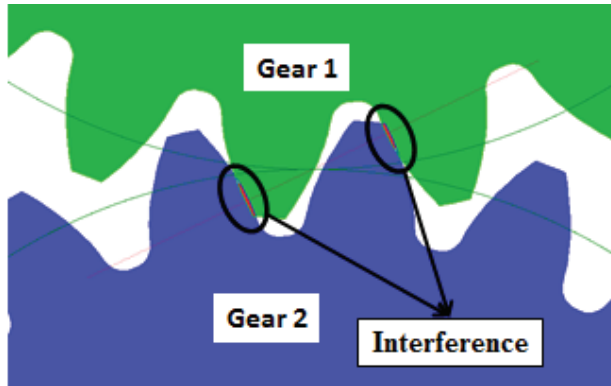


Figure 9: Interference in gears

The *tip to root clearance* constraint ensures that the inter-axis distance between the two gears is sufficiently large enough so that the tooth tip of one tooth does not intersect the bottom land of the other teeth.

The mathematical expressions which govern the meshing constraints are shown in table 2 below [22,23].

**Table 2: Expressions for meshing constraints**

Meshing constraints	Contact ratio	$\frac{2}{\cos\alpha} \cdot \frac{(\sqrt{R_o^2 - R_b^2} - R \cdot \sin\alpha)}{\frac{2 \cdot \pi \cdot R}{Z}} > 1$	(6)
	Interference	$R_o^2 < R_b^2 + 4 \cdot R^2 \cdot \sin^2\alpha$	(7)
	Tip to root clearance	$R_o + R_r < 2 \cdot R$	(8)

**3.3.2 Manufacturing Constraints**

Manufacturing constraints ensure the correct manufacturability of the gears based on the use of a rack type cutter. There are two different constraints which fall into this category as explained below.

*Pointed Teeth* constraint ensures that the thickness of the teeth at the tip of the gears is greater than zero hence preventing wear and tear of the gears during operation.

*Undercutting* is the phenomenon due to which some material is removed at the root of the gear because of the interference between the cutter and the gear during the manufacturing process. One of the reasons for undercutting is large negative shift coefficients which lead to removal of more material by the cutter near the root of the gear. Since in gear pumps the teeth are not highly stressed as in other applications, a certain degree of undercutting is permitted until the thickness of the teeth is greater than a certain minimum value. Figure 10 shown below, depicts the undercut tooth profile generated due to large negative profile shift coefficients.

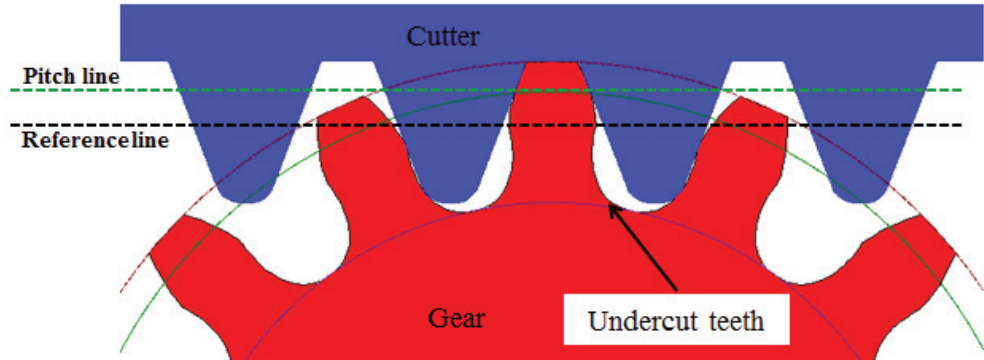


**Figure 10: Undercut gear**

The mathematical expressions which govern the manufacturing constraints are shown in table 3 below [22].

**Table 3: Expressions for manufacturing constraints**

Manufacturing constraints	Pointed teeth	$2 \cdot R_o \cdot \left( \frac{\pi}{2 \cdot z} + \text{inv}\alpha - \text{inv}\alpha_o \right) > 0.0$ <p style="text-align: center;">Where,</p> $\alpha_o = \cos^{-1} \left( \frac{R_b}{R_o} \right)$	(9)
	Undercutting	$x < h_{fp} - \rho_{fp} + \rho_{fp} \cdot \sin\alpha - \frac{z}{2} \cdot \sin^2\alpha$	(10)

### 3.3.3 Geometrical Constraints

The geometrical constraints ensure that the different calculated values based on the design variables are physically possible. The mathematical expressions governing the geometrical constraints are given in table 4 below.

**Table 4: Expressions for geometrical constraints**

Geometrical Constraints	$addendum > 0$	(11)
	$dedendum > 0$	(12)
	$R_r > 0$	(13)
	$R_o > R > R_r$	(14)

Additionally, the facewidth (b) of the gears is calculated based on the desired displacement of the unit (pump/motor),  $V_d$ , given as input parameter of the optimization procedure. Therefore, once the gear profile is predicted the facewidth is calculated based on the eq. (15) below,

$$V_d = 2 \cdot \pi \cdot b \left( R_o^2 - R^2 \left( 1 + \frac{\pi \cdot \cos^2\alpha}{3 \cdot z^2} \right) \right) \quad (15)$$

It is also necessary that the facewidth of the gears is not too small or not too large; therefore the aspect ratio of the gears defines as the ratio of facewidth to the pitch radius should fall within a certain range of values, as shown in eq. (16) below.

$$\left( \frac{b}{R} \right)_{MIN} \leq \left( \frac{b}{R} \right) \leq \left( \frac{b}{R} \right)_{MAX} \quad (16)$$

### 3.3.4 Constraints Pertaining to Groove Profiles

The design of the grooves/recesses machined on the bearing block greatly affects the performance of the machine especially in terms of internal pressure peaks and cavitation effects [10]. Even though the optimization algorithm can determine the optimal position of the grooves based on a random starting point, providing an initial configuration as a function of gear profile can significantly reduce the simulation time. Hence the procedure to identify the initial position based on the evolution of the trapped volume is described.

Figure 11 below shows the angular position at which the trapped volume begins and ends. A representative position of the grooves is also shown for clarity.

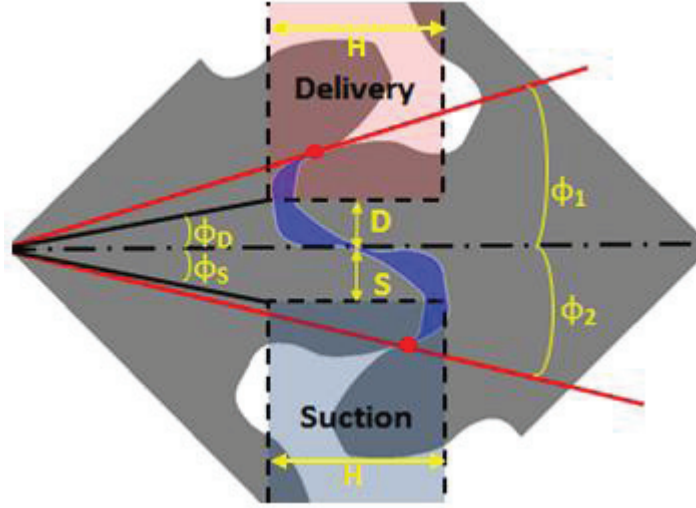


**Figure 11: Angular position of trapped volume and the grooves**

The angular position at which the trapped volume starts occurring,  $\phi_1$  and the angular position at which trapped volume finishes,  $\phi_2$  can be calculated using the expressions,

$$\phi_1 = -\frac{\sqrt{R_o^2 - R_b^2} - R \cdot \sin \alpha}{R_b} + \frac{2\pi}{z} \quad (17)$$

$$\phi_2 = \frac{\sqrt{R_o^2 - R_b^2} - R \cdot \sin \alpha}{R_b} \quad (18)$$

and the angular position at which the trapped volume is minimum can be calculated by the expression,

$$\phi_{MIN} = \frac{\pi}{z} \quad (19)$$

$\phi_D$  represents the angle at which the delivery groove closes connection between the trapped volume and the delivery port and  $\phi_S$  represents the angle at which the suction groove opens connection between the trapped volume and the suction port. The vertical distance 'D' and 'S' of the delivery and the suction grooves respectively from the line joining the center of the two-axis can be calculated using the expressions,

$$S = R \cdot \phi_S \cdot \cos^2 \alpha \quad (20)$$

$$D = \left( R \cdot \phi_D \cdot \cos \alpha - \frac{2\pi \cdot R_b}{z} \right) \cos \alpha \quad (21)$$

As previously mentioned, the dimension H is assumed to be a constant for a particular gear design to reduce the number of variables and hence the computational time. The expression for H, is given by,

$$H = 2 \cdot (R - R_r) \quad (22)$$

The constraint functions which govern the extreme values of the groove geometry ensuring realistic and feasible designs of grooves are shown in table 5.

**Table 5: Constraints governing the groove profiles**

<b>Grooves Constraints</b>	$\phi_{MIN} < \phi_D < \phi_1$	(23)
	$\phi_2 < \phi_S < \phi_{MIN}$	(24)

### 3.4. Optimization Methodology

One of the main features of this work is represented by the usage of a multi-objective optimization algorithm. The optimization workflow has been implemented in modeFRONTIER<sup>®</sup>, a multi-objective optimization environment which allows the flexibility of integrating different software. For the case of this study, HYGESim was integrated with KISSsoft<sup>®</sup> and Pro-ENGINEER<sup>®</sup>, for the geometrical generation of gears and lateral bushes, and with and MATLAB<sup>®</sup>, for the calculation of objective functions.

The chosen optimization algorithm is the Fast Multi-Objective Genetic Algorithm (FMOGA) which incorporates Response Surface (RS) methodologies to speed up the process. An initial database of designs spanning the entire domain uniformly is used to train RS (mathematical expression of OFs in terms of the design variables) based on the objective functions evaluated by HYGESim. Following this step, a virtual optimization of the RS is performed. The designs optimized virtually are then validated with the help of HYGESim and hence these newly evaluated designs enrich the design space for the next iteration. In this way, the RS becomes more and more accurate and representative of the actual OFs at the end of every iteration of the generic algorithm. The optimization algorithm follows the analogy of the natural evolution process by incorporating processes like selection (select best designs from the database), crossover (reproduce new designs by combining properties of the designs selected previously) and mutation (introducing a random effect to explore the entire design space) [24]. After several iterations, the Pareto optimum design can be identified which represent a solution with a reasonable compromise of all the OFs.

## 4. RESULTS

In this section the results of the outcomes of the extensive optimization process has been summarized. A total of 68 gear profiles were analyzed with 60 lateral bush designs for each gear profile considered. These designs form a sufficiently large population for an approximate prediction of the various interaction effects on the basis of a simple two-level analysis of variance (ANOVA). Firstly, the different interesting interaction effects between the input factors and the OFs have been depicted qualitatively. This will help in understanding the complex relationships between the design features and the performance of the unit. Secondly, the optimal design of the gears and the lateral bush has also been presented. In this reference case a 11.2 cm<sup>3</sup>/rev pump operating at 1000 rpm and 100 bar at the outlet is considered. This permits the direct comparison with a commercial solution



deeply studied by the authors in past works. Nevertheless, the workflow is generalized and can be applied to any case of displacement and operating conditions.

#### 4.1. Qualitative Results

The main aim of this section is to identify the effect of the design variables pertaining to the gears on the OFs as well as to determine the different interaction effects between the combinations of design variables which contribute significantly to the OFs. Since the OFs of a particular gear profile is based on the optimal later bush design, the parameters pertaining to the grooves are not taken into consideration for the qualitative analysis. The effects have been represented using normal probability plot which are effective in communicating the most important effects. The effects corresponding to each factor have been evaluated using Box-whisker plots assuming two levels for each variable. The normal probability plots represent the effects (main and interaction) against normal probability [25,26]. The irrelevant/negligible effects will lie along a straight line which passes through the origin, whereas the significant effects will lie far away from the straight line.

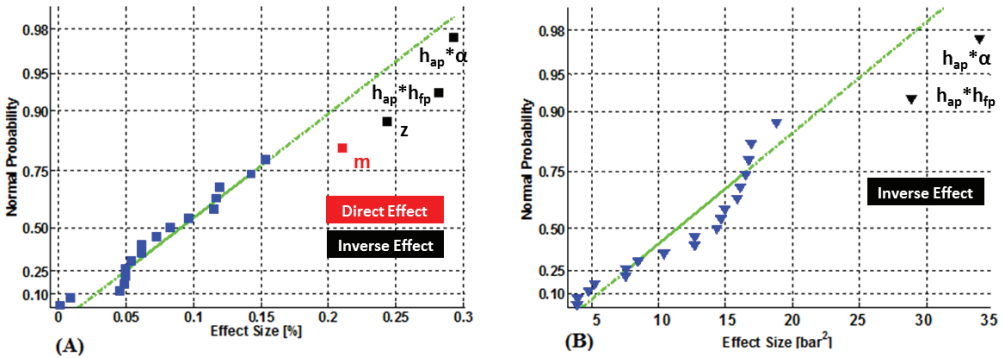


**Figure 12: (A) Normal probability plot for volumetric efficiency (B) Normal probability plot for pressure ripple**

The two levels considered for the ANOVA where: 1) low level, values lying between the minimum value of the design variable and its mean value, 2) high level, values lying between the mean of the design variable and its maximum value. A direct effect refers to an increase in the particular OF for an increase in the effect considered and an inverse effect refers to a decrease in the particular OF for an increase in the interaction under consideration. The different interaction effects which influence the most interesting OFs (OF1 and OF4) have been plotted in figure 12. From figure 12(A) it can be seen that the most important effects which influence OF<sub>4</sub> have been highlighted in red and black. The 1<sup>st</sup> order effects which are significant in case of the OF<sub>4</sub> are  $m$  (direct),  $z$  (inverse) and  $h_{ap}$  (inverse). Similarly for OF<sub>1</sub> it can be seen from figure 12 that there are complex 2<sup>nd</sup> order interaction effects which have a great influence on the performance of the machine. Although this analysis strongly depends on the assumed range of variation of the input parameters, these considerations are significant to show mutual effects between parameters strongly complicate the problem, and analysis based on the so called one-factor-at-a-time approach can become unsuccessful. Rather all these interaction effects need to be considered simultaneously to enable the proper evaluation of the pump performance. The optimization procedure discussed in this paper proves to be a powerful tool to capture all the complicated relations between the design variables and hence determine the optimal

design of the machine. To understand the interaction effects Radial Basis Functions (RBF) were used to interpolate the OFs for different designs since they have been proven to be a very powerful interpolation tool especially when the data points are scattered and not on a regular grid. These RBFs are a linear combination of several similar spherical symmetric functions, centered at the design points [27]. These interpolating functions help in visualizing the influence of the interaction effects on the OFs as depicted in the figures below.

From the normal probability plots it can be seen that the interaction effects  $h_{ap}*\alpha$  and  $h_{ap}*h_{fp}$  appear as inverse effects in both the cases of OF<sub>1</sub> and OF<sub>4</sub> (figure 13). But OF<sub>1</sub> is intended to be minimized and OF<sub>4</sub> is intended to be maximized. Therefore this effect is contradictory and critical in both the OFs.

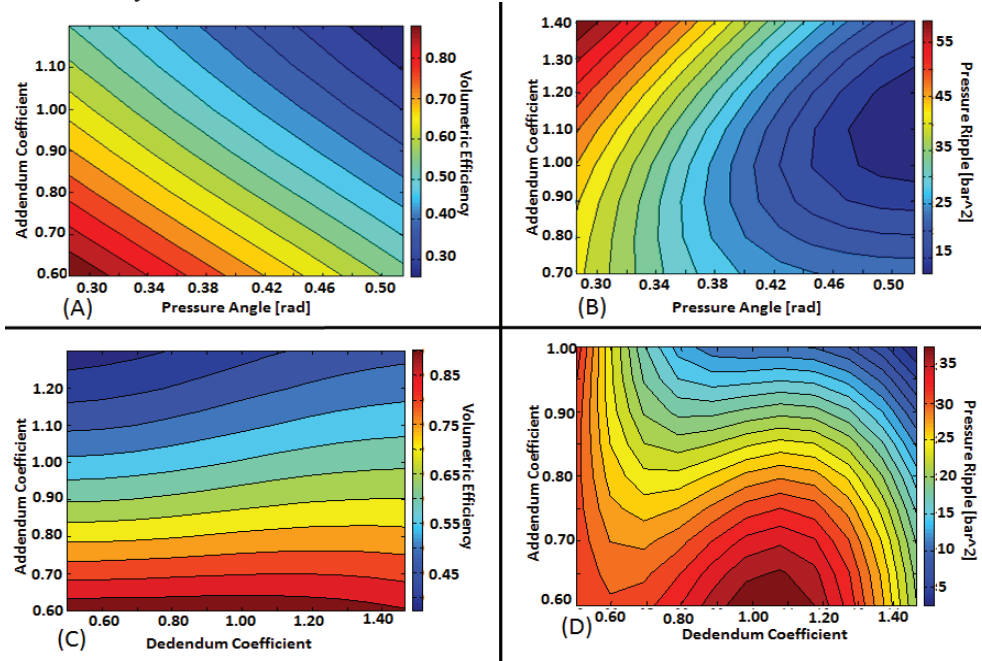


**Figure 13: (A) OF<sub>4</sub> vs.  $h_{ap}$  and  $\alpha$  (B) OF<sub>1</sub> vs.  $h_{ap}$  and  $\alpha$  (C) OF<sub>4</sub> vs.  $h_{ap}$  and  $h_{fp}$  (D) OF<sub>1</sub> vs.  $h_{ap}$  and  $h_{fp}$**

Figure 13, shows just the contribution of the major contradicting interaction effects of OF<sub>1</sub> and OF<sub>4</sub> maintaining all the other parameters constant. It can be interpreted from figure 13 that the volumetric efficiency increases with decreasing  $h_{ap}*\alpha$  and decreasing  $h_{ap}*h_{fp}$ . Conversely, pressure ripple decreases with increasing  $h_{ap}*\alpha$  and increasing  $h_{ap}*h_{fp}$ .

Similar analysis of the normal probability plots for the pressure peak (OF<sub>2</sub>) and local cavitation effects (OF<sub>3</sub>) were studied to identify the most important interaction effects. It was seen that almost all of the effects were irrelevant except for the combination  $h_{fp}*\rho_{fp}$ . This effect corresponds to the amount of undercut in a particular gear. It is seen that when the amount of undercut increases, this increases the trapped volume during meshing process. Therefore, the fluid has more volume to occupy and hence the pressure peak is reduced (figure 14(A)).

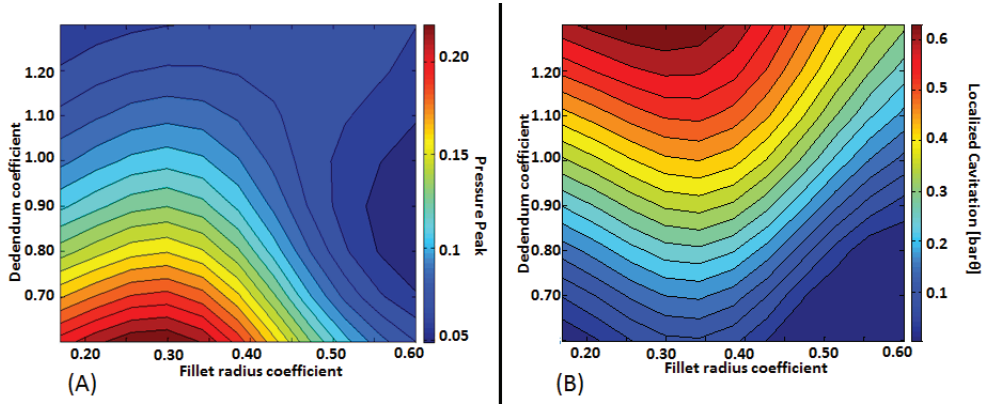


**Figure 14: (A) Pressure peak as a function of  $h_{fp}$  and  $\rho_{fp}$  (B) Cavitation as a function of  $h_{fp}$  and  $\rho_{fp}$**

Similar consideration can be done as concerns  $OF_3$  (localized cavitation): from figure 14(B) one can observe that when the level of undercut increases, localized cavitation effects are higher. This is due to the fact that, during the meshing process, when the tooth space volume opens, the fluid has more volume in an undercut gear to expand and hence the pressure can fall below its saturation pressure causing cavitation.

**4.2 Optimal Design**

This section presents the optimal design generated at the end of the optimization process. The chosen configuration is at a Pareto optimum of all the four OFs considered in this research.

**Table 6: Parameters of the optimal gear pump design**

Variable	Value	Unit
$m$	2.150	mm
$z$	10	-
$R$	11.541	mm
$h_{ap}$	0.586	-
$h_{fp}$	1.378	-
$\rho_{fp}$	0.300	-
$\alpha$	25.44	°
$b$	33.43	mm
$D$	1.950	mm
$S$	3.890	mm

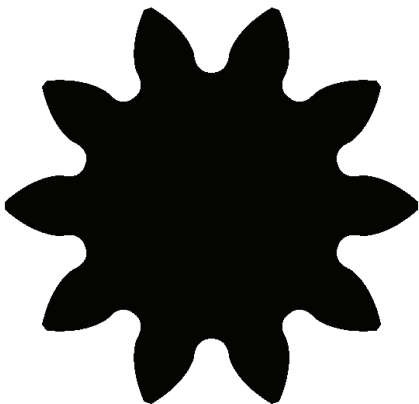


**Figure 15: Gear profile of the optimal design**

The efficacy of the proposed optimization methodology can be highlighted by comparing the optimal design with the commercial solution taken as reference. As reported in figures. 16 and 17, significant reduction in the delivery pressure pulsations is obtained.

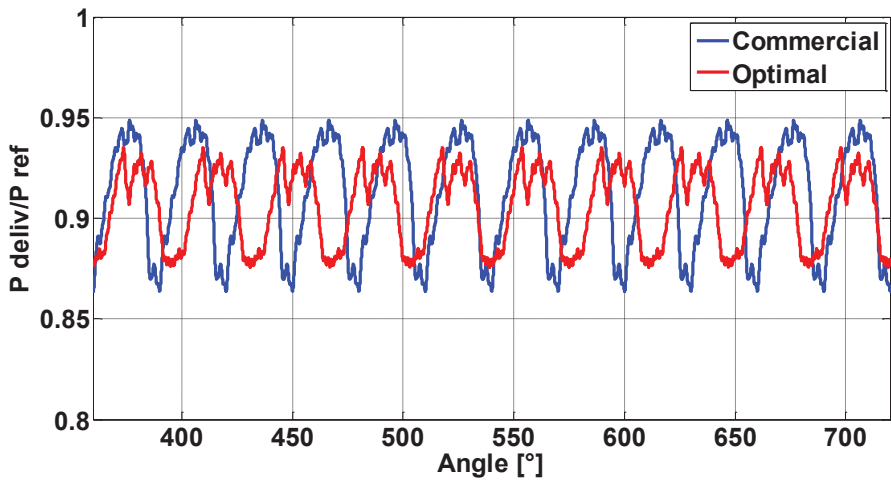


Figure 16: Plot of Delivery Pressure for the commercial and optimal design

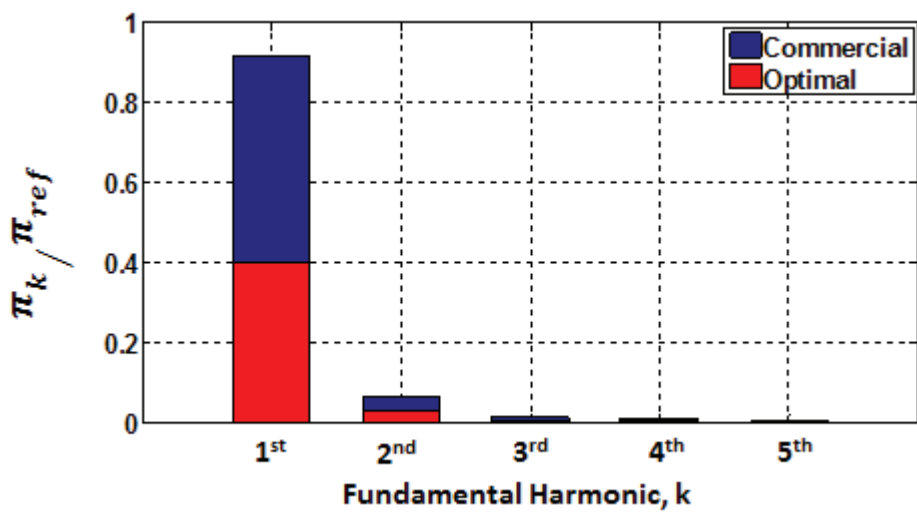
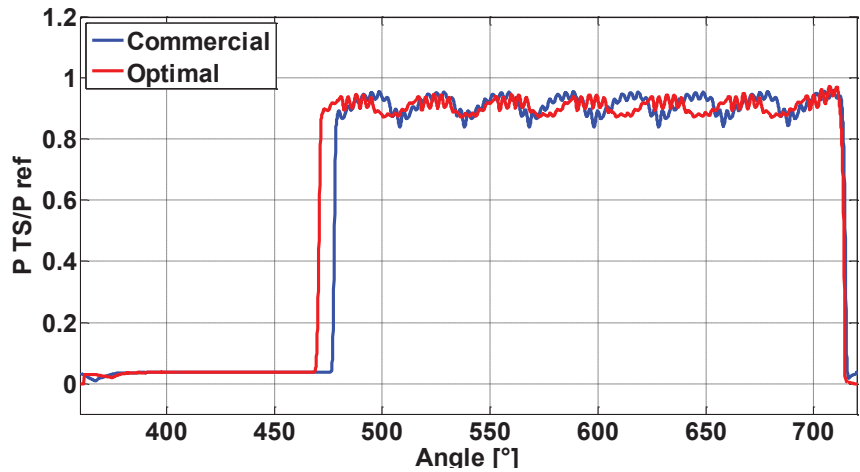


Figure 17: Plot of energy possessed by each harmonic of the pressure ripple for the commercial and optimal design



**Figure 18: Plot of Tooth Space Pressure for the commercial and optimal design**

From figures 16 and 17, it can be seen that the optimal design predicted in this work has shown a significant reduction in the pressure ripple and hence it would lead to quieter operation of the pump. In figure 18 it can be seen that the tooth space pressures follows similar trends in both the designs.

**Table 7: Summary of OFs for the commercial and optimal design**

	Pressure Ripple, OF <sub>1</sub> [%]	Pressure Peak, OF <sub>2</sub> [%]	Localized Cavitation, OF <sub>3</sub> [%]	Volumetric Efficiency, OF <sub>4</sub> [%]
<b>Commercial</b>	100.0	100.0	100.0	100.0
<b>Optimal</b>	43.8	125.7	84.7	101.3

From table 7, it can be seen that the optimal design shows much better performance compared to the optimal design. Significant reduction of the pressure ripple by more than 50% has been obtained as well as the efficiency seems to be higher by more than 1%. Also, the contact ratio for the selected gear pair is around 1.16 which is within the usual practical range of 1.15-1.20; hence it also assures that the power transmission is also smooth. Even though the pressure peak seems to be a little higher, the overall performance has been improved taking all the OFs into consideration.

**5. CONCLUSION**

In this paper a numerical optimization procedure for designing gear pump as a “whole” has been developed. Particularly, the major parts of the machine such as the gear and the lateral bushes have been optimized. The procedure takes into consideration all the necessary constraints which prevail in the manufacturing of gear machines and also to obtain smooth operation of the unit. The performance of the machine was analyzed based on four objective functions namely: delivery pressure oscillations, internal pressure peaks, localized cavitation and volumetric efficiency. Multi-objective genetic algorithms combined with

response surface methods were used for better simulation speeds. The problem of optimizing the gear machine is inherently complex with prevalent mutual interactions between the design variables as documented in this paper and hence cannot be solved using simplified approaches. Thanks to the optimization process developed in this research, the optimal configuration can be identified considering all the different interactions simultaneously. The optimal design of the gear machine has been provided and its performance was compared with an existing commercial design.

## ACKNOWLEDGMENTS

The authors would like to express their gratitude to LMS Engineering Innovation® for providing the software LMS Imagine.Lab AMESIM® for the development of HYGESim tool. The authors would sincerely like to thank the technical support team of ESTECO SpA (in particular Mr. Zhendan Xue) for their constant guidance while building the optimization workflow and continued support of the software modeFRONTIER.

## NOMENCLATURE

$\eta_v$	Volumetric Efficiency	
$Q_{avg}$	Average delivery flow rate	[l/min]
$P_{D,avg}$	Average delivery pressure	[bar]
$P_{TSV,peak}$	Peak pressure in the tooth space volume	[bar]
$V_d$	Displacement of the pump	[cm <sup>3</sup> ]
$f_k$	$k^{th}$ fundamental frequency of the FFT of the delivery pressure ripple	[Hz]
$\pi_k$	Sum of squares of the amplitude of the FFT of the delivery Pressure ripple for the $k^{th}$ fundamental harmonic	[bar <sup>2</sup> ]
$\pi_{ref}$	Sum of squares of the amplitude of the FFT of the reference delivery Pressure ripple	[bar <sup>2</sup> ]
$\Delta_f$	Frequency interval considered for the calculation of energy	[Hz]
$P(f_k)$	Total energy of the waveform	[bar <sup>2</sup> ]
$N$	Number of fundamental frequencies of interest	
$m$	Normal module	[mm]
$h_{ap}$	Addendum coefficient	
$h_{fp}$	Dedendum coefficient	
$\rho_{fp}$	Fillet radius coefficient	
$\alpha$	Pressure angle	[rad]
$R$	Pitch radius of the gears	[mm]
$R_b$	Base radius of the gears	[mm]
$R_o$	Outer radius of the gears	[mm]
$R_r$	Root radius of the gears	[mm]
$x$	Profile shift coefficient	
$b$	Face width of the gears	[mm]
$\phi_1$	Angular position at which the trapped volume begins to exist	[rad]
$\phi_2$	Angular position at which the trapped volume ceases to exist	[rad]

$\phi_{MIN}$	Angular position at which the trapped volume is a minimum	[rad]
$\phi_D$	Angle at which the delivery groove closes connection between the trapped volume and the delivery groove	[rad]
$\phi_S$	Angle at which the delivery groove closes connection between the trapped volume and the suction groove	[rad]
D	Vertical distance of the delivery groove from the line joining the axis of the two gears	[mm]
S	Vertical distance of the suction groove from the line joining the axis of the two gears	[mm]
H	Horizontal length of the suction/delivery grooves	[mm]

### Abbreviations

TS	Tooth Space
TSV	Tooth Space Volume
OF	Objective Function
OA	Optimization Algorithm
GA	Genetic Algorithm
RS	Response Surface
RSM	Response Surface Methodology
ANOVA	Analysis of variance
Ref	Reference
Deliv	Delivery
peak	Peak Value
avg	Average Value

### REFERENCES

- [1] Eaton, M., Edge, K., *Modelling and Simulation of Pressures within the Meshing Teeth of Gear Pumps*, Int. Cnf. On Recent Advantages in Aerospace Actuation Systems and Components, June 13-15, 2001, Toulouse, France
- [2] Borghi, M., Milani, M., Zardin, B., Patrinieri, F., *The influence of cavitation and aeration on gear pump and motors meshing volume pressures*, ASME-IMECE 2006, Chicago, IL (USA)
- [3] Manco S., Nervegna, N., *Pressure Transient in an External Gear Hydraulic Pump*, Second JHPS, International Symposium on Fluid Power, 2003, Tokyo, Japan
- [4] Wustmann, W., Helduser, S., Wimmer, W., *CFD Simulation of the reversing process in external gear pumps*, 6th International Fluid Power Conference, 2008, Dresden, Germany
- [5] Casoli, P., Vacca, A., Berta, G.L. *A Numerical Model for the Simulation of Flow in Hydraulic External Gear Machines*, Power Transmission and Motion Control, PTMC, 2006, Bath
- [6] Casoli, P., Vacca, A., Berta, G.L. *Potentials of a Numerical Tool for the Simulation of Flow in External Gear Machines*. SICFP07, The Tenth Scandinavian International Conference on Fluid Power, 2007, Tampere, Finland

- [7] Vacca A., Guidetti M., 2011, *Modeling and Experimental Validation of External Spur Gear Machines for Fluid Power Applications*, Elsevier Simulation Modelling Practice and Theory, 19 (2011),pp. 2007–2031
- [8] Manring, N.D., Kasaragadda, S.B., *The Theoretical Flow Ripple of an External Gear Pump*, *Journal of Dynamic Systems, Measurement and Control*, 125 (2003)
- [9] Wang, S., Sakurai, H., Kasarekar, A., *The Optimal Design in External Gear Pumps and Motors*, IEEE/ASME Transactions on Mechatronics, Vol 16, No.5 (2011)
- [10] Vaseena, A., Vacca, A., *Design Optimization of The Sliding Elements of External Gear Machines*, 6th FPNI-PhD Symposium 2010, West Lafayette,
- [11] Casoli, P., Vacca, A., Berta, G.L., *Optimization of Relevant Design Parameters of External Gear Pumps*, 7th JFPS International Symposium on Fluid Power, 2008, Toyama, Japan
- [12] Dhar S., Vacca A., *A Novel CFD- Axial Motion Coupled Model for the Axial Balance of Lateral Bushings in External Gear Machines*, Elsevier Simulation Modelling Practice and Theory, 2012
- [13] Dhar S., Vacca A., Lettini A., *A Fluid – Structure Interaction model to analyze Axial Balance in External Gear Machines*, 8th IFK International Fluid Power Conference, 2012, Dresden, Germany
- [14] Klop, R., Vacca, A., Ivantysynova, M., 2009, *A Method of Characteristics Based Coupled Pump/Line Model to Predict Noise Sources of Hydrostatic Transmission*, Bath/ASME Symposium on Fluid Power & Motion Control, 2009, Hollywood, California
- [15] Casoli, P., Vacca, A., Franzoni, G., Guidetti, M., *Effects of Some Relevant Design Parameters on External Gear Pumps Operating: Numerical Predictions and Experimental Investigations*, 6IFK Internationales Fluidtechnisches Kolloquium 2008, Dresden, Germany
- [16] LMS.Imagine SA, HYD Advanced Fluid Properties, Technical Bulletin no. 117, rev 8B, December 2008, 2008.
- [17] P. Casoli, A. Vacca, G. Franzoni, G.L. Berta., *Modelling of fluid properties in hydraulic positive displacement machines*. Elsevier Simulation Modelling Practice and Theory, 14 (2006), pp. 1059–1072
- [18] Vacca A., Dhar S., Opperwall T., 2011, *A Coupled Lumped Parameter and CFD Approach for Modeling External Gear Machines*, SICFP2011 The Twelfth Scandinavian International Conference on Fluid Power, May 18-20, 2011, Tampere, Finland
- [19] *Method for Specifying the Geometry of Spur and Helical Gears*, AGMA 913-A98, American Gear Manufacturers Association, 1998
- [20] Kollek, Waclaw, Osinski, P., *Modeling and Design of Gear Pumps*, Oficyna Wydawnicza Politechniki Wroclawskiej, Wroclaw, 2009
- [21] Ivantysyn, J., Ivantysynova, M., *Hydrostatic Pumps and Motors*, Tech Books In., 2003, New Delhi, India



- [22] Litvin, F.L., Fuentes, A., *Gear Geometry and Applied Theory*, 2004, 2nd edition, Cambridge University Press
- [23] Trautshold, R., *Gear Design and Production Rules and Working Formulas*, 1955, Columbia Grpahs
- [24] Goldberg, D.E., *Genetic Algorithms in Search, Optimization and Machine Learning*, Addison Wesley Longman Publishing Co., Boston, MA, USA, 1989
- [25] Antony, J., *Design of Experiments for Engineers and Scientists*, Butterworth Heinemann, 2006
- [26] Vacca, A., Cerutti, M., *Analysis and Optimization of a Two-Way Valve Using Response Surface Methodology*, International Journal of Fluid Power, Vol. 8, November 2007
- [27] Buhmann, Martin, D., *Radial Basis Functions: Theory and Implementations*, Cambridge University Press, 2003

# Friction measurement of plunger bushing contact in fuel injection pumps

**Sebastian Drumm, Stefan Heitzig, Hubertus Murrenhoff**

Institute for Fluid Power Drives and Controls of RWTH Aachen University  
Steinbachstraße 53, 52074 Aachen, Germany  
sebastian.drumm@ifas.rwth-aachen.de

## ABSTRACT

The Cluster of Excellence “Tailor made fuels from biomass” (TMFB), funded by the German research foundation (DFG), is an interdisciplinary collaboration of about 20 institutes and 65 researchers. The aim of the project is to find a new route to synthesise tailored fuels based on biomass. Furthermore, the combustion and injection system shall be optimized by reconsidering the new fuel as a design element. Task of the authors is to develop a guide-line for designing an injection system adapted to these fuels. The focus is especially on high pressure pumping of the new fuels within common rail systems.

To measure friction forces in a radial piston fuel injection pump a test rig has been designed and set up. It is developed to investigate the axial friction forces in the plunger bushing contact as well as the transversal forces which act on this contact. The test rig is designed to analyze the effects of different materials and coatings, different micro and macro geometries and different types of fuel.

In this paper the test bench and first measurement results with diesel as a reference fuel will be shown and discussed.

## 1 INTRODUCTION FOR COMMON RAIL PUMPS

Common rail pumps for Diesel applications are usually lubricated by the fuel itself. In **Figure 1** the common rail pump CP1 from Bosch is shown as an example. The pump is designed as a radial piston pump as common rail pumps usually are. All gaps are lubricated by the diesel fuel. The tribological contacts are between eccentric shaft and polygon ring, between polygon ring and piston plate, and between piston and bushing. The suggested fuels in the project TMFB have different hydraulic and tribological characteristics. Most of the fuels have a lower viscosity and a poor lubricity. This has significant influence on the tribological systems in the injection pump.

The aim is to develop tribological contacts that are lubricated mostly by hydrodynamic lubrication films and not with mixed friction. The type of lubrication influences the friction in the contact which shall be measured with a test bench. The most critical tribological contact is allocated between piston and bushing and the contact between polygon ring and piston plate between which the friction shall be measured.

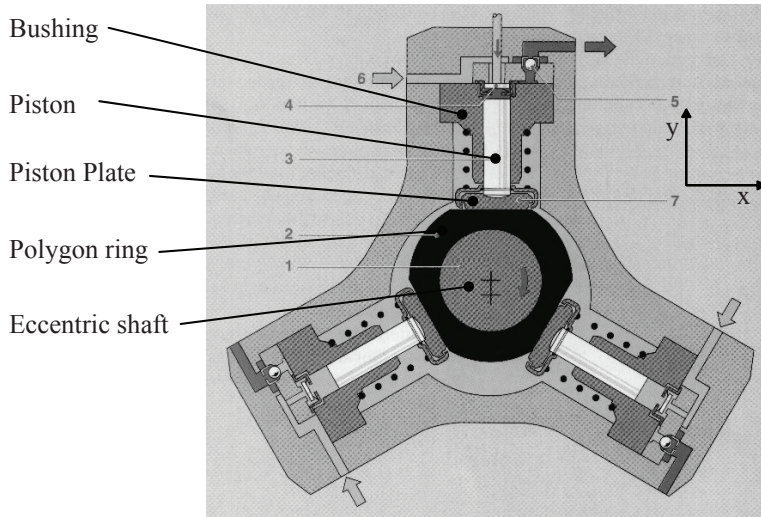


**Figure 1: Common Rail Pump CP1 (Bosch), total displacement 0.677 cm<sup>3</sup>**

To measure friction forces in tribological contacts of hydraulic pumps different test rigs were developed [1], [2], [3], [4], [5]. The measurement principle chosen for the developed test rig in this paper can be compared with the test rig developed by Breuer [6] who measured the friction forces in the piston bushing contact of an axial piston pump. In order to measure friction in the described contacts one bushing is mounted to a force measuring platform so that forces in axial (y-direction) and in radial direction (x-direction) can be investigated. The forces in axial direction are used to measure friction in the piston – bushing contact and the forces in radial direction will be used to measure friction in the contact polygon ring – piston plate. In this paper the design of the test bench will be shown and first measurement results with diesel as a reference fuel are discussed.

## 2 DESIGN OF THE TEST RIG FOR FRICTION MEASUREMENTS

All frictions are measured at one of the three pistons. Therefore one bushing is mounted to the force measuring platform as shown in the test rig concept in **Figure 2**. The force measuring platform consists of 4 force measuring cells which are mounted between platform and base frame. The axial forces induced by the pressure in the piston chamber are expected to be much higher than the friction forces in axial direction. To measure the friction forces without the influences of the pressure force, a compensation piston is used. This piston has the same diameter (6.5 mm) as the measured piston and is mounted opposite to the measured piston. Thus the forces generated by pressure are led directly to the base frame. In that way it is achieved that the force sensors in axial direction measure only the forces generated by friction. The volumes of the measured piston and the compensation piston are connected. So the dead volume will be larger compared to the remaining pistons. Also, the leakage of this volume will be approximately doubled by the leakage at the compensation piston. So it is expected that the pressure increase at the start of the pumping stroke will be slower than at the other pistons.

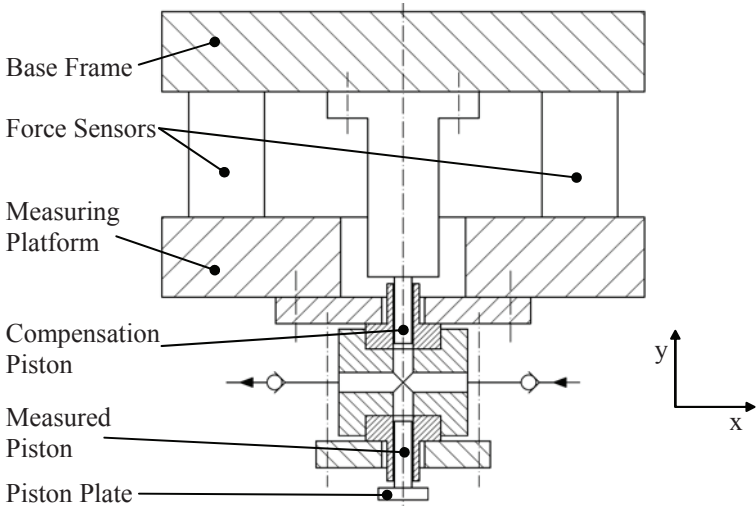


**Figure 2: Friction Measurement Concept**

In **Figure 3** the hydraulic diagram of the test rig is shown. The test rig is supplied from the tank via a fuel supply pump. To achieve a constant supply pressure of 6 bar a pressure relieve valve is used. The separation from pressure an suction side of the single pistons is done by check valves at each piston. The pressure in the volume of the measured piston shall be detected by a dynamic pressure sensor. The flow of the pistons is pumped to two different high pressure rails. One rail is connected to the measured piston while the other rail is supplied by the unmodified pitons. The pressure in each pressure rail is controlled by a pressure relieve valve. With the use of two pressure rails it is achieved that only low pressure connections are installed between the force measuring platform and the base frame of the test rig. In that way no additional forces by pressure pulsation in the high pressure system is induced to the force measuring system.

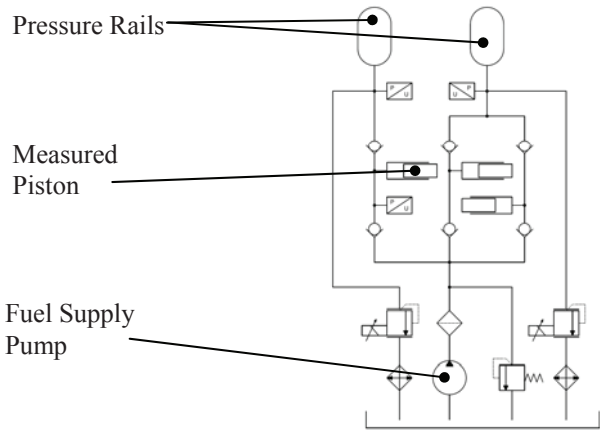


**Figure 3: Hydraulic diagram of the test rig**

**Figure 4** depicts the design of the test rig is shown in a cross section, radial and axial. The test rig is driven by an electric motor and a flywheel is used to achieve a constant rotational speed. The rotational speed and the angle of revolution is detected by an angle sensor. To enable an easy change of the eccentric shaft it is connected by an extra coupling to the driving shaft. The measured piston has a radial position to the eccentric shaft and is connected by the polygon ring.

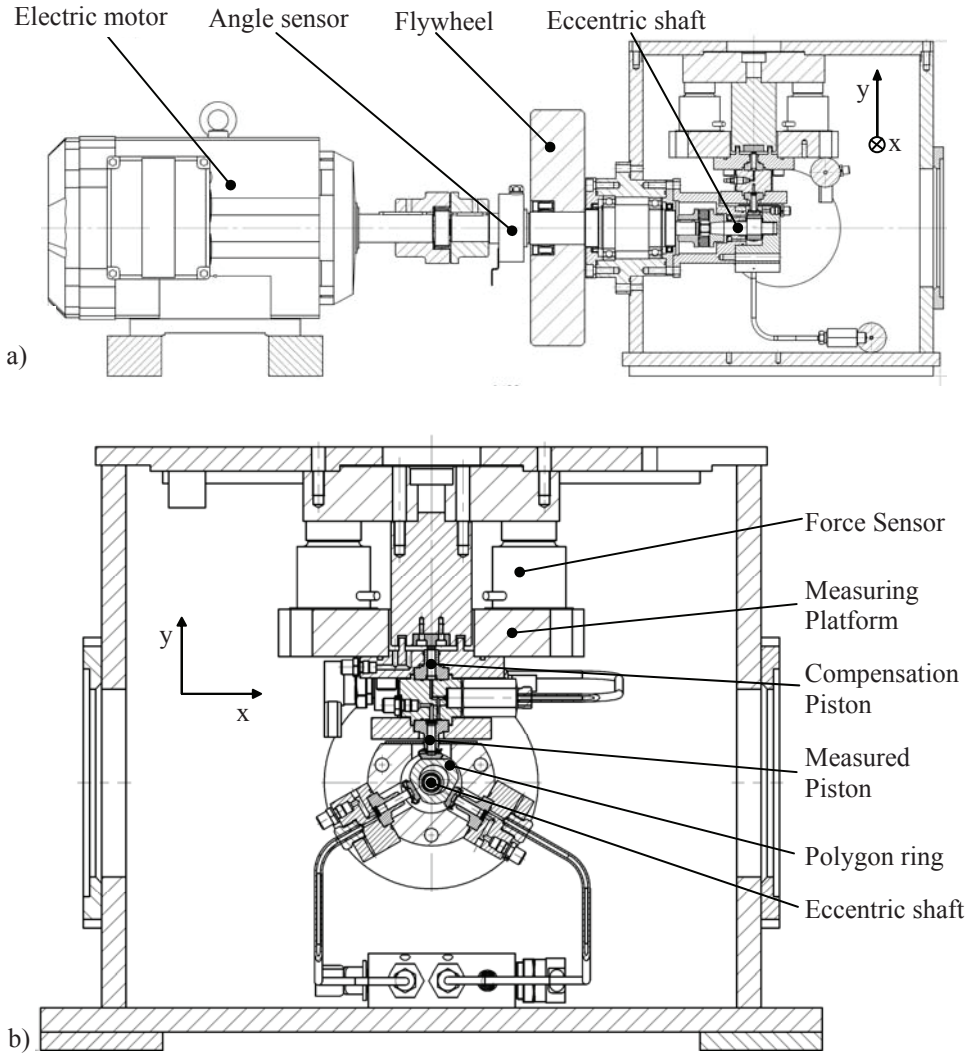


**Figure 4: Test Rig, Cross Sections: a) axial, b) radial**

The bushing of the measured position is clamped together with the bushing of the compensation piston. Between these two bushings a valve block is located where the separation from the suction and the high pressure side is integrated with check valves.

Additionally a dynamic pressure sensor is mounted to the valve block to measure the pressure build-up of the measured piston. The compensation piston is used to carry the pressure forces of the measured piston directly to the base frame.

To set up all forces that have an influence on the behaviour of the polygon ring, all three pistons are integrated in the test rig and generate a pressure. To avoid that a pulsating pressure in the high pressure system carries a load on the force measuring system two different high pressure rails are used: one for the measuring piston on the force measuring platform and one for the two other pistons.

It is possible to change the position of the whole measuring platform with the measured piston in x-direction. In that way the eccentricity of the piston can be changed.

### 3 MEASUREMENT RESULTS OF FRICTION

The test rig has been set up recently and the first measurements were performed. In the following these results will be shown and discussed. In **Figure 5** friction forces and pressures of one revolution are shown against the rotation angle at rotational speed of 500 1/min and displacement of the piston axis in x-direction against the eccentric axis of -1.5 mm. The plot starts at the outer dead centre of the piston at a rotational angle of 0° and ends again at the outer dead centre of the piston at a rotational angle of 360°.

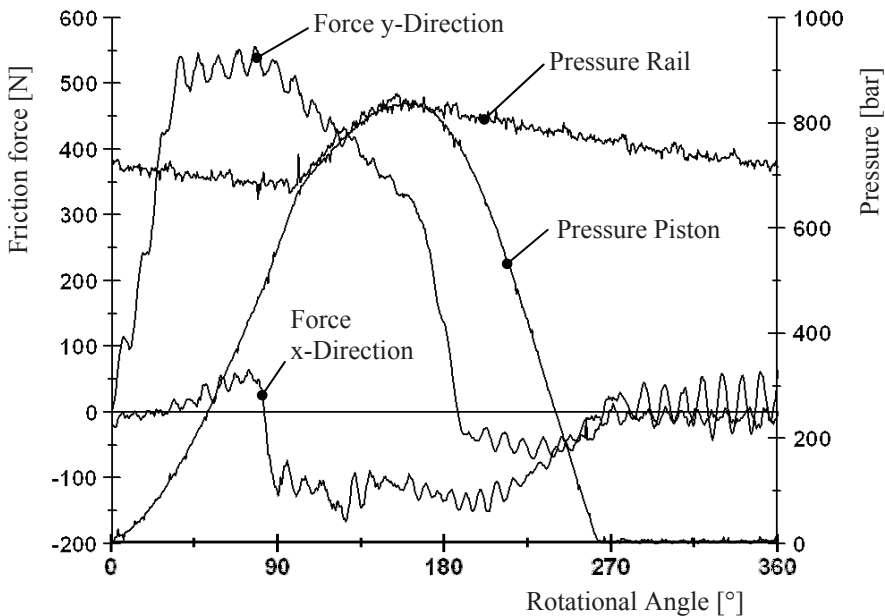


**Figure 5: Friction Measurement**

The pressure in the piston chamber starts at the lower dead centre with 5 bar being set by the supply pressure. With further compression pressure rises. At a rotational angle of about

90 ° the pressure in the piston chamber reaches the pressure level of the rail. At this point the check valve from the piston chamber to the rail opens and a flow rate to the rail develops. From this point the pressure in the piston chamber and the rail rise simultaneously with a lower slope than the pressure rise in the piston chamber before. The upper dead centre is reached at 180 °. Here, the highest pressure in the piston chamber is reached with 840 bar. Starting at this point the pressure in the piston chamber is decompressed until a rotation angel of 260°. At this point the pressure of the supply system is reached again which fills the piston chamber.

The pressure in the pressure rail starts linear decreasing at the lower dead centre until it rises simultaneously with the pressure in the piston chamber between 90 and 180°. After the upper dead centre is reached, it decreases again with an almost linear behaviour.

An ideal shape of the pressure in the piston chamber would be a rectangular profile. This pressure would jump at the lower dead centre from the supply pressure to a constant rail pressure. At the upper dead centre this pressure would drop at once to the supply pressure on which it would remain constantly until the next cycle starts. There are two reasons which cause a slower pressure increase. The first reason is an additional leakage flow rate at the compensation piston. This approximately doubles the leakage flow rate. The second and more important reason is the dead volume which is larger than in an original pump. With adding a compensating piston, the volume is already more than doubled with the connection bore of the two pistons. In this first measurement the dead volume is even larger because an absolute pressure sensor is used which is mounted with the help of an adapter which also has a large volume. This together enlarges the dead volume of the piston to approximately five times of the displacement of the piston. For further experiments a dynamic pressure sensor will be used which will reduce the dead volume significantly.

The friction forces in y-direction, which is the friction between the piston and the bushing, rises at the beginning of the cycle and reaches a maximum of 550 N. The friction force in y-direction remains positive until the upper dead centre is reached. After that, it changes the direction and is negative until the pressure in the piston chamber is relieved to the supply pressure. After that, the friction alternates around zero with an amplitude of approximately 150 N. The friction force in x-direction, which is the friction force between the piston plate and the polygon ring, starts climbing in positive direction until a rotation angle of 90°. From this point between the piston plate and the polygon ring changes the direction and so the friction force drops to negative values. The friction force in x-direction remains negative till the rotational angle of 270° where the direction of the movement is changed again. After that the friction force alternates around zero.

To analyse the reproducibility, in **Figure 6** the measurement of friction forces and pressure of 16 revolutions in one row are shown plotted over the rotational angle. The rotational speed is 500 1/min, the eccentricity of the piston axis against the eccentric axis is +0.5 mm. The characteristics of pressures and friction forces are similar to the operation point shown in Figure 5. The differences are a higher maximum pressure at the upper dead centre of 1000 bar and a lower friction force in y-direction with a maximum of 380 N. It can be taken from the diagram that the measured curves from all 16 revolutions are close to each other. The curves of the piston pressure show the smallest deviation compared with the other measurements. All measurements cover a bandwidth smaller than 10 bar. The pressure



measurements of the rail pressure are placed in a bandwidth of approximately 20 bar. This equates the bandwidth of the measurement noise of the rail pressure already shown in figure 5. The plots of the force measurement are all enclosed in a bandwidth of less than 100 N. It is noticeable that the characteristics of the ripples in the force measurement are reproducible and do not occur accidentally. They can emerge from stick-slip effects or from vibrations in the structure. If the waves emerge from vibrations this can be detected by measurements of acceleration of the structure in future work.

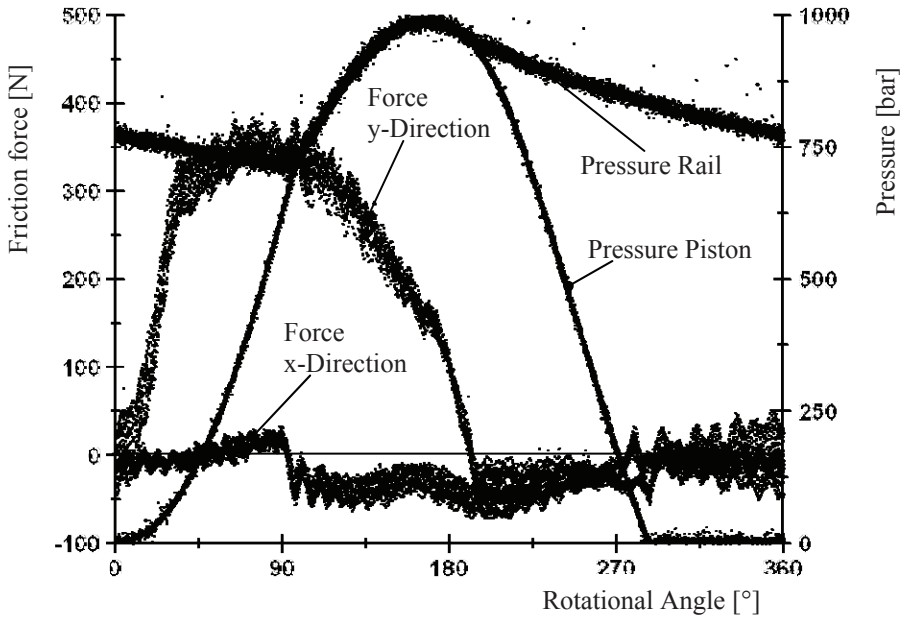


**Figure 6: Reproducibility of Friction Measurement of 16 revolutions**

#### 4 CONCLUSION AND OUTLOOK

To develop injection pumps for alternative fuels, a test rig to measure friction forces in tribological contacts has been developed and set up. The test rig was brought into operation and first test measurement were done. The measurement results have shown that the test rig is suitable to analyse the friction forces depending on the rotational angle at different operation conditions. By reducing the dead volume of the piston chamber, the build up of the pressure in the position chamber will be steeper and therewith more realistic. Also the regulation of the rail pressure will be improved. In the ongoing work the test rig will be used to validate EHD simulation models of the tribological contacts. In the ongoing research on this topic the simulation models will be used to optimise the geometry of the tribological contacts. The optimised tribological parts will be measured again in the test rig.



## ACKNOWLEDGMENTS

This work was performed as part of the Cluster of Excellence "Tailor-Made Fuels from Biomass", which is funded by the Excellence Initiative by the German federal and state government to promote science and research at German universities. The authors thank for the support of their work.

## REFERENCES

- [1] K.-Th. Renius: Untersuchungen zur Reibung zwischen Kolben und Zylinder bei Schrägscheiben-Axialkolbenmaschinen. In: VDI Forschungsheft 561, VDI-Verlag, Düsseldorf, 1974
- [2] O. Koehler: Anlaufreibungsverluste eines Schrägscheiben-Axialkolben-Motors. In: Ölhydraulik und Pneumatik Nr. 31, Jahrgang 11, 1987
- [3] S. Donders: Kolbenmaschinen für HFA-Flüssigkeiten – Verlustanteile einer Schrägscheibeneinheit. Verlag Mainz, Aachen, 1998
- [4] A. Kleist: Berechnung von Dicht- und Lagerfugen in hydrostatischen Maschinen. Shaker Verlag, Aachen, 2002
- [5] R. Lasaar: Eine Untersuchung zur mikro- und makrogeometrischen Gestaltung der Kolben-/Zylinderbaugruppe von Schrägscheibenmaschinen. VDI Verlag, Düsseldorf, 2003
- [6] D. Breuer: Reibung am Arbeitskolben von Schrägscheibenmaschinen im Langsamlauf. Shaker Verlag, Aachen, 2007

# Geometric Features of Gerotor Pumps Analytic vs Cad Methods

**Gianluca Carconi\*; Cristian D'Arcano; Nicola Nervegna; Massimo Rundo**

Politecnico di Torino - Energy Department  
The Fluid Power Research Laboratory (FPRL)  
Corso Duca degli Abruzzi 24  
Torino, 10129 - Italy

Phone: +39 0110904432, Fax: +39 0110904599

Mail: nicola.nervegna@polito.it

\*Randit S.r.l., Torino, Italy

## ABSTRACT

Accurate simulation models of gerotor pumps require knowledge of geometric features of these units. Instantaneous volumes of chambers as well as their volume derivatives lead to kinematic flow rate, flow ripple index, displacement. Flow passage areas between a chamber and the inlet/delivery volumes during a complete shaft revolution also need to be known. General analytical methods (integral-derivative and derivative-integral) have been developed for the calculation of geometric quantities of gear as well as vane pumps and will be reported in the paper with specific emphasis on gerotor units. The approach leading to these geometric informations has traditionally been grounded on a 2D analysis of involved features.

However, in the last decade, there has been a progressive and relentless development and use of 3D CAD software that has led to the possibility of having at hand a virtual representation of these positive displacement machines.

Accordingly, a novel method that requires the 3D model of the gerotor pump is presented and the paper demonstrates how geometric features of the unit can be obtained. Main characteristics of this methodology are the use of parametric relations that define the relative position of the rotating gears, and the use of *virtual components*. A validation of this proposed approach is discussed contrasting analytic and CAD-model based outcomes.

This methodology has been successful also in axial piston machines as well as for the determination of flow passage areas of complex proportional direction spool valves.

**Keywords:** positive displacement pumps; Modelling; Simulation;

## 1. INTRODUCTION

Along more than two decades the Fluid Power Research Laboratory (FPRL) has developed and experimentally validated simulation models for axial piston pumps and motors [1],

external [2] and internal gear (gerotor) pumps [3], radial pistons [4] as well as variable and fixed displacement vane pumps [5]. All have generally evolved in AMESim, elaborating proprietary libraries leading to an accurate prediction of the main hydraulic and mechanical quantities; recently, a multibody software code has also been proposed for the analysis of axial piston pumps [6]. In the course of these studies a recurrent aspect had to be faced relative to an often tedious and error prone analysis of geometric features of these hydrostatic machines. It is well known that modelling of positive displacement units involves knowledge of volumes and volumes variation to appraise ideal flow rate and absorbed torque along with the flow and torque ripple characteristics. Similarly portplate timing and suction-delivery flow passage areas represent another issue that must be resolved. Recognition of these quantities form the backbone of an accurate and rigorous modelling procedure.

One significant contribution in this line of reasoning was provided by research works performed at the Maha Research Centre of Purdue University in the USA. A software tool named *AVAS* (Automated Valve Plate Area Search) [7] was developed for the evaluation of flow passage areas in axial piston pumps following connections of a variable volume chamber with the portplate during a complete barrel revolution. Another tool, *SUEZ* [8], further aimed at finding optimal kidney ports geometries to minimize fluid borne noise. However, these findings were strictly oriented at piston pumps and to the authors present knowledge, no extensions have been published to convey a general outlook and methodology for further developments. In addition availability of those tools seems to be restricted as they work within *CASPAR* [9],[10] and in essence are to be retained as proprietary codes.

## 2. GEOMETRIC FEATURES

### 2.1 Simulation approaches

The geometric quantities in positive displacement pumps are mainly dependent on the control volumes selected for the modelling. Two rather diverse approaches exist involving a different number of differential equations. The first ( $2+X$ ) implies two variable volumes for inlet and delivery capacities and a various number  $X$  of fixed or variable volumes associated with trapped chambers. Inlet and delivery volumes include connected chambers that are lumped together and with inlet/outlet ducts. Instead the second approach ( $N+2$ ) considers two fixed volumes for inlet and delivery capacities and a control volume associated with each of the  $N$  variable chambers.

This last methodology is more suitable for the simulation of volumetric machines where variable volume chambers are well defined (e.g. piston and vane pumps), while its application to external gear pumps/motors becomes more complex. On the other hand, with this approach each chamber pressure evolution can be individually observed during a complete shaft revolution, leading to improved predictions of pump performance.

### 2.2 Quantities depending on volume

Regardless of the method, to each  $j$ -th control volume the equation expressing the pressure derivative in an open system must be applied:

$$\frac{dp_j}{dt} = \frac{\beta}{V_j} \left( Q_j - \omega \cdot \frac{dV_j}{d\theta} \right) \quad (1)$$

being:

- $V_j$  the volume of the  $j$ -th hydraulic capacity;
- $\vartheta, \omega$  the shaft angular position / speed;
- $\beta$  the fluid bulk modulus;
- $Q_j$  the net ingoing volumetric flow rate.

The volume derivative is also necessary for the evaluation of the kinematic (theoretical) flow rate defined as:

$$Q_{th}(\vartheta) = \omega \sum_{j=1}^{N_v} F_j(\vartheta) \quad (2)$$

where:

$$F_j(\vartheta) = -\min\left(\frac{dV_j}{d\vartheta}, 0\right) \quad (3)$$

and  $N_v$  is the number of variable volumes into which the pump is divided. The flow ripple index is defined as:

$$\delta_Q = \frac{\max(Q_{th}) - \min(Q_{th})}{\bar{Q}} \quad (4)$$

where:

$$\bar{Q} = \frac{1}{\Theta} \int_0^{\Theta} Q_{th}(\vartheta) d\vartheta \quad (5)$$

being  $\Theta$  the angular period of the function  $Q_{th}$ .

The pump displacement can be always evaluated starting from the kinematic flow rate:

$$V = \bar{Q} / \omega \quad (6)$$

Optionally it can also be calculated from the unit displacement  $V_0$  of a single chamber:

$$V = n_c \cdot N \cdot V_0 \quad (7)$$

being  $n_c$  the number of cycles per shaft revolution and  $N$  the number of variable chambers.

The ideal  $T_{th}$  and indicated  $T_{ind}$  torques are function of the volume derivative:

$$T_{th} = p_{out} \sum_{j=1}^{N_v} F_j(\vartheta) \quad (8)$$

$$T_{ind} = - \sum_{j=1}^{N_v} \left( p_j \cdot \frac{dV_j}{d\vartheta} \right) \quad (9)$$

being  $p_{out}$  the pressure at the outlet port.

### 2.3 Quantities depending on flow area

In case of single chamber approach (model  $N+2$ ), it is necessary to calculate the passage

areas  $A_i$  and  $A_d$  respectively between a chamber and the inlet/delivery volumes during a complete shaft revolution. The ingoing/outgoing flow rate through the port plate is evaluated using eq. (10) valid for turbulent regime:

$$Q = C_e A(\theta) \sqrt{\frac{2\Delta p}{\rho}} \quad (10)$$

The approach (2+X) does not require the evaluation of the passage area since all the chambers connected to inlet/outlet volumes are lumped together.

### 2.4 Analytical methods

Two different approaches are possible for the calculation of the geometric quantities, as described in [11]: the integral-derivative (ID) and the derivative-integral (DI). The former evaluates the volume or the passage area by integration of the equations defining the contour of the chamber, then the volume variation is calculated by derivation. The latter performs a direct evaluation of the volume derivative based on kinematic considerations, afterwards the volume or area is calculated by integration of the angular derivative. This last approach, when applicable, is more accurate and it is particularly suitable for gear pumps as well as for vane pumps.

Two different methods can be used for the direct calculation of the volume derivative. The first technique, also called vector-ray method, consists in the assessment of the area swept by the segments joining the centre rotation of the rotor and the contact points (between gears or vane and internal stator track) delimiting the chamber. The second technique consists in the evaluation of the torque on the shaft generated by the pressure in the  $j$ -th chamber, based on eq. (9).

## 3. AN APPLICATION CASE STUDY

### 3.1 Gerotor pump

All the analytic methods will be discussed with reference to a gerotor pump (Figure 1). The unit consists of an internal gear having one tooth less than the external. Each gear rotates about its respective centre  $O_i$  and  $O_e$  with a transmission ratio of  $(N-1)/N$ .

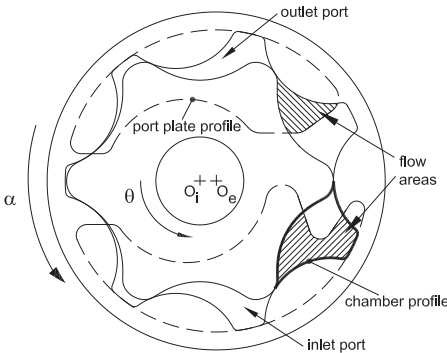


**Fig. 1. Schematic representation of a gerotor pump**

Since in this type of machine the number of cycles per shaft revolution is lower than one, the

use of the angular position  $\alpha$  of the outer gear as independent variable is to be preferred in order to obtain functions with period of  $2\pi$ .

### 3.2 DI approach with vector-ray method

Two control volumes (see Figure 2) are considered:

- $V_i$  relative to the internal gear and bounded by the polyline  $1O_i2$  and the line of contacts;
- $V_e$  relative to the external gear and bounded by the arc 3-4, the line of contacts comprised between 1 and 2 and the two segments 2-3 and 1-4.

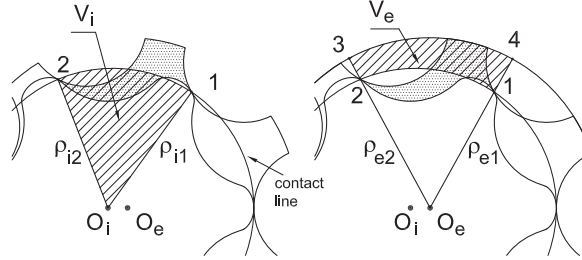


**Fig. 2. DI vector-ray method, control volumes and symbols**

If a rotation is impressed on gears,  $V_i$  and  $V_e$  change due to volumes swept by vector rays  $\rho_{i1}$  and  $\rho_{i2}$  for the inner gear and by  $\rho_{e1}$  and  $\rho_{e2}$  for the outer gear. However contact points as well as vector rays rotate a different angle than gears so that the gearing solid volume comprised in control volumes is variable. Accounting for this, it is possible to evaluate the net volume change of chambers. Considering an infinitesimal rotation  $d\theta$  of the inner gear, after some intermediate calculation shown in [11], the corresponding variation of the volume  $V_i$  is:

$$dV_i = \frac{1}{2}H \cdot (\rho_{i2}^2 - \rho_{i1}^2) \cdot d\theta \quad (11)$$

In a similar manner the variation of the volume  $V_e$  after a rotation  $d\alpha$  of the outer gear is:

$$dV_e = \frac{1}{2}H \cdot (\rho_{e1}^2 - \rho_{e2}^2) \cdot d\alpha \quad (12)$$

Therefore the total variation of the chamber can be written as:

$$\frac{dV_j}{d\alpha} = \frac{1}{2}H \left[ (\rho_{e1}^2 - \rho_{e2}^2) + (\rho_{i2}^2 - \rho_{i1}^2) \frac{N}{N-1} \right] \quad (13)$$

The vector rays expressions are given by the equation of the line of contact in polar coordinates.

This method can also be used for the evaluation of the passage area in case of very simple geometries; in this case some rotating vector-rays in eq. (13) must be substituted by fixed segments representing the port plate rims.

### 3.3 DI approach with torque method

The pressure  $p_j$  acting in the chamber produces two torques  $T_i$  and  $T_e$  respectively on the

internal and external gear (Figure 3).

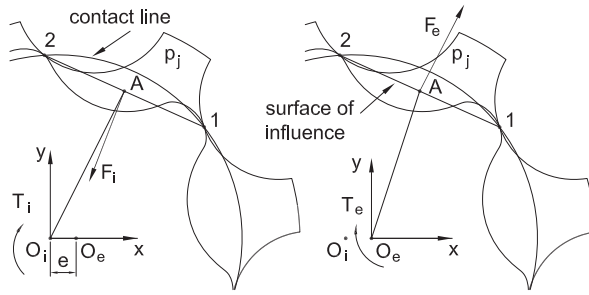


**Fig. 3. DI torque method, forces and surfaces**

In the reference frame with centre  $O_i$  the torque  $T_i$  is:

$$T_i = \overline{O_i A} \times F_i \quad (14)$$

where:

$$\overline{O_i A} = \begin{bmatrix} (x_1 + x_2)/2 \\ (y_1 + y_2)/2 \\ 0 \end{bmatrix}; F_i = \begin{bmatrix} (y_1 - y_2) \cdot H \cdot p_j \\ (x_2 - x_1) \cdot H \cdot p_j \\ 0 \end{bmatrix} \quad (15)$$

Equation (14) yields:

$$T_i = \begin{bmatrix} 0 \\ 0 \\ \frac{1}{2} H \cdot p_j (x_2^2 - x_1^2 + y_2^2 - y_1^2) \end{bmatrix} \quad (16)$$

and therefore:

$$|T_i| = \frac{1}{2} H \cdot p_j (\rho_{i2}^2 - \rho_{i1}^2) \quad (17)$$

While in the reference frame with centre  $O_e$ :

$$\overline{O_e A} = \begin{bmatrix} (x_1 + x_2)/2 \\ (y_1 + y_2)/2 \\ 0 \end{bmatrix}; F_e = \begin{bmatrix} (y_2 - y_1) \cdot H \cdot p_j \\ (x_1 - x_2) \cdot H \cdot p_j \\ 0 \end{bmatrix} \quad (18)$$

and therefore the torque  $T_e$  is:

$$|T_e| = \frac{1}{2} H \cdot p_j (\rho_{e1}^2 - \rho_{e2}^2) \quad (19)$$

The torque on the external gear necessary to balance pressure in the  $j$ -th chamber is:

$$|T_j| = -|T_e| \frac{N}{N-1} |T_i| = -p_j \cdot \frac{dV_j}{d\alpha} \quad (20)$$

By substituting expressions (17) and (19), eq. (13) is obtained.

### 3.4 ID approach

For the DI approach the equation of the contact line was only required; instead the ID method needs also the equations of both gears profiles. With reference to Figure 4, the chamber volume in a generic angular position  $\alpha_0$  is:

$$V_j(\alpha_0) = \frac{1}{2}H \left( \int_{\psi_{e1}}^{\psi_{e2}} \rho_e^2 d\psi - \int_{\psi_{i1}}^{\psi_{i2}} \rho_i^2 d\psi \right) \quad (21)$$

being  $\psi_1$  and  $\psi_2$  the phase of vector rays in correspondence of the contact points 1 and 2, while  $\rho_e(\psi, \alpha_0)$  and  $\rho_i(\psi, \alpha_0)$  are the equations of the gear profiles in polar coordinates.

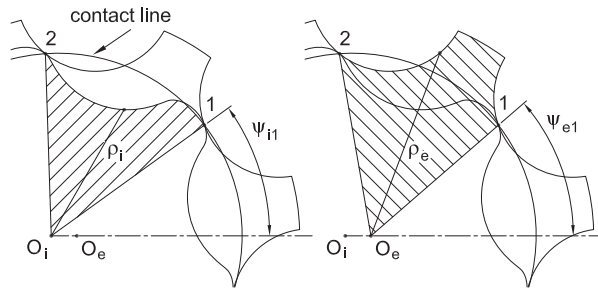


**Fig. 4. ID approach, gears profiles and symbols**

Eq. (21) must be applied for several values of the angle  $\alpha$  in the range  $0-2\pi$  in order to obtain the complete volume history.

### 3.5 Graphical-analytical methods

These approaches can be used for the evaluation of flow passage areas in case of complex geometry, where the port plate profile cannot be easily defined by analytical equations. The starting point is represented by the 2D drawing of the port plate that must be converted in a file containing the x-y coordinates of the passage area contour. This can be done with automatic procedures available in the CAD software (e.g. AutoLISP routines) or by means of digitizing programs.

The obtained data are processed in order to calculate the area in common with the chamber port. To this purpose, algorithms for the evaluation of the common area of overlapping polygons can be used. The procedure must be applied for different angular positions of the shaft.

## 4. THE CAD APPROACH METHODOLOGY

As already mentioned in the Introduction, in the last twenty years computing resources capable of assisting research activities have evolved in multiple directions: from advanced simulation environments, to highly intensive calculation codes, to diversified software ambients aimed at enacting a full portrayal of components, mechanisms and machines. And, in particular, these last resources have been profitably used to generate accurate and faithful 3D descriptions of fluid power components and systems. Nowadays, having at hand a rather



extensive database of high quality three-dimensional models originally developed in house from FPRL or re-worked from manufacturers communications, the idea has matured about the fact that these *CAD 3D parametric solid modellers* have already and definitely reached the degree of reliability, completeness and richness of tools leading to the possibility of performing automatic or at least relatively fast and precise evaluations of nominal geometric characteristics cited in paragraphs 2.2 and 2.3. Therefore a novel approach is now possible to overcome difficulties inherent with analytic investigations.

To demonstrate the feasibility of the approach a high-end commercial software from PTC (Creo Elements/Pro, formerly known as Pro/ENGINEER) was selected. The choice was based on the availability of operations and tools that other mid-level software, at least to our present knowledge, do not yet incorporate. To be more explicit we are referring to the creation of measures and relational features capable of identifying characteristics as areas, volumes etc. of the fluid power unit under scrutiny while tracking their evolution as a motion parameter is varying within the simulation study.

The methodology that has been developed can be synthesized in a series of fundamental steps, that do obviously differ in some details depending on the unit and the characteristics being sought, but that altogether propounds a general framework within which it is possible to progress with relative ease and confidence:

- Develop, starting from real hardware components, their 3D parts models, or import them in the PTC software if already available;
- Bring together all parts in an assembly, building all constraints mates so to match the number of degrees of freedom (DOF) of the real unit;
- Create  $n$  global parameters, equal to the assembly DOF, and associate these parameters, through mathematical relations, to dimensions linked with constraints so to guarantee the correct motion of the assembly parts;
- Create *virtual parts* representative of fluid volumes by copying and filling cavities within real parts; the geometries of *virtual parts*, pending on the unit type, mode of operation and assembly creation, might be dependent or not on a position parameter. These parts may, for example, be representative of inlet and delivery volumes, variable volume chambers, gaps in between spool lands etc.
- (if necessary) Intersect *virtual parts* so to generate *intersection parts* that might represent flow passage areas or common (*shared*) volumes;
- Create distance, area or volume features (depending on the analysis) within *virtual parts*, so to quantitatively appraise stipulated (user defined) characteristics also when these vary with time;
- Create *relational features* to further combine analyses features or to transfer measurements data from the parts to the assembly level;
- Create multiple assemblies configurations to evaluate the variable chamber volume derivative;
- Run the simulation to evaluate and visually inspect parameters plots identified by *relational features*;
- Export obtained results for post-processing purposes.

As stated a characteristic of this methodology lies in the use of *virtual parts*: by inheriting from real components their own geometry based on parent/child relations and on position parameters introduced to define the assembly motion, *virtual parts* do represent oil volumes within the pump unit on which geometric quantities can be measured at each instant of the

pump duty cycle.

Coming to the analysis of the gerotor pump characteristics, the procedure is described in the following paragraphs. The adopted modelling, with reference to possibilities set forth in paragraph 2.1, is identified as type  $N+2$ .

In detail the above methodology has been applied to the gerotor pump shown in Figure 5.

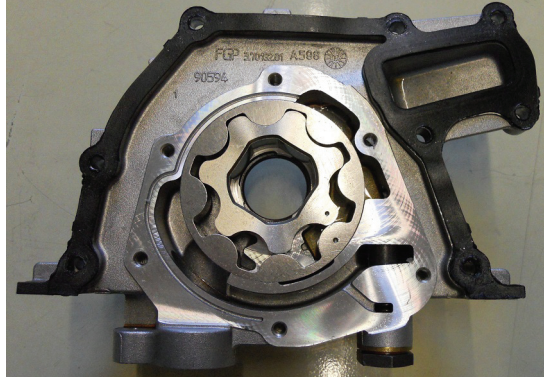


**Fig. 5. Digital image of the real gerotor pump**

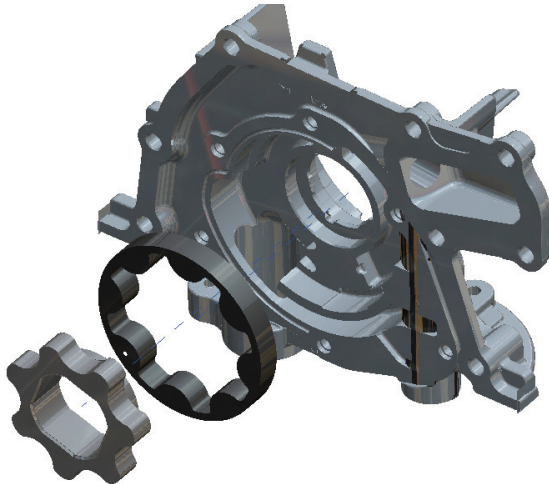


**Fig. 6. Exploded view of pump components**

#### **4.1 Creation and assembly of real model parts in Pro/E**

The first step consisted in creating part models of the main components of the pump i.e. the casing and the two gears with circular arcs profiles. In fact these parts have been imported from existing models via STEP files. Thereafter, parts shown in the exploded view in Figure 6 have been assembled applying, for each mobile element, appropriate constraint mates that only allow rotation about fixed axes. Gears axes were so constrained to be col-linear with respective axes in the casing (rotation centres  $O_i$  and  $O_e$ ) and their front planes made coincident with the plane surfaces of the casing.

The horizontal plane of each gear has been selected and mated with the fixed global horizontal plane of the assembly. In Figure 7 this is shown for the external gear where mating of the gear-assembly horizontal planes has been effected introducing an angular offset. This was also done for the inner gear-assembly planes. These offsets named *alfa\_outer* and *theta\_inner* correspond to rotational angles  $\alpha$  and  $\vartheta$  of the external and internal gear with respect to the fixed reference plane of the assembly. Obviously, to guarantee a proper performance of the assembly, the two gears must be set in a correct initial position. A subsequent step consisted in linking the two angular measures with a unique global rota-

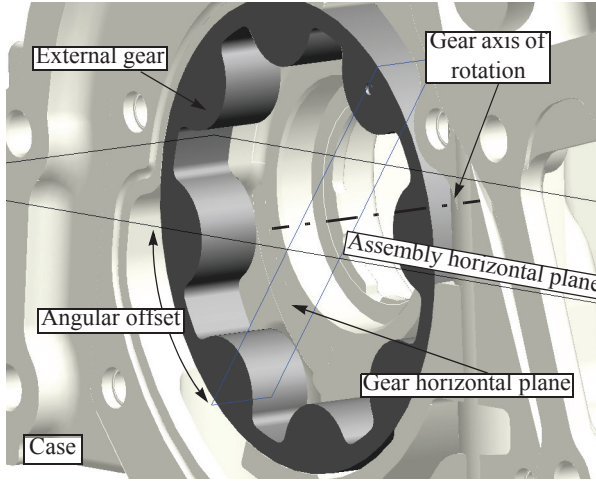


**Fig. 7. Constraint mates on the external gear horizontal plane**

tion parameter named *ANGLE* defined previously at the assembly level, whose value defines the desired angular position of the assembly. The parameter value can either be entered manually or made variable within a simulation.

In this last case, to perform a correct simulation of all involved geometric features, two strategies have been assessed that are mutually exclusive.

In the first strategy, relations have been enforced that directly link the control parameter *ANGLE* with the angular rotation  $\alpha$  of the external gear through the *alfa\_outer* parameter. As to the inner gear its parameter *theta\_inner* is defined through the gearing transmission ratio. The governing relations become:

$$\begin{aligned} \text{alfa\_outer} &= \text{ANGLE} \\ \text{theta\_inner} &= \text{ANGLE} \cdot N/(N-1) \end{aligned} \quad (22)$$

These have been slightly modified using the function “*floor*” so to keep angle values lower than  $2\pi$ . Alternatively, the control parameter *ANGLE* can be associated with the internal gear angle  $\vartheta$ .

The example in Figure 8 shows a front view of the assembly corresponding to a rotation angle of the external gear  $\alpha = 70^\circ$ . Notice the gears rotation centres and the reference planes.

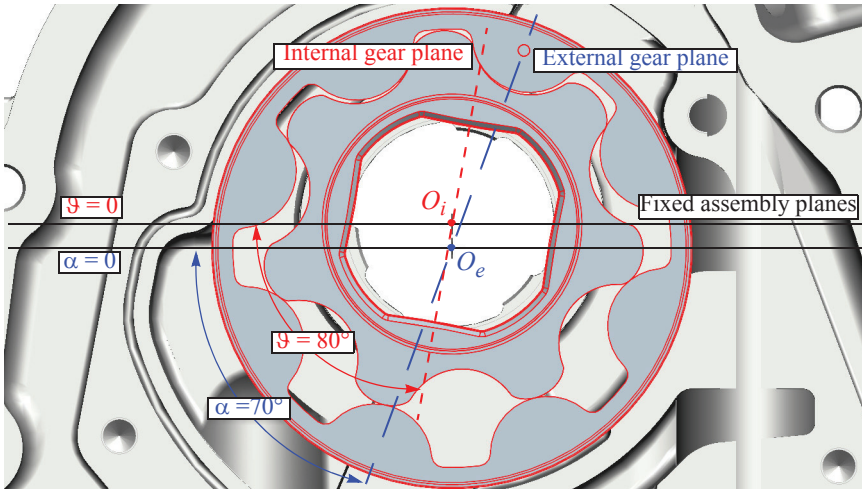


Fig. 8. Assembly close-up front view with  $\alpha = 70$  degrees

#### 4.2 Creation of virtual models

The main virtual model of the gerotor pump is the one representing a variable volume chamber. This allows the evaluation of displacement whereupon the inlet and delivery passage flow areas along with the kinematic flow ripple can be derived through appropriate actions. The chamber is built by copying from the assembly into a new part the teeth profiles of the engaging gears along with the external surface of the outer gear. These geometries are identified in Figure 9.

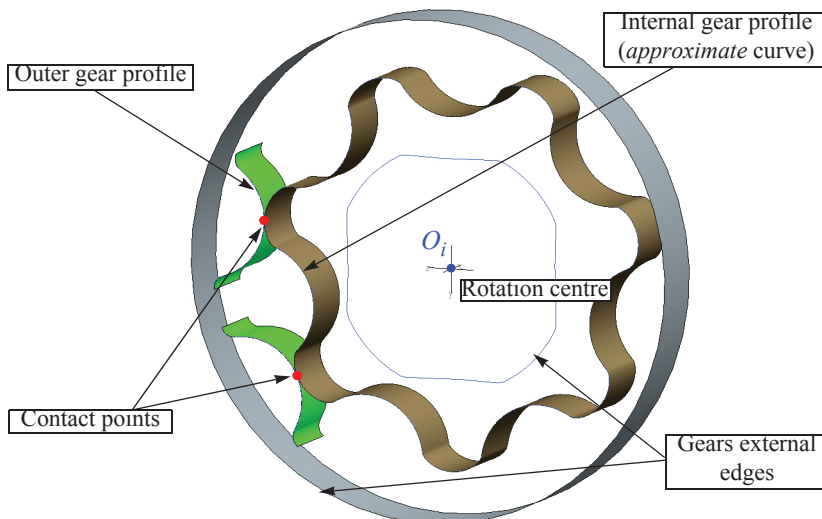
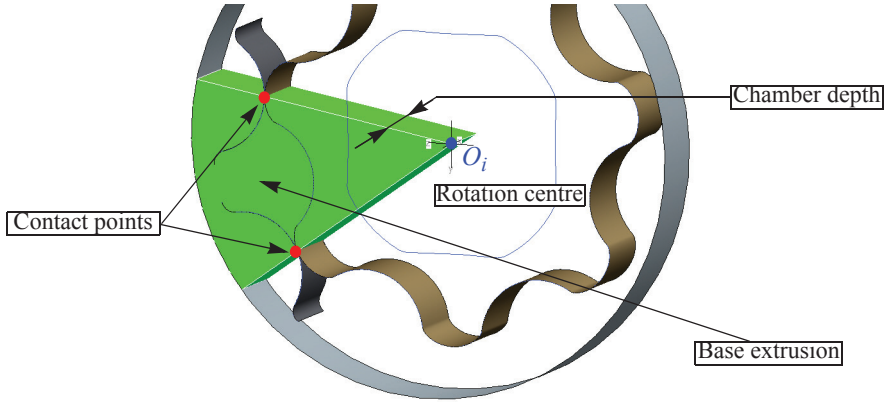


Fig. 9. Geometries to identify the variable volume chamber

The rim of the internal gear was further elaborated through the option “*Approximate*” so to generate a  $G2$  (with curvature continuity) curve. By so doing just one reference has been



**Fig. 10. Base extrusion of the variable volume chamber**

used to identify the entire profile of the gear. This curve, together with the profile of just two teeth of the outer gear, allows to univocally recognize the gears two contact points without overlapping references. These points identify the chamber as it rotates and changes in shape as gears engage.

Utilizing contact points, the external rim and the external gear centre of rotation, an elementary volume (circular sector) has been extruded whose thickness was made equal to the real chamber depth (shown in Figure 10).

Through the “cut out” function and extruded cuts procedures the volume occupied by the two gears was removed. By so doing the nominal oil volume within the chamber was obtained. This volume automatically varies with the rotation parameter *ANGLE* and is highlighted in Figure 11.

Additional virtual components representing the suction and delivery volumes have been obtained by copying the timing rims profiles in the casing and extruding them in space. The two virtual components inserted in the appropriate locations in the casing are shown in Figure 12.

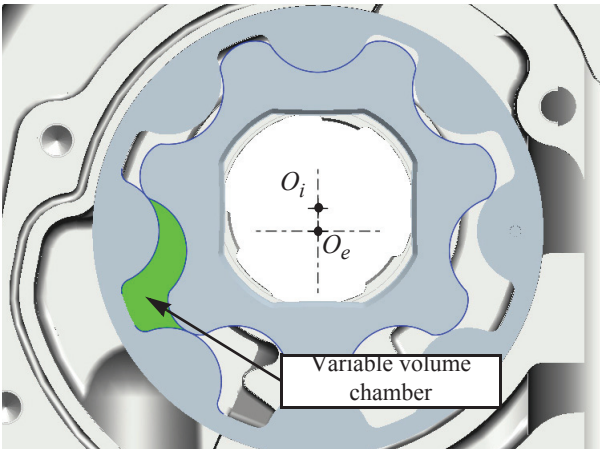


**Fig. 11. View of the variable volume chamber within the assembly**

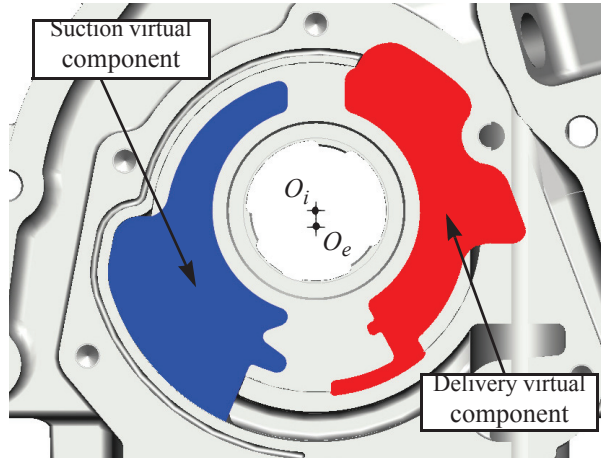


**Fig. 12. Suction and delivery volumes in the casing**

The extrusion of these two components was so effected to generate a modest intersection with the chamber volume. As this communicates with either suction or delivery ambients a variable flow passage area is being originated. By so doing two new “*virtual intersection parts*” were created whose volumes correspond to the intersections of the variable volume chamber with the suction and delivery ambients (see Figure 13, where the passage towards delivery ambient has been highlighted).

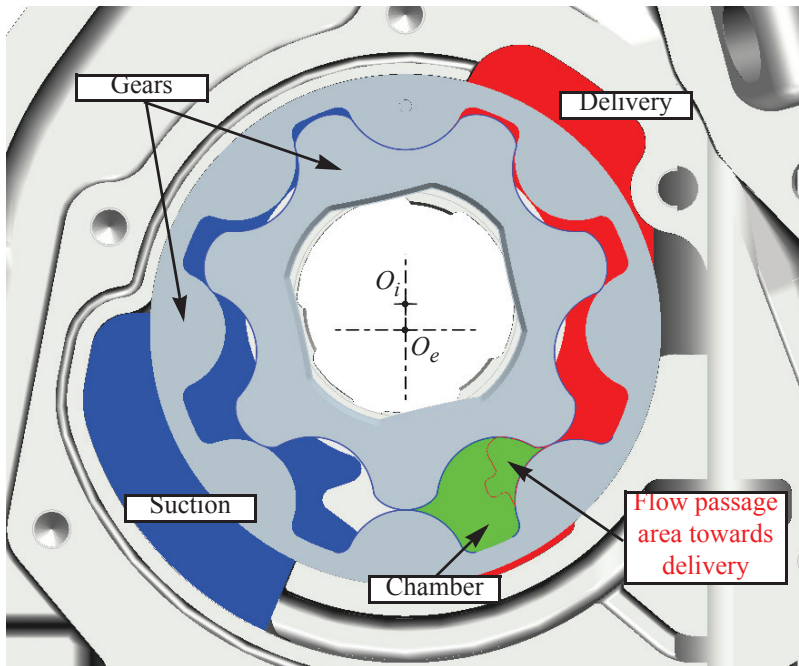


**Fig. 13. Virtual components: chamber, suction and delivery ( $\alpha = 90$  degrees)**



### 4.3 Creation of analysis and relational features - Sensitivity Analysis

Geometric quantities to be measured and tracked during simulations should now be specified: more precisely the chamber volume and its front area, along with the intersection front areas of the chamber with suction and delivery ambients.

At component level these quantities have been evaluated setting up an *analysis feature* that, through selection of a specific region, allows quantitative informations about an area (as shown in Figure 14) or a volume. Thereafter, these features have been upgraded to the assembly level via *relational features*. Analysis features generate parameters that convey

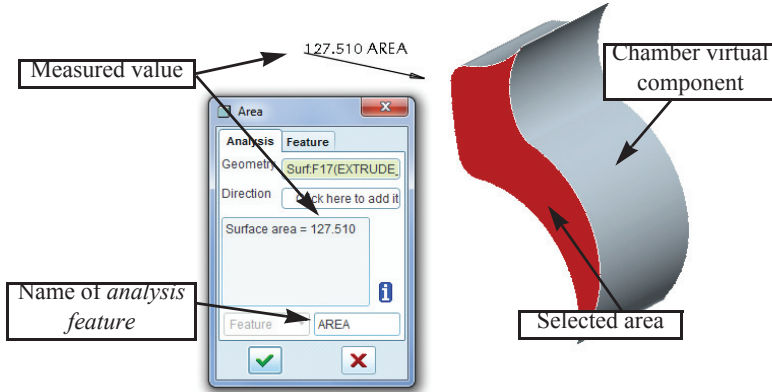


Fig. 14. Measure of chamber frontal area with an *analysis feature*

measured data and depend on the position parameter. These form the object of simulation studies (*Sensitivity Analysis*) and are evaluated, plotted or stored as position parameters change within a prescribed range and according to a number of steps defined by the user.

Since the gerotor pump completes a timing cycle in one revolution of the external gear, the unrolling of volume and flow areas with suction and delivery ambients was monitored for a single chamber with reference to that gear. Accordingly relations expressed in equation (22) have been used. Furthermore the assumption was made that all remaining chambers would behave as the simulated one due account being taken of the intervening angular shift  $\Pi = 360^\circ/N = 45^\circ$ .

### 4.4 Chamber volume derivative

To determine the chamber volume variation (as function of the shaft rotation angle) three configurations of the base assembly were generated. Leaving the central configuration unchanged, in the other two relations were introduced modifying their *ANGLE* parameter of a quantity defined by a new global parameter *DTHETA*. The intent was that of generating two specific geometric layouts for gears engagement and, namely, one in advance, the other in delay when confronted with the base assembly. The extent of either advance or delay is designated by *DTHETA*.

Gears rotation control within each configuration may follow either of two approaches introduced in paragraph 4.1. However, in the present context it is certainly expedient to evaluate derivatives as functions of shaft rotation angle  $\vartheta$ .

Thus, for every angular position of the base assembly, due account is taken of chamber vol-

umes data for the advanced and delayed configurations. If  $\vartheta^*$  references the angular condition of the base assembly and  $\Delta\theta$  the angular shift associated with parameter  $DTHETA$ , the chamber volume derivative can be approximated, through a central finite difference, as:

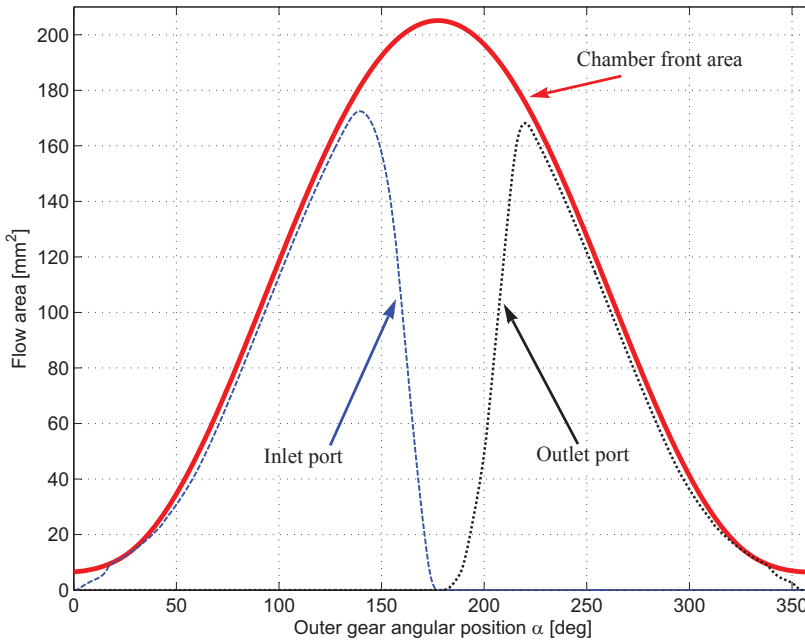
$$\frac{\Delta V}{\Delta \vartheta} = \frac{V(\vartheta^* + \Delta\theta) - V(\vartheta^* - \Delta\theta)}{2 \cdot \Delta\theta} \quad (23)$$

thereafter the equation can be profitably used in a relation feature. Finally, the evaluation of function  $F_j(\vartheta)$  leads to the determination of flow and torque through equations (2) and (8).

#### 4.5 Simulations

In Figure 15 for one revolution of the external gear (data captured every degree) simulation results are plotted for flow passage areas towards suction and delivery ambients and the frontal area of the  $j$ -th chamber. The chamber volume is simply the product between the frontal area and the gears thickness.

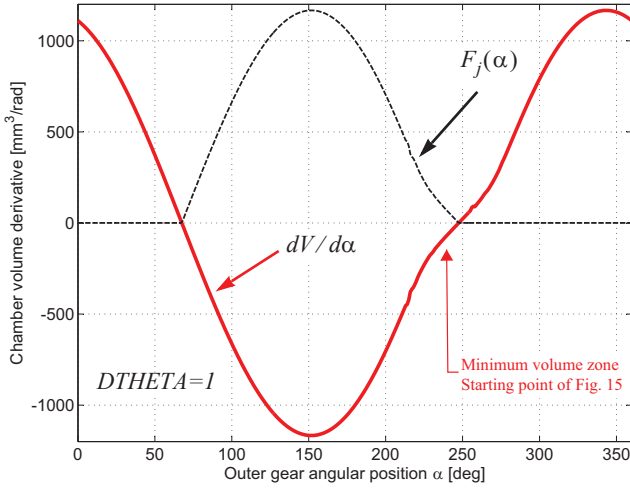
These outcomes are not confronted with analytic results, since the difference between the two data sets is not perceptible on the graphs. However, plots have been deliberately shifted  $250^\circ$  in respect to the references shown in Figure 8 to guarantee a clear reading.



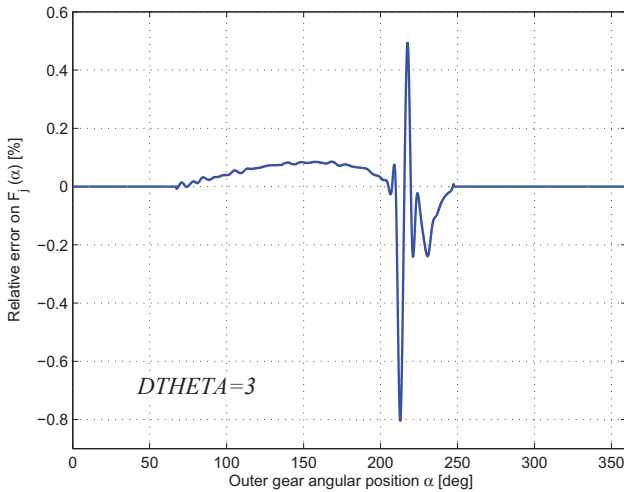
**Fig. 15. Simulation outcomes for flow passage areas**

Figure 16 illustrates chamber volume derivative and the corresponding function  $F_j(\alpha)$ , both evaluated for one revolution of the external gear. In this case,  $DTHETA$  has been set equal to 1. These results have been confronted with those stemming from the analytical  $DI$  method presented in paragraph 3.2: in Figure 17 the relative error between the kinematic functions  $F_j(\alpha)$  is presented. Slight discrepancies exist in the zone of minimum chamber volume,





**Fig. 16. Simulation outcome for chamber derivative  $dV/d\alpha$**



**Fig. 17. Relative error between analytical and simulated results for  $F_j(\alpha)$**

reaching a maximum relative error of  $0.8\%$  when confronted with the mean value of the analytical function  $F_j(\alpha)$ . These differences are triggered by software faults in detecting the contact points between the gears. In turn these imperfections are generated from various sources: precision in the construction of gears profiles, absolute tolerance chosen in the regeneration of the model, numerical accuracy of the software.

The AMESim model [12] shown in Figure 18 has been used to evaluate the kinematic flow ripple from data collected via simulations: submodel **A** requires text files with the punctual values of chamber volume and its derivative, while submodel **B** loads data of the flow passage areas. These values are then interpolated, duplicated and shifted of the required angle to generate the kinematic flow ripple inside submodel **C**.

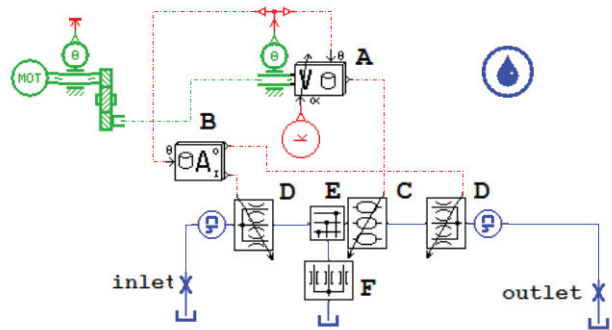


Fig. 18. AMESim model used for flow ripple calculation

This solution allows the study of the influence of the parameter *DTHETA* on the accuracy of the outcomes, particularly on the flow ripple. The analytic flow ripple index, evaluated according to eq. (4), is equal to  $\delta_Q = 4,703\%$ .

Choosing this as the reference value, the relative error of the flow ripple index obtained by simulations has been estimated at different values of parameter *DTHETA*. Matching the expectations, accuracy improves in a quasi-linear manner with the decrease of the interval where the derivative is evaluated. However, a linear increase of the required simulation time (Table 1) is observed, linked to the higher number of compelled reconstructions of the 3D model. On the other hand, there is an increase of the punctual differences between analytical and simulated results in the area of minimum volume. As already stated the model is strongly influenced by possibly defective identification of gears contact points.

Table 1. Simulation time and relative error as a function of parameter *DTHETA*

<i>DTHETA</i> [deg]	Simulation time [s]	Relative error on $\delta_Q$ [%]
3	103	0.56
2	155	0.33
1	309	0.29
0.5	617	0.11
0.2	1584	0.02
0.1	3326	0.02

5. CONCLUSIONS

Quantitative knowledge of geometric features of a fluid power pump during its entire work cycle (variable chambers volumes, flow passage areas to and from timing slots, etc) is an essential prerequisite in the assessment of a simulation model to the purpose of providing adequate predictive performance of the unit being analysed.

This research work has laid down a general methodology to attain, in a CAD 3D environment, the sought informations making use of “virtual components” and “analysis features”. “Real” components essential to the scope are gathered into an assembly and motion is applied through one or more control parameters via mathematical relations. In turn, “virtual

components”, representing fluid volumes within the pump are spawned (in a parent-child relationship) from their real counterparts and inherit respective geometries and locations. Thereafter, through an automatic change of motion control parameters values, simulations are performed and geometric quantities measured with appropriate features. Results are then further combined to yield, for example, volume derivatives as functions of the selected motion parameter.

Despite the fact that the paper has only addressed an application to a gerotor pump, the purported methodology is intrinsically so general to allow attainment of geometric features of hydrostatic pumps/motors belonging to the axial, vane and external gear families. In this respect, extensive investigations on such units do confirm the excellent matching with analytical results.

If the approach is analytic, a possible redesign of pump timing rims constrains to a complete reformulation of descriptive equations. Conversely, following the CAD proposition the methodology stays unchanged and, therefore, if effected validation studies are sufficiently robust, then confidence in obtained results might set aside the former approach.

One further advance is viable. This is related to the unfolding of “macros” to perform some of the envisaged operations automatically: even not-expert users could then profit of the whole procedure. One final aspect is worth noting and namely investigating the possibility of porting the procedure within other “high-end” CAD environments.

## NOMENCLATURE

$A$ (9)	passage area between chamber and inlet/outlet volume	$\text{m}^2$
$C_e$	discharge coefficient	-
$\mathbf{F}_e, \mathbf{F}_i$	force acting on outer and inner gear	N
$F_j$ (9)	kinematic function for the $j$ -th variable volume chamber	$\text{m}^3/\text{rad}$
$H$	gears thickness	m
$N_V, N$	number of variable volumes in a generic pump	-
$n_c$	number of cycles per shaft revolution	1/rev
$O_e, O_i$	centre of rotation of outer and inner gear	
$p_j$	pressure in the $j$ -th hydraulic capacity	Pa
$p_{out}$	pressure at the outlet port	Pa
$\bar{Q}$	flow rate through port plate	$\text{m}^3/\text{s}$
$\bar{Q}$	integral average of kinematic flow rate	$\text{m}^3/\text{s}$
$Q_j$	net ingoing volumetric flow rate in the $j$ -th hydraulic capacity	$\text{m}^3/\text{s}$
$Q_{th}$	kinematic (theoretical) flow rate of the pump	$\text{m}^3/\text{s}$
$T_e, T_i$	pressure induced torque on outer and inner gear	Nm
$T_j$	balancing torque on external gear for the $j$ -th chamber	Nm
$T_{ind}$	indicated torque at pump shaft	Nm
$T_{th}$	ideal torque at pump shaft	Nm
$t$	time	s
$V$	pump total displacement	$\text{m}^3/\text{rev}$

$V_0$	unit displacement of a pump single chamber	$\text{m}^3$
$V_e, V_i$	control volume relative to outer and inner gear	$\text{m}^3$
$V_j$	volume of the $j$ -th hydraulic capacity	$\text{m}^3$
$x_I, x_2, y_I, y_2$	geometrical coordinates of contact points between gears	m
$\alpha$	angular position of outer gear	rad
$\beta$	fluid bulk modulus	Pa
$\Theta$	angular period of evaluation of $Q_{th}$	rad
$\Delta\theta$	angular shift associated with $DTHETA$	rad
$\Delta p$	pressure differential between chamber and inlet/outlet	Pa
$\delta_Q$	flow ripple index	-
$\vartheta$	internal gear angular position	rad
$\vartheta^*$	generic angular position of base assembly	rad
$\Pi$	angular shift between two consecutive chambers	rad
$\rho$	fluid density	$\text{kg/m}^3$
$\rho_{e1}, \rho_{e2}, \rho_{i1}, \rho_{i2}$	vector rays for outer and inner gear	m
$\rho_e, \rho_i (\psi, \alpha_0)$	equations of outer/inner gear profile in polar coordinates	
$\Psi_{e1}, \Psi_{e2}, \Psi_{i1}, \Psi_{i2}$	phase of vector rays for outer and inner gear	rad
$\omega$	shaft speed	rad/s

## ACRONYMS

DI	derivative-integral analytical method
ID	integral-derivative analytical method
$N$	variable chambers in a control volume simulation approach
$X$	variable/fixed volumes in a trapped chamber simulation approach
<i>ANGLE</i>	global parameter defining assembly angular position (in Pro/E)
<i>DTHETA</i>	global parameter defining advance/delay between assemblies (in Pro/E)
<i>alfa_outer</i>	rotational angle $\alpha$ of outer gear (in Pro/ENGINEER)
<i>theta_inner</i>	rotational angle $\vartheta$ of internal gear (in Pro/ENGINEER)

## REFERENCES

- [1] Gilardino, L., Mancò, S., Nervegna, N. and Viotto, F., An Experience in Simulation: the case of a Variable Displacement Axial Piston Pump, *Proc. of the Fourth JHPS International Symposium*, Tokyo, Japan, 1999, pp. 85-91.
- [2] Mancò, S. and Nervegna, N., Simulation of an External Gear Pump and Experimental Verification, *Proc. of the First JHPS International Symposium*, Tokyo, Japan, 1989.
- [3] Mancò, S., Nervegna, N., Rundo, M. et Al., Gerotor Lubricating Oil Pump for IC Engines, *SAE Trans. 1998 - Journal of Engines*, Vol. 107, pp. 2267-2283. SAE Paper

982689.

- [4] Caretto, R., Mancò, S., Nervegna, N. and Rundo, M., Modelling, Simulation and Experimental Studies on a Variable Displacement Radial Piston Pump Prototype for Automotive Applications, *ASME Fluid Power Systems and Technology 1996 Collected Papers*, Vol. 3, pp.1-9.
- [5] Mancò, S., Nervegna, N., Rundo, M. and Armenio, G., Modelling and Simulation of Variable Displacement Vane Pumps for IC Engine Lubrication, *SAE Technical Paper 2001-01-1601*, 2001.
- [6] Roccatello, A., Mancò, S. and Nervegna, N., Modelling a Variable Displacement Axial Piston Pump in a Multibody Simulation Environment, *ASME Trans. 2007 - Journal of Dynamic Systems, Measurement and Control*, Vol. 129, No. 4, pp. 456-468.
- [7] Ivantysynova, M., Huang, C. and Christiansen, S.-K., Computer aided valve plate design - an effective way to reduce noise, *Proc. of SAE Commercial Vehicle Engineering Congress & Exhibition 2004*, Chicago, USA. SAE Technical Paper 2004-01-2621.
- [8] Ivantysynova, M. and Christiansen, S.-K., Automatic Valve Plate Design based on optimized Pressure Profile, *Proc. of IFPE Technical Conference 2005*, Las Vegas, USA, pp. 519-529. Technical Paper NCFP I05-14.1.
- [9] Wieczorek, U. and Ivantysynova, M., CASPAR - A Computer Aided Design Tool for Axial Piston Machines, *Proc. of Bath Workshop on Power transmission and Motion Control - PTMC 2000*, Bath, UK, pp. 113 - 126.
- [10] Wieczorek, U. and Ivantysynova, M., Computer Aided Optimization of Bearing and Sealing Gaps in Hydrostatic Machines - The Simulation Tool CASPAR, *Int. Journal of Fluid Power*, Vol. 3 (2002), No. 1, pp. 7-20.
- [11] Fabiani, M., Mancò, S., Nervegna, N., Rundo, M. et Al., Modelling and Simulation of Gerotor Gearing in Lubricating Oil Pumps, *SAE Trans. 1999 - Journal of Engines*, Section 3, Vol. 108, pp. 989-1003. SAE Technical Paper 1999-01-0626.
- [12] Mancò, S., Nervegna, N. and Rundo, M., A Contribution to the Design of Hydraulic Lube Pumps, *Int. Journal of Fluid Power*, Vol. 3 (2002), No. 1, pp. 21-31.

## BIBLIOGRAPHY

- [13] Babbone, R., Bottazzi, D., Cagni, G., Grasselli, F. and Milani, M., CAE Design of Orbit Annular Machines, *Proc. of the Twelfth Scandinavian International Conference on Fluid Power*, Tampere, Finland, 2011.
- [14] Ham, Y.-B., Kim, D.-M., Gu, J.-S., Jeon, S.-H. and Kim, S.-D., An Analysis of the Volumetric Displacement of an Hydraulic Gerotor Motor, *Proc. of the Twelfth Scandinavian International Conference on Fluid Power*, Tampere, Finland, 2011.

# Efficient Fluid Power



# Thermal Insulation in Enhancing Performance Characteristics of Hydraulic Accumulator

**J. Juhala, J. Kajaste, M. Pietola**

Aalto University

School of Engineering

Department of Engineering Design and Production

P.O.Box 14400

FIN-00076 Aalto, Finland

email: [jyri.juhala@aalto.fi](mailto:jyri.juhala@aalto.fi)

## ABSTRACT

The hydraulic accumulator as an energy storage component in hydraulically operated regenerative systems is not perfect. Further energy losses in form of heat transfer from gas to walls of the accumulator and to surroundings is a well-known problem. Quick filling of the accumulator is nearly adiabatic process where the temperature of gas increases. The stored hydraulic energy escapes in form of heat from gas through the walls of the accumulator to the environment.

The efficiency of hydraulic accumulator can be improved by using different heat recovery or insulation methods. Several methods to improve the energy efficiency of hydraulic accumulators can be found on the literature; preventing convection, restraining the raise of temperature during the compression or using thermal insulation.

The aim of this study is to design and test one potential insulation method to improve the characteristics of hydraulic accumulator which is used as energy storage. The results of this study consist of multi-disciplinary simulations and measurements of insulated piston type hydraulic accumulator. The results demonstrate that certain thermal insulation can improve the energy efficiency of accumulator significantly.

## 1 INTRODUCTION

In hydraulic regenerative systems, where releasing potential (or kinetic) energy is stored and used to compensate the need of external energy in next work cycle, the effectiveness performance could be enhanced - even significantly. On the other hand, every energy conversion from one form to another induces losses since none of conversions are ideal and the number of conversions in regenerative operations should be kept to minimum. In hydraulic power transmission operated machines this means that the releasing potential and



kinetic energy which is first converted to hydraulic energy should be stored in that form and further conversions, e.g. into electric, should be avoided.

The energy efficiency of accumulator can be improved by using different heat recovery methods. The escaping energy, in form of heat, from gas to walls and to the environment can be avoided by blocking the gas flow inside the accumulator using elastomeric foam (porous material), since in gases and liquids the convection is the primary method of heat transfer [1, 2]. Apart from that, the rise of temperature can be prevented by attaching the heat regenerator inside the gas volume [3, 4]. The third method is to block the heat transfer between the compressed gas and the surroundings by using certain thermal insulation, which can be located either outside or inside accumulator (in gas volume). The latter one is preferable since it prohibits the heat transferring from gas to accumulator structure.

This study describes the multiphysics model of hydraulic accumulator and introduces the experimental tests made with prototype. The simulation results of simulation model are validated using test data from measurements of the original piston type hydraulic accumulator. The experimental study of modified accumulator attached with thermal insulation is also presented.

## 2 INSULATED ACCUMULATOR AND EXPERIMENTAL TEST SETUP

### 2.1 Insulation concept

To prevent the energy to escape from the compressed gas to surroundings a special insulation method was developed. The idea is to put heat insulation material inside the accumulator but to keep the body of the accumulator in same form as in the reference (original) version. The schematic drawing of the insulation is presented in *Figure 1*. In *Fig. 1* the number 1 indicates the insulating material which is aerogel [5], the number 2 is the inner tube which purpose is to provide sliding surface for the piston of the accumulator as the insulating material is porous and for that reason is not suitable to act as an opposite surface for the sealing of the piston.

The construction of the accumulator is implemented so that the pressure in both sides of the inner tube is the same. This is done by drilling holes through the inner tube at top part of the construction (number 3 in *Fig. 1*). These holes allows the gas to flow from main gas chamber (5 in *Fig. 1*) to the chamber filled with insulating material (number 1 in *Fig. 1*) keeping the pressure difference over the inner tube near zero, which means that inner tube is not carrying the gas pressure but the pressure is supported by the outer structure (number 4 in *Fig. 1*). This offers possibility to manufacture the wall thickness to as thin as possible to minimize the heat capacity affected to compressed nitrogen.

In this study, the inner tube is manufactured using stainless steel but it can be produced using any other material which fulfils the requirements. The material of the inner tube must tolerate the chemical effects caused by hydraulic fluid, the operating temperature of the accumulator (including the peak temperature at the end of the compression phase) and offer well enough surfaces for piston sealing.

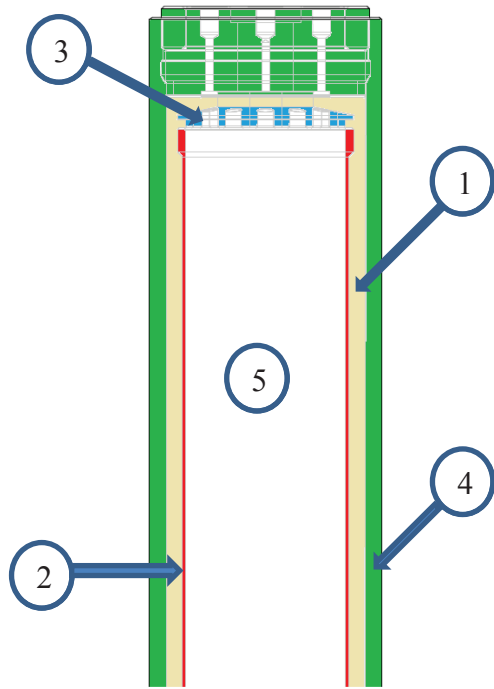


Figure 1: Schematic drawing of the insulation method.

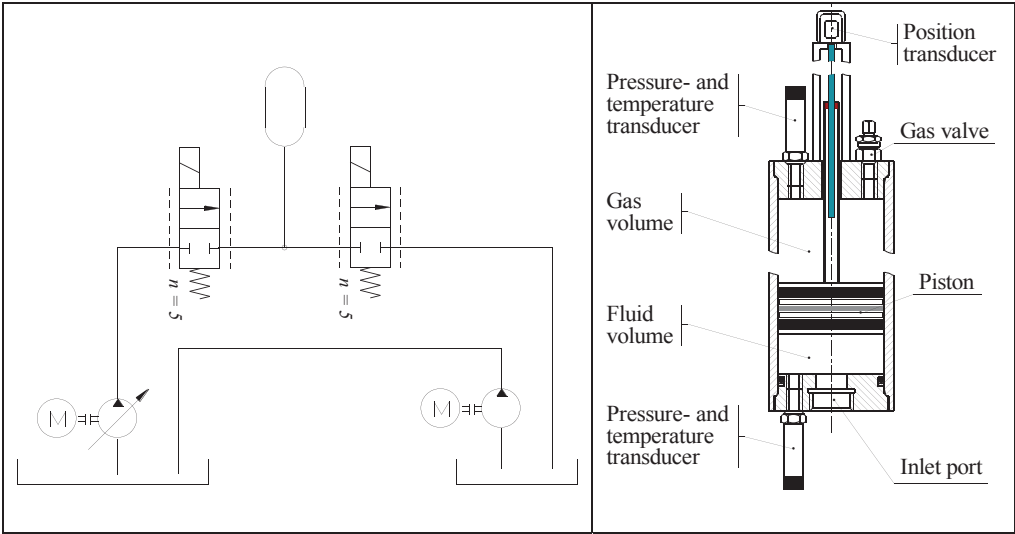


Figure 2: Hydraulic circuit of the test setup (left) and schematic drawing of piston type accumulator with sensors (right).

## 2.2. Measurement test setup

The experimental test-rig was built using two DFCUs (Digital Flow Control Unit) with five parallel connected on/off valves. The digital hydraulic was chosen to control the inflow/outflow to accumulator as it offers leak free characteristics for holding phase.

The hydraulic circuit consists of the main pump unit, two digital flow control units (DFCUs), the hydraulic accumulator under investigations and separate buffer tank with an additional pump. The separate tank and pump are attached to the test system to shorten the tank line. The hydraulic circuit of the test setup is illustrated in *Fig. 2*.

The measured quantities are pressures in both chambers of accumulator and close to the valve blocks; flow rate to/from the accumulator, the location of the piston; temperature of gas and oil. In the measurements of the insulated accumulator, one temperature sensor was attached between the aerogel and the wall of accumulator (outer tube) so that the sensor is not in contact with the wall. The location of the temperature sensors is shown in *Fig. 3* and same locations were used in the simulations.

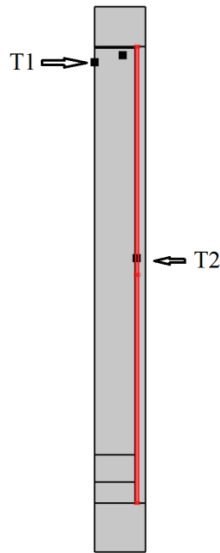


**Figure 3: Location of temperature sensors in insulated accumulator.**

## 2.2. Test cycle

The measurement (and simulation) procedure consists of three stages; the compressing phase, holding phase and decompressing phase.

In the compressing phase the accumulator is driven using reference flow rate of 30 l/min for the digital hydraulic flow controller to adjust the inflow rate to the accumulator under investigation. The filling process is continued until the gas volume has reduced from 6 litres to 3 litres which observed using the position transducer attached to piston.

After the compressing phase, the valves are closed for 60 seconds. The duration of the holding phase was chosen to one minute because almost all the heat escapes during that time period and authors also expect it to be typical storing time in regenerative systems e.g. in hydraulic hybrid vehicles.

The holding period is followed by the decompressing phase where the stored hydraulic energy is run down with the same flow rate as in the compressing phase.

### 3 SIMULATION MODEL

The multidisciplinary model of the piston type hydraulic accumulator is implemented using Comsol Multiphysics software, which is multidisciplinary finite element method (FEM) simulation software [6]. The model of the accumulator is mainly the same as used in previous study [4] and it is composed of three physical phenomena; heat transfer, turbulent flow system (Navier-Stokes) and moving mesh (movement of the piston).

The heat transfer and the flow system of the nitrogen is modelled using Conjugate Heat Transfer module with turbulent flow. The subdomain of gas volume is set as fluid and for the walls of gas volume a boundary condition is set to be “Wall, no slip”. As the heat transfer in gasses is mainly done by the natural convection, the volume force ( $\rho\mathbf{g}$ ) is added to subdomain of the gas chamber. The outside temperature of the accumulator’s structure is expected to stay at constant room temperature and the boundary condition is  $T = T_{room}$ , for temperature at outer wall.

The simulation software does not recognize the change of the gas volume, which is modelled using the moving mesh module. The rise of the pressure during the compression phase is modelled as turbulent inflow to the gas volume with normal inflow velocity as the accumulator piston since the moving piston produces kind of “inflow” to compressing gas volume. The boundary condition for inlet is the average inflow speed, which is same as the piston velocity. The equations for turbulent flow system and heat transfer are presented in detail in [6].

The rise of temperature of the nitrogen during the compression phase is simulated using the heat source  $Q$  in the subdomain of the gas volume.  $Q$  is calculated using the ideal gas law and the equations of adiabatic process. First the amount of nitrogen in moles is calculated from ideal gas law using initial values:

$$pV = nRT \rightarrow n = \frac{p_0 V_0}{RT_0} \quad (1)$$

The amount of nitrogen is used to calculate work done during adiabatic compressing phase

$$W = -\alpha nRT_0 \left[ \left( \frac{V}{V_0} \right)^{1-1.4} - 1 \right] \quad (2)$$

By derivation of (2) we get the total power for the heat source  $Q$  at the subdomain of gas

$$Q = \frac{dW}{dt} \quad (3)$$

The mesh for the calculation is automatically generated using Comsol software's automatic physics controlled mesh feature with setting of element size is imposed to "Extra coarse". The mesh of normal accumulator is illustrated in *Fig. 4(left)*.

The moving mesh decreases the quality of the mesh elements as single mesh element stretch when the piston moves. *Figure 4(right)* shows the mesh quality at situation when the compression has completed, red colour indicates good mesh quality while blue colour is for poor mesh quality. It can be seen that mesh elements which are in worse condition after the movement of the piston are mainly located in the oil volume. This is not a problem, since the effect of oil (heat transfer and flow in oil volume) to the temperature of gas is negligible.

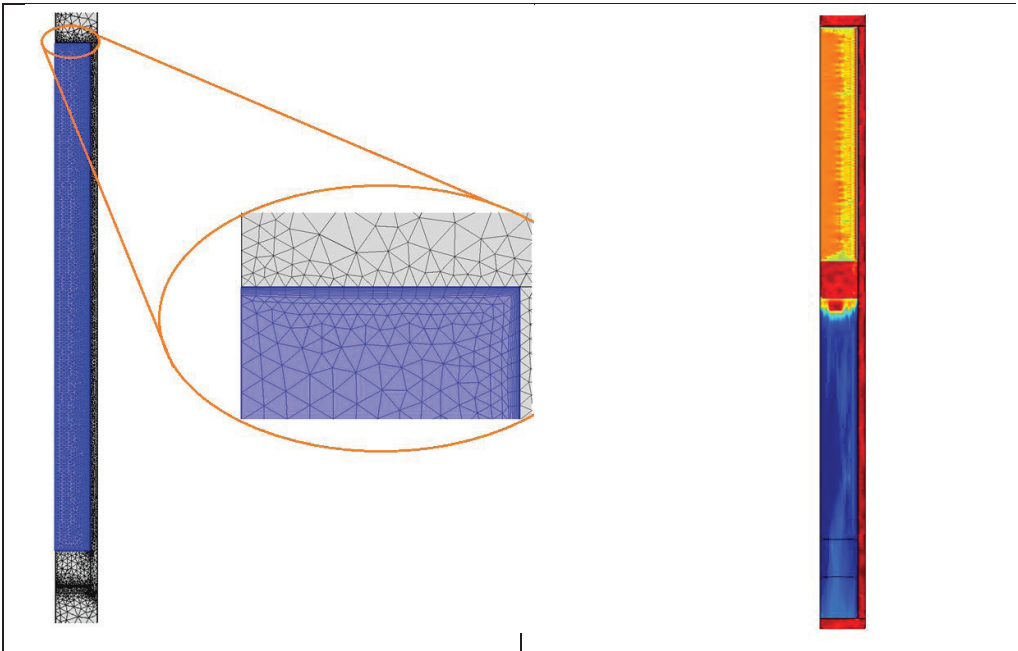


**Figure 4: Automatically generated physics controlled mesh of normal accumulator (left) and the quality of mesh elements after compression ( $t=6s$ ).**

### 3.1 Differences in model of the insulated accumulator

The model of the insulated version of the hydraulic accumulator is basically the same as the model of the normal accumulator. However, the geometry differs from the normal version as the thermal insulation material and the sliding pipe was added to construction. The

geometry properties were simplified so that the thickness of the insulating material and the inner tube were equivalent to real prototype.

In the model of insulated accumulator also three extra materials were added to simulation model; stainless steel 304L (the inner tube), aerogel (the main insulating material) and polyoxymethylene POM (small plate in top of the construction acting as insulating layer between gas and the top part of the accumulator). Comsol software offers good library of various materials which are described as functions of required quantities, but some of them are only partially modelled e.g. the heat capacity of POM is not implemented. The missing material property (the heat capacity of polyoxymethylene) were obtained from the literature [7] and attached to the model as a function of the temperature.

## 4 RESULTS

The results of the simulation model of hydraulic accumulator are presented in the following section. Also the experimental results of the original accumulator and the thermally insulated one are introduced.

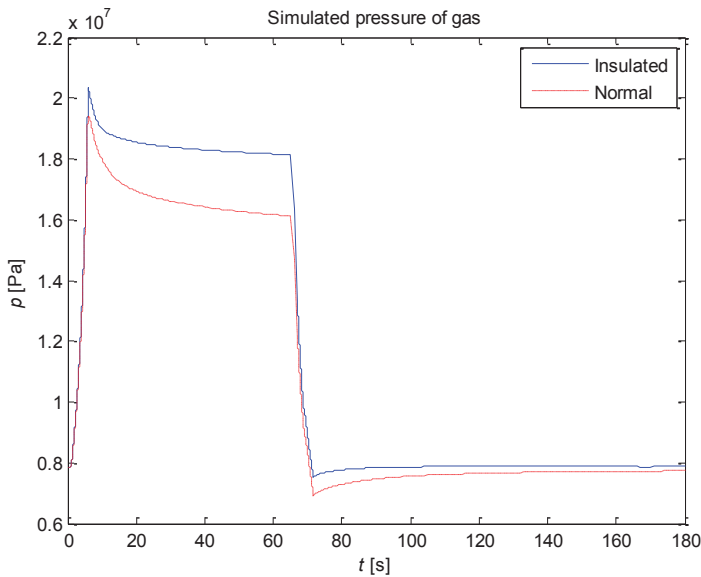


**Figure 5: Simulated pressure of the nitrogen in normal and insulated accumulator**

### 4.1 Simulation results

The results of simulations of both of the accumulators are presented in *Figures 5-7*. *Figure 5* shows the simulated pressure behaviour of the nitrogen inside the accumulator; the dash-dot line represents the unmodified accumulator and the solid curve depicts the insulated one.

Figure 6 presents the simulated temperature of the gas in both normal and insulated accumulator. The locations of sensors  $T_1$  and  $T_2$  are according to Fig 3. The figure shows clearly that the insulation is functional as temperature  $T_2$  is not increasing as much as  $T_1$  inside the insulated accumulator.

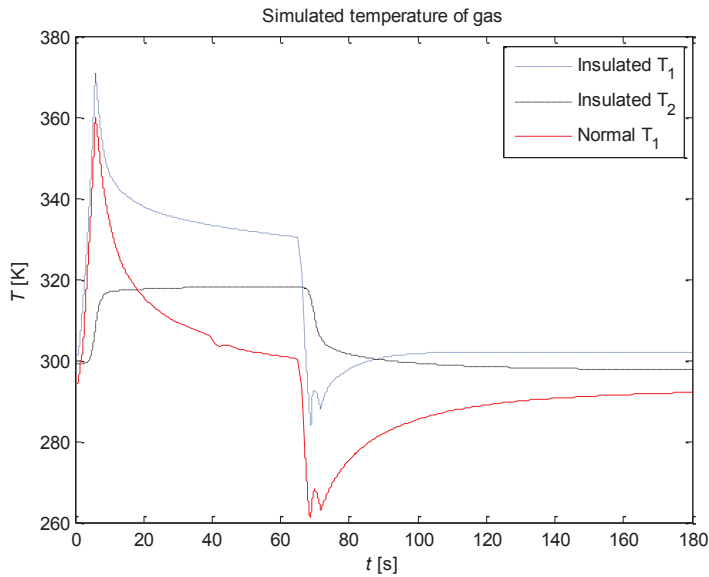


Figure 6: Simulated temperature behavior of the gas.

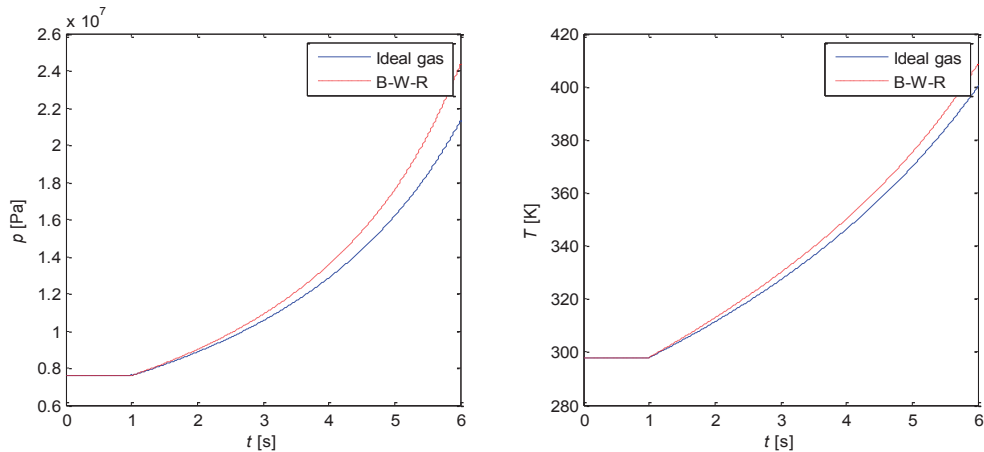


Figure 7: Comparison between Ideal gas equations and B-W-R equations during the compression phase.

In the multiphysics simulations the pressure and temperature were modelled using equations from ideal gas law which are well-known to be inaccurate when applied to real

gases –especially at the higher pressure levels. To show the differences in temperature and pressure between simulations with ideal gas and real gas, a simple simulation of compressing period has been carried out using Simulink software. The “real gas” of this simulation is implemented using Benedict-Webb-Rubin equation of state which is described in [1, 8]. The results of simulations are shown in *Fig. 7*.

#### 4.2 Results of experimental tests

The results of experimental tests are presented in *Figures 8-10*. *Figure 8* presents the measured pressure of both of the accumulators during the measurement cycle. Figure shows that the pressure decreases less during the holding phase in insulated accumulator.

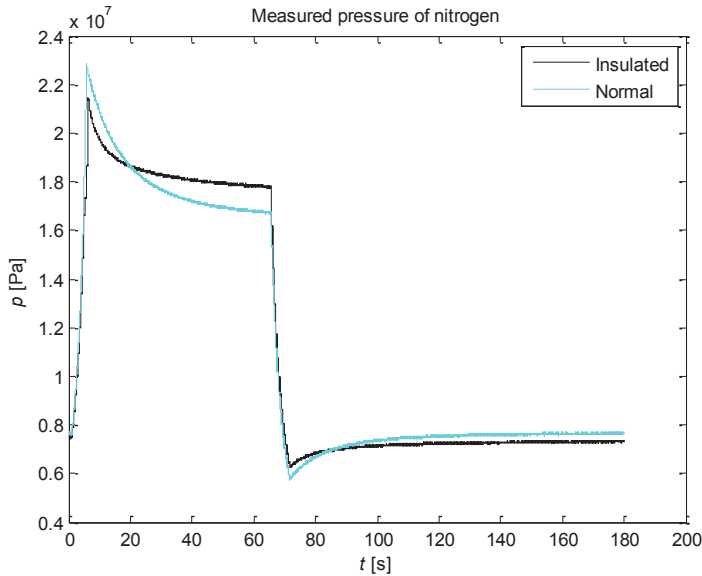


**Figure 8: Pressure inside the gas chamber.**

*Figure 9* illustrates the measured temperature behaviour in both the insulated and the original accumulator. The locations of the temperature transducers are presented in *Fig 3*. The figure shows that temperature does not rise as much in insulated accumulator at location T1 as in the original accumulator.



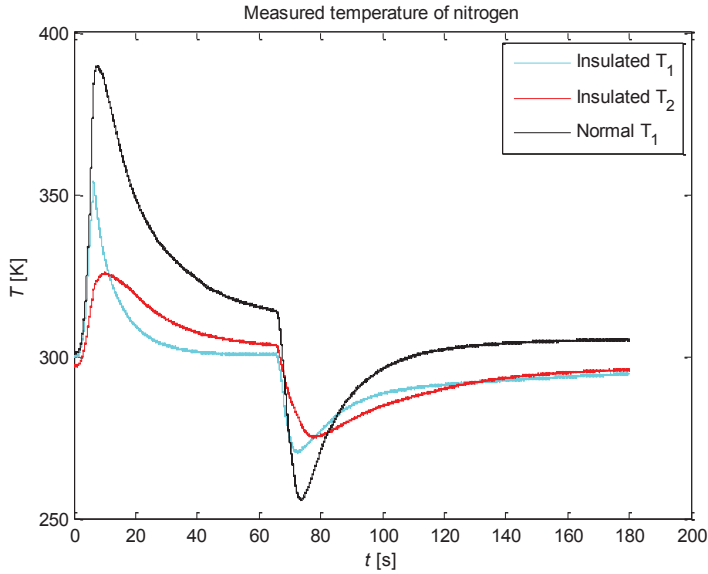


Figure 9: Temperature of the nitrogen

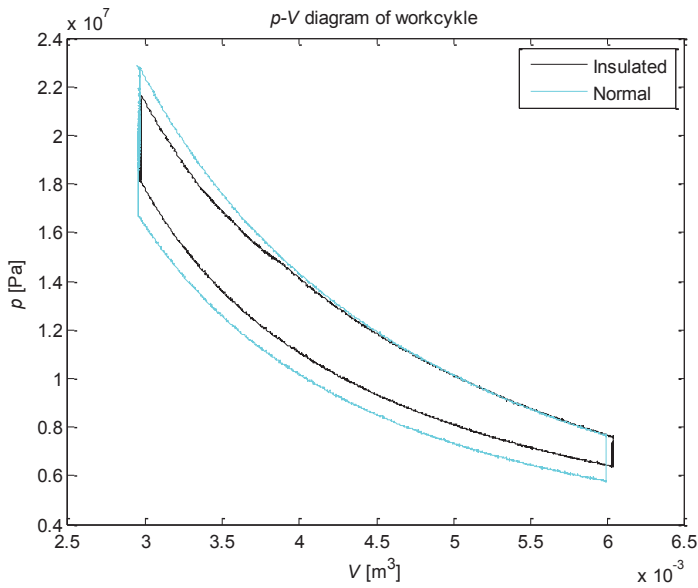


Figure 10:  $p$ - $V$  diagram of the work cycle.

Figure 10 shows the  $p$ - $V$ –diagram of the measured work cycle. The figure manifests that the insulation concept improve the efficiency significantly. The efficiency of the accumulator has increased from approx. 72,5 %  $\rightarrow$  80 % by using the heat insulation.

## 5 DISCUSSION AND CONCLUSIONS

A new concept for thermally insulating the hydraulic piston type accumulator was introduced, modelled using multidisciplinary simulation software and functional prototype was manufactured.

The results of multiphysics simulations show that the final values of pressure at the end of the compressing phase were slightly lower than in the measurements. This is expected to be partly a consequence of inaccuracy of the ideal gas law and for that reason it is advisable to use the real gas equations e.g. Benedict-Webb-Rubin equation of state in simulations. Other reason for differences in pressure between simulations and measurements of insulated accumulator is the uncertainty of the volume of the gas. The amount of nitrogen in insulating chamber (number 1 in *Fig. 1*) is difficult to estimate as the insulating material, aerogel, is porous material.

The temperature of nitrogen in normal accumulator was acting as expected. In the compression phase the temperature rose slightly more in measurements than in the simulations which also indicates the requirement to use more accurate gas models. Instead of that, the temperature behaviour of the insulated accumulator had substantial difference. The measured temperature at location T1 rose only to 354 K at the end of compressing phase although the simulations expected the temperature to rise up to 370 K. This is expected to be measurement error because the pressure behaviour does not support the temperature curve. The position of the temperature transducer may be too close to or even touching the cover of accumulator in spite of extra effort used during the assembling of the prototype.

The results of the experimental tests of insulated accumulator show that the energy balance of piston type accumulator can be improved. The results manifest that gas temperature of insulated accumulator does not increase as much as with original one and the pressure of the gas in insulated version decreases less during the holding period.

However, thermal insulation seems to be a potential option to improve the energy efficiency of hydraulic accumulator. The results showed improvement from circa 72 % up to 80 per cent, which means that there are still possibilities for future improvements. Authors will continue their work and will publish another method for improving the energy balance of accumulator and combine earlier presented methods to the following prototypes. Also, the multidisciplinary model of piston type accumulator with real gas equations will be introduced in near future.

## ACKNOWLEDGEMENT

This study is related to MIDE/HybLab and EFFIMA/DiHy projects which are funded by Aalto University and Finnish Metals and Engineering Competence Cluster (Fimecc Ltd.).

## REFERENCES

- [1] Juhala, J. et al. 2010. Energy losses in piston type hydraulic accumulator. 7th International Fluid Power Conference (7th IFK), March 22-24, Aachen, Germany. ISBN 978-3-940565-93-8
- [2] Pourmovahed, A., Beachley, N.H., Fronczak, F.J. Modeling of a hydraulic energy regeneration system – Part I: Analytical treatment. Transactions of the ASME, Vol. 114, No. 1, March, 1992. pp. 160165.
- [3] Stroganov, A., Sheshin, L. Accumulator efficiency improvement: Heat insulation or regeneration. The 11th Scandinavian International Conference on Fluid Power, SICFP'09, June 24, 2009, Linköping, Sweden. 13 p. ISBN 978-952-15-1761-7 (CD-ROM).
- [4] Juhala, J., Pietola, M. HYDRAULIC ACCUMULATOR AS ENERGY STORAGE. Proceedings of the ASME 2011 International Mechanical Engineering Congress & Exposition, IMECE2011, November 11-17, 2011, Denver, Colorado, USA
- [5] Aspen Aerogels, Inc. Data sheet of Pyrogel 6650. Available at [http://www.aerogel.com/products/pdf/Pyrogel\\_6650\\_DS.pdf](http://www.aerogel.com/products/pdf/Pyrogel_6650_DS.pdf) (visited 15.4.2012)
- [6] COMSOL, Comsol Multiphysics User's Guide ver. 4.2a. Comsol software documentation.
- [7] Srivastava Shweta, et. al. Phonons and Heat Capacity of Polyoxymethylene. Journal of Applied Polymer Science, Vol. 122, 1376-1381 (2011)
- [8] Otis, D. A. and Pourmovahed, A. *An Algorithm for Computing Nonflow Gas Processes in Gas Springs and Hydropneumatic Accumulators*. Journal of Dynamic Systems, Measurements, and Control, March 1985, Vol. 107, pp. 93-96

## NOMENCLATURE

$g$	gravity, 9,81 [m/s <sup>2</sup> ]
$k$	thermal conductivity [W/(m K)]
$n$	number of moles
$p$	pressure [Pa]
$p_0$	pressure at beginning of test cycle [Pa]
$Q$	heat source [W/m <sup>3</sup> ]
$R$	universal gas constant, 8,314472 [J/(mol K)]
$t$	time [s]
$T$	temperature [K]
$T_0$	temperature at beginning of test cycle [K]
$T_1, T_2$	temperature sensors
$T_{\text{room}}$	room temperature [K]
$V$	volume [m <sup>3</sup> ]
$V_0$	volume at beginning of test cycle [m <sup>3</sup> ]
$W$	work of adiabatic process [J]
$\alpha$	number of degrees of freedom divided by 2 (= 5/2 for diatomic gas)
$\rho$	density [kg/m <sup>3</sup> ]

# Energy-efficient electrohydraulic compact drives for low power applications

**Dipl.-Ing. Sebastian Michel, Professor Dr.-Ing. Jürgen Weber**

Technische Universität Dresden

Institute of Fluid Power

01062 Dresden, Germany

Phone +49 351 463 33705, Fax +49 351 463 32136

E-mail: [michel@ifd.mw.tu-dresden.de](mailto:michel@ifd.mw.tu-dresden.de)

## Abstract

This paper focuses on the systematic development and investigation of new energy-efficient electrohydraulic compact drives. Configured as speed-controlled turn-key assembly, the concept combines the advantages of electromechanical drives (good energy-efficiency, compact design, user-friendliness) and the advantages of hydraulic drives (reliability, large forces, good overload protection). A systematic approach for the analysis of existing solutions that manage the unequal flows of the differential cylinder is shown. Regarding the price-sensitivity in the low power sector, the minimal use of (auxiliary) components is aimed at. Out of the derived solution space, the preferred variants for low power applications were selected. Prototypes were built up to proof and analyse the functionality of the concepts experimentally. Apart from the static and dynamic performance, the energy-efficiency was particularly examined. Finally, a comparison with electromechanical drives, which were tested on a test rig as well, is done.

**KEYWORDS:** Electric-hydrostatic actuator, energy-efficiency, compact-drive, low power applications

## 1 Introduction

Low power linear drives ( $P < 5$  kW) are used in a wide field of applications, ranging from actuators in metal cutting and forming machine tools via plastic and processing machines to building automation. Further fields of applications include mobile working and hoisting machines as well as automotive and aeronautic applications.

Although hydraulic cylinders are ideally suited for translational motions, hydraulic drives are increasingly displaced by electromechanical drives in this power class. The reasons for this are that electromechanical drives feature a good energy-efficiency on the one hand and an ease of use on the other hand. Designed as turn-key assembly, they offer advantages, such as simple installation, compact design and low maintenance for the user.

Disadvantages like for example increased wear, difficult overload protection and lower load forces are accepted.

In contrast, currently available valve controlled hydraulic drives offer high reliability, high load forces, high transmissions and easy overload protection. However, they are also marked by high power losses and higher efforts on installation, space and maintenance. This includes not only the installation of a separate power pack, but also a costly pipe layout towards the actuator, which has to be connected by qualified staff. Furthermore, in particular in machine tools, a decentralisation of the drives is desired. **Figure 1** shows the drive structures which are currently available in the area of low power applications including their advantages and disadvantages.

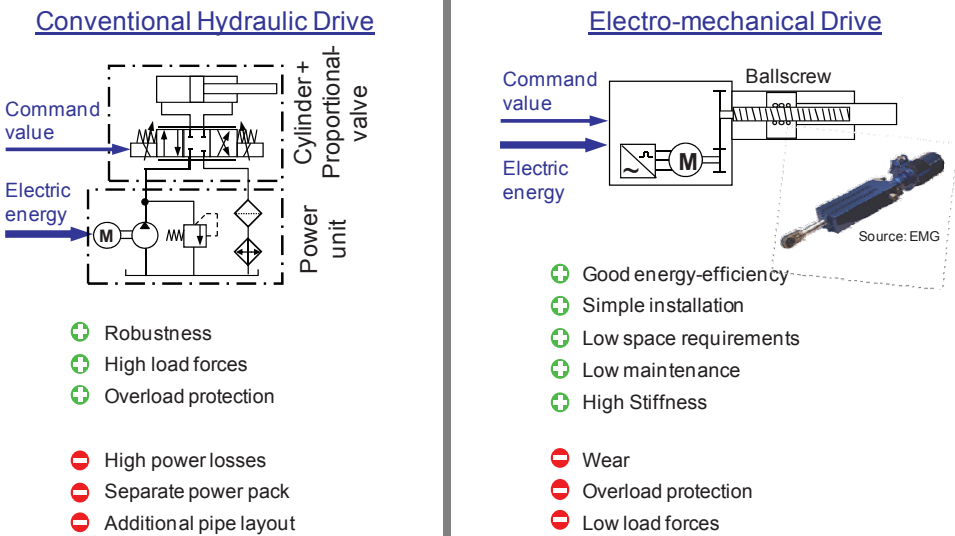


**Figure 1: State of the art in low power applications**

Hence, a new concept for hydraulic drives has to be found to meet the increased user requirements in the low power class. This concept has to feature the following characteristics:

- Compactness
- Energy-efficiency
- User-friendliness
- Cost-efficiency

Looking to the aircraft industry, a trend to energy-efficient compact drives has been noticed for several years. Here, highly integrated turn-key assemblies are used which consist of a speed controlled motor, pump, double rod cylinder and valves for auxiliary functions.

These so-called electric-hydrostatic actuators (EHA) achieve high energy-efficiency by controlling the velocity of the piston with the speed of the pump. The investigations of Rühlicke (1), Klug (2) and Neubert (3) have shown that – especially under part load – high efficiency can be achieved using this configuration. Consequently, with EHA's-structure, the disadvantages of current hydraulic drives in terms of energy-efficiency and user-friendliness are reduced significantly. Series applications in commercial aircrafts are already known – for example as secondary actuators for flaps in the Airbus A380 (4). However, the double rod cylinder installed in the EHA has a negative effect on the load force and in particular on the installation space. Furthermore they are very cost-intensive, since they have been developed for the special requirements of aircraft applications (Kazmeier (5), Bildstein (6)). For these reasons, currently available EHA's do not fulfil the claimed features in terms of compactness and cost-efficiency and are not suitable for industrial or mobile applications.

Only recently, a few hydraulic compact drive products for use in industrial applications have appeared on the market. Instead of a double rod cylinder a single rod cylinder is used. Thus, these products achieve higher compactness and better cost-efficiency. However, systematic investigations on compact drives for industrial low power applications have not yet been carried out.

Consequently, this paper focuses on the systematic development and the systematic investigation of concepts for electrohydraulic compact drives, which feature the aforementioned characteristics needed to meet the requirements in low power applications. Chapter 2 and 3 describe the basic configuration and the systematic approach followed by the results showing the basic functionality and operation of preferred variants (chapter 4). A special focus is set on the results regarding energy-efficiency (chapter 5). In order to evaluate the performance of the developed compact drives, a comparison to electromechanical drives is done in chapter 6.

## 2 Basic configuration and challenges

The basic idea for the compact drive concept is to design a turn-key assembly which features only electrical and mechanical interfaces. With respect to a good energy-efficiency, the compact drive is based on the EHA-principle. In order to minimize the installation space, a single rod cylinder is used instead of a double rod cylinder. The schematic structure of the compact drive concept is illustrated in **Figure 2**.

The introduced concept combines the advantages of standard hydraulic drives (reliability, large forces, good overload protection) and the advantages of electromechanical drives (good energy-efficiency, less required space, low maintenance effort, easy plug and play connectivity). Most disadvantages of current conventional hydraulic drives in low power applications are minimized or eliminated.

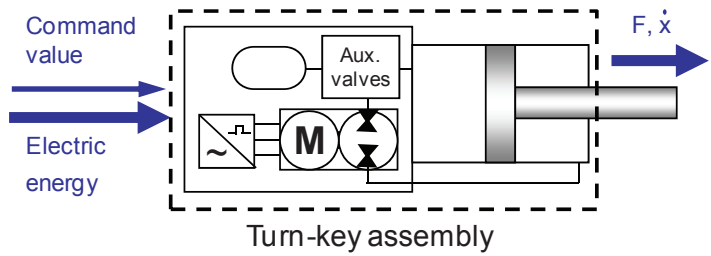


**Figure 2: Schematic structure of the investigated compact drive concept**

In case of using a single rod cylinder combined with a pump control, the main challenge is the management of unequal volume flows of the cylinder. The balancing volume flow caused by the rod has to be charged or discharged in accordance with the direction of motion. By now, several variants for managing the balancing volume flow were disclosed in a various number of publications and patents (e.g. (7), (8), (9), (10), (11)). Furthermore, scientific research has been conducted investigating specific circuit configurations (e.g. (1), (3), (12) and (13)). With a special focus on the requirements of low power applications, a methodological investigation of the various options for managing the balancing volume flow is needed.

**3 Solution space and preferred variants**

Based on a comprehensive analysis of the state of research, a solution space for the pump control of a single rod cylinder could be derived. This solution space classifies the existing variants according to the number of used pumps, the number of used drives and the type of circuit. **Figure 3** shows the derived solution matrix.

With regard to a compact and reasonably priced design of low power application drives, the grey highlighted fields in the matrix with one drive and one pump unit are of particular interest. The further division into systems with switching or pressure valves and systems without any valves – as illustrated in Figure 3 on the right hand side – is appropriate.

	Single rod cylinder				1 Pump, 1 Drive		
	1 Pump	2 Pumps		3 Pumps	Without switching valves		With switching valves
	1 Drive		2 Drives	1 Drive	Without valves	With pressure v.	
Open circuit							
Closed circuit							

**Figure 3: Solution matrix for the pump control of a single rod cylinder, General (left) and in particular with one pump (right)**

In order to derive the preferred variants out of the solution space, a design methodological evaluation in accordance with the Kepner-Tregoe method was carried out. Evaluation criteria were chosen with particular attention to the specific requirements of low power applications, such as compact design, use of standard components and low costs. Owing to the numerous application fields of compact drives, different load cases were evaluated separately, as shown in **Figure 4**. The complexity of motion increases from case A to D.

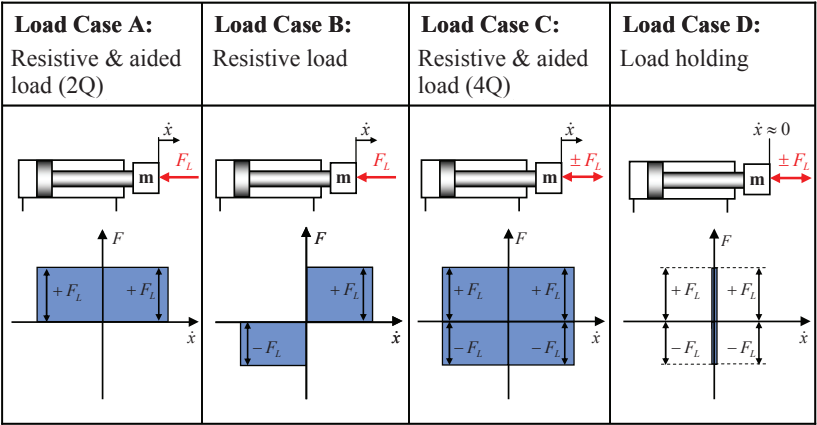
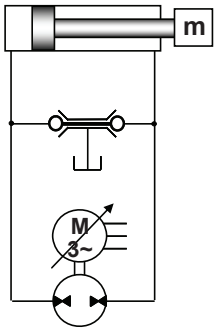


**Figure 4: Different load cases for the design methodological evaluation**

The evaluation led to different preferred variants for different load cases. For simple drive tasks (load case A and B), a simple design is of prime importance, whereby the dynamic stability is the decisive factor for enhanced drive tasks with switching loads (load case C and D). **Figure 5** illustrates the preferred variants of the evaluation. The variants are built in a closed circuit manner and characterized by their simplicity and robustness.

Variant „Inverse shuttle Valve“



Variant „Double gear pump“

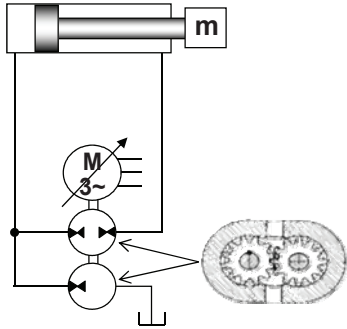


**Figure 5: Circuit diagram of the preferred variants of the evaluation**

In the first variant “Inverse shuttle valve” only one pump unit is used. The balancing volume flow is charged and discharged by means of only one pressure-controlled auxiliary valve that features the characteristic of an “inverse” shuttle valve. This means the low pressure side of the cylinder is always connected to the tank reservoir. Thus, the balancing



volume flow is always charged and discharged on the low pressure side of the cylinder. In this feature, the variant “Inverse shuttle valve” is similar to the investigated actuator of Rahmfeld and, later on, Williamson, where this function is realized via two piloted check valves. A detailed operation description of the variant “Inverse shuttle valve” is provided in (14). The advantage of this variant is the flexibility in terms of design since there is no geometrical restriction between the displacement volume of the pump, the piston areas of the cylinder and the auxiliary valves. Therefore, the “Inverse shuttle valve” is best suited for load cases A and B, and also able to handle load cases C and D (switching loads). However, there are dynamic limits for the operation of this concept. A detailed description of the dynamic limits can also be found in (14).

The second variant “Double gear pump” uses two external gear pumps, which are arranged on a common shaft. The balancing volume flow is charged and discharged by the pump, which is connected to the piston chamber of the cylinder and the tank reservoir. Due to the same pump speed, the displacement volumes are strictly geometrically linked to the piston areas of the cylinder in order to avoid pressure peaks and cavitation on the suction ports of the pumps. Therefore, the displacement volume ratio of the pumps has to match the piston area ratio  $\phi$  of the cylinder. Furthermore, anti-cavitation valves should be adopted. Although this variant is in terms of design not as flexible as the other, it is particularly appropriate for enhanced drive tasks with switching loads.

#### 4 Demonstrators and examination of performance

To examine the static and dynamic performance of the preferred variants, demonstrators were built up. With respect to price-sensitivity, the demonstrators were designed with the proviso to keep the amount of auxiliary components as low as possible. For the variant “Inverse shuttle valve”, a spool valve was used in the design instead of a poppet valve. Those valves commonly used as hot oil shuttle valves, are widespread commercially available. **Figure 6** shows the developed demonstrators.

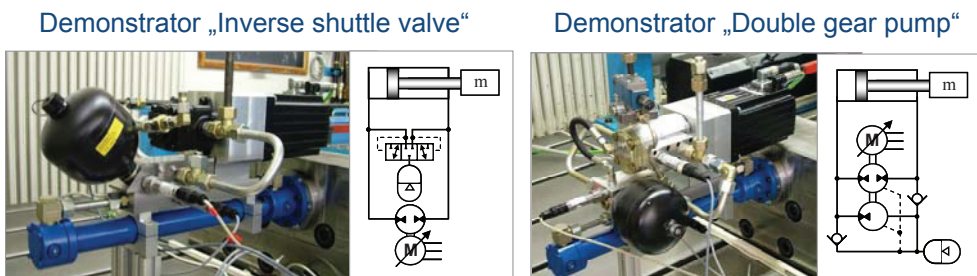


**Figure 6: Demonstrators of the preferred variants**

Following the systematic approach, the demonstrators were tested in terms of the different load cases and dynamic excitations on a test rig. The test rig is designed as electrohydraulic load axis and allows for application of the different load cases on the demonstrators.

In **Figure 7**, experimental results for load case B (Resistive load) are illustrated as examples. For the experiments, the drives executed a given profile of extending and retracting in an open loop control manner. The pump speed magnitude was constant both for extending and retracting. The initial pressure of the accumulator was set to  $p_{acc} = 2,5$  bar. The graphs show the principal functionality of the pump controlled single rod cylinder with a minimum of throttle losses by means of the inverse shuttle valve and the double gear pump.

Due to the dominant inertial loads, the shown reversal process represents an enhanced motion profile for the drives. While the maximum acceleration of variant “Inverse shuttle valve” is limited, variant “Double gear pump” could be applied with the maximum acceleration rate of the electric motor. Thus, in the experiments, accelerations of up to  $15 \text{ m/s}^2$  could be achieved. The experiments could also prove the concept functionality in the load cases A, C and D.

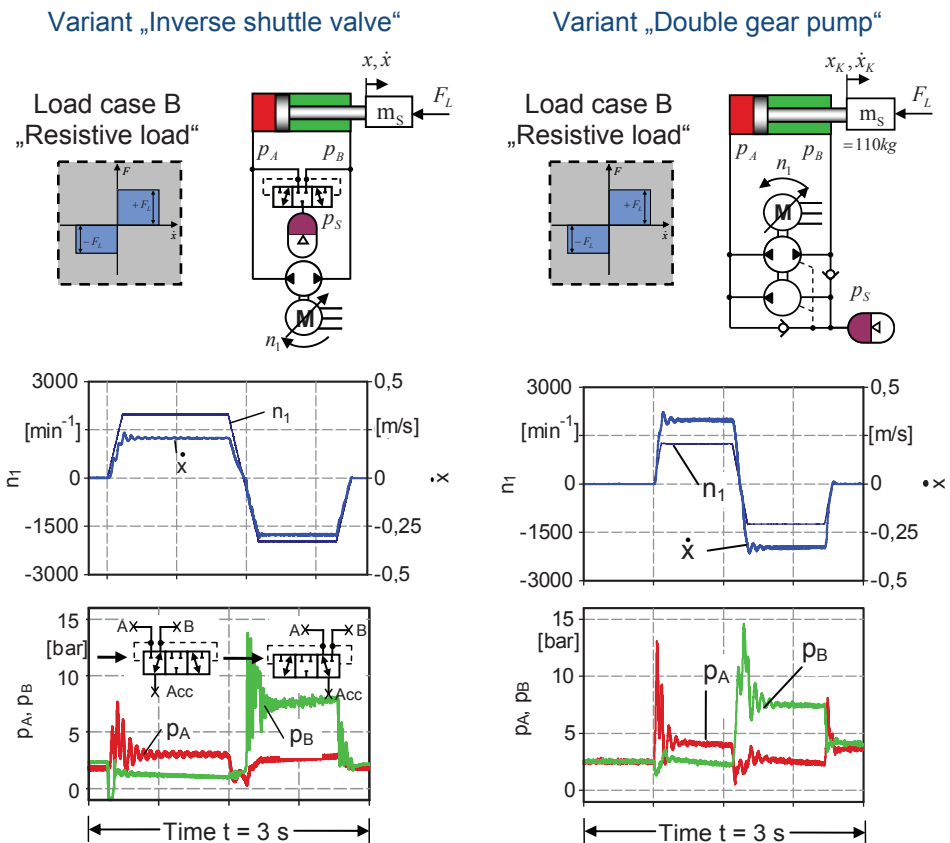


**Figure 7: Test Results for the load case B “Resistive load”**

The graphs show that no pressure peaks or cavitation occurs with the minimal equipment of auxiliary valves. Only in a few cases a hydraulic restraint appeared while applying a load in retracting direction for variant “Double gear pump”. Due to a leakage flow from the piston

side of the pump to the rod side of the pump, the pressure rose in both cylinder chambers to a certain level. This behaviour was not repeatable and can be referred to the operation of the axial bearings in the gear pumps, which compensate the axial gap. Since they are configured for a minimal speed of  $n = 800 \text{ rev/min}$ , a correct operation for lower speeds can not be assured. Coulomb friction and restraint torques lead to complex interrelations for the operation of the axial bearings, which cannot be predicted. Here, a further improvement of the pumps for lower speeds is necessary. Otherwise, a double gear pump in an open circuit manner is recommended.

## 5 Energy-efficiency of the electrohydraulic compact drives

An important feature of electrohydraulic compact drives is their energy-efficiency. Therefore, the demonstrators were examined in terms of their energy-efficiency on a test rig as illustrated in **Figure 8**.

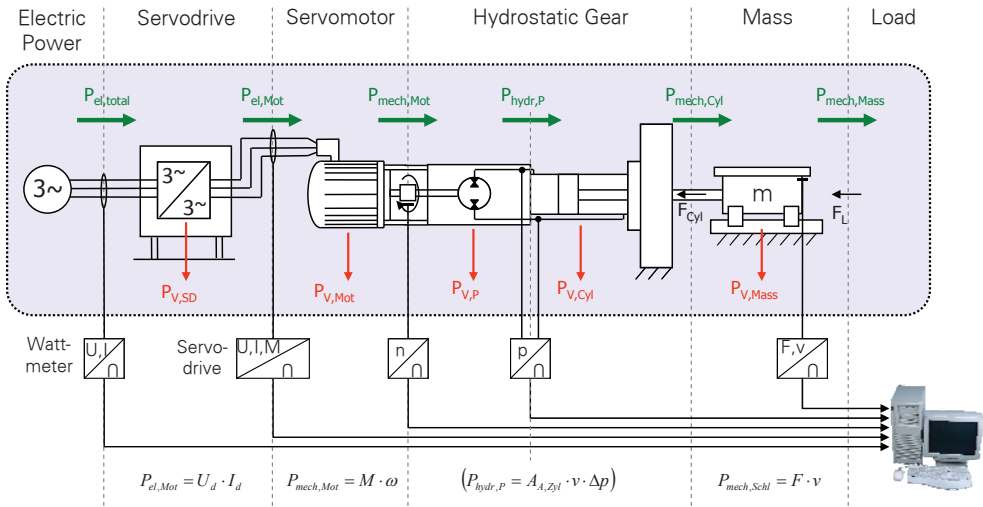


**Figure 8: Test rig for examining the energy-efficiency of the demonstrators exemplarily for variant “Inverse shuttle valve”**

The power is measured at each interface, starting from the electrical power input via the servodrive and the servo motor to the hydrostatic gear and the connected mass. In all experiments, the same servodrive and servo motor was used. With these measurements, the efficiency of each component  $i$  can be calculated by:

$$\eta_i = \frac{P_{out,i}}{P_{in,i}} \quad (1)$$

By measuring different operating points, a static efficiency map could be recorded. **Figure 9** illustrates the overall efficiency maps of the preferred variants. The parameters load and velocity are normalised to the nominal parameters of the electromechanical drive

(EMD), which is presented in chapter 6. In areas of high workload both variants achieve a reasonably good efficiency. In these operation areas efficiency remains on a plateau and falls significantly towards lower velocities and loads. Reasons for this are lower volumetric and electrical efficiency at lower velocities as well as lower hydro-mechanical efficiency at lower loads. For the variant “Inverse shuttle valve” an overall efficiency of up to 65 % and for the variant “Double gear pump” an overall efficiency of up to 55 % was measured.

As can be seen at the efficiency map of variant “Double gear pump”, the graph could only be recorded to half of the nominal load of the electromechanical drive. The reason for this is an oversized pump unit, which had to be used for the demonstrator. Using standard components, no smaller pump unit was commercially available. With the oversized pump, the electric motor was not able to deliver the required torque for higher loads. Also, the pump unit in the demonstrator “Inverse shuttle valve” is not ideally sized, since no smaller component was commercially available. It is obvious that oversized components have a negative effect on the efficiency – not only on the hydraulic components but also on the electric ones. The efficiency of the electric drive is also strongly dependent on the operating point. This means that the usage of optimal components leads to improved efficiency.

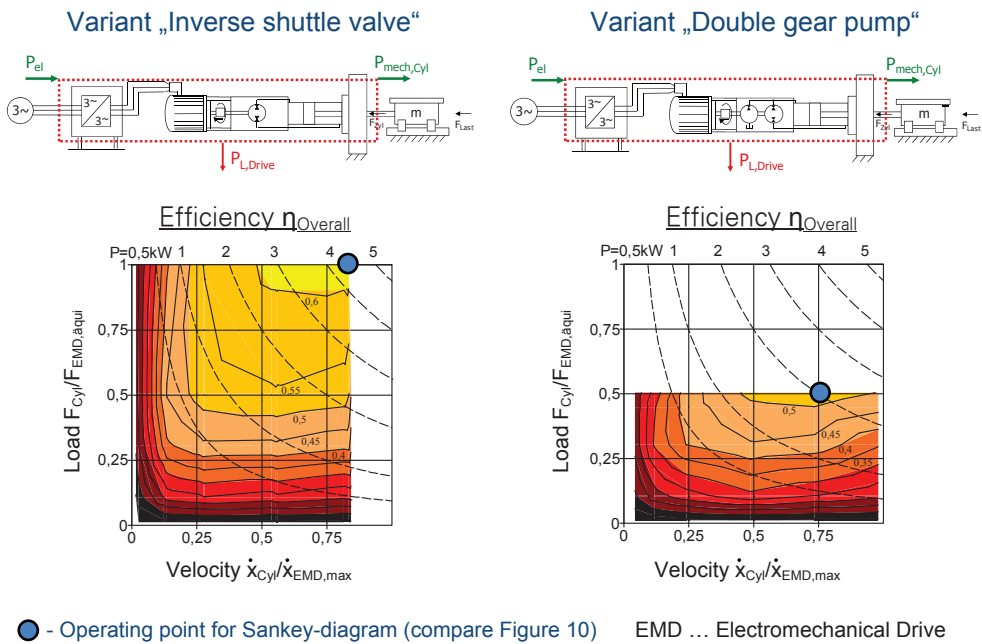


**Figure 9: Energy-efficiency of the hydrostatic gears of the demonstrators**

Looking at the Sankey-diagrams in **Figure 10**, the proportion of energy loss of each component compared to the whole system becomes clear. At the referred operating points (marked with a circle in Figure 9) both the hydrostatic gears show a total loss of energy of about 25 %. The electric drive in variant “Inverse shuttle valve” has a total loss of 13 %. In contrast, the electric drive in variant “Double gear pump” has a total loss of about 21 %. The reason for this is that, due to the lower transmission ratio of variant “Double gear

pump”, the electric drive has to deliver a much higher torque at lower speeds. In those operating points, the efficiency of electric drives significantly decreases.

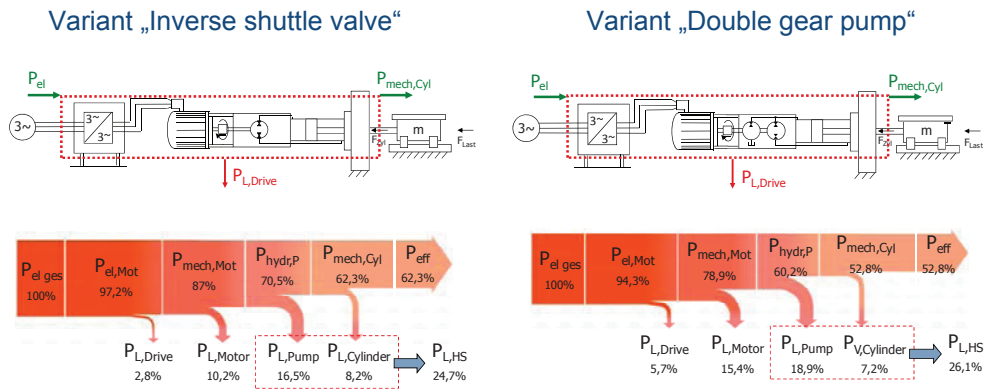


Figure 10: Sankey-diagrams of the demonstrators

Looking from another point of view, these results show the potential of electrohydraulic compact drives. With the inherent characteristic of hydraulic gears that small pumps can work with a higher shaft speed than ball screw drives, not only the efficiency of the hydraulic gear could be improved significantly with optimal components, but also the electric drive could work in better efficiency areas or even could be down-sized.

The level of efficiency that can be achieved with optimally sized components is estimated at 72.3% (**Figure 11**). This is supported by extrapolated data derived on basis of the range of efficiency of a 2-quadrant-pump at the scale needed.

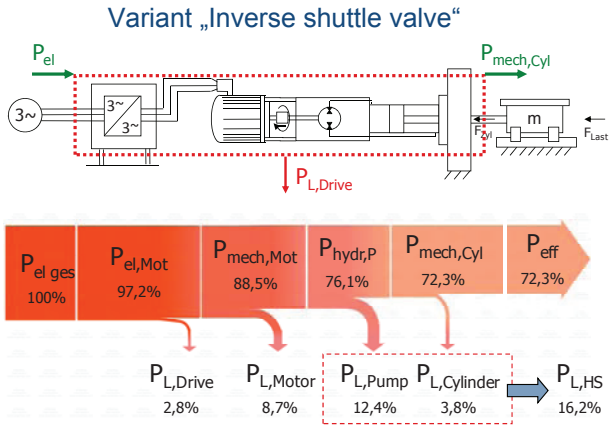
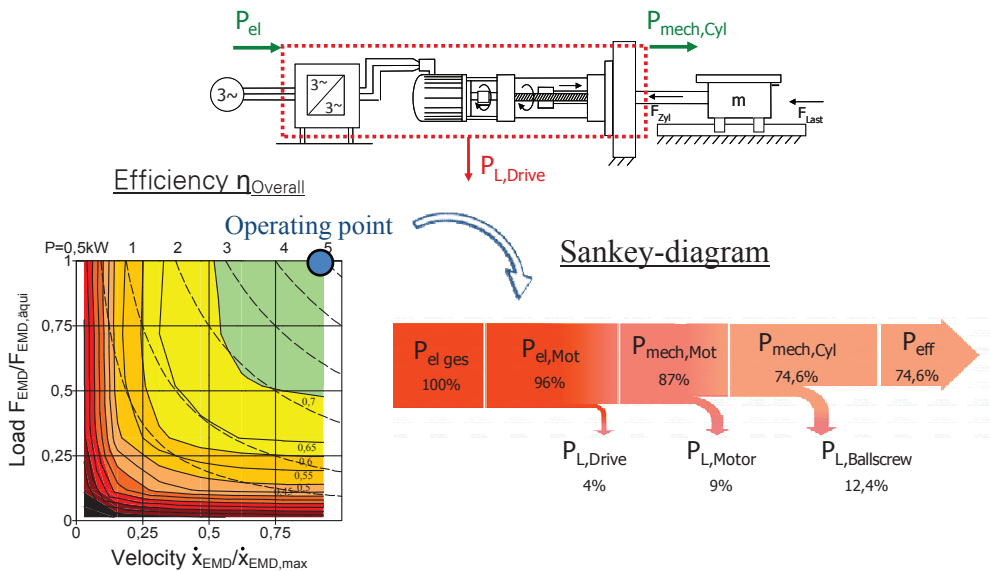


Figure 11: Sankey diagram (extrapolated) for a hydraulic compact drive with optimally sized components

## 6 Comparison to electromechanical drives

In order to evaluate the efficiency of the developed electrohydraulic concept, a comparison to electromechanical drives is appropriate. Information on technological characteristics of electromechanical drives are mostly spread by manufacturers itself. In data sheets, for example, information on energy efficiency is given only in a generalized way by a single value for a specific operating point. An efficiency map is missing. Also scientific works to screw drives are few and far between. Therefore, a commercially available electromechanical drive with a ball screw was tested experimentally, in order to analyse the efficiency of these drives. The experiments were carried out analogues to the experiments in chapter 5 using the same test rig including the same servodrive and servo motor.

**Figure 12** shows the overall electromechanical drive efficiency. Analogue to electrohydraulic drives, a plateau with a good efficiency can be recognized in areas of high workload, which falls significantly towards lower speeds and forces. This decrease can also be referred to a lower electric and mechanical efficiency in these operating points. Near the nominal operating point, the overall efficiency of the axis is 74.6%. 13% of the losses are due the electric drive and 12.4% to the ball screw drive.



**Figure 12: Efficiency map (left) and Sankey diagram (right) of an electromechanical drive**

Comparing the drives it becomes clear that the electrohydraulic prototypes are in an efficiency range similar to that achieved in electromechanical drives, which are already developed for series production. In particular in part-load operation and in periods of downtime, a substantial increase in energy efficiency as opposed to valve-controlled drives can be noticed. Apart from their energy efficiency both technologies are notable for their

high degree of user friendliness and compact design – due to the fact that electrohydraulic and electromechanical compact drives have the same structure.

On the basis of equivalent energy efficiency and user friendliness, further technological criteria can be used for the comparison and evaluation of the drives. These are stated in **Table 1** and can be assigned to the categories operating characteristics, construction, safety and application. In dependence to the requirements of the particular application, the most suitable drive technology can be selected objectively as a result of the evaluation of drives.

Due to their inherent characteristics, hydraulic drives offer clear advantages generating higher forces and also with regards to robustness. Although electromechanical drives are extremely stiff, this, conversely, means that they also have poorer capabilities to absorb impacts. Furthermore, the maximum acceleration of ball screws is, unlike that of hydraulic cylinders, technologically limited.

Category	Criterion	Elektrohydraulic compact drive	Elektromechanical compact drive*
Operating characteristics	Energy efficiency	++**	++
	Robustness	++	o
	High forces	++	o
	Stiffness	o	++
	Impact absorption	++	--
	Max. acceleration	++	+
	Thermal characteristics	?	+
Design	Installation space	++	++
	Nominal speed of drive assembly	++	-
	Variable transmissions	++	--
Safety	Overload protection	++	o
	Fail-safe	++	-
Applica- tion	User friendliness	++	++
	Durability / Maintenance effort	?	o+

\* with ball srew    \*\* expected

**Table 1: Comparison of the characteristics of electrohydraulic and electromechanical compact drives**

In terms of design the maximum speed of the spindle or the pump is an important criterion. Ball screws have to be operated with lower speeds than small pumps because of critical maximum ball speeds and bending vibrations. Depending on the design, this may be factor 1.5. This has far-reaching consequences for the reachable maximum speed or conversely for the size of the electric motor that has to be applied. If one considers the possibility of enhancing electrohydraulic compact drives with a switchable transmission (rapid speed / working speed), these drives can, under certain circumstances, be considerably better designed for the application requirements than electromechanical axes that allow only fixed transmissions.

Regarding safety, hydraulic compact axes are also to be evaluated positive. While controlled overload protection and fail-safe functions can be realised relatively easy, a fail-safe function for electromechanical drives can only be realised with more effort.

Of course, thermal characteristics and the predicted durability and maintenance effort are important features, which influence the performance and acceptance of electrohydraulic drives reasonably. These aspects, which were not investigated in detail in recent works, shall be focussed in future works.

## 7 Conclusion

Low power linear drives ( $P < 5 \text{ kW}$ ) are used in a wide field of applications. In this paper, a systematic approach for the development of new electrohydraulic compact drives was introduced, which emphasises enhanced energy-efficiency, user-friendliness, small installation space and minimal maintenance of the drive. Designed as a turn-key assembly, the new compact drive uses a pump control in combination with a single rod cylinder based on the EHA-principle. For the particular challenge to manage the unequal volume flows of a single rod cylinder, a systematic solution space was developed to provide an overview of the various design options. Following the systematic approach, a design methodological evaluation with the selection of preferred variants was carried out with particular attention to the specific requirements of low power applications. The preferred variants are characterized by their simplicity and robustness. To examine the performance and the energy-efficiency of the compact drives, demonstrators were built up and tested in experiments. Experimental results presented in this paper show the basic functionality of the systems. A special focus was set on the examination of the energy-efficiency of the compact drives. Furthermore, a comparison with electromechanical drives was done. Here, a commercially available electromechanical drive was tested experimentally as well. The results show, that electrohydraulic compact drives achieve a similar good efficiency and user-friendliness as electromechanical drives. Against this background further criterions for the comparison were included, where hydraulic drives feature some unique characteristics due to inherent technological advantages. In future works, the thermal characteristics and durability of electrohydraulic compact drives shall be focussed.



## 8 Acknowledgements

The presented research results were obtained within the research project “Energy-efficient electrohydraulic drives for low power applications” supported by the VDMA Fluid Power Association.

## References

- (1) Rühlicke, I.           Elektrohydraulische Antriebssysteme mit drehzahlveränderbarer Pumpe, Dissertation, TU Dresden, 1997
- (2) Klug, D.                Hydraulische Antriebe mit drehzahlgeregeltem Elektromotor  
Dissertation, TU Chemnitz, 2000
- (3) Neubert, T.            Untersuchungen von drehzahlgeregelten Pumpen,  
Dissertation, TU Dresden, 2002
- (4) Maré, J.-C.            From Douglas DC3 to Airbus A380 – Seventy Years of innovation in Aerospace Hydraulics, 4. Internationales Fluidtechnisches Kolloquium, Dresden, Proceedings II p. 95-106, 2004
- (5) Kazmeier, B            Energieverbrauchsoptimierte Regelung eines elektrohydraulischen Linearantriebs kleiner Leistung mit drehzahlgeregeltem Elektromotor und Verstellpumpe, Dissertation, TU Hamburg-Harburg, 1998
- (6) Bildstein, M.           Application of electro-hydrostatic actuators (EHA) for future aircraft primary flight controls, 1. Internationales Fluidtechnisches Kolloquium, Aachen, Proceedings I S. 93-105, 1998
- (7) Hewett, A. J.           Hydraulic Circuit Flow Control. Patent US 5,329,767, 1994
- (8) Eisenbacher, E.       Hydraulischer Antrieb zur Nockenwellenverstellung einer Brennkraftmaschine, Offenlegungsschrift DE 42 27 001 A1, 1994

- (9) Sebode, G. et al.      Hydroseilaufzug, Patent DE 197 15 224 C4, 1999
  
- (10) Pinter, R. et al.      Hydraulische Betätigungsanordnung, Patent EP 0 803 630 B1, 2002
  
- (11) Dantlgraber, J.      Hydrostatic Drive Unit, Patent WO 2008/037306 A1. 2008
  
- (12) Rahmfeld, R.      Development and Control of Energy Saving Hydraulic Servo Drives for Mobile Systems, Dissertation, TU Hamburg-Harburg, 2002
  
- (13) Williamson, C.,  
Ivantysynova, M.      The Effect of Pump Efficiency on Displacement-Controlled Actuator Systems, Tenth Scandinavian International conference on Fluid Power (SICFP'07), Tampere, 2007, Proceedings Vol. 2, pp. 301-326
  
- (14) Michel, S.,  
Weber, J.      Electrohydraulic Compact Drives for Low Power Applications considering Energy-efficiency and High Inertial Loads, Seventh FPNI-PhD-Symposium, Reggio Emilia, Proceedings, 2012



# Optimizing Hydraulic Energy Recovery System of Reach Truck

**H. Hänninen, J. Kajaste and M. Pietola**

Department of Engineering Design and Production  
Aalto University, School of Engineering, Espoo, Finland  
henri.hanninen@aalto.fi

## ABSTRACT

When improving the energy efficiency of a work machine, an energy recovery system is in many cases an effective solution. In lift/lower -function of a reach truck mast, a direct hydraulic recovery system with hydraulic accumulators and a Digital Flow Control Unit (DFCU) has been proven as a very viable option. In this kind of system however, the pre-load pressure of accumulator gas chamber has a critical influence on the overall performance of the recovery system, and therefore method for its optimization based on work cycle related parameter values (e.g. load) is needed.

In this study a new simplified model for optimizing accumulator parameters is created based on analytical assessment on hydraulic losses with given system topology. The model approach was needed since the system contains time dependent and partly interdependent variables, both internal and external. The functionality of this model is validated with measurements utilizing the full size truck test system.

In addition, system hardware and effectiveness of DFCU-controller were improved compared to previously published results. Measurements with different loads and fork velocities were carried out utilizing load optimized pre-load pressure settings. In the best case, energy consumption reduction was measured to exceed 50 per cent with the round trip efficiency of the hydraulic recovery system nearing 90 per cent.

**Keywords:** Reach truck, energy recovery, energy regeneration, optimization, hydraulic accumulator

## 1 INTRODUCTION

Increasing energy prices, tightening regulations and public view on energy and environmental issues have prompted to research focusing on energy efficiency of machines and processes. When focusing on machines' internal energy consumption (improvements on work cycles etc. excluded), energy efficiency improvements can be obtained by using higher efficiency components or by redesigning system topology and, in addition, by retrieving and storing machines' internal kinetic and/or potential energy.

Most of the commercially available energy recovery systems today are based on electric recovery and are used in passenger transportation and more specifically in automobiles. Usage of other energy storage types is fairly scanty compared to the previous. Some commercial systems utilizing hydraulic recovery can however be found. For example, kinetic energy recovery system to be used in trucks [1] or potential energy recovery system implemented to a very narrow aisle truck (subtype of fork lifts) [2]. When concerning research on hydraulic energy recovery, there can be found many studies on the subject in literature. For example, Achten et al. have researched on hydraulic regenerative drivelines on vehicles [3] and Yang et al. on hydraulic elevators [4].

For a typical reach truck there are only two subsystems that can be prudently modified to allow energy recovery. These are the masts lift and lower function in addition to the driveline of the machine. In the case of other functions of the machine, there is no potential energy to be recovered and kinetic energy levels are too low for any reasonable recovery system. Due to the fact that driveline testing facilities are beyond the available resources of this project, this study is focused merely on the lift and lower function of the reach truck's mast system. Since the mast system is hydraulically operated the usage of hydraulic energy recovery is well justified starting point since it enables avoiding unnecessary energy form conversions (hydraulic-electric-hydraulic).

This study is a part of HybLab-project which aims in significant reductions in energy consumption of work machines. Previously in this project, a fully functional hydraulic recovery circuit for reach trucks' lift/lower function has been built and measured using a realistic work cycle [5]. However, a work cycle of a reach truck in normal operational conditions includes arbitrary sequences with random parameters such as lift height and load. Thus, in real usage a "factory set" value for accumulator pre-load pressure would be un-optimal in most cases which creates the need to re-set this value to one optimized for current work cycle. In order to achieve this efficiently, a novel approach was needed since optimization based on previously created full system simulation model, or using measurements with test system, would be too time consuming when executed in sufficiently wide scope of variable values. This need for faster optimization procedure necessitates an analytical approach for simplification of the given system and creation of a model for optimization based on the previous.

## 2 METHODS

This section describes the studied system set-up and basis for optimization in this system.

### 2.1 System set-up

The main components in the studied energy recovering system are the pressure accumulators and the digital flow control unit (DFCU), illustrated in **Figure 1**. The DFCU consists of two individually adjustable control edges containing five poppet-type on/off-valves each, coupled with different sized orifices. In figure 1, these two metering edges are drawn with modified symbols of a proportional 2/2 valve, which is the most established drawing symbol for a DFCU [6]. The individual adjustability of control edges are needed for dynamic division of volume flows between accumulator package and tank. The division is achieved with a cost-function based controller [7] written in C-code running in xPC-target [7] written in C-code running in xPC-target (MATLAB/Simulink) machine.

The poppet-type valves enable virtually leakage free operation, which is crucial for this system since leakage from accumulators would result in loss of stored energy.

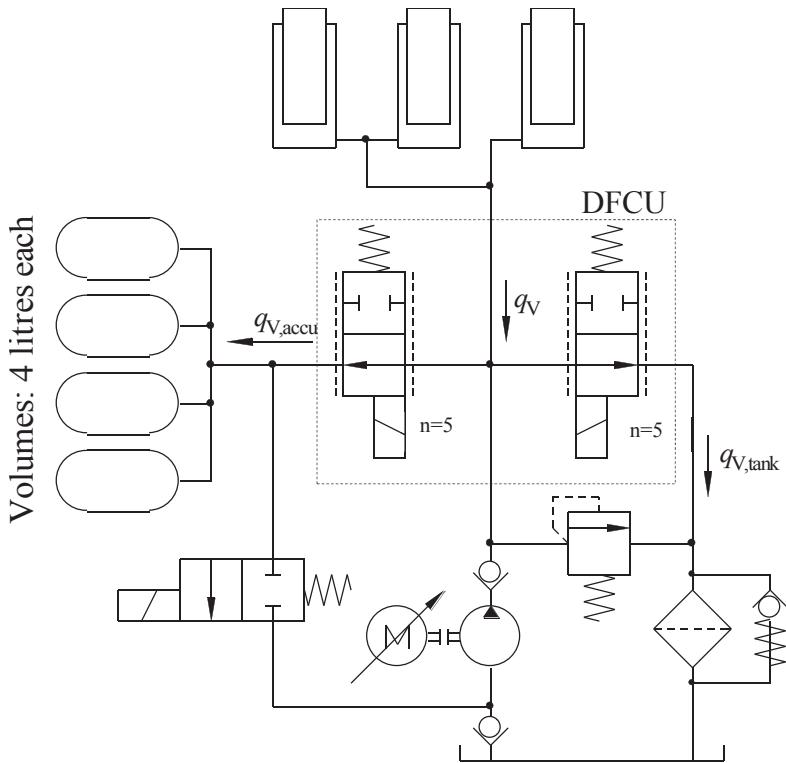


**Figure 1.** Simplified circuit diagram of test system, lifting cylinders (plunger type) on top

## 2.2 Basis for optimization

The recovered energy is stored as pressurized fluid in the hydraulic accumulator or accumulators. The energy content of accumulator is given with,

$$W_{\text{accu}} = \int p_{\text{accu}} V_{\text{oil}} dV \quad (1)$$

where  $p_{\text{accu}}$  is the pressure of hydraulic fluid inside accumulator and  $V_{\text{oil}}$  is its volume. The energy content is at its local maximum after each lowering phase of mast system, and therefore when optimising the efficiency of the energy recovery system, the goal is to optimize the sum of these local energy maxima over the studied work cycle. This method assumes that all energy collected at phase  $x$  is completely used in phase  $x+1$ .

$$E_t = \sum_1^{\text{cycles}} E_{\text{cmax}} \quad (2)$$

The two variables in equation (1) have multiple dependencies, including cross-dependencies. The boundary conditions for the two are:

$$V_{\text{oil}} \leq V_{\text{accu}} \quad (3)$$

$$p_{\text{accu}} \geq p_{\text{pre-load}} \quad (4)$$

and for  $p_{\text{accu}}$  while loading the accumulator

$$p_{\text{accu}} \leq p_{\text{cyl}} - p_{\text{losses}} \quad (5)$$

The truck used in this study contains two lift height dependant stages with different piston areas, which leads to two different pressure levels in mast input. In the lower portion of height range (free lift zone) only forks and their support structure is moved, and in upper zone part of the mast structure is moved. The system pressure when operating free lift zone is hereafter referred as  $p_{\text{cyl1}}$  and in the upper portion as  $p_{\text{cyl2}}$ .

$$p_{\text{cyl1}} < p_{\text{cyl2}} \quad (6)$$

and

$$p_{\text{cyl}} = p_{\text{cyl1}} \text{ when } h_{\text{lif}} < h_{\text{mast\_switch}}, \text{ otherwise } p_{\text{cyl}} = p_{\text{cyl2}} \quad (7)$$

The mast is velocity controlled, and hence the desired volume flow from mast while lowering is user set. Let us assume that the operator uses highest available descent velocity, which is true for most real operating situations. This translates roughly to a 45 l/min flow from the mast.

The two sources of significant losses in the system are direct losses to tank via DFCU:s cylinder-tank control edge (B-edge), and pressure losses in cylinder-accumulator control edge (later: A-edge) (**Figure 2.**).

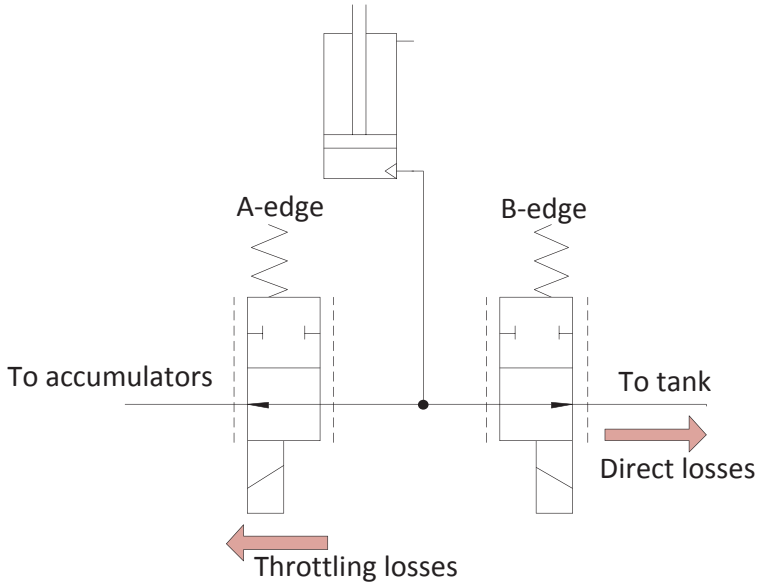


**Figure 2. Hydraulic losses when controlling the flow in lowering motion**

The former is given with

$$E_{\text{loss1}} = p_{\text{cyl}} \int_1^2 q_{v,\text{tank}} dt \quad (8)$$

where 1 refers to initial condition and 2 to end condition.  $q_{v,\text{tank}}$  is greater than zero when  $\Delta p$  across A-edge is larger than  $\Delta p_{\text{min}}$ . As stated before, there are five individual valves with different chokes on each of them on one control edge. It has been noticed that usage of theoretical flow equation causes some slight errors in actual flows. This due to the fact that in addition to the chokes the DFCU-block contains additional restrictions (such as bends etc.). In order to guarantee a good operation of the controller, a modified flow equation must be used for flow calculations

$$q_v = \sum_{n=1}^5 K_n \Delta p_{\text{min}}^{z_n} \quad (9)$$

The values of  $K$  and  $z$  are individually identified via measurements for each coupling of poppet valve and orifice [5]. When concerning the losses in A-edge, they depend on  $\Delta p$  across it.

$$E_{\text{loss2}} = \int (p_{\text{cyl}} - p_{\text{accu}}) \cdot q_{v,\text{accu}} dt \quad (10)$$

The pressure in accumulator depends on its pre-load pressure, initial gas volume, its characteristics and loading speed. The pressure-volume relationship is (polytropic process)

$$p_1 V_1^\kappa = p_2 V_2^\kappa \quad (11)$$

where sub index 1 refers to initial condition and 2 to end condition. In this case, initial condition is empty accumulator with preloaded gas pressure and the pressure in the accumulator is given with



$$p_2 = p_{\text{accu}} = \frac{p_1 V_1^\kappa}{V_2^\kappa} = \frac{P_{\text{preload}} V_1^\kappa}{(V_1 - \int q_{V,\text{accu}} dt)^\kappa} \quad (12)$$

This yields to a total loss of

$$E_{\text{loss,tot}} = E_{\text{loss1}} + E_{\text{loss2}} = p_{\text{cyl}} \int q_{v,\text{tank}} dt + \int (p_{\text{cyl}} - \frac{P_{\text{preload}} V_1^\kappa}{(V_1 - \int q_{V,\text{accu}} dt)^\kappa}) \cdot q_{v,\text{accu}} dt \quad (13)$$

When  $\Delta p$  is less than  $\Delta p_{\text{min}}$ . If  $\Delta p$  is greater than  $\Delta p_{\text{min}}$  equation (13) simplifies to

$$E_{\text{loss,tot}} = E_{\text{loss2}} = \int (p_{\text{cyl}} - \frac{P_{\text{preload}} V_1^\kappa}{(V_1 - \int q_{V,\text{accu}} dt)^\kappa}) \cdot q_{v,\text{accu}} dt \quad (14)$$

In order to maximize  $E_{\text{accu}}$ ,  $E_{\text{loss,tot}}$  must be minimized since potential energy is either stored to accumulators or lost in previously described manner. The equation (13) must be iteratively solved since the division of  $q_v$  alters along with the charging of accumulators. In this study this has been conducted by creating a Simulink based model using the previous equations. This analytical model has operation height dependent case structure (for the two different mast phases) with simplified flow-mast height relation calculation (dynamics of mast, such as mass and elasticity are not included). For the division of  $q_v$  the same C-code based controller, as used in the full truck model simulations, has been utilized.

### 2.3 Measurement system and measurements

The measurement system was instrumented for previous studies with a broad range of transducers covering pressures, flows, temperatures, rotational speed, torque, load forces and load position [8]. For this study, the flow transducers were however bypassed for minimizing the flow losses. In addition to these, one of the accumulators was instrumented for measuring piston position, gas chamber pressure and temperature of the gas. Measurements were carried out using Simulink xPC Target software, which included also a controller for the DFCU. The controller defines which valves of the DFCU (both control edges) are to be opened and which closed in order to fulfill simultaneously the charging of the accumulators and the demanded lowering speed. The controller calculates the flow through control edges using data from pressure transducers.

After the initial measurements, presented at [5], the test platform was modified by reducing flow losses within the system. In addition to the above mentioned bypassing of flow transducers, this also entailed shortening of flow lines and increasing the cross-sectional flow areas, where feasible. The DFCU-controller parameters (weighting coefficients) were also iteratively “tuned” (via measurements). The previously used parameter values emphasized the precision of the set volume flow value which led to too excessive usage of valves on B-edge (and though to undesired losses). The tuned controller allows more error between demanded and calculated flow thus reducing the unwanted usage of B-edge. With these the flow error still remains very small (<1 l/min), and would be unnoticeable from operators point of view.

For validation of the optimization model, measurements were carried out with differing pre-load pressure settings in 10 bar intervals. Closer to the expected optimal pre-load pressure point the interval was changed to 5 bar (both below and above the point). The measurement points were 10, 20, 30, 35, 40, 45, 50, 60 and 70 bars. The total accumulator volume used, was selected to be 16 liters, travel distance was 2.7 m and the velocity 0.4 m/s. For each

pre-load pressure setting, the measurement included three phases; lifting without assistance, lowering with recovery on and lifting with assistance on. The loss results are derived from the difference of electric power drawn from battery pack between non-assisted and assisted lifts.

The energy consumption reduction measurements were conducted using three different external loads and for each, three lifting/lowering velocities. The selected loads were 500, 1000 and 1500 kg and velocities 0.2, 0.3 and 0.4 m/s. As with validation measurements, these measurements consisted of the same three phases. And the energy consumption reduction ratio is defined as

$$\Gamma_s = \frac{E_{\text{unassisted}} - E_{\text{assisted}}}{E_{\text{unassisted}}}, \quad (15)$$

where  $E_{\text{assisted}}$  is the energy consumption (calculated from the measured electric power drawn from the battery pack) with the hydraulic assistance on and  $E_{\text{unassisted}}$  is the energy consumption with the assistance off. The energy consumptions for both the assisted and unassisted cases are defined as

$$E = \int_{t_0}^{t_1} P dt = \int_{t_0}^{t_1} (U \cdot I) dt \quad (16)$$

Since the energies are calculated from discrete measurements, (16) is discretized to

$$\Delta E = \sum P \cdot \Delta t = \sum U \cdot I \cdot \Delta t \quad (17)$$

where  $\Delta t$  is the sampling interval.

The total efficiency of the recovery circuit is calculated as a ratio between the energy used for assisting (energy consumption difference between un-assisted and assisted lifts) and the total recoverable energy (potential energy), defined as

$$\eta_{\text{rec}} = \frac{E_{\text{unassisted}} - E_{\text{assisted}}}{(m_{\text{struc}} + m_{\text{load}}) \cdot g \cdot h} \quad (18)$$

where  $m_{\text{struc}}$  is the mass of moving structural parts,  $m_{\text{load}}$  is the used external load,  $g$  is the acceleration of gravity (9.816 m/s used) and the  $h$  is the measured operating height. This value is similar to round trip efficiency (given to for example electric double layer capacitor) but it also includes the energy type conversions.

### 3 RESULTS

This section includes the results obtained from the energy loss equations and validation of these utilizing measurements with selected parameters. In addition, the results of energy consumption measurements with optimized pre-load pressure setting values are depicted.

#### 3.1 Validation of analytical model by loss minima comparison

The measured loss values are derived from measured electrical power drawn from battery and hence natively include all powertrain losses as the analytical model includes only hydraulic losses in DFCU flow division and charging the accumulators. Therefore, the analytical model and measured losses are not commensurate by means of energy values, the

validation will be based on comparing the position of their minima in the pre-load pressure axis.

**Figure 3** illustrates measured energy losses versus simulated direct hydraulic losses obtained from the analytical model. The operation cycle for these is lifting and lowering static load of 1000 kg using operational height of 2.7 meters and velocity of 0.4 m/s. The total oil volume of accumulators is set to 16 liters.

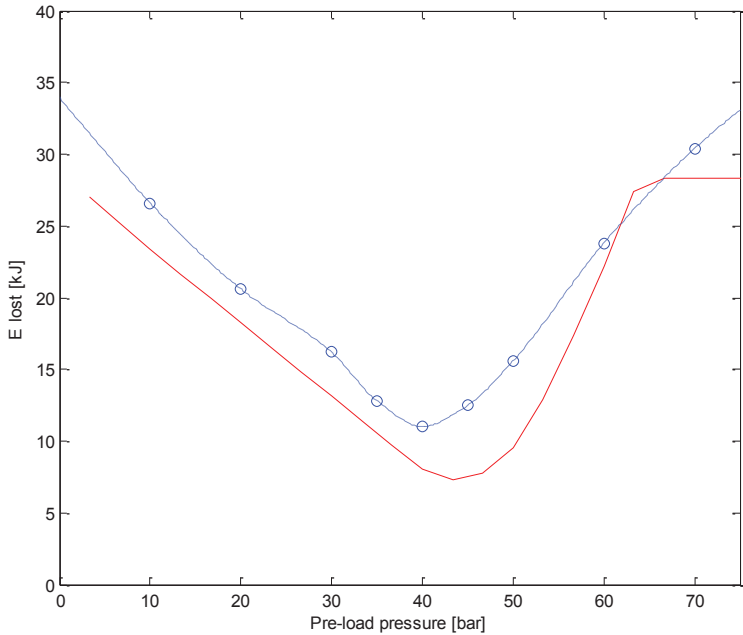


**Figure 3. Loss minima comparison. Measured values: blue dots. Results of analytical model: red line. Parameters: Lift height: 2.7 m, load 1000 kg, velocity 0.4 m/s and accumulator capacity 16 l.**

In addition to finding the correct pre-load pressure setting the model created can be used for assessment of effect of accumulator's volume and pressure setting on the overall performance of the system. In **figure 4** are illustrated simulated energy losses as a function of pre-load pressure using six different sized accumulators.

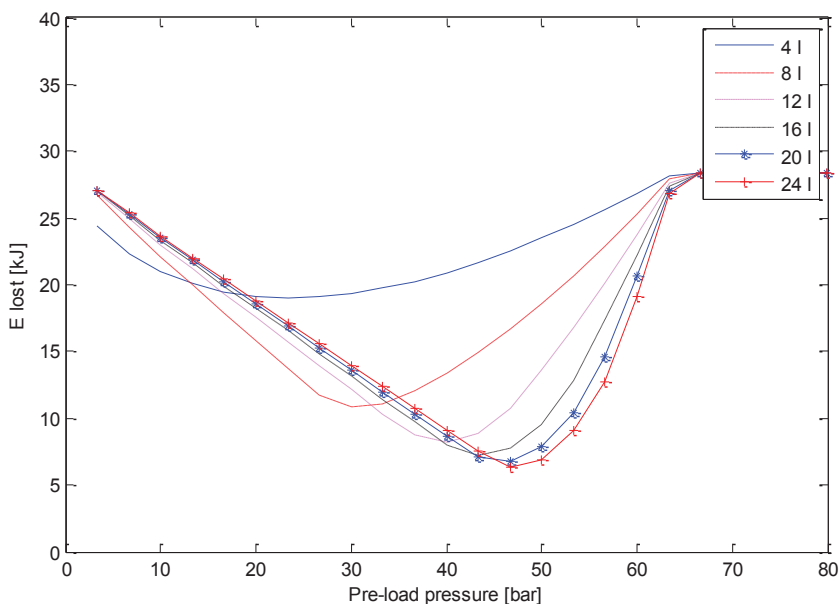


**Figure 4. Energy losses for six accumulator volumes; Optimal pre-load setting for each accumulator is in the minimum of energy losses. Operation values: Lowering from 2.7 meters (load 1000 kg,  $v=0.4$  m/s).**

### 3.3 Energy consumption measurements

The energy consumption reduction ratios with three external loads using three velocities are presented in **table 1**.

**Table 1. Measured energy consumption reductions. Constant load in lifting and lowering, operating height 1.6 m**

Velocity [m/s]	Load [kg]		
	500	1000	1500
0.4	26 %	41 %	45 %
0.3	30 %	42 %	50 %
0.2	31 %	45 %	53 %

The total efficiencies of the energy recovery system in these tests are depicted in **figure 5**. The total efficiency, defined by equation (18), describes the ratio of how much of the available potential energy during lowering was reused for assisting energy in next lifting motion.

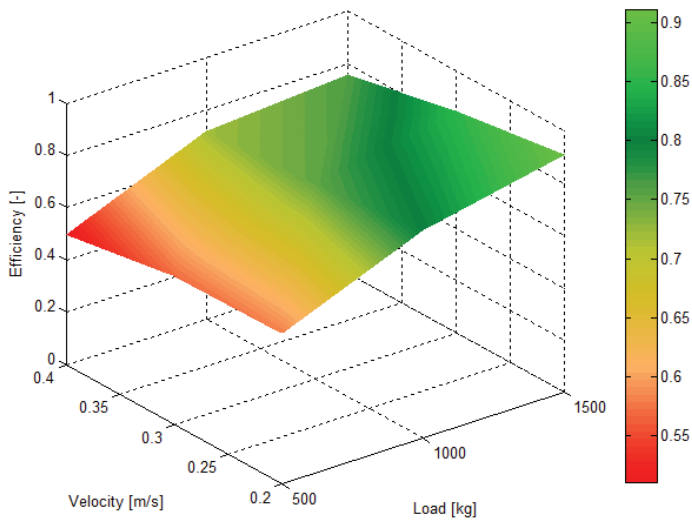


**Figure 5. Total efficiency of energy recovery and re-use**

In addition to the previous energy consumption measurements, three measurements were carried out using so called order picking cycle. In this case the lifts were done without external load and lowering with three different loads. Operating height was set to 2.7 m and velocity to 0.4 m/s, results in **table 2**.

**Table 2. Energy consumption reductions. Order picking cycle - lowering with indicated load; lifting without external load, operating height 2.7 m**

Load [kg]		
500	1000	1500
39 %	79 %	120 %

It can be observed that this type of operation cycle transforms to energy positive when lowered load exceeds approximately 1250 kg. This means, that with certain specific work cycles this machine could in theory rely solely on power collected from lowering masses ( it also verified that the controller of induction motor (that is driving the pump) is capable of charging the trucks main battery).

## 4 DISCUSSION

Based on the validation measurements, the created simplified model was found to be fairly accurate for pre-load pressure optimization. The difference in the positions of loss minima (on the pre-load pressure axis) was found to be approximately 5 bar (figure 3). Most of this error is expected to arise from the throttling losses between the DFCU A-edge and accumulators in the test system (losses in hoses, accumulator divider block etc.). This error will be analysed and factored in to the next revision of the model.

In addition, the created analytical model has some simplifications, which can bring about some inaccuracies to the energy loss calculations with some operation parameter values. One of these is the assumption of isothermal loading and unloading of the accumulator ( $\kappa=1$  in eq 11). Based on measurements, this assumption is fairly accurate using large accumulator sizes. However, with decreasing accumulator volumes the error of this assumption increases, as the true value of the polytropic constant increases. To increase the accuracy of the model with small accumulator capacities the polytropic constant should be adaptable and hold times should be factored in. Another factor that causes some inaccuracies is the possible changes in operating parameters in some of the system's components that were excluded from the model created. For example; with different hydraulic assistance power the power requirement of the pump alters, thus shifting the operation point of the induction motor (and changing its efficiency).

The model can also be used for assessing or optimizing the accumulator volume for a system with known operational work cycle parameters. From figure 4, it can be observed that with given parameter values the additional benefit of increasing accumulator volume drastically decreases after the volume of 12 liters.

The energy consumption measurements with optimized accumulator pre-load pressure settings indicated energy consumption reductions between 26 and 53 per cent compared to a machine without energy recovery and re-use system. The calculated total efficiencies of the energy regeneration system were between 50 and 91 per cent, being most efficient with high loads and low velocities.

In these measurements, the used accumulator volume of 16 liters was sufficient for maintaining the thermal losses in accumulators relatively small (low relative loading flow and hence low temperature gain in gas). If a significantly lower volume had been used, the thermal losses of accumulator would have become more significant and the reduction of these losses would have required attention. In literature, there are many examples on research in modelling the thermodynamic behaviour of accumulators and in to methods of improving the efficiency [9,10].

When concerning the task of altering pre-load pressure settings on such system, it is evident that the upcoming work cycle should be known, and in addition remain relatively constant for sufficient duration. Such cases can be found for example in warehouses and material handling tasks in industry. When operating in mixed goods warehouses with variable loads it would not be prudent to alter pre-load pressure setting to match every task. With such operating parameters, a more adaptable recovery system topology should be considered instead of the direct recovery system studied here. For addressing this, an alternative

recovery circuit based on indirect hydraulic recovery utilizing a hydraulic transformer has been designed. Even though this new system is expected to have a lower peak efficiency (than optimized direct system), simulations [11] suggests that it has better overall efficiency.

## 5 CONCLUSIONS

A mathematical model of hydraulic energy losses was created and implemented using Simulink. This enabled fast calculations for evaluating the effect of different parameters on the system's effectiveness. These parameters include the parameters of the recovery system and also work cycle related parameters. The analytical model can be used for optimization of accumulator volume and pre-load pressure and for comparison of direct hydraulic losses with given system topology. It cannot, however, be used for system energy usage or total energy loss calculations. The functioning of this model was validated with measurements.

The measurements with load optimized accumulator pre-load pressure settings yielded energy consumption reductions ratios between 26 and 53 per cent compared to a machine without energy recovery and re-use system. The total efficiencies of the energy regeneration system were found to be between 50 and 91 per cent, being most efficient with high loads and low velocities.

## ACKNOWLEDGEMENTS

This study is related to MIDE/HybLab-project which is funded by Aalto University. The cooperation of M.Sc. Jyri Juhala at the Department of Engineering Design and Production of School of Engineering of Aalto University is greatly appreciated.

## NOMENCLATURE

$E$	Energy	[J]
$n$	index of poppet valve	[-]
$p_{accu}$	pressure of accumulator (hyd.)	[Pa]
$p_{cyl}$	pressure at cylinder assembly	[Pa]
$p_{pre-load}$	initial pressure of accumulator (gas)	[Pa]
$q_V$	volume flow	[m <sup>3</sup> /s]
$t$	time	[s]
$V_{accu}$	total accumulator oil volume	[m <sup>3</sup> ]
$V_{oil}$	oil volume inside accumulator	[m <sup>3</sup> ]
$\Gamma_s$	consumption reduction ratio	[-]
$\eta_{rec}$	efficiency of recovery	[-]
$\kappa$	polytropic index	[-]

DFCU                      Digital Flow Control Unit

## REFERENCES

- [1] Gannon , Mary C., 2009. Hydraulic hybrids on rise. *Hydraulics & Pneumatics*, Vol 62, 7 2009. p. 26-31.
- [2] Toyota Materail Handling Europe. Facts about BT-ALS. <http://www.toyota-forklifts.se/SiteCollectionDocuments/PDF%20files/Facts-about-BT-ALS.pdf>. Retrieved, 03.07.2012
- [3] P. Achten, G. Vael, T. Kohmäscher, M. Ibrahim-Sokar, Energy efficiency of the Hydrid, Proc. Int. Fluid Power Conference 6th IFK, 2008
- [4] Huayong Yang, Wei Sun, and Bing Xu. New Investigation in Energy Regeneration of Hydraulic Elevators. *IEEE/ASME TRANSACTIONS ON MECHATRONICS*. 2007, vol 12, issue 5. p. 519-526. Available; <http://ieeexplore.ieee.org/stamp/stamp.jsp?tp=&arnumber=4351935>. Retrieved 03.07.2012
- [5] Hänninen, H., Kauranne, H., Sinkkonen, A., Pietola, M. Study on Energy Usage of Reach Truck Equipped with Energy Recovery System, The Proceedings of The 12th Scandinavian International Conference on Fluid Power (SICFP'11) Volume 3, May 18-20 2011 Tampere, Finland. p.179-188, ISBN 978-952-15-2520-9
- [6] Linjama, M., Laamanen, A. and Vilenius, M. Is it time for digital hydraulics? The Eighth Scandinavian International Conference on Fluid Power (SICFP'03). Tampere, Finland, May 7-9, 2003.
- [7] Juhala, J; Kauranne, H; Kajaste, J; Pietola, M,. 2009. Improving energy efficiency of work machine with Digital Hydraulics and pressure accumulator. The 11th Scandinavian International Conference on Fluid Power (SICPF'09), Linköping, Sweden, June 2-4, 2009. 15 p. ISBN: 978-91-7393-588-3
- [8] Sinkkonen, A., Kauranne, H., Hänninen H., Pietola, M, 2011. Analysis of Energy Balance in Electrohydraulic Forklift. The 12th Scandinavian International Conference on Fluid Power (SICPF'11), Tampere, Finland, May 18-20, 2011. p.193-204, ISBN 978-952-15-2518-6
- [9] Pourmovahed, A., Baum, S.A., Fronczak, F.J., Beachley, N.H. Experimental evaluation of hydraulic accumulator efficiency with and without elastomeric foam. *Journal of Propulsion and Power*, Vol. 4, March-April, 1988. pp. 185-192.
- [10] Stroganov, A., Sheshin, L. Accumulator efficiency improvement: Heat insulation or regeneration. The 11th Scandinavian International Conference on Fluid Power, SICFP'09, June 2-4, 2009, Linköping, Sweden. 13 p. ISBN 978-952-15-1761-7 (CDROM).
- [11] Hänninen H., Juhala, J, Sinkkonen, A., Hentunen, A., H, Pietola, M, 2010. Comparing hybrid power transmission systems of work machines. The 7th International Fluid Power Conference (IFK), 22.-24.3.2010, Aachen, Germany. p. 189-200, ISBN 978-3-940565-92-1





# Minimizing the Power Dissipation in the Piston-Cylinder Gap Using a Barrel-Shaped Piston

**Kim A. Stelson, Professor and Director**

**Feng Wang, Postdoctoral Associate**

Center for Compact and Efficient Fluid Power

Department of Mechanical Engineering

University of Minnesota

Minneapolis, MN 55455, U.S.A.

## ABSTRACT

A hydraulic piston pump is a key component of a hydrostatic drive. Improving the efficiency of these piston units will improve overall hydrostatic drive efficiency. There are many losses in a piston unit, including the losses between piston and cylinder, cylinder barrel and valve plate, swash plate and slipper, etc. To improve the efficiency of a piston unit, the piston-cylinder assembly is studied in this paper. In a conventional piston unit design, the piston is a cylinder. In this paper, a barrel-shaped piston design is studied to minimize the power dissipation in the piston-cylinder gap. To conduct a comparison, the power dissipation in the gap with a cylindrical-shaped piston is selected as the baseline. In the analysis, it is assumed that the flow in the gap is laminar and the fluid is incompressible. The flow velocity distribution, the pressure gradient, the leakage flow and the viscous friction are studied. It is shown that in some cases, a barrel-shaped piston can have higher efficiency than a cylindrical piston. The optimum curvature of the piston and the minimum power dissipation can be determined, providing a theoretical way to design barrel-shaped pistons. The analysis is validated with CFD simulation.

**KEYWORDS:** barrel-shaped piston, piston-cylinder assembly, gap flow, efficiency, power dissipation, optimization, hydrostatic drive.

## 1. INTRODUCTION

Hydraulic pumps and motors are essential components in a hydrostatic drive, and highly efficient pumps and motors are necessary to improve efficiency. There are several types of pumps and motors of which the piston type is most popular due to its high efficiency, high-pressure rating and variable function. There are three types of piston units, axial, bent axis and radial piston. Despite of the different unit types, there is a common and essential element inside these units, the piston-cylinder assembly. The power dissipation in the piston-cylinder gap is just one portion of the power losses in a piston pump. Other losses such as the loss between cylinder block and valve plate and the loss between swash plate

and slippers needs to be investigated to give a comprehensive understanding on how the efficiency of piston unit is influenced by these losses.

The piston moves cyclically inside the cylinder bore. The gap between the piston and cylinder is filled with fluid. The gap seals the fluid, provides lubrication and supports radial loads. There is leakage in the gap and viscous friction on the moving piston. The leakage is caused by the pressure difference along the gap while the viscous friction is caused by the viscous drag between fluid and moving piston. The leakage and viscous friction influence the drive efficiency of the piston-cylinder assembly and therefore influence the efficiency of the whole piston unit.

Some studies were conducted to improve the efficiency of the piston-cylinder assembly by optimizing the gap clearance. Gap leakage increases while the viscous friction decreases as the gap clearance increases. There is an optimum gap clearance that achieves maximum overall efficiency as a trade-off between viscous friction and leakage energy losses [1,2,3].

There are also some studies on how the fluid viscosity influences the efficiency. When the oil viscosity increases, the gap leakage decreases while the viscous friction increases. There is also optimum fluid viscosity to achieve maximum overall efficiency [4, 5]. A dimensionless viscosity that combines the fluid viscosity, pressure and piston velocity is defined to obtain the optimum viscosity, which can be found in [6].

There are also some efforts to improve efficiency using high bulk modulus fluids. Air or other gasses in the fluid is the main factor reducing the bulk modulus. High bulk modulus fluid has less compressibility, reducing volume change and increasing volumetric efficiency [7,8].

There are many studies on the leakage flow, viscous friction and power dissipation in the piston-cylinder gap for cylindrical pistons [9,10,11,12,13,14,15,16]. Gap shapes other than cylindrical; such as converging wedge, diverging wedge, secant wedge, exponential wedge, tapered land and Rayleigh step shapes; are studied as hydrodynamic bearings [17,18,19]. Some commercial piston units use barrel-shaped pistons to achieve higher efficiency. However, no study has been found to theoretically investigate how the higher efficiency is achieved by using barrel-shaped pistons.

In this paper, a barrel-shaped piston is studied to minimize the power dissipation in the piston-cylinder gap. The power dissipation in a gap with a cylindrical-shaped piston is selected as the baseline. The flow is assumed to be laminar, Newtonian and incompressible. The analysis is based on the one-dimensional Reynolds equation.

## 2. BASIC EQUATIONS

Consider a barrel-shaped piston moving inside a cylindrical bore in a piston pump, as shown in **Figure 1**. The barrel-shaped piston has a diameter,  $D$ , and length,  $L$ . The radius of the barrel shape,  $R$ , is much larger than the piston diameter and length. The piston is centered inside the cylinder. The central gap height,  $h_0$ , is in the middle of the piston, as shown in **Figure 1**. For pumping, the pressure on the left of piston is the tank pressure, zero, and the pressure on the right of piston is the load pressure,  $p_s$ . The piston moves to the right against

the pressure force, with velocity,  $U$ . Since the piston diameter is much larger than the gap height, the flow between the piston and cylinder can be approximated as flow between two flat plates.

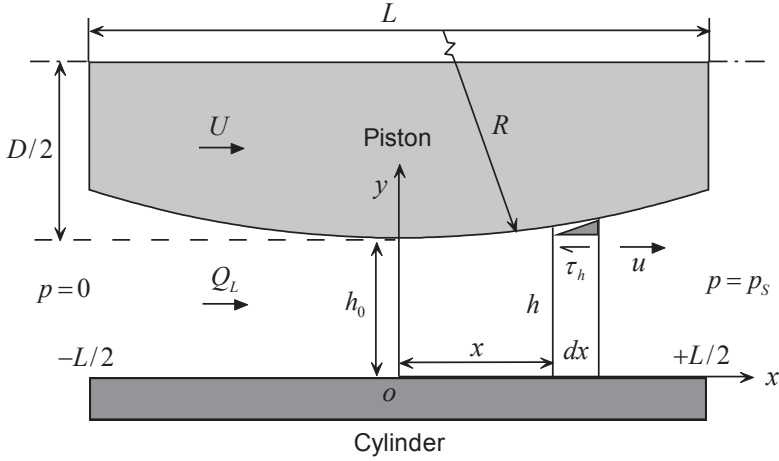


**Figure 1 Flow between cylindrical bore and barrel-shaped piston**

Based on Newton's law of viscosity and the Reynolds equation, the velocity of the fluid in the gap,  $u$ , is [20]:

$$u = \frac{1}{2\mu} \frac{\partial p}{\partial x} y^2 + C_1 y + C_2 \quad (1)$$

where  $\mu$  is the viscosity of the fluid,  $P$  is the pressure, and  $x, y$  are the coordinates within the gap.  $C_1$  and  $C_2$  are the coefficients determined by the boundary conditions.

The boundary condition is that the velocity of the fluid on the stationary cylinder is zero, and the velocity of the fluid on the piston is the same as the velocity of the piston:

$$u = 0 \text{ at } y = 0 \quad (2)$$

$$u = U \text{ at } y = h \quad (3)$$

where  $h$  is the gap height at the coordinate,  $x$ .

This yields:

$$C_1 = \frac{U}{h} - \frac{1}{2\mu} \frac{\partial p}{\partial x} h \quad (4)$$

$$C_2 = 0 \quad (5)$$

Therefore the velocity of the fluid in the gap is:

$$u = \frac{U}{h}y + \frac{1}{2\mu} \frac{\partial p}{\partial x} (y^2 - yh) \quad (6)$$

### 3. LEAKAGE FLOW

The leakage flow in the gap,  $Q_L$ , is:

$$Q_L = \pi D \int_0^h u dy = \frac{\pi D U h}{2} - \frac{\pi D h^3}{12\mu} \frac{\partial p}{\partial x} \quad (7)$$

The pressure gradient along the x-axis is:

$$\frac{\partial p}{\partial x} = \frac{12\mu}{\pi D h^3} \left( \frac{\pi D U h}{2} - Q_L \right) \quad (8)$$

The total pressure drop along the x-axis is the integration of the pressure gradient, which is  $p_s$ :

$$\int_{-L/2}^{L/2} \frac{\partial p}{\partial x} dx = p_s \quad (9)$$

Therefore the total pressure drop along the x-axis is:

$$p_s = 6\mu U \int_{-L/2}^{L/2} \frac{1}{h^2} dx - \frac{12\mu Q_L}{\pi D} \int_{-L/2}^{L/2} \frac{1}{h^3} dx \quad (10)$$

The piston shape is assumed as a parabola, the gap height  $h$  at the coordinate,  $x$ , is:

$$h \approx h_0 + \frac{x^2}{2R} = h_0 \left( 1 + \frac{x^2}{2R h_0} \right) \quad (11)$$

The following expressions are made using Taylor series expansions with the maximum order of four:

$$\frac{1}{h} \approx \frac{1}{h_0} \left( 1 - \frac{x^2}{2R h_0} + \frac{x^4}{4R^2 h_0^2} \right) \quad (12)$$

$$\frac{1}{h^2} \approx \frac{1}{h_0^2} \left( 1 - \frac{x^2}{R h_0} + \frac{3x^4}{4R^2 h_0^2} \right) \quad (13)$$

$$\frac{1}{h^3} \approx \frac{1}{h_0^3} \left( 1 - \frac{3x^2}{2R h_0} + \frac{3x^4}{2R^2 h_0^2} \right) \quad (14)$$

The following integrations are made:

$$\int_{-L/2}^{L/2} \frac{1}{h^2} dx = \frac{L}{h_0^2} \left(1 - \frac{L^2}{12Rh_0} + \frac{3L^4}{320R^2h_0^2}\right) \quad (15)$$

$$\int_{-L/2}^{L/2} \frac{1}{h^3} dx = \frac{L}{h_0^3} \left(1 - \frac{L^2}{8Rh_0} + \frac{3L^4}{160R^2h_0^2}\right) \quad (16)$$

Substituting Eq. (15) and (16) into Eq. (10):

$$p_s = \frac{6\mu UL}{h_0^2} \left(1 - \frac{L^2}{12Rh_0} + \frac{3L^4}{320R^2h_0^2}\right) - \frac{12\mu Q_L L}{\pi D h_0^3} \left(1 - \frac{L^2}{8Rh_0} + \frac{3L^4}{160R^2h_0^2}\right) \quad (17)$$

Therefore the leakage flow is:

$$Q_L = \frac{\pi D h_0 U}{2} \frac{1 - \frac{L^2}{12Rh_0} + \frac{3L^4}{320R^2h_0^2}}{1 - \frac{L^2}{8Rh_0} + \frac{3L^4}{160R^2h_0^2}} - \frac{p_s \pi D h_0^3}{12\mu L} \frac{1}{1 - \frac{L^2}{8Rh_0} + \frac{3L^4}{160R^2h_0^2}} \quad (18)$$

Since  $\frac{L^2}{8Rh_0} - \frac{3L^4}{160R^2h_0^2} \ll 1$ , the following approximation is made:

$$\frac{1}{1 - \frac{L^2}{8Rh_0} + \frac{3L^4}{160R^2h_0^2}} \approx 1 + \frac{L^2}{8Rh_0} - \frac{L^4}{320R^2h_0^2} \quad (19)$$

Therefore the leakage flow in the gap is:

$$Q_L \approx \frac{\pi D h_0 U}{2} \left(1 + \frac{L^2}{24Rh_0} - \frac{L^4}{240R^2h_0^2}\right) - \frac{p_s \pi D h_0^3}{12\mu L} \left(1 + \frac{L^2}{8Rh_0} - \frac{L^4}{320R^2h_0^2}\right) \quad (20)$$

The leakage flow is defined with the same direction as the piston movement, the actual flow of the piston,  $Q_a$ , is:

$$\begin{aligned} Q_a &= \frac{\pi D^2 U}{4} + Q_L \\ &= \frac{\pi D U}{4} \left[ D + 2h_0 \left(1 + \frac{L^2}{24Rh_0} - \frac{L^4}{240R^2h_0^2}\right) \right] - \frac{p_s \pi D h_0^3}{12\mu L} \left(1 + \frac{L^2}{8Rh_0} - \frac{L^4}{320R^2h_0^2}\right) \end{aligned} \quad (21)$$

Defining an equivalent piston diameter  $D_e$ :

$$D_e = \sqrt{D[D + 2h_0(1 + \frac{L^2}{24Rh_0} - \frac{L^4}{240R^2h_0^2})]} \quad (22)$$

The equivalent piston diameter is slightly larger than the piston diameter. Therefore the actual flow of the piston is:

$$Q_a = \frac{\pi D_e^2 U}{4} - \frac{p_s \pi D h_0^3}{12 \mu L} (1 + \frac{L^2}{8Rh_0} - \frac{L^4}{320R^2h_0^2}) \quad (23)$$

#### 4. VISCOUS FRICTION

Substituting Eq. (20) into Eq. (8), the pressure gradient along the x-axis is:

$$\begin{aligned} \frac{\partial p}{\partial x} = \frac{6\mu U}{h_0^2} & \left( \frac{x^2}{2Rh_0} - \frac{3x^4}{4R^2h_0^2} - \frac{L^2}{24Rh_0} + \frac{x^2 L^2}{16R^2h_0^2} + \frac{L^4}{240R^2h_0^2} \right) \\ & + \frac{p_s}{L} \left( 1 - \frac{3x^2}{2Rh_0} + \frac{3x^4}{2R^2h_0^2} + \frac{L^2}{8Rh_0} - \frac{3x^2 L^2}{16R^2h_0^2} - \frac{L^4}{320R^2h_0^2} \right) \end{aligned} \quad (24)$$

According to Newton's law of viscosity, the shear stress is:

$$\tau = \mu \frac{du}{dy} = \mu \frac{U}{h} + \frac{1}{2} \frac{\partial p}{\partial x} (2y - h) \quad (25)$$

At  $y = h$ , the shear stress is:

$$\tau_h = \mu \frac{U}{h} + \frac{h}{2} \frac{\partial p}{\partial x} \quad (26)$$

The viscous friction force on the piston caused by a fluid element of length  $dx$  is:

$$dF_f = \tau_h dA_h = \pi D \tau_h dx \quad (27)$$

The total viscous friction on the piston,  $F_f$ , is:

$$\begin{aligned} F_f &= \pi D \int_{-L/2}^{L/2} \tau_h dx \\ &\approx \frac{p_s \pi D h_0}{2} \left( 1 + \frac{L^2}{24Rh_0} - \frac{L^4}{240R^2h_0^2} \right) + \frac{\pi D \mu U L}{h_0} \left( 1 - \frac{L^2}{24Rh_0} + \frac{7L^4}{960R^2h_0^2} \right) \end{aligned} \quad (28)$$

The actual drive force on the piston,  $F_a$ , is the sum of the pressure force and the viscous friction force:

$$\begin{aligned}
F_a &= \frac{p_s \pi D^2}{4} + F_f \\
&\approx \frac{p_s \pi D}{4} \left[ D + 2h_0 \left( 1 + \frac{L^2}{24Rh_0} - \frac{L^4}{240R^2h_0^2} \right) \right] + \frac{\pi D \mu UL}{h_0} \left( 1 - \frac{L^2}{24Rh_0} + \frac{7L^4}{960R^2h_0^2} \right)
\end{aligned} \quad (29)$$

Substituting the equivalent piston diameter as defined in Eq. (22), the actual drive force is:

$$F_a \approx \frac{p_s \pi D_e^2}{4} + \frac{\pi D \mu UL}{h_0} \left( 1 - \frac{L^2}{24Rh_0} + \frac{7L^4}{960R^2h_0^2} \right) \quad (30)$$

## 5. POWER DISSIPATION

For a single piston in a piston pump, the input power is the mechanical power that drives the piston against the load and the output power is the hydraulic power. The power dissipation in the gap,  $P_d$ , is the difference between these two powers, considering the piston curvature  $\kappa = 1/R$ :

$$\begin{aligned}
P_d &= F_a U - p_s Q_a \\
&= \frac{\pi D \mu U^2 L}{h_0} \left[ 1 + \frac{1}{3} \left( \frac{p_s h_0^2}{2 \mu UL} \right)^2 \right] - \kappa \frac{\pi D \mu U^2 L^3}{24 h_0^2} \left[ 1 - \left( \frac{p_s h_0^2}{2 \mu UL} \right)^2 \right] + \kappa^2 \frac{7 \pi D \mu U^2 L^5}{960 h_0^3} \left[ 1 - \frac{1}{7} \left( \frac{p_s h_0^2}{2 \mu UL} \right)^2 \right]
\end{aligned} \quad (31)$$

A dimensionless factor that combines the load pressure, central gap clearance, fluid viscosity, piston velocity and piston length,  $\lambda$ , is defined:

$$\lambda = \frac{p_s h_0^2}{2 \mu UL} \quad (32)$$

Therefore the power dissipation in the barrel-shaped piston is:

$$P_d = \frac{\pi D \mu U^2 L}{h_0} \left( 1 + \frac{1}{3} \lambda^2 \right) - \kappa \frac{\pi D \mu U^2 L^3}{24 h_0^2} (1 - \lambda^2) + \kappa^2 \frac{7 \pi D \mu U^2 L^5}{960 h_0^3} \left( 1 - \frac{1}{7} \lambda^2 \right) \quad (33)$$

It is shown in Eq. (33) that the power dissipation in the barrel-shaped piston is a quadratic function of the piston curvature, creating the possibility of reducing the power dissipation with a barrel-shaped piston. When the curvature is zero, Eq. (33) reduces to the case of a cylindrical gap as shown in [6].

As it is shown in some textbooks [1,2,4], the optimum gap clearance with a cylindrical-shaped piston,  $h_{0\_op}$ , is:



$$h_{0\_op} = \sqrt{\frac{2\mu UL}{p_s}} \quad (34)$$

Considering the situation when the central gap clearance is near the optimum gap clearance:

$$h_0 = h_{0\_op}(1 + \varepsilon) \quad (35)$$

where  $\varepsilon$  is the deviation from the optimum gap clearance.

The dimensionless factor is:

$$\lambda = (1 + \varepsilon)^2 \approx 1 + 2\varepsilon \quad (36)$$

Therefore the power dissipation is:

$$P_d = \frac{4\pi D\mu U^2 L}{3h_{0\_op}} + \kappa \frac{\pi D\mu U^2 L^3}{24h_{0\_op}^2} \frac{4\varepsilon}{1+2\varepsilon} + \kappa^2 \frac{\pi D\mu U^2 L^5}{960h_{0\_op}^3} \frac{6-4\varepsilon}{1+3\varepsilon} \quad (37)$$

Differentiating the power and setting the derivative equal to zero, the optimum piston curvature for minimum power dissipation is:

$$\kappa_{op} = -\frac{20h_{0\_op}}{L^2} \frac{4\varepsilon}{1+2\varepsilon} \frac{1+3\varepsilon}{6-4\varepsilon} \quad (38)$$

With this optimum piston curvature, the power dissipation is:

$$P_{d\_min} = \frac{4\pi D\mu U^2 L}{3h_{0\_op}} - \frac{5\pi D\mu U^2 L}{12h_{0\_op}} \frac{(4\varepsilon)^2}{(1+2\varepsilon)^2} \frac{(1+3\varepsilon)}{(6-4\varepsilon)} \quad (39)$$

The following three cases are discussed.

1. If  $\varepsilon = 0$ , the central gap clearance is the same as the optimum gap clearance. The dimensionless factor in this case is  $\lambda = 1$ , and the optimum piston curvature to get the minimum power dissipation in this case is  $\kappa_{op} = 0$ . This is a cylindrical-shaped piston, meaning that the barrel-shaped piston does not help to reduce the power dissipation.

The minimum power dissipation in this case is:

$$P_{d\_min} = \frac{4\pi D\mu U^2 L}{3h_{0\_op}} \quad (40)$$

2. If  $\varepsilon > 0$ , the central gap clearance is larger than the optimum gap clearance. The dimensionless factor in this case is  $\lambda > 1$ , and the optimum piston curvature to get the minimum power dissipation in this case is  $\kappa_{op} < 0$ . This is the negative barrel or concave case.

3. If  $\varepsilon < 0$  , central gap clearance is smaller than the optimum gap clearance. The dimensionless factor in this case is  $\lambda < 1$  , and the optimum piston curvature to get the minimum power dissipation in this case is  $\kappa_{op} > 0$  . This is the positive barrel or convex case.

The power dissipation as a function of the piston curvature at different central gap clearances is shown in **Figure 2**.

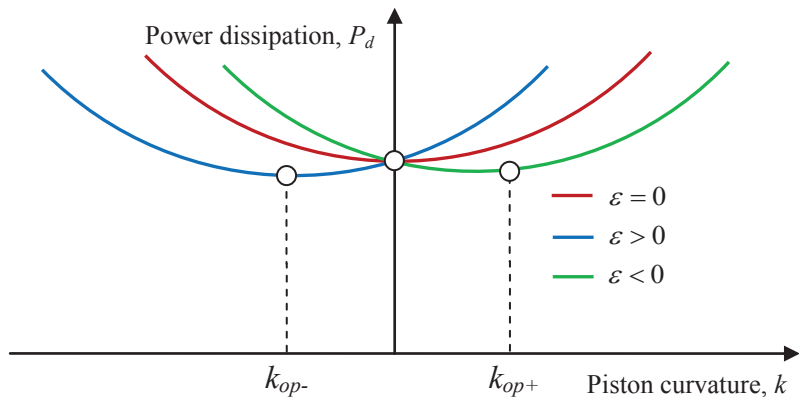


**Figure 2 Power dissipation as a function of piston curvature at different central gap clearances**

The CFD simulation has been conducted to verify the analysis. The piston-cylinder assembly geometry and the mesh are built in Gambit and solved in Fluent. Since the gap between the piston and cylinder is axisymmetric, a 2D gap profile is used to simplify the model. The simulation parameters are shown in **Table 1**. The number of cells solved in the simulation is 200,000.

**Table 1 CFD simulation parameters**

Parameter	Value	Unit
piston diameter	1.0E-02	m
piston length	4.0E-02	m
optimum gap clearance	1.4751E-05	m
load pressure	2.00E+07	pa
oil density	850	kg/m <sup>3</sup>
oil viscosity	2.72E-02	pa.s
piston velocity	2.0	m/s

The CFD simulation results are shown in **Table 2**. It is shown that when the central gap clearance is the same as the optimum gap clearance, the minimum power dissipation occurs at zero piston curvature, which is a cylindrical piston. When the central gap clearance is larger than the optimum gap clearance, the minimum power dissipation occurs for a negative piston curvature. When the central gap clearance is smaller than the optimum gap clearance, the minimum power dissipation occurs for a positive piston curvature. These

conform to the analysis results shown in **Figure 2**. In the CFD results, the power dissipations with zero piston curvature at different central gap clearances are not identical, which are different from the analysis results shown in **Figure 2**. This discrepancy comes from approximations in the analysis since the CFD result is expected to be more accurate than the analysis.

Typical parameters were used in the CFD model. In this analysis  $\lambda$  ranged from 0.81 to 1.21. The optimum curvature varied from  $-0.0143$  to  $0.0101 \text{ m}^{-1}$  where  $0.0101 \text{ m}^{-1}$  corresponds to a piston radius of 99 m.

**Table 2 Power dissipation in the piston-cylinder gap (unit: W, CFD results)**

	Piston curvature ( $\text{m}^{-1}$ )		
	$k_{op-}=-0.0143$	$k=0$	$k_{op+}=0.0101$
$\epsilon = -0.1$	13.41	12.87	12.75
$\epsilon = 0$	12.85	12.64	12.69
$\epsilon = +0.1$	12.71	12.79	12.99

## 6. CONCLUSIONS

The power dissipation in the piston-cylinder gap with a barrel-shaped piston is studied in this paper. It is assumed that the gap flow is laminar Newtonian flow and the fluid is incompressible. The analysis is based on one-dimensional Reynolds equation and Newton's law of viscosity. The temperature effect is not taken into consideration in the analysis.

The fluid velocity distribution, pressure distribution, leakage flow and viscous friction in the piston-cylinder gap are studied. A dimensionless factor which includes the load pressure, central gap height, fluid viscosity, piston velocity and length is defined to aid the analysis. It is shown that the power dissipation in the barrel-shaped piston can be expressed as a quadratic function of the curvature of the piston. The optimum curvature of the piston for minimum power dissipation can be determined.

The analysis shows that a barrel-shaped piston, concave or convex, can be more efficient than a cylindrical-shaped piston in some conditions. The results have been validated through numerical simulation. The current study is for pumping, but can easily be extended to motoring.

## ACKNOWLEDGMENTS

This research was supported by the Center for Compact and Efficient Fluid Power, a National Science Foundation Engineering Research Center funded under cooperative agreement number EEC-0540834.

## REFERENCES

- [1] J. Ivantysyn and M. Ivantysynova, *Hydrostatic Pumps and Motors*, Tech Books International, New Delhi, 2003.
- [2] Y. Lu, *Technical Manual of Hydraulics and Pneumatics (in Chinese)*, China Machine Press, Beijing, 2002, pp. 34-36.
- [3] H. Merritt, *Hydraulic Control Systems*, New York: Wiley, 1967.
- [4] C. He, *Hydraulic Components (in Chinese)*, China Machine Press, Beijing, 1981, pp. 16-22.
- [5] W. E. Wilson, "Rotary-Pump Theory," *Transaction of ASME*, vol. 68, 1946, pp. 371-384.
- [6] K. A. Stelson and F. Wang, "A simplified model to optimize positive-displacement hydraulic pump and motor efficiency," in *Proc. Bath/ASME Symp. Fluid Power Motion Control*, Bath, UK, 2010, pp. 417-429.
- [7] T. Tsubouchi, H. Kamimura, and J. Shinoda, "Development of oily high bulk modulus fluid," *Proc. 7th JFPS International Symposium on Fluid Power*, Toyama, 2008, pp. 329-334.
- [8] T. Tsubouchi and J. Shinoda. "Oily high bulk modulus fluid of new concept for hydraulic fluid," *Proc. 7th International Fluid Power Conference*, Aachen, Germany, 2010.
- [9] M. Ivantysynova and R. Lasaar, "An investigation into micro- and macro geometric design of piston/cylinder assembly of swash plate machines," *International Journal of Fluid Power*, vol. 5, no. 1, 2004, pp. 23-36.
- [10] M. Pelosi and M. Ivantysynova, "A novel fluid-structure interaction model for lubricating gaps of piston machines," *WIT Transactions on the Built Environment*, vol. 105, 2009, pp. 13-24.
- [11] A. H. MacIraith and M. P. Fitzgerald, "Analysis of controlled clearance seals," *Metrologia*, vol. 29, no. 4, 1992, pp. 285-293.
- [12] M. P. Fitzgerald and A. H. McIraith, "Analysis of piston-cylinder systems and the calculation of effective areas," *Metrologia*, vol. 30, no. 6, 1994, pp. 631-634.
- [13] U. Wiecek and M. Ivantysynova, "Computer aided optimization of bearing and sealing gaps in hydrostatic machines – the simulation tool CASPAR," *International Journal of Fluid Power*, vol. 3, no. 1, 2002, pp. 7-20.
- [14] Y. Fang and M. Shirakashi, "Mixed lubrication characteristics between the piston and cylinder in hydraulic piston pump-motor," *Journal of Tribology, Transaction of ASME*, vol. 117, 1995, pp. 80-85.
- [15] A. Yamaguchi, "Motion of the piston in piston pumps and motors. Theoretical discussion in relation to solid contact force and power loss," *JSME Int. J Ser B*, vol.43, no.2, 2000, pp. 213-218.
- [16] K. Tanaka, K. Kyogoku, T. Nakahara, "Lubrication characteristics on sliding surfaces between piston and cylinder in a piston pump and motor. Effects of running-in, profile of piston top and stiffness," *JSME Int. Journal. Ser C.*, vol.42, no.4, 1999, pp. 1031-1040.
- [17] A. Cameron, *Basic Lubrication Theory*, New York: Halsted Press, 1981, pp. 52-79.
- [18] R. C. Binder, *Fluid Mechanics*, New York: Prentice-Hall, 1955, pp. 344-364.
- [19] W. A. Gross, *Fluid Film Lubrication*, New York: Wiley, 1980, pp. 74-134.
- [20] W. E. Wilson, *Positive-Displacement Pumps and Fluid Motors*. Sir Issac Pittman and Sons, London, 1950, pp. 100-106.



# Digital Hydraulics



# Digital Hydraulic Pressure Relief Function

**M. Ketonen, M. Huova, M. Heikkilä, M. Linjama, P. Boström\*, M. Waldén\***

Dept. of Intelligent Hydraulics and Automation, Tampere University of Technology, Tampere, Finland, miikka.ketonen@tut.fi

\* Dept. of Information Technologies, Åbo Akademi, Turku, Finland

## ABSTRACT

Digital hydraulics offers an alternative for traditional proportional and servo valves by means of parallel connected 2/2-way on/off valves and intelligent control. Programmability of digital hydraulic valve systems enables versatile use of the control valve which reduces the number of valve types needed in a hydraulic system. In this paper, the functionality of a traditional hydro-mechanical pressure relief valve is realized with a control algorithm integrated to a digital hydraulic control system to remove pressure peaks that often emerge in the chamber between the actuator and the control valve. Digital hydraulic pressure relief function enables parameter changes via controller user interface. The maximum pressure setting and the behaviour of the controller can be set based on the system characteristics.

Simulation study is performed to determine the operation limits in terms of hydraulic capacity of the controlled volume and a valve response time. Test system is built to verify simulations. This paper represents a new method to eliminate unwanted pressure peaks in a hydraulic system. It summarizes the operation limits for different valve and system configurations. A PNM-coded digital valve system is studied and it is noticed to react faster than a PCM-coded valve system.

**Keywords:** Digital hydraulics, Digital fluid power, Digital valve system, pressure relief, controller design, design by contract, PNM

## 1 INTRODUCTION

Digital fluid power has been studied with increasing intensity in the past decade and it is gaining interest amongst several large component and machine developers. Study of digital hydraulics has been expanded in recent years not only to comprehend valve systems (i.e. 1 & 2), but also switching transformers (3), pumps (4) and multi-chamber cylinders (5).

Two different approaches to digital hydraulic valve systems (DVSSs) are to use PWM-controlled switching of on/off –valves or to connect several on/off –valves in parallel as presented in figure 1. One of the main benefits of using a DVS is the flexibility and programmability since each meter-in and meter-out edge can be controlled independently.



Parallel connection ensures that the opening of the valve is always at least as fast as the slowest on/off –valve. Since the effective opening area is the sum of flow areas of open on/off valves, only discrete flow levels can be achieved. Number of discrete values – known as *states* – can be maximized by setting individual valve capacities according to binary coding (1:2:4:...) i.e. to use *pulse code modulation* (PCM). In this way  $n^2-1$  discrete flow rates can be achieved with  $n$  number of valves. Parallel connection of on/off -valves forms a basic digital hydraulic valve unit called *Digital Flow Control Unit* (DFCU). Example of a cylinder control with a DVS is presented in figure 1.

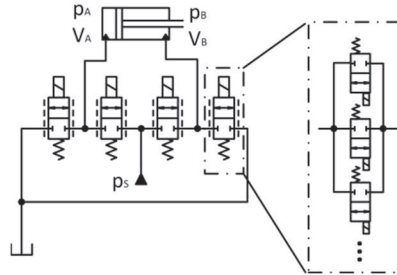


**Figure 1: Actuator control with digital valve system with four digital flow control units (DFCUs) containing parallel connected on/off valves.**

PCM-coding with binary or similar coding schemes e.g. Fibonacci-code (6) has been the practice in recent years. However this has some drawbacks and limitations which could be eliminated by connecting parallel valves with equal flow capacities i.e. by using *pulse number modulation* (PNM) in valve coding (7). The Biggest obstacle for the development of PNM-coded digital valve systems is the lack of fast, inexpensive on/off –valves on market. Miniature valves have been one of the main research objectives in the field of digital hydraulics (8).

Typically different valve functions have required separate valve types in hydraulic systems. Programmability of digital hydraulics enabled functionalities of a pressure reduce valve and a flow control valve to be developed with DFCUs in (9) and (10). Those are few possible applications where programmability of the valve could be used. A Digital valve system requires a sophisticated control system to exploit its full potential. Because control algorithms are getting more and more sophisticated, contract based design methods commonly used in object oriented programming have been developed to assure good quality of the controller (11 & 12). Systematic design of a digital hydraulic controller with a modified V-model advocated in the software relevant part of the standard IEC61508 used to certify safety critical industrial equipment has been studied and are yet to be published. These methods are also used in the study of this paper.

Pressure relief method studied in this paper is intended to replace relief valves located at the proximity of an actuator by utilizing the DVS used to control the actuator. The Purpose of the relief valve is to prevent sudden pressure peaks that often emerge with high payloads and in sudden changes of the movement direction. Actuator is thus protected from high pressures that could be hazardous to the system. The valve response time along with the stability are the most important aspects in operation of a pressure relief valve (PRV) when the purpose of the valve is to act as a shock valve. The Overshoot of the valve depends on

the response time and on the hydraulic capacity of the controlled volume. Hydraulic capacitance is determined with the equation

$$C_h = \frac{V}{B_e} \quad (1)$$

where  $V$  is the volume of the chamber and  $B_e$  is the effective bulk modulus of the system. Derivative of the pressure is then obtained from the equation

$$\frac{dp}{dt} = \frac{\Sigma Q}{C_h} \quad (2)$$

where  $\Sigma Q$  is the sum of the inflow and the outflow.

## 2 PRESSURE RELIEF CONTROLLER

Operating principle of the pressure relief function (PRF) is to use pressure sensors and feed-back control. Flow is passed through the valves from the pressure side to the tank side when the user set maximum pressure level is reached. The PRF is designed to act against sudden pressure peaks in the actuator chambers and therefore improving the static properties with more complex control algorithm is neglected in this study. The PRF controls the DFCUs on the meter-out edges as seen in figure 2.

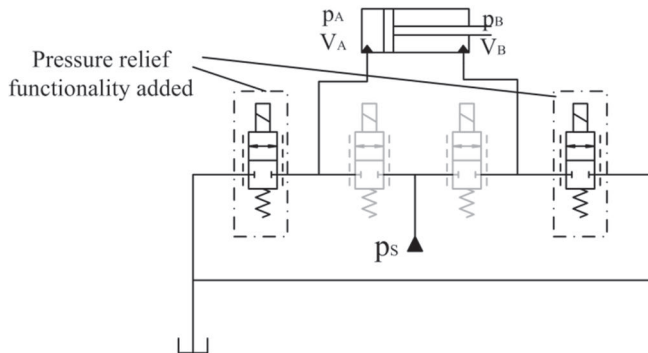


**Figure 2: Additional pressure relief functionality in a digital valve system.**

After the pressure relief algorithm is integrated to the control algorithm user can adjust the main parameters via the user interface of the system. User set cracking pressure determines the pressure level in which the tank side DFCU starts to open and corresponds to the spring pre-load of a traditional hydro-mechanical valve. New feature in the digital hydraulic pressure relief function is the ability to adjust the pressure-flow sensitivity online. This corresponds to changing the spring stiffness of a traditional hydro-mechanical pressure relief valve. Limitations for the performance are determined by the characteristics of the digital valve system and by the controlled volume. Shock relief valves are usually sized according to the possible port flows of the actuators i.e. the nominal flows. The DFCUs which actuates the PRF are sized according to a proper small pressure drop across the valve

with the nominal flow and therefore only small states of the DFCU are likely to be used with high cracking pressures.

Dynamic behaviour of the digital hydraulic pressure relief in a specific volume is determined by the dynamics of the on/off -valves and by the controller pressure-flow sensitivity. Smaller pressure rise gives more aggressive behaviour which corresponds to a growing proportional gain of the controller. Same phenomenon can be seen with hydro-mechanical PRVs when stiffness of the spring changes.

Inputs to the controller are the measured chamber pressures and the outputs of the main actuator controller. Block presentation example of a PRF integrated to a model based velocity controller presented by Linjama et. al. (1) is shown in figure 3. Similarly, any extra features, e.g. anti-cavitation, could be incorporated to an existing controller.

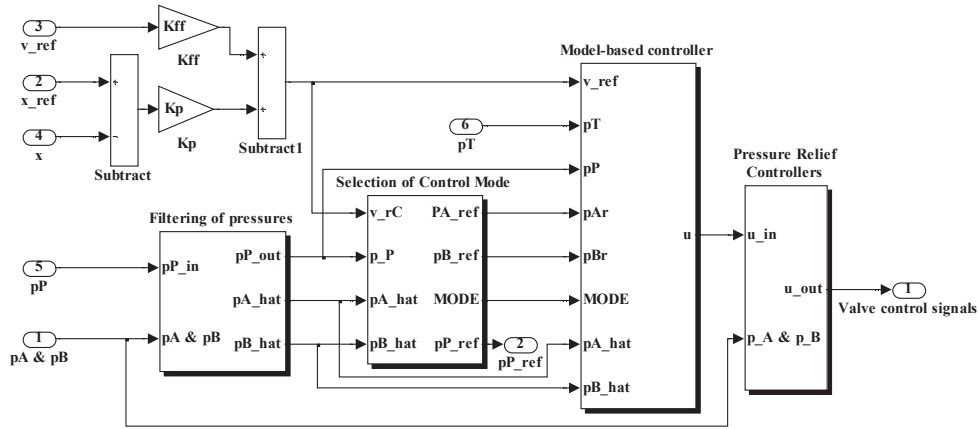
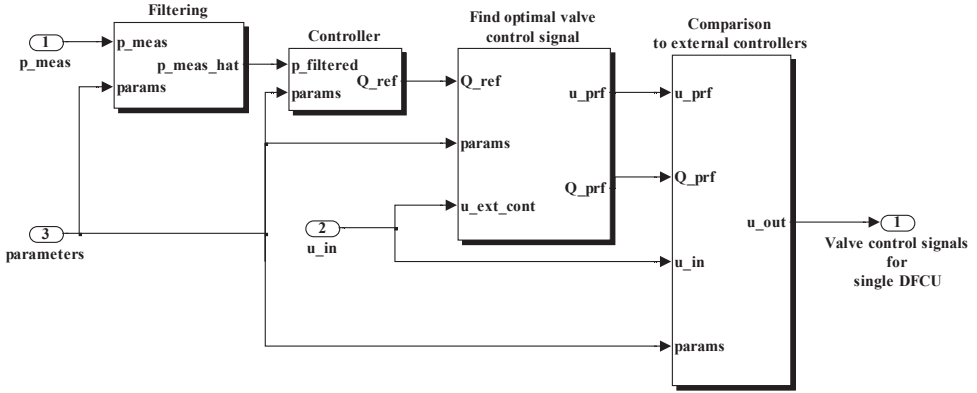


Figure 3: Modification of the controller proposed in (2).

## 2.1 Structure of the controller

Structure of the PRF is presented in figure 4. PRF consists of filtering of the pressure, controller which selects the optimal flow to tank, finding an optimal state and comparing the control signals to the ones from the actuator velocity controller.



**Figure 4: Structure of the pressure relief controller.**

Due to the noise in a measured pressure signal, filtering is preferred to decrease the switching frequency of the valves. Low-pass filtering and an addition of a small hysteresis reduces the number of valve switching significantly. In experiments a non-linear filtering by taking the median value of five samples with a sample time of 0.5 ms and a hysteresis of 1 % of the cracking pressure decreased the number of switching to one third compared to having only an analogue low-pass filtering with a cut-off frequency of 230Hz. Since the response time is crucial for the chamber relief functionality filtering is kept as small as possible and could even be eliminated from the PRF if pressure peaks do not emerge often in the system.

*Controller* calculates a proper reference flow of a DFCU by a simple equation of

$$Q_{REF} = u_{PRF\_out} \cdot \sum_{i=1}^{n_1} (\bar{Q}_{NOM})_i \quad (3)$$

where  $\bar{Q}_{NOM}$  is a vector of nominal flow rates through each on/off valve at the user set cracking pressure.  $u_{PRF\_out}$  is a proportional factor from 0 to 1 defined as

$$\begin{aligned} u_{PRF\_out} &= \frac{p_{filtered} - p_{cracking}}{p_{max} - p_{cracking}}, p_{cracking} \leq p_{filtered} \leq p_{max} \\ u_{PRF\_out} &= 0, p_{filtered} < p_{cracking} \\ u_{PRF\_out} &= 1, p_{filtered} > p_{max} \end{aligned} \quad (4)$$

where  $p_{filtered}$  is the filtered pressure,  $p_{cracking}$  is the user set cracking pressure parameter and

$$p_{max} = p_{cracking} \cdot \left( 1 + \frac{p_{max\_rel}}{100} \right) \quad (5)$$

where  $p_{max\_rel}$  is the user set parameter that defines the pressure-flow sensitivity of the controller i.e. the pressure rise with respect to the flow through the DFCU.

*Find optimal valve control signal* finds the opening combination that realizes a flow rate that is bigger than but closest to the one determined by the controller. This block also takes an advantage of the PNM-coding by using independent control of the valves with a fast sample time. This enables faster reaction to pressure peaks since a new state of a DFCU can be determined with faster intervals than with PCM-coding. Control principle is that each valve can be commanded to a new value after the time duration of the valve response time has passed independently of other on/off –valves. With the PCM-coded DFCUs, the sample time must always be slightly bigger than the valve response time because the uncertainties in the valve openings can cause large pressure peaks. Comparison of control strategies for PNM- and binary coded DFCUs are presented in figure 5.

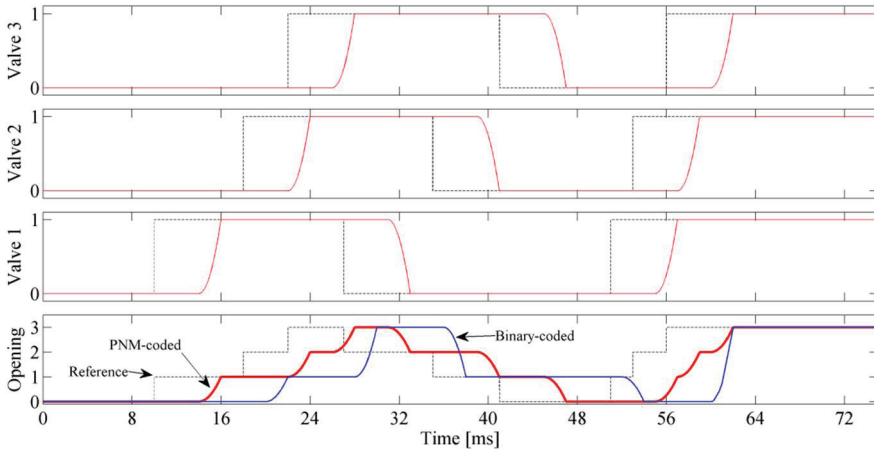


**Figure 5: Example of PNM control strategy. Valve delay 4 ms, total response time 7 ms, fast sample time 1 ms and slow sample time 8 ms.**

## 2.2 Simulations

Simulation model used is presented in figure 6. It consists of a volume, a PRF-controller and a model of the DFCU. The main controller output is kept as a zero vector and the tank pressure is set to zero. The pressure that is generated in the volume is modeled by substituting eq. 1 into eq. 2 and taking an integral of the derivative of the pressure. The effective bulk modulus and the volume of the chamber determine the pressure gradient when certain stepwise flow is directed to the chamber. No transmission line dynamics are included into the model. The static model of the DFCU calculates the sum of the flows through each of the on/off –valves with the equation:

$$Q = \sum_{i=n}^i kv_i \cdot \Delta p^{x_i} \quad (6)$$

in which  $kv_i$  is the individual flow-gain of the valve,  $\Delta p$  is the pressure difference over the valve,  $x_i$  is the exponential term of the valve model and  $n$  is the number of valves in the DFCU. Dynamics of the DFCU are modeled as a delay phase and a following constant

acceleration phase. Delay phase is known to be usually longer than the acceleration phase and therefore delay/response time ratio of 0.6 was used.

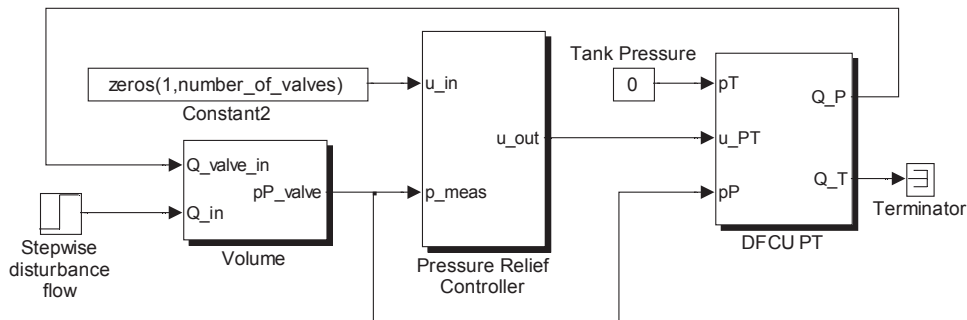


**Figure 6: Simulink model for the simulations of the pressure relief function**

Simulation studies show the valve behavior with 10, 2 and 0,5 ms switching time valves in figure 7. Hydraulic capacitance of the system is set to a small value for which the system barely remains stable. Stepwise flow of 75 l/min is applied to the volume with a constant bulk modulus of 1500 MPa. Cracking pressure is set to 16 MPa and the pressure-flow sensitivity to 50 % which in this case equals to 0.05 MPa/(l/min). The Nominal flow rate and the resolution of the DFCU are constant: 100 l/min @ 3 MPa and 64 respectively.

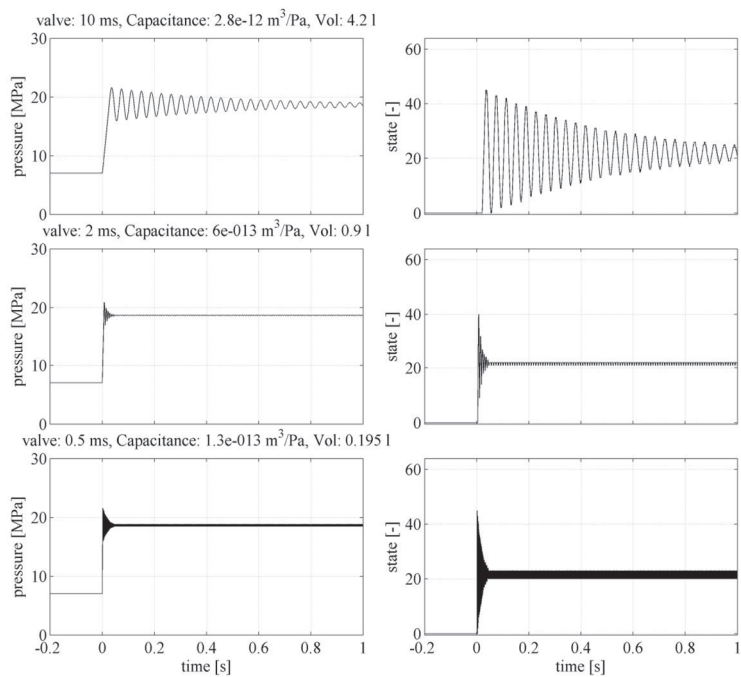


**Figure 7: Effect of valve response time to the minimum capacitance of the system.**

It can be noticed that fast response times are needed for relatively small volumes in order to avoid the instability with a constant disturbance flow. Instability relates to the fact that only discrete opening values are possible with a DFCU and as the hydraulic capacitance decreases the difference between the “too large state” and the “too small state” increases. For large enough hydraulic capacitances the difference between the states remains small and the response can be seen as marginally stable.

Since volumes in actuator chambers vary according to the actuator position, a minimum volume consisting of only hoses or pipes and dead volumes of an actuator can be quite small and therefore fast valves are needed in many applications. However, these values of hydraulic capacitances are only valid for a DFCU with a nominal flow of 100 l/min @ 3MPa and with stepwise flow of 75 l/min. Corresponding operating limits for any system with the same relation between the nominal valve flow and the disturbance flow is theoretically directly proportional as presented in table 1. Simulations of figure 7 are the ones numbered as 1, 4 and 7:

**Table 1: Effect of the nominal flow of a DFCU to the operation limits with a disturbance flow of 75 % of the nominal flow.**

Simulation	$t_{\text{RESPONSE}}$ [ms]	Vol. [l]	$B_{\text{EFF}}$ [MPa]	$Q_{\text{DFCU @ 3MPa}}$ [l/min]
1.	10	4,20	1500	100
2.	10	2.10	1500	50
3.	10	1,05	1500	25
4.	2	0,90	1500	100
5.	2	0,45	1500	50
6.	2	0,23	1500	25
7.	0,5	0,20	1500	100
8.	0,5	0,10	1500	50
9.	0,5	0,05	1500	25

Faster response with a PNM-coded DFCU can be seen with 10 ms switching time valves in figure 8. PNM-coded system has smaller fluctuations in the state diagram compared to binary-coded system which yields smaller settling time for the pressure. With faster 2 ms switching time both coding methods give fast settling times due to relatively large hydraulic capacitance in relation to valve response time.

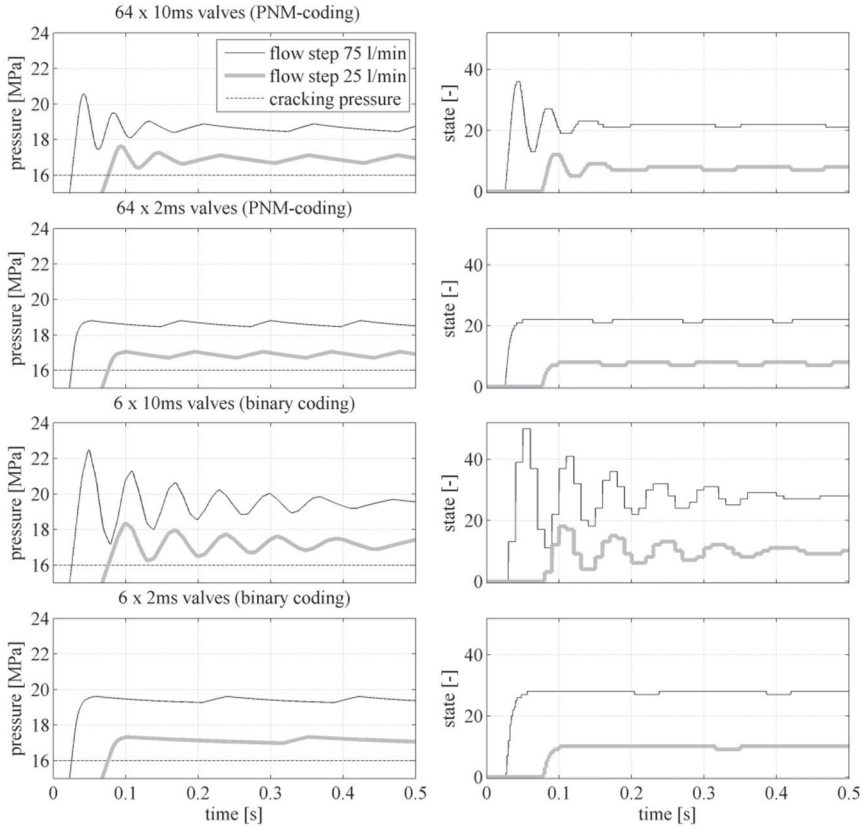


**Figure 8: Simulated responses of the pressure relief function with PNM- and binary-coded DFCUs. DFCU resolution 64/63, valve nominal flows 100 l/min @ 3 MPa, Volume 5.3 l and Bulk modulus 1500 MPa.**

### 3 TEST SYSTEM

For the validation of the pressure relief function and for comparison to traditional pressure relief valves, experimental test system is build. A DFCU is designed for relatively large flows with a small pressure drop. Better behavior of the pressure relief function with respect to the pressure ripple could have been achieved with a smaller nominal flow of the DFCU, but in this case the idea is to implement the pressure relief controller to a digital valve system that is designed for controlling an actuator.

Valve system consists of 16 parallel connected equal sized Bosch Rexroth KSDEU on/off –valves with 12 VDC coils. An emptied 5 liter accumulator is placed before the valves to give a total control volume of 6.7 liters. Valves are equipped with 1.6 mm orifices to achieve a total flow rate of 82 l/min @ 1.5 MPa. Valve openings and closings are boosted with booster electronics that provides a pull-in voltage of 48 V. Valve delays are measured to be around 5 ms and response time less than 10 ms. Effective bulk modulus is measured to be around 1900 MPa and remaining relatively constant with pressures larger than 5 MPa.



Hydraulic medium used is Shell Tellus S46 with a temperature of  $40 \pm 2$  °C. The PNM-coded DFCU of the test system is modified from an existing 4-way digital valve system used in previous studies by connecting ports A and B, and respectively P and T together as illustrated in figure 9.

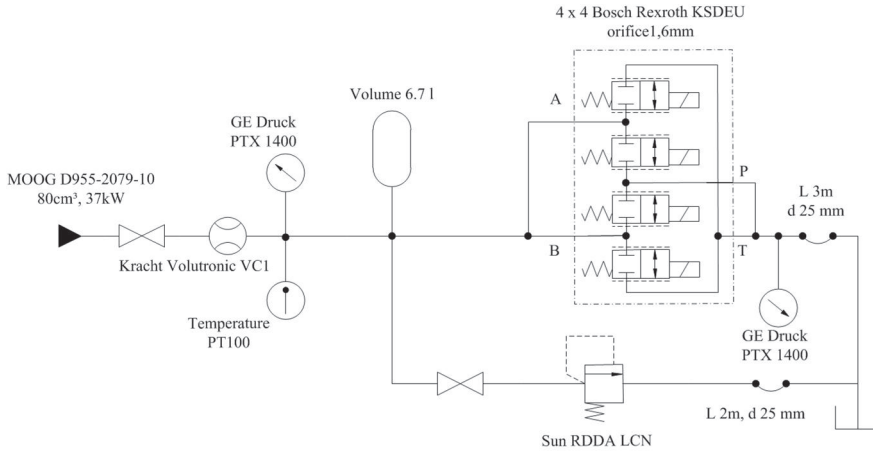


**Figure 9: Schematics of the test system.**

The selected pressure relief valve for the comparison is Sun Hydraulics RDDA LCN with a nominal flow of 95 l/min and a pressure range from 7 to 42 MPa. The valve is directly operated and a typical response time of 2 ms is mentioned in the data sheet.

## 4 EXPERIMENTAL RESULTS

Valve measurements are conducted by measuring step responses of the controller by creating different pressure gradients with constant disturbance flows from 10 to 75 l/min. High pressure gradients are created by allowing a constant flow from the pump to the tank through a number of valves of the DFCU and then rapidly closing all valves as illustrated in figure 10.

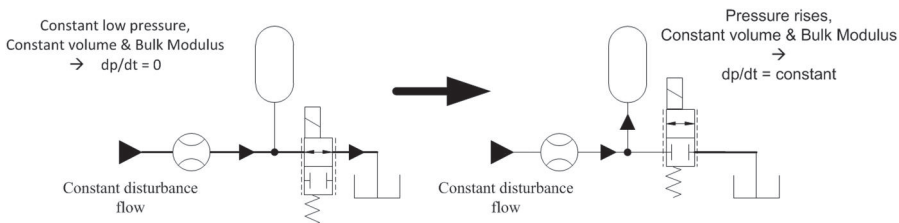


**Figure 10: Constant pressure gradient with constant flow from the pump unit.**

Comparison of the Sun Hydraulic RDDA LCN and the digital hydraulic valve system is presented in figure 11. The DFCU resolution is poor which is observed as a rather large ripple in the steady state pressure. Big flow rates of the valves reduce the number of valves used with high pressure differences. With a pressure setting of 16 MPa and a disturbance

flow of 75 l/min, states 3 and 4 are alternating in the steady state. Aggressiveness of the controller is kept same in the measurements of figure 11 so that percentual pressure rise is equal with different pressure settings. With a pressure setting of 4 MPa it can be seen that optimal DFCU state is found for disturbance flow of 75 l/min and the valve switching is stopped. Frequency of the pressure ripple varies according to the difference between the disturbance flow from the pump and the closest achievable flow through the DFCU.

Pressure overshoot with the PRF is appearing to be smaller than with the analogue valve with all pressure settings and disturbance flows over 25 l/min. Pressure rise with a small pressure setting with the analogue valve is relatively high. Minimum pressure setting was declared to be 7 MPa and therefore different valve should have been used with cracking pressure of 4 MPa.

Changes in the DFCU state at the beginning of the opening with a disturbance flow of 75 l/min and a pressure setting of 16 MPa is presented in figure 12. First state of the DFCU is commanded only 0.5 ms after the pressure has exceeded the set cracking pressure of 16 MPa. Pressure rise is fully stopped 11 ms later. With a binary coded DFCU the delay could have been up to 11 to 12 ms due to the lower sample time. The worst case total time to the fully stopped pressure gradient would have been around 20 ms when the valve response time is included.

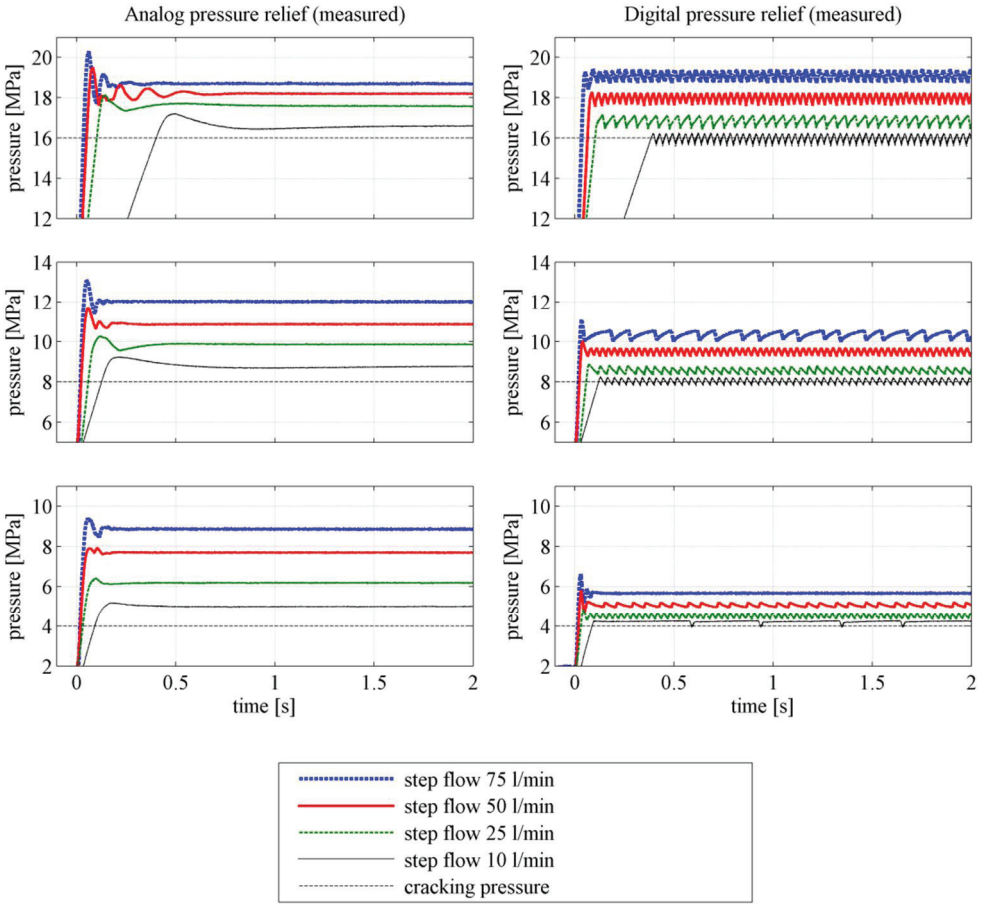


**Figure 11: Step responses of the Sun Hydraulics RDDA LCN (analogue) and the digital hydraulic valve system with 16 bit PNM-coded DFCU.**

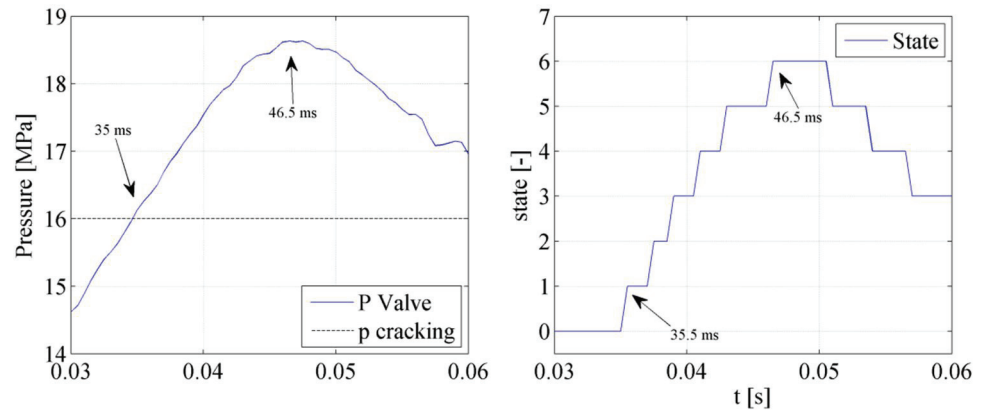


**Figure 12: Close up of pressure and valve state behaviour.**

## 5 CONCLUSIONS AND DISCUSSION

Programmability of the digital hydraulic valve systems makes it possible to integrate different valve functionalities to the digital control valve of an actuator. The pressure relief functionality studied in this paper is a new way to realize pressure peak elimination. This approach offers the possibility to set the cracking pressure via control panel while traditionally this has required manual work in case of fast acting shock relief valves. Also the spring properties have traditionally been fixed for some flow and pressure range. With a digital hydraulic solution properties such as pressure-flow sensitivity and hysteresis can be tuned online allowing a wide operating range.

The responses of the built test system shows that with relatively large disturbance flows the pressure peaks suppresses faster with PRF than with the analogue comparison valve. Simulation studies showed also good behaviour with small hydraulic capacitances when valves with response time of 2 ms are used. Comparison of the measured analogue valve and the simulation of a DFCU with 64 bit resolution and 2 ms switching time valves is shown in figure 13.

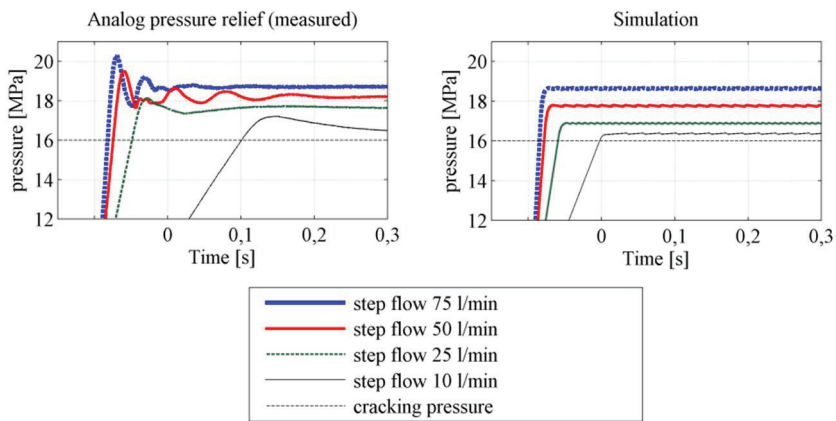


**Figure 13: Comparison of hydro mechanical pressure relief valve and a digital valve system with 64-bit DFCU with 2 ms valves.**

Digital hydraulics offers also fault tolerance as several valves are connected in parallel. Hydro mechanical valves are independent of electricity which is not the case with digital hydraulic valve system. Availability of electricity has to be ensured with safety critical systems to the digital hydraulic controller by auxiliary power sources if main power source is inoperative. Also effort should be made to improve the quality of the control algorithms especially with safety critical projects.

## ACKNOWLEDGEMENT

This research is supported by the project Digital Hydraulics (DiHy), which is part of the Finnish Metals and Engineering Competence Cluster, FIMECC-program EFFIMA.

## ABBREVIATIONS

PRF	Pressure Relief Function
DFCU	Digital Flow Control Unit
PNM	Pulse Number Modulation
PCM	Pulse Code Modulation
PRV	Pressure Relief Valve

## REFERENCES

- (1) Linjama et. al. 2007. Design and implementation of energy saving digital hydraulic control system. The Tenth Scandinavian International Conference on Fluid Power, Tampere, Finland.
- (2) Schepers, I., Weiler, D., Weber, J., Analysis of Control Methods for Switching Valve Configurations that Control Die Casting Machines as an Example, The 8th International Conference on Fluid Power (8th IFK), Dresden , Germany, March 26 - 28, 2012.
- (3) Kogler, H., Scheidl, R., The Hydraulic Buck Converter Exploiting the Load Capacitance. The 8th International Conference on Fluid Power (8th IFK), Dresden, Germany, March 26 - 28, 2012.
- (4) Heikkilä, M. & Linjama, M. 2011. Direct connection of digital hydraulic power management system and double acting cylinder – a simulation study. The Fourth Workshop on Digital Fluid Power, Linz, Austria.
- (5) NorrDigi<sup>TM</sup>. Norrhydro Oy, website: <http://www.norrhydro.com>, Retrieved June 6, 2012
- (6) Laamanen, A., Linjama, M., Vilenius, M., Pressure Peak Phenomenon in Digital Hydraulic Systems – a Theoretical Study. Power Transmission and Motion Control, PTMC2005, Bath, UK 7-9.9.2005.
- (7) Linjama, M., Fundamentals of Digital Microhydraulics, The 8th International Conference on Fluid Power (8th IFK), Dresden , Germany, March 26 - 28, 2012.
- (8) Karvonen, M., Juhola, M., Ahola, V. Söderlund, L. & Linjama, M. 2010. A miniature needle valve. In: Laamanen A. & Linjama M. (eds.). Proceedings of the Third Workshop on Digital Fluid Power, October 13-14, 2010, Tampere, Finland, pp. 61-78.
- (9) Ijas, M., Mäkinen, E., Linjama, M., Digital Hydraulic Pressure Con-trol. Proceedings of the 11th Scandinavian International Conference on Fluid Power SICFP'09, Linköping, Sweden, June 2-4, 2009.
- (10) Huova, M., Płaska, M., Siivonen, M., Linjama, M., Waldén, M., Vilenius, M., Sere, K.. Controller design of digital flow control valve. Proceedings of the 11th Scandinavian International Conference on Fluid Power SICFP'09, Linköping, Sweden, June 2-4, 2009.
- (11) Pontus Boström, Contract-Based Verification of Simulink Models. In: Shengchao Qin, Zongyan Qiu (Eds.), 13th International Conference on Formal Engineering Methods, ICFEM 2011, LNCS 6991, 291-306, Springer, 2011.
- (12) Boström, P., Linjama, M., Morel, L., Siivonen, L., Walden, M., Design and Validation of Digital Controllers for Hydraulics Systems, The Tenth Scandinavian International Conference on Fluid Power, SICFP'07, Tampere, Finland 21 – 23.3, 2007

# Analysis of Dynamic Properties of a Fast Switching On-Off Valve for Digital Displacement Pumps

Daniel B. Rømer, Per Johansen, Henrik C. Pedersen & Torben O. Andersen

Department of Energy Technology, Aalborg University, 9220 Aalborg East, Denmark

## ABSTRACT

The shift towards digital fluid power systems set new requirements for the components with regard to dynamic performance, reliability and controllability. Especially for valves to be used in digital displacement motors and pumps the requirements are extreme, as the allowed switching times for the valves are inversely proportional to the revolution speed. The focus of the current paper is on a prototype of a high efficient, one-stage, fast switching on-off valve, with special attention on the actuation side. Experimental measurement data is used to evaluate the developed system model.

**Keywords:** Modelling, Simulation, Digital displacement, One-stage valve, fast switching, Solenoid actuation, Magnetic Equivalent Circuit, Suction model

## 1 INTRODUCTION

Digital displacement pump/motors are upcoming technology, where each cylinder chamber is either enabled or disabled on a stroke by stroke basis, achieved by use of individual controlled valves. This effectively varies the unit displacement, a technique initially developed in the 80's at Edinburgh University [1]. This technique has shown to offer high part-load efficiency which can expand the use of fluid power in the industry, and has recently been announced to be a key part of a 7MW wind turbine being developed [2]. For this technology to be further developed there is a need for fast, efficient valves with the durability to withstand billions of operation cycles.

Until now, most research within the field have been conducted within the company Artemis Intelligent Power, where one-stage poppet valves with solenoid actuation is the main design concept [3, 4]. Other researchers have conducted work on a digital pump using modified commercial spool valves with solenoid actuation [5], but only mediocre efficiency is obtained using non-integrated valves for the cylinder chambers. In the field of fast switching on-off valves with high flow rates much research have been conducted [6, 7, 8]. However, while fast switching and appropriate flow rates are achieved for some concepts, they uses pilot

stage actuation and are thus more complex than a one-stage valve concept. As pointed out in [1], the actuation for a digital fluid power pump/motor valve does not need to be capable of opening against higher pressure differentials, and a direct electro-magnetic actuation is therefore possible and desirable for a simple robust valve actuation system. This benefit comes at the cost of requiring very accurate valve timing and estimations of bulk modulus. However, precise computer control together with fast acting valves and pressure chamber models seems to be able to overcome this difficulty.

In the present effort, a prototype electronic controlled seat valve is designed, with the aim of achieving fast switching times together with a low pressure loss. The basis for the project is a seat valve suitable for connecting the pressure chamber in a digital displacement pump to the low pressure manifold, having a maximum load pressure of 350 bar and a target shaft rotation speed of 1500RPM.

## 2 VALVE DESCRIPTION

The prototype valve suitable for meeting the requirements for a digital fluid power pump/motor is presented in figure 1. Flow is conducted through the inside of the valve plunger, and the plunger is actuated using two linear variable reluctance actuators (solenoids). As oppose to [3], the valve is bi-directional and do not utilize permanent magnets.

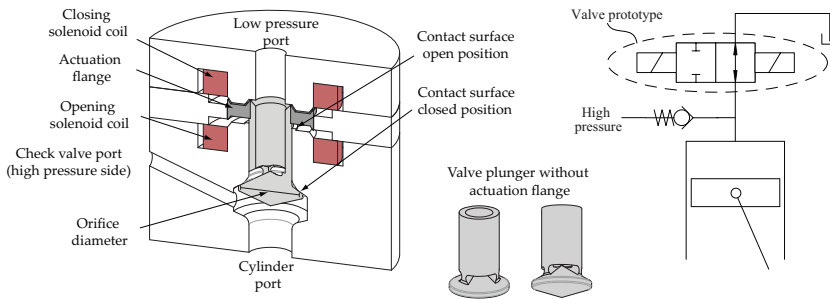


**Figure 1: Prototype low pressure valve section view**

To obtain a fast switching valve, the mass of plunger and actuation flange was sought minimized by considering material stresses calculated using structural FEM, and an aluminium alloy was chosen as plunger material. Furthermore, the end position contact surfaces were made small and a relatively loose guidance tolerance was selected to minimize valve movement friction forces. The actuation flange is designed with conical part at the inner and outer radius [9], leading to an enhanced available force in the weak actuation positions (large air gaps) compared to an actuation using purely flat parallel surfaces, thus improving the force vs. position actuation characteristic.

Dimensions and specifications of the prototype valve is given in table 1.

**Table 1: Dimensions and specifications of the prototype valve**

Orifice diameter	21 mm	Plunger material	Alu-alloy 7075-T6
Stroke length	1.55 mm	Flange material	Carbon steel
Moving mass	39 g	Actuation method	Dual solenoid
Closing switching time	3 ms	Guidance gap plunger	20 $\mu\text{m}$
Pressure loss @ 10 l/min	<0.1 bar	Guidance gap flange	100 $\mu\text{m}$

The principle of the dual solenoid actuation is shown in figure 2, where either the closing coil or the opening coil is energized to attract the actuation flange up or down respectively. Each magnetic circuit seeks to minimize the flux path reluctance, and therefore an actuation force is generated trying to minimize the primary air gaps shown in figure 2.

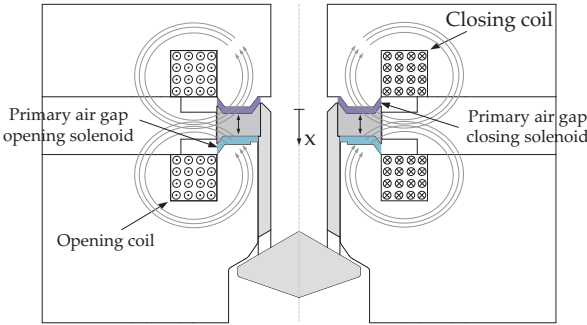


**Figure 2: Valve actuation, the valve opens/closes by energizing the corresponding coil.**

The solenoid actuation concept is simple and offers durable moving members, compared to other actuation concepts using moving permanent magnets or moving coils. It is in the nature of a solenoid to provide large forces for small currents when the air gap is small, and the valve actuation therefore uses little energy for holding the valve open (eg. idle operation). A disadvantage, however, is the need for two separate actuation coils, each requiring power electronics for current control. Furthermore, magnetic diffusion times will be significant due to the non-laminated magnetic circuit.

### 3 VALVE DYNAMICS MODEL

The valve dynamics model consists of two main parts; the valve movement part and the actuation part. The modelling is described in the following sections.

#### 3.1 Valve movement model

To accurately model the valve movement, a simple viscous friction model is not adequate. In particular, when the valve plunger is moved close to the end positions, increased damping is present. When driving the valve plunger away from a contact surface, a so called suction effect occurs, and when forcing the plunger towards a contact surface, a flow displacement effect is present close to valve impact. A valve movement model including these effects is



given by:

$$F_{act} - F_{damp} - F_{suct} = m\ddot{x} \quad (1)$$

where  $m$  is the total moving mass,  $F_{act}$  is the actuation force,  $F_{damp}$  the force arising from motion damping and  $F_{suct}$  the force resulting from suction effect. When modelling a complete digital pump/motor additional force terms should be added to account for pressure and flow forces.

### 3.1.1 Plunger damping force

The damping force opposes valve plunger movement. The damping force is modelled dependent on both plunger velocity and position, as given in equation (2).

$$F_{damp} = B_v(x, \text{sign}(\dot{x})) \dot{x} + B_D \text{sign}(\dot{x}) \dot{x}^2 \quad (2)$$

where  $B_D$  is a constant drag coefficient and the viscous damping coefficient  $B_v(x, \text{sign}(\dot{x}))$  is modelled as a constant term and a position dependent term to accommodate for the increased damping observed near the end positions of plunger movement, where oil is displaced from the contact surface between spool and housing as shown in figure 3. A similar situation is present when the plunger is opening and the plunger stroke is near open position.

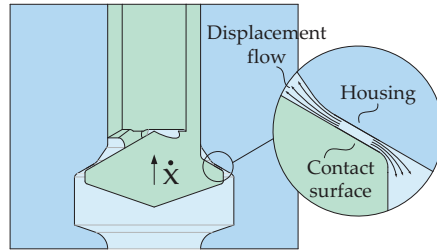


**Figure 3: Displacement flow near closed valve position**

The viscous damping coefficient is therefore modelled as:

$$B_v = \begin{cases} B_0 + B_{near,op} e^{-\frac{l_{sl}-x}{x_{0,op}}} & \text{for } \dot{x} > 0 \\ B_0 + B_{near,cl} e^{-\frac{x}{x_{0,cl}}} & \text{for } \dot{x} < 0 \end{cases} \quad (3)$$

The exponential division coefficients  $x_{0,op}$  and  $x_{0,cl}$ , influences the rate of decrease for the exponential terms, and denotes the distance where the exponential term has decreased to  $e^{-1} \approx 37\%$ . The constant damping term  $B_0$  sets the minimum value of  $B_v$ , which is dominant for plunger positions between open and closed position.

The movement model parameters  $B_0$ ,  $B_{near}$ ,  $x_0$  and  $B_D$  depend on the valve geometry, and are found based on experimental measurement.  $B_0$  may, however, be estimated by calculating the friction force between two parallel plates.

### 3.1.2 Plunger suction force

In addition to the friction force, a force opposing the plunger movement is present when initializing plunger movement from either the open or closed position. When attempting to

pull the plunger away from an end position, a vacuum is created in the contact surface region, opposing the plunger movement. This suction force is denoted  $F_{suct}$ . The force needed to overcome the suction effect and initiate plunger motion depends on both the magnitude of the externally applied force as well as time, and is modelled as two variable orifices and corresponding control volumes as illustrated in figure 4.

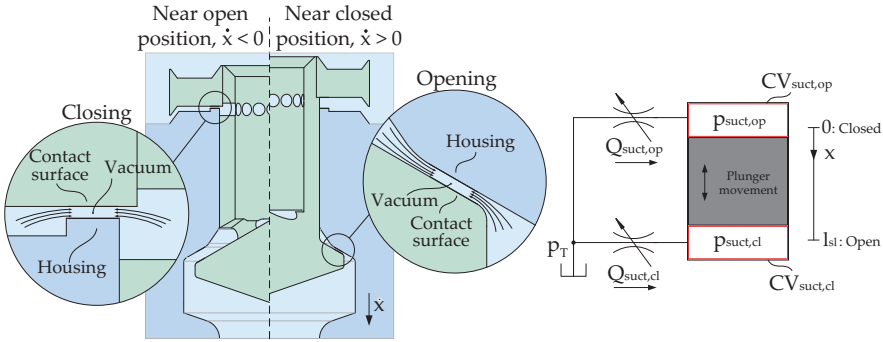


**Figure 4: Plunger suction principle and the utilized suction model**

The two variable orifices in the suction model are described by considering the flow into the vacuum region to be steady laminar flow between two parallel plates. The distance between the parallel plates is  $h$  and the length of the flow path between the plates is  $l$ . By letting the distance between the plates be dependent on the plunger position  $x$ , the wanted effect, where the oil flow is restricted to a large degree initially and decreased rapidly as a movement is initiated, is obtained. This is wanted for control volume  $CV_{suct,op}$  or  $CV_{suct,cl}$  when the plunger is at the closed or open position respectively. The flow model for  $CV_{suct,op}$  is:

$$Q_{suct,op} = \frac{2h_{suct,op}(x)^3}{3\mu l_{suct,op}} (p_T - p_{suct,op}) \quad \text{where} \quad h_{suct,op} = \begin{cases} x + h_{i,op} & \text{for } \dot{x} > 0 \\ l_{sl} & \text{for } \dot{x} \leq 0 \end{cases} \quad (4)$$

where  $h_{i,op}$  is the initial distance between parallel plates,  $l_{suct,op}$  the length of flow paths between parallel plates and  $p_{suct,op}$  the pressure of  $CV_{suct,op}$ . As the plate distance is cubed, the flow restriction is effectively limited to plunger positions near the open and closed position. Notice that a small initial plate distance is included to limit the flow restriction for  $x = 0$ , which is necessary to get correspondence between measurements and model. If the small initial distance is not included, the model too aggressively prevents plunger movement. This need for an initial distance may be a result of material surface imperfections at or close to the contact surface of the valve.

The pressure  $p_{suct,op}$  present in the suction control volume is modelled using the continuity equation as shown in (5). The oil stiffness is modelled as being pressure dependent including the effects of entrained air [10],

$$\dot{p}_{suct,op} = (Q_{suct,op} - A_{suct,op}\dot{x}) \frac{\beta_{eff}(p_{suct,op})}{V_{0,suct,op} + A_{suct,op}x} \quad (5)$$

$$\beta_{eff}(p_{suct,op}) = \frac{\beta_F}{1 + \alpha \left( \frac{p_0}{p_{suct,op}} \right)^{\frac{1}{\kappa}} \left( \frac{\beta_F}{\kappa p_{suct,op}} - 1 \right)} \quad (6)$$

where  $A_{suct,op}$  is the parallel plates area,  $V_{0,suct,op}$  the initial volume for  $CV_{suct,op}$ ,  $\beta_F$  the stiffness of oil,  $\alpha$  the volumetric content of entrained air at atmospheric pressure  $p_0$  and  $\kappa$  the adiabatic constant for air. Similar equations are used for  $CV_{suct,cl}$ , however here  $x$  is replaced with  $l_{sl} - x$ .

Physically the initial volumes for the control volumes approaches zero when the two parallel surfaces are in close contact. However, to avoid numerical instability, a relatively large initial volume and parallel plate's area must be included. Even though these values differ from the physical interpretation, the model suction characteristic is maintained.

The suction force  $F_{suct}$  is applied to the plunger using the suction control volume pressures:

$$F_{suct} = \begin{cases} A_{suct,op} p_{suct,op} & \text{for } \dot{x} > 0 \\ A_{suct,cl} p_{suct,cl} & \text{for } \dot{x} < 0 \end{cases} \quad (7)$$

### 3.2 Valve actuation model

The valve actuation system for each direction consist of a servo amplifier connected to the solenoid coil, and is modelled as indicated in figure 5. The static magnetic force model, magnetic diffusion model and electric circuit model is described next.

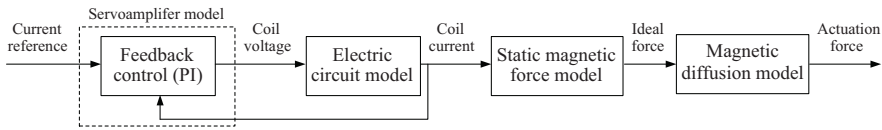


Figure 5: Actuation model overview

#### 3.2.1 Static magnetic force model

Lumped parameter Magnetic Equivalent Circuits (MEC) have been shown to offer accurate modelling results compared to measurements [11, 12], and different levels of MEC complexity can be deployed depending on the magnetic operation range and system geometry. The ferromagnetic material used within the prototype valve saturates at larger flux densities, however the intended operation range of the actuation is within the linear region, and these effects are thus discarded in the MEC for simplicity. Furthermore, as the magnetic reluctance of the circuit in the linear operation range is mainly determined by the air gap reluctances, only the air gap reluctances are included in the MEC model. Material saturation and flux leakage are, however, included in the FEM models, cf. figure 9.

The magnetic circuit geometry determines the static behaviour of the valve actuator, by determining the circuit reluctance  $\mathcal{R}_{eq}$ . Hopkinson's law states that the relationship between Magneto-Motive Force (MMF) and circuit flux  $\Phi$  may be described as:

$$MMF = Ni = \Phi \mathcal{R}_{eq}(x) \quad (8)$$

The circuit flux and coil self-inductance is related by:

$$L(x) i = N \Phi \Rightarrow L(x) = \frac{N^2}{\mathcal{R}_{eq}(x)} \quad (9)$$

Following the assumption of linear magnetic properties, the solenoid force may be calculated using the magnetic circuit co-energy as [13]:

$$F(x, i) = \frac{1}{2} \frac{\partial L(x)}{\partial x} i^2 = -\frac{1}{2} N^2 i^2 \frac{\frac{d}{dx}(\mathcal{R}_{eq}(x))}{\mathcal{R}_{eq}(x)^2} \quad (10)$$

For a given position the actuation force has a quadratic relation to the coil current, and force is generated in the direction seeking to minimise the circuit reluctance, independent on current direction.

#### **Analytic estimation of circuit reluctance $\mathcal{R}_{eq}$**

The reluctance model includes three main air gap reluctances  $\mathcal{R}_{op}$ ,  $\mathcal{R}_{cl}$  and  $\mathcal{R}_{flange}$  as illustrated to the left in figure 6.

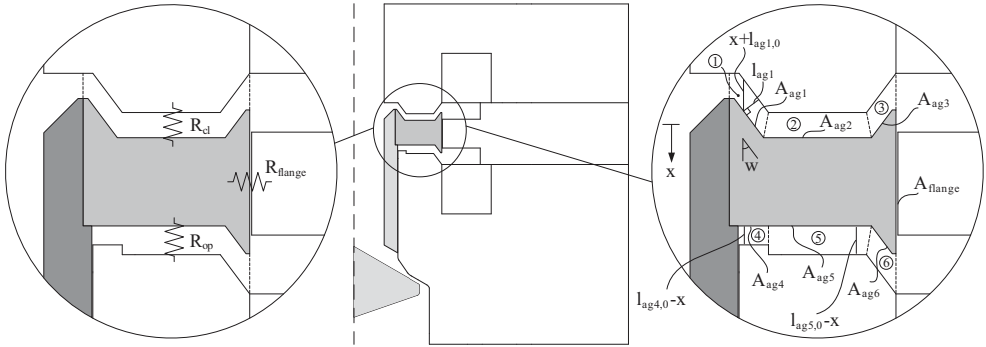


**Figure 6: Elements in reluctance model**

Considering the magnetic circuits driven by the two coils as shown in figure 7, enables the equivalent reluctance to be calculated as given in (11) and (12).

$$\begin{aligned} \mathcal{R}_{eq,op}(x) &= \mathcal{R}_{op}(x) + \mathcal{R}_{cl}(x) \parallel \mathcal{R}_{flange} \\ &= \mathcal{R}_{op}(x) + \frac{\mathcal{R}_{cl}(x) \mathcal{R}_{flange}}{\mathcal{R}_{cl}(x) + \mathcal{R}_{flange}} \end{aligned} \quad (11)$$

$$\begin{aligned} \mathcal{R}_{eq,cl}(x) &= \mathcal{R}_{op}(x) \parallel \mathcal{R}_{flange} + \mathcal{R}_{cl}(x) \\ &= \mathcal{R}_{cl}(x) + \frac{\mathcal{R}_{op}(x) \mathcal{R}_{flange}}{\mathcal{R}_{op}(x) + \mathcal{R}_{flange}} \end{aligned} \quad (12)$$

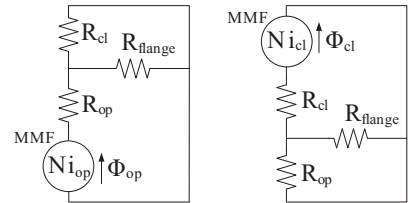


**Figure 7: Equivalent circuits**

The reluctance of each air gap element are described by,

$$\mathcal{R} = \frac{l}{\mu A} \quad (13)$$

where  $l$  is the length between parallel air gap plates,  $\mu$  the permeability of air and  $A$  the area of each plate.

To estimate the reluctances  $\mathcal{R}_{op}(x)$  and  $\mathcal{R}_{cl}(x)$ , each air gap is estimated as three reluctances connected in parallel with constant air gap area. The air gap determining  $\mathcal{R}_{cl}$  is divided into air gap element 1,2 and 3 as shown to the right in figure 6. Similarly,  $\mathcal{R}_{op}$  is divided in element 4,5 and 6. In total yielding:

$$\mathcal{R}_{eq,op}(x) = \mathcal{R}_{op}(x) + \frac{\mathcal{R}_{cl}(x) l_{flange}}{\mu A_{flange} \left( \mathcal{R}_{cl}(x) + \frac{l_{flange}}{\mu A_{flange}} \right)} \quad (14)$$

$$\mathcal{R}_{eq,cl}(x) = \mathcal{R}_{cl}(x) + \frac{\mathcal{R}_{op}(x) l_{flange}}{\mu A_{flange} \left( \mathcal{R}_{op}(x) + \frac{l_{flange}}{\mu A_{flange}} \right)} \quad (15)$$

with

$$\mathcal{R}_{op}(x) = \left( \frac{\mu A_{ag4}}{l_{ag4}(x)} + \frac{\mu A_{ag5}}{l_{ag5}(x)} + \frac{\mu A_{ag6}}{l_{ag6}(x)} \right)^{-1} \quad (16)$$

$$l_{ag1} = l_{ag3} = (x + l_{ag1,0}) \sin w \quad (18)$$

$$l_{ag2} = x + l_{ag1,0} \quad (19)$$

$$l_{ag4} = l_{ag4,0} - x \quad (20)$$

$$\mathcal{R}_{cl}(x) = \left( \frac{\mu A_{ag1}}{l_{ag1}(x)} + \frac{\mu A_{ag2}}{l_{ag2}(x)} + \frac{\mu A_{ag3}}{l_{ag3}(x)} \right)^{-1} \quad (17)$$

$$l_{ag5} = l_{ag5,0} - x \quad (21)$$

$$l_{ag6} = (l_{ag5,0} - x) \sin w \quad (22)$$

The static actuation model, equation (10), discards magnetic transient effects, eg. the actuation force follows the coil current without delay. However, due to Eddy-currents within the non-laminated material, a considerable magnetic diffusion time is expected. The result is a delayed actuation force and also a decreased inductance. This effect on actuation force is included by adding a filter to the actuation model, as described in the next section.

### 3.2.2 Magnetic diffusion model

The transient behaviour of the valve actuation is modelled using the FEM software package OPERA-2D, which solves the axisymmetric vector diffusion equation with Dirichlet boundary conditions, having the magnetic vector potential  $A$  as the unknown variable:

$$\nabla \times \left( \frac{1}{\mu} \nabla \times A \right) = J_s - \sigma \frac{\partial A}{\partial t} \quad (23)$$

where  $J_s$  is the source current density, and  $\sigma \frac{\partial A}{\partial t}$  are the induced (Eddy) currents. All transient simulations are performed by initially applying a voltage step, which is maintained until a predefined current limit is reached, whereupon the source is switched to a current source maintaining the wanted maximum actuation current. This source behaviour approximates the servo amplifier used for experimental measurements.

In a 1-dimensional case, where a conducting material of width  $d$  is subjected to a step in external magnetic field  $B_0$ , the solution of the magnetic diffusion may be described in the form [14],

$$B_x(z,t) = B_0 \left( 1 - \sum_{n \text{ odd}} \frac{4}{n\pi} \sin \left( \frac{n\pi z}{d} \right) e^{-\frac{n^2}{\tau} t} \right) \quad (24)$$

where  $x$  is in the direction of the external field and  $z$  runs along the width of the conducting material. The opposing term (representing the effect of Eddy-currents) decays exponentially. Assuming the magnetic diffusion of the valve actuation to behave in a somewhat similar manner to this simplified example, the magnetic diffusion is modelled as a position dependent first order system:

$$G_d = \frac{1}{\tau_d(x)s + 1} \quad (25)$$

where the magnetic diffusion time constant is modelled as proportional to the coil self-inductance,  $\tau_d(x) = \gamma_d L(x)$ .  $\tau_d(x)$  ranges from 4 ms (open) to 11 ms (closed) for the closing actuation of the prototype valve. In figure 8, a comparison of the modelled transient actuation behaviour and the first order actuation force model is given, showing similar characteristics.

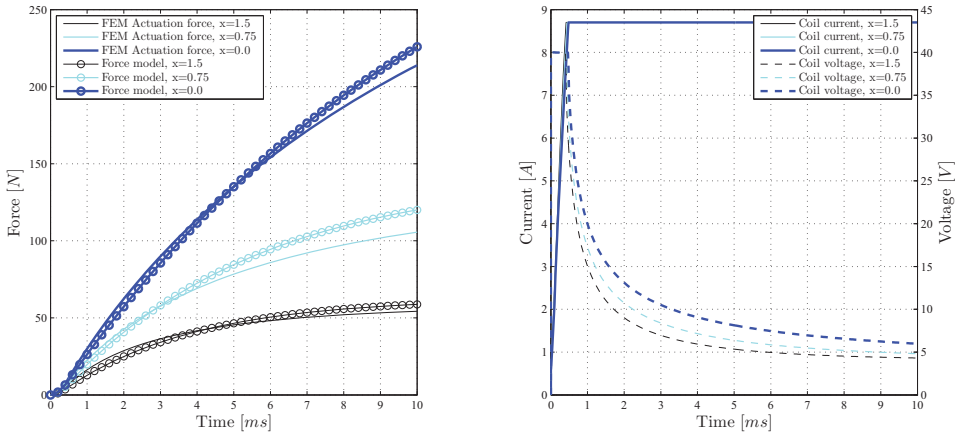


**Figure 8: Transient actuation force simulations for three plunger positions with corresponding voltages and currents. A simple first order actuation force model is plotted along with the FEM simulation results.**

### 3.2.3 Electric circuit model

To model the coil current, each coil is modelled using a lumped parameter approach. The voltage-current relationship for each coil circuit is given as,

$$v = R_{coil} i + \frac{d}{dt} (L_{trans}(x) i) = R_{coil} i + \frac{dL_{trans}(x)}{dx} \frac{dx}{dt} i + L_{trans}(x) \frac{di}{dt} \quad (26)$$

The transient self-inductance  $L_{trans}(x)$  used in the electric circuit model differs from the static self-inductance  $L(x)$ , as a result of eddy-currents effectively limiting the rate of change of magnetic flux when applying a voltage step, leading to a (transiently) lowered self-inductance. The transient self-inductance  $L_{trans}$  is determined from the transient FEM simulations, taken as a mean inductance in the period from zero time to the time where the maximum allowable current is reached (right hand side of figure 8, 0-0.5 ms).

In equation (26),  $\frac{di}{dt}$  is isolated and integrated. To supply voltage and current for the prototype valve, a servo amplifier is used. This servo amplifier utilizes closed loop PI current control, with PWM voltage as output. A simple model of this current control loop is included in the dynamic valve model.

## 4 EXPERIMENTAL SETUP

The experimental measurement is conducted by use of two measurement setups. Both setups uses a programmable DSP for control and data acquisition, two servo amplifiers for current control and AD conversion boards.

### 4.1 Fixed position setup

In this setup the valve plunger is connected to a force gauge, and a number of measurements are conducted with the plunger fixed in various positions. The plunger position is measured by means of a laser distance meter with a resolution of  $0.05 \mu\text{m}$ . The coil current is controlled to wanted DC-values to test the static performance of the valve actuation using PWM voltage ( $\pm 40 \text{ V}$  mean).

### 4.2 Dynamic valve test setup

In this setup the valve assembly is filled with hydraulic oil at atmospheric pressure, and actuated to switch between open and closed states. Position measurement with the laser distance meter was not possible in the closed assembly, and a position sensor based on a permanent magnet and a Hall Effect sensor is fitted. In these measurements, the actuation current is controlled to give approximately constant actuation force independent on plunger position.

## 5 MEASUREMENT RESULTS

Results from measurements on the prototype valve are given below. In addition to these valve actuation/movement measurements, flow-pressure measurement have been performed showing a pressure drop in the range 0-0.45 bar for flow rates of 0-27 l/min respectively.

### 5.1 Static actuation performance

The static performance for three different plunger positions are presented in figure 9, shown together with the corresponding FEM analysis and analytic model forces.

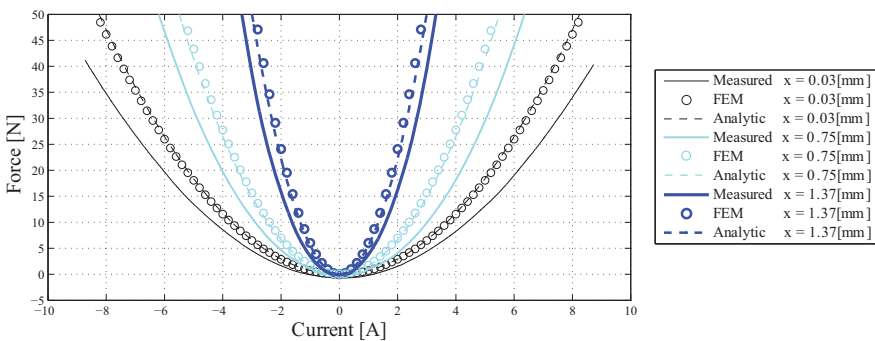


**Figure 9: Forces for opening solenoid at three fixed plunger positions.**

Good correspondence between the FEM analysis and the analytic model are seen, however some deviation is present in comparison with the measured actuation forces. The models predict the change in actuation force for different positions and the parabolic characteristic well, but the measured force levels are lower than the models.

The lower actuation force measured is assumed to be caused by an increased magnetic reluctance, and thereby reduced circuit flux leading to lowered generated force, as a result of the PWM voltage controlled current. This PWM voltage applies alternating voltages with a switch frequency of 50 kHz, leading to the presence of Eddy-currents even when a steady average current level is achieved.

As the parabolic characteristic of the actuation force with respect to current is well predicted by the model, a correction of the model may easily be applied, by adding a reluctance contribution to equation (14) and (15), whereby the modelled steady state force for a given position and current corresponds to the measurements. This correction is used as basis for comparing the dynamic measurements with the valve model in the next section, in order to better evaluate the valve movement model.

## 5.2 Dynamic valve test

In order to generate the model results presented in this section, the valve actuation model (figure 5) is combined with the valve movement model (equation (1)), which then solves the plunger movement  $x$  given some current reference. An appropriate current reference is calculated from a desired constant actuation force  $F_{ref}$  using the plunger position  $x$ , based on equation (10).

The effects of the suction force in the valve movement model is most apparent when using a relatively small actuation force and initialising movement from different positions. Referring to figure 10, it is seen that no suction effect is present for movements with initial positions away from open or closed valve state. A modest suction effect is present when initiating movement from the open position ( $x=1.55$ ), and a considerable suction effect is present when opening from closed position ( $x=0$ ). This difference between opening and closing of the valve is expected based on the difference in contact surface area, and is well captured by the model.

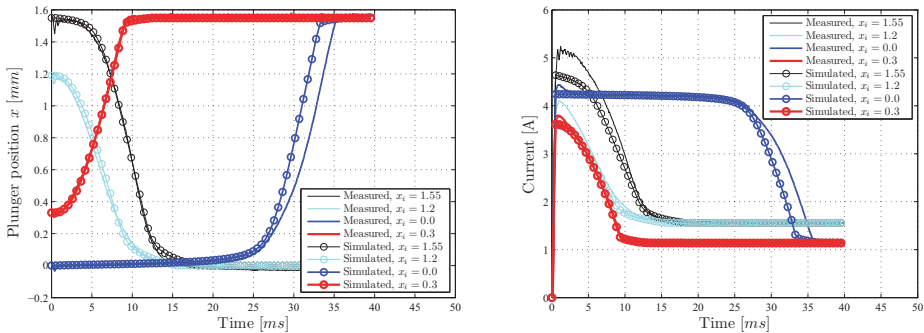


**Figure 10: Measured and simulated valve response for different initial positions and directions, with a relatively small actuation force of  $F_{ref} = 10$  N applied. Oil temperature  $20^\circ\text{C}$**



The valve closing response for different actuation forces are shown in figure 11. The dynamic behaviour is largely captured by the developed model for different actuation forces, and a valve closing switching time of 3 ms is obtained, suitable for use in a digital fluid power pump/motor. The oscillatory behaviour seen at larger currents are a result of unwanted disturbance in the position measurement, giving an oscillating current reference. Only the simulated coil voltages are shown, as PWM voltages was used in the measurements.

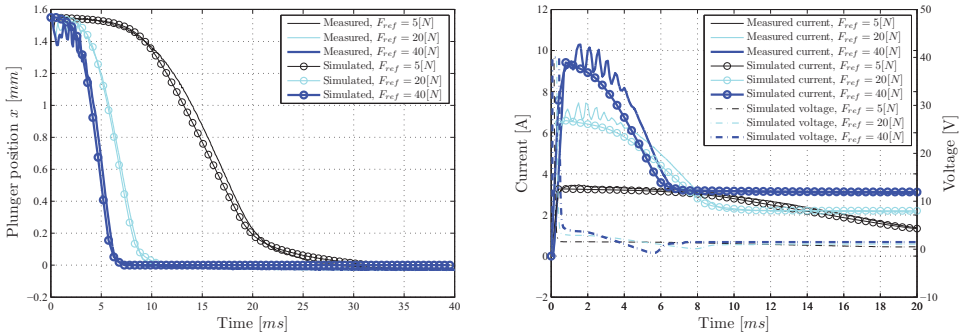


**Figure 11: Valve closing response for various actuation force references. Oil temperature  $20^{\circ}\text{C}$**

Opening valve responses are shown in figure 12, where an increased switching time of 4.5 ms is obtained due to the larger suction force compared to valve closing. This result, however, is of less importance compared to valve closing, as valve opening force is performed by fluid pressure forces in digital pump operation, as the valve is self-acting when opening, and the second solenoid is used for keeping the valve open.

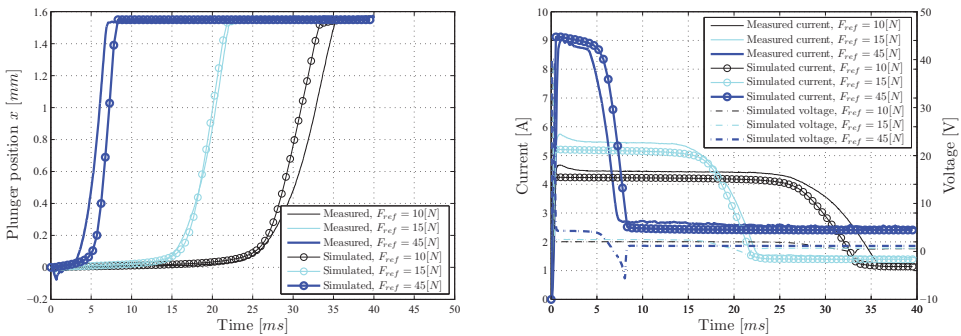


**Figure 12: Valve opening response for various actuation force references. Oil temperature  $20^{\circ}\text{C}$**

## 6 CONCLUSIONS

A functional prototype of a valve suitable for a digital displacement pump has been developed, and the corresponding models have been verified by means of experimental measurements. A closing time of 3 ms has been measured, showing that the valve actuation is appropriate for a fast switching on-off valve for use in a digital displacement pump. An opening transition time of 4.5 ms is measured using the valve actuation to provide opening forces.

Methods for modelling the suction and near-end damping effect are presented, giving good correspondence with measurement. However, guidelines for predicting the model coefficients based on geometry remains a topic for further research.

An analytic, static, solenoid actuation force model is developed, and this force model is combined with a position dependent first order filter to account for magnetic diffusion time. A reduction of the measured static force compared to the model predictions is seen, which is caused by the PWM voltage excitation. The diffusion time constant is relatively large compared to the valve transition time, which indicates a dominating effect of the Eddy-currents, showing a weakness in the actuator design.

Further work includes force measurements using DC voltage source, and examination of ways to improve the transient actuation performance, including material laminations or alternative magnetic circuit materials.

## PARAMETERS

$l_{sl}$	1.55 mm	Valve stroke length
$B_0$	16.8 Ns/m	Constant viscous friction coefficient
$B_{near,op} / B_{near,cl}$	2000/7500 Ns/m	Friction coefficient, opening/closing
$x_{0,op} / x_{0,cl}$	20/50 $\mu$ m	Exponent division value, opening/closing
$B_{D,op} / B_{D,cl}$	200/250 Ns <sup>2</sup> /m <sup>2</sup>	Drag coefficient, opening/closing
$A_{suct,op} / A_{suct,cl}$	12.5/7.6 cm <sup>2</sup>	Plates area for opening/closing
$V_{0,suct,op} / V_{0,suct,cl}$	10.4/8.3 cm <sup>3</sup>	Initial volumes for $CV_{suct}$
$h_{i,op} / h_{i,cl}$	26/45 $\mu$ m	Initial distance, opening/closing
$\beta_F$	16000 bar	Oil stiffness
$\alpha$	0.5 %	Volumetric content of entrained air
$l_{suct,op} / l_{suct,cl}$	1.6/1.6 mm	Length of flow path, opening/closing
$l_{ag1,0} / l_{ag4,0} / l_{ag5,0}$	0.55/1.7/2.2 mm	Initial distance element 1/4/5, for $x = 0$
$l_{flange}$	0.1 mm	Flange air gap length
$A_{ag1} / A_{ag2} / A_{ag3}$	133.5/377.0/170.0 mm <sup>2</sup>	Air gap area element 1/2/3
$A_{ag4} / A_{ag5} / A_{ag6}$	51.2/377.0/170.0 mm <sup>2</sup>	Air gap area element 4/5/6
$A_{flange}$	527.8 mm <sup>2</sup>	Flange air gap area
$w$	37 deg	Flange angle
$N$	92	Coil winding number
$R_{coil}$	0.48 $\Omega$	Coil ohmic resistance
$\gamma_d$	0.85	Magnetic time constant inductance factor

## REFERENCES

- [1] W. Rampen, *The Development of Digital Displacement Technology*, ch. Keynote address, pp. 12–17. Fluid Power and Motion Control (FPMC), 2010.
- [2] Mitsubishi, “Seaangel - the future of offshore wind.” MPSE Brochure, 2011.
- [3] W. Rampen, J. Almond, and S. Salter, “The digital displacement pump/motor operating cycle: Experimental results demonstrating the fundamental characteristics,” in *International Fluid Power Workshop, Bath*, 1994.
- [4] S. Salter and H. S. Rampen, William, “Improved fluid-working machine,” 12 1990. Patent No. EP 0494236 B1.
- [5] J. Tammisto, M. Huova, M. Heikkilä, M. Linjama, and K. Huhtala, “Measured characteristics of an in-line pump with independently controlled pistons,” in *7th International Fluid Power Conference*, 2010.
- [6] J. Pohl, M. Sethson, P. Krus, and J. Palmberg, “Modelling and validation of a fast switching valve intended for combustion engine valve trains,” *Proceedings of The Institution Of Mechanical Engineers Part I*, vol. 216, 2002.
- [7] B. Winkler and R. Scheidl, “Development of a fast seat type switching valve for big flow rates,” in *The Tenth Scandinavian International Conference on Fluid Power*, vol. 10, pp. 137–146, 2007.
- [8] B. Winkler, A. Ploekinger, and R. Scheidl, “A novel piloted fast switching multi poppet valve,” *International Journal of Fluid Power*, vol. 11, pp. 7–14, 2010.
- [9] B. Lequesne, “Finite-element analysis of a constant-force solenoid for fluid flow control,” *IEEE Transactions on Industry Applications*, vol. 24, pp. 574–581, 1988.
- [10] M. H. Kim, S., “Measurement of effective bulk modulus for hydraulic oil at low pressure,” *Journal of Fluids Engineering, Transactions of the ASME*, vol. 134, no. 2, 2012.
- [11] M. Batdorff and J. Lumkes, “High fidelity magnetic equivalent circuit in an axisymmetric electromagnetic actuator,” *IEEE Transactions on Magnetics*, vol. 45, 2009.
- [12] J. Reuter, S. Maerkl, and M. Jaekle, “Optimized control strategies for fast switching solenoid valves,” *International Journal of Fluid Power*, vol. 11, pp. 23–33, 2010.
- [13] S. Cetinkunt, *Mechatronics*. John Wiley and Sons, Inc., 2006.
- [14] H. H. Woodson and J. R. Melcher, *Electromechanical Dynamics*. John Wiley and Sons, Inc., 1968.

# Active control of pressure pulsation in a switched inertance hydraulic system using a rectangular-wave reference signal

Min Pan, Nigel Johnston, Andrew Hillis  
University of Bath

## ABSTRACT

The nature of digital hydraulic systems may cause severe pressure pulsation problems. For example, switched inertance hydraulic systems (SIHS) can be used to adjust or control flow and pressure by a means that does not rely on dissipation of power, but they have noise problems due to the pulsed nature of the flow. An effective method to reduce the noise is needed that doesn't impair the system performance and efficiency. In this paper, active control of fluid-borne noise is described using an adaptive control system. A rectangular wave signal was used as the reference signal in the adaptive control algorithm. The rectangular waveform corresponds to the demand signal for the switched valve and contains all the necessary harmonics. Using this rectangular signal, more harmonics can be cancelled compared with using a sinusoidal reference signal and only one adaptive filter is needed for noise attenuation, which simplifies the controller and computation.

A "switched inertance hydraulic system" in a flow booster configuration was used as the test rig. Experimental results show an acceptable cancellation was achieved by using this method. It can be concluded that the method is a promising solution for a compromise between noise cancellation and computation speed requirement.

## 1 INTRODUCTION

In most fluid power hydraulic systems, the speed and force of a load are controlled by using valves to throttle the flow and control the hydraulic pressure or reduce the flowrate. This is a simple but extremely inefficient method as the excess energy is lost as heat. The switched inertance hydraulic system (SIHS) is one of the alternative methods which can provide varied flow and pressure by a means that does not rely on dissipation of power [1]. Brown presented a number of switched reactance devices which provided good results both in simulation and experimentally [2, 3]. The flow or pressure from such devices can be controlled by changing the mark-space ratio, that is, the ratio of the widths of the positive and negative cycles. However, such systems suffer from noise problems [1-3]. This is because the pulsed nature of a high-speed switching valve introduces severe pressure ripple into the inlet and outlet lines. The pressure pulsation could result in serious noise and

vibration problems. A method is needed to reduce the pulsation without impairing the static or dynamic performance characteristics or reducing the system efficiency.

An active device, which senses and cancels the pressure pulsation, has been applied successfully in a SIHS based on sinusoidal reference signals [4]. This is a very promising solution for reducing the pressure pulsation in digital hydraulic systems. It has several advantages over passive noise control systems, being effective for low frequency cancellation and a wide range of frequencies without impairing the system's dynamic response. It has a quick adaptive response, and is robust and versatile. It consists of a number of narrowband adaptive notch filters acting in parallel, each based on a sinusoidal reference signal at a multiple of the fundamental frequency of the switching valve. The outputs of these notch filters are added together to drive one fast-acting valve. The number of harmonics that can be cancelled is limited by the computational speed of the digital controller.

In this paper an alternative approach is used whereby the pulse signal that is used to drive the switching valve for the SIHS is used as the reference signal. The pulse signal takes the form of a rectangular wave with unequal width positive and negative pulses. The pressure or flow output of the SIHS is changed by changing the mark-space ratio (ratio of positive to negative pulse width). This has a number of possible advantages:

- the controller is simplified and computation may be decreased;
- a greater number of harmonics may be cancelled;
- the reference signal follows changes in the SIHS mark-space ratio, which should result in reduced adaptation time when the mark-space ratio changes.

In this paper, firstly the SIHS is introduced and the pressure pulsation problem presented. The principle of the adaptive least mean square (LMS) filter and details of the design of the noise controller are described. A piezoelectric valve was selected and used as the actuator for noise cancellation in terms of its fast response and high frequency bandwidth [5]. The adaptive cancellation filter using a rectangular-wave reference signal was implemented based on a dSPACE 1005 board.

## 2 SWITCHED INERTANCE HYDRAULIC SYSTEMS

Two basic modes can be configured by reversing the inlet and outlet connections in a three-port SIHS. In one mode it acts as a flow booster; in the other it performs as a pressure booster [1]. Figure 1 (a) shows the arrangement of a flow booster. It consists of a high-speed switching valve with one common port, two switched ports and a long, small diameter 'inertance' tube. The common port is connected alternately to high pressure (HP) supply port and then the low pressure (LP) supply port.

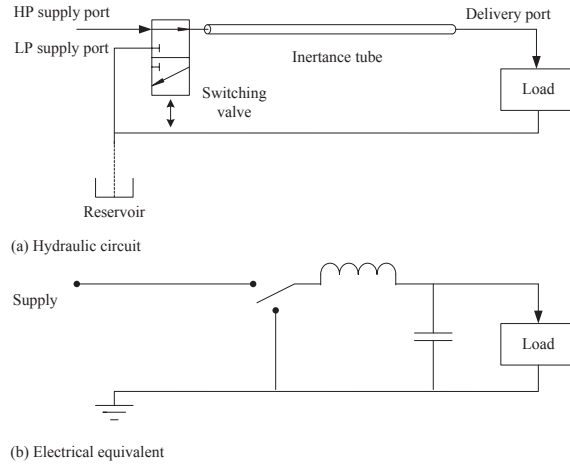


**Figure 1 Schematic diagram of flow booster arrangement [1]**

The switching valve operates cyclically and rapidly such that the supply and boost ports are opened alternately. The delivery port might connect to a loading system. When the valve is connected to the HP supply port, flow passes from the HP supply port to the delivery port and a high speed fluid occurs in the inertia line. When the valve is open to the LP supply port, fluid is drawn from the LP supply port to the delivery port by large momentum of the fluid in the inertia line. As long as the valve is switched quickly, the delivery flow will only reduce slightly due to small deceleration of fluid velocity during this phase, as shown in Figure 2.

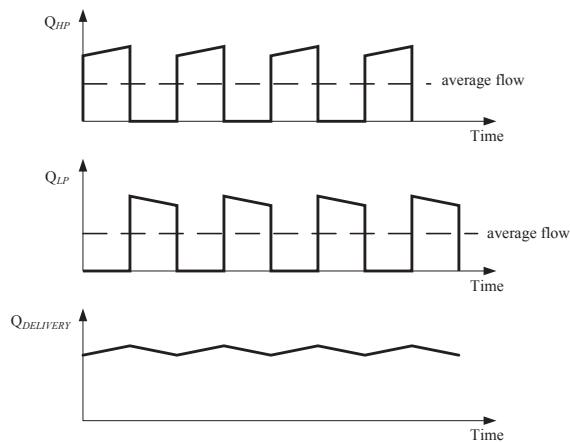


**Figure 2 Idealized operation of flow booster [1]**

However, noise problems may be an issue, as severe pressure pulsation is introduced when the high speed switching valve switches cyclically between the HP supply port and LP supply port. Furthermore the real pulsation may be considerably worse than the idealised operation shown in figure 2 because of wave effects [6]. The pulsation is a periodic narrowband signal, which has a fundamental frequency determined by the valve switching frequency.

### 3 CONTROLLER DESIGN

#### 3.1 Least mean square (LMS) adaptive noise control method

The LMS algorithm is widely applied in the field of active noise control (ANC) since it was originally developed by Widrow and Hoff in 1960 [7]. The conventional structure of ANC system is shown in Figure 3 where the noise canceller employs an adaptive filter  $W(z)$  which operates with the inputs of the reference signal  $x(n)$  and residual error signal  $e(n)$  by using the LMS algorithm [8].

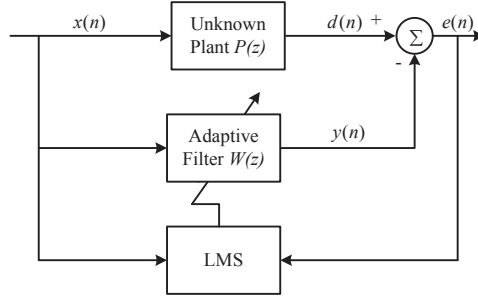


Figure 3 Block diagram of a conventional ANC system [8]

The filter output  $y(n)$  is subtracted from the desired signal  $d(n)$  to produce the residual error  $e(n)$ . The LMS algorithm applies a special estimate of the gradient to minimize the mean-square value of the output  $e(n)$ , which is used to control the adjustments of the tap weights in the adaptive filter, thereby causing  $y(n)$  to approach  $d(n)$ . Thus,  $e(n)$  would decrease to zero when the output of the filter  $W(z)$  equals to the desired signal  $d(n)$ .

The weight update can be presented as follows,

$$\mathbf{w}(n+1) = \mathbf{w}(n) + \mu \mathbf{x}(n)e(n) \quad (1)$$

where

$$\mathbf{w}(n) = [w_0(n) \quad w_1(n) \quad \cdots \quad w_{M-1}(n)]^T$$

$$\mathbf{x}(n) = [x(n) \quad x(n-1) \quad \cdots \quad x(n-M+1)]^T$$

and  $\mu$  is the convergence rate,  $M$  is the length of the filter.

$$y(n) = \mathbf{w}^T(n) \mathbf{x}(n) \quad (2)$$

$$e(n) = d(n) - y(n) \quad (3)$$

In practice, an actuator is normally introduced to generate the physical anti-noise signal, such as the anti-pressure pulsation required in a SIHS. This can cause instability due to additional system dynamics  $S(z)$ , as shown in Figure 4.  $S(z)$  normally depends on the dynamics of the actuator and also the characteristics of the whole system. Morgan [9] proposed a solution which is placing an identical filter in the reference signal path to the weight update of the LMS algorithm.

The reference signal  $x(n)$  is filtered so as to compensate for the effect of secondary path  $S(z)$  in the adaptation loop. This algorithm is known as filtered-X LMS (FXLMS), which can be given as

$$\mathbf{w}(n+1) = \mathbf{w}(n) + \mu \mathbf{x}'(n)e(n) \quad (4)$$

$$\mathbf{x}'(n) = \hat{S}^T(n) \mathbf{x}(n) \quad (5)$$

where

$$\mathbf{x}'(n) = [x'(n) \quad x'(n-1) \quad \cdots \quad x'(n-M+1)]^T$$

is the filtered reference signal and  $\hat{S}(z)$  is the estimated value of  $S(z)$ .

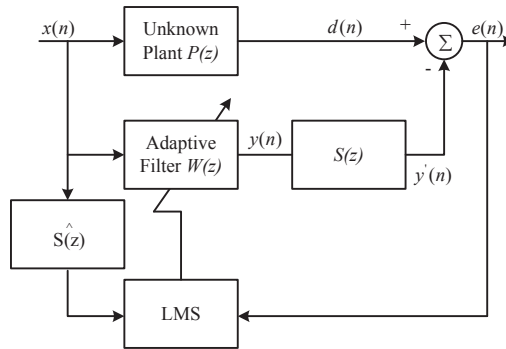


**Figure 4 Block diagram of ANC system using Filtered-X LMS algorithm [9]**

Figure 4 shows a conventional structure of the FXLMS algorithm, which is effective for both broadband and narrowband noise cancellation. For broadband noise cancellation, the reference signal can be the driving signal  $x(n)$  of the primary plant  $P(z)$ . However, sometimes the feedback effect of the cancellation path could degrade system performance due to the inaccuracy of  $x(n)$ . The feedback effect is because the actuator can generate waves propagating both upstream and downstream. Therefore, the anti-noise output to the actuator not only cancels noise downstream by minimizing the error signal measured by the pressure transducer but also propagates upstream to the reference sensor, resulting in a corrupted reference signal  $x(n)$ .

$x(n)$  can be also measured or estimated by using the information of the primary noise before switching on the noise canceller, but, in this case, the characteristics of the primary noise should be well known beforehand. For example, the harmonics of the SIHS are highly depended on the system switching frequency. Thus, the harmonics contained in  $x(n)$  can be estimated by using the switching frequency in practice.

### 3.2 Noise attenuator design

Periodic noise contains tones at the fundamental frequency and at several harmonic frequencies. These multiple sinusoidal signals can be cancelled by using a reference signal which contains the same harmonics as the signal. Sinusoidal waves can be used as reference



signals. This technique has been used very successfully [4]. Multiple controllers are implemented in parallel, one for each harmonic to be cancelled.

Equation (6), (7) and (8) summarize the adaptive LMS algorithm applied in an individual controller [10]:

$$y(n) = \sum_{l=0}^{L-1} w_l(n)x(n-l) \quad (6)$$

$$w_l(n+1) = w_l(n) + \mu x'(n-l)e(n) \quad l = 0, 1, \dots, L-1 \quad (7)$$

$$x'(n) = \sum_{l=0}^{L-1} \hat{s}_l x(n-l) \quad (8)$$

where  $y(n)$  is the output and  $w_l(n)$  is the tap weights of the filter, and  $x(n)$  and  $x'(n)$  are the reference and filtered reference signals respectively.  $\mu$  is the convergence rate and  $L$  is the length of the filter.

From Equations (6) and (8), the output convolution  $y(n)$  and the filtered reference signal  $x'(n)$  both need  $L$  multiplications and  $L-1$  additions. Therefore, the combination of sinusoidal signals can result in complex computation. Because of this heavy computational load, the number of harmonics that can be cancelled is limited.

Using a rectangular-wave reference signal, the wave can be considered to take only the values 1 or 0. This has considerable advantage in the FXLMS algorithm because  $y(n)$  and  $x'(n)$  can be simply computed as a small number of additions. However, the sample frequency must be chosen high enough so that aliasing effects do not seriously limit performance [10].

Figure 5 shows a schematic diagram of the flow booster system with pressure pulsation cancellation. The noise attenuator was based on a dSPACE 1005 control board. The anti-noise signal is generated by a piezoelectrically actuated valve, which was arranged in parallel with the load. A loading valve was used for adjusting the delivery pressure and flow at the end of the system.

For the noise controller, a pressure transducer was arranged at the downstream end of the tube to measure the pressure pulsation as the error signal  $e(n)$ . An output  $y(n)$  of an adaptive filter  $W(z)$  is produced to drive the piezoelectric actuator of the valve. A rectangular reference signal  $x(n)$  is filtered by the estimation of the secondary path  $S(z)$  and the LMS algorithm is employed for the cancellation filter  $W(z)$ . The secondary path  $S(z)$  is a transfer function between the piezoelectric valve and the response at the pressure transducer.

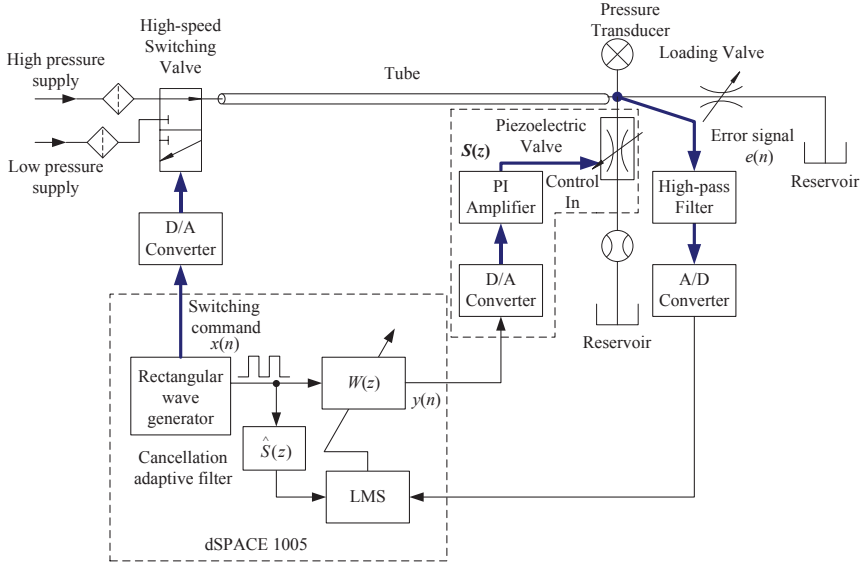


**Figure 5 Schematic of the noise canceller in a flow booster using a rectangular-wave reference signal**

A rectangular reference signal  $x(t)$  can be expressed as [10]

$$x(t) = \begin{cases} A & kT_0 - \frac{\tau}{2} \leq t < kT_0 + \frac{\tau}{2} \\ 0 & kT_0 + \frac{\tau}{2} \leq t < (k+1)T_0 - \frac{\tau}{2} \end{cases} \quad (9)$$

where  $\tau$  and  $T_0$  is the width and the period of the rectangular wave and  $k$  is an integer, as shown in Figure 6.

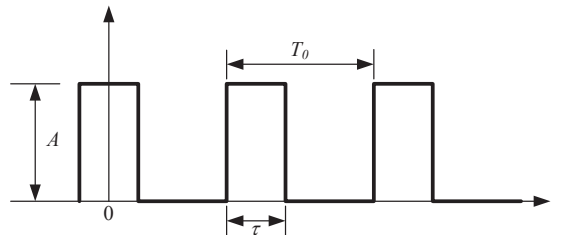


**Figure 6 Rectangular-wave reference signal [10]**

The frequency components are at the fundamental frequency  $2\pi/T_0$  and its harmonics. However, sometimes all significant harmonic components can not be adequately represented by the rectangular wave. For example, when  $\tau/T_0 = 0.5$  the reference signal

only contains odd harmonics and it would not be effective for cancelling even harmonics. Ideally, at frequencies where the harmonic amplitudes of the reference signal are zero, the primary noise would also have zero amplitude. However in practice this is not the case because of nonlinearities, although the harmonics are likely to be small.

There are many high-order harmonics in  $x(t)$ , which above a certain frequency, are not significant in the primary noise. Satisfactory performance can be achieved for [10]

$$\frac{\tau}{T_0} \leq \frac{1}{2M} \quad (10)$$

where  $M$  is the largest significant harmonic index of the primary noise.

## 4 EXPERIMENTAL RESULTS

### 4.1 Piezoelectric valve dynamics

The steady state flow characteristics for the piezoelectric valve as a function of applied voltage and pressure drop across the valve are shown in Figure 7. The applied voltage of the piezoelectric actuator ranged from -200V to 800V. The flow increases as the pressure drop increases and applied voltage decreases. When the applied voltage equals -200V, the piezoelectric valve is fully opened; when the applied voltage equals 800V, the valve is closed off. However, it can be seen that a significant leakage flowrate occurs even when the valve is at the nominally closed position [5]. This is mainly due to distortion caused by the high pressure forces. At an applied voltage of 400V a flowrate of 10L/min is produced at pressure drop of 4bar. This state is applied as the mean condition of the noise attenuator in the experiments. A digital Butterworth high-pass filter was designed with a cutoff frequency of 3 Hz to eliminate the mean pressure value measured from the pressure transducer.

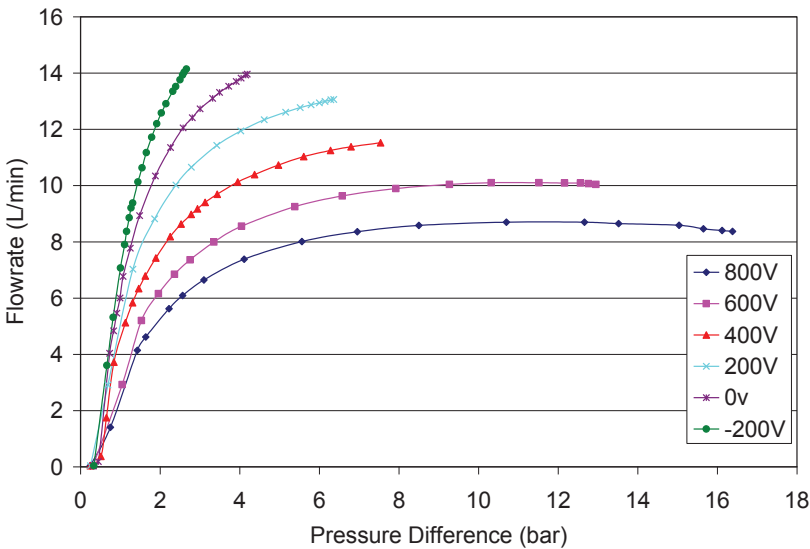
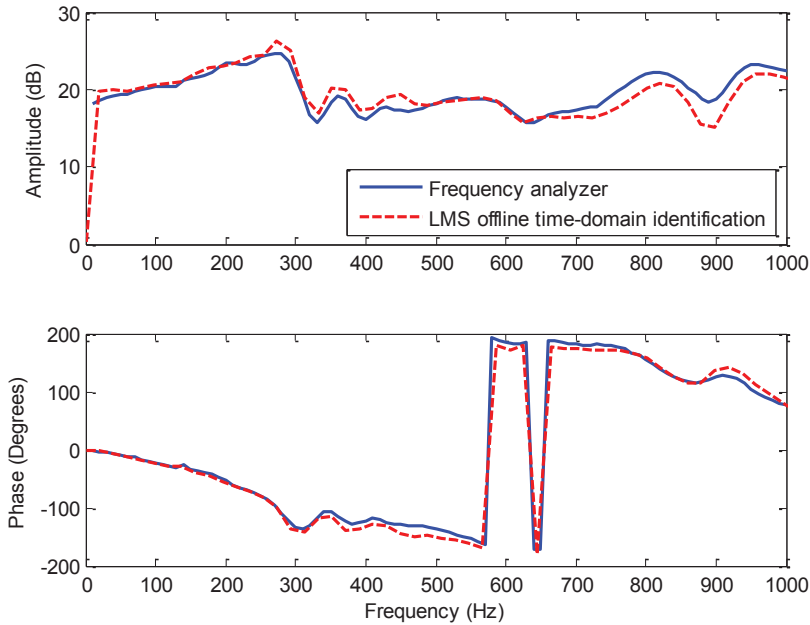


Figure 7 Steady state flow characteristics for the piezoelectric valve

## 4.2 Secondary path identification

The characteristics of the secondary path  $S(z)$  are significant for the FXLMS algorithm. In applications in which  $S(z)$  is initially unknown,  $S(z)$  may be estimated off-line then transferred to the controller and evaluated in real time. [10]. Figure 8 shows the magnitude and phase characteristics of  $S(z)$ , where the applied voltage of the piezoelectric actuator is 400V.



**Figure 8 Magnitude and phase characteristics of the secondary path  $S(z)$**

The results were achieved by using a frequency analyzer and the LMS offline identification technique. It can be seen that the amplitude and phase curves obtained from the LMS offline technique agree well with the results achieved from the frequency analyzer. This shows that the LMS filter was effective for the identification of the unknown plant. It also provides a promising method for using on-line identification technique of the secondary path in time-varying conditions of the system [4].

## 4.3 Pressure pulsation cancellation

Experiments were performed under switching conditions in a flow booster configuration. The high supply pressure was fixed at 30 bar, the low pressure at 6 bar and the delivery flow was 3 L/min. A servovalve was used for the high-speed switching, which was driven by a square wave with the amplitude from -5V to 5V and duty cycle of 50%. The valve is fully open with the driving voltage of -10V or 10V. A small delivery flowrate and half opening of the valve were used in order to avoid cavitation and excessively large pressure pulsation. The switching frequency of the servovalve was 40Hz and the flowrate was 8.4L/min.

Five significant harmonic components were considered in the cancellation. Using Equation (10), the duty cycle of the rectangular-wave reference signal was selected at 10% as an example in the experiments. In this case, the frequencies of 40Hz, 80Hz, 120Hz, 160Hz and 200Hz can be represented. The length of the cancellation filter was 512 and the sampling period was 0.3ms.

Figure 9 shows the cancellation using the designed noise controller. The result in Figure 8 was used as the estimated characteristics of the secondary path  $\hat{S}(z)$ . The convergence rate of the controller was  $\mu=5\times10^{-5}$ . A Hamming window was used to minimize the maximum side lobe in the spectral analysis.

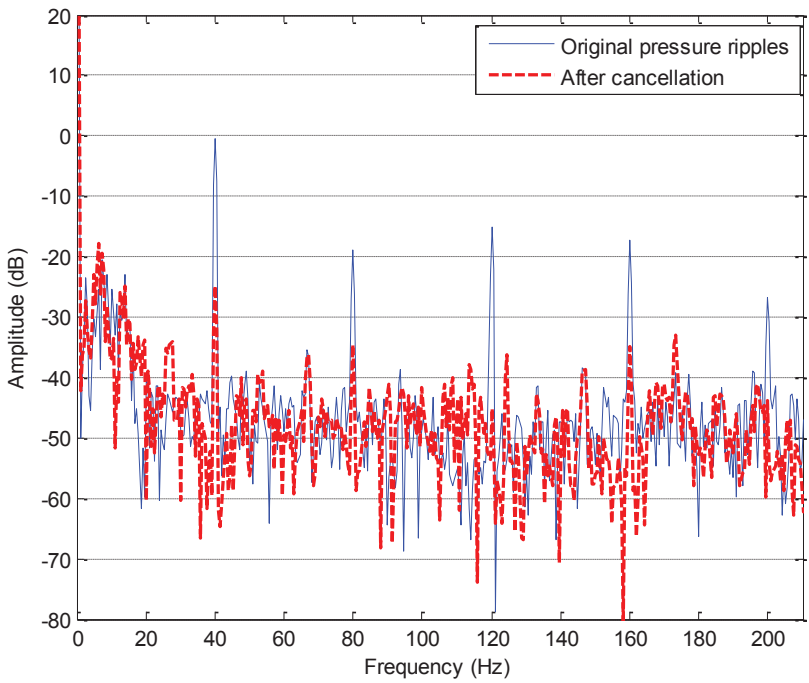


**Figure 9 Multiple frequency cancellation**

The pressure pulsation was decreased by 24.6dB at the fundamental frequency of 40Hz. The amplitudes of the original pressure pulsation and after cancellation at different frequencies are listed in Table 1. The average cancellation of different harmonics is 20.7dB, which would be acceptable for many applications in practice.

**Table 1 Results of cancellation at different harmonics using LMS offline time-domain technique**

Frequency (Hz)	40	80	120	160	200
Original pressure pulsation (dB)	-0.43	-18.9	-15.2	-17.4	-26.8
After cancellation (dB)	-25.0	-34.6	-45.6	-35.9	-41.3
Total reduction (dB)	24.6	15.7	30.4	18.5	14.5

## 5 COMPARISON AND DISCUSSION

The results obtained using the noise controller with sinusoidal waves as the reference signals [4] were used for comparison. Figure 10 shows the comparison of the results. The same length of 512 was applied for the cancellation filter. The sampling period was 0.3ms. As can be seen, the cancellation using a sinusoidal reference signal was about 20dB better than using the rectangular wave at the frequency of 40Hz and 80Hz. However, only three harmonics can be considered due to the computation capability of the hardware. The reason of the better performance is a notch filter can be formed automatically at each reference frequency when sinusoids are applied to adaptive filters [11]. Thus, every sinusoidal component of the interference will be effectively cancelled as long as references signal including these components. However, the frequencies of the reference sinusoids need to be measured or estimated accurately in order to achieve good cancellation.

For the method of using a rectangular reference signal, only a fundamental frequency of the primary noise is required, and only one cancellation filter is needed for the primary noise attenuation at all harmonics. In these experiments, the filter length of 512 is not ideally short for computation. But with the rectangular-wave reference signal of 10% duty cycle and system sampling period of 0.3ms, only 8 sampling points during '1' period were valid for computation. This can significantly decrease the computational load, and in this condition, two more harmonics were able to be cancelled. Therefore, it can be concluded that the method of using a rectangular reference signal can provide an acceptable noise cancellation with the advantage of simple computation.

Equation (10) gives an estimated relationship of the largest significant cancelled harmonic index and the duty cycle of the rectangular wave. The length of the cancellation filter determines the number of weights which are used for attenuation. Better noise cancellation can be obtained by using a longer length filter. However, this could result in a more complex computation. Moreover, the selection of the sampling period needs to be considered beforehand in order to avoid the aliasing. The optimization study for the length of the cancellation filter, duty cycle of the rectangular-wave reference signal and the sampling period is continuing.

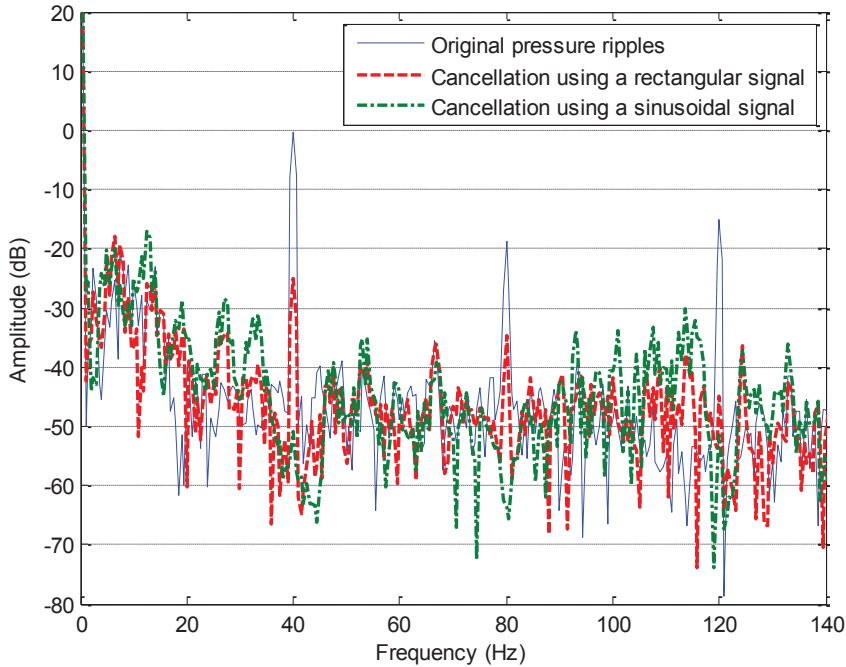


**Figure 10 Comparison of the cancellation using rectangular and sinusoidal waves as the reference signals**

## 6 CONCLUSIONS

This paper presented an active adaptive noise control method for attenuating pressure pulsation using a rectangular-wave reference signal. The designed controller has been implemented experimentally for pressure pulsation cancellation in a flow booster. Experimental results show that acceptable cancellation (about 20dB) can be achieved. The alternative method with using sinusoidal reference signals produces better cancellation (about 40 dB), but has greater computation requirements and consequently fewer harmonics can be cancelled. The proposed controller shows good ability for noise cancellation and less computation requirement. It can be concluded that the method is a promising solution in practical applications for a compromise between noise cancellation and computational hardware requirements.

## REFERENCES

- [1] D. N. Johnston, "A switched inertance device for efficient control of pressure and flow," *Bath/ASME Fluid Power and Motion Control Symposium*, Hollywood, USA, pp.1-8. 2009.
- [2] F. T. Brown, S. Tentarelli, and S. Ramachandran, "A hydraulic rotary switched-inertance servo-transformer," *Journal of Dynamic Systems, Measurement, and Control*, vol. 110, pp.144-150, 1988.
- [3] F. T. Brown, "Switch reactance hydraulics: a new way to control fluid power," *Proc. National conference on Fluid Power, Chicago*, Feb-Mar, pp.25-34, 1987.
- [4] M. Pan, "Active control of pressure pulsation in a switched inertance hydraulic system," *PhD thesis, University of Bath*, 2012.
- [5] D. Branson, D. N. Johnston, D. Tilley, C. Bowen, and P. Keogh, "Piezoelectric Actuation in a High Bandwidth Valve," *Ferroelectrics*, vol. 408, pp. 32-40, 2010.
- [6] P.Wang, S.Kudzma, D. N. Johnston, A. Plummer, A.J.Hillis, "The influence of wave effects on digital switching valve performance," *The Fourth workshop on Digital Fluid Power*, Linz, Austria, 2011.
- [7] B. Widrow and M. E. Hoff, "Adaptive switching circuits," *IRE WESCON Convention Record, Part4*, IRE, New York, pp. 96-104, 1960.
- [8] S. Haykin, "Adaptive filter theory," *New Jersey, Prentice-Hall Inc*, 1996.
- [9] D. Morgan, "An analysis of multiple correlation cancellation loops with a filter in the auxiliary path," *IEEE Transactions on Acoustics Speech and Signal Processing*, vol. 28, pp. 454-467, 1980.
- [10] S. Kuo and D. Morgan, *Active noise control systems: algorithms and DSP implementations*: John Wiley & Sons, Inc. New York, NY, USA, 1995.
- [11] J.R.Glover,Jr, "Adaptive noise canceling applied to sinusoidal interferences," *IEEE Transactions on Acoustics, Speech and Signal Processing*, vol. 25, pp. 484-491, 1977.
- [12] B. Widrow, J.R.Glover,Jr, J.M.McCool, J. Kaunitz, C.S.Williams, R.H.Hearn, J.R. Zeidler, E. Dong, Jr, and R.C. Goodlin, "Adaptive noise cancelling: Principles and applications," *Proceedings of the IEEE*, vol. 63, pp. 1692-1716, 1975.
- [13] S. Kuo and D. Morgan, "Active noise control: a tutorial review," *Proceedings of the IEEE*, vol. 87, pp. 943-973, 1999.





# Control I



# A Sliding Mode Controller Based on the Interacting Multiple Model Strategy

M. A. El Sayed<sup>1</sup>, S. A. Gadsden, and S. R. Habibi

Centre for Mechatronics and Hybrid Technology Research

Department of Mechanical Engineering, McMaster University, Canada

[abugabma@mcmaster.ca](mailto:abugabma@mcmaster.ca), [gadsden@mcmaster.ca](mailto:gadsden@mcmaster.ca), and [habibi@mcmaster.ca](mailto:habibi@mcmaster.ca)

## ABSTRACT

Sliding mode controllers (SMCs) are a form of variable structure control, which utilizes a discontinuous switching plane along some desired trajectory. This plane is often referred to as a sliding surface, in which the objective is to keep the state values along this surface by minimizing the state errors (between the desired trajectory and the estimated or actual values). Ideally, if the state value is off or away from the surface, a switching gain would be used to push the state towards the sliding surface. This switching brings an inherent amount of stability; and as such, SMCs have become a popular control strategy for systems with modelling uncertainty. Furthermore, some systems behave according to a number of different models (or operating regimes). In these scenarios, it is desirable to implement adaptive estimation algorithms, which ‘adapt’ themselves to certain types of uncertainties or models in an effort to minimize the state estimation error and improve tracking performance. One type of adaptive estimation technique includes the multiple model (MM) algorithm and its interactive form (IMM). For the MM methods, a Bayesian or probability based framework is used. Essentially, based on some prior probabilities of each model being correct (i.e., the system is behaving according a finite number of modes) the corresponding updated probabilities are calculated. This paper introduces a new type of sliding mode controller based on the interacting multiple model strategy (SMC-IMM). The SMC-IMM method is applied on an electrohydrostatic actuator, and the results are compared with the standard SMC strategy.

## 1 INTRODUCTION

Variable structure systems with sliding mode control have gained international attention following Utkin's paper [1] and book [2]. Since then, there has been considerable progress in this field. Many applications have been reported, for example, an SMC-based controller was applied to a tracking problem with a three degree of freedom manipulator [3]. Simulation results demonstrate that SMC provides perfect tracking capabilities with minimum tracking error.

---

<sup>1</sup> Both M. A. El Sayed and S. A. Gadsden contributed equally to this paper, and are co-first authors.

A continuous SMC control strategy has been implemented in a Cartesian pneumatic robot in [4]. In this research, the performance of the SMC is compared to the linear proportional-velocity-acceleration (PVA) controller. The SMC provides an improvement over the PVA regarding trajectory tracking precision with minimal tuning effort. In addition, the discontinuous nature of the SMC helps in providing a measure of friction compensation. In this research, the importance of the boundary layer approach to eliminating chatter with SMC was also highlighted. A robust SMC and adaptive control strategy has been applied to a two-degrees of freedom robotic arm in [5]. The robotic arm was required to track a circular trajectory with a period of 4 sec. The adaptive control is used to estimate unknown disturbances and environmental factors while the SMC is used to overcome the dynamic system model uncertainties. Experimental results show the robustness of the proposed SMC to track trajectories with bounded errors. An SMC strategy with an integral switching surface in an electro-pneumatic rotary actuator has been proposed in [6]. First, a nonlinear model of the servo drive is attained, the developed model was found to be nonlinear with respect to the state variables and the control input. Accordingly, model linearization and transformation was carried out with respect to a new control input in order to apply the nonlinear discontinuous controller. Experimental results show the advantage of the SMC with integral switching surface over standard SMC in terms of tracking error.

A recently proposed robust state and parameter estimation strategy referred to as the variable structure filter (VSF) combined with the SMC strategy has been proposed in [7]. The proposed combined strategy is referred to as SMCF and it results in increased robustness in both, control and state estimation given bounded parametric uncertainties and noise. In addition, the proposed strategy can achieve high regulation rates or short settling time. The proposed strategy has been applied to a high precision electro-hydrostatic actuator (EHA) system. From the plant, some of the outputs can be physically measured and they might contain measurement uncertainties. These outputs are fed into the VSF to estimate the full set of internal system states. These estimated states may be integrated into a trajectory following sliding mode controller. The sliding mode controller uses information contained in the state estimates besides the reference input to produce a discontinuous control signal to attain trajectory following. One of the major considerations in the SMC and the VSF are their chattering phenomenon due to the discontinuous action. Chattering can be removed by using a smoothing boundary layer [2].

A fuzzy sliding mode controller for flight simulator servo system is presented in [8]. The stand-alone SMC provides strong robustness against parameter variations and external disturbances but the chattering produced by SMC limits its application to practical systems. In this research, by using fuzzy control, the chattering can be effectively reduced. At the same time, the optimal fuzzy reasoning is adopted in fuzzy control. Simulation and real system experiment results confirm the effectiveness of the proposed control method. An adaptive sliding mode control for regenerative braking in hybrid vehicles is presented in [9]. In this research, a nonlinear control strategy based on adaptive sliding-mode control (ASMC) is implemented to tackle the problem of engine torque control during regenerative braking mode. The ASMC-based controller combines the partially known inverse dynamic model of the engine. Numerical and experimental results show performance enhancement of the proposed strategy compared to a high-gain PID controller and to the conventional smooth sliding mode controller regarding tracking error, chattering elimination capability, and robustness to disturbance.

In this paper, a new type of sliding mode controller based on the interacting multiple model strategy (SMC-IMM) is proposed. The SMC-IMM method is applied on an electrohydraulic actuator, and the results are compared with the standard SMC strategy. The paper is organized as follows. Section 2 describes SMC in more detail, followed by a section on the IMM method. Section 4 provides an overview of the SMC-IMM method. The problem statement and results are provided in Section 5. The main findings of the paper are then summarized in the conclusion.

## 2 SLIDING MODE CONTROL THEORY

Sliding mode control (SMC) is known for its ability to provide robustness and stability in the presence of uncertainties. Misawa proposed a discrete sliding mode control method for nonlinear systems with uncertainties that do not satisfy the matching condition [10]. Later in [11], this design was extended for linear systems and was reported to provide good results. Wang adopted Misawa's control technique to design a controller for an EHA prototype for trajectory tracking applications [12]. Using an accurate model of the EHA's nonlinear friction in the controller design, his results indicated that the controller was able to provide precise tracking while suppressing the chatter in acceleration and velocity profiles. In [13], Wang's controller is shown susceptible to high frequency limit cycle oscillations when the uncertainty associated with the friction characteristics increased. This oscillation is more noticeable in the acceleration profile. The simulation results clearly show that chattering can be eliminated by expanding the SMC boundary layer thickness, at the expense of reducing the positional precision [13].

Consider a single input linear dynamical system as follows:

$$x_{k+1} = \hat{F}x_k + \hat{G}u_k + w_k \quad (2.1)$$

where  $A$  and  $B$  are the system and input matrices respectively,  $x$  refers to the state vector,  $u$  is the system input, and  $w$  refers to uncertainties present in the system (e.g., modelling errors or system noise). The uncertainties  $w$  are assumed to be bound such that:

$$\gamma \geq |Cw| \quad (2.2)$$

In trajectory tracking mode, the objective is to force the system to follow a desired trajectory  $x_d$ . This objective can be restated as driving the tracking error ( $e_k = x_{d,k} - x_k$ ) as close as possible to zero. A sliding manifold is defined as:

$$\Sigma = \{e_k | s_k = Ce_k = 0\} \quad (2.3)$$

where  $C$  is the sliding surface parameter vector, and with a smoothing boundary layer defined by:

$$\Psi = \{e_k | |s_k| = |Ce_k| \leq \psi\} \quad (2.4)$$

In this paper, the control strategy will be based on Misawa's SMC control structure [10,11]. The control input may be defined as follows [10,11]:

$$u_k = u_{eq,k} - (C\hat{G})^{-1}s_k + (C\hat{G})^{-1}K_c \text{sat}\left(\frac{s_k}{\psi}\right) \quad (2.5)$$

where  $u_{eq}$  refers to the equivalent control component, and the remainder is the switching control component. The follow is also defined:

$$u_{eq,k} = (C\hat{G})^{-1}C(x_{d,k+1} - \hat{F}x_k) \quad (2.6)$$

$$K_c = \gamma + 2\epsilon, \quad \psi \geq \gamma + \epsilon \quad (2.7)$$

$$\text{sat}\left(\frac{s_k}{\psi}\right) = \begin{cases} +1 & \text{if } s > \psi \\ \frac{s}{\psi} & \text{if } |s| \leq \psi \\ -1 & \text{if } s < -\psi \end{cases} \quad (2.8)$$

where  $\epsilon$  is an arbitrary positive constant. However, a major drawback in Misawa's SMC derivation is the assumption that the uncertainties  $w$  are bounded by a constant [10,11]. This assumption is not realistic since  $w$  is inherently dependent on the system states. Accordingly, a new gain calculation is required, where a variable gain may be used to compensate for the uncertainties. A variable gain and boundary layer were introduced in [14], and are defined as follows:

$$K_c = C\tilde{F}_{max}|e_k| + C\tilde{F}_{max}|x_{d,k}| + C\tilde{G}_{max}u_{max} + Cv_{max} + 2\epsilon \quad (2.9)$$

$$\psi = C\tilde{F}_{max}|e_k| + C\tilde{F}_{max}|x_{d,k}| + C\tilde{G}_{max}u_{max} + Cv_{max} + \epsilon \quad (2.10)$$

where  $\tilde{F}_{max}$  and  $\tilde{G}_{max}$  are the upper bounds on the uncertainties in the system matrix and the input matrix respectively,  $u_{max}$  is the maximum allowable input, and  $v_{max}$  is the maximum noise amplitude. In trajectory tracking, the system may be forced to follow some desired trajectory by implementing (2.5) through (2.10).

### 3 THE INTERACTING MULTIPLE MODEL STRATEGY

In nature, many systems behave according to a number of different models (modes, or operating regimes). For example, in target tracking, a target may travel straight (i.e., uniform motion) or turn (i.e., undergo a coordinated turn) [15]. Furthermore, a system may experience different types of noises (i.e., white or 'coloured') [16]. In these scenarios, it is desirable to implement adaptive estimation algorithms, which 'adapt' themselves to certain types of uncertainties or models in an effort to minimize the state estimation error [15]. One type of adaptive estimation technique includes the 'multiple model' (MM) algorithm [17]; which include the following: static MM [18], dynamic MM [15], generalized pseudo-Bayesian (GPB) [19,20,21,22], and the interacting multiple model (IMM) [15,23,24]. For the MM methods, a Bayesian framework is used (i.e., probability based). Essentially, based on some prior probabilities of each model being correct (i.e., the system is behaving according a finite number of modes), the corresponding updated probabilities are calculated and implemented [15].

Throughout this paper, it will be assumed that all of the models are linear with the presence of Gaussian noise; however, nonlinear models could be used via linearization [15]. Each MM method requires estimation of the states and their corresponding probability. The most popular strategy that has been implemented in the MM framework remains the Kalman filter (KF), and is referred to as the IMM-KF [16]. The interacting multiple model (IMM) estimation algorithm is conceptually requires  $r$  number of filters (such as the KF) that operate in parallel [15]. The state estimate is calculated under each possible current model, with a mixed initial condition (i.e., a different combination of the previous model-conditioned estimates) [15]. Furthermore, according to and as presented in [15,24], the input to the filter matched to  $M_j$  is obtained from an interaction of the  $r$  filters, which consists of the mixing of the estimates  $\hat{x}_{i,k|k}$  and weightings  $\mu_{i|j,k|k}$  (mixing probabilities). This is equivalent to merging taking place at the beginning of each estimation cycle, which limits the number of filters to  $r$  [24]. The IMM strategy has shown to be very effective, and is more computationally efficient than other multiple model algorithms [15]. The following figure helps to explain the IMM method more effectively.

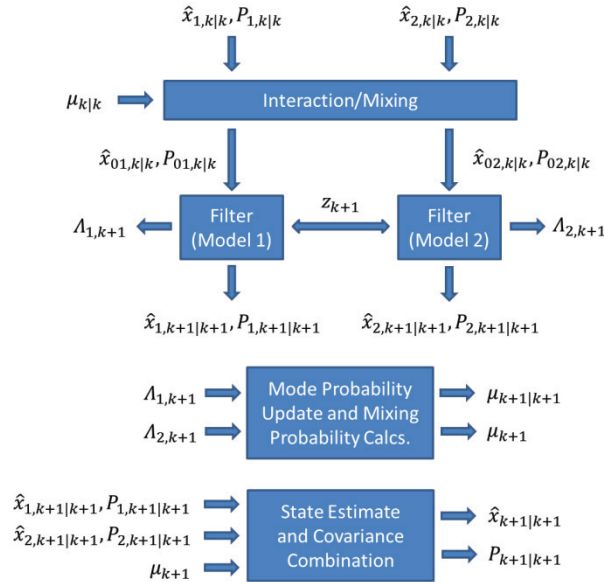


**Figure 1: IMM estimator for two models (adapted from [15,25])**

The IMM estimator consists of five main steps: calculation of the mixing probabilities, mixing stage, mode-matched filtering, mode probability update, and state estimate and covariance combination. The first step involves calculating the mixing probabilities (i.e., the probability of the system currently in mode  $i$ , and switching to mode  $j$  at the next step). These are calculated using the following two equations [15]:

$$\mu_{i|j,k|k} = \frac{1}{\bar{c}_j} p_{ij} \mu_{i,k} \quad (3.1)$$



$$\bar{c}_j = \sum_{i=1}^r p_{ij} \mu_{i,k} \quad (3.2)$$

The mixing probabilities  $\mu_{i|j,k|k}$  are used in the mixing stage, next. In addition to the mixing probabilities, the previous mode-matched states  $\hat{x}_{i,k|k}$  and covariance's  $P_{i,k|k}$  are also used to calculate the mixed initial conditions (states and covariance) for the filter matched to  $M_j$ . The mixed initial conditions are found respectively as follows [15]:

$$\hat{x}_{0j,k|k} = \sum_{i=1}^r \hat{x}_{i,k|k} \mu_{i|j,k|k} \quad (3.3)$$

$$P_{0j,k|k} = \sum_{i=1}^r \mu_{i|j,k|k} \{P_{i,k|k} + (\hat{x}_{i,k|k} - \hat{x}_{0j,k|k})(\hat{x}_{i,k|k} - \hat{x}_{0j,k|k})^T\} \quad (3.4)$$

The next step involves mode-matched filtering, which involves using (3.3) and (3.4) as inputs to the filter matched to  $M_j$ . Each filter also uses the measurement  $z_{k+1}$  and input to the system  $u_k$  (if any). The likelihood functions are calculated for each mode-matched filter as follows [15]:

$$\Lambda_{j,k+1} = \mathcal{N}(z_{k+1}; \hat{z}_{j,k+1|k}, S_{j,k+1}) \quad (3.5)$$

Equation (3.5) may be solved by each filter as follows [15,16]:

$$\Lambda_{j,k+1} = \frac{1}{\sqrt{|2\pi S_{j,k+1}|_{\text{Abs}}}} \exp\left(\frac{-\frac{1}{2} e_{j,z,k+1|k}^T e_{j,z,k+1|k}}{S_{j,k+1}}\right) \quad (3.6)$$

Utilizing the likelihood functions from each filter, the mode probability may be updated by [15]:

$$\mu_{j,k} = \frac{1}{c} \Lambda_{j,k+1} \sum_{i=1}^r p_{ij} \mu_{i,k} \quad (3.7)$$

where the normalizing constant is defined as [15]:

$$c = \sum_{j=1}^r \Lambda_{j,k+1} \sum_{i=1}^r p_{ij} \mu_{i,k} \quad (3.8)$$

Finally, the overall state estimates (3.9) and covariance (3.10) are calculated. However, note that for this paper, one is mainly interested in utilizing (3.7) for determining the system behavior in an effort to improve controller accuracy.

$$\hat{x}_{k+1|k+1} = \sum_{j=1}^r \mu_{j,k+1} \hat{x}_{j,k+1|k+1} \quad (3.9)$$

$$P_{k+1|k+1} = \sum_{j=1}^r \mu_{j,k+1} \left\{ P_{j,k+1|k+1} + (\hat{x}_{j,k+1|k+1} - \hat{x}_{k+1|k+1})(\hat{x}_{j,k+1|k+1} - \hat{x}_{k+1|k+1})^T \right\} \quad (3.10)$$

Equations (3.1) through (3.10) summarize the IMM estimator strategy, and are used recursively. Note that (3.9) and (3.10) are used for output purposes only, and are not part of the algorithm recursions [15]. The IMM strategy has successfully been applied to a number of estimation problems [26]; ranging from target tracking in a traffic controller setting [27] to fault detection and diagnosis [28,29].

#### 4 AN SMC BASED ON THE IMM STRATEGY

In this paper, it is proposed that combining the SMC method (Section 2) with the IMM strategy (Section 3) will improve the overall trajectory tracking accuracy, particularly in systems that are not well defined. The basic principle and concept of the SMC-IMM strategy may be summarized by the following figure.

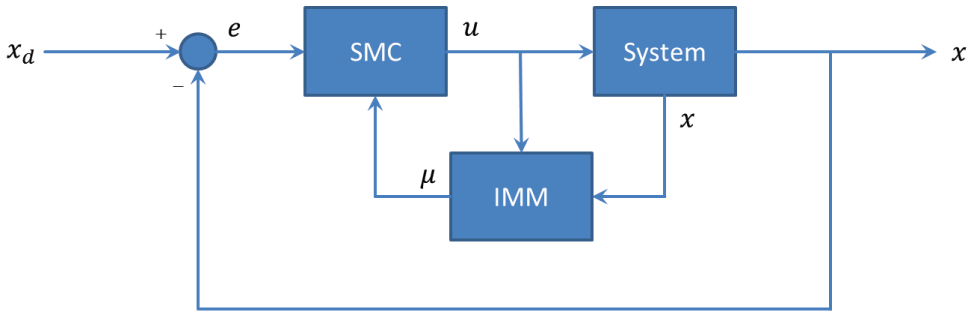


**Figure 2: Proposed SMC-IMM strategy**

In the SMC-IMM strategy, the SMC utilizes the tracking error  $e$  and the mode likelihood probability  $\mu$  (a value between 0 and 1), to generate a ‘weighted’ system input  $u$ . The IMM requires the system input and the output from the system  $x$  (or  $z$  if using measurements) in order to calculate the mode probability as per (3.7). If the system is being measured, a Kalman filter (KF) or smooth variable structure filter (SVSF) may be implemented to reduce the effects of unwanted noise [25]. Essentially, the SMC-IMM strategy utilizes the IMM mode probabilities to formulate ‘weighted’ system and input matrices in an effort to capture the actual dynamics of the system. In this case, the controller input is modified as follows:

$$u_k = u_{eq,k} - (C\hat{G}_{\mu,k})^{-1} s_k + (C\hat{G}_{\mu,k})^{-1} K_c \text{sat}\left(\frac{s_k}{\psi}\right) \quad (4.1)$$

$$u_{eq,k} = (C\hat{G}_{\mu,k})^{-1}C(x_{d,k+1} - \hat{F}_{\mu,k}x_k) \quad (4.2)$$

where  $\hat{G}_{\mu,k} = \sum_{i=1}^r \mu_{i,k} \hat{G}_i$  and  $\hat{F}_{\mu,k} = \sum_{i=1}^r \mu_{i,k} \hat{F}_i$ . Recall that  $r$  refers to the number of operating modes (e.g., normal operation, and various levels of faults). Equations (4.1) and (4.2) are used with (2.9) and (2.10) to generate the system input required to force the system to follow the desired trajectory.

## 5 SIMULATION PROBLEM AND RESULTS

### 5.1 Problem

In this paper, an electrohydrostatic actuator (EHA) was studied. An EHA is an emerging type of actuator typically used in the aerospace industry. EHAs are self-contained units comprised of their own pump, hydraulic circuit, and actuating cylinder [30]. The main components of an EHA include a variable speed motor, an external gear pump, an accumulator, inner circuitry check valves, a cylinder (or actuator), and a bi-directional pressure relief mechanism. A mathematical model for the EHA has been described in detail in [14,25]. For the purposes of this paper, only the main state space equations will be explored. The input to the system is the rotational speed of the pump  $\omega_p$ , with typical units of rad/s. In this setup, the sample rate for this simulation was defined as  $T = 0.1$  ms. The state space equations are defined as follows:

$$x_{1,k+1} = x_{1,k} + Tx_{2,k} + Tw_{1,k} \quad (5.1)$$

$$x_{2,k+1} = x_{2,k} + Tx_{3,k} + Tw_{2,k} \quad (5.2)$$

$$\begin{aligned} x_{1,k+1} = & \left[ 1 - T \left( \frac{BV_0 + M\beta_e L}{MV_0} \right) \right] x_{3,k} - T \frac{(A^2 + BL)\beta_e}{MV_0} x_{2,k} \\ & - T \left[ \frac{2B_2 V_0 x_{2,k} x_{3,k}}{MV_0} + \frac{\beta_e L (B_2 x_{2,k}^2 + B_0)}{MV_0} \right] \text{sign}(x_{2,k}) \\ & + T \frac{AD_p \beta_e}{MV_0} u_k + Tw_{3,k} \end{aligned} \quad (5.3)$$

Note that  $A$  refers to the piston cross-sectional area,  $B_{\#}$  represents the load friction present in the system,  $\beta_e$  is the effective bulk modulus (i.e., the ‘stiffness’ in the hydraulic circuit),  $D_p$  refers to the pump displacement,  $L$  represents the leakage coefficient,  $M$  is the load mass (i.e., weight of the cylinders), and  $V_0$  is the initial cylinder volume. The values used to obtain a linear normal operating model are summarized in the appendix. Two more models were created based on a severe friction fault (the friction was increased 3 times) and a severe leakage fault (the leakage coefficient was increased 4 times). The normal, friction fault, and leakage fault system matrices are respectively defined as follows:

$$F_1 = \begin{bmatrix} 1 & 0.0001 & 0 \\ 0 & 1 & 0.0001 \\ 0 & -41.0258 & 0.6099 \end{bmatrix} \quad (5.4)$$

$$F_2 = \begin{bmatrix} 1 & 0.0001 & 0 \\ 0 & 1 & 0.0001 \\ 0 & -51.8627 & 0.2226 \end{bmatrix} \quad (5.5)$$

$$F_3 = \begin{bmatrix} 1 & 0.0001 & 0 \\ 0 & 1 & 0.0001 \\ 0 & -73.5364 & 0.6015 \end{bmatrix} \quad (5.6)$$

Note that all three input gain matrices remained the same, and were calculated as follows:

$$G = \begin{bmatrix} 0 \\ 0 \\ 0.0135 \end{bmatrix} \quad (5.7)$$

The important SMC parameters were defined by:

$$C = [2500 \quad 100 \quad 1] \quad (5.8)$$

$$\tilde{F}_{max} = \begin{bmatrix} 0 & 0 & 0 \\ 0 & 0 & 0 \\ 0 & 8.6695 & 0.3099 \end{bmatrix} \quad (5.9)$$

Note also that artificial system and measurement noise was added to the simulation problem to make it more challenging. The zero-mean Gaussian noise was generated using system and measurement noise covariance's  $Q$  and  $R$  which were diagonal matrices with elements equal to  $1 \times 10^{-6}$ . Furthermore, even when the system was operating 'normally', there was still a modelling error of 20% added for both controllers (SMC and SMC-IMM) to overcome. The desired position, velocity, and acceleration trajectories are shown in the following three figures.

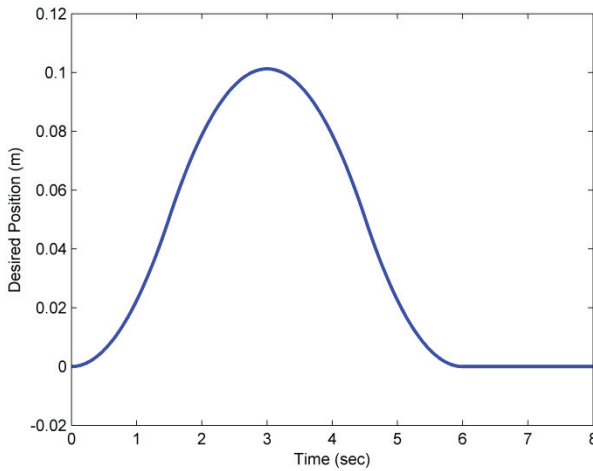


**Figure 3: Desired EHA position trajectory**

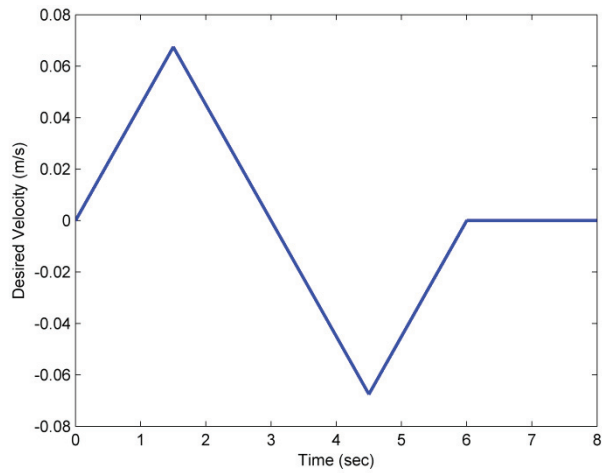


**Figure 4: Desired EHA velocity trajectory**

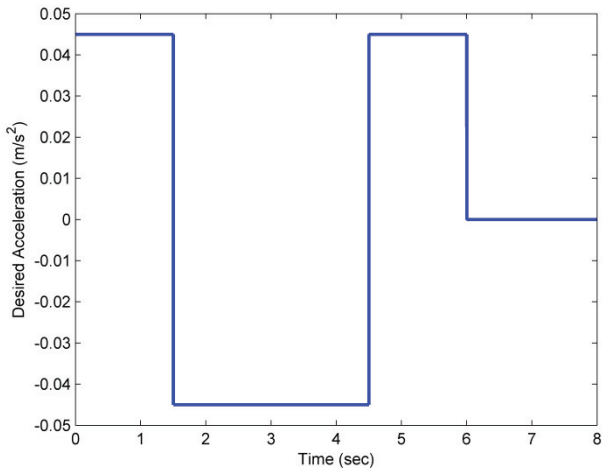


**Figure 5: Desired EHA acceleration trajectory**

Note that for the first 1.5 second, the system behaved normally. A friction fault was injected at 1.5 seconds and lasted for 1.5 seconds. At 3 seconds, a 1.5 second leakage fault was implemented. At 4.5 seconds, the leakage fault was removed and a friction fault was injected again. The system operated normally during the last two seconds.

**5.2 Results**

The results of implementing the standard SMC and proposed SMC-IMM on the EHA are shown in this subsection. As an example, the following figure shows the normal mode probability calculated by the IMM.

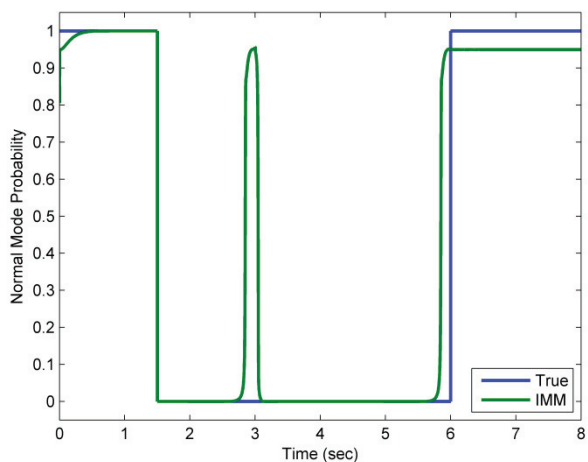


**Figure 6: True and estimated normal mode probability**

Note that the estimated normal mode probability closely follows the true normal mode probability. However, at around 3 seconds the IMM has trouble distinguishing between the three modes, and the normal mode is misclassified. This is most likely due to the fact that all three models behave similarly around this point in the trajectory. The following three figures represent the trajectory tracking (position, velocity, and acceleration) errors for the SMC and SMC-IMM methodologies.

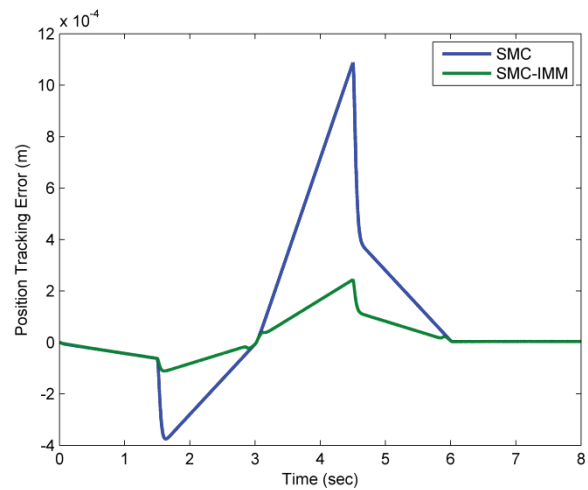


**Figure 7: Position tracking error for SMC and SMC-IMM**

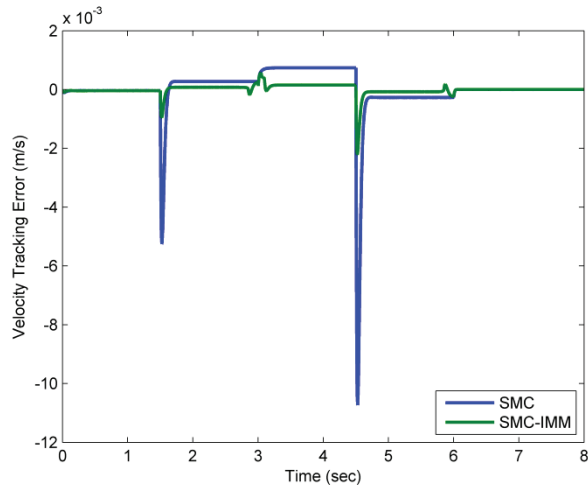


**Figure 8: Velocity tracking error for SMC and SMC-IMM**

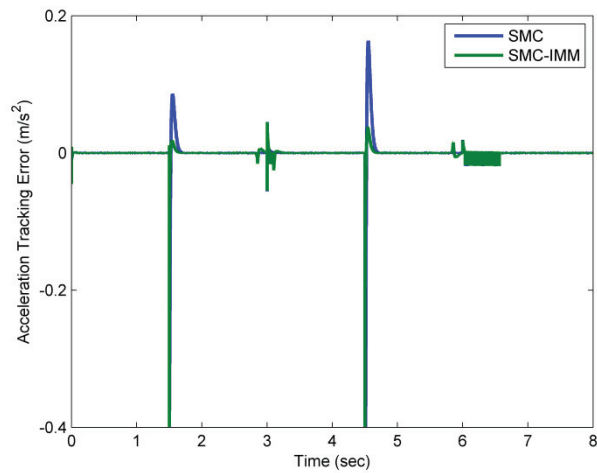


**Figure 9: Acceleration tracking error for SMC and SMC-IMM**

As shown in the above figures, the SMC-IMM strategy is able to overcome the modelling uncertainties, and improves the trajectory tracking accuracy by nearly 4 times when compared with the standard SMC. Furthermore, the introduction of system changes (i.e., faults) causes the tracking error to spike. The magnitude of this error is considerably smaller with the proposed strategy, which makes for a smoother controller motion in the presence of faults.

## 6 CONCLUSION

In this paper, a new type of sliding mode controller based on the interacting multiple model strategy (SMC-IMM) was proposed. The SMC-IMM method was applied on an electrohydraulic actuator, and the results were compared with the standard SMC strategy. As demonstrated in the paper, the proposed SMC-IMM method was found to provide more accurate trajectory following when compared with the standard SMC strategy. In fact, the tracking error was reduced by over 4 times, which is a significant improvement. Future work will involve: implementation of the method on an EHA system in real-time, utilization of filtering strategies to remove noise, and the development of the proof of stability.

## 7 REFERENCES

- [1] V. Utkin, "Variable Structure Systems with Sliding Modes," *IEEE Transactions on Automatic Control*, vol. 2, pp. 212-222, 1977.
- [2] V. Utkin, *Sliding Modes and Their Application in Variable Structure Systems*, 1st ed. Moscow, U.S.S.R.: Mir (English), 1978.
- [3] F. Harashima and J. H. H. Xu, "Tracking Control of Robot Manipulators Using Sliding Mode," *IEEE Transactions on Power Electronics*, pp. 169-176, 1987.
- [4] X. Yang, "Continuous Sliding Mode Control of a Cartesian Pneumatic Robot," Queen's University, Kingston, Ontario, Master's Thesis 2001.
- [5] A. R. R. J. Lanzon, "Trajectory/Force Control for Robotic Manipulation Using Sliding Mode and Adaptive Control," in *American Control Conference*, San Diego, California, 1999, pp. 1940-1944.
- [6] M. Bouri and D. Thomasset, "Sliding Control of an Electropneumatic Actuator Using an Integral Switching Surface," *IEEE Transactions on Control Systems Technology*, vol. 9, pp. 368-375, 2002.
- [7] S. Wang, R. Burton, and S. R. Habibi, "Sliding Mode Controller and Filter Applied to an Electrohydraulic Actuator System," *ASME Journal of Dynamic Systems, Measurement and Control*, vol. 133, no. 2, 2011.
- [8] Y. Wu, W. Le, and Y. Liu, "Fuzzy Sliding Mode Control Based on Optimal Fuzzy Reasoning and Its Application on Simulator Turntable," in *7th International Conference on System Simulation and Scientific Computing*, 2008, p. 765.
- [9] A. Fazeli, M. Zeinali, and A. Khajepour, "Application of Adaptive Sliding Mode Control for Regenerative Braking Torque Control," *ASME Dynamic Systems and Control Division*, vol. 1, no. 11, 2011.
- [10] E. Misawa, "Discrete Time Sliding Mode Control for Nonlinear Systems with Unmatched Uncertainties and Uncertain Control Vector," *ASME Journal of Dynamic Systems, Measurement and Control*, vol. 119, no. 3, pp. 503-512, 1997.
- [11] E. Misawa, "Discrete Time Sliding Mode Control: The Linear Case," *ASME Journal of Dynamic Systems, Measurement and Control*, vol. 119, no. 4, pp. 819-21, 1997.
- [12] S. Wang, S. R. Habibi, and R. Burton, "Sliding Mode Control for a Model of an Electrohydraulic Actuator System with Discontinuous Nonlinear Friction," in *American Control Conference*, 2006, p. 38.
- [13] M. A. El Sayed and S. R. Habibi, "Multiple Sliding Mode Control for an Electrohydraulic Actuator System," in *ASME Fluid Power and Motion Control Symposium*, Bath, UK, 2010, pp. 353-364.
- [14] M. A. El Sayed, "Multiple Inner-Loop Control of an Electrohydraulic Actuator," McMaster University, Hamilton, Ontario, Ph.D. Thesis 2012.
- [15] Y. Bar-Shalom, X. Rong Li, and T. Kirubarajan, *Estimation with Applications to Tracking and Navigation*. New York: John Wiley and Sons, Inc., 2001.
- [16] M. S. Grewal and A. P. Andrews, *Kalman Filtering: Theory and Practice Using MATLAB*, 3rd ed. New York: John Wiley and Sons, Inc., 2008.
- [17] X. R. Li, *Advances in Aerospace Systems Dynamics and Control Systems (Volume 76)*, C. T. Leondes, Ed. New York, USA: Academic Press, 1996.
- [18] D. T. Magill, "Optimal Adaptive Estimation of Sampled Stochastic Processes," *IEEE Transactions on*



*Automatic Control*, vol. AC-10, pp. 434-439, 1965.

- [19] G. A. Ackerson and K. S. Fu, "On State Estimation in Switching Environments," *IEEE Transactions on Automatic Control*, vol. AC-15, no. 1, pp. 10-17, January 1970.
- [20] A. G. Jaffer and S. C. Gupta, "Recursive Bayesian Estimation with Uncertain Observation," *IEEE Transactions on Information Theory*, vol. IT-17, pp. 614-616, September 1971.
- [21] A. G. Jaffer and S. C. Gupta, "Optimal Sequential Estimation of Discrete Processes with Markov Interrupted Observations," *IEEE Transactions on Automatic Control*, vol. AC-16, pp. 417-475, October 1971.
- [22] C. B. Chang and M. Athans, "State Estimation for Discrete Systems with Switching Parameters," *IEEE Transactions on Aerospace and Electronic Systems*, vol. AES-14, no. 5, pp. 418-425, May 1978.
- [23] H. A. P. Blom, "An Efficient Filter for Abruptly Changing Systems," in *23rd IEEE Conference on Decision and Control*, Las Vegas, Nevada, December, 1984.
- [24] H. A. P. Blom and Y. Bar-Shalom, "The Interacting Multiple Model Algorithm for Systems with Markovian Switching Coefficients," *IEEE Transactions on Automatic Control*, vol. AC-33, no. 8, pp. 780-783, August 1988.
- [25] S. A. Gadsden, "Smooth Variable Structure Filtering: Theory and Applications," Department of Mechanical Engineering, McMaster University, Hamilton, Ontario, Ph.D. Thesis 2011.
- [26] E. Mazor, A. Averbuch, Y. Bar-Shalom, and J. Dayan, "Interacting Multiple Model Methods in Target Tracking: A Survey," *IEEE Transactions on Aerospace and Electronic Systems*, vol. 34, no. 1, pp. 103-123, January 1998.
- [27] H. Wang, T. Kirubarajan, and Y. Bar-Shalom, "Precision Large Scale Air Traffic Surveillance Using an IMM Estimator with Assignment," *IEEE Transactions on Aerospace and Electronic Systems*, vol. 35, no. 1, pp. 255-266, January 1999.
- [28] Y. M. Zhang and X. R. Li, "Detection and Diagnosis of Sensor and Actuator Failures Using IMM Estimator," *IEEE Transactions on Aerospace and Electronic Systems*, vol. 34, pp. 1293-1313, October 1998.
- [29] S. Kim, J. Choi, and Y. Kim, "Fault Detection and Diagnosis of Aircraft Actuators Using Fuzzy-Tuning IMM Filter," *IEEE Transactions on Aerospace and Electronic Systems*, vol. 44, no. 3, pp. 940-952, July 2008.
- [30] S. R. Habibi, "The Smooth Variable Structure Filter," *Proceedings of the IEEE*, vol. 95, no. 5, pp. 1026-1059, 2007.

## 8 APPENDIX

The following is a list of important EHA parameters and their corresponding values.

**Table 1. Important EHA Parameter Values**

Parameter	Physical Significance	EHA Model Value
$A$	Piston Area	$1.52 \times 10^{-3} \text{ m}^2$
$D_p$	Pump Displacement	$6.876 \times 10^{-7} \text{ m}^3/\text{rad}$
$M$	Load Mass	$7.376 \text{ kg}$
$V_0$	Initial Cylinder Volume	$2.1789 \times 10^{-4} \text{ m}^3$
$x_0$	Maximum Cylinder Stroke	$0.14335 \text{ m}$
$\beta_e$	Effective Bulk Modulus	$2.1 \times 10^8 \text{ Pa}$
$B$	Friction Damping Term	$28,569 \text{ Ns/m}$
$B_0$	Second Friction Term	$25 \text{ Ns/m}$
$B_2$	Third Friction Term	$0 \text{ Ns/m}$
$L$	Leakage Coefficient	$2.903 \times 10^{-11} \text{ Nm/s}$

# Hydraulic servoactuator for adaptive force control of fast trains pantographs

**Davide Ferrara, Giovanni Jacazio, Andrea Mornacchi, Stefano Pastorelli, Massimo Sorli**

Politecnico di Torino, Italy - Department of Mechanical and Aerospace Engineering

## ABSTRACT

Quality of current collection is a critical issue in high speed trains to reduce wear of the sliding surfaces, electrical arcs and electromagnetic interferences. Over the years, several studies were performed and different solutions proposed to improve the quality of current collection. These studies were primarily focused to pantograph kinematics, dynamics of the pantograph-catenary system, and estimation of the contact force between pantograph and overhead catenary, while less attention was given to the actuation system developing the control force on the pantograph. A research activity was hence conducted to develop a control and actuation system providing optimum control of the contact force. This was done with specific reference to the pantographs of Alstom high speed tilting trains. The paper first presents an overview of the past work in this field, outlines the characteristics of the pantograph-catenary system and analyses the factors acting as error sources for the force control system: variations of catenary height, uncertainty of the force measurement, signals noise, aerodynamic forces. The paper then describes architecture and characteristics of the force control and actuation system that was eventually defined for attaining the optimum force control; the system uses a combination of adaptive control and hydraulic actuation to obtain an accurate, fast responding and long life system. A dedicated mathematical model was developed and validated for simulating the system performance. The results of the system behaviour over the whole expected range of operating, service and environmental conditions are presented together with a conclusive assessment of its accuracy and robustness.

## 1 PROBLEM STATEMENT

Maintaining a constant, or quasi-constant contact force between the pantograph and the catenary has always been a major issue for trains collecting the electrical power from an overhead wire (Figure 1). A good quality of current collection, as well as the pantograph life, is in fact obtained when the contact pressure between pantograph and overhead catenary is kept within a well defined range. Large contact forces lead to a rapid wear of the sliding surfaces, while a low contact force tends to increase the electrical resistance and make the pantograph-catenary system more prone to temporary losses of contact eventually leading to electrical arcs with a consequent components damaging.

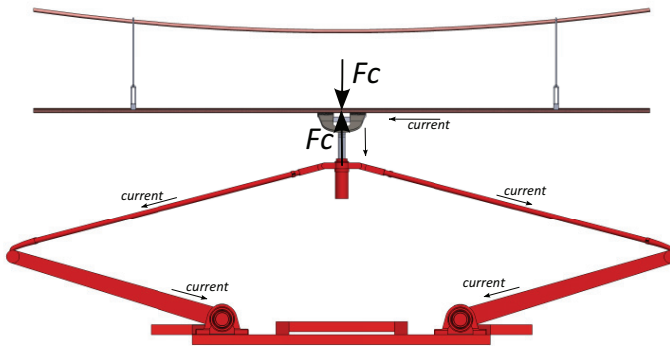


**Figure 1: Pantograph-catenary contact and current collection**

To generate the contact force, the pantographs are normally spring loaded; it is a simple and reliable solution, which however gives rise to large variations of the contact force in service. This is due to several factors such as catenary geometry, variation of the catenary height at level crossings and in tunnels, dynamics of the entire pantograph-catenary system and aerodynamic forces. In order to reduce the variations of the contact force during the train ride, several studies were performed aimed at developing force generation systems in which the contact force between pantograph and catenary is actively controlled and maintained quasi constant. Most of the past research effort was focused to the study of the pantograph-catenary system dynamics and of the control strategy, while the actuator generating the force received relatively little attention. However the actuator is a fundamental component of the active force control system, whose overall performance is highly dependent of the characteristics of the actuator with its associated control components. Moreover, the control law of the force servoloop must be tuned to the actuator characteristics in order to obtain the system best dynamic response and accuracy.

The most critical design issues for the servoactuator controlling the pantograph contact force are: life, dynamic response and control accuracy while subjected to rapid variations of the catenary height and to external disturbances, force measuring technique and sensitivity to the electrical noise.

Life is a critical issue because the catenary geometry determines a continuous periodical variation of the distance between the overhead wire and the train roof, which entails a continuous cycling travel of the actuator. For a train in revenue service, a total of about 30000 cycles a day can be expected, which corresponds to about 11 millions cycles per year and to more than 200 millions of cycles for a 20 years life. This large number of cycles is critical for electromechanical actuators made up by an electric motor, a gear drive and a ballscrew, since the wear associated to the operation of the mechanical components will limit the actuator life and periodical replacements must be planned. Pneumatic actuators could be more suitable to

withstand this large number of cycles, but they fall short of meeting the necessary dynamic response.

Dynamic response and force control accuracy are in fact a second main design issue because a bandwidth of at least 10 Hz is necessary to promptly counteract the variations of the catenary height and the external disturbances; furthermore, large and rapid changes of the catenary height can occur when a train passes along a level crossing, or at the entrance and exit of a tunnel, and the required force must be ensured during these transients while the actuator travels at high speed. These control requirements can hardly be met by pneumatic force control systems supplied by the typical 9 to 10 bar pressure of the trains air production systems. Determining the exact value of the contact force between the pantograph and the catenary is not an easy job. A direct measurement with a force sensor is obviously not possible because electrical current must flow through the contact area. A way for determining the contact force is to measure the force just under the shoe that makes up the uppermost portion of the pantograph, and correct that force by means of an appropriate algorithm that takes into account shoe acceleration and mass, as well as train speed, as it will be outlined further in this paper.

As briefly stated above, electromechanical actuators present the problem of wear of their internal parts as a result of the very large number of cycles, while pneumatic actuators exhibit a large compliance which thwarts their dynamic response. Hydraulic servoactuators thus seem to be the most suitable actuation technology for a pantograph force control system. These servoactuators can withstand very large number of cycles, as it is proven from their use in the aircraft primary flight controls, and show excellent frequency response and large dynamic stiffness. The main problem for hydraulic actuators is that hydraulics is normally not present in trains, which make use of compressed air for operation of brakes, doors, pantographs and other utilities. This is certainly true, however, most of the tilting trains do have hydraulics on board to supply the actuators controlling the carbody tilting when the train negotiates a curve. Therefore, the use of hydraulic servoactuators seems the logical choice for a pantograph force control system of tilting trains equipped with a hydraulic tilting system.

This paper presents the results of a research activity aimed at defining a hydraulic force control system for the pantographs of high speed tilting trains, and at assessing its performance. Though the scope of the work is focused to a specific train category, it is actually wider since it can well be envisaged to equip non-tilting trains with small and compact hydraulic power packs providing the small amount of average flow required by the pantograph actuator operation.

## **2 PAST WORK ON HYDRAULIC FORCE CONTROL SYSTEMS FOR PANTOGRAPHS**

Most of the research activities on active force control systems for pantographs considered the use of electromechanical or pneumatic actuators to develop the controlled force. A design concept that is found in several proposed designs is to exploit the already existing pneumatic actuator used to lift the pantograph providing it with the capability of modulating the pressure, thereby controlling its output force. This is an interesting solution since it does not

require the installation of a new actuator and uses an actuation technology well known in railways applications (4). However, the slow response of low pressure pneumatic actuators creates the need of developing complex control strategies performing predictive estimates of the control signals based upon processing the information of the pantograph state with a pantograph/catenary dynamic model. The solution is interesting, but is very sensitive to the variations of the characteristics of the components of the entire system made up by catenary, pantograph, actuator and pneumatic system, thus a good force control accuracy cannot in general be ensured.

A research on a hydraulic servo-operated pantograph for high speed trains (1) was performed about 40 years ago by the United Aircraft Corporation under a grant of the US Department of Commerce that perceived the merits of high speed trains and the associated need of improving the pantographs performance. Two different design solutions were proposed in that research activity, based on either one or two hydraulic actuators with their flows modulated by a mechanically driven flow control valve. The two-actuators solution entailed a complex construction, but it was a very effective design concept because each of the two actuators was optimized for a specific task. The larger and slower actuator was designed to make up for the changes of the catenary height, while the smaller and faster actuator was designed to cancel out the disturbances generated by the catenary droppers. The processing capabilities available at the time when that research activity was performed stymied the possibility of fully exploiting the merits of a hydraulic servo-operated pantograph, but the idea of using the hydraulic actuation technology for developing an accurate pantograph force control system remains valid. The computing capabilities nowadays available offer the possibility of implementing control algorithms for servovalve operated hydraulic actuators able to promptly respond to the control signals resulting from optimized control laws. This was the ground for the research activity presented in this paper which eventually defined a hydraulic servo-operated pantograph using a combination of adaptive control and hydraulic actuation to obtain an accurate, fast responding and long life system.

### 3 PANTOGRAPH-CATENARY DYNAMICS

The development of an analytical model of the pantograph-catenary system is a complex task because the system is made up by two nonlinear subsystems and furthermore one of these two, the overhead line, is a distributed parameter system requiring very complex modelling.

Actually, there are several different ways to model the overall system. Most authors describe the pantograph with a linear lumped-parameters model (either with two or three masses) while describe the catenary with a finite element model (2), (3), (4). This solution is certainly the most accurate one, but it demands large computing power and long computation time. Moreover, the purpose of modelling the catenary system in this research is to assess the merits of the pantograph force control system and its ability to react to periodical and random disturbances, and this assessment can be positively obtained also if the catenary is described with a lower resolution mathematical model. The pantograph-catenary model hence used for the system simulation consists of two lumped-parameters models: a two-degrees-of-freedom model for the pantograph and a space-varying model for the overhead line, as presented in (5).

The overhead line can have different configurations, but generally consists of one or two contact wires (1 in Fig. 2) which are held in tension horizontally and are zigzagged relatively to the centre line of the track to ensure even wear of the train's pantograph sliding underneath. The contacts wires are linked to the catenary wire (2 in Fig. 2) by means of droppers (3 in Fig. 2), with both wires supported regularly at any 60 m ( $l$  in Fig. 2) by a mast. For this work specific reference was made to the overhead line model 1805, which is the most common version in the Italian railway system. Figure 2 shows also the droppers layout in the 1805 model. The mathematical models for the catenary and for the pantograph used in the analysis of the pantograph force control system are briefly outlined in the following.

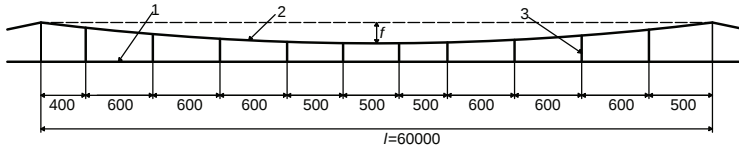


**Figure 2: Catenary outline (dimensions in mm)**

### 3.1 Catenary mathematical model

The mathematical model describing the catenary was developed with the purpose of representing the dynamic characteristics that are mostly important in determining the force exchange with the underlying pantograph, neglecting other features that have a minor effect on the contact force. This allows to take in due account the catenary dynamics without relying on an unnecessary complex mathematical model. The mathematical model used to describe the catenary dynamics has the following main features:

- A single-degree-of-freedom model describes the vertical displacement of the contact wire
- The overhead line is straight without zigzags
- The catenary wire is not deformable
- There are no singular points of contact wire like railroad switch or waste and debris

The lumped parameter model of the catenary is shown in figure 3. The contact wire inertia is represented by the mass  $M_{con}$  interfacing with the catenary wire by means of a connection with stiffness  $K_{con}$  and damping coefficient  $C_{con}$ . Mass, stiffness and damping coefficient are not constant values, but are space dependent parameters that are functions of the position of the contact point  $x$  between wire and shoe along each span. Figure 4 shows the diagrams of these parameters along a span between any two masts supporting the catenary. The parameters variation along the length between two masts consists of a global variation determined by the distance from the nearest mast and a superimposed local variation determined by the distance from the nearest dropper. The actual values for the catenary parameters are those for the 1805 catenary model.

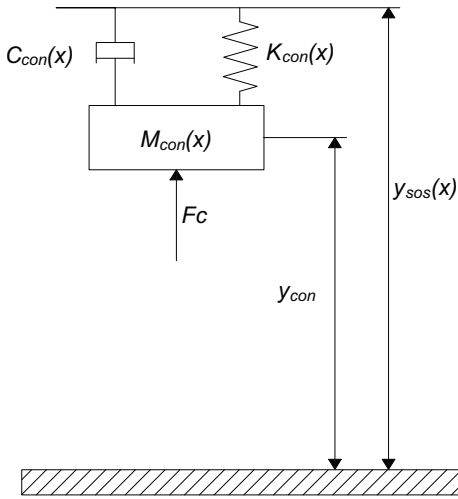


Figure 3: Overhead line model

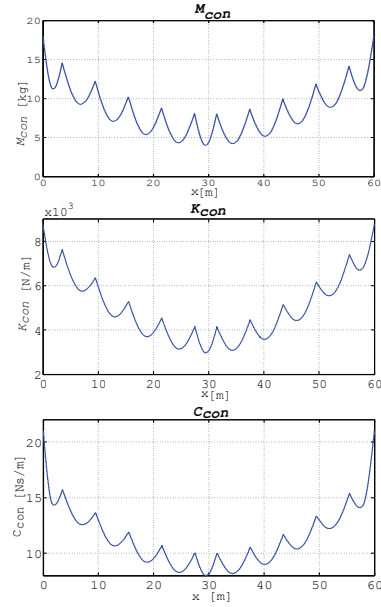


Figure 4: Variation of catenary dynamic parameters

The contact force  $F_c$  developed by the pantograph is applied to the mass  $M_{con}$ ; this force has an upward (positive) direction under normal operating conditions when there is contact between pantograph shoe and wire, and is set to zero in case of separation between these two parts.

It is important to emphasize that all vertical positions in the model are referred to the rails; this is instrumental in allowing a correct description of the change of the height of the overhead line that occurs in tunnels and at level crossings. Based on the above definitions, the catenary dynamics can be represented by the following equation, where  $y_{con}$  is the distance between contact wire and rail,  $y_{sos}$  is the distance between catenary wire and rail, and  $l0_{con}$  is the free length of the equivalent spring:

$$M_{con}(x)(\ddot{y}_{con} + g) + C_{con}(x)\dot{y}_{con} - K_{con}(x)(y_{sos} - y_{con} - l0_{con}) = F_c \quad (1)$$

### 3.2 Pantograph mathematical model

The pantograph considered for this work is the 52 FS AV model, which is used in several fast trains, such as the "Pendolino". This pantograph has a symmetrical construction and can well be described by a two-degree-of-freedom model: one for the lower frame and one for the upper frame (4). In addition, the pantograph model has a further non-inertial degree of freedom to describe the deformation of the shoe at the contact point. This degree of freedom is thus simply described by a combination of stiffness and damping without inertia. As for the catenary model, all variables defining the positions of the different parts of the pantograph represent the vertical distances from the rail.

The model schematic of Fig. 5 also shows the four external forces acting on the pantograph. Two forces act on the lower part of the pantograph:  $F_{stat}$  is the force generated by the pneumatic actuator used to lift the pantograph and is almost constant during the train travel; the other force  $F_{att}$  is the controlled force developed by the hydraulic servoactuator. The upper part of the pantograph is subjected to two external forces: the contact force  $F_C$  exchanged between shoe and wire, and the force  $F_{ae}$  resulting from the aerodynamic disturbances acting on the pantograph arch.

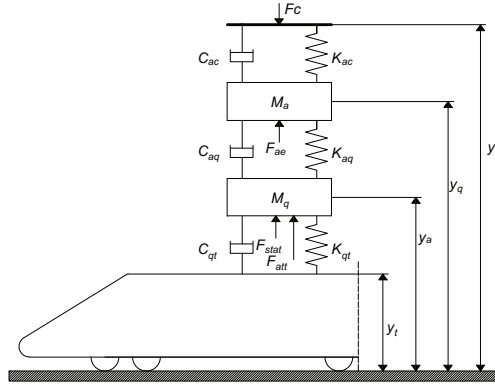


**Figure 5: Pantograph model diagram**

The dynamics of the system shown in Fig. 5 is described by the system of linear dynamic equations (2). It must be noted that the equation defining the relative position between shoe (distance from the rail  $y_c$ ) and upper mass  $M_a$  (distance from the rail  $y_a$ ) can have two different expressions depending on whether there is, or not, contact between shoe and wire. If contact exists ( $F_C > 0$ ), the positions of shoe and wire coincide ( $y_c = y_{con}$ ); in case of separation between shoe and wire, the contact force  $F_C$  is set to zero and the shoe position  $y_c$  becomes independent from the wire position since the shoe can move freely.

$$\begin{cases} C_{ac}(\dot{y}_a + \dot{y}_{con}) + K_{ac}(y_a - y_{con}) = F_C & \text{if } F_C > 0 \\ C_{ac}(\dot{y}_a + \dot{y}_c) + K_{ac}(y_a - y_c) = 0 & \text{if } F_C = 0 \\ M_a(\ddot{y}_a + g) - C_{aq}(\dot{y}_q - \dot{y}_a) - K_{aq}(l_{0aq} + y_q - y_a) + C_{ac}(\dot{y}_a - \dot{y}_c) - K_{ac}(y_a - y_c) = F_{ae} \\ M_q(\ddot{y}_q + g) - C_{qt}(\dot{y}_t - \dot{y}_q) - K_{qt}(l_{0qt} + y_t - y_q) + C_{aq}(\dot{y}_q - \dot{y}_a) + K_{aq}(l_{0aq} + y_q - y_a) = F_{stat} + F_{att} \end{cases} \quad (2)$$

In these equations  $l_{0qt}$  and  $l_{0aq}$  are the free lengths of the equivalent springs.

#### 4 EXTERNAL FORCE AND DISTURBANCES

Particular attention was paid during the research activity to consider all external factors that could possibly act as disturbances for the force control system and eventually affect the contact force. Three different factors were identified as potential disturbances:

- Aerodynamic force acting on the pantograph
- Electrical interference



- Change of height of overhead wire

The first two factors depend on the environmental conditions; they are not deterministic and a suitable model was prepared to take into account their effects. The third factor can be easily described from the known geometry of the catenary at level crossings and in tunnels. This is actually a rare occurrence when fast trains run along new tracks, but it is more frequent when the trains travel along older tracks, which is still the case for several trains in revenue service. These disturbance factors are briefly discussed hereunder.

#### 4.1 Aerodynamic force

The aerodynamic force is generated from the airflow impinging on the pantograph. Although air flows over the whole pantograph, the major contribution to the vertical component of the force is by far given by the flow over the upper part of the pantograph. The lift coefficient for the upper frame is in fact much larger than that for the lower frame. The values of the lift coefficients of the pantograph for different directions of the airstream are available from dedicated wind tunnel tests (11). The airflow over the pantograph actually consists of two independent components: the flow resulting from the train motion and the atmospheric wind. The first component was modelled as a vector always parallel to the rail direction (yaw angle = 0) and with a magnitude equal to the train velocity, while the wind modelling required a more careful analysis. The atmospheric wind was modelled as the sum of two vectors, each defined by two randomly time-variant numbers. The first number defines the wind velocity, while the second number defines its angle with respect to the track. The two vectors describe two different wind characteristics: one vector describes the wind turbulence and is randomly varying between 0 and 6 m/s with a high frequency content, while the second vector describes wind gusts and is varying between 0 and 19 km/h (equal to 3<sup>rd</sup> grade on the Beaufort scale) (13) with a randomly generated basis for both amplitude and direction of the gust. When running the simulations, the parameters of the resulting wind vector computed at each simulation time step were used to calculate the aerodynamic force and the lift coefficient, thereby allowing to determine a representative time history of the vertical component of the aerodynamic force acting on the pantograph.

#### 4.2 Electrical interference

While operating, the pantograph is immersed in a very severe electromagnetic environment determined by the collection of a large electrical current from a high voltage supply line. This generates an intense electromagnetic field disturbing the signals generated by the pantograph transducers. The resulting electromagnetic interference was simulated in the model as the sum of two sinusoidally varying signals, at 50 and 120 Hz, with randomly varying amplitudes. The lower frequency corresponds to that of the alternating current of the Italian power lines, while 120 Hz is a value simulating a higher frequency noise that was selected on the basis of information received by the trains' operators. In both cases the maximum amplitude of the disturbance was assumed to be equal to 0.4% of the full scale signal, which is consistent with the measurements for trains in service.

#### 4.3 Change of height of overhead wire

The change of height of overhead wire is typical of the old railways lines; it occurs at level crossings and in tunnels and is obtained by rising or lowering the catenary wire along a ramp approach in order to limit the oscillations of the horn. The transition ramp generally takes

place over two spans, hence over 120 m length, and the maximum height variation is normally 0.5 m.

## 5 HYDRAULIC SERVOACTUATOR

The key feature of the actively controlled pantograph is its actuation system consisting of a servovalve controlled double-acting hydraulic linear actuator whose rod end is connected to an extension of one of the arms of the pantograph lower frame as schematically shown in Fig. 5. The force developed by the hydraulic actuator is converted into a moment about the pantograph arm hinge and eventually into a force applied to the pantograph shoe in contact with the overhead wire. The hydraulic servoactuator is comprised of a hydraulic ram and a valve module. The hydraulic ram is a double acting piston jack with low friction characteristics ensured by a proper selection and sizing of the seals. The servoactuator is connected to a 28MPa hydraulic power supply, which is the prevailing type of hydraulic power supply for the high speed tilting trains manufactured by Alstom. The actuator is sized to provide a stall load of 6600 N, corresponding to a force of 746 N at the shoe, which is well above the maximum specified force for this type of pantographs. The relevant specification (13) recommends for the worst operating conditions a contact force  $F_c$  equal to:

$$F_c = 110 + 0.00092V^2 \quad (3)$$

where  $V$  is the train speed measured in m/s and  $F_c$  is the force in N. It must be noted that the conversion from actuator force and contact force is determined by the pantograph kinematics, which essentially is an off-centre rod-crank mechanism.

The hydraulic schematics of the servoactuator is shown in Fig. 6, which also shows the components and signals of the force control system. The valve module is comprised of a five-ports electrohydraulic servovalve with internal electrical feedback, a by-pass valve for actuator floating and emergency unloading, two cross-port pressure differential limiting valves (PPR) for actuator load limiting, that accept a pilot signal from the electrically operated valve DPR, pressure (AHP) and return (ALP) accumulators for minimising the effect of the hydraulic line dynamics on the transient response of the force control system. Moreover, the valve module includes a calibrated orifice (BP) for creating an internal cross port leakage, as required to optimise the force control dynamic performance, a manual valve (MV) for ensuring full by-pass during maintenance operations, and a dedicated filter for the servovalve first stage. The electronic control unit generates the servovalve input voltage and the energizing signal to the DPR valve to hydraulically arm the loading actuator.

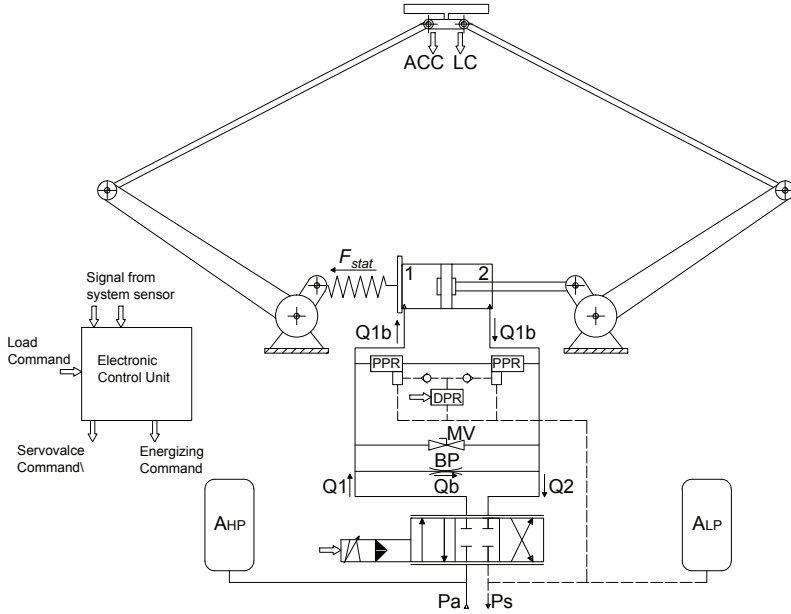


**Figure 6: Concept layout of hydraulic servoactuator and pantograph**

## 6 FORCE CONTROL LAW

Force control systems for high dynamic performance have been developed for different applications, some of which are described in (6), (7), (8), (9), (10), (12).

The control law used to regulate the force that the hydraulic actuator develops onto the pantograph follows the same general philosophy of that described in (8), (10), (12); it is essentially built around a modified PID controller with the addition of a gain variable blocks that optimise the system performance according to the operating conditions. The block diagram of the resulting control law is illustrated in Figure 7, where  $F_{CSET}$  is the required contact force and  $F_{CF/B}$  is the feedback signal. The control law is organized such that only an integrator is present in the forward path of the control loop, while the proportional and derivative gains act on the feedback signal; this arrangement is more effective than a conventional PID control. It improves the system accuracy since it allows a large value of the integrator gain to be set whilst maintaining a good stability margin due to the beneficial effect of the proportional and derivative internal feedback loops. To this effect, it is instrumental to have a 16 bit A/D converter and a minimum computation time to allow performing a fairly accurate time derivative of the force signal, with little noise superimposed on the true signal.

In order to get the best performance of the force control system over its whole operational range, the control loop gain is made adaptive to the actual force developed by the actuator. This is obtained by changing the values of the block  $Y$  in the diagram of Figure 7.

The adaptive gain  $Y$  is a function of the actual force developed by the actuator and is instru-

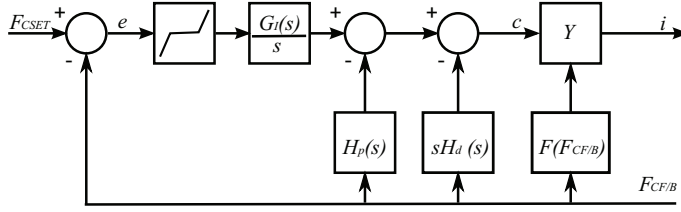


**Figure 7: Block diagram of the force control law**

mental in compensating the non-linear pressure/flow relationship of the servovalve and of the bypass orifice. In order to maintain an approximately constant stability margin over the whole range of operating conditions, the adaptive gain  $Y$  varies as a function of the measured actuator force  $F$  according to the following shaping function:

$$Y = \left( \frac{C_1}{C_2 + C_3 \left| \frac{F}{A_m} \right|} \right)^D \quad (4)$$

where  $A_m$  is the actuator mean area and  $C_1, C_2, C_3, D$  are suitable coefficients that were tuned to obtain the optimum system performance.

### 6.1 Feedback signal

Design and operation of the pantograph make the measurement of the contact force a critical issue. Direct measurement is obviously not possible because the installation of a load cell between wire and shoe would prevent the current collection. The solution identified as the most effective was to measure the force exchanged between the upper and lower frame of the pantograph, and correct it with calculated values of the forces acting on the upper frame. The value of the contact force  $F_{CF/B}$  used as a feedback signal in the force servoloop is then given by the following relationship:

$$F_{CF/B} = F_{aq} + F_{ae} - F_{ia} - F_{pa} \quad (5)$$

where  $F_{aq}$  is the force exchanged between the upper and the lower frame,  $F_{ia}$  and  $F_{pa}$  are respectively the inertia force and the weight of the upper frame, and  $F_{ae}$  is the aerodynamic force. The force  $F_{aq}$  exchanged between lower and upper frame can be measured by a load cell, while the weight  $F_{pa}$  is a design parameter and it is a known quantity. The evaluation of the inertia force  $F_{ia}$  requires an accelerometer to be placed on the upper frame to measure the vertical component of the acceleration. From the measured value of the vertical acceleration, and the known value of the mass of the upper frame, the inertia force can be computed. The evaluation of the aerodynamic force would require the measurement of the local air velocity. However, since the main contribution is by far given by the train velocity, which is a known quantity, the errors induced by neglecting the atmospheric wind are little and do not justify the installation of an air velocity sensor, with the associated cost and possibility of failure. As a conclusion, the vertical component of the aerodynamic force is determined from the square of the train velocity and the pantograph coefficient of lift. In order to validate the procedure used

to calculate the contact force, a comparison was made between the measurements performed on a train traveling at 250 km/h and the contact force computed with the above outlined procedure for a train traveling at that speed along the same track. The comparison results are shown in Fig. 8.

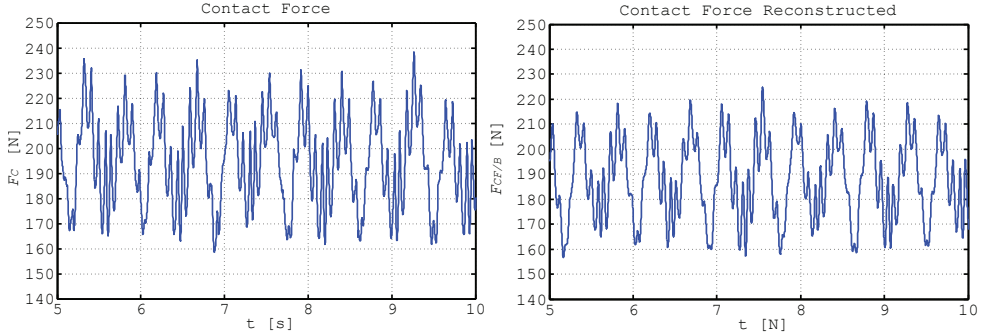


**Figure 8: Comparison between contact force and reconstructed force**

## 7 SIMULATION CODE

The equations defined in the previous sections of this paper made up the basis for writing a simulation code of the overall system consisting of hydraulic servoactuator with its electronic controller, pantograph and overhead catenary. The model is therefore of a "physical-based" type, in which all system components are modelled with equations representative of their physical characteristics. In particular, for the modelling of the hydraulic servoactuator the detailed characteristics of the servovalve are duly addressed. The 1<sup>ST</sup> stage dynamics is described by a modified second order transfer function that includes modeling of the 1<sup>ST</sup> stage end-of-travel. The pressure-flow characteristics of the 1<sup>ST</sup> stage are described by the equations relating pressure and flow through the 1<sup>ST</sup> stage internal passageways, which in turn determine the velocity of the 2<sup>ND</sup> stage spool and eventually its position, by also taking into account the spool end-of-travels. Once the spool position is known, the pressure/flow characteristics of the servovalve are determined. The servovalve model accurately describes the flow through each of the four internal passageways taking into account the actual passage area, which depends on spool displacement, valve laps and radial clearance between spool and sleeve. Also, the variation of the flow discharge coefficient with the Reynolds number, with the corner radius and with the aspect ratio of the control port is taken into account. Piston inertia, viscous and coulomb frictions are duly considered in the actuator model.

The pantograph simulation code implements the two-degree-of-freedom model for the pantograph and the space-varying model for the overhead line described in section 3 of this paper. It also implements the equations representative of the aerodynamic and electrical disturbances acting on the pantograph as defined in section 4 of this paper. A good confidence on the model accuracy was gained by comparing the time histories of measured and computed contact force as shown previously in Fig. 8.

## 8 SYSTEM PERFORMANCE ASSESSMENT

A wide simulation campaign was conducted to assess the performance of the pantograph force control system over the whole range of the operating conditions expected for a train in revenue service. Variations of train speed, catenary height, aerodynamic and electrical disturbances, and environmental conditions were duly considered.

### 8.1 Simulation at 250 km/h

The first simulation for assessing the force control system merits was carried out assuming a constant train speed of 250 km/h. The results obtained were then compared with the requirements established by the technical regulation for pantographs of the Italian railway lines. The difference between the contact forces  $F_c$  for the passive and active pantographs are clearly shown in the diagrams of Fig. 9 which represent only a part of all duration of the simulation. At a first glance, the introduction of the hydraulic force control system does not seem to bring a particular advantage; however, when the actual values of the contact force are properly examined, it can be seen that it leads to a decrease of the average contact force, bringing it close to the required value. Some reduction of the amplitude of the force oscillations is obtained, as well as the complete absence of separations between shoe and overhead wire. A clear summary of the advantages gained by the introduction of the hydraulic force control system is provided by Table I in which the technical specifications required for pantograph qualification are compared with the results obtained for the two configurations.

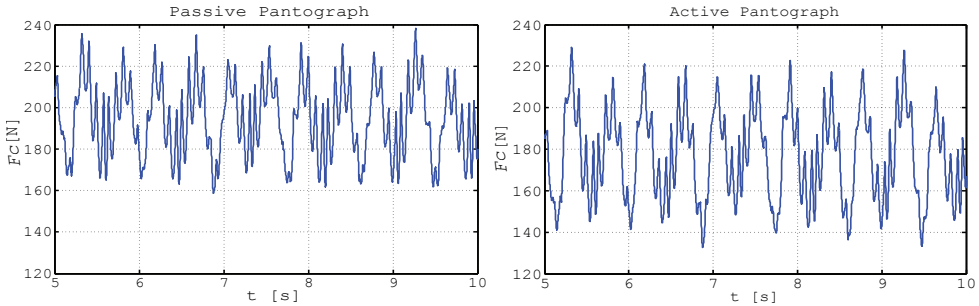


Figure 9: Time history of contact force at 250 km/h for passive and active pantograph

Table I: Comparison between active and passive pantograph at 250 km/h

	Regulation	Active	Passive
$F_{cmean}$	170 [N]	178 [N]	195 [N]
$F_{cmax}$	400 [N]	237 [N]	245[N]
$0.3F_{cmean} - \sigma$	> 0.00 [N]	32.34 [N]	40.95[N]
$NQ$	< 0.200%	0.000%	0.017%

In this table,  $0.3F_{cmean} - \sigma$  indicates if the force remains inside a tolerance band of about 3 sigma. The parameter  $NQ$  reported in the above table is a very important parameter to

determine the quality of the current collection.  $NQ$  is defined as (13):

$$NQ = \frac{\sum t_{dist}}{T_{oss}} * 100 \quad (6)$$

where  $t_{dist}$  is duration of each individual separation between pantograph shoe and overhead wire, and  $T_{oss}$  is the total duration of the test. The active pantograph greatly improves the parameter  $NQ$  since no separation occurs, thereby improving the current collection and the useful life of the shoe.

### 8.2 Simulation at 300 km/h

The improvements introduced by the hydraulic force control system are even more evident for a train traveling at 300 km/h, where a passive pantograph performance is poor with frequent losses of the contact between shoe and wire. For this operating condition the quality coefficient  $NQ$  of passive pantograph is more than twice than the specified limit. On the contrary, no separation occurs for the active pantograph. The comparison between active and passive pantograph performance for this operating condition is clearly shown by the following Fig. 10 and table II. The active pantograph allows a reduction of the contact force, which significantly reduces the frictional forces, and prevents contact losses, thereby ensuring an excellent current collection and minimum probability of generation of electric arcs.

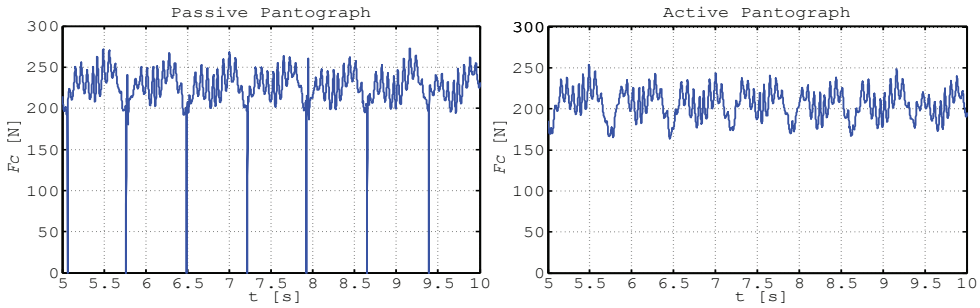


**Figure 10:** Time history of contact force at 300 km/h for passive and active pantograph

**Table II:** Comparison between active and passive pantograph at 300 km/h

	Regulation	Active	Passive
$F_{cmean}$	197 [N]	206 [N]	227 [N]
$F_{cmax}$	400 [N]	270 [N]	510[N]
$0.3F_{cmean} - \sigma$	> 0.00 [N]	43.36 [N]	42.36[N]
$NQ$	< 0.200%	0.000%	0.480%

### 8.3 Simulation of travel in tunnel

A simulation was performed with the purpose to verify the behavior of the active pantograph in response to the variation of the catenary height associated with a tunnel. The simulation was run for the case of a train entering into a tunnel with 500 m length which requires a

**Table III: Comparison between active and passive pantograph at 150 km/h in a tunnel**

	Regulation	Active	Passive
$F_{cmean}$	132 [N]	136 [N]	184 [N]
$F_{cmax}$	300 [N]	173 [N]	334[N]
$0.3F_{cmean} - \sigma$	$> 0.00$ [N]	30.78 [N]	-8.29[N]
$NQ$	$< 0.100\%$	0.000%	0.000%

reduction of 0.2 m height of the overhead wire. For a passive pantograph this height reduction leads to an increase of the contact force as clearly shown in the right diagram of Fig. 11.

For an active pantograph, the force control system appropriately reacts to the height variation of the catenary and maintains an approximately constant force, as shown in the right diagram of Fig. 11. Table III reports the performance summary for passive and active pantographs when the train travels in a tunnel.

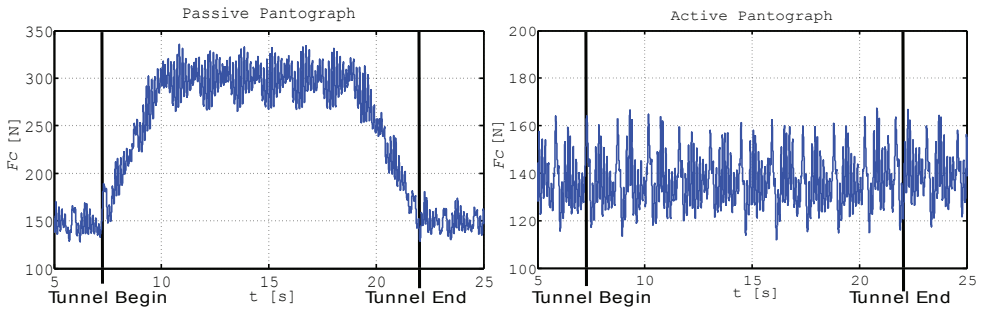


**Figure 11: Time history of contact force at 150 km/h for passive and active pantograph in a tunnel**

### 9 CONCLUSIONS

The pantograph force control system described in this paper was devised to accurately control the contact force between pantograph and wire for the possible range of operating and environmental conditions encountered by a train while in service. To achieve that, a non-linear, adaptive control strategy was devised to generate the control signals to a servovalve controlled hydraulic actuator able to accurately control the pantograph /catenary contact force. The system merits were verified by using a properly developed mathematical model implemented as a Matlab/Simulink software code to evaluate the system performance for the expected range of operating and environmental conditions. It was shown that the force control system is able to always maintain the contact force between pantograph and overhead catenary within the specified range, thereby contributing to minimise pantograph and contact wire wear and increase their life.



## REFERENCES

- (1) United Aircraft Corporation, Design and development of a servo-operated pantograph for high speed trains, July, 1970, Stratford, CT, USA
- (2) Gostling R.J., Hobbs A.E.W., The interaction of pantograph and overhead equipment: practical applications of a new theoretical method, Proceeding of Institution of Mechanical Engineering, Volume 197C, pp. 61-69, 1983
- (3) Vinayagalingam T., Computer evaluation of controlled pantograph for current collection from simple catenary overhead equipment at high speed, Journal of Dynamic System, Measurement and Control, Volume 105, pp. 287-294, 1983
- (4) Diana G., Fossati F. and Resta F., High speed railway: collecting pantograph active control and overhead lines diagnostic solutions, Vehicle System Dynamics, Volume 30, pp. 69-84, 1998
- (5) Allotta B., Pisano A., et al., VSC of a servo-actuated ATR90-type pantograph, Proceeding of the 44th IEEE Conference on Decision and Control, and the European Control Conference, pp. 590-595, December 12-15, 2005, Seville, Spain
- (6) Karam W., Maré J.C., Comparison of EMA et HA performance for dynamic load simulators, Proceedings of the Power Transmission and Motion Control, pp. 211-224, September 7-9, 2006, Bath, England
- (7) Karam W., Maré J.C., The performance of force controlled electromechanical actuator around null speed, Proceedings of Power Transmission and Motion Control Symposium - PTMC 2007, September 12th-14th, 2007 Bath, UK
- (8) Jacazio G. and Balossini G., Real-time loading actuator control for an advanced aerospace test rig, Proceedings of the Institution of Mechanical Engineers, Part I: Journal of Systems and Control Engineering, Volume 221, Number 2/2007, pp. 199-210
- (9) Karam W., Maré J.C., Force control of a roller-screw electro-mechanical actuator for dynamic loading of aerospace actuators, Proceeding Bath/ASME Symposium on Fluid Power and Motion Control, Bath, September 10 -12, 2008
- (10) Jacazio G. and Balossini G., The Iron bird for the M346 advanced trainer, Presented at the SAE A6 meeting on Aerospace fluid power and actuation systems, October 13-16, 2008, Portland
- (11) Gregoire R., Collina A. et al., Some considerations on the aerodynamic of high speed pantograph: CFD and wind tunnel test, Proceeding of BBAA VI International Colloquium on: Bluff Bodies Aerodynamic & Applications, July 20-24, 2008, Milano
- (12) Jacazio G. and Balossini G., A mechatronic active force control system for real time test loading of an aircraft landing gear, Proceedings of the ASME 2009 International Design Engineering Technical Conferences & Computers and Information in Engineering Conference IDETC/CIE 2009, August 30 - September 2, 2009, San Diego; Paper DETC2009-86148
- (13) Rete Ferroviaria Italiana, Prove da eseguire per la caratterizzazione di un pantografo a  $3kV_{cc}$  (*Italian Railways Network, Tests to performed for assessing the characteristics of a  $3 kV_{dc}$  pantograph*), 2008

## LIST OF SYMBOL

$A_m$	Actuator mean area	$l0_{aq}, l0_{qt}$	Rests of pantograph equivalent spring
$C_1, C_2, C_3$	Coefficients of the shaping function	$M_a, M_q$	Masses of pantograph frame
$C_{ac}, C_{aq}, C_{qt}$	Damping coefficients of pantograph frame	$M_{con}$	Mass of overhead wire
$C_{con}$	Damping coefficient of overhead wire	$NQ$	Index of caption quality
$D$	Exponent of the shaping function	$s$	Laplace variable
$F_{ae}$	Aerodynamic force	$t_{dis}$	Duration of each individual separation
$F_{aq}$	Force exchange between the upper and lower frame	$T_{oss}$	Duration of the test
$F_{att}$	Controlled force developed	$V$	Velocity of train
$F_C$	Contact force	$x$	Position of contact point along each span
$F_{CF/B}$	Reconstructed contact force	$y_a$	Absolute position of upper frame
$F_{CSET}$	Required contact force	$y_{con}$	Absolute position of contact wire
$F_{ia}$	Inertia force of upper frame	$y_c$	Absolute position of shoe
$F_{pa}$	Weight force of upper frame	$y_a$	Absolute position of lower frame
$F_{stat}$	Force by pneumatic spring	$y_{sos}$	Absolute position of catenary wire
$K_{ac}, K_{aq}, K_{qt}$	Stiffness coefficient of pantograph frame	$y_t$	Absolute position of roof of train
$K_{con}$	Stiffness coefficient of overhead wire	$\sigma$	Standard deviation of contact force



# Issues of sensor noise, bandwidth and sampling time in PID pressure control

**Matthias Liermann**

American University of Beirut  
matthias.liermann@aub.edu.lb

## ABSTRACT

Electro-hydraulic pressure control is needed for the operation of hydraulic service manifolds at constant pressure or to control forces of actuators in many industrial applications. As opposed to position control of hydraulic actuators, where model-based control classical design is rarely practical, it works well for pressure control. Model-based PID control design is of particular interest, because it allows direct implementation on existing applications with existing controls. This paper builds on previous work by the author on model-based PID control design. It extends the scope of view by analyzing the influence of sensor dynamics and sampling frequency on the control performance. The analysis shows that these factors have a significant influence on the control performance in particular when high-response valves are used. The paper concludes with practical recommendations for sensor bandwidth and sampling time for a given valve.

## 1 NOMENCLATURE

Symbol	Units	Description
$B_V$	$\frac{m^3}{s\sqrt{Pa}}$	valve flow coefficient
$C_H$	$\frac{m^3}{Pa}$	hydraulic capacity
$D_V$	-	valve damping ratio
$E'_{oil}$	Pa	effective bulk modulus of oil
$G_{PID}(z)$	-	discrete PID transfer function
$K_D$	$\frac{s}{Pa}$	derivative PID gain
$K_I$	$\frac{1}{Pa s}$	integral PID gain
$K_P$	$\frac{1}{Pa}$	proportional PID gain
$K_V$	-	valve gain
$p_A$	Pa	pressure in chamber A
$p_{A,ref}$	Pa	reference pressure for chamber A
$p_{A,ZOH}(t)$	Pa	zero order hold pressure measurement value between $t$ and $t + T_S$
$p_{nom}$	Pa	nominal pressure
$p_{res}$	Pa	reservoir pressure

Symbol	Units	Description
$p_{\text{sup}}$	Pa	supply pressure
$Q_A$	$\frac{\text{m}^3}{\text{s}}$	volumetric flow rate
$Q_{\text{nom}}$	$\frac{\text{m}^3}{\text{s}}$	nominal flow at nominal pressure
$T_{\text{cd}}$	s	computing time delay
$T_D$	s	derivative time constant
$T_S$	s	loop cycle time
$U$	-	measurement signal value
$u$	-	control signal
$V$	$\text{m}^3$	volume
$V_{\text{Qu}}$	$\frac{\text{m}^3}{\text{s}}$	flow gain
$x_v$	-	partial valve opening
$y(t)$	-	discrete output of PID control between $t$ and $t + T_S$
$\omega_n$	$\frac{1}{\text{s}}$	dominant natural frequency of system
$\omega_{pc}$	$\frac{1}{\text{s}}$	phase cross-over frequency
$\omega_{\text{PID}}$	$\frac{1}{\text{s}}$	natural frequency characterizing zeros of PID
$\omega_S$	$\frac{\text{rad}}{\text{s}}$	sensor natural frequency
$\omega_V$	$\frac{\text{rad}}{\text{s}}$	valve natural undamped frequency
$\phi_m$	$\frac{\text{rad}}{\text{s}}$	phase margin
$\zeta_S$	-	sensor damping ratio

## 2 INTRODUCTION

PID feedback is almost exclusively used for industrial pressure control. It has the necessary ingredients to shape the dynamic response but is difficult to parameterize. The parameterization in practice is based on tuning experience of experts. Feedback gain formulas or tuning rules have been developed to parameterize PID control based on plant parameters which are known by commissioning engineers [1, 2, 7]. They are very helpful and have proven to be effective in many cases. However, it has been reported from practice that in some cases they lead to low damped or even unstable systems. In the derivation of the tuning rules it is assumed that the controller is implemented continuously and that sensor dynamics are negligible. The purpose of this paper is to investigate, in which ranges of sensor natural frequency and control system sampling time this assumption is valid. The paper shows that especially with the use of high response valves with low damping ratio care must be taken to choose sensors which have sufficiently large bandwidth and that the control sampling is not too coarse. The analysis is done on the basis of the frequency response of the hybrid continuous/discrete open loop dynamics. Chapter 4 presents a chart for practical use which shows how to pair valve and sensor natural frequency with sampling time.

**Figure 1** shows a hydraulic load frame as a typical application for pressure control. It consists of four precision machined poles which connect the adjustable cross-head to the base. The hydraulic cylinder is mounted on top of the cross-head. Its motion and force is controlled by servo-valve actuation. Usually a digital control unit is used to facilitate safe plant operation and to close the loop between force or pressure measurement and valve actuation.



**Figure 1: Servo-hydraulic load frame**

**Figure 2** shows a schematic of the hydraulic circuit and the pressure control scheme commonly used in industrial controllers. The pressure is picked up by a pressure transducer with a certain dynamics and noise characteristics. The controller evaluates the error and generates a control signal  $u$  with proportional plus integral plus derivative action. The derivative action is only applied on the measurement signal and not on the input signal to avoid the set-point kick phenomenon when the input signal changes quickly. This type of PID feedback is referred to in literature as PI-D feedback, [10]. A digital control unit can only process measurements at discrete time steps and usually outputs the results right away with a slight computational delay. This delay is usually much smaller than the cycle time. Cycle times depend on the processor speed and the size of the control program. Typical industrial controllers operate at cycle times of  $T_S = 0.25$  ms and larger.

### 3 MODELING

This section describes the mathematical model of the plant depicted in Figure 2. For reference and further details, see [9, 7]. At first, the model for the hydraulic system is presented including the valve dynamics. The flow is described by the orifice equation and the pressure

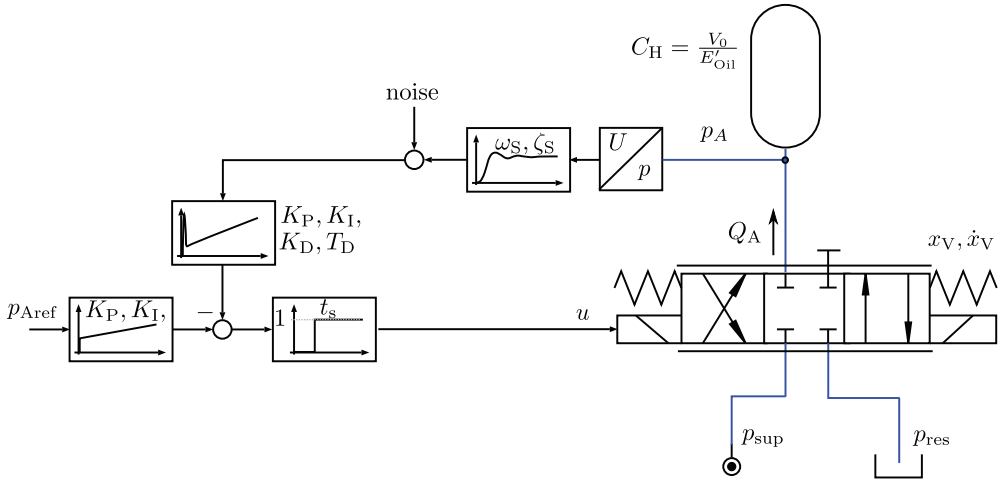


**Figure 2: Pressure control using PI-D feedback**

build-up equation is derived from the mass conservation principle for the pressurized volume. Then, the sensor and real-time control system dynamics are discussed and a discrete-time model is given.

### 3.1 Valve and controlled volume

The control valve used for pressure control is usually a spool type valve. The dynamics can be approximated satisfactorily by a 2<sup>nd</sup> order element. **Figure 3** exemplarily shows the measured and approximated bode diagram of a Bosch NG6 High Response Valve. The diagram characterizes the dynamics of the electro-mechanical system. The input signal is a sinusoidal command signal  $u$ . The response signal, for which the diagram is plotted, is the spool percent opening  $x_V$ , not the flow. Two curves are plotted for small signal and large signal response. This shows that obviously the valve does not behave linear. Among other factors, this is due to current limitation of the electric actuation. In the small signal domain the valve has a higher bandwidth and a small overshoot. This indicates a damping ratio below 0.7. In pressure control applications, the valve usually operates around its center position. Therefore the small signal Bode diagram should be chosen for identification of valve parameters. The identified parameters are the damping ratio  $D_V$  and the natural undamped (angular) frequency  $\omega_V$ . It is evident that the match of magnitude and phase curves is good for frequencies below the bandwidth (-3dB frequency) of the valve.

$$\frac{x_V(s)}{u(s)} = \frac{K_V \omega_V^2}{s^2 + 2D_V \omega_V s + \omega_V^2} \quad (1)$$

The flow  $Q_A$  through the valve is a function of pressure difference and valve opening. Typically the flow is expressed as a function of the spool percent opening  $x_V$ .

$$Q_{A_{in}} = B_V x_V \sqrt{p_{sup} - p_A} \quad \text{for } x_V \geq 0 \quad (2)$$

$$Q_{A_{out}} = B_V x_V \sqrt{p_A - p_{res}} \quad \text{for } x_V < 0 \quad (3)$$

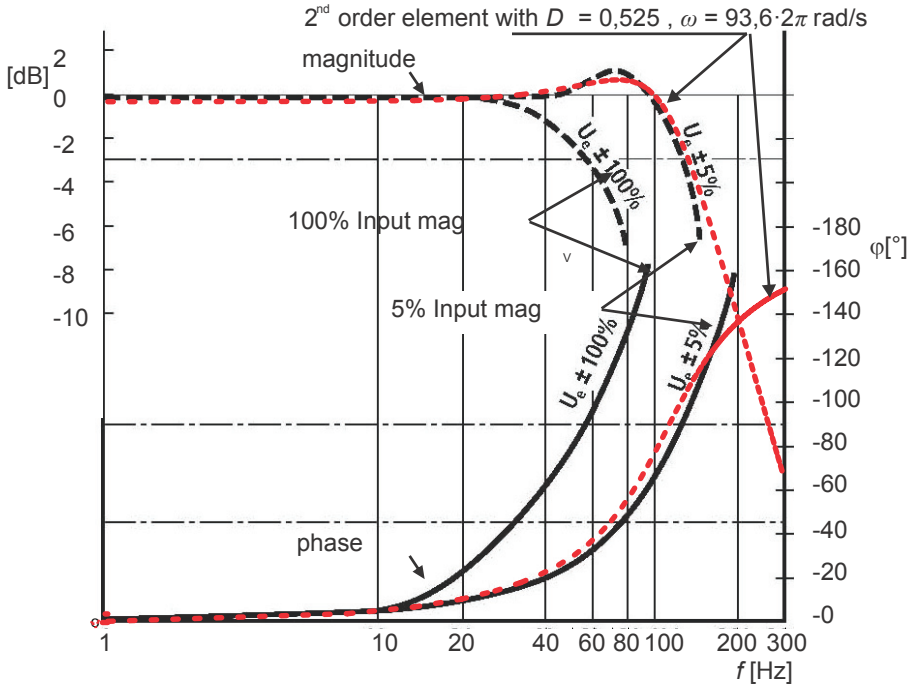


**Figure 3: Valve dynamics approximated as 2<sup>nd</sup> order element**

The valve flow coefficient  $B_V$  is a parameter which includes information about the maximum cross-sectional flow area, the discharge coefficient and the fluid density. It is obtained through measurement and can be calculated from data given in the valve data-sheet.

$$B_V = \frac{Q_{nom}}{\sqrt{p_{nom}}} \quad (4)$$

The nominal flow  $Q_{nom}$  is measured at a nominal pressure difference  $p_{nom}$  of typically 35 bar across each valve land.

For analysis and model-based control design it is desirable to obtain a linearized flow equation for conditions around an operating point. Linearizing Eq. 2 and Eq. 3 breaks the product of percent valve opening and square root of pressure difference into sums of linear independent terms. The first term characterizes the sensitivity of flow on change in pressure difference, the other term characterizes the sensitivity on the change of valve position. A dimensional analysis shows that the latter term is large in comparison with the first. Therefore, in many works on pressure control, the sensitivity on change of pressure difference is neglected [12, 3, 9]. The simplified linearized flow equation then is

$$\Delta Q_A = \frac{V_{Qu}}{K_V} \Delta x_V \quad (5)$$



The flow gain  $V_{Qu}$  is the derivative of flow with respect to valve input signal calculated at operating point conditions. It is obtained from Eq. 2 and Eq. 3 using the valve gain  $K_V$  which describes the proportionality of valve percent opening and input signal.

$$V_{Qu} = \frac{\partial Q_A}{\partial u} = \frac{\partial Q_A}{\partial (K_V x_V)} \quad (6)$$

The flow gain is different depending on whether the inflow or outflow pressure difference is taken into account. For stability analysis the higher value should be considered as this is usually the more critical case:

$$V_{Qu_{in}} = \frac{B_V}{K_V} \sqrt{p_{sup} - p_A} \quad (7)$$

The continuity principle states that the sum of rates of mass flows going in and out is equal to the change of mass in the controlled volume. Assuming that the volume is constant, this statement leads to the pressure build-up equation, which states that the pressure gradient is proportional to the net flow into the volume.

$$\dot{p}_A = \frac{1}{C_H} Q_A \quad (8)$$

$$V_{Qu_{out}} = \frac{B_V}{K_V} \sqrt{p_A - p_{res}} \quad (9)$$

The hydraulic capacity  $C_H$  is the ratio between Volume  $V$  and (effective) bulk modulus  $E'_{oil}$ . It should be noted that this factor is difficult to predict accurately for a given setup, on which pressure control should be applied. The volume  $V$  may be well known if engineering drawings exist, but often it has to be estimated. Sometimes it may be subject to change, for example if pressure control is applied with a cylinder in different positions. The effective bulk modulus is also difficult to know precisely. It depends significantly on pressure, the compliance of components and possibly contained air in the system [6].

Based on the foregoing analysis, an approximated linear model of the electro-hydraulic open loop system is given by

$$\frac{p_A(s)}{u(s)} = \frac{V_{Qu}}{C_H} \frac{\omega_V^2}{s[s^2 + 2D_V \omega_V s + \omega_V^2]} \quad (10)$$

### 3.2 Sensor and control

Even though the controller in most cases is implemented using deterministic real time control, it is common practice to derive model-based feedback dynamics assuming continuous implementation. The works [2, 7] make this assumption and propose model-based tuning rules for PI-D feedback. The open loop transfer function assuming continuous implementation of PID control is

$$\frac{p_A(s)}{u(s)} = \frac{V_{Qu}}{C_H} \frac{\omega_V^2 (K_D s^2 + K_P s + K_I)}{s^2 (s^2 + 2D_V \omega_V s + \omega_V^2) (T_D s + 1)} \quad (11)$$

with the PID gains  $K_P$ ,  $K_I$  and  $K_D$  and  $T_D$  the derivative time constant. The derivative time constant approximates the behavior of a practical implementation of a PID control, since an ideal differentiation is impossible.

Liermann proposes the following gain formulas in [7] based on a frequency response design approach:

$$K_{PFR} = K_I \frac{2D_V}{\omega_{PID}} \quad (12)$$

$$K_{IFR} = \frac{2C_H \omega_V^2 \omega_{PID}^2}{9V_{Qu}} \sqrt{\frac{16 + 9D_V^2}{81\omega_{PID}^4 - 18\omega_{PID}^2 \omega_V^2 + \omega_V^4 + 36D_V^2 \omega_{PID}^2 \omega_V^2}} \quad (13)$$

$$K_{DFR} = \frac{K_I}{\omega_{PID}^2} \quad (14)$$

with  $\omega_{PID}$  being the natural frequency of the PID transfer function zeros:

$$\omega_{PID} = \frac{\omega_V}{12} \left( \sqrt{16 + 9D_V^2} - 3D_V \right) \quad (15)$$

These tuning rules, or gain formulas, give a tailored set of parameters  $K_P$ ,  $K_I$  and  $K_D$  which are optimal with respect to the design idea. It is assumed that plant parameters are known although this is rarely the case in practice. However, the rules have the advantage that the capacity  $C_H$ , which is the major modeling uncertainty, appears in all three equations only as a multiplying factor and therefore can be used as a single tuning parameter. By scaling this parameter the control can be adjusted to make up for the major modeling errors. This approach requires less expert knowledge and commissioning time than having to adjust all parameters independently. The result is a good transient response which is also very robust, if the assumption is valid, that sensor dynamics and sampling can be neglected.

However, when the sampling time  $T_S$  of the control is close to the dominant time constant of the system, or the sensor bandwidth is close to the valve bandwidth, this assumption is violated. Franklin et al propose in [4] that a complete discrete analysis is recommended when the sample time is larger than  $\frac{1}{10\omega_h}$ , with  $\omega_h$  the dominant natural frequency of the system. This is the case if high response valves with natural frequencies around 80-300 Hz are used and sampling times are between 0.1-5 ms. Also, the sensor natural frequency may not be negligible. Industrial thick or thin film pressure sensors have a natural frequency depending on the filtering of the transducer electronics between 200-1200 Hz. Some have natural frequencies that are as low as 20 Hz due to signal conditioning.

**Figure 4** shows the system block diagram explicitly using discrete control. The PI-D control is implemented in form of a difference equation based on discrete time values of present and past control cycles, [8].

$$y(t) = y(t - T_s) + K_P \left( \left( 1 + \frac{T_S K_I}{K_P} + \frac{K_D}{K_P T_S} \right) p_{A,ZOH}(t) - \left( 1 + 2 \frac{K_D}{K_P T_S} \right) p_{A,ZOH}(t - T_S) \dots \right. \\ \left. \dots + \frac{K_D}{K_P T_S} p_{A,ZOH}(t - 2T_S) \right) \quad (16)$$

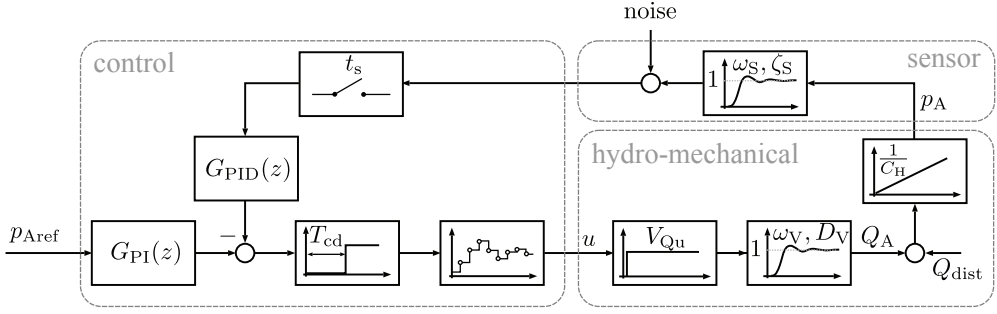


**Figure 4: Block diagram of pressure control with discrete control**

The pressure  $p_A$  is picked up at discrete times with  $\Delta t = T_S$  and processed as  $p_{A,ZOH}$  by the discrete control. The computing time delay  $T_{cd}$  is the time needed to execute the computation and to update the output. It should be much less than the cycle time in order to be neglected. Usually it is assumed that the computation itself takes place instantly,  $T_{cd} = 0$ . Shin and Cui have investigated the effect of computing time delay on control performance in [11]. Also see discussion in [5]. The effect of computation delay is neglected in the following analysis. The difference equation can then be represented as discrete transfer function:

$$G_{PID}(z) = K_P \frac{(1 + \frac{T_S K_I}{K_P} + \frac{K_D}{K_P T_S})z^2 - (1 + 2 \frac{K_D}{K_P T_S})z + \frac{K_D}{K_P T_S}}{z^2 - z} \quad (17)$$

The next section presents a dimensionless frequency response stability analysis. The result of the analysis is a directive how to pair valve and sensor bandwidth with sampling time to avoid low damped system behavior or even unstable systems.

## 4 STABILITY ANALYSIS

The open loop dynamics consist of a continuous physical system Eq. 10 and a discrete control Eq. 17. It cannot be represented in a single expression due to the hybrid nature of combined discrete and continuous system. But the stability analysis of discrete systems is analogous to continuous systems and the Nyquist criterion applies in the same way. The requirement for stability of non-minimum phase systems is that the magnitude of the frequency response of the open loop has to be smaller than unity at the frequency  $\omega_{pc}$  where the phase crosses  $-180^\circ$ . In other terms, the open loop phase at gain cross-over frequency  $\omega_{gc}$ , where the gain crosses unity, has to be larger than  $-180^\circ$ . The phase margin  $\phi_m = 180 + \phi(\omega_{gc})$  is the amount of additional phase lag, which the system tolerates at the gain cross-over frequency  $\omega_{gc}$ , before it would become unstable.

### 4.1 Impact of added phase lag from sensor and control on stability margin

The following analysis is normalized to the valve frequency  $\omega_V$ . **Figure 5** shows the Bode plot of the open loop with and without control. The parameters are listed in the top right corner of the plot. The valve damping  $D_V = 0.525$  is read from the valve bode plot which is

shown in Figure 3. The sensor damping ratio  $\zeta_s = 0.89$  is chosen slightly over-damped, its natural frequency  $\omega_s$  four times larger than the valve natural frequency. The control sampling time is half of the inverse of the valve natural frequency. The Bode plots of continuous and discrete open loop are given for comparison. Comparing the phase plot with and without controller reveals the objective of the PID control. The PID provides positive phase shift and increases the phase margin. The magnitude curve is lifted to a level that the gain cross-over frequency is at a frequency with large phase margin. The sensor dynamics are four times larger than the valve dynamics and hence do not have large influence on the bode diagram. If plotted without sensor dynamics the bodeplot lies almost identically on the curve of the open loop that includes sensor dynamics. Therefore it is not plotted for better readability. However, it is evident how the sampling time of the discrete system reduces the phase margin to  $31.8^\circ$  compared to  $46^\circ$  of the continuous system.

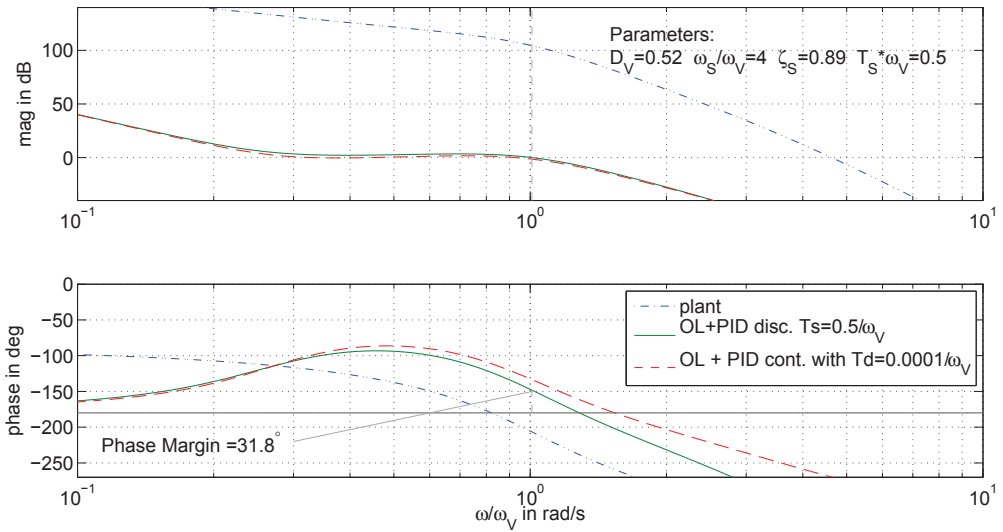


**Figure 5: Influence of added phase lag from sensor and control on stability margin**

The sensor dynamics  $\omega_s$  and the digital control sampling time  $T_s$  both add additional phase lag. This was neglected in the design of the feedback gain formulas [2, 7]. The negative influence becomes significant if the ratio between the natural frequency of the sensor and the valve  $\omega_s/\omega_v$  is not high enough or sampling time  $T_s$  is close to system time constant  $\frac{1}{\omega_v}$ . The impact of decreased phase margin on the system behavior is exemplary shown in **Figure 6**. The noise step responses for varying sampling time show to which degree noise can be damped in the system. If oscillation can be seen in the noise step response it can be expected that the realized pressure control causes rattling or may become unstable. The simulation clearly shows how increasing of the sampling time leads to low damped system behavior. In the next section the influence of sensor dynamics and sampling time is illustrated for a wide range of possible values. Based on this data a recommendation can be made on pairing valve, sensor and sampling time for good system behavior.

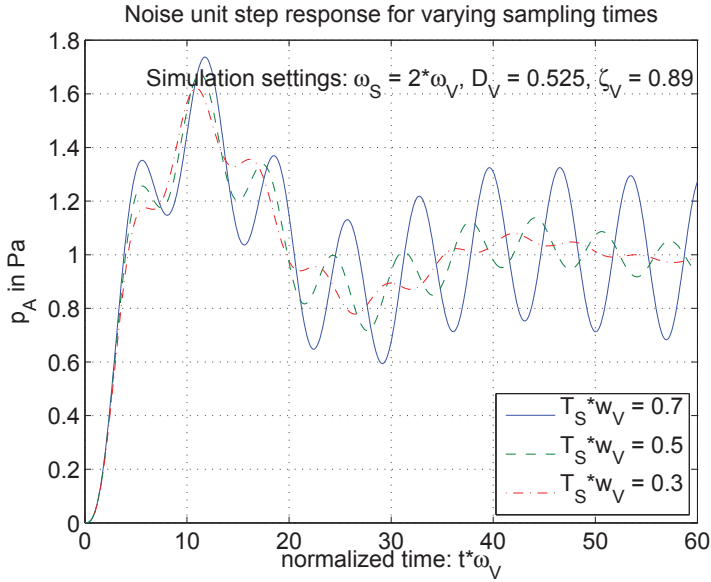


Figure 6: Noise step responses for different sampling times

## 5 PAIRING OF VALVE NATURAL FREQUENCY WITH SAMPLING TIME AND SENSOR DYNAMICS

This paper assumes that the tuning rules as published in [7] are used to parameterize PID pressure control hardware. They provide a good and robust first guess set of parameters and allow single parameter tuning. The tuning rules are model-based and make the assumption that the valve transfer function has a dominant pair of complex conjugate poles. This assumption becomes invalid if the sensor dynamics are not significantly higher than the valve dynamics. But also, if discrete control is used, the sampling time should be small enough. As shown in the previous section, a coarse sampling decreases the phase margin and leads to a low damped or unstable closed loop.

This section gives quantitative results how to pair sensor and valve dynamics with sampling time. As an example, we assume that the high response valve is used for the pressure control with data according to Figure 3, with  $D_v = 0.525$  and  $\omega_v = 93.6 \frac{\text{rad}}{\text{s}}$ . Then the question is, which sampling time should be used and which natural frequency the sensor should have. **Figure 7** shows a three dimensional diagram of the phase margin as a function of pairing this valve with a range of possible sampling times and natural frequencies of sensors, assuming that the sensor damping ratio would be characterized by  $\zeta_s = 0.8$ . We can read from the diagram that, assuming we had a natural frequency of the sensor around  $500 \text{ Hz} = 3141 \frac{\text{rad}}{\text{s}}$ , we would need a sampling time of at less than  $\frac{0.464}{\omega_v} = 0.79 \text{ ms}$  to guarantee a phase margin

of  $40^\circ$ .

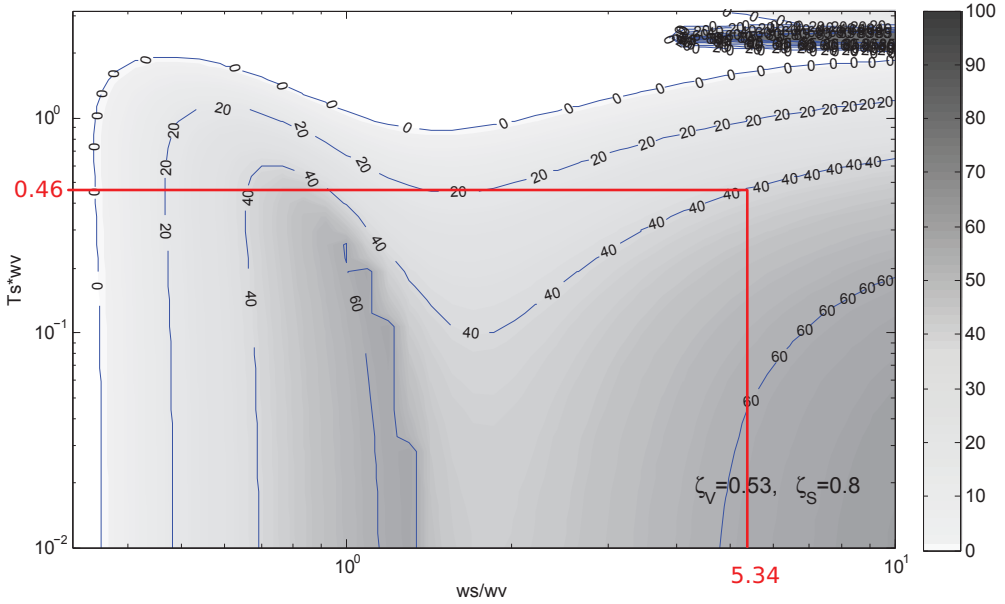


**Figure 7: Phase margin for pressure control using high response valve as a function of normalized sampling time  $T_S \omega_V$  and normalized sensor natural frequency  $\frac{\omega_S}{\omega_V}$**

This result is generalized in **Figure 8** which shows nine phase margin plots for various selected valve- and sensor damping ratios. The sets of damping ratios of valve and sensor are:

$$D_V = [0.53, 0.89, 1.5]; \quad \zeta_S = [0.53, 0.89, 1.5] \quad (18)$$

For each plot the normalized sampling time  $T_S \omega_V$  and sensor natural frequency  $\frac{\omega_S}{\omega_V}$  are varied between:

$$0.001 \leq T_S \omega_V \leq 3.16 \quad (19)$$

$$0.316 \leq \frac{\omega_S}{\omega_V} \leq 10 \quad (20)$$

The results reveal that pressure controls with valves that have a damping ratio of  $D_V \leq 0.89$  tolerate much larger sampling times and slower sensor dynamics than valves with damping ratio as low as 0.53 as depicted in Figure 3. For such low valve damping the tuning rules proposed in [7] require sampling times of  $T_S \leq \frac{0.5}{\omega_V}$  and sensor dynamics of  $\omega_S \geq 3\omega_V$  to have a safe phase margin guaranteed above  $\phi_m \geq 40$ . This means that the high response valve with the data shown in Figure 3 should be paired with a sensor that has a natural frequency of  $\omega_S \geq 3 \cdot 93.6 \cdot 2\pi \frac{\text{rad}}{\text{s}} = 280.8 \cdot 2\pi \frac{\text{rad}}{\text{s}}$ . Accordingly, the control should have a sampling time of  $T_S \leq 5 \text{ ms}$ .

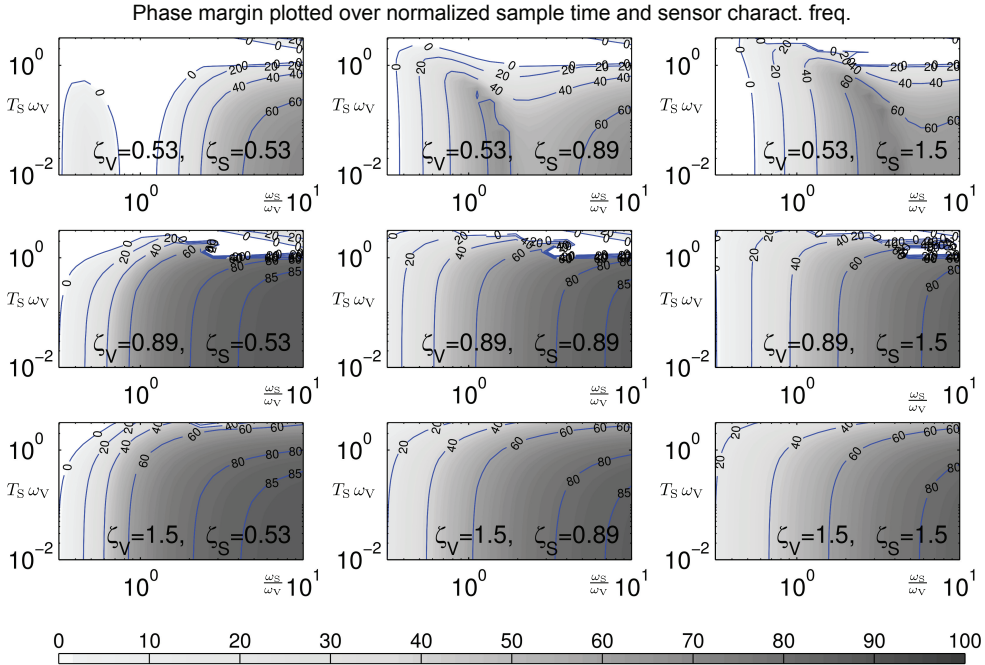


**Figure 8: Phase margin plots for different pairs of damping ratios of valve and sensor. Each plot shows phase margin over normalized sampling time and sensor characteristic frequency**

## 6 CONCLUSION

This paper presents analysis of the influence of sensor dynamics and frequency of discrete sampling on the effectiveness of PID tuning rules for standard hydraulic pressure control. The phase margin of the hybrid continuous/discrete open loop is plotted against varying sensor natural frequency and control sampling time in Figure 8 to help choose the right sensor, sampling time, and valve. Assuming that the phase margin should be at least  $40^\circ$  this normalized plot is a quick reference for the commissioning engineer whether the tuning rules are applicable or not. The results show that the robustness of the PID tuning rules is good if valves with damping ratios larger than 0.7 are used.

The phase margin plots of Figure 8 are theoretical results. The approximation of the dynamic behavior of the valve and sensor as a second order element is widely accepted. It is assumed that the natural frequency and damping ratio of valve and sensor are known. If natural frequency and damping ratio are not read or estimated correctly from the data sheet, the phase margin for the closed loop cannot be accurately predicted with the plots in Figure 8. However, choosing a minimum phase margin of  $40^\circ$  should provide a sufficient degree of robustness against parameter uncertainties.

## 7 ACKNOWLEDGEMENTS

The author expresses thanks to the University Research Board of the American University of Beirut for funding this research.

## REFERENCES

- [1] Ufuk Bakirdogen and Matthias Liermann. Simulation study on pressure control using nonlinear input/output linearization method and classical pid approach. In A. R. Plummer D. N. Johnston, editor, *FPMC 2010 Bath/ASME Symposium on Fluid Power and Motion Control, September 15-17 2010, Bath, UK*, pages 323–338. Hadleys Ltd, 2010.
- [2] Christoph Boes, Walter Lenz, and Jürgen Müller. Digital servo valves with fieldbus interface in closed loop applications. In *8th Scandinavian International Conference on Fluid Power 2003*, pages 845–856, Tampere, 2003.
- [3] Ingbert Forster. *Elektrohydraulische Lastsimulation [Electro-hydraulic load simulator]*. PhD thesis, RWTH Aachen University, 1988.
- [4] Gene F. Franklin, J. David Powell, and Abbas Emami-Naeini. *Feedback control of dynamic systems*. Pearson Ed, 2010.
- [5] A. Gambier. Real-time control systems: A tutorial. In *2004 5th Asian Control Conference*, 2004.
- [6] Jaroslav Ivantysyn and Monika Ivantysynova. *Hydrostatic pumps and motors*. Akademia Books International, 2001.
- [7] Matthias Liermann. Pid tuning rule for pressure control applications. *International Journal of Fluid Power*, to be published in November, 2012.
- [8] Jan Lunze. *Regelungstechnik 2*. Springer, 2010.
- [9] Hubertus Murrenhoff. *Servohydraulik - geregelte hydraulische Antriebe [Servo-hydraulics - closed loop controlled hydraulic drives]*. Shaker, Aachen, 2008.
- [10] Katsuhiko Ogata. *Modern Control Engineering*. Pearson Education, 2010.
- [11] Kang G Shin and Xianzhong Cui. Effects of computing time delay on real-time control systems. In *American Control Conference*, 1988, pages 1071 –1076, 1988.
- [12] Friedhelm Zehner. *Vorgesteuerte Druckventile mit direkter hydraulisch - mechanischer und elektrischer Druckmessung [Pilot operated pressure valves with direct hydro-mechanic and electric pressure sensing]*. PhD thesis, RWTH Aachen University, 1987.





# Overshoot and steady-state error of hydraulic press driven by DCV-positioned pump-controlled asymmetric cylinder

Jianfeng Tao<sup>1\*</sup>, Haiyan Yang<sup>1</sup>, Guofang Gong<sup>2</sup>, Chengliang Liu<sup>1</sup>

1.School of Mechanical Engineering, Shanghai Jiao-tong University, Shanghai 200240, China

2.State Key Laboratory of Fluid Power Transmission and Control, Zhejiang University, Hangzhou 310027, China

## ABSTRACT

Pump-controlled asymmetric cylinder systems positioned by directional control valves (DCV) are becoming more widely used on hydraulic press applications. However, there is a lack of appropriate theoretical methods for analyzing a system's important positioning indices: the overshoot and the steady-state error. In this paper, a hydraulic press circuit configuration and operating principle of pump-controlled asymmetric system are introduced. Using flow continuity and force balance equations, the system dynamic behavior is described. The overshoot and steady-state error are analyzed and the approximate calculation methods are proposed. The results of the theoretical analysis indicate that when the system parameters are fixed, the maximum overshoot is primarily determined by the cylinder's approach speed, and the steady-state error is proportional to the cylinder's unbalanced force at the moment when the DCV is closed. These results have been verified by simulation and experiment.

**Keywords:** pump-controlled asymmetric cylinder, hydraulic press, directional control valve, overshoot, steady-state error, position control

## 1 INTRODUCTION

Because of their excellent energy-saving characteristics, pump-controlled hydraulic systems have been actively researched for many years and an early systematic analysis can be found in H.E. Merritt's famous textbook<sup>[1]</sup>. With the development of the technology of electrically-controlled proportional pumps<sup>[2-5]</sup>, pump-controlled hydraulic systems are used

---

\*Corresponding author.

Inst. Of Mechatronics Control and Logistics Equipment, School of Mechanical Engineering, Shanghai Jiaotong University,

No.800 Dongchuan Road, Shanghai 200240, P.R. China

Tel. & Fax.:+862134206053. Email: jftao@sjtu.edu.cn.

in many applications, including aircraft <sup>[6, 7]</sup>, mobile machines <sup>[8-11]</sup>, and construction equipment <sup>[12, 13]</sup>. Another promising area for such systems is hydraulic press applications <sup>[14-17]</sup>.

In the literature [1-16], most of the emphasis is on closed-circuit pump-controlled asymmetric cylinder systems (CCPCAC systems), which are not only energy-saving but also space-saving. Usually, CCPCAC systems use bidirectional pumps and have complex circuit configurations to balance the unequal flow rates entering and leaving the cylinder volumes, and to achieve a dynamic performance comparable to a valve-controlled cylinder. For position control, such systems are controlled by a feedback control algorithm. These characteristics increase the cost of CCPCAC systems. In [17], an open-circuit pump-controlled asymmetric cylinder (OCPCAC) system with a unidirectional pump and a proportional valve is presented for a velocity control and clamping force control system on an injection molding machine. It is clear that such a system can also be used to fulfill the positioning function with a closed-loop position control algorithm, but the problem is that an expensive proportional valve is needed. In [18, 19], two extremely similar OCPCAC systems, which are driven by an electrically-controlled proportional unidirectional pump and positioned by a directional control valve, are recommended. These systems operate in the following way: the pump controls the actuator speed when approaching the desired position, and the position sensor, such as a magnetic or photoelectric switch, monitors the system's position; when the system reaches the desired position, the directional control valve blocks the cylinder's working chambers and stops the motion of the cylinder. The system is very simple and cheap, and has excellent energy-saving characteristics. However, there is a lack of theory to guide the system design, and it can take engineers a long time, using trial-and-error techniques to obtain satisfactory results for position overshoot and steady-state error.

In this paper, we model the OCPCAC system is using traditional hydraulic modeling methods and focus on the analysis of the system's overshoot and steady-state positioning error. In Section 2, the OCPCAC system and working principle are described in detail. In Section 3, the system is modeled using the flow continuity and force balance equations and, the system overshoot and steady-state error are analyzed, and the limitation of the overshoot and steady-state error is deduced, in Section 4. In Section 5, the model and the analysis are validated by comparison between the results obtained from simulation and experiment. The conclusions are presented in Section 6.

## 2 SYSTEM DESCRIPTION

A simplified structure of an OCPCAC system positioned by a directional control valve, which is applied to a hydraulic press application, is depicted in Fig.1. The system consists of a variable speed electrically-controlled unidirectional pump (1), directional control valves (DCV, 2,6), an asymmetric cylinder (3), a pre-fill valve (4), a pre-fill tank (5), a proportional relief valve (PRV, 7), a safety valve (8), an oil tank (9), a displacement sensor (10) and a motion controller (11). The loads acting on the cylinder are gravity, the load mass, a spring force, and frictional damping.

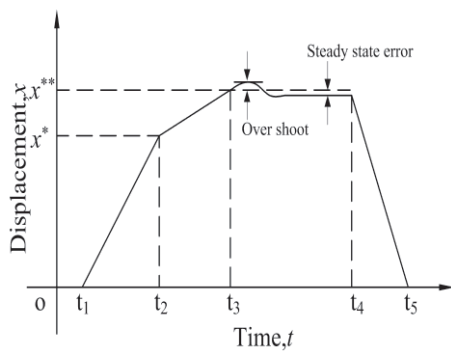
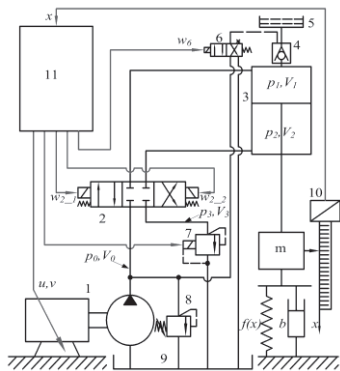


**Fig.1 Pump-controlled asymmetric cylinder Fig.2 Typical system displacement output**

To stop the cylinder, the motion controller sets the pump's flow and pressure commands to be zero, and sets DCV (2) to its central position. To move the cylinder down, the controller sets the pump flow and pressure commands to certain non-zero values, and positions valve (2) in the left position. In the case when rapid downward movement is required, the working pressure of PRV (7) is set to the minimum value, and DCV (6) is set to the right spool position, so that the cylinder can get enough compensated flow from the pre-fill tank through the pre-fill valve. The controller adjusts the commands to the pump and valves according to the signal from the displacement sensor. In the case of slow downward movement, the pump's flow command is reduced and the working pressure at valve (7) is set to a suitable value. When the cylinder reaches the desired position, DCV (2) returns to its central position, and the pump stops outputting flow, so that the cylinder stops at the right position within a specified accuracy band. To move the cylinder up, the controller sets DCV (2) to the right spool position, and at the same time, adjusts the pump's output flow and pressure commands. When the cylinder returns to its original position, the controller stops the pump, closes DCV (2), and prepares for the next cycle. To ensure the pre-fill tank has enough oil for the next cycle, DCV (6) is usually in its left position when the cylinder moves up, so that some of the return oil from the upper chamber flows to the pre-fill tank. Usually the working pressure of PRV (7) is set to zero to reduce the resistance when the cylinder's moving upward. A typical response for the system displacement is illustrated in Fig.2. Table.1 shows the typical operation of the electrical solenoids, pump input and PRV working pressure setting.

**Table.1 Typical solenoids operation, pump inputs and PRV working pressure setting**

System action (time interval)	Launching condition	Solenoids input			Pump inputs		Prop. relief valve, $p_{prv\_set}$
		$w_{2\_1}$	$w_{2\_2}$	$w_6$	$u$	$v$	
Preparing( $0-t_1$ )	$t \geq 0$	X	X	X	0	0	$8mg/A_2$
Quick moving down( $t_1-t_2$ )	$t \geq t_1$	O	X	X	$0.5 u_{max}$	$0.625 v_{max}$	0
Slow moving down( $t_2-t_3$ )	$x \geq x^*$	O	X	X	$0.25 u_{max}$	$0.625 v_{max}$	$8mg/A_2$
Position holding( $t_3-t_4$ )	$x \geq x^{**}$	X	X	X	0	0	$8mg/A_2$
Returning( $t_4-t_5$ )	$t-t_3 \geq T_{hold}$	X	O	O	$0.5 u_{max}$	$0.625 v_{max}$	0

Note: O-solenoid on,  $w_{2\_x}$  or  $w_6=24V$ ; X-solenoid off.  $w_{2\_x}$  or  $w_6=0V$ .

Essentially, the aforementioned positioning method is an open-loop control method. The displacement sensor in the system is used only for monitoring and launching the corresponding commands, such as the inputs to the electrical solenoids, the pump and the PRV. Therefore, the displacement sensor can be a cheap one, such as a magnetic or photoelectric switch. However, there is no feedback mechanism to regulate the system's overshoot and steady-state error, which are important performance characteristics of position control systems. Hence, a calculation model or approximate evaluation method for these two parameters is very important and helpful for system design.

### 3 SYSTEM MODELING

The system must be modeled to allow the position overshoot and steady-state error to be determined. To simplify the system model, we assume all pressures are uniform, no line losses or dynamics, negligible minor losses, constant fluid density and temperature, zero cylinder external and internal leakage, and laminar flow. Under these conditions, the system behavior is modeled when the cylinder is moving down and position holding (overshoot and steady-state error are irrelevant to the operation) as follows:

For a constant-pressure-variable-flow electrically-controlled proportional pump (variable-speed type), considering the dead zone, saturation, and leakage, the pump output flow can be determined as follows

$$q_o = \begin{cases} q_i - K_{c_p} \cdot p_0 & , p_o < p_i \\ q_i - K_{c_p} \cdot p_i - K_{p_p} \cdot (p_0 - p_i) & , p_o \geq p_i \end{cases} \quad (1)$$

and representing the pump's dynamics with first-order elements

$$\mathcal{L}(p_i) = \frac{p_{\max} \mathcal{L}(\text{sat}(u))}{u_{\max} (T_p s + 1)} \quad (2)$$

$$\mathcal{L}(q_i) = \frac{q_{\max} \mathcal{L}(\text{sat}(v))}{v_{\max} (T_q s + 1)} \quad (3)$$

$$\text{where } \text{sat}(u) = \begin{cases} u_{\min}, & u < u_{\min} \\ u, & u_{\min} \leq u \leq u_{\max} \\ u_{\max}, & u > u_{\max} \end{cases} \quad \text{and} \quad \text{sat}(v) = \begin{cases} v_{\min}, & v < v_{\min} \\ v, & v_{\min} \leq v \leq v_{\max} \\ v_{\max}, & v > v_{\max} \end{cases}.$$

For the volume between the pump and DCV (2), the flow continuity equation can be written as

$$q_o = \frac{V_0}{E_y} \dot{p}_0 + K_{ce} p_0 + q_{dcv1} \quad (4)$$

where  $q_{dcv1}$  is the flow leaving the volume through DCV (2), determined by

$$q_{dcv1} = x_{dcv} K_{q\_dcv} \sqrt{|p_0 - p_1|} \operatorname{sgn}(p_0 - p_1) \quad (5)$$

The spool motion dynamics associated with DCV(2) is represented by

$$\mathcal{L}(x_{dcv}) = \frac{K_{x\_dcv} \mathcal{L}(w_{2\_1})}{T_{sv}s + 1} \quad (6)$$

The flow continuity equations of the chamber between DCV (2) and the cylinder's upper chamber and that between DCV (2) and the cylinder's lower chamber can be expressed by

$$q_{dcv1} + q_{pfv} = \frac{V_1(x)}{E_y} \dot{p}_1 + A_1 \dot{x} \quad (7)$$

$$A_2 \dot{x} = \frac{V_2(x)}{E_y} \dot{p}_2 + q_{dcv2} \quad (8)$$

where the effects of the piston motion on the fluid volumes are given by  $V_1(x) = V_{10} + A_1 x$  and  $V_2(x) = V_{20} - A_2 x$  ;

The flow leaving DCV (2) and the pre-fill valve are given by

$$q_{dcv2} = x_{dcv} K_{q\_dcv} \sqrt{|p_2 - p_3|} \operatorname{sgn}(p_2 - p_3) \quad (9)$$

$$q_{pfv} = \begin{cases} 0 & , p_{pfv} < p_1 \\ K_{q\_pfv}(p_{pfv} - p_1) & , p_{pfv} \geq p_1 \end{cases} \quad (10)$$

The continuity equation for the volume between DCV (2) and the PRV is given by

$$q_{dcv2} = \frac{V_3}{E_y} \dot{p}_3 + q_{prv} \quad (11)$$

The flow passed by the PRV is governed by

$$q_{prv} = \begin{cases} 0 & , p_3 < p_{prv\_set} \\ K_{q\_prv}(p_3 - p_{prv\_set}) & , p_3 \geq p_{prv\_set} \end{cases} \quad (12)$$

Neglecting the friction force and considering nonlinear spring force  $f(x)$ , Newton's second law is used to obtain the cylinder's force balance equation as follows

$$p_1 \cdot A_1 - p_2 \cdot A_2 + mg = m\ddot{x} + b\dot{x} + f(x) \quad (13)$$

#### 4 OVERSHOOT AND STEADY-STATE ERROR

Since the system described by Eqs.(1)-(13) is nonlinear, it is difficult to obtain the exact solution of the overshoot and the steady-state error. Hence, an approximate calculation for the overshoot and steady-state error under specific assumptions, in order to provide some guidance for system design.

Here, the approaching speed  $\dot{x}_{app}$  is defined as the speed at which the cylinder first approaches the desired position. Referring to Fig.1, the overshoot and steady-state error are defined as  $\Delta x_{os}$  and  $\Delta x_{sse}$  respectively, and are defined as the follows:

$$\Delta x_{os} = \max_{t \in [t_3, t_4]} (x(t) - x^{**}) \quad (14)$$

$$\Delta x_{sse} = \lim_{t \rightarrow t_4} (x(t) - x^{**}) \quad (15)$$

To obtain the approximate formulation of overshoot defined by Eq.(14), we assume that the effect of the piston motion on the cylinder working chamber volumes, the dynamics of DCV (2), and the damping force can be neglected, that is,  $V_1(x) \approx V_{10} + A_1 x^{**}$ ,  $V_2(x) \approx V_{20} - A_2 x^{**}$ ,  $T_{sv} = 0$  and  $b = 0$ . Then, according to Eqs.(7), (8) and (13), we obtain

$$\frac{V_{10} + A_1 x^{**}}{E_y} \dot{p}_1 + A_1 \dot{x} = 0 \quad (16)$$

$$\frac{V_{20} - A_2 x^{**}}{E_y} \dot{p}_2 - A_2 \dot{x} = 0 \quad (17)$$

$$p_1 \cdot A_1 - p_2 \cdot A_2 + mg = m\ddot{x} + f(x) \quad (18)$$

Solving Eqs.(17) and (18), we get

$$p_1 = -\frac{E_y A_1}{V_{10} + A_1 x^{**}} \Delta x + p_1(t_3) \quad (19)$$

$$p_2 = \frac{E_y A_2}{V_{20} - A_2 x^{**}} \Delta x + p_2(t_3) \quad (20)$$

where  $p_1(t_3)$  and  $p_2(t_3)$  are respectively the pressure in the cylinder's upper and lower chambers at the moment when the DCV completely closes. Substituting Eqs.(19) and (20) into Eq.(18), and integrating Eq.(18) with respect to  $\Delta x$ , we obtain

$$\left( f'(x^{**}) + \frac{E_y A_1^2}{V_{10} + A_1 x^{**}} + \frac{E_y A_2^2}{V_{20} - A_2 x^{**}} \right) \Delta x^2 - 2(p_1(t_3)A_1 - p_2(t_3)A_2 + mg - f(x^{**}))\Delta x + m(\dot{x}^2 - \dot{x}_{app}^2) = 0 \quad (21)$$

where  $\Delta x = x - x^{**}$ , and  $f(x)$  is approximated by  $f(x^{**}) + f'(x^{**})\Delta x$ . For the actual system, we note that

$$p_1(t_3)A_1 - p_2(t_3)A_2 + mg - f(x^{**}) \leq 0 \quad (22)$$

Then, the positive extremum of the overshoot can be approximated by

$$(\Delta x_{os})^+ \approx \dot{x}_{app} \sqrt{\frac{m}{f'(x^{**}) + \frac{E_y A_1^2}{V_{10} + A_1 x^{**}} + \frac{E_y A_2^2}{V_{20} - A_2 x^{**}}}} \quad (23)$$

To calculate the overshoot using Eq.(23), the approach speed  $\dot{x}_{app}$  must be known. For a flow setting  $q_i$  corresponding to the flow command signal  $v$ , assuming that the external leakage,  $\dot{p}_0$  and  $\dot{p}_1$  can be neglected and noting that  $q_{pfv}$  is usually zero when the cylinder moves down slowly, we can obtain an approximate approaching speed calculation method from Eqs.(1)-(7), that is

$$\dot{x}_{app} \approx \frac{q_{\max} \cdot v}{A_1 \cdot v_{\max}} \quad (24)$$

Noting that  $\dot{x} = 0$  and  $\ddot{x} = 0$  when the system is stable, substituting these conditions and Eqs.(19) and (20) into Eq.(18), allows  $\Delta x$  to be determined as follows

$$\left( \frac{E_y A_1^2}{V_{10} + A_1 x^{**}} + \frac{E_y A_2^2}{V_{20} - A_2 x^{**}} + f'(x^{**}) \right) \Delta x = p_1(t_3)A_1 - p_2(t_3) \cdot A_2 + mg - f(x^{**}) \quad (25)$$

As the PRV coefficient  $K_{q_{prv}}$  is usually a large number. According to Eq.(12), it can be assumed that

$$p_2(t_3) \approx p_{prv\_set} \quad (26)$$

Applying Eq.(22) again, it can be deduced that the steady-state error is negative, and it achieves its negative extremum at  $p_1(t_3) = 0$ , that is,



$$(\Delta x_{sse})^- \approx \frac{-p_2(t_3) \cdot A_2 + mg - f(x^{**})}{\frac{E_y A_1^2}{V_{10} + A_1 x^{**}} + \frac{E_y A_2^2}{V_{20} - A_2 x^{**}} + f'(x^{**})} \quad (27)$$

Considering the dynamics of the DCV in Eq. (6),  $x^{**}$  in Eqs. (23) and (27) is replaced with  $x_a^{**}$ , that is,

$$x_a^{**} \approx x^{**} + T_{sv} \dot{x}_{app} \quad (28)$$

so that, the calculation accuracy is improved.

## 5 SIMULATION AND EXPERIMENT

**Table.2 Primary parameters**

Parameters	values	Parameters	values
$E_y$	$8.8 \times 10^8 \text{ Pa}$	$V_0$	$4 \times 10^{-4} \text{ m}^3$
$K_{c\_p}$	$2.66 \times 10^{-13} \text{ m}^3 \cdot \text{s}^{-1} \cdot \text{Pa}^{-1}$	$V_{10}$	$1 \times 10^{-5} \text{ m}^3$
$K_{p\_p}$	$5.28 \times 10^{-9} \text{ m}^3 \cdot \text{s}^{-1} \cdot \text{Pa}^{-1}$	$A_1$	$7.84 \times 10^{-2} \text{ m}^2$
$p_{\max}$	$20.6 \times 10^6 \text{ Pa}$	$V_{20}$	$7.6 \times 10^{-3} \text{ m}^3$
$q_{\max}$	$1.3 \times 10^{-3} \text{ m}^3 \cdot \text{s}^{-1}$	$A_2$	$1.88 \times 10^{-2} \text{ m}^2$
$u_{\max}$	$10 \text{ V}$	$V_3$	$4 \times 10^{-4} \text{ m}^3$
$u_{\min}$	$0.025 \text{ V}$	$k_{q\_dcv}$	$5.7 \times 10^{-7} \text{ m}^3 \cdot \text{s}^{-1} \cdot \text{Pa}^{-0.5}$
$v_{\max}$	$10 \text{ V}$	$T_{sv}$	$0.065 \text{ s}$
$v_{\min}$	$0.025 \text{ V}$	$m$	$530 \text{ Kg}$
$T_p$	$0.05 \text{ s}$	$b$	$200 \text{ N} \cdot \text{s} \cdot \text{m}^{-1}$
$K_{ce}$	$1.01 \times 10^{-11} \text{ m}^3 \cdot \text{s}^{-1} \cdot \text{Pa}^{-1}$	$k_{q\_prv}$	$8.24 \times 10^{-7} \text{ m}^3 \cdot \text{s}^{-1} \cdot \text{Pa}^{-1}$
$K_{q\_pfv}$	$1.48 \times 10^{-5} \text{ m}^3 \cdot \text{s}^{-1} \cdot \text{Pa}^{-1}$		

To verify the model, simulation and experiment testing have been undertaken. Fig.3 shows the press used in the experiment, which is driven by a Daikin's Super Unit pump (SUT00-8021). The valves are controlled by PLC from Mitsubishi Company, and the pump is controlled by an industrial computer from Advantech Company. System displacement and pressures are also sampled by Advantech's data acquisition cards in the industrial computer. The primary parameters used in the simulation model are listed in Table.2. To simplify the experiment and simulation, the nonlinear spring force term,  $f(x)$  was zero.

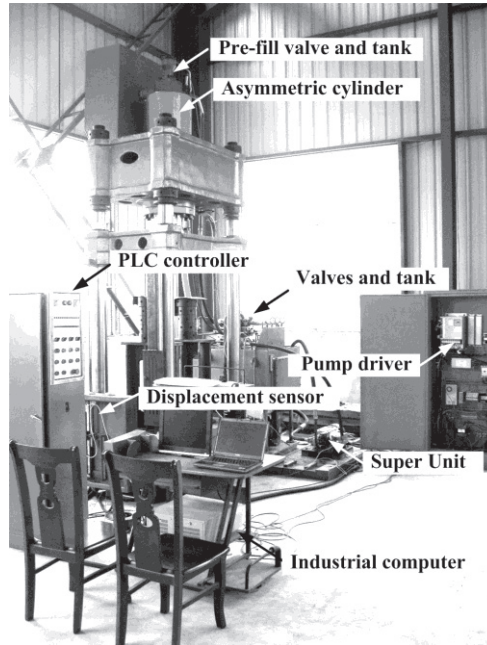


Fig.3 Hydraulic press for experiment

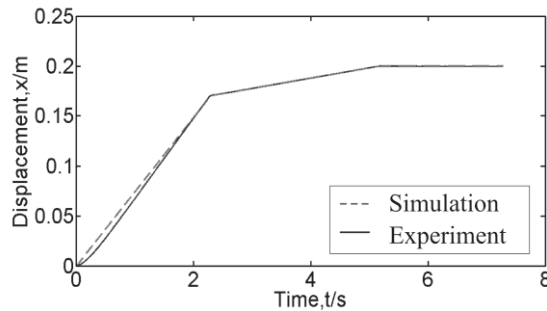


Fig.4 Simulated and experimental result

Fig.4 shows the simulated and experimental displacements obtained using the inputs listed in Table.1, and  $x^*=0.17\text{m}$  and  $x^{**}=0.1993\text{m}$ . As shown in Fig.4, for the system operation of slow when the actuator is moving down slowly with position holding, the simulated displacement is in close agreement with the experimental displacement. The difference between the traces at the beginning of the operation occurs when the actuator is moving quickly downwards, which may due to the pump's unmodeled dynamics. Since the overshoot and steady-state error are performance characteristics the operation when the actuator is slowly moving downwards and position holding, the comparison in Fig.4 illustrates that the model is valid for the analysis of the overshoot and steady-state error.

To check the analysis of the overshoot and steady-state error in Section 4, the experimental overshoot and steady-state error from 5.1 seconds shown in Fig.5. As can be seen from Fig.5, the maximum overshoot is  $4.2 \times 10^{-6}\text{m}$  and the steady-state error is  $1.2 \times 10^{-4}\text{m}$ .

From Eqs. (25), (27) and (28), the calculated value of the overshoot is  $1.18 \times 10^{-5} \text{ m}$  and that of the steady-state error is  $3.75 \times 10^{-4} \text{ m}$ . The calculated results are larger than those of the experiment, but the magnitudes are considered to be sufficiently close. The errors between the calculated and the experimental values are mainly caused by the assumptions of zero damping and the DCV closing in the force-balanced situation. However, as a design guide, the results obtained from Eqs. (25) and (27) are conservative and of sufficient accuracy. In fact, as shown in Fig.5, at the point where the DCV completely closes ( $t=5.222\text{s}$ ), the acceleration is  $-3.845 \times 10^{-3} \text{ m/s}^2$ . Hence, the assumption made in Eq. (25) that the unbalanced force is non-negative is reasonable.

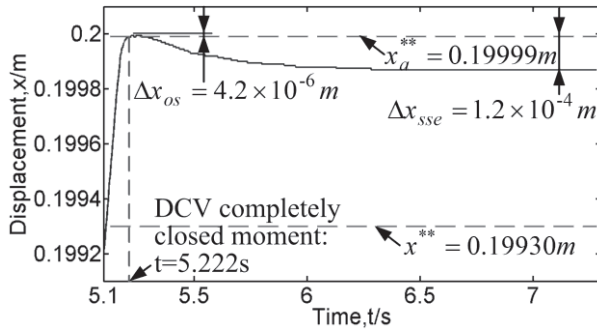


Fig.5 Overshoot & steady-state error

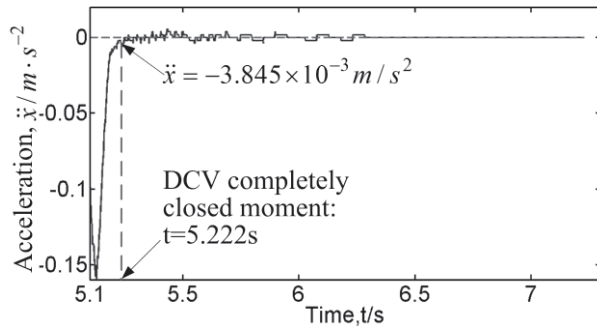


Fig.6 Acceleration at DCV closing moment

## 6 CONCLUSIONS

In this paper, a pump-controlled asymmetric cylinder system positioned by directional control valves, used more and more on industrial machines for its excellent energy-saving performance, is presented. A mathematical model is described that allows the overshoot and steady-state error to be predicted for a hydraulic press application. The results of theoretical analysis show that the overshoot is proportional to the cylinder approach speed and the steady-state error is proportional to the unbalanced force acting on the cylinder at the moment when the DCV completely closes. Based on the mathematic model, calculation

methods for the limitations of the overshoot and steady-state error are deduced. Experimental results verify that the proposed model and the calculation method are valid.

## NOMENCLATURE

$E_y$	Effective bulk modulus of system( Pa )
$q_o$	Pump's output flow( $\text{m}^3 \cdot \text{s}^{-1}$ )
$p_o$	Pump's output pressure( Pa )
$K_{c\_p}$	Pump's flow coefficient at constant flow operation( $\text{m}^3 \cdot \text{s}^{-1} \cdot \text{Pa}^{-1}$ )
$K_{p\_p}$	Pump's flow coefficient at constant pressure operation( $\text{m}^3 \cdot \text{s}^{-1} \cdot \text{Pa}^{-1}$ )
$p_{\max}$	Pump's maximum controllable output pressure( Pa )
$p_i$	Pump's setting pressure( Pa )
$p_1$	Pressure in cylinder's upper chamber( Pa )
$p_2$	Pressure in cylinder's lower chamber( Pa )
$p_3$	Pressure in the chamber between DCV(2) and PRV( Pa )
$T_p$	Settling time of pump's setting pressure( s )
$q_{\max}$	Pump's maximum controllable output flow( $\text{m}^3 \cdot \text{s}^{-1}$ )
$q_i$	Pump's setting flow( $\text{m}^3 \cdot \text{s}^{-1}$ )
$T_q$	Settling time of pump's setting flow( s )
$u, u_{\max}, u_{\min}$	Pump's pressure command, and its upper and lower limitations( V )
$v, v_{\max}, v_{\min}$	Pump's flow command, and its upper and lower limitations( V )
$\text{sat}(\cdot)$	Saturation function
$V_0$	Volume between pump output port and directional control valve input port( $\text{m}^3$ )
$K_{ce}$	External leakage of the volume between pump output port and directional control valve input port( $\text{m}^3 \cdot \text{s}^{-1} \cdot \text{Pa}^{-1}$ )
$q_{dcv1}, q_{dcv2}$	Flows in and out of directional control valve( $\text{m}^3 \cdot \text{s}^{-1}$ )
$K_{q\_dcv}$	Flow coefficient of directional control valve ( $\text{m}^3 \cdot \text{s}^{-1} \cdot \text{Pa}^{-0.5}$ )
$x_{dcv}$	Displacement of directional control valve's spool( m )
$w_{2\_1}, w_{2\_2}, w_6$	Control input of directional control valves' solenoids( V )
$K_{x\_dcv}$	Displacement coefficient of directional control valve( $\text{V} \cdot \text{m}^{-1}$ )
$T_{sv}$	Settling time of directional control valve's displacement( s )
$q_{pfv}$	Output flow of pre-fill valve( $\text{m}^3 \cdot \text{s}^{-1}$ )

$p_{pfv}$	Pressure at input port of PFV( Pa )
$K_{q\_pfv}$	Flow coefficient of pre-fill valve ( $\text{m}^3 \cdot \text{s}^{-1} \cdot \text{Pa}^{-1}$ )
$V_1, V_{10}$	Volume and initial volume of cylinder's upper chamber( $\text{m}^3$ )
$A_1$	Cross-sectional area of the piston end without rod( $\text{m}^2$ )
$V_2, V_{20}$	Volume and initial volume of cylinder's lower chamber( $\text{m}^3$ )
$A_2$	Cross-sectional area of the piston end with rod( $\text{m}^2$ )
$V_3$	Volume between directional control valve and proportional relief valve( $\text{m}^3$ )
$\text{sgn}(\cdot)$	Sign function
$q_{prv}$	Output flow of proportional relief valve( $\text{m}^3 \cdot \text{s}^{-1}$ )
$p_{prv\_set}$	Proportional relief valve's setting pressure( Pa )
$K_{q\_prv}$	Flow coefficient of proportional relief valve( $\text{m}^3 \cdot \text{s}^{-1} \cdot \text{Pa}^{-1}$ )
$x$	Cylinder displacement( m )
$x^*$	Switching position from quick moving down to slow moving down( m )
$x^{**}$	Switching position from slow moving down to position holding( m )
$x_a^{**}$	Actual position at directional control valve completely closing moment( m )
$\Delta x$	Displacement variation respect to $x^{**}$ ( m )
$\Delta x_{os}, (\Delta x_{os})^+$	Overshoot and its positive extremum ( m )
$\Delta x_{sse}, (\Delta x_{sse})^-$	Steady-state error and its negative extremum( m )
$\dot{x}$	Cylinder velocity( $\text{m} \cdot \text{s}^{-1}$ )
$\dot{x}_{app}$	Cylinder approaching speed( $\text{m} \cdot \text{s}^{-1}$ )
$m$	Mass of cylinder rod and load( Kg )
$b$	Damping coefficient( $\text{N} \cdot \text{s} \cdot \text{m}^{-1}$ )
$f(x)$	Nonlinear spring force function(N)
$t_1, t_2, t_3, t_4, t_5$	Switching times of system( s )
$T_{hold}$	Position holding time( s )

## ACKNOWLEDGMENTS

This research is sponsored by the National Natural Science Foundation (No. 50805090, 50975172), Special Program of Technology Support System Construction for Shanghai Major Technique Equipments (No. ZX08070) and State Key Laboratory of Mechanical System and Vibration of Shanghai Jiaotong University (No. MSV-2010-05).

## REFERENCES

- [1] H.E. Merritt, Hydraulic Control Systems. Willey, New York, 1967, pp.152-157.
- [2] Parker Hannifin GmbH-Hydraulic Controls Division, Installation and setup manual Electro-hydraulic control for PV series- Variable displacement axial piston pump, <http://www.parker.com/literature/Literature%20Files/hydraulicpump/serv/PVI017-UK.pdf>.
- [3] S. Helduser, Electric - Hydrostatic drive - An innovative energy-saving power and motion control system, *Proceedings of the Institution of Mechanical Engineers, Part I: Journal of Systems and Control Engineering* 1999,213 (5), pp.427-437.
- [4] T. Neubert, J. Wolff, S. Helduser & H. Späth, Untersuchung elektrischer Antriebssysteme am Beispiel von Hydraulikpumpen, *Antriebstechnik* 2004, 43 1, pp.34-41.
- [5] ISO 17559-2003, Hydraulic Fluid Power - Electrically Controlled Hydraulic Pumps - Test Methods to Determine Performance Characteristics, 2003.
- [6] R. Navarro, "Performance of an Electro-Hydrostatic Actuator on the F-18 Systems Research Aircraft", Research report. NASA/TM-97-206224, October 1997.
- [7] D. Liviu, C. Jenica-Ileana, A. L. Mihai, N. T. Alexandru , Electro-hydrostatic Servo-actuators for Aircraft, In: *Proceedings of the 7th WSEAS international conference on System science and simulation in engineering, Venice, Italy, November 21-23, 2008*, pp.217-222.
- [8] M. Ivantysynova, Displacement Controlled Linear and Rotary Drives for Mobile Machines with Automatic Motion Control, SAE Technical PAPER Series (2000-01-2562), 2000.
- [9] J. I. Yoon, A. K. Kwan, D. Q. Truong, "A Study on An Energy Saving Electro-Hydraulic Excavator". In: *Proceeding of .ICROS-SICE Int. Joint Conference 2009, Fukuoka, Japan, Aug. 18-21, 2009*, pp.3825-3830.
- [10] J. Zimmerman, M. Ivantysynova, Effect of installed hydraulic corner power on the energy consumption and performance of multi-actuator displacement controlled mobile machines, In: *Proceedings of the ASME Dynamic Systems and Control Conference 2009, Hollywood, California, USA, Oct.12-14, 2009*, pp. 1783-1790.
- [11] J. Y. Alaydi, Mathematical Modeling for Pump Controlled System of Hydraulic Drive Unit of Single Bucket Excavator Digging Mechanism, *Jordan Journal of Mechanical and Industrial Engineering* 2008, 2 (3), pp.157-162.

- [12] B. Xia, P. Feng, H. Yang, Modeling and analysis on servo adjustment of bidirectional variable displacement pump in hydraulic drive system of the cutter head in a shield tunneling machine, *Applied Mechanics and Materials* 2011, 44-47, pp.1380-1386.
- [13] K. Sanada, A study on full-electric control system of hydro static transmission for construction machines, In: *SICE Annual Conference 2004, Sapporo, Japan, Aug. 4-6, 2004*: 561-565.
- [14] P. Buchner, Pump control systems in metal forming technology, *Olhydraulik und Pneumatik* 2003, 47 6, pp.404-408.
- [15] D. Lovrec, M. Kastrevc, S. Ulaga, Electro-hydraulic load sensing with a speed-controlled hydraulic supply system on forming-machines, *International Journal of Advanced Manufacturing Technology* 2009, 41, pp.1066–1075.
- [16] S.G. Wei1, S.D. Zhao, J.M. Zheng, Y. Zhang, Self-tuning dead-zone compensation fuzzy logic controller for a switched-reluctance-motor direct-drive hydraulic press, *Proceedings of the Institution of Mechanical Engineers, Part I: Journal of Systems and Control Engineering* 2009, 223, pp.647-659.
- [17] Chiang, M.H., Yang, F.L., Chen, Y.N. and Yeh, Y.P., Integrated Control of Clamping Force and Energy-Saving in Hydraulic Injection Moulding Machines Using Decoupling Fuzzy Sliding-Mode Control, *International Journal of Advanced Manufacturing Technology*, 2005, 27 (1-2), pp.53-62.
- [18] K. Takaku, H. Hiraide, K. Oba, Application of the “asr series” ac servo motor driven hydraulic pump to injection molding machines, In: *Proceedings of the 7th JFPS International Symposium on Fluid Power, Toyama, Japan, 2008*, pp.127-130.
- [19] T. Imamura, Y. Sawada, M. Ichikawa and H. Nakamura, Energy-saving hybrid hydraulic system comprising highly efficient ipm motor and inverter, for injection molding and manufacturing machine, In: *Proceedings of the 7th JFPS International Symposium on Fluid Power, Toyama , Japan, 2008*, pp.117-120.

# Pneumatics I





# A Pneumatic Position Servo Based on On/Off Valve Actuated Muscle Actuators in Opposing Pair Configuration

**Ville Jouppila, Asko Ellman**

Tampere University of Technology, Department of Mechanics and Design  
Korkeakoulunkatu 6, 33101 Tampere, Finland  
ville.jouppila@tut.fi, asko.ellman@tut.fi

## ABSTRACT

Pneumatic muscle actuator is a novel type of actuator which has even higher force to weight ratio than a cylinder. In addition, muscle actuator introduces a stick slip free operation giving an interesting option for positioning systems. However, due to highly nonlinear characteristics of the actuator and pneumatic system, obtaining a good control performance is a real challenge. Instead of using relatively expensive servo valve, a proposal for controlling pneumatic muscle actuators in an opposing pair configuration by four low-cost on/off valves with a PWM strategy is introduced. PWM-technique allows control laws derived for servo valves to be used with on/off valves. As the overall pneumatic system is highly nonlinear and not completely known, a sliding mode control (SMC) strategy is chosen for control law.

The system with on/off valves is formulated in a nonlinear SISO canonical control form for which the SMC control law can be designed. The same approach is used also for servo valve approach enabling a direct comparison of these approaches. The SMC control algorithms designed for this pneumatic position servo system and their performance is compared experimentally with sinusoidal tracking tasks. The robustness of the approaches is verified by varying loading conditions of the system.

**Keywords:** Pneumatic muscle actuator, pulse width modulation (PWM), on/off valve, servo-pneumatics, sliding mode control (SMC)

## 1 INTRODUCTION

Pneumatic systems have many properties that make them attractive for use in a variety of environments. High force-to-weight ratios, cleanliness, compactness, ease of maintenance, and the safety of pneumatic actuators offer desirable features for many industrial designs. In addition, a pneumatic McKibben muscle actuator provides an even higher force-to-weight ratio compared with other conventional designs, and is able to operate in a wide range of environments. However, there are a number of nonlinearities present in the system, which makes it rather difficult and complex to control accurately. Nonlinear characteristics of the muscle actuator, air compressibility, friction, and nonlinear airflow through the

valves are the main reason that pneumatic systems are commonly avoided for advanced applications. Literature demonstrates that a large number of control strategies have been proposed to handle the effects of nonlinearities present. These include the following: adaptive control strategies (1,2,3), nonlinear PID (4), neural networks (5), and fuzzy controllers (6,7). In (8,9) a sliding mode control (SMC) strategy was applied to a muscle actuator system, but only simulation results of the effectiveness of the strategy were presented. Other SMC approaches are presented in (10-12). In the most recent work (12) a SMC strategy was applied to control the muscle actuator system in an opposing pair configuration (similar system as used in this work as a reference to on/off valve approach) using a servo valve. Experimental results with sinusoidal tracking (with amplitude 7.5 mm and frequency 0.5 – 1.5 Hz) and payload mass 10.8 kg showed accuracies of  $\pm 0.5$  mm to  $\pm 1.2$  mm. In this work, SMC strategy was chosen for the control of the muscle actuator since the system studied was highly nonlinear and not well-defined. Previous SMC studies have demonstrated that it is an efficient and robust control strategy for pneumatic actuator applications. However, in these studies, a proportional or servo valve has been used to control the actuator. In this paper, the on/off valves are chosen for the control of the muscle actuator system in order to provide a low cost alternative to servo-pneumatic systems.

In recent years, effort has been made to develop inexpensive servo-pneumatic systems using on/off solenoid valves with pulse-width modulation (PWM). In a PWM-controlled system, the power to an actuator is delivered with discrete packets of energy via a valve that is either completely on or completely off. If the PWM frequency is significantly faster than the system dynamics (i.e. dynamics of the actuator and load), the system will respond in a manner similar to the continuous case. Unlike the continuous case, little to no power is dissipated in the process. Specifically, in the ideal on-state, no flow resistance is offered, and thus no power is dissipated as the flow orifice is fully opened. In the ideal off-state, no flow occurs (if flow to atmosphere is blocked), and thus no power is dissipated. A PWM-controlled system is therefore capable of delivering a significant amount of controlled power to an actuator while dissipating essentially none. Previous works have shown the potential of PWM-controlled pneumatics (13-18). In (19), a modified PWM valve pulsing algorithm was developed that enabled the use of multiple on/off solenoid valves instead of costly servo valves. The proposed algorithm (with a continuous state feedback controller) was successfully implemented, and demonstrated its effectiveness on pneumatic cylinder experiments. In (20), a nonlinear state-space averaged model and a sliding mode controller with PWM was introduced for the control of a single degree of freedom pneumatic positioning system with a cylinder. Sinusoidal tracking with amplitude of 20 mm and frequencies from 0.25 to 1 Hz reportedly had accuracies from  $\pm 1$  mm to  $\pm 3.5$  mm. In (21), a sliding mode controller without PWM for a double-acting cylinder using four low-cost solenoid valves was introduced. The sinusoidal tracking error for a stroke  $\pm 20$  mm at 0.5 Hz was less than  $\pm 2$  mm. In (22) three linearization approaches for PWM-driven servo-pneumatic systems with a cylinder and a single on/off valve were introduced. Improved performances were achieved by using simple linear controllers with velocity feedback instead of complex and costly nonlinear ones although no real comparison was introduced. Tracking accuracies for a sinusoidal input with amplitude 20 mm at 1 Hz and 2 Hz were less than  $\pm 0.5$  mm and  $\pm 1.5$  mm, respectively.

In this paper, a muscle actuator system with two Festo Fluidic Muscle (MAS10-300 mm) actuators mounted horizontally and coupled to a linear slide carrying a payload is studied

(Fig. 1). The system is controlled by 4 on/off valves where an individual valve is used for controlling the inflow and outflow of each muscle actuator. The valves are operated with a PWM-based signal by controlling the PWM duty ratio. For a comparison to on/off valve approach, a servo valve approach is also presented. The SMC controller is designed in the Matlab Simulink environment and is coded by a real-time windows target toolbox, where reference values are generated, data from the sensors (potentiometer, pressures) are read, and the controller output signal is calculated. The output signal is then distributed to an electronic amplifier that supplies the sufficient power to actuate the valves. Actuator pressures and the displacement of the actuator (potentiometer) are measured. The other kinematic states (velocity and acceleration) are obtained by differentiation of the position signal; which adds noise that the controller needs to overcome.

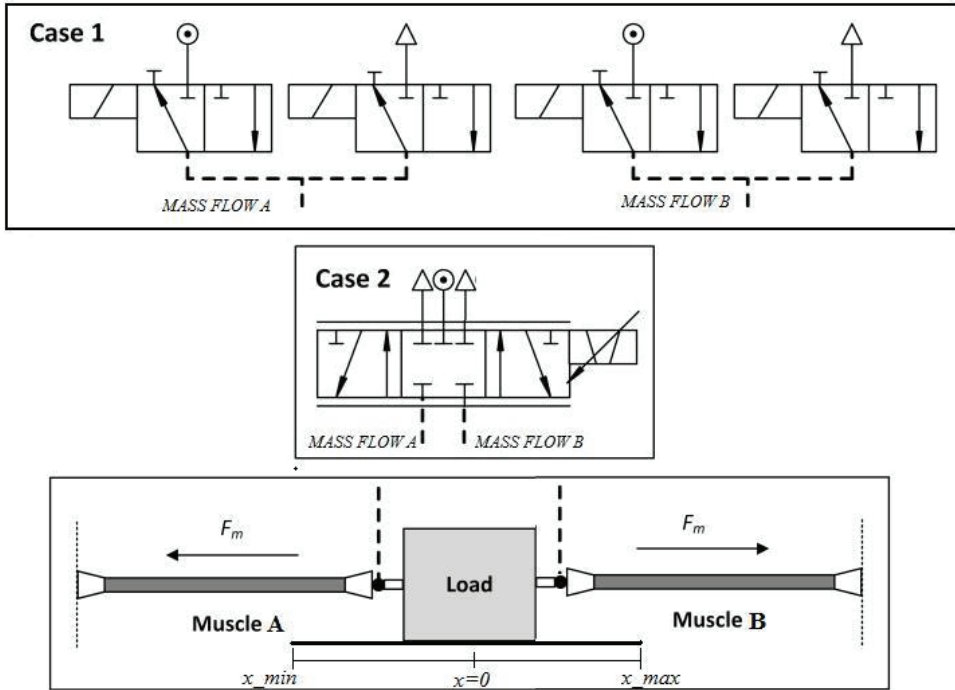


**Figure 1: A Muscle Actuator System Controlled by 4 On/Off Valves and Servo Valve**

## 2 MODELING OF THE PNEUMATIC SYSTEM

### 2.1 Load Dynamics

The load dynamics of the system can be written as

$$M\ddot{x} = F_B - F_A - B\dot{x} - F_{ext} \quad (1)$$

where  $M$  is the total payload,  $B$  is the viscous friction coefficient,  $F_A$  and  $F_B$  are the actuation forces of the muscle actuators and  $F_{ext}$  is the external force. Coulomb and static friction that are present in the real system are neglected in the control design and can be considered as modeling uncertainties and disturbances.

## 2.2 Muscle Actuator Force Dynamics

The pneumatic McKibben muscle actuator consists of a rubber tube with a non-extensible fiber surrounding. The physical configuration causes the muscle to have variable-stiffness spring-like characteristics and being very light-weight compared to other types of actuators (23, 24). During pressurization, the muscle widens in diameter and shortens in length, and the maximum force is obtained at the beginning of the contraction and decreases with increasing contraction. The generated force is unidirectional and its maximum contraction is typically 20% to 25% of the nominal length. The advantage of the muscle actuator over the traditional cylinder is the higher force to weight ratio and the stick-slip free motion at low velocities. On the other hand, the force-to-contraction relation at different pressure levels is highly nonlinear, and adds to the difficulty of effectively modelling the muscle actuator. As with all actuation systems, effective application of pneumatic muscle actuators relies on being able to accurately model and predict the forces that will be generated under any operating conditions. Figure 2 illustrates the nonlinear relationship between the force, pressure and displacement for the muscle actuators working in opposing pair configuration. Since the pneumatic muscle actuator is assumed to be non-stretchable, it is necessary, to initially contract both muscles of respectively  $x_{0A}=x_{0B}=x_0$ . Typically the initial contraction/displacement is determined as half the maximum stroke with an initial reference pressure  $p_{A0}=p_{B0}=p_0$ . In a typical configuration, the movement is produced by a pressure differential variation between the muscle actuator.

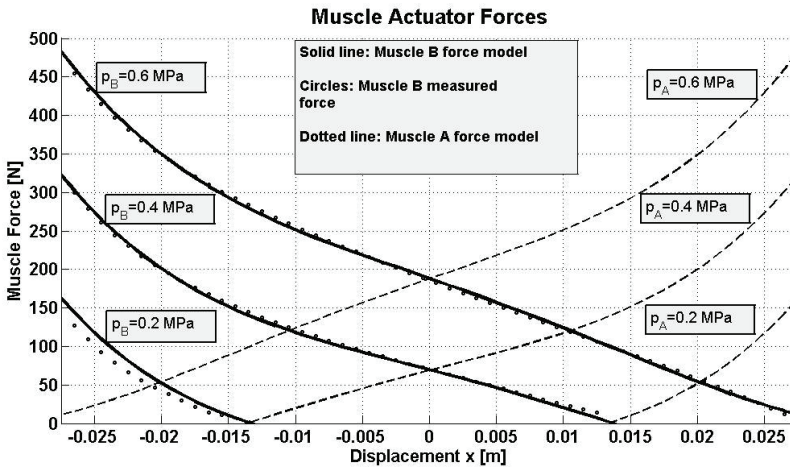


Figure 2: Nonlinear muscle actuator force characteristics

The nonlinear muscle forces can be described by equations

$$\begin{aligned}
F_A(x, p_A) &= a_0 + a_1(x_0 - x) + a_2(x_0 - x)^2 + a_3(x_0 - x)^3 + a_4(x_0 - x)^4 \\
&\quad - (p_{\max} - p_A) \left( \frac{k_0 - k_1(x_0 - x)}{k_2} \right) \\
F_B(x, p_B) &= a_0 + a_1(x_0 + x) + a_2(x_0 + x)^2 + a_3(x_0 + x)^3 + a_4(x_0 + x)^4 \\
&\quad - (p_{\max} - p_B) \left( \frac{k_0 - k_1(x_0 + x)}{k_2} \right)
\end{aligned} \tag{2}$$

where  $p_{\max}$  (=0.6 MPa) is the maximum muscle pressure, and  $a_{0-3}$ ,  $k_0$  [N],  $k_1$  [N/m] and  $k_2$  [Pa] are coefficients to match the model and measured data, respectively. The details of the actuator force modeling can be found in our previous work (25).

### 2.3 Pressure Dynamics

For calculating the pressure inside the actuators, it is assumed that the air is an ideal gas and the change of air is adiabatic, such that the pressure change is as follows:

$$\dot{p}_{A,B} = \frac{kRT}{V_{A,B}(x)} \dot{m}_{A,B} - \frac{kp_{A,B} \dot{V}_{A,B}}{V_{A,B}(x)} \tag{3}$$

where  $k$  (=1.4 for adiabatic process),  $R$ ,  $T$ ,  $V_{A,B}$  and  $\dot{m}_{A,B}$  denote the specific heat ratio, universal gas constant, air temperature, volume of the actuators and mass flow rate into the actuator. The volume of the muscle actuators can be described by a linear approximation (25)

$$V_A = V_0 - v_1 x, \quad V_B = V_0 + v_1 \tag{4}$$

### 2.4 Valve Mass Flow Dynamics

The on/off solenoid valve (Festo MHE2,  $Q_N=100$  l/min) is controlled with the duty ratio  $u_{duty}$  of the PWM-modulated signal. The switching frequency  $f_{PWM}$  and the duty ratio determine how long the valve is open and closed during time period  $T_{PWM}$  ( $=1/f_{PWM}$ ). PWM-technique allows control laws derived for servo valves to be used with on/off valves. It should be noted, that the PWM switching frequency has a significant effect on the system performance as the final control signal for the valve is updated at the PWM frequency used. In order to provide sufficient performance the PWM frequency should be significantly higher than the natural frequency of the system. On the other hand, the bandwidth (300 Hz) of the used valve sets the limit to the maximum reasonable PWM frequency. The PWM frequency used in this work is 100 Hz.

For a comparison to on/off valve approach, a servo valve (FESTO MPYE-5-M5-010-B,  $Q_N=100$  l/min) with the same nominal flow capacity is also used to control the system. The spool position of the servo valve is controlled by a control voltage signal (0-10 V) where the spool is in the center position with control signal 5 V. Due to high bandwidth (125 Hz) the spool dynamics can be ignored and the valve control signal can be calculated based on the desired spool position.

The mass flow rate through the control valve is one of the major nonlinearities in pneumatic systems. Thus, the modeling of valve flow characteristics plays an important role, when a sufficient performance of pneumatic servo systems is required. A traditional equation for modeling the mass flow is based on a flow of an ideal gas through a converging nozzle, and related to the valve control signal by the following relation:

$$\dot{m}(p_u, p_d) = U\Psi(p_u, p_d),$$

$$\Psi(p_u, p_d) = \begin{cases} Cp_{up} & \frac{p_{down}}{p_{up}} \leq b \\ Cp_{up} \sqrt{1 - \frac{\left(\frac{p_{down}}{p_{up}} - b\right)^2}{1 - b}}, & \frac{p_{down}}{p_{up}} \geq b \end{cases} \quad (5)$$

where  $p_u$  and  $p_d$  are the upstream and downstream pressures, respectively,  $C$  is the valve conductance, and  $b$  is the critical pressure ratio that divides the flow regimes into unchoked and choked flow through the orifice, and  $U$  is the control signal. The definition of valve control signal is defined here as a normalized control signal  $[-1 \dots 1]$ . In case of on/off valve approach, the control signal is directly the desired duty ratio  $U = u_{duty}$  and in case of servo valve  $U = G^{-1} * U_{servo}$ . Note that, a positive valve command will pressurize the muscle B and exhaust the muscle A, while a negative command corresponds to opposite. The resulting equations for mass flow rates are

$$\dot{m}_A = -U\Psi_A, \quad \Psi_A = \begin{cases} \Psi(p_A, p_{atm}), & \text{if } U \geq 0 \\ \Psi(p_s, p_A), & \text{if } U < 0 \end{cases}$$

$$\dot{m}_B = U\Psi_B, \quad \Psi_B = \begin{cases} \Psi(p_s, p_B), & \text{if } U \geq 0 \\ \Psi(p_B, p_{atm}), & \text{if } U < 0 \end{cases} \quad (6)$$

where  $p_s$  is the supply pressure ( $=0.65$  MPa (abs.)). Figure 3 shows a comparison of the estimated mass flow rate (Eq. (5)) and experimental data for servo valve while charging actuator B. The parameters of the equation (5) are obtained by searching the best fit for the experimental data. It can be seen that the model is capable of providing sufficient accuracy at higher control signals, while the modeling accuracy degrades at small control signals. Similar modeling approach is used also for negative control signals while discharging actuator B. Note, that the servo valve is assumed to be symmetric for mass flow rates A and B. Figure 3 illustrates also the measured mass flow rate as a function of control signal with constant pressure drop across the valve. Note the dead zone and linearity of the curves. Due to a valve dead zone, compensation is added to the final control signal of a servo valve as follows

$$U_{servo} = \begin{cases} U_0 - GU + u_{dz} \text{sign}(U), & \text{if } U \leq 0 \\ U_0 + GU + u_{dz} \text{sign}(U), & \text{if } U > 0 \end{cases} \quad (7)$$

where  $U_0=5\text{V}$  and  $u_{dz}=0.25\text{V}$  is experimentally determined dead zone range.

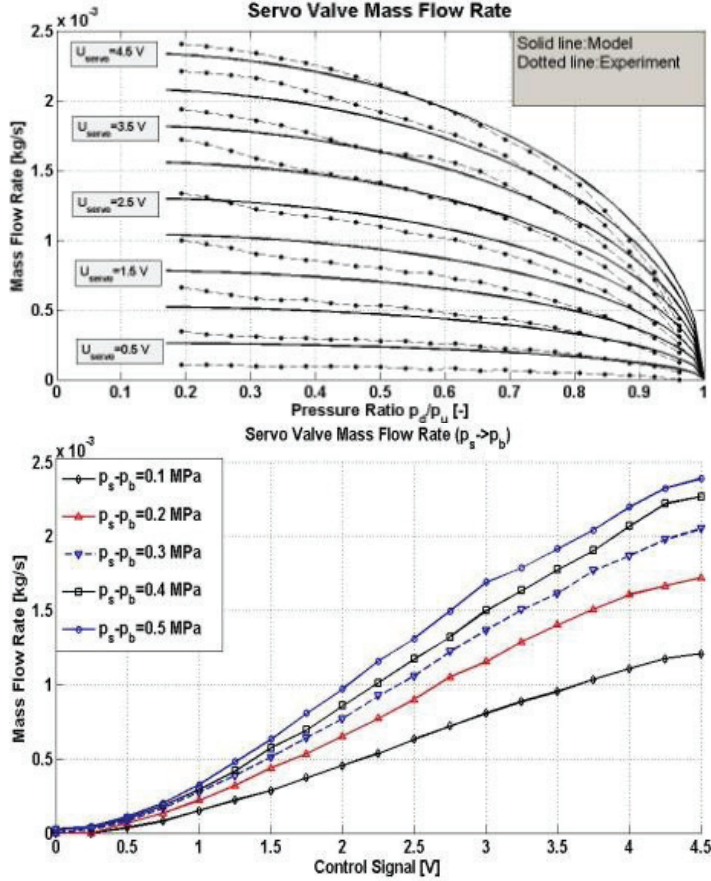


**Figure 3: Servo valve mass flow rate while charging actuator B**

Similar modeling approach can be utilized with a PWM controlled on/off valve where the control signal is PWM duty ratio (-1...1). Figure 4 illustrates that the traditional flow equation can reasonably well describe the nonlinear flow characteristics. Note also the linear region between control signals 0.1 and 0.9 and the valve dead zone with control values less than 0.05 and flow saturation with control values higher than 0.9. With a dead zone compensation ( $u_{dz}=0.05$ ) the respective valve control signals are



$$\begin{aligned}
 u_{dutyA\_in}, u_{dutyB\_out} &= \begin{cases} U + u_{dz}, & \text{if } U < 0 \\ 0 & \text{if } U \geq 0 \end{cases} \\
 u_{dutyA\_out}, u_{dutyB\_in} &= \begin{cases} U + u_{dz}, & \text{if } U > 0 \\ 0 & \text{if } U \leq 0 \end{cases}
 \end{aligned} \quad (8)$$

Note that this kind of modeling approach results in identical controller structure providing a possibility for a direct comparison of on/off and servo approaches.

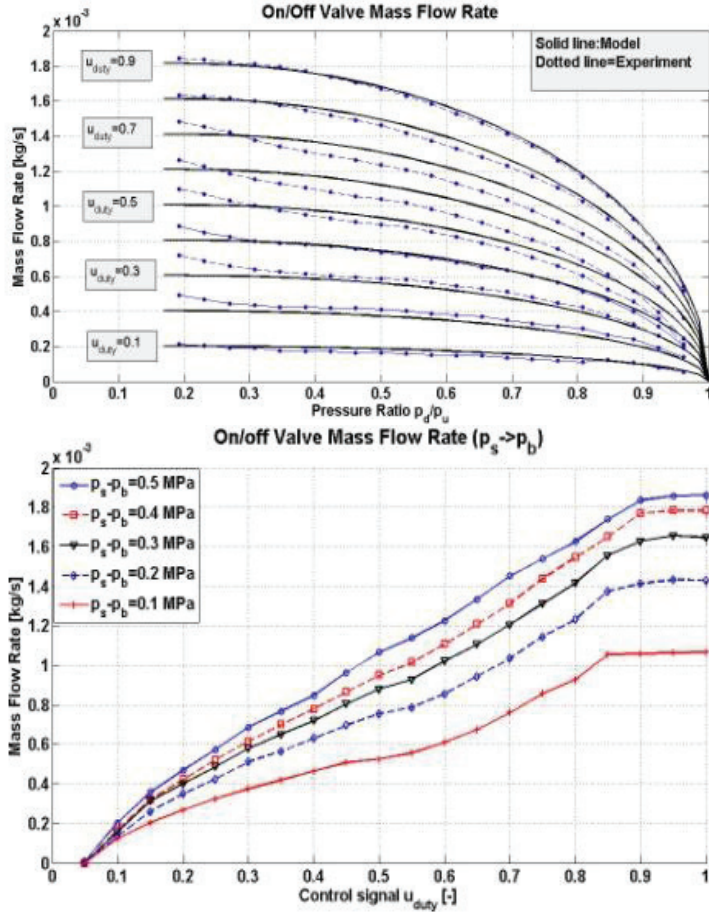


Figure 4: On/off valve mass flow rate while charging actuator B

## 2.5 Overall system model

The full nonlinear SISO model from the control input  $U$  to the displacement of the load  $x$  can be defined as

$$\ddot{x} = f(\mathbf{x}) + b(\mathbf{x})U \Rightarrow \ddot{x} = \frac{K}{M}\dot{x} - \frac{B}{M}\ddot{x} + \left( \frac{C_a\psi_a + C_b\psi_b}{M} \right)U \quad \text{where}$$

$$f(\mathbf{x}) = \frac{K}{M}\dot{x} - \frac{B}{M}\ddot{x}, \quad b(\mathbf{x}) = \frac{C_a\psi_a + C_b\psi_b}{M}$$

$$K = 2a_1 + 4a_2x_0 + 6a_3x_0^2 + 8a_4x_0^3 + 3x^2(2a_3 + 8a_4x_0)$$

$$- \frac{k_1}{k_2}(p_A + p_B - 2p_{\max}) - \left( \frac{k_0 - k_1(x_0 + x)}{k_2} \right) \frac{kv_1 p_B}{V_B(x)}$$

$$- \left( \frac{k_0 - k_1(x_0 - x)}{k_2} \right) \frac{kv_1 p_A}{V_A(x)}$$

$$C_a = - \left( \frac{k_0 - k_1(x_0 - x)}{k_2} \right) \frac{kRT}{V_A(x)}, \quad C_b = \left( \frac{k_0 - k_1(x_0 + x)}{k_2} \right) \frac{kRT}{V_B(x)}$$

The state vector  $\mathbf{x}$  consists of the pressure in each muscle actuator, along with the position, velocity and acceleration of the load

$$\mathbf{x} = [x \quad \dot{x} \quad \ddot{x} \quad p_A \quad p_B]^T \quad (10)$$

### 3 SLIDING MODE CONTROL (SMC) DESIGN

SMC is a form of variable structure control and regarded as one of the most effective nonlinear robust control approaches (26, 27). SMC utilizes a discontinuous switching plane along some desired trajectory. The plane is often referred to as a sliding surface  $S$  that models the desired closed loop performance in the state variable space. The objective is to keep the state values along this surface by minimizing the state errors (between the desired trajectory and the estimated or actual values). Then, the control law is designed so that the system state trajectories are forced towards the sliding surface and stay on it. The choice of the control law that satisfies the following sliding condition is:

$$S\dot{S} < 0 \quad (11)$$

which ensures the attractivity of the sliding surface in the state space. The switching brings inherent stability and robustness to the control strategy, while also introducing chattering (high-frequency switching) that is undesirable in practice and can excite un-modelled dynamics. A boundary layer may be introduced along the sliding surface in order to saturate and smooth out the chattering within a region referred as the smoothing boundary region.

The sliding surface for this configuration is selected as

$$S = (\ddot{x} - \ddot{x}_d) + 2\lambda\xi(\dot{x} - \dot{x}_d) + \lambda^2(x - x_d) = \ddot{e} + 2\lambda\xi\dot{e} + \lambda^2e \quad (12)$$

with  $\lambda > 0$  (control bandwidth) and  $\zeta$  damping ratio. A robust control law can be obtained by combining an equivalent control component  $u_{eq}$  with a robust switching component  $u_{sw}$  (27)

$$U = u_{eq} + u_{sw} \quad (13)$$

where the equivalent control component is used to achieve the desired motion on the sliding surface

$$\dot{S} = 0 \Rightarrow u_{eq} = \frac{\ddot{x}_d - \hat{f}(\mathbf{x}) - 2\lambda\zeta\dot{e} + \lambda^2 e}{\hat{b}(\mathbf{x})}, \quad (14)$$

$$\hat{b}(\mathbf{x}) = \sqrt{b_{\min}(x)b_{\max}(x)}, \quad \hat{f}(\mathbf{x}) = \frac{f_{\min}(\mathbf{x}) + f_{\max}(\mathbf{x})}{2}$$

where  $\hat{f}(\mathbf{x})$  and  $\hat{b}(\mathbf{x})$  are the nominal or estimate values of  $f(\mathbf{x})$  and  $b(\mathbf{x})$ , respectively. In order to satisfy the reaching condition Eq.(14), the switching control component that accommodates the model uncertainties and disturbances is defined as follows

$$u_{sw} = -\frac{K_{SMC}}{\hat{b}(\mathbf{x})} \text{sat}\left(\frac{S}{\Phi}\right)$$

$$K_{SMC} \geq \beta(F(\mathbf{x}) + \eta) + (\beta - 1) |\hat{b}(\mathbf{x}) \cdot u_{eq}|, \quad (15)$$

$$\beta = \sqrt{\frac{b_{\max}(x)}{b_{\min}(x)}}, \quad |f(\mathbf{x}) - \hat{f}(\mathbf{x})| \leq F(\mathbf{x}) = \alpha \hat{f}(\mathbf{x})$$

where  $\beta$  is the gain margin,  $F(\mathbf{x})$  is the estimation error on  $f(\mathbf{x})$ ,  $\alpha$  is the uncertainty factor, and  $\Phi$  is the boundary layer thickness.

## 4 RESULTS

Experiments were conducted to demonstrate the performance of the SMC strategy with aforementioned control strategies. For the implementation of the sliding mode control law, the system states including the pressure in the muscle actuators, the position, velocity, and acceleration of the load are required. The velocity was obtained by differentiating the measured position signal which was then filtered by 2<sup>nd</sup> order Butterworth low pass filter with cut-off frequency 65 Hz. The acceleration estimate was obtained by differentiating the velocity estimate and filtering it by similar low-pass filter with cut-off frequency 50 Hz. The cut-off frequencies for the filters were found with the help of simulations and finally tuned experimentally to provide optimal result. It should be noted, that in order to obtain acceleration estimate for the SMC controller, also a direct measurement of acceleration, estimation of acceleration using pressure measurement or using state estimation strategies such as extended Kalman filter for nonlinear systems, could also been used here.

The experiments were performed with sinusoidal tracking (amplitude 15 mm) for frequencies 0.25, 0.50, 0.75, 1.0, 1.5 and 2.0 Hz. Each experiment was repeated 5 times to gauge the repeatability of the closed-loop performance and root mean square error (RMSE) values were used as performance indicator.

Initial controller tuning was done with the help of simulations and final tuning was done with the experimental setup in order to guarantee a sufficient accuracy for sinusoidal tracking in normal conditions ( $M=2$  kg). Also, in the controller tuning a focus was to avoid significant chattering in the control signal. For the servo valve configuration, the control parameters were  $\lambda=85$  rad/s,  $\zeta=0.3$ ,  $K_{SMC}=3000$  and  $\Phi=50$ . Note that the damping ratio was set to a small value in order to minimize the amplification of noise in the estimated velocity and acceleration signals. In order to compare the valve approaches similar set of parameters were used with the on/off valve approach. However, the performance was also studied with higher gains by decreasing the boundary layer thickness resulting in a better tracking accuracy at the cost of increased control signal chattering with both valve configurations.

#### 4.1 Normal conditions

The mean RMSE values and maximum tracking errors for the control performance of the servo valve and 4 on/off valves configuration with SMC approach for sinusoidal tracking with nominal payload ( $M=2$  kg) are gathered in Table 1. It can be seen that on/off valve approach results in only 22 % poorer performance in total than the servo valve approach for the whole input frequency range. However, the majority of this difference becomes at higher input frequencies (1.5 and 2.0 Hz) as the servo valve is capable of providing more flow than on/off valves (see Figures 3 and 4). At lower input frequencies ( $< 1$  Hz) on/off valve approach is capable of providing surprisingly good performance as the performance is almost identical to servo valve approach. It is notable that servo valve approach provides better accuracy in terms of maximum tracking error in overall. The maximum error occurs mostly at times when the direction of movement is changed when the effect of muscle actuator hysteresis is the most significant. With servo valve approach the control loop is much faster (1 ms) than with on/off valve approach (10 ms) resulting in better response at motion reversals. Figures 5-7 illustrates the performance of the approaches for 0.25, 1.0 and 1.5 Hz sinusoidal tracking.

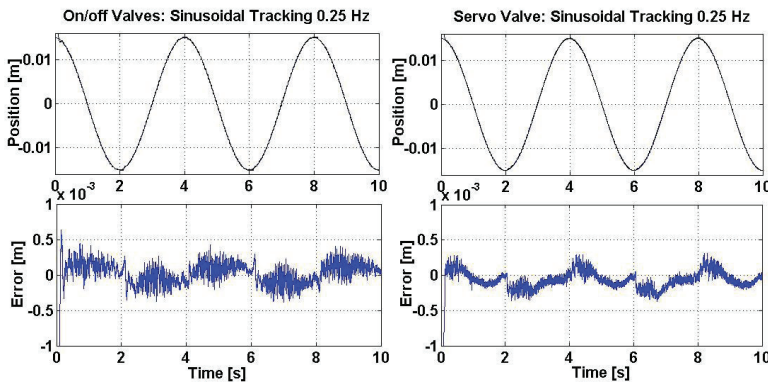
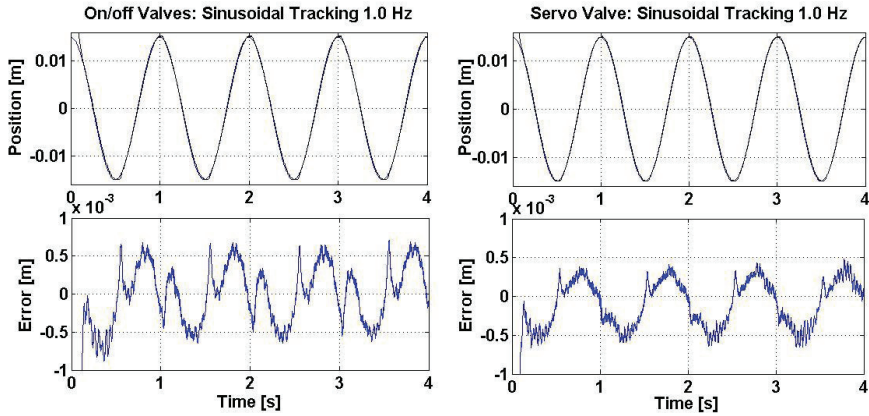


Figure 5: Sinusoidal tracking 0.25 Hz

Frequency of the sine trajectory	<i>On/Off Valves</i>	<i>Tracking error</i>	<i>Servo valve</i>	<i>Tracking error</i>
0.25 Hz	0.143 (-0 %)	-0.4...+0.4 mm	0.144	-0.35...+0.35 mm
0.5 Hz	0.195 (+0 %)	-0.5...+0.6 mm	0.195	-0.5...+0.3 mm
0.75 Hz	0.220 (-8%)	-0.5...+0.6 mm	0.240	-0.6...+0.3 mm
1.0 Hz	0.348 (+7 %)	-0.6...+0.7 mm	0.324	-0.6...+0.45 mm
1.5 Hz	0.725 (+45 %)	-1.1...+1.5 mm	0.500	-0.8...+0.7 mm
2.0 Hz	1.126 (+50 %)	-1.5...+2 mm	0.750	-1.15...+1.0 mm
Sum RMSE	2.757 (+22%)	-----	2.153	-----

**Table 1: Comparison of RMSE (mm) values and maximum tracking error of the valve configurations with nominal payload mass  $M=2$  kg and SMC approach.**



**Figure 6: Sinusoidal Tracking 1 Hz**

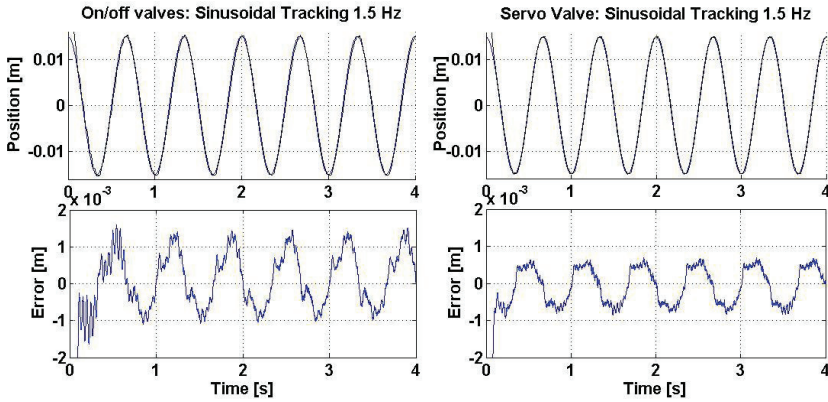


**Figure 7: Sinusoidal Tracking 1.5 Hz**

#### 4.2 Robustness to payload variation

Although there has been many studies on PWM servo-pneumatics most of them lack analysis of robustness to parameter variations in the process. In this paper, the robustness analysis in terms of increased payload mass is performed. Figure 8 illustrates the resulting control performance of the approaches as a function of increased payload. The sum of the mean RMSE values of control performances for sinusoidal tracking at 0.25, 0.5, 0.75 and 1.0 Hz is used as a robustness indicator. It is interesting to see, that servo valve approach is extremely robust to increased payload mass as the tracking performance is maintained up to  $M=6$  kg. In contrast, the on/off valve approach is capable of maintaining reasonable robustness up to  $M=4$  kg after which the performance starts to degrade more clearly. A significantly better robustness of servo valve approach is due its faster control loop combined with smaller noise in the system. As the SMC strategy is quite sensitive to delay and noise, it starts to affect the performance with PWM strategy that results in a 10 ms control delay and more noise due to PWM switching. In order to demonstrate the effect of control delay, the servo valve approach was used with a sampling time  $T_s=10$  ms that corresponds with the PWM 100 Hz. It can be seen, that the control delay degrades the control performance especially at higher payload masses decreasing the robustness of the controller. With on/off valve approach the effect of control delay and system noise has a more significant effect on the performance.

Another critical factor affecting the controller performances is the value of damping ratio used in the sliding surface design. A smaller damping ratio significantly decreases the magnitude of sensor noise (velocity, acceleration) and in the nominal case a higher value of damping ratio than 0.3 resulted in a poor performance due to magnified noise. It should be noted, that the damping ratio determines the damping properties of the control dynamics. Thus, a small value will provide fast response with low damping resulting in a poor performance with increased system inertia. A higher damping ratio will provide better damping properties with slower response resulting in better performance especially with increased inertia. For that reason, the controllers were not able to provide good results with payload masses much higher than  $M=6$  kg with a damping ratio 0.3.

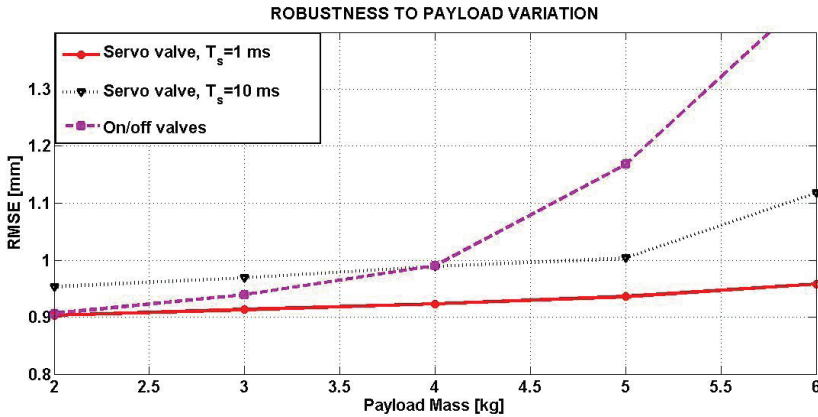


Figure 8: Robustness to Increased Payload

## 5 CONCLUSIONS

This paper provides a low-cost approach to control pneumatic systems by using high-speed on/off valves instead of costly proportional and servo valves. The mechatronic system under study consisted of pneumatic muscle actuators in the opposing pair configuration driven by four PWM operated on/off valves. In order to provide a comparison between on/off valve and servo valve approaches, a full nonlinear modelling of the system in SISO canonical control form was derived for which SMC strategy was applied. As the resulting controller structure was same for both valve configurations, a direct comparison between the approaches was possible. In nominal conditions, the on/off valve approach resulted in good results as the tracking accuracy was almost identical with the servo valve approach. In terms of maximum tracking error, the servo valve approach provided slightly better performance due to its faster control response at motion reversals when the muscle actuator hysteresis is the most significant. At higher tracking frequencies servo valve approach performed better mostly due to its higher flow capacity compared to on/off valve approach. The robustness of the approaches was tested by increasing the payload mass up to 6 kg. It was noted, that servo valve approach was extremely robust against it, but the performance of on/off valve approach started to degrade clearly at higher payloads. This difference between the approaches is caused by the combination of PWM switching introduced control delay and higher system noise that significantly affects the performance of SMC controlled PWM approaches. However, the results indicate that on/off valve approach can provide a reasonable performance and an interesting option for servo-pneumatic systems with limited uncertainties and parameter variations.

## References

- [1] Caldwell, D. G.; Medrano-Cerda, G. A.; & Goodwin, M. J. (1995). Control of Pneumatic Muscle Actuators. *IEEE Control Systems Magazine*, 15, No.1, pp. 40-48.



- [2] Lilly, J. (2003). Adaptive Tracking for Pneumatic Muscle Actuators in Bicep and Tricep Configurations. *IEEE Transaction of Neural Systems and Rehabilitation Engineering*, 11, No. 3, ss. 333-339.
- [3] Medrano-Cerda, G. A.; Bowler, C. J.; & Caldwell, D. G. (1995). Adaptive Position Control of Antagonistic Pneumatic Muscle Actuators. *IEEE/RSJ International Conference on Intelligent Robots and Systems*, 1, ss. 378-383. Pittsburgh, USA.
- [4] Than, T.; & Ahn, K. (2006). Nonlinear PID Control to Improve the Control Performance of 2 Axes Pneumatic Artificial Muscle Manipulator Using Neural Networks. *Mechatronics*, 16, 577-587.
- [5] Hesselroth, T.; Sarkar, K.; Van der Smagt, P.; & Schulten, K. (1994). Neural Network Control of a Pneumatic Robot Arm. *IEEE Transaction of Systems, Man and Cybernetics*, 24, No. 1, ss. 28-38.
- [6] Chan, S. W.; Lilly, J. H.; Repperger, D. W.; & Berlin, J. E. (2003). Fuzzy PD+I Learning Control for a Pneumatic Muscle. *Proceedings of 2003 IEEE International Conference on Fuzzy Systems*, (ss. 278-283). St Louis, USA.
- [7] Balasubramanian, K.; & Rattan, K. S. (2003). Feedforward Control of a Nonlinear Pneumatic Muscle System Using Fuzzy Logic. *IEEE International Conference of Fuzzy Systems*, 1, ss. 272-277.
- [8] Lilly, J. H.; & Yang, L. (2005). Sliding Mode Tracking for Pneumatic Muscle Actuators in Opposing Pair Configuration. *IEEE Transactions on Control Systems Technology*, 13, ss. 550-558.
- [9] Carbonell, P.; Jiang, Z. P.; & Repperger, D. W. (2001). Nonlinear Control of a Pneumatic Muscle Actuator: Backstepping vs. Sliding Mode. *Proceedings of the IEEE International Conference on Control Applications*, (ss. 167-172).
- [10] Tondu, B.; & Lopez, P. (2000). Modeling and Control of McKibben Artificial Muscle. *IEEE Control Systems Magazine*, (ss. 15-38).
- [11] Aschemann, H.; & Schindele, D. (2008). Sliding-mode Control of a High-Speed Linear Axis Driven by Pneumatic Muscle Actuators. *IEEE Transactions on Industrial Electronics*, 11 (55), 3855-3864.
- [12] Shen, X.; Zhang, J.; Barth, E.; & Goldfarb, M. (2006). Nonlinear Model-Based Control of Pulse Width Modulated Pneumatic Servo Systems. *ASME Journal of Dynamic Systems, Measurement and Control*, 128, 663-669.
- [13] Morita, Y. S.; Shimizu, M.; & Kagawa, T. (1985). An Analysis of Pneumatic PWM and Its Application to a Manipulator. *Proceedings of International Symposium of Fluid Control and Measurement*, (ss. 3-8). Tokyo, Japan.
- [14] Noritsugu, T. (1986). Development of PWM Mode Electro-Pneumatic Servomechanism, Part I-II: *Journal of Fluid Control*, 17-1, 65-80.
- [15] Lai, J. Y.; Singh, R.; & Menq, C. H. (1992). Development of PWM mode Position Control for a Pneumatic Servo System. *Journal of the Chinese Society of Mechanical Engineers*, 13 (1), 86-95.
- [16] Paul, A. K.; Mishra, J. K.; & Radke, M. G. (1994). Reduced Order Sliding Mode Control for Pneumatic Actuator. *IEEE Transaction on Control Systems Technology*, 2 (30), 271-276.
- [17] Van Varseveld, R. B.; & Bone, G. M. (1997). Accurate Position Control of a Pneumatic Actuator Using On/Off Solenoid Valves. *IEEE/ASME Transaction on Mechatronics*, 2 (30), 195-2004.



- [18] Barth, E. J.;Zhang, J.;& Goldfarb, M. (2003). Control Design for Relative Stability in a PWM-Controlled Pneumatic Systems. *ASME Journal of Dynamic Systems, Measurement and Control* , 125 (3), 504-508.
- [19] Ahn, K.;& Yokota, S. (2005). Intelligent Switching Control of Pneumatic Actuator using On/Off Solenoid Valves. *Mechatronics* , 15, 683-702.
- [20] Shen, X.;Zhang, J.;Barth, E.;& Goldfarb, M. (2006). Nonlinear Model-Based Control of Pulse Width Modulated Pneumatic Servo Systems. *ASME Journal of Dynamic Systems, Measurement and Control* , 128, 663-669.
- [21] Nguyen, T.;Leavitt, J.;Jabbari, F.;& Bobrow, J. E. (2007). Accurate Sliding-Mode Control of Pneumatic Systems Using Low-Cost Solenoid Valves. *IEEE/ASME Transactions on Mechatronics* , 12 (2), 216-219.
- [22]Taghizadeh, M.;Ghaffari, A.;& Najafi, F. (2008). A Linearization Approach in Control of PWM-driven Servo-Pneumatic Systems. *Proceedings of the 40th Southeastern Symposium on System Theory*, (ss. 395-399). New Orleans, LA, USA.
- [23] Schulte, R. A. (1962). The Characteristics of the McKibben Artificial Muscle. *The Applications of External Power in Prosthetics and Orthotics* , 94-115.
- [24] Chou, P.;& Hannaford, B. (1996). Measurement and Modeling of a McKibben Pneumatic Artificial Muscles. *IEEE Transaction on Robotics and Automation* , 12 (1).
- [25] Jouppila, V. T.;Gadsden, S. A.;& Ellman, A. U. (2010). Modeling and Identifiacation of a Pneumatic Muscle Actuator System Controlled by an On/Off Solenoid Valve. *Proceedings of 7th International Fluid Power Conference*, (s. 16). Aachen, Germany.
- [26] Utkin,V. I., Sliding Modes and Their Application in Variable Strucure Systems. Moscow, Russia: MIR Publishers, 1978.
- [27] Slotine, J. J. and Li, W., Applied Nonlinear Control. Englewood Cliffs, New Jersey, USA: Prentice-Hall, 1991.

# Implementation and Analysis of a Pneumatic Pipe Model

Jan Elvers

Hubertus Murrenhoff

RWTH Aachen University, Germany

Institute for Fluid Power Drives and Controls (IFAS)

## ABSTRACT

The use of system simulation software is state of the art in the design of fluid power systems. In pneumatics the influence of pipe and hose elements is often approximated through resistances, which has several disadvantages. Delay times are missing, parameterization often is guesswork and pressure wave effects are neglected. To improve the accuracy of system simulations, pneumatic pipe models play an important part. Besides eliminating the aforementioned disadvantages they also affect the calculation of the speed of pressure build-up in chambers and reaction times of cylinders. In the first part of the paper the development and implementation of a one-dimensional pneumatic pipe model is presented. It is based on the method of characteristics for the simulation of pneumatic applications. The model especially considers friction and heat transfer as those effects are of special interest in pneumatic pipe networks. In the second part the influence of key parameters will be discussed and the simulation results are compared with measurements on a newly designed test bench. The pipe model is a necessary component in simulation of pneumatic networks. In further works a distributor model will be developed which connects several pipe models to represent pneumatic networks.

## 1 NOMENCLATURE

$c$	Speed of sound	[ m/s ]
$m$	Mass	[ kg ]
$\dot{m}$	Mass flow	[ kg/s ]
$p$	Pressure	[ N/m <sup>2</sup> ]
$\dot{q}$	Heat flow per fluid mass	[ W/kg/s ]
$t$	Time	[ s ]
$u$	Flow velocity	[ m/s ]

$A$	Cross section or wall surface (depending on context)	[ m <sup>2</sup> ]
$D$	Pipe diameter	[ m ]
$L$	Pipe length	[ m ]
$Q$	Heat	[ W ]
$R$	Specific gas constant	[ J/kg/K ]
$T$	Temperature	[ K ]
$T_w$	Wall temperature	[ K ]
$\alpha$	Heat transfer coefficient	[ W/m <sup>2</sup> /K ]
$\Delta t$	Time step	[ s ]
$\Delta x$	Pipe element length	[ m ]
$\kappa$	Isentropic exponent	[ – ]
$\lambda$	Friction coefficient	[ – ]
$\rho$	Density	[ kg/m <sup>3</sup> ]

## 2 INTRODUCTION

In the past pipes and hoses were often neglected in the one-dimensional simulation of pneumatic systems to save calculation time and to reduce the overall size of the simulation model. In recent years this has begun to change because faster computers are becoming available and complex systems, for example valve clusters which are connected to drives by long lines, need to be entirely simulated in order to obtain more information about their transient behaviour [1].

Many mathematical pipe models have been derived and developed from the Navier-Stokes equations, but remarkably few have been published in a way that tries to take a general look at the fundamental problem. The mathematical model is an absolute necessity for the description of pipe flow but hardly sufficing. Additional information of value concerns the implementation of the computing scheme as well as the realization of necessary boundary conditions in the program.

Early attempts at pipe models were concentrated parameter models [2]. The pipe was basically cut into volumes connected by resistances which allowed an approximation of pressure losses. But the reduction of a continuous system to a series of concentrated volumes with piecewise constant values of pressure and temperature is problematic. To improve the underlying inaccuracies the number of volumes was increased which correspondingly decreases the size. Small volumes behave as stiff systems which need small time steps to calculate. This increased complexity leads to long simulation durations. The next idea was to treat the problem as distributed parameters. Some converted the governing partial differential equations into transfer functions [6], which observe pressure and volume flow rate, while others used finite difference schemes to solve the simplified

governing equations [7]. Commercial software packages like AMESim or SimulationX offer distributed parameter models for the calculation of pipe flow. However, the program code of those models has not been disclosed so far. It is therefore unclear how different models are set up and how the calculations are carried out inside the block model. Universally applicable pneumatic pipe models which consider pressure, momentum and temperature are quite rare which is why the Fluid Power Association of the German Engineering Federation (VDMA) decided to support research in this field of fluid power. The aim is to develop a simulation model which is able to accurately calculate pressure wave propagation in pneumatic lines. This paper aims to show an exemplary development of a working pipe model block which can be added and connected to a system simulation model.

### 3 MODEL

The basics for the description of pipe flow are the Navier-Stokes equations coupled with an equation of state. In this case air is treated as a perfect gas. As the Navier-Stokes equations have been discussed in great detail in numerous publications, it will be refrained from repeating this discussion. **Equation 1** shows the Navier-Stokes equations (conservation of mass, momentum and energy) as a system of partial differential equations, where  $A$  is a  $(3 \times 3)$  matrix and  $d$  is a column vector of length 3, which includes the dissipative effects of friction and heat transfer. The subscripts  $t$  and  $x$  denote the derivatives after time and location.

$$u_t + A(x, t, u)u_x + d(x, t, u) = 0$$

$$\text{with } u(x, t) = \begin{pmatrix} p \\ \rho v \\ T \end{pmatrix}; \quad A(x, t, u) = \begin{pmatrix} -(\kappa - 1)\frac{RT\rho v}{p} & \kappa RT & \kappa R\rho v \\ 1 - \frac{RT(\rho v)^2}{p^2} & 2\frac{RT\rho v}{p} & \frac{R(\rho v)^2}{p} \\ -(\kappa - 1)\frac{RT^2\rho v}{p^2} & (\kappa - 1)\frac{RT^2}{p} & \kappa\frac{RT\rho v}{p} \end{pmatrix} \quad (1)$$

$$d(x, t, u) = \begin{pmatrix} (\kappa - 1)\left(-\frac{p}{RT}\dot{q} + \rho v X\right) \\ \frac{p}{RT}X \\ -(\kappa - 1)\left(\frac{1}{R}\dot{q} - \frac{T\rho v}{p}X\right) \end{pmatrix}$$

This system can be transformed into normal form which leads to a system of ordinary differential equations whose solutions follow so called characteristic curves. The authors refrain from showing the transformation of the equations as information on this procedure is available in mathematical standard works. The method itself has been used in gas dynamics for a long time to calculate flows, e.g. see the description by Shapiro [5] in 1953 or Sauer in 1966 [8].

### 3.1 Simplifications

The presented pipe model makes use of the following simplifications: the flow is one-dimensional, therefore speed is averaged over the pipe's cross section, the friction forces are Reynolds number dependent and heat transfer is described by wall temperature and heat transfer coefficient. The method of characteristics is used to solve the equations. This method has already been applied to the problem of hydraulic pipe and hose models. E.g. Theissen used it for the calculation of oscillating pipe flows in association with frequency dependent friction [3]. Applying the method of characteristics to the hyperbolic system of differential equations leads to a system of ordinary differential equations whose solutions travel along the so called characteristic curves. Also called eigenvalues, the characteristics are the flow velocity, flow velocity with added speed of sound and finally the flow velocity with subtracted speed of sound. The flow velocity affects friction and heat transfer and vice versa heat transfer and friction affect the flow velocity while pressure disturbances propagate with speed of sound in both directions of the pipe. Additional information on the method of characteristics is available in [5].

### 3.2 Method of characteristics

To calculate the solutions for a pipe the differential equations need to be turned into difference equations. These can be implemented in a computer program by using an explicit difference scheme. The pipe is divided into  $k+1$  nodes, and therefore  $k$  elements. As the solutions are known for all nodes at the old time step, the difference equations can be used to calculate all values for the new time step. Considering a given point  $i$ , an approximation for the propagation speed is given by the characteristic speeds  $u(i)+c(i)$  and  $u(i)-c(i)$ . Multiplying with the simulation time step width gives the distances  $\Delta x_A$  and  $\Delta x_B$ . Linear interpolations of the values at these points are used for the calculation of all variables for the point  $i$  at the new time step using the difference equations.

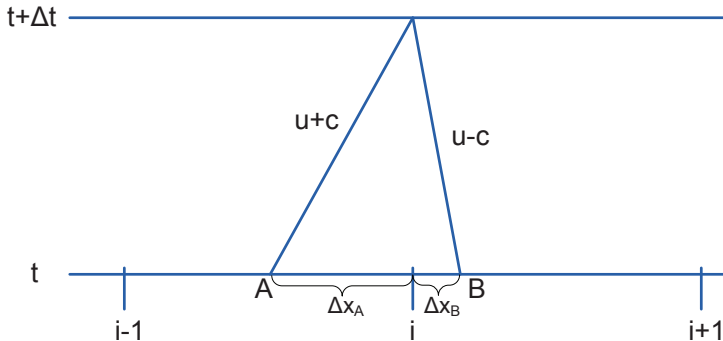


**Figure 1: Basic principle of the method of characteristics**

Considering that flow velocity and speed of sound are hardly constant but instead changing and therefore the characteristics are resembling curves far more than straight lines, accuracy is improved by adjusting the characteristics by averaging the new values  $u(i, t+\Delta t)$  and  $c(i, t+\Delta t)$  and the old values  $u(i, t)$  and  $c(i, t)$ . This leads to new points  $A$  and  $B$ . The new values are iteratively adjusted until an abort criterion is reached. A very useful criterion is the change of the characteristic speeds between two iterations. If the difference is smaller than

a predefined threshold, the calculated values are deemed accurate enough and the iteration is finished for the current time step.

### 3.3 Stability

Transforming the system of hyperbolic partial differential equations and solving the simpler ordinary differential equations does not automatically lead to a stable procedure. Of utmost importance is the correct choice of dependent variables. Momentum, pressure and temperature are a stable combination and were used in this study. Because the used differentiation scheme is an explicit one, another important stability condition, named after Courant, Friedrichs and Lewy, has to be met.

$$\frac{(|u| + c) \cdot \Delta t}{\Delta x} \leq CFL < 1 \quad (2)$$

The condition describes that the maximum propagation speed has to be smaller than the speed needed for information to travel through an element during a time step. Therefore the ratio of time step and element length depends solely on the CFL number. As can be seen in **equation 2** the minimum length of each pipe element is defined by the time step width multiplied with the highest propagation speed. By choosing smaller CFL numbers the pipe is divided into longer elements which reduces the number of elements and leads to swifter calculation.

### 3.4 Boundary Conditions

The inside parts of the pipe model are dependent on given values which were initial conditions at the beginning of the calculation or calculated values from the last simulation time step. But what about both pipe ends? There, one of the three characteristics is missing. To compensate for this lack of information, data from connected volumes is used. In the case of inflow, the pressure and temperature of the connected volume at the new time step are used as additional information so that momentum can be calculated.

In the other case (outflow) only the pressure is used as an initial starting point. As we have two characteristics, the new values of temperature and momentum are calculated. It is then necessary to calculate flow velocity and sonic velocity to identify a physically impossible supersonic condition at the output element as this leads to an instable behaviour of the simulation model. The way to remedy this situation is to iteratively adjust the pressure in the outflow node. The following expression is used to find the correct outflow pressure by setting  $u$  to the value of the sonic velocity  $c$ .

$$\dot{m} = u \cdot A \cdot \rho = \frac{u \cdot A \cdot p}{R \cdot T} \Leftrightarrow p = \frac{\dot{m} \cdot R \cdot T}{u \cdot A} \quad (3)$$

Half of the difference between this pressure and the pressure calculated during the previous iteration step is added to latter. This new value is then used for the calculation of temperature and momentum. The algorithm is applied until the found pressure changes are small and flow velocity is identical to local sonic speed.

### 3.5 Friction and Heat transfer

A simple model is chosen to account for friction effects. Pressure losses are estimated to be dependent on the momentary flow velocity, density and the geometric properties. This leads to the Darcy-Weisbach equation which is utilized in the presented pipe model for the description of friction effects.

$$\Delta p = \lambda \cdot \frac{L}{D} \cdot \frac{\rho}{2} \cdot u^2 \quad (4)$$

The friction coefficient  $\lambda$  is assumed to be only dependent on the momentary Reynolds number. To further simplify the calculation of friction it is assumed that the simulated pipes are smooth. Accordingly, the authors use the friction values presented in **Table 1** in the consideration of friction effects [4].

**Table 1: Friction Coefficient  $\lambda$**

$0 < \text{Re} < 2320$	$\lambda = \frac{64}{\text{Re}}$	laminar flow
$2320 \leq \text{Re} < 3906$	$\lambda = \frac{0,028}{2300^b} \cdot \text{Re}^b$ with $b = 0.68467$	transition laminar/turbulent
$3906 \leq \text{Re} < 10^5$	$\lambda = (100 \cdot \text{Re})^{-\frac{1}{4}}$	turbulent flow (Blasius)
$10^5 \leq \text{Re}$	$\lambda = 0,018$	turbulent flow

Heat transfer is a potentially highly complex matter, but it needs to be reduced to a general solution by assuming simplified conditions so that it can be used in a general pipe model. The temperature of the pipe wall is considered to be constant while the heat capacity of the pipe material is neglected. The underlying heat transfer problem is reduced to the contact area between pipe wall and fluid. This kind of heat transfer problem is describable by the following equation which utilizes an averaged heat transfer coefficient  $\alpha$ .

$$Q = -\alpha \cdot A \cdot (T - T_w) \cdot \Delta t \quad (5)$$

By substituting  $A$  with the surface area of a pipe element, relating the transferred heat to the fluid mass and to the time interval, the following equation is used in the pipe model.

$$\dot{q} = \frac{Q}{m \cdot \Delta t} = \frac{-\alpha \cdot \pi \cdot D \cdot \Delta x \cdot (T - T_w) \cdot \Delta t}{\frac{\pi}{4} D^2 \cdot \rho \cdot \Delta x \cdot \Delta t} = -\frac{4 \cdot \alpha \cdot T \cdot R}{D \cdot p} (T - T_w) \quad (6)$$

It is possible to consider heat exchange in a very general manner by defining the heat transfer coefficient  $\alpha$ . This simple treatment of heat transfer was partly chosen because of its easy implementation and partly, because sufficient data for the correct parameterization

of more sophisticated models often is lacking. In future work the heat transfer model can be adjusted to accommodate more complex situations. Improvements that directly come to mind are incorporating pipe wall heat capacity, addition of heat transfer between outer pipe wall and the environment as well as consideration of fluid speed and pressure in the calculation of heat transfer.

### 3.6 Parameters

The implemented pipe model needs to be parameterized before starting the simulation. Important tuning parameters are the geometric dimensions of the pipe, initial conditions (pressure, temperature), heat transfer coefficient and wall temperature, expected maximum sonic velocity, the threshold for the change of characteristics (in m/s) and finally the factor which adjusts the length of the pipe elements (range between 1 and 20 which is  $1/\text{CFL}$ ). Other parameters which should be kept unchanged from presets include the dynamic viscosity of air and the isentropic exponent.

## 4 MEASUREMENTS AND VALIDATION

### 4.1 Mass Balance and Propagation Speed

Validation of a simulation model is important in achieving reliability. As a first test the model was used to simulate a pressure equalization process of two volumes connected with a pipe under differing simulation parameters. It appears to work stable for pressure steps of up to 16 bar, pipe lengths from 0.1 m up to 20 m, pipe diameters from 2 mm up to 25 mm, different time step size from  $1 \cdot 10^{-6}$  s up to  $5 \cdot 10^{-5}$  s and even different starting temperatures. **Figure 2** shows the results of an exemplary calculation of a pressure step from 1 bar to 6 bar at the front end of a pipe ( $D = 8$  mm,  $L = 1$  m). For further information on simulation parameters see **Table 2**. Evident are the time delay for the pressure step to reach the pipe end, pressure reduction through friction and the development of steady conditions for both pressure and velocity after 0.005 s.

**Table 2: Simulation parameters**

Parameter	Value	Parameter	Value
Volumes connected to line	5 l	Temperature (system)	293.15 K
Starting pressure Volume 1	6 bar	Length (line)	1 m
Starting pressure Volume 2 and line	1 bar	Diameter (line)	8 mm
Time step	$10^{-5}$ s	Solver	ODE4
CFL-number	0.703	Number of nodes	96



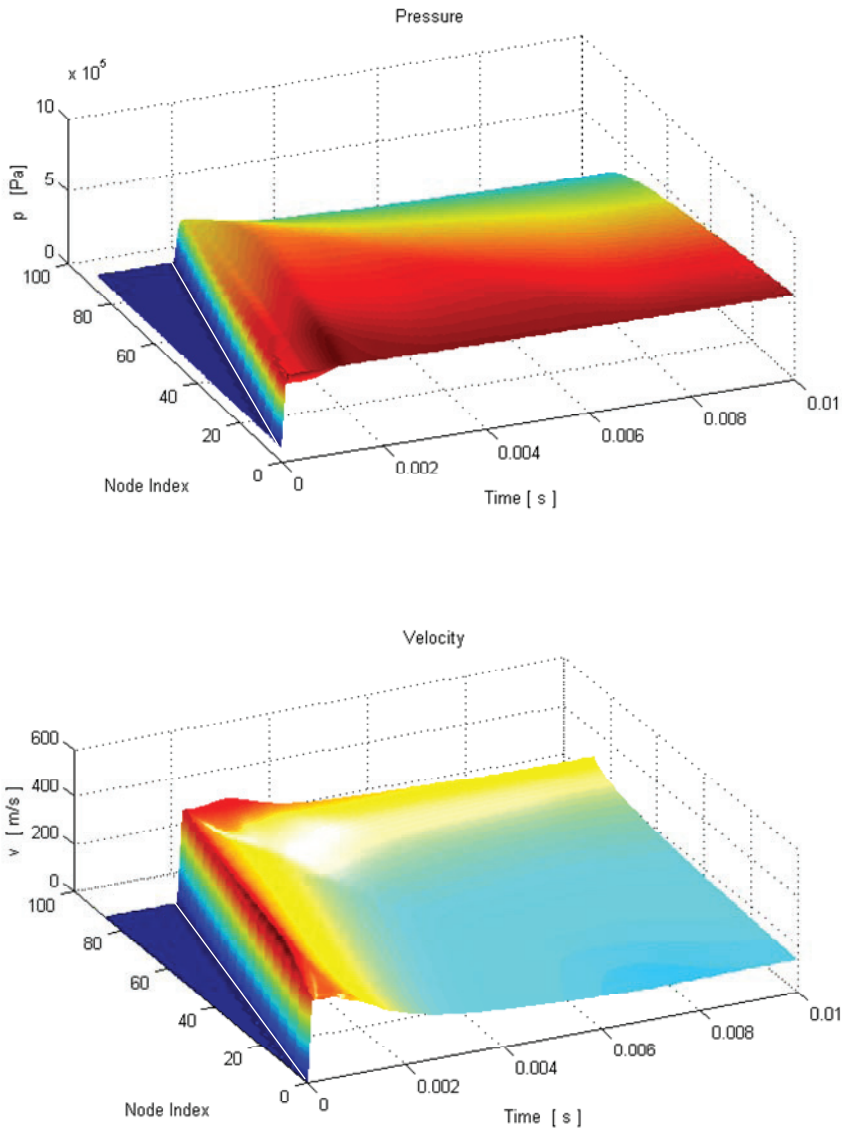


**Figure 2: Pressure and Velocity Propagation through the Pipe**

As a second test the conservation of mass was investigated in order to get information about the accuracy of the model. Especially important is the chosen time step of the simulation as it has the highest impact on accuracy. Three different time step sizes were used on the identical problem of the aforementioned pressure equalization process as is presented in **Table 3**.

**Table 3: Mass Balance after Pressure Equalization Process**

Simulation Time Step	Mass after simulation in relation to mass before simulation
$1 \cdot 10^{-6}$ s	99.05 %
$5 \cdot 10^{-6}$ s	98.01 %
$1 \cdot 10^{-5}$ s	96.97 %

The table data clearly indicates that the chosen time step size affects the accuracy of the simulation. It can be noted at this point that bigger step sizes lead to larger deviations but the error is still bounded.

The comparison of measured and simulated travel time of pressure step was the third test of the implemented pipe model. A 3.4 m long hose with a diameter of 4 mm was pressurized via a fast acting switching valve. Pressure transducers at the beginning and the end of the hose were used to measure the travel time of the pressure jump (1 bar to 1.7 bar). The data was compared to the simulation results of a similar system which represented the testing apparatus. In reality the pressure jump traveled the distance in a time of 9.2 ms while the simulated result was 8.7 ms. This strongly indicates that the model is accurate enough for modeling pressure wave propagation as the results from measurement and simulation are to a huge extent (5 %) in agreement.

#### 4.2 Influence of Element Length and Simulation Time Step

As described in 3.3 the CFL-Number defines the ratio between local and temporal discretisation and delivers a minimal element length. It is then possible to increase the length of those pipe elements. The authors expect a decrease in simulation duration as the number of elements is linked to the number of calculations. A test was conducted to verify and quantify this hypothesis. The simulated system calculated a pressure equalization and consisted of a pipe with a length of 5 m and a diameter of 8 mm which connected two volumes ( $V = 10$  l). The first volume had a pressure of 6 bar and was connected at the beginning of the simulation to the pipe and the second volume which had a pressure of 1 bar. In a first step the time step was varied starting from  $10^{-6}$  s to  $5 \cdot 10^{-5}$  s. In a second step the size of the pipe elements was adjusted. All pipe element lengths were expressed as multiples of the smallest length defined by the CFL condition. Criteria for the test were simulation duration and the pressure build-up in the second volume. **Figure 3** shows the results of the simulation study. It is important to note, that a step size of  $5 \cdot 10^{-5}$  s combined with longer pipe elements does not allow a stable computation. So there are no results for elements longer than factor 10.

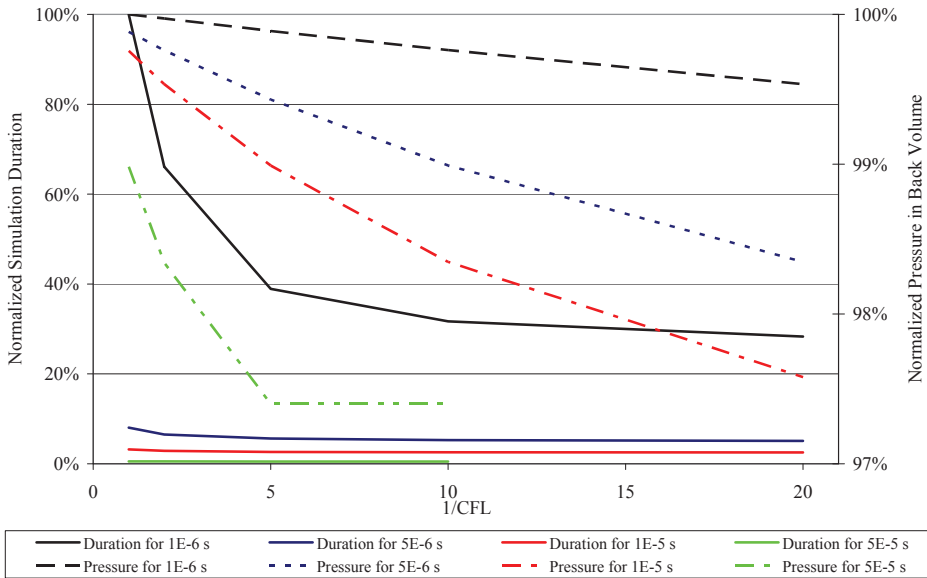


**Figure 3: Simulation Duration and Back Pressure Difference depending on Time Step and Element Length**

The simulation run with the smallest time step size ( $10^{-6}$  s) and smallest pipe elements (factor 1) gives the most accurate results which are therefore used to normalize all other findings. There are two main conclusions to be drawn: Firstly, an increase of the element length greatly reduces the simulation duration. As can be seen for the smallest time step size, an elongation of the pipe elements beyond the minimum length by a factor of 5 leads to a decrease in simulation duration of 60 %. Secondly, the time step size affects the mass balance. This can be shown as follows. Increasing time steps lead to increasing deviations in the calculation of the pressure build-up in the back volume. Additionally, an increasing element length leads to larger deviations as well. This means that a gain in simulation time is paid with a loss of precision. In the case of the smallest time step size combined with the longer elements (factor 5) this leads to a loss of accuracy of about 2 %. The curve which depicts the normalized pressure in the back volume for the biggest time step shows that using longer element lengths does not have to imply a decrease in precision. It is much more important to find the correct ratio of time step width and element length. Especially while using small time step widths the use of larger element lengths is most beneficial.

## 5 CONCLUSIONS

This paper presents an exemplary path to the development of a pneumatic pipe model based on the method of characteristics for the simulation of pressure wave propagation. It was shown how to incorporate heat transfer and friction into the model. Of particular interest were problems of the implementation into a working simulation model which is able to work under very general conditions. The model was shown to be working under stationary

and simple transient conditions like pressure equalization of two volumes connected by a pipe or hose. Further works include more validations with measured system responses as well as the development of a distributor model, for example a T-fitting, which shall be connected to the pipe model and enable the user to design a pneumatic network.

The authors would like to thank the Fluid Power Association of the German Engineering Federation (VDMA) for financing and supporting the research.

## 6 References

1. **Kefer, J.; Krichel, S.**, Modeling and Simulation of Pneumatic Systems with focus on Tubes, 8th International Fluid Power Conference , 2012, Dresden
2. **Bala, H.-P.**, Durchflussmessungen und stroemungstechnische Kenngroessen, o+p Oelhydraulik und Pneumatik, vol. 29, 1985
3. **Theissen, H.**, Die Berücksichtigung instationärer Rohrströmung bei der Simulation hydraulischer Anlagen, Dissertation, 1983, Aachen
4. **Truckenbrodt, E.**, Fluidmechanik, Band I, Grundlagen und elementare Strömungsvorgänge dichtebeständiger Fluide. Springer, Berlin-Heidelberg-New York, 1989
5. **Shapiro, A.**, The Dynamics and Thermodynamics of Compressible Fluid Flow, vol. II, Robert E. Krieger Publishing Co., 1954, Florida
6. **Franco, W.; Sorli, M.**, Time Domain models for pneumatic transmission lines, in Burrows, Edge and Johnson (eds.), Power Transmission and motion control, Bath, 2004, pp 257 – 269
7. **Mitushiro, N.; Kawashima, K.; Kagawa, T.**, Analysis of pneumatic pipeline using CCUP (CIP-combined and unific procedure) method, SICE Annual Conference 2010, Taipei, pp. 1670 – 1675
8. **Sauer, R.**, Nichtstationäre Probleme der Gasdynamik, Springer, Berlin, 1966



# Investigation on the Efficiency of Pneumatic System Using Air Power

**Toshiharu Kagawa\***, **Maolin Cai\*\***, and **Xin Li\***

\* Precision and Intelligence Laboratory, Tokyo Institute of Technology, R2-45, 4259 Nagatsuta-chou, Midori-ku, Yokohama, 226-8503, Japan

\*\* School of Automatic Science and Electrical Engineering, Beihang University, Beijing, People's Republic of China

## ABSTRACT

In these decades, pneumatic systems are widely used not only in factory automation but also in bio measurement because of its inherent advantages of generating little heat and magnetic free, etc. However, few reports on energy consumption of pneumatic systems can be found due to lack of available energy assessment. In this study, the authors propose a definition of pneumatic energy called as air power that is composed of expansion power and transmission power. Based on the definition of air power, we analyze the energy loss and efficiency of pneumatic system by dividing pneumatic system to four parts: air production, air cleaning, air transmission and actuator. In air production, we discuss the adiabatic and isothermal efficiencies of a compressor, and define the overall efficiency of compressor with air power. In air cleaning, energy efficiency of air filter is investigated and general data are given. In air transmission, the energy losses due to pressure loss in pipe and air leaks are discussed, and the energy saving effect of a regulator is shown. In air consumption, the energy distribution in a cylinder meter-out actuating circuit is clarified. These efficiency analysis and discussion would be helpful to an energy-saving equipment selection and system design.

## 1. INTRODUCTION

The demands of industrialization have increasingly required the use of compressed air in factories and workshops since the 1960s. Compared with oil or electric systems, compressed air systems are cleaner, cheaper, and easier to maintain. However, compressed air systems can be expensive to operate [1]. The cost for producing 0.6 MPa ~ 0.9 MPa compressed air in Japan averages around U.S. \$0.02–0.03 per cubic meter, with the compressor's electricity responsible for 80% ~ 90% of the cost. In fact, compressed air systems typically consume 10% to 20% of the total electricity in manufacturing factories, reaching 40 billion kilowatt hour per year in Japan.

A significant portion of the energy consumed by compressed air systems is wasted due to improper settings and operation, as well as air leaks and inappropriate equipment, addressing these concerns typically saves about 30%. Therefore, improving the efficiency of compressed air systems and reducing air consumption is essential for minimizing energy costs. Air volume or flow rate is typically used to represent air consumption because there is no standard method for determining the power consumed by compressed air flow. This paper proposes a new concept, called air power, to represent this power. In hydraulics, fluid

power is calculated by multiplying the gauge pressure and the fluid's volumetric flow rate. This method, however, cannot be applied to air because it assumes incompressibility. The electrical power applied to a compressor, which is the energy source for the air power, is not proportional to its pressure output for a given flow rate. Therefore, the role of air pressure must be studied. Using only the flow rate does not specify the power lost in the supply pipes or supplied to the actuators, which are considered extremely important for streamlining energy consumption. Therefore, air power must be sufficiently defined and quantified. This paper uses a typical compressed air system to derive a general equation of air power. Then, based on the definition of air power, we analyzed the energy loss and efficiency of a pneumatic system by dividing a pneumatic system to four parts: air production, air cleaning, transmission and pneumatic actuator.

### Nomenclature

$e$ : available energy of a unit mass of air, J/kg	$G$ : mass flow rate, kg/s
$E$ : energy, J	$m$ : mass of air, kg
$P$ : air power, W	$p$ : air pressure, Pa
$h$ : enthalpy of a unit mass of air, J/kg	$Q$ : volumetric flow rate, m <sup>3</sup> /s
$R$ : gas constant, J/(kg K)	$T$ : temperature, K
$s$ : entropy of a unit mass of air, J/(K kg)	$V$ : volume, m <sup>3</sup>
$W$ : work, J	$\kappa$ : specific heat ratio
$\eta$ : Efficiency, %	

## 2. PROPOSAL OF AIR POWER

In this section, we discuss the definition of air power in terms of the energy conversion for the state change of air. For simplicity, two ideal processes are discussed, in which there are no losses. In the first process, compressed air is produced in a simple piston-type compressor. The other process involves a pneumatic cylinder consuming compressed air. These two processes are depicted in Fig. 1 [2, 3].

### 2.1 Ideal Production of Compressed Air

It is well known that air compression requires the least amount of work in an isothermal process. Assuming that there is no friction or air leak, the ideal process is described as follows.

1. Suck: Pull the piston from position A to B to suck air from the atmosphere in a quasi-static process.
2. Compress: Close Valve 1 and push the piston from Position B to C to compress the air quasi-statically until the air pressure reaches  $p_s$ . This process is considered an isothermal process.
3. Supply: Open Valve 1 and close Valve 2. Then push the piston from Position C to A to completely expel the compressed air under constant pressure  $p_s$ . The compressed air is supplied to the cylinder on the right.

Using the equation  $p_a V_a = p_s V_s$  for isothermal compression, the required mechanical work for producing compressed air of pressure  $p_s$  and volume  $V_s$  is

$$W'_i = W'_{i1} + W'_{i2} + W'_{i3} = 0 + \int_{V_a}^{V_s} (p_a - p) dV + (p_s - p_a) V_s = p_s V_s \ln \frac{p_s}{p_a} \quad (1)$$

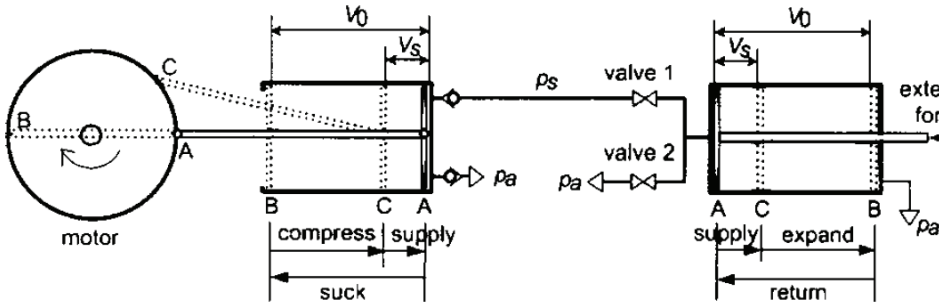


Figure 1: Ideal production and ideal consumption of compressed air

## 2.2 Ideal Consumption of Compressed Air

The actuator most often used in compressed air systems is a pneumatic cylinder. Assuming that there is no friction or air leak, the ideal scenario for performing the maximum level of mechanical work is described as follows.

1. Supply: This step is identical to Step 3 in Section 2.1. The piston is pushed from Position A to C at a constant pressure of  $p_s$  in a quasi-static process.
2. Expand: Close Valve 1 and expand the supplied air quasi-statically until it reaches the atmospheric state. During this process, the piston is pushed from Position C to B. The air state change is considered isothermal.
3. Return: Open Valve 2 and pull back the piston from Position B to A in a quasi-static process.

The work done in these steps can be calculated by Eq. 2. This equation also represents the work-producing potential of compressed air at a pressure  $p_s$  and a volume  $V_s$ .

$$W_o' = W_{o1}' + W_{o2}' + W_{o3}' = (p_s - p_a)V_s + \int_{V_s}^{V_a} (p - p_a)dV + 0 = p_s V_s \ln \frac{p_s}{p_a} \quad (2)$$

It can be seen that air state changes for ideal consumption are the opposite of those for ideal production. The state changes for a unit mass of air are depicted by the  $P$ - $V$  diagram in Fig. 2. The area of ABCA represents the mechanical work calculated by Eqs. 1 and 2.

From this figure it is evident that the energy produced is completely consumed without any loss. In addition, it is clear that the compressed air is used to transmit the energy. The transmitted amount of air can be determined from its pressure and volume, which will be employed by the proposed air power calculation.

## 2.3 Definition of Air Power

A quasi-static process is sometimes referred to as a reversible process [4]. In thermodynamics, an isothermal process is also considered a reversible process. Therefore, it can be said that  $p_s V_s \ln(p_s/p_a)$  represents the mechanical work exchanged in a reversible process. In actual processes, however, losses due to friction are inevitable. Therefore, the following relationship is more realistic:

$$W_i \geq p_s V_s \ln \frac{p_s}{p_a} \geq W_o \quad (3)$$

Eq. 3 suggests that air power should be represented by  $p_s V_s \ln(p_s/p_a)$ . To verify this assertion, a thermodynamics term called energy is used to derive a general conclusion. Energy represents the work producing potential that can be extracted from a substance. In this study, this output potential of compressed air is its available energy. Therefore, the available energy per unit mass of air can be expressed by Eq. 4 [3].



$$e = (h - h_a) - T_a(s - s_a) \quad (4)$$

It can be easily proven that  $e$  is related to the mechanical work done in the production and consumption of compressed air as follows [2, 3]:

$$W_i \geq m \cdot e \geq W_o \quad (5)$$

In this equation, the quantities are equal if they refer to reversible processes. When the air temperature is  $T_\infty$ , Eq. 4 can be expanded to

$$e = (h - h_a) - T_a(s - s_a)|_{T=T_a} = \frac{pV}{m} \ln \frac{p}{p_a} \quad (6)$$

Eq. 3 can be obtained by combining Eqs. 5 and 6. Therefore, the available energy represents the air power energy, so air power can be defined as the flux of the available energy that can be extracted from flowing air as it undergoes a reversible process from a given state to the atmospheric state. This definition of air power is expressed as

$$P = G[(h - h_a) - T_a(s - s_a)] \quad (7)$$

Fig. 5 shows the position of air power in compressed air systems using this definition. Because  $h$  and  $s$  are both functions of air pressure and temperature, air power can be calculated as follows by expanding Eq. 7:

$$P = GRT_a \left[ \ln \frac{p}{p_a} + \frac{\kappa}{\kappa-1} \left( \frac{T}{T_a} - 1 - \ln \frac{T}{T_a} \right) \right] \quad (8)$$

Generally, compressed air flows at atmospheric temperature in pipes. According to Boyle-Charles Law,  $GRT_a = pQ = p_aQ_a$  at atmospheric temperature, where  $Q$  and  $Q_a$  are the volumetric flow rate at a compressed state and at atmospheric state, respectively. Substituting this equation and  $T = T_a$  into Eq. 8, air power at atmospheric temperature can be reduced to

$$P = GRT_a \ln \frac{p}{p_a} = pQ \ln \frac{p}{p_a} = p_aQ_a \ln \frac{p}{p_a} \quad (9)$$

Therefore, air power is proportional to flow rate. Table 1 provides examples of air power under various pressures at a flow rate of 1000 l/min. This table reveals that the unit of air power is kilowatt which is as the same as for electric power. This will facilitate the management of air energy consumption in factories.

This definition of air power will make it easy to determine energy losses due to pressure losses and air leaks, and will enable the investigation of internal energy distributions in current compressed air systems.

## 2.4 Composition of Air Power

It can be seen from the previous discussion on ideal processes that the air power

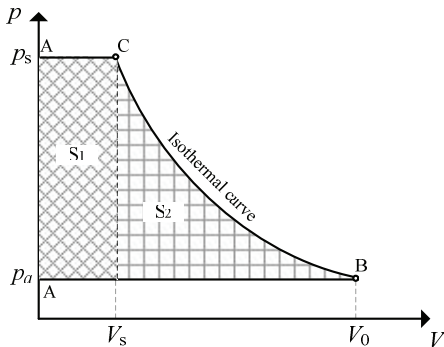


Figure 2:  $p$ - $V$  diagram of ideal production and consumption

Table 1 A calculation example of air power

Flow rate L/min(ANR)	Pressure MPa (abs)	Air power kW
1000	0.4	2.32
	0.6	3.00
	0.8	3.49
	1.0	3.87

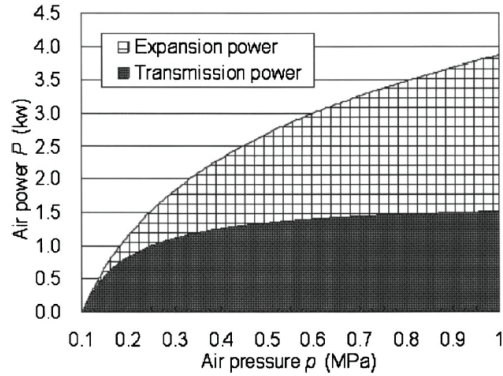


Figure 3: Composition of air power

equation should be composed of two parts. The first part represents the transmission power, which addresses the power required to push the air downstream. The second part represents the expansion power, which addresses the available work due to air expansion.  $P_t$  and  $P_e$  are used to represent these two parts, respectively, and can be calculated using the following equations.

$$P = P_t + P_e \quad (10)$$

$$P_t = (p - p_a)Q = p_a Q_a \left(1 - \frac{p_a}{p}\right) \quad (11)$$

$$P_e = pQ \ln \frac{p}{p_a} - (p - p_a)Q = p_a Q_a \left(\ln \frac{p}{p_a} + \frac{p_a}{p} - 1\right) \quad (12)$$

In  $p$ - $V$  diagram shown in Fig. 4,  $P_t$  and  $P_e$  are equal to the areas of  $S_1$  and  $S_2$ , respectively.

Fig. 3 displays a representative example using Eqs. 11 and 12. This figure indicates that the transmission power and expansion power are identical when the air pressure is equal to 0.52 MPa. The higher the air pressure, the larger the ratio of expansion power. Because the air supply pressure in factories ranges between 0.6 MPa and 1.0 MPa, the expansion power is typically larger than the transmission power for compressed air systems.

As shown in Eq. 11, transmission power for air is calculated using the same expression as hydraulic power. However, flowing air contains not only transmission power, but also expansion power. Even when the upstream supply is shut off, compressed air can still perform work by expanding, unlike liquids. This is the significant difference in the power transmission between compressible and incompressible fluids. Therefore, both transmission power and expansion power must be considered when analyzing the power of flowing air.

### 3. ANALYSIS ON THE EFFICIENCY OF PNEUMATIC SYSTEM

In this section, we divide a pneumatic system to the four parts: air production, cleaning, transmission and consumption, and discuss the energy efficiency of each part respectively by using the definition of air power.

#### 3.1 Efficiency of Compressed Air Production

Compressed air is produced by air compressor. The usually used compressor types are screw, piston, vane and centrifugal type. Generally, compressors are driven by an electric motor, whose energy source is electricity. If high-pressure compressed air is required; several

stages of compression may be employed. One or two intercooler is usually used for cooling compressed air to decrease the power requirement. When selecting a compressor installation, several factors should be considered. These include efficiency, capacity (flow rate output and power), and pressure range, the quality of air, the cooling system, future adaptability, noise levels and ease of maintenance [5].

### 3.1.1 Energy losses in compressor

The efficiency of electric motors generally varies between 80 and 96%. Smaller motors (<10kW) are generally less efficient. Efficiencies can be raised to as high as 98% with high efficiency motors and variables speed drive [6]. The power output of motor is usually transmitted by belt. Belt drives have typical efficiencies of above 95% [5]. For the power arriving at the compression mechanism, the energy losses due to mechanical friction and mixture, air leak and insufficient cooling will happen. The total amount of these losses is the greatest part of the overall loss. Generally, these losses account for 20-40% and vary with compressor type, size and cooling condition. Except for the electricity to motor, electricity is also required by intercooler, after-cooler. This part of electricity consumption is around 10% of the motor.

### 3.1.2 Adiabatic efficiency and isothermal efficiency

It is known that less power will be required if air is compressed near an isothermal process. However, it is a fact that air compression is actually rapid and this makes it near an adiabatic process. This may be the reason why the overall adiabatic efficiency is usually used for assessing the efficiency of compressor. Furthermore, the overall adiabatic efficiency is always higher than the overall isothermal efficiency. The two efficiencies are defined as follows.

$$\eta_{tad} = (P_{tad} / P_e) \times 100\% \quad (13)$$

$$\eta_{tis} = (P_{tis} / P_e) \times 100\% \quad (14)$$

where  $P_{tad}$  is theoretical adiabatic power,  $P_{tis}$  is theoretical isothermal power,  $P_e$  is the total electricity supplied to compressor.

The overall adiabatic efficiency indicate better performance index, which, however, is different from the actual cases. The actual cases are more near to the overall isothermal efficiency because the air with high temperature after an adiabatic compression should be cooled before supplied to pneumatic equipment. Therefore, the theoretical adiabatic power cannot indicate the minimum power requirement for compression. Furthermore, the overall adiabatic efficiency depends on the number of internal compression stages, not just the input

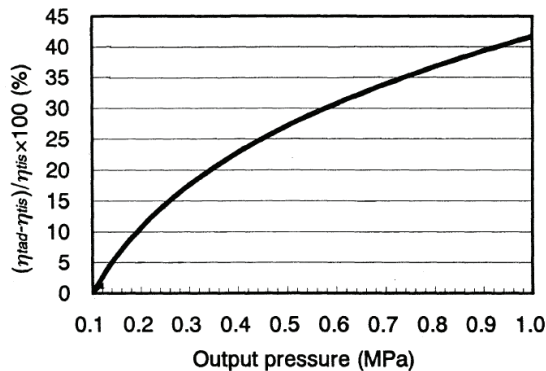


Figure 4: Comparison between the overall adiabatic efficiency and he overall isothermal efficiency

of shaft power and the output of compressed air. Fig. 4 shows the difference between the two efficiencies under the same input and output. As shown in Fig. 4, the overall adiabatic efficiency is 37% higher than the overall isothermal efficiency when the output pressure is 0.8MPa under one stage compression.

Assuming the temperature of the compressed air is the room temperature; the energy output of the compressor is very near to  $P_{tis}$  and can be easily calculated by Eq. 9 with the measured values of pressure and flow rate. The overall efficiency defined above involves all the losses in compressor. It is an easy and practical index for a user to evaluate compressor performance. Fig. 5 shows the data of some typical compressors on the present market [2, 3]. As shown in Fig. 5, the overall efficiency of compressor has a range of 35-50% when motor power is less than 10kW, 40-60% when motor power is10-100kW and 50-70% when motor power is larger than 100kW.

In ISO1217-Displacement Compressors Acceptance Tests, specific energy, defined as the ratio of required motor power and air output volume, is prescribed as an energy performance index. The minimum specific energy for compressing air to 0.8MPa is 0.06kWh/m3. However, in practice, only very large piston compressors are able to approach this figure. The energy consumption of a good installation is more likely to be

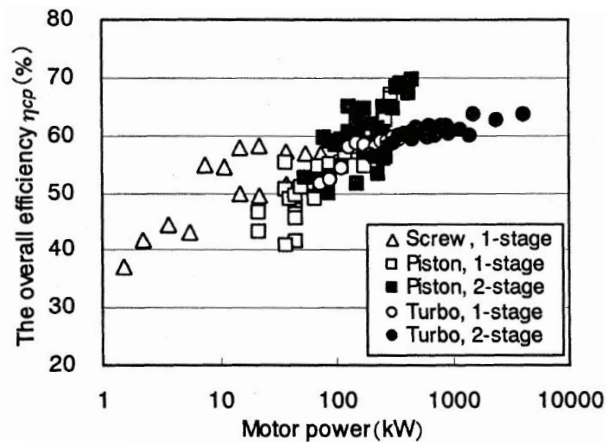


Figure 5: The overall efficiencies of compressors

Table 2 Some typical compressor features

Type	Capacity Nm/s (0.8MPa)	Specific energy kWh/m <sup>3</sup>	Efficiency %
Piston	< 20	0.133	39.6
	20 – 200	0.095	55.4
	200 – 2000	0.072	73.1
Vane	< 20	0.125	42.1
	20 – 200	0.100	52.7
Screw	< 20	0.116	45.4
	20 – 200	0.100	52.7
	200 – 2000	0.092	57.2
Centrifugal	400 – 1000	0.091	57.9
	1000 – 2000	0.083	63.4

0.08-0.12kWh/m<sup>3</sup>. Table 2 shows the actual values of some typical compressors [7]. Given that motor power is only 90% of the total electricity consumption; their overall efficiencies can be calculated and shown in the right of the table. Compared with the specific energy, the overall efficiency is easy to understand, and also necessary for evaluating the efficiency of the whole pneumatic system.

### 3.2 Efficiency of Air Cleaning

After being produced, compressed air will be cleaned by air filter before transmitted to pipe network. In pipe network, the equipment most used to clean air is filter. There are all kinds of filters developed to remove different contaminations such as water, oil, dust, etc. While compressed air flows through a filter, the power loss is determined by the pressure loss there. Generally, as a characteristic, the relation graph between flow rate and pressure loss is given in product catalogue. With this graph, the energy-transfer efficiency of filter can be given by

$$\eta_{fl} = \frac{P_2}{P_1} \times 100\% = \frac{\ln((p_1 - \Delta p_{fl})/p_a)}{\ln(p_1/p_a)} \times 100\% \quad (15)$$

where  $\Delta p_{fl}$  refers the pressure loss. The power loss is expressed as

$$\Delta P_{fl} = p_a Q_a \ln \frac{p_1}{p_1 - \Delta p_{fl}} \quad (16)$$

A calculation example is shown in Fig. 6. By calculating the efficiencies of a number of filters on the market at the condition of the maximum flow rate, it is concluded that a filter for main pipe is always above 99%, and a filter with a performance under 5  $\mu$ m for terminal device is always around 95%.

### 3.3 Efficiency in air transmission

In transmission through pipe, pressure loss and air leak are the two factors resulting in air power loss.

#### 3.3.1 Pressure Loss through Pipe

Pressure loss, denoted by  $\Delta p_{pp}$  occurs along pipe and at joints. Although some theoretical equations for calculating pressure loss were presented in books and previous research reports, as a matter of fact, it is difficult to obtain calculation results with good precision. It is because the pipe network in factories is very complicated and the state of air

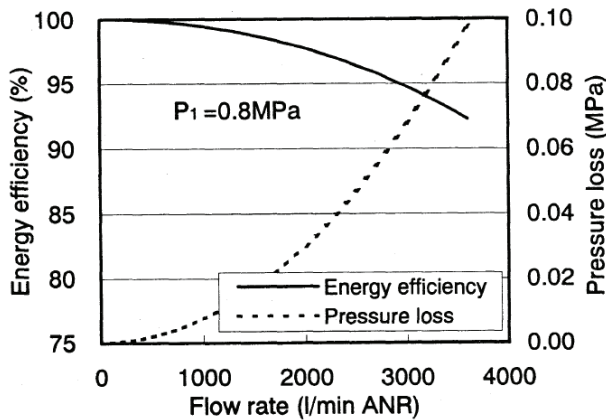


Figure 6: Pressure loss and energy efficiency of an air filter

flow, such as velocity distribution, is not the same as assumed in theoretical calculation. Therefore, compared with this theoretical calculation, measurement is recommended. Given  $\Delta p_{pp}$  as the measured pressure loss, the power loss is

$$\Delta P_{pp} = p_a Q_a \ln \frac{p_1}{p_1 - \Delta p_{pp}} \quad (17)$$

### 3.3.2 Air Leaks

The gradual loss of pressure in the system when no air is being used means there are air leaks. These can account for as much as 10-40% of air consumption in factories although permissible air leaks should be 5% or less in industrial installation [8].

Leaks frequently occur at the pipe, hose joints, valves, fittings and terminal equipment. There are several ways to check for air leaks. The total leak of the system can be checked using a flow meter in the supply line while there is no user on the system. Given  $Q_{lka}$  as the flow rate of leaks and  $p_1$  as the system pressure, the power loss is

$$\Delta P_{lk} = p_a Q_{lka} \ln \frac{p_1}{p_a} \quad (18)$$

### 3.3.3 Regulator

Pressure regulation is also required at the pipe network, especially just before the terminal equipment. The function of a regulator is not only making the output pressure stable, but also reducing it to meet the supply requirement as a power limiter. Therefore, regulator can cut down the air consumption in the terminal equipment. However, power loss will inevitably occur due to pressure reduction. The lost power can be calculated by

$$\Delta P_{rg} = p_a Q_a \ln \frac{p_1}{p_2} \quad (19)$$

Taking a simple actuating system including an air cylinder actuator and a pressure regulator as a calculation example, the cylinder with a size of  $\Phi 25\text{mm} \times 250\text{mm}$  is driven by the reduced pressure. The supplied energy to cylinder and the lost energy in the regulator per one cycle actuation are calculated and shown in Fig. 7. It can be seen that the lower the reduced pressure output is, the less the total energy consumption is, however, the ratio of energy loss and used energy becomes bigger.

### 3.4 Efficiency in air actuator

In this paper, the efficiency and energy distribution in an air cylinder is discussed. Fig. 8 is a typical meter-out cylinder circuit. One actuating cycle of the air cylinder is to lift a load

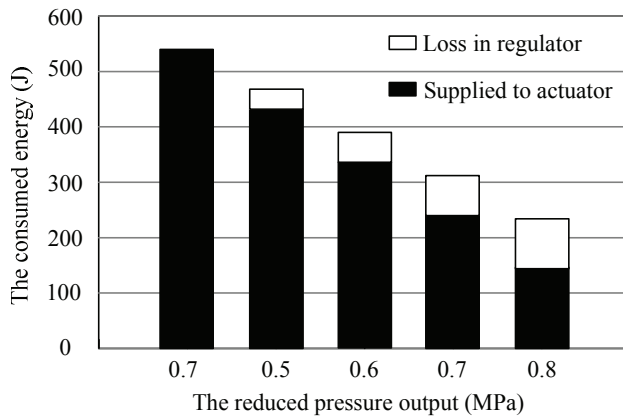


Figure 7: The energy consumption in a regulator and cylinder

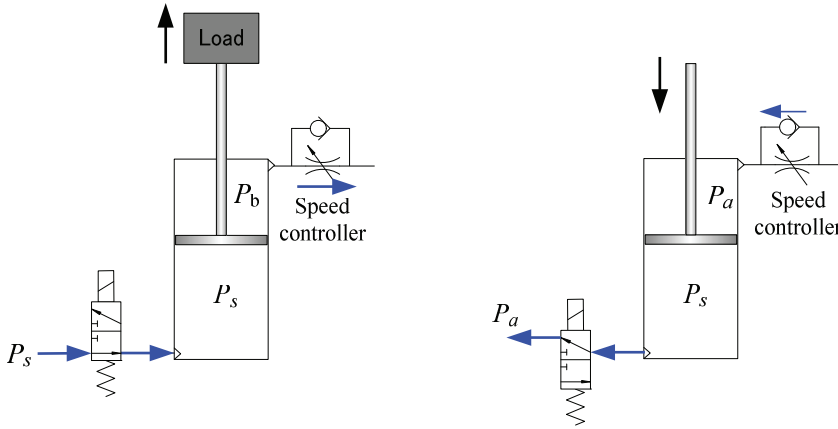


Figure 8: A meter-out cylinder circuit and actuating cycle

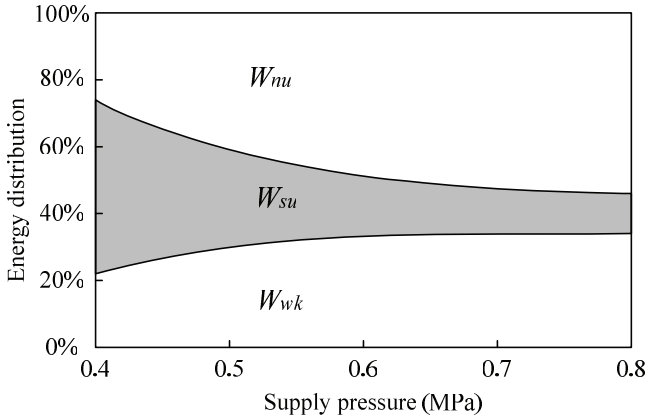


Figure 9: Energy distribution in an ideal meter-out cycle actuation

and then return to the initial position. The speed-controller is installed for controlling the velocity of the piston by raising the back pressure  $p_b$ . When lifting the load, the energy consumption can be given by

$$E_{cyi} = p_s V \ln \frac{p_s}{p_a} \quad (20)$$

where  $V$  is the total volume of the cylinder,  $p_s$  is the supply pressure. Here, air leaks and electricity driving valve are relatively little and neglected. Given  $W_{wk}$  as the mechanical work output, the efficiency can be easily calculated as follows.

$$\eta_{cy} = \frac{W_{wk}}{E_{cyi}} \times 100\% \quad (21)$$

The back pressure  $p_b$  applies a resistance force, which causes an energy loss. This part of energy can be considered as the energy used for velocity control, and represented by  $W_{sc}$ .

Besides  $W_{wk}$  and  $W_{sc}$ , much of supplied energy, denoted by  $W_{nu}$ , is exhausted to the atmosphere without being used when the piston returns to the initial position. Fig. 9 shows the energy distribution in an actuating cycle of meter-out control at different supply pressure settings. It is known that, only about half of supplied energy is effectively used for

doing mechanical work and controlling piston velocity. The rest energy is exhausted without being used. Therefore, taking full of advantage of the exhausted energy is the key to energy-saving design for air cylinders.

#### 4. CONCLUSION

This study introduced the derivation of air power by using typical ideal production and ideal consumption of compressed air. Air power is defined as a property of compressed air and uses a thermodynamics concept to assess the energy of compressed air. It is composed of two parts, transmission power and expansion power. The transmission power is the power required to push the air downstream. The expansion power is the available work due to air expansion. Based on the concept of air power, we analyzed the energy loss and efficiency of a pneumatic system by dividing a pneumatic system to four parts: air production, air cleaning, transmission and pneumatic actuator. In air production, we discussed the adiabatic and isothermal efficiencies of a compressor, and defined the overall efficiency of compressor with air power. In air cleaning, energy efficiency of air filter was investigated and some general data were given. In air transmission, the energy losses due to pressure loss in pipe and air leaks were discussed, and the energy saving effect of a regulator was shown. In air consumption, the energy distribution in an air cylinder was clarified. These efficiency analysis and discussion would be helpful to an energy-saving equipment selection and system design.

#### REFERENCES

1. Energy Efficiency Office: Compressing Air Costs, Good Practice Guide No. 126, United Kingdom, 1994.
2. Cai, Maolin, Kawashima, Kenji, Kagawa, Toshiharu: Power assessment of flowing compressed air, *Journal of Fluids Engineering, Transactions of the ASME*, v 128, n 2, p 402-405, 2006.
3. Kagawa, Toshiharu, Cai, Maolin, Kawashima, Kenji: Energy assessment in pneumatic systems and air power meter, *Power Transmission and Motion Control 2002*, p337-386, 2002.
4. Li, Kam: *Applied Thermodynamics: Availability Method and Energy Conversion*, Taylor & Francis, London, 1995.
5. CADDET: Saving energy with efficient compressed air systems, CADDET Energy Efficiency, Max Brochure 06, 2000
6. CADDET: Saving energy with industrial motors and drives, CADDET Energy Efficiency, Max Brochure 02, 2000
7. Novem: Efficient compressed air system in industry, the Netherlands, 1996
8. Dutch National Team: Compressed air: savings of 30% are quite normal, CADDET Energy Efficiency, Newsletter No.3, 1999





# Sliding Mode Control of an MRI-Compatible Pneumatically Actuated Robot

David B. Comber, Diana Cardona, Robert J. Webster, III, Eric J. Barth

Department of Mechanical Engineering, Vanderbilt University

## ABSTRACT

Magnetically sensitive environments such as MRI scanners preclude the use of traditional electromagnetic actuators. Pneumatic piston-cylinders are well-suited actuators for MRI-guided robots, but the nonlinear dynamics of the working fluid creates a challenging controls problem. Precision control of the actuators is needed for the robot to achieve high targeting accuracy. This paper reports a five degree-of-freedom MRI-compatible robot and a sliding mode controller for high-accuracy position tracking. Mean steady-state errors for needle translation and rotation in free space are 0.006 mm and 0.3 degrees, respectively.

## 1 INTRODUCTION

One of the world's oldest recognized diseases, epilepsy affects more than 50 million patients globally (1). In as many as 30 percent of cases, anticonvulsant medications fail to provide seizure control and the patient is left at risk for sudden unexplained death in epilepsy (1). For these patients, surgical resection of the hippocampus, where seizures commonly begin, is a potentially permanent cure, yet the rate of undertreatment exceeds 50 percent in several developed nations (2-4). Hence, there is a compelling case to develop a minimally invasive alternative to surgery.

There are several motivations for a procedure of this kind to use real-time MRI guidance. This technology can provide high-quality images to locate the tip of a needle in soft tissue, and MRI can be used to monitor the delivery of thermal therapy through MR thermometry. However, the closed bore of the MRI scanner limits access to the patient such that a surgical robot is essentially required to do the procedure.

Because traditional electromagnetic actuators are not MRI-compatible, MRI-guided robots have generally used one of two forms of actuation: piezoelectric or fluid power. It has been demonstrated that pneumatic piston-cylinders do not reduce the signal-to-noise ratio (SNR) of the scanner, while piezoelectric motors have a moderate to severe impact (5). Like pneumatics, hydraulic actuators also can be fully compatible because the fundamental principles of actuation are free from electronics.

For surgical applications, pneumatic actuation has several key advantages over hydraulics. In the event of a system leak, hydraulic fluid creates a mess, even if the fluid is sterile, and these leaks can pose a safety hazard to the patient or clinicians. Furthermore, because standard hydraulic fluids are not sterilizable, water or saline is typically used. These fluids can cause system corrosion, and their poor lubrication properties can lead to stick-slip behavior.

In selecting a type of actuation, it is important to also consider how easily the surgical robot can integrate with existing operating rooms. The gas supply for pneumatic robots can come directly from the nitrogen tanks or instrument air supplies that are already available in hospitals. Thus, while hydraulic robots require an auxiliary supply system, pneumatic robots can easily integrate into existing hospital facilities.

Despite the nonlinearities of compressible gas dynamics, high precision control for pneumatics is feasible and has been demonstrated to sub-millimeter accuracy for MRI-compatible piston-cylinders (6). In needle tip placement experiments, a pneumatic robot for prostate brachytherapy has achieved 0.94 mm rms error (7). This paper reports a 5-dof pneumatic robot design for the treatment of epilepsy by hyperthermal ablation. The design and implementation of a sliding mode controller is described. The accuracies in free space for the robot mechanisms approach the resolution of the encoders.

## 2 MECHANICAL DESIGN

There are several challenging constraints on the design of a surgical robot for intraoperative MRI use. Its dimensions are limited by the bore diameter of the scanner, the allowable materials for parts are restricted to plastics and small amounts of non-magnetic metals, and most electronics must be remotely located several meters away from the scanner. Additionally, the mechanisms must be low friction to allow for precision control of the actuators.

Using these design objectives, a five degree-of-freedom prototype has been designed and manufactured. It is designed to steer an active cannula, a type of continuum robot capable of curving around critical structures in the brain. This needle is made up of three concentric tubes as shown in Fig. 1. An outer, straight titanium tube reaches from the back of the skull to the tail of the hippocampus. The middle and inner tubes are superelastic nitinol. The middle tube is pre-curved to fit the desired needle trajectory for ablation. Thus it requires two degrees of freedom, translation and rotation. Likewise, the innermost nitinol tube is designed to translate and rotate the ablator with a catheter, thus delivering the thermal therapy. In Fig. 1, the active cannula is shown delivering the ablator to the hippocampus, which was modeled in CAD from sagittal and horizontal photographs of a dissected hippocampus.

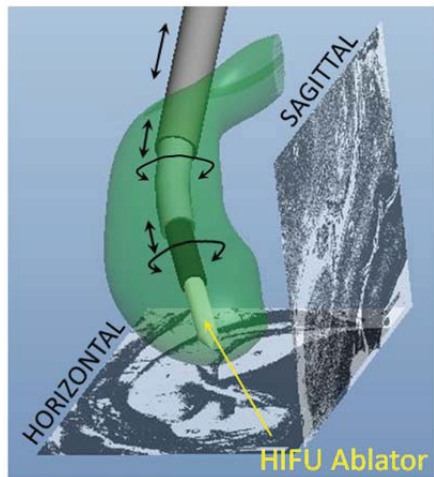


**Figure 1: Degrees of freedom for active cannula to deliver ablator to hippocampus**

### 2.1 Mechanism Design for Needle Translation

For translation of the three needle tubes, a compact, modular design was developed using specialty MRI compatible pneumatic cylinders (Airpot Airpel E9 Non-Magnetic). The concept for translation of the outermost tube is presented in Fig. 2. The piston rod is fixed to the front plate of the robot, which also serves as a needle guide. The needle tube is fixed to a sliding plate, which is supported by a pair of linear bearings and guide shafts. The cylinder is fixed to the sliding plate such that the movement of the cylinder, rather than the piston, provides actuation.

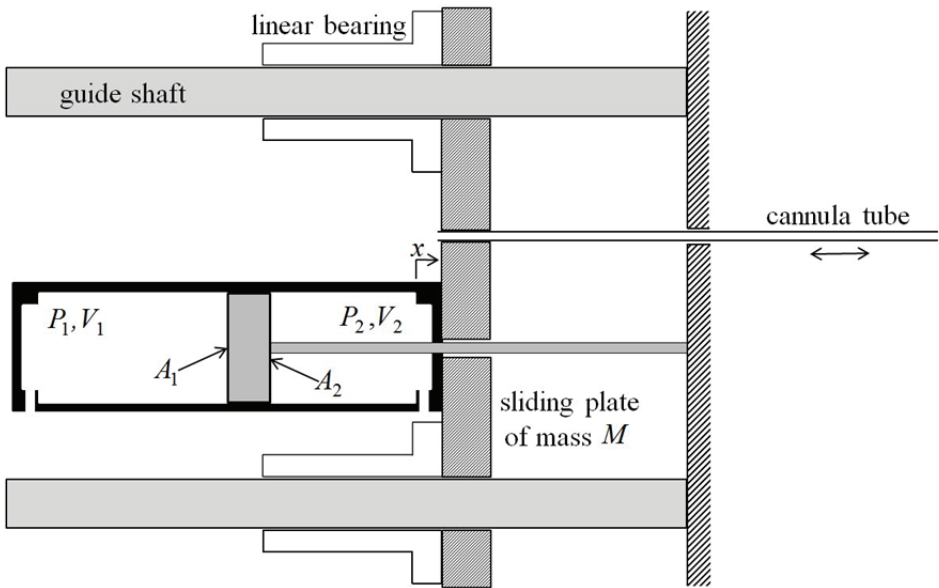


**Figure 2: Sliding plate with piston-cylinder actuator to translate cannula tube**

Similarly, two additional sliding plates translate the middle and innermost tubes. These translations are relative motions, because the piston rods are fixed to the first and the second sliding plates, respectively, as opposed to the stationary front plate with needle guide. The photograph of the robot in Fig. 3 shows the resulting mechanisms for needle tube translation.

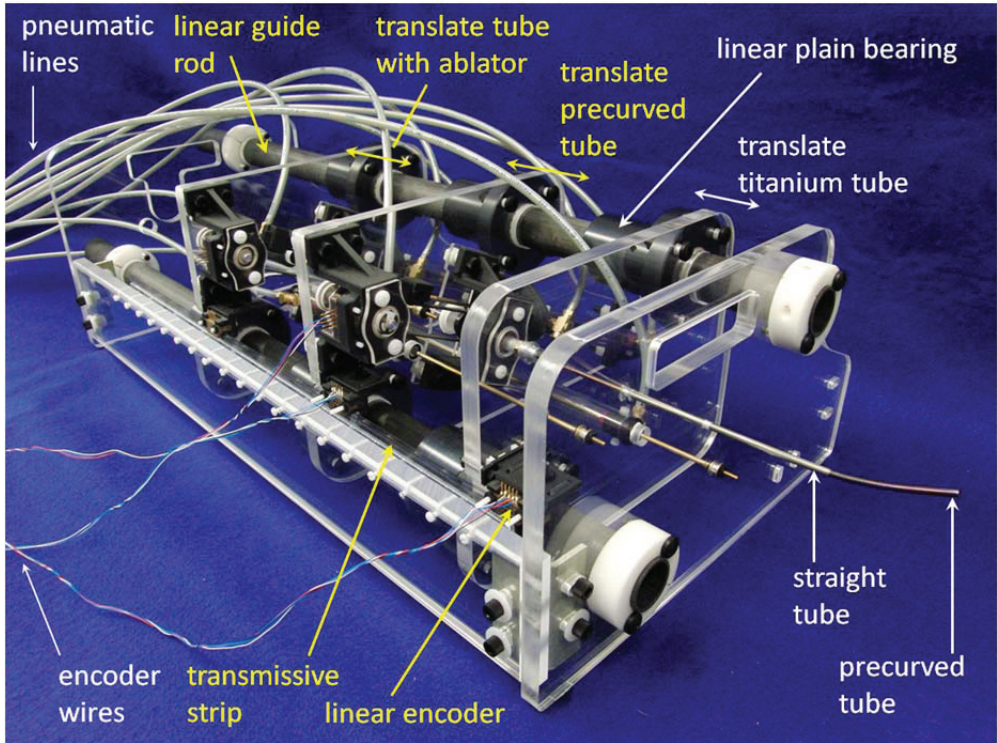


**Figure 3: Photograph of five degree-of-freedom robot**

## 2.2 Mechanism design for needle rotation

A low-friction, compact mechanism was needed to convert the linear motion of the actuator to rotation of the needle tubes. This transmission was designed to mount directly to the sliding plate, thus providing a modular design to both translate and rotate the needle tube. The tube clamps onto a hollow shaft, which is supported by a pair of ball bearings. The shaft and tube rotate when the piston and rod translate the linear portion of a timing belt. A photograph of one transmission on the robot is shown in Fig. 4.

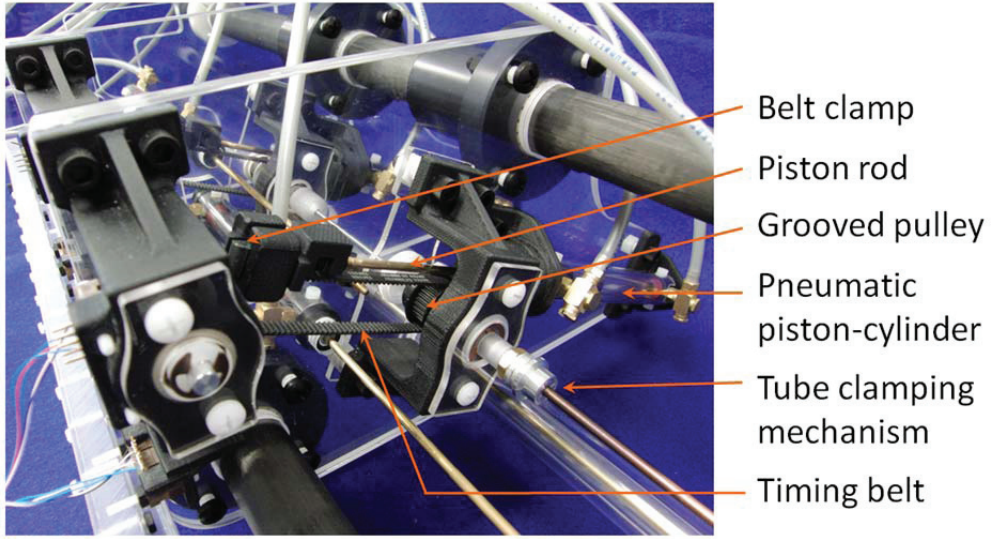


**Figure 4: Transmission for rotary motion of needle tube**

### 3 ROBOTIC SYSTEM DYNAMICS

The system dynamics for the robot include the equations of motion for the linear and rotary mechanisms as well as the gas dynamics for the piston-cylinders. For each actuator, a four-way spool valve controls the mass flow to both cylinder chambers.

#### 3.1 Equation of Motion for the Sliding Plate

Using the quantities defined in Fig. 2, the equation of motion for each sliding plate is readily derived by Newton's Second Law. In Eq. 1, actuation force in the positive  $x$  direction corresponds to chamber 2 pressure  $P_2$  and negative force corresponds to chamber 1 pressure  $P_1$ . Noting that the moving part of the actuator is the cylinder, not the piston, there are an additional two forces due to atmospheric pressure acting upon both ends of the cylinder. Finally, there is an unknown friction force  $F_f$ .

$$M\ddot{x} = P_2A_2 - P_1A_1 + P_{atm}A_1 - P_{atm}A_2 - F_f \quad (1)$$

Defining the piston rod cross-sectional area as  $A_r = A_1 - A_2$ , a simplified equation of motion is obtained. Anticipating that the robustness of the sliding mode controller can provide sufficient compensation for the unknown friction force,  $F_f$  is neglected, and the result is

$$M\ddot{x} = P_2A_2 - P_1A_1 + P_{atm}A_r \quad (2)$$

#### 3.2 Equation of Motion for Tube Rotation Mechanism

A similar equation of motion for the linear-to-rotary mechanism can be derived. The mechanism behavior is more traditional in that the cylinder is stationary while the piston and



rod move. Thus, in keeping with the convention of  $P_2$  denoting the rod-side pressure, the equation of motion is

$$M_{eff}\ddot{x} = P_1A_1 - P_2A_2 - P_{atm}A_r \quad (3)$$

where  $M_{eff}$  is the effective inertia of the piston, rod, timing belt, belt clamp, and rotating components. Again, the friction force has been neglected.

### 3.3 Actuator-Valve Dynamics

A four-way spool valve was selected to control the actuator. For this type of actuator-valve system, a thorough derivation of the gas dynamics model can be found in (8). These dynamics include the thermodynamics of the compressible gas in either cylinder chamber, as well as the mass flow through the valve orifice. Since a percutaneous intervention in the brain is a relatively slow-going operation, the required bandwidth for the robot is low. Therefore, the pressure dynamics are assumed to behave isothermally. From the mathematical model described in (8), the time derivative of each chamber pressure  $\dot{P}_i$ ,  $i = 1, 2$ , is given for the isothermal case as

$$\dot{P}_i = \frac{RT}{V_i} \dot{m}_i - \frac{P_i \dot{V}_i}{V_i} \quad (4)$$

where  $R$  is the specific ideal gas constant and  $T$  is the ambient temperature. To provide a single input from the controller to the 4-way spool valve, the mass flows  $\dot{m}_i$  into the chambers can be expressed as the product of valve orifice area  $A_v$  and area-normalized mass flow  $\Psi_i$ :

$$\begin{aligned} \dot{m}_1 &= -A_v \Psi_1(P_u, P_d) \\ \dot{m}_2 &= A_v \Psi_2(P_u, P_d) \end{aligned} \quad (5)$$

where the area-normalized mass flows are defined as

$$\Psi_1(P_u, P_d) = \begin{cases} \Psi(P_1, P_{atm}) & \text{for } A_v \geq 0 \\ \Psi(P_s, P_1) & \text{for } A_v < 0 \end{cases} \quad \text{and} \quad \Psi_2(P_u, P_d) = \begin{cases} \Psi(P_s, P_2) & \text{for } A_v \geq 0 \\ \Psi(P_2, P_{atm}) & \text{for } A_v < 0 \end{cases} \quad (6)$$

The area-normalized mass flow is a function of the pressures,  $P_u$  and  $P_d$ , upstream and downstream of the orifice, given in (9) as

$$\Psi(P_u, P_d) = \begin{cases} \frac{C_1 C_f P_u}{\sqrt{T}} & \text{if } \frac{P_d}{P_u} \leq C_r \text{ (choked)} \\ \frac{C_2 C_f P_u}{\sqrt{T}} \left( \frac{P_d}{P_u} \right)^{1/k} \sqrt{1 - \left( \frac{P_d}{P_u} \right)^{(k-1)/k}} & \text{otherwise (unchoked)} \end{cases} \quad (7)$$

For the isothermal case, the temperature  $T$  of the flow is equal to ambient. The ratio of specific heats is  $k = c_p/c_v$ , and  $C_f$  is the dimensionless discharge coefficient dependent on valve orifice geometry. The pressure ratio  $C_r$  defines the flow as choked or unchoked, and the constants are given by

$$C_r = \left( \frac{2}{k+1} \right)^{\frac{k}{k-1}} \quad (8)$$

$$C_1 = \sqrt{\frac{k}{R} \left( \frac{2}{k+1} \right)^{(k+1)/(k-1)}} \quad \text{and} \quad C_2 = \sqrt{\frac{2k}{R(k-1)}} \quad (9)$$

The gas dynamics are fully described by Eqs. 4 to 9 and relate the spool valve command to equation of motion given by Eq. 2. For control of the actuators and mechanisms described by Eq. 3, the sign of the valve command is opposite that which appears in Eq. 5, and thus the direction of mass flow is opposite of that in Eq. 6.

## 4 CONTROL DESIGN

A robust controller was required in order to handle the nonlinearity of the gas dynamics as well as the uncertainty of the friction force. Sliding mode control (SMC) is particularly well suited to provide robust control of nonlinear systems with unknown parameters. In prior work, sub-millimeter precision SMC control was achieved for the same type of MRI-compatible actuators now used on the 5-dof robot (6).

### 4.1 Control Law

A suitable SMC control law was formulated by choosing a third-order sliding surface acting on the integral of the position error:

$$s = \left( \frac{d}{dt} + \lambda \right)^3 \int e = \ddot{e} + 3\lambda\dot{e} + 3\lambda^2 e + \lambda^3 \int e \quad (10)$$

where  $e = x - x_d$ ,  $x_d$  is the desired position, and  $\lambda$  is the desired closed-loop poles of the error dynamics. The system dynamics are third-order in position, as the affine control variable  $A_v$  appears by taking the time derivative of Eq. 2 and substituting in Eq. 4 to obtain

$$M\ddot{x} = A_2 \left( \frac{RT}{V_2} \dot{m}_2 - \frac{P_2 \dot{V}_2}{V_2} \right) - A_1 \left( \frac{RT}{V_1} \dot{m}_1 - \frac{P_1 \dot{V}_1}{V_1} \right) \quad (11)$$

To achieve stable error dynamics, the Lyapunov candidate function  $V = \frac{1}{2}s^2$  was chosen, and its time derivative,  $\dot{V} = s\dot{s}$ , was set equal to a negative definite function of choice. The function  $\dot{V}_{desired} = -\eta s \cdot \text{sat}(s)$  is a desirable choice because it forces the  $s$  dynamics to exhibit a smooth, exponential decay behavior:



$$\dot{s} = -\eta \text{sat}(s) \quad (12)$$

where the saturation function  $\text{sat}(s)$  is bounded at  $\pm 1$ , and  $\eta$  is the robustness constant of choice. The control law was obtained by taking the time derivative of Eq. 10, setting the result equal to Eq. 12, and substituting in Eq. 11. Solving the result for the command  $A_v$ :

$$A_v = \frac{\ddot{x}_d + f(P_i, V_i, \dot{x}) - 3\lambda\ddot{e} - 3\lambda^2\dot{e} - \lambda^3e - \eta\text{sat}(s)}{g(V_i, \Psi_i)} \quad (13)$$

where the functions  $f$  and  $g$  are given by

$$f(P_i, V_i, \dot{x}) = \frac{1}{M} \left( A_1^2 \frac{P_1}{V_1} + A_2^2 \frac{P_2}{V_2} \right) \dot{x} \quad (14)$$

$$g(V_i, \Psi_i) = \frac{RT}{M} \left( \frac{A_1}{V_1} \Psi_1 + \frac{A_2}{V_2} \Psi_2 \right) \quad (15)$$

In Eq. 14, velocity has been introduced by noting that  $\dot{V}_1 = -A_1\dot{x}$  and  $\dot{V}_2 = A_2\dot{x}$ . The control law provides a Lyapunov-stable closed-loop error dynamics for the sliding mode controller.

#### 4.2 Control Electronics and Settings

To make the electronics MRI-compatible, five optical encoders were used for sensing linear and rotary positions of the actuators. A linear transmissive strip with 197 lines per cm (500 lines per inch) is used with three linear encoders to sense position of the three sliding plates. Two rotary encoders with 1250 counts per revolution provide angular position of the needle tubes. The encoders provided a clean signal that was digitally differentiated to provide velocity and acceleration, with second-order low pass filters at 100 Hz. For each actuator, additional electronics were one Festo 4-way spool valve and two 0-16 bar Festo pressure sensors to measure both chamber pressures.

Control accuracy was also improved through careful measurement of three dead volumes in the system: the pressure sensor with its fitting and the entry ports to each of the two cylinder chambers, with their fittings. Measurements were obtained using a syringe with 0.01 mL increments and isopropyl alcohol. This fluid has a low surface tension and thus it provided an accurate measurement because very few air bubbles were formed.

## 5 RESULTS

The controller was tested on the robot with the needle moving in free space. Position tracking of the sliding plate is shown in Fig. 5, where the reference signal is a 0.25 Hz square wave of 30 mm peak-to-peak amplitude. For this test the supply pressure of 310 kPa gage (45 psi) was capable of producing a maximum force of 21.0 N (4.72 lbf). The mean steady-state error was 6 microns, which is one half the resolution of the linear encoder when

it is read in quadrature. Shown in Fig. 6, the steady-state error appears to be less than the encoder resolution, but this is simply because the reference position is not an exact multiple of the encoder counts. Optimal values for the control parameters were  $\lambda = 20 \text{ Hz}$  and  $\eta = 2 \text{ m}^3/\text{sec}$ .

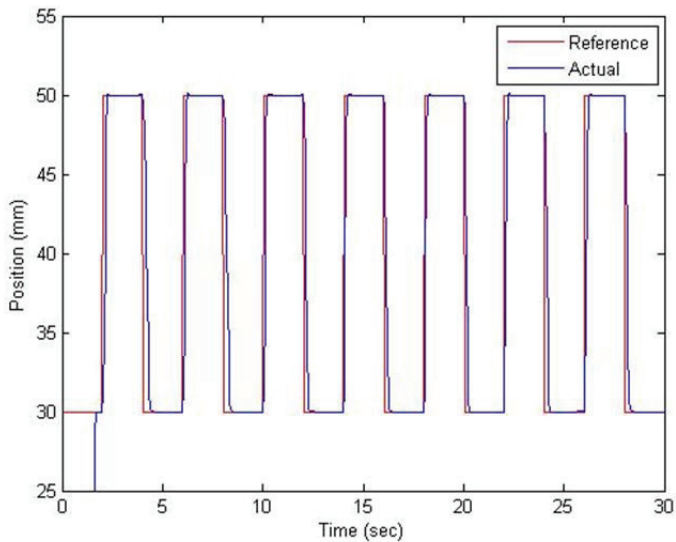


Figure 5: Position tracking for translation of sliding plate

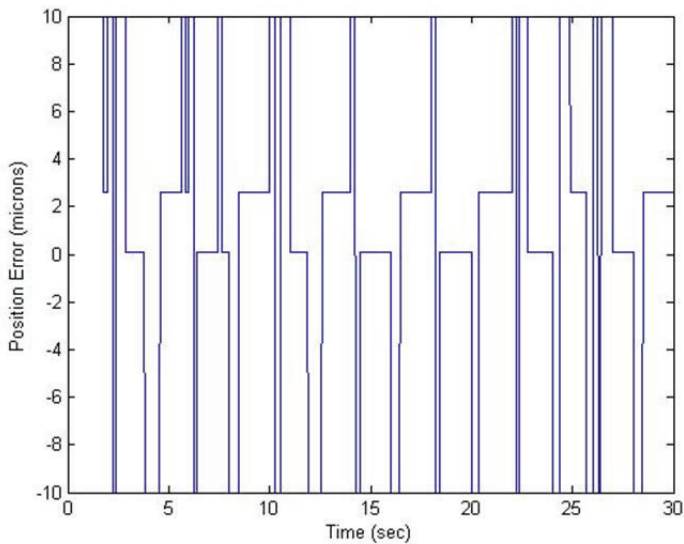
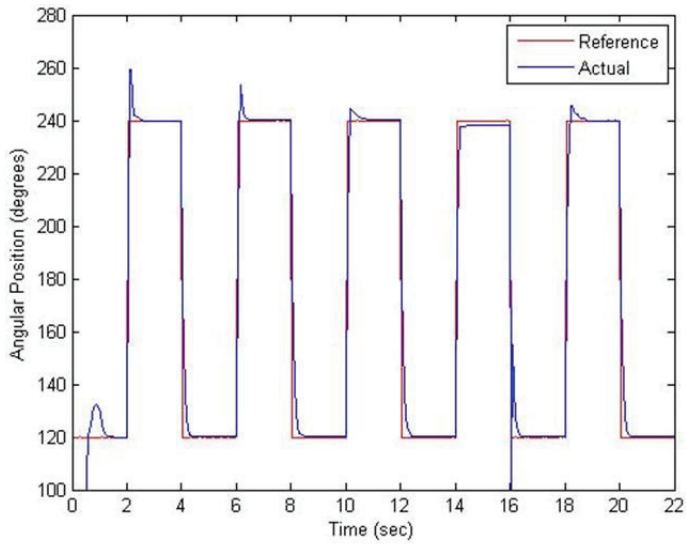
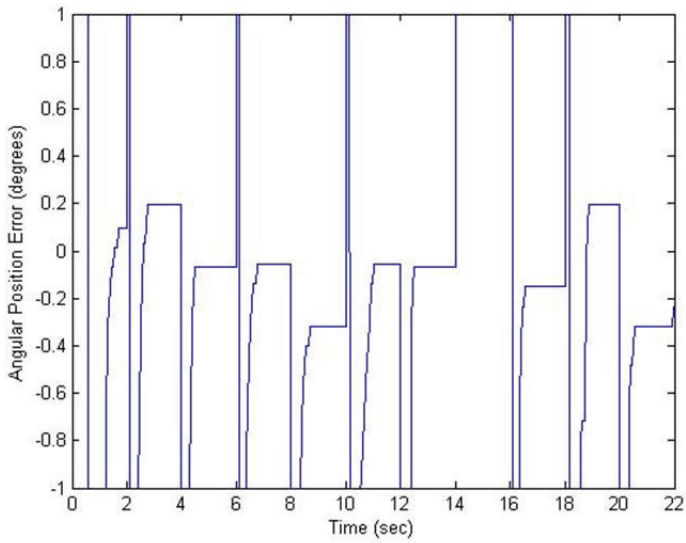


Figure 6: Steady-state position error for translation of sliding plate

Similarly, controller performance for rotation of the needle tube is shown in Figs. 7 and 8. The reference was a 0.25 Hz square wave with peak-to-peak amplitude of 120 degrees. The controller achieved a mean steady-state error of 0.3 degrees with the control parameters tuned to  $\lambda = 15$  Hz and  $\eta = 2$  m<sup>3</sup>/sec.



**Figure 7: Angular position tracking for rotation of needle tube**



**Figure 8: Steady-state angular position error for rotation of needle tube**

## 5 CONCLUSION

An ideal solution for MRI-compatible robots, pneumatic actuators can easily integrate with the nitrogen or instrument air supply in hospitals. As the supply is sterile and inert, leakage is not a safety concern. Furthermore, pneumatic actuators do not reduce the scanner SNR. In light of these advantages, a 5-dof robot was designed and built to steer an active cannula by pneumatic actuation. The robot provides both translation and rotation to needle tubes by a modular design, such that additional tubes could easily be added to the cannula. Thus, while the robot was originally designed for a specific clinical application, the design could easily be modified for treatment of tumors or other disorders in the brain.

Using sliding mode control, high accuracy position tracking has been achieved for both the translation and rotation actuators. Since typical MRI resolutions are 1 mm, the reported accuracy of the controller suggests the robot has the potential to produce excellent results for needle tip targeting experiments, which will be conducted in future research.

## REFERENCES

- (1) Kwan, P. and Brodie, M. J., 2000, "Early Identification of Refractory Epilepsy," *N Engl J Med*, **342**(5), pp. 314-319.
- (2) de Flon, P., Kumlien, E., Reuterwall, C., and Mattsson, P., 2010, "Empirical Evidence of Underutilization of Referrals for Epilepsy Surgery Evaluation," *European Journal of Neurology*, **17**, pp. 619-625.
- (3) Engel, J., Jr., Wiebe, S., French, J., Sperling, M., Williamson, P., Spencer, D., Gumnit, R., Zahn, C., Westbrook, E., and Enos, B., 2003, "Practice Parameter: Temporal Lobe and Localized Neocortical Resections for Epilepsy," *Epilepsia*, **44**(6), pp. 741-751.
- (4) Lhatoo, S. D., Solomon, J. K., McEvoy, A. W., Kitchen, N. D., Shorvon, S. D., and Sander, J. W., 2003, "A Prospective Study of the Requirement for and the Provision of Epilepsy Surgery in the United Kingdom," *Epilepsia*, **44**(5), pp. 673-676.
- (5) Fischer, G. S., Krieger, A., Iordachita, I., Csoma, C., Whitcomb, L. L., and Fichtinger, G., 2008, "MRI Compatibility of Robot Actuation Techniques – A Comparative Study," *Int Conf Medical Image Computing and Computer Assisted Intervention*, New York, NY, **5242**, pp. 509-517.
- (6) Comber, D. B. and Barth, E. J., 2011, "Precision Position Tracking of MR-Compatible Pneumatic Piston-Cylinder Using Sliding Mode Control," DSCC2011-5960, *Proc. DSCC & Bath/ASME Symp. Fluid Power and Motion Control*, Arlington, VA, pp. 1-7.
- (7) Fischer, G., Iordachita, I., Csoma, C., Tokuda, J., DiMaio, S., Tempany, C., Hata, N., and Fichtinger, G., 2008, "MRI-Compatible Pneumatic Robot for Transperineal Prostate Needle Placement," *IEEE/ASME Trans. Mechatronics*, **13**(3), pp. 295-305.
- (8) Richer, E. and Hurmuzlu, Y., 2000, "A High Performance Pneumatic Force Actuator System: Part 1—Nonlinear Mathematical Model," *ASME J. Dyn. Syst., Meas. Control*, **122**(3), pp. 416-425.
- (9) Ben-Dov, D., and Salcudean, S., 1995, "A Force-Controlled Pneumatic Actuator," *IEEE Trans. Robotics & Automation*, **11**(6), pp. 906-911.



## Control II



# A Combined Multiple Inner Loop Control Strategy for an Electro-Hydraulic Actuator

**Mohammed A. El Sayed and Saeid Habibi**

Center for Mechatronics and Hybrid Technology,  
Mechanical Engineering Department, McMaster University,  
abugabma@mcmaster.ca, habibi@mcmaster.ca

## ABSTRACT

This article presents the development of a combined multiple inner-loop (MIL) control strategy and multiple sliding mode control (MSMC) strategy for improving the performance of hydrostatic actuation systems. In these actuators, the presence of nonlinearities associated with pump/motor static friction and backlash, pressure drop in the piping system, and non-linear friction at the load have a significant effect on the performance and positional accuracy of the system.

For trajectory tracking applications, the MSMC control strategy incorporated a double sliding mode controllers in an inner/outer loop format, where the secondary (inner-loop) sliding mode controller provided an additional control input that compensated for the uncertainty in the friction characteristics. The purpose of the combined method is to include additional feedback from the motor in the MSMC strategy to enhance its accuracy in trajectory tracking applications. A differential velocity/position feedback was added in an inner loop format. Experimental results supported by theoretical analysis indicated that the added control input proved effective in further enhancing the trajectory tracking positional accuracy.

## 1 INTRODUCTION

Hydraulic systems are commonly used for actuation and manipulation of heavy loads. They are found in a variety of different industries, such as in automotive, manufacturing, robotics, construction, and aerospace. Conventional hydraulic systems use a centralized constant pressure supply system. Pressurized fluid is then channeled to actuators using servo-valves. The advantages of these systems are their high torque to mass ratio, and the ability to control speed and direction with relative accuracy, [1]. However, according to [2, 3, 4], there are also disadvantages such as the requirement of a bulky centralized supply, leakage, noise, and reduced energy efficiency due to orifice flow and the requirement for maintaining a constant supply pressure.

Electro-Hydrostatic Actuation systems (EHA) alleviate many of the above mentioned short-



comings of servo-valve controlled hydraulic systems. In the EHA position control is achieved by regulating the pumping action. Here, a fixed or a variable displacement pump can be used to move oil from one chamber of the actuator to the other. Fixed displacement gear pumps have been successfully used for precision control of inertial loads. Load manipulation is achieved by changing the speed and the direction of the pump with an electrical servomotor. A high precision EHA was prototyped in [2, 5, 6] and has achieved sub-micron resolution. In this EHA, two control loops were used. These consisted of an outer-loop proportional controller and a high gain inner-loop pump velocity controller. The later was reported to desensitize the system to dead-band caused by friction at the pump motor interface. In [7], a gain scheduled proportional controller, and a fuzzy controller were applied to the outer position control loop to improve the positional accuracy. A further study involved re-tuning of the gain scheduled proportional controller to improve its performance in trajectory tracking applications in [8], and reported that chatter is observed in both load velocity and acceleration, which is linked to the nonlinear behavior of friction at the load, [9, 10, 11, 12]. It was stated that using sliding mode control suppresses the chattering effect, thus resulting in improved velocity and acceleration profiles.

In [8], sliding mode control was proven as a very effective tool in suppressing the friction induced limit cycle oscillations. The effectiveness of this strategy is dependent on adjusting the smoothing boundary layer thickness for the switching component of the control signal. However, it should be noted that the role of the smoothing boundary layer has been to date targeted to eliminating chatter caused by the switching action and uncertainties in sliding mode control, [13, 14, 15, 16]. Larger system uncertainties require a larger boundary layer thickness in order to effectively eliminate the chatter. Because of the correspondence of the boundary layer thickness with the amount of error in trajectory tracking, a larger boundary layer thickness would increase the amount of error present in the positional accuracy; a tighter boundary layer thickness on the other hand, will improve the positional accuracy at the expense of inducing chatter.

In [17], a new form of sliding mode control with a secondary inner-loop was introduced. This inner-loop provided a secondary boundary layer thickness that added an additional degree of freedom and was effective in overcoming static friction. Theoretical analysis along with simulation and experimental results confirmed the effectiveness of this strategy in suppressing the friction induced limit cycle oscillations, while maintaining the level of accuracy.

Despite the MSMC strategy's success in improving the EHA's positional accuracy, further improvements are possible because the MSMC only incorporated feedback from the load side. Accordingly, it is expected that combining the Multiple Inner Loop (MIL), and the Multiple Sliding Mode Control (MSMC) strategies would further enhance the EHA's performance. The combination will provide an additional control input based on the differential velocity and differential position feedback, which will improve the accuracy by providing additional compensation for the free-play, and the friction dead-band. In this paper the combined control strategy is presented and applied to on the experimental setup to test its effectiveness.

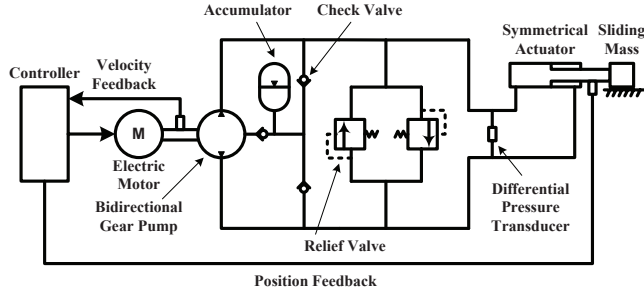


Figure 1: The EHA circuit diagram,[7]

## 2 THE ELECTRO-HYDRAULIC ACTUATOR

In this paper the EHA system of Fig. 1 will be used with its design details given in [6]. This system consists of an electric motor, a gear pump, a symmetrical actuator, pressure and position sensors, an accumulator, pressure relief sub-circuit, and optional filtering sub-circuit. The pump only operates when control action is needed, and thus the system has the advantage of an overall better energy efficiency in comparison to swash plate hydrostatic and valve controlled hydraulic systems, [6]. However, volumetric efficiency is compromised at very low pump speeds, and a dead-band is present, resulting in an effect similar to backlash. This problem was overcome by the use of a high gain pump-speed inner loop controller. As for the outer positional control loop, a simple proportional control strategy was used, and a final resolution of 100 nm was reported, [6].

A detailed derivation of the EHA dynamic equations is presented in [6]. Where, a linear simulation model of the EHA was constructed by considering its components as follows:

### 2.1 Linear Symmetrical Actuator

As previously stated the dynamic significance of the accumulator flow can be assumed negligible, resulting in a simplification of the model such that pump inlet/outlet flows are assumed to be equal to the outlet/inlet flows of the piston, i.e.  $Q_a = Q_1$  and  $Q_b = Q_2$ . Where  $Q_a$  and  $Q_b$  denote pump in/outlet flows and,  $Q_1$  and  $Q_2$  are those of the linear symmetrical piston.

The piston has an area of  $A$ , and the piston rod is directly connected to a mass of  $M$  that moves on a horizontal slide. A friction force  $f_{friction}(\dot{x})$  is present and will be characterized by using Chinniah's quadratic friction model as defined by equation (1).

$$f_{friction} = \begin{cases} B\dot{x} + (B_2\dot{x}^2 + B_0) & \dot{x} > 0, \\ B\dot{x} - (B_2\dot{x}^2 + B_0) & \dot{x} < 0, \end{cases} \quad (1)$$

note that  $B, B_0, B_2$  are the coefficients of the quadratic function. Chinniah's friction model for the EHA prototype reported in [18] and [6] is illustrated by Figure 2. It should be further noted that Chinniah's friction model will be used in the development of the computer simulation model. However, for the purpose of obtaining a linear transfer function of the EHA,

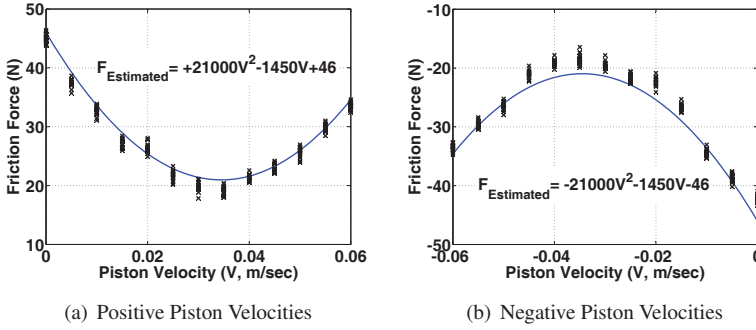


**Figure 2: Quadratic Friction Model,[18].**

the friction model will be substituted with a linear friction model, as defined by the following equation.

$$f_{friction}(\dot{x}) = B\dot{x} + \tilde{f}_{friction}, \quad (2)$$

where  $B$  is the viscous friction coefficient and  $\tilde{f}_{friction}$  is the uncertainties associated with the linearized friction model.

Equations (3) to (7) summarize the equations of motion of the linear symmetrical actuator, and are used to derive the transfer function  $G_{cylinder}$  relating load flow to actuator force given by equation (8). The hydraulic cylinder/mechanical load block diagram is presented by Figure 3, and the actuator flow equations are:

$$q_a = A\dot{x} + \frac{A(x_o + x)}{\beta_e} \frac{dp_1}{dt} + Lp_1, \quad (3)$$

$$q_b = A\dot{x} - \frac{A(x_o - x)}{\beta_e} \frac{dp_2}{dt} - Lp_2, \quad (4)$$

where  $x_o$  is the actuator mean position,  $p_1$  and  $p_2$  are the actuator chambers pressures,  $\beta_e$  is the hydraulic bulk modulus, and  $L$  is the Leakage coefficient. For a load directly attached to the actuator, the load equation is:

$$f = (p_1 - p_2)A = M\ddot{x} + f_{friction}(\dot{x}). \quad (5)$$

For:

$$q_L = \frac{q_a + q_b}{2}. \quad (6)$$

Since  $\frac{dp_a}{dt} \approx \frac{dp_1}{dt}$ ,  $\frac{dp_b}{dt} \approx \frac{dp_2}{dt}$ , and due to the symmetry of the actuator  $\frac{dp_1}{dt} \approx -\frac{dp_2}{dt}$  [[6]], Then from equations (3), (4), and (5):

$$q_L = A\dot{x} + \frac{x_o}{2\beta_e} \dot{f} + \frac{L}{2A} f. \quad (7)$$

From equations (3) to (7), then the transfer function linking the cylinder load flow to its output force is obtained as:

$$G_{cylinder} = \frac{1}{\left(\frac{x_o}{2\beta_e}\right)p + \left(\frac{L}{2A}\right)} = \frac{F}{Q_L - Apx}. \quad (8)$$

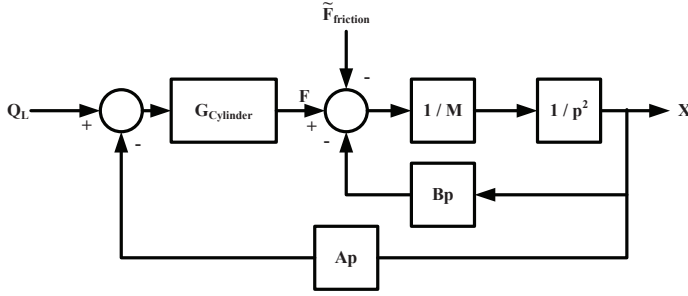


**Figure 3: Hydraulic Cylinder/Mechanical Load Block Diagram**

## 2.2 Hydraulic Pump

The hydraulic pump converts the mechanical energy, provided by the electric motor, to fluid flow. A bidirectional fixed displacement gear pump was used in the EHA system. The pump had three ports. Two large diameter input/output ports are directly connected to the symmetrical linear actuator by solid tubing. The third port is a case drain provided for pump leakage. It should be noted that the EHA's precision is dependant on the pump volumetric displacement. Thus, a smaller volumetric displacement provides a higher resolution, and a lower rod speed. This presents a trade-off between maximum speed and positioning resolution.

Equation (9) represents the hydraulic pump element and is used in conjunction with equations (5), and (7) to derive the hydraulic circuit transfer function  $G_H$  given by equation (10). The hydraulic circuit/mechanical load block diagram is presented by Figure 4.

$$q_L = D_p \omega_p - \frac{\xi}{A} f - \frac{x_o}{2\beta_e} \dot{f} - 2\xi p_{pipe}, \quad (9)$$

$$G_H = \frac{1}{\frac{x_o}{\beta_e} p + \frac{\frac{L}{2} + \xi}{A}} = \frac{F}{D_p \omega_p - Apx - 2\xi p_{pipe}}, \quad (10)$$

where  $q_L$  is the load hydraulic flow,  $D_p$  is the hydraulic pump volumetric displacement,  $\omega_p$  is pump rotational velocity, and  $\xi$  is the pump cross-port leakage coefficient.

## 2.3 Electric Motor

A high performance brush-less DC servo motor is used to drive the hydraulic pump. The model of the motor is well established and presented here in a summarized form, [19, 20].

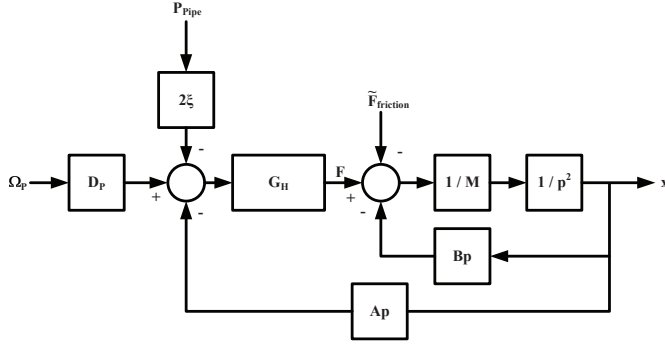


**Figure 4: Hydraulic Circuit/Mechanical Load Block Diagram**

The following equations characterizes the motor dynamics:

$$i_c = G_{e1}(v_c - K_\omega \omega_m), \quad (11)$$

$$G_{e1} = \frac{\frac{1}{R_c}}{\frac{L_c}{R_c}p + 1}, \quad (12)$$

$$t_m = K_e i_c, \quad (13)$$

$$t_m = J_{pm} \dot{\omega}_m + (K_{pvisc} + K_{fric}) \omega_m + t_{DB} + D_p(p_a - p_b), \quad (14)$$

where  $\omega_m$ ,  $i_c$ ,  $v_c$ ,  $L_c$ ,  $R_c$ ,  $K_e$ ,  $K_\omega$ ,  $K_{fric}$ ,  $K_{pvisc}$  are the electric motor speed, current, voltage, resistance, inductance, torque constant, back emf, the coefficient of friction, and the coefficient of viscosity respectively,  $J_{pm}$  is the combined motor and pump inertia,  $t_{DB}$  is the static friction torque, and  $P_a$ ,  $P_b$  are the pump port pressures. The electric motor/pump block diagram is shown in Figure 5. From equations (11) to (14), the transfer function of the electrical motor can be obtained as:

$$G_{e2} = \frac{1}{J_{pm}p + (K_e K_\omega G_{e1} + K_{pvisc} + K_{fric})} = \frac{\Omega_m}{K_e G_{e1} V_c - F \frac{D_p}{A} - 2D_p P_{pipe} - t_{DB}}. \quad (15)$$

By combining the electrical motor and the hydraulic circuit block diagrams, the complete EHA block diagram can be obtained as shown in Figure 6.

### 3 MULTIPLE INNER-LOOP CONTROL (MIL)

Further to [21], the control strategy of the EHA prototype involves two control loops: a proportional control outer loop, and a high-gain proportional/integral inner loop controller as shown in Fig. 7. This control strategy desensitizes the system to dead-band caused by friction at the pump motor interface as reported in [6].

According to [22], the effect of free-play associated with backlash in gear trains occurs when the system is at rest or when it is changing direction. Accordingly, within the dead zone

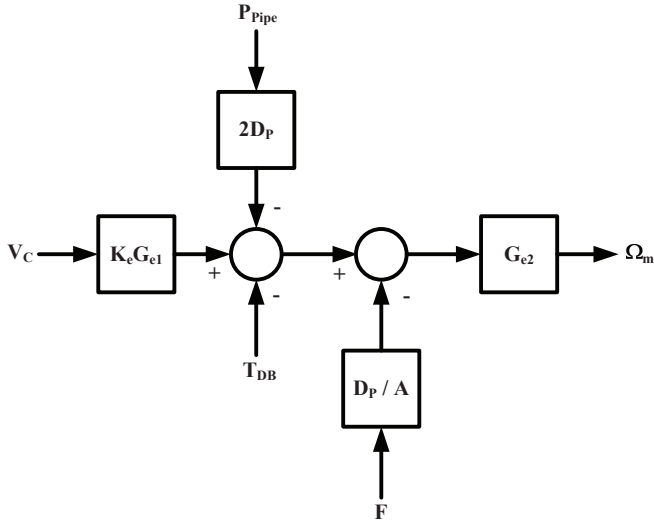


**Figure 5: Electric Motor/Pump Block Diagram**

associated with backlash both the position and velocity of the driving motor and the load would respectively differ. In such a case, a feedback signal that would amplify and correct for the differential velocity and position within the dead-zone region constitutes the essence of a second inner-loop feedback strategy as proposed in [23]. The inner-loop feedback term is constructed by using both the differential position and velocity between the load and the motor. Figure 8 represents the EHA block diagram with the proposed control strategy highlighted.

#### 4 MULTIPLE SLIDING MODE CONTROL (MSMC)

Sliding mode control is known for its ability to provide robustness and stability in the presence of uncertainties. [24] proposed a discrete sliding mode control method for nonlinear systems with uncertainties that do not satisfy the matching condition. Later in [25], this design was extended for linear systems and was reported to provide good results. Wang adopted Misawa's control technique to design a controller for an EHA prototype for trajectory tracking applications, [8]. Using an accurate model of the EHA's nonlinear friction in the controller design, his results indicated that the controller was able to provide accurate tracking while suppressing the chatter in acceleration and velocity profiles. In [17], it is shown Wang's controller is susceptible to high frequency limit cycle oscillations when the uncertainty associated with the friction characteristics increased. This oscillation is more noticeable in the acceleration profile, as shown in figure 9. Figure 10 shows the simulation results reported in [17], where it is clearly evident that chattering can be eliminated by expanding the SMC boundary layer thickness, at the expense of reducing the positional accuracy.

The results indicate that a trade off between tracking accuracy and chatter elimination exists

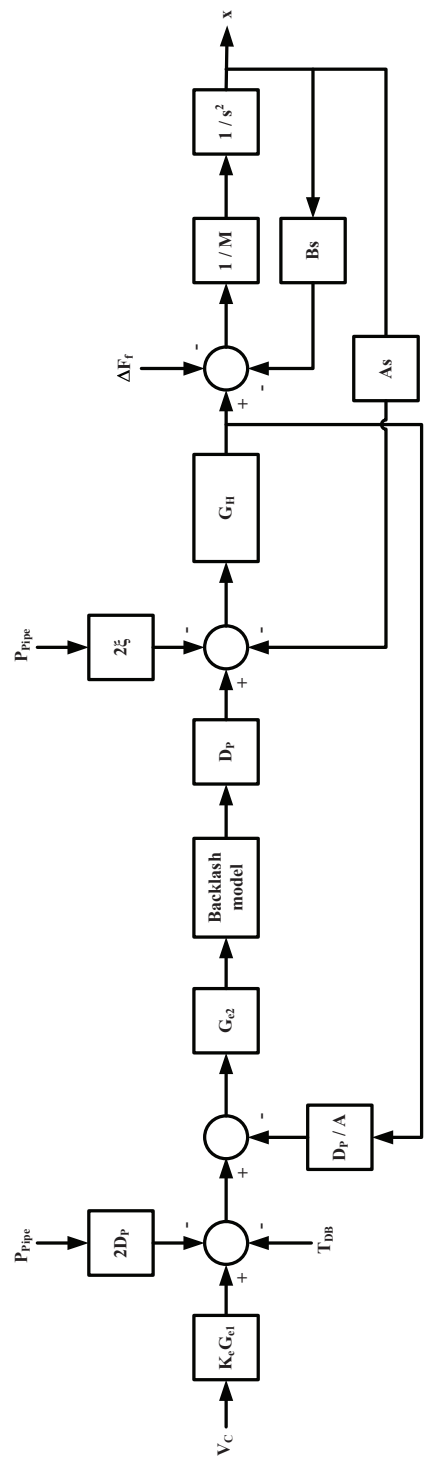


Figure 6: Complete EHA Block Diagram

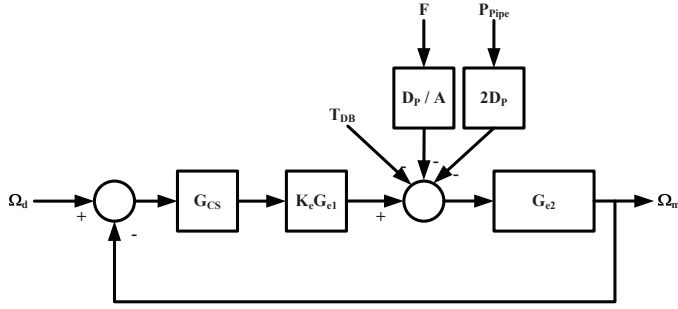


Figure 7: Electric motor inner control loop [6]

in SMC. This trade off is attributed to the use of a single boundary layer  $\psi$ , associated with all tracking errors (position, velocity, and acceleration) grouped together. The boundary layer is defined for  $s = C_1 \times \tilde{x} + C_2 \times \dot{\tilde{x}} + C_3 \times \ddot{\tilde{x}}$  that represents the distance to the sliding surface. Since friction uncertainty has a more significant effect on the acceleration tracking error, the boundary layer has to be expanded to accommodate for this uncertainty. Chattering in the acceleration tracking and its associated errors is orders of magnitude higher than those of position and velocity, thus overshadowing their consideration. To remove all chattering, the boundary layer  $\psi$  has to be expanded to accommodate acceleration induced chattering and disproportionately compromises the tracking error in both position and velocity profiles.

To provide greater flexibility in dealing with this effect a secondary inner-loop SMC controller was proposed in [17] to improve position and velocity accuracy while suppressing chattering that is most prevalent in acceleration trajectory. The secondary controller is a reduced order controller, such that it uses the error in position and velocity to derive a secondary sliding surface  $s_2 = C_1 \times \tilde{x} + C_2 \times \dot{\tilde{x}}$  with a secondary boundary layer  $\psi_2$ . The output of this controller is then used to apply a correction to the desired acceleration trajectory to compensate for the inaccuracy in the friction model. It can be used to eliminate the chatter and compensate for static friction without compromising the positional accuracy. In the next section, the mathematical representation of this strategy will be presented.

Consider a single input linear dynamical system of the form shown in equation (16):

$$\mathbf{x}_{k+1} = \hat{\Phi} \mathbf{x}_k + \hat{\mathbf{G}} u_k + \mathbf{w}_k. \quad (16)$$

It is assumed that the terms  $\hat{\Phi} \in \mathbb{R}^{n \times n}$  and  $\hat{\mathbf{G}} \in \mathbb{R}^{n \times 1}$  are known, and that the uncertainties satisfy the matching conditions, where the system uncertainties  $(\tilde{\Phi}, \tilde{\mathbf{G}})$  and the system noise  $\mathbf{v}_k \in \mathbb{R}^{n \times 1}$  can all be lumped into a single vector function  $\mathbf{w}_k \in \mathbb{R}^{n \times 1}$ . Furthermore, the uncertainties  $(\mathbf{w})$  are assumed to be bounded such that:

$$|\mathbf{C} \mathbf{w}| \leq \gamma. \quad (17)$$

In trajectory tracking mode, the objective is to force the system to follow a desired trajectory  $\mathbf{x}_d$ , this objective can be restated as driving the tracking error  $(\mathbf{e}_k = \mathbf{x}_{d,k} - \mathbf{x}_k)$  as close as





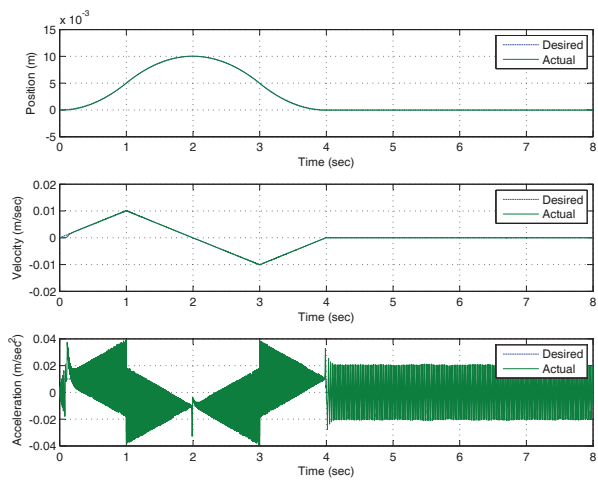


**Figure 9: EHA SMC Simulation Results, Inaccurate Friction, and Small Boundary Layer Thickness**

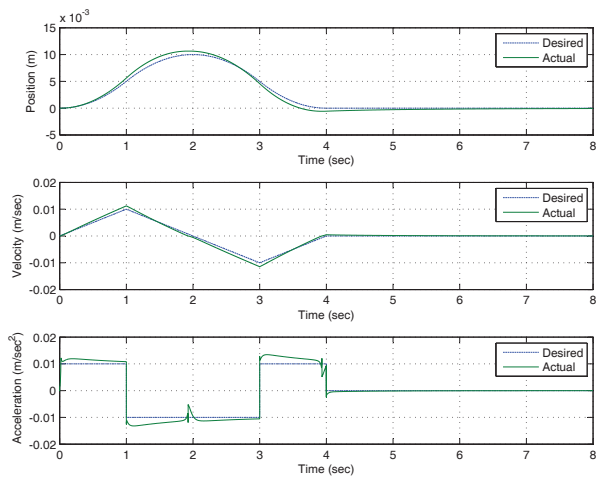


**Figure 10: EHA SMC Simulation Results, Inaccurate Friction, and Large Boundary Layer Thickness**

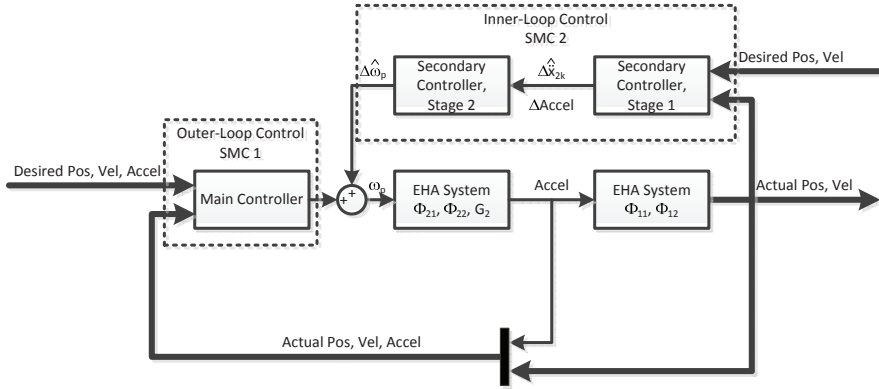


**Figure 11: MSMC Strategy Basic Structure**

possible to zero. A sliding manifold is defined as:

$$\Sigma = \{\mathbf{e}_k | s_k = \mathbf{C}\mathbf{e}_k = 0\}, \quad (18)$$

where  $\mathbf{C} \in \mathbb{R}^{1 \times n}$  is the sliding surface parameter vector, and with a smoothing boundary layer:

$$\Psi = \{\mathbf{e}_k | |s_k| = |\mathbf{C}\mathbf{e}_k| \leq \psi\}. \quad (19)$$

Consider a linear dynamical system of the form shown of equation (16). Partitioning the system to reflect the system inputs such that:

$$\mathbf{C} = (\mathbf{C}_1 \quad \mathbf{C}_2), \quad (20)$$

$$\mathbf{x} = (\mathbf{x}_1^T \quad x_2^T)^T, \quad (21)$$

$$\hat{\Phi} = \begin{pmatrix} \hat{\Phi}_{11} & \hat{\Phi}_{12} \\ \hat{\Phi}_{21} & \hat{\Phi}_{22} \end{pmatrix}, \quad (22)$$

$$\hat{\mathbf{G}} = \begin{pmatrix} 0_{n-1} \\ \hat{G}_2 \end{pmatrix}, \quad (23)$$

where  $\mathbf{x}_1 \in \mathbb{R}^{n-1 \times 1}$ ,  $x_2 \in \mathbb{R}^{1 \times 1}$ ,  $\mathbf{C}_1 \in \mathbb{R}^{n-1 \times 1}$ ,  $\mathbf{C}_2 \in \mathbb{R}^{1 \times 1}$ . Accordingly, the system of equation (16) can be rewritten as:

$$\mathbf{x}_{1,k+1} = \hat{\Phi}_{11}\mathbf{x}_{1,k} + \hat{\Phi}_{12}x_{2,k}, \quad (24)$$

$$x_{2,k+1} = \hat{\Phi}_{21}\mathbf{x}_{1,k} + \hat{\Phi}_{22}x_{2,k} + \hat{G}_2u_k + \mathbf{w}_k. \quad (25)$$

For the purpose of control, it is assumed that full state feedback is available. Accordingly, the measurement equation is defined as:

$$\mathbf{z}_k = \mathbf{I}\mathbf{x}_k. \quad (26)$$

The MSMC control strategy uses two SMC controllers ( $SMC_1$ ,  $SMC_2$ ) in an additive form,  $u_{MSMC} = u_{SMC_1} + u_{SMC_2}$ . The basic structure of the MSMC strategy is shown in Figure 11, the hypothesis is:

- By considering the overall EHA system model, where the input is the pump rotational speed ( $\omega_p$ ) and the outputs are the load position, velocity, and acceleration ( $x, \dot{x}, \ddot{x}$ ). Accordingly, the sliding surface parameters  $\mathbf{C}$  will be a vector with three elements such that  $\mathbf{C} = [C_{e1}, C_{e2}, C_{e3}]$ . Designing the first SMC controller (outer-loop main controller) with a sliding surface  $s = C_{e1}e + C_{e2}\dot{e} + C_{e3}\ddot{e}$ , and a boundary layer  $\psi$  large enough to accommodate for the friction model inaccuracy, would eliminate chatter.
- The EHA system model is then partitioned into two sub-systems:
  1. A sub-system with the pump rotational speed as an input and the EHA load acceleration as an output according to the lower partition of equations (21) to (24), such that:

$$\ddot{x}_{k+1} = \hat{\Phi}_{21}\ddot{x}_k + G_2\omega_p + \hat{\Phi}_{21} \begin{bmatrix} x_k \\ \dot{x}_k \end{bmatrix} + \mathbf{w}_k. \quad (27)$$

2. A sub-system with the load acceleration as the input and the load position and velocity as the outputs according to the upper partition of equations (21) to (24), such that:

$$\begin{bmatrix} x_{k+1} \\ \dot{x}_{k+1} \end{bmatrix} = \hat{\Phi}_{11} \begin{bmatrix} x_k \\ \dot{x}_k \end{bmatrix} + \hat{\Phi}_{12}\ddot{x}_k. \quad (28)$$

The tracking precision is then enhanced by using a secondary SMC controller with two stages according to Figure 11 and equations (27) and (28), such that:

**Stage 1** A sliding surface  $s_1 = C_{e1}e + C_{e2}\dot{e}$  and a boundary layer  $\psi_1$  are defined to obtain the required position and velocity tracking accuracies. **In this stage, the trajectory tracking errors ( $e, \dot{e}$ ) are used in conjunction with the aforementioned sub-system of equation (28), to create an estimate for the change in acceleration required to enhance the load position and velocity precision of tracking ( $\Delta\hat{\ddot{x}}_{k+1}$ ).** Further to equation (27), it is found that:

$$\begin{aligned} \Delta\hat{\ddot{x}}_{k+1} = \bar{\ddot{x}}_{k+1} - \ddot{x}_{k+1} &= \hat{\Phi}_{22}\ddot{x}_k + \hat{\Phi}_{22} \begin{bmatrix} x_k \\ \dot{x}_k \end{bmatrix} + \hat{G}_2\bar{\omega}_p \\ &\quad - \hat{\Phi}_{22}\ddot{x}_k - \hat{\Phi}_{22} \begin{bmatrix} x_k \\ \dot{x}_k \end{bmatrix} - \hat{G}_2\omega_p, \end{aligned} \quad (29)$$

$$\Delta\hat{\ddot{x}}_{k+1} = \hat{G}_2\bar{\omega}_p - \hat{G}_2\omega_p = \hat{G}_2\Delta\hat{\omega}_p. \quad (30)$$

**Stage 2** Using the acceleration correction term ( $\Delta\hat{\ddot{x}}_{k+1}$ ), the corresponding ( $\Delta Input = \Delta\hat{\omega}_p$ ) is calculated using a sliding surface  $s_2 = C_{e3}\Delta\hat{\ddot{x}}_{k+1}$  and a boundary layer  $\psi_2$ .

#### 4.1 Sliding Mode Control

In this research, the MSMC will use Misawa's SMC control structure which can be found in [24, 25]. In this section, this method will be presented before being revised and used in the formulation of the new MSMC control strategy.

The control input is defined using Misawa's method as, [25]:

$$u_k = u_{eq,k} - (\mathbf{C}\hat{\mathbf{G}})^{-1} s_k + (\mathbf{C}\hat{\mathbf{G}})^{-1} K_c \text{sat} \left( \frac{s_k}{\psi} \right), \quad (31)$$

where

$$u_{eq,k} = (\mathbf{C}\hat{\mathbf{G}})^{-1} \mathbf{C} (\mathbf{x}_{d,k+1} - \hat{\Phi} \mathbf{x}_k), \quad (32)$$

$$K_c = \gamma + 2\varepsilon, \quad \psi \geq \gamma + \varepsilon, \quad (33)$$

$$\text{sat} \left( \frac{s}{\psi} \right) = \begin{cases} +1 & \text{if } s > \psi, \\ \frac{s}{\psi} & \text{if } |s| \leq \psi, \\ -1 & \text{if } s < -\psi, \end{cases} \quad (34)$$

and  $\varepsilon$  is an arbitrary positive constant.

A major drawback in [24] SMC derivation is the assumption that the uncertainties  $\mathbf{w}_k$  are bounded by a constant, this assumption is not realistic, since  $\mathbf{w}_k$  is inherently dependant on the system states. Accordingly, a new gain calculation is needed, where a variable gain will be used to compensate for the uncertainties that relate to the system states. If modeling errors are considered in  $\mathbf{w}$ , then the system uncertainties in  $\mathbf{w}_k$  are obtained as:

$$\mathbf{w}_k = \tilde{\Phi} \mathbf{x}_k + \tilde{\mathbf{G}} u_k + \mathbf{v}_k, \quad (35)$$

where  $\tilde{\Phi} = \Phi - \hat{\Phi}$ ,  $\tilde{\mathbf{G}} = \mathbf{G} - \hat{\mathbf{G}}$ , and  $\mathbf{v}_k$  are the system matrix uncertainty, the input matrix uncertainty, and the system noise respectively. Accordingly the uncertainties bound of equation (17) is rewritten as:

$$\gamma(\mathbf{x}_k) \geq |\mathbf{C} (\tilde{\Phi} \mathbf{x}_k + \tilde{\mathbf{G}} u_k + \mathbf{v}_k)|. \quad (36)$$

The stability condition of equation (36) is satisfied by selecting  $\gamma$  such that:

$$\gamma(\mathbf{x}_k) \geq \mathbf{C} \tilde{\Phi}_{max} |\mathbf{x}_k| + \mathbf{C} \tilde{\mathbf{G}}_{max} u_{max} + \mathbf{C} \mathbf{v}_{max}, \quad (37)$$

where  $\tilde{\Phi}_{max}$  and  $\tilde{\mathbf{G}}_{max}$  are the upper bounds on the uncertainties in the system matrix and the input matrix,  $\mathbf{v}_{max}$  is the maximum noise amplitude, and  $u_{max}$  is the maximum allowable input ( $\pm 10$  volts for the EHA system). Substituting  $|\mathbf{x}_k - \mathbf{x}_{d,k}| + |\mathbf{x}_{d,k}| = |\mathbf{e}_k| + |\mathbf{x}_{d,k}| \geq |\mathbf{x}_k|$  in equation (36), the condition of equation (17) is satisfied by selecting  $\gamma$  as:

$$\gamma(\mathbf{e}_k) = \mathbf{C} \tilde{\Phi}_{max} |\mathbf{e}_k| + \mathbf{C} \tilde{\Phi}_{max} |\mathbf{x}_{d,k}| + \mathbf{C} \tilde{\mathbf{G}}_{max} u_{max} + \mathbf{C} \mathbf{v}_{max}. \quad (38)$$

Substituting equation (38) in the gain and boundary layer calculations of equation (33) results in:

$$K_c = \mathbf{C} \tilde{\Phi}_{max} |\mathbf{e}_k| + \mathbf{C} \tilde{\Phi}_{max} |\mathbf{x}_{d,k}| + \mathbf{C} \tilde{\mathbf{G}}_{max} u_{max} + \mathbf{C} \mathbf{v}_{max} + 2\varepsilon, \quad (39)$$

$$\psi = \mathbf{C} \tilde{\Phi}_{max} |\mathbf{e}_k| + \mathbf{C} \tilde{\Phi}_{max} |\mathbf{x}_{d,k}| + \mathbf{C} \tilde{\mathbf{G}}_{max} u_{max} + \mathbf{C} \mathbf{v}_{max} + \varepsilon. \quad (40)$$

## 4.2 MSMC Mathematical Formulation

The multiple sliding mode control strategy as shown in Figure 11 is composed of two control elements in an additive form, consisting of:

**SMC 1-** A main outer loop controller that utilizes the system model of equation (16) to derive a control action to follow trajectories associated with position, velocity, and acceleration. For this element, the same strategy as in the previous section is followed where the estimated equivalent control law for the system of equation (16), is obtained from equation (32) as:

$$\hat{u}_{eq,k} = (\mathbf{C}\hat{\mathbf{G}})^{-1} \mathbf{C} (\mathbf{x}_{d,k+1} - \hat{\Phi}\mathbf{x}_k). \quad (41)$$

Consider the ideal sliding motion such that:

$$s_k = s_{k+1} = s_{k+2} = \dots = 0. \quad (42)$$

From the definition of the sliding manifold given by equation (18), then under ideal sliding mode conditions:

$$\mathbf{C}\mathbf{e}_{k+1} = \mathbf{C} (\mathbf{x}_{d,k+1} - \mathbf{x}_{k+1}) = 0. \quad (43)$$

Substituting equation (16) in equation (43) results in:

$$\mathbf{C} (\mathbf{x}_{d,k+1} - \hat{\Phi}\mathbf{x}_k - \hat{\mathbf{G}}\mathbf{u}_k - \mathbf{w}_k) = 0, \quad (44)$$

where  $u_{eq}$  is obtained from equation (44) as:

$$\hat{u}_{eq,k} = (\mathbf{C}\hat{\mathbf{G}})^{-1} \mathbf{C} (\mathbf{x}_{d,k+1} - \hat{\Phi}\mathbf{x}_k), \quad (45)$$

$$u_{SMC1} = \hat{u}_{eq,k} - (\mathbf{C}\hat{\mathbf{G}})^{-1} s_k + (\mathbf{C}\hat{\mathbf{G}})^{-1} K_c \text{sat} \left( \frac{s_k}{\psi_c} \right), \quad (46)$$

where  $K_c = \mathbf{C}\tilde{\Phi}_{max} |\mathbf{e}_k| + \mathbf{C}\tilde{\Phi}_{max} |\mathbf{x}_{d,k}| + \mathbf{C}\tilde{\mathbf{G}}_{max} u_{max} + \mathbf{C}\mathbf{v}_{max} + 2\varepsilon$ ,  $\psi_c = \mathbf{C}\tilde{\Phi}_{max} |\mathbf{e}_k| + \mathbf{C}\tilde{\Phi}_{max} |\mathbf{x}_{d,k}| + \mathbf{C}\tilde{\mathbf{G}}_{max} u_{max} + \mathbf{C}\mathbf{v}_{max} + \varepsilon$ , and  $\varepsilon$  is an arbitrary positive constant.

**SMC 2-** A secondary inner-loop controller consisting of two cascaded stages, such that:

**Stage 1** Considering the upper system partition of equation (24), restated here for clarity as:

$$\mathbf{x}_{1,k+1} = \hat{\Phi}_{11}\mathbf{x}_{1,k} + \hat{\Phi}_{12}\mathbf{x}_{2,k}. \quad (47)$$

By assuming that the control input to the first partition is  $u_2 = \mathbf{x}_{2,k}$ , and using sliding mode control of equations (31) and (32), with a sliding surface  $s_1 = \mathbf{C}_1 (\mathbf{x}_{1d,k} - \mathbf{x}_{1,k})$  and a tighter boundary layer  $\psi_1$ , an estimate of the required change in the second partition state vector  $\Delta\hat{\mathbf{x}}_{2,k}$  is found as:

$$\begin{aligned} \Delta\hat{\mathbf{x}}_{2d,k} &= (\mathbf{C}_1\hat{\Phi}_{12})^{-1} \mathbf{C}_1 (\mathbf{x}_{1d,k+1} - \hat{\Phi}_{11}\mathbf{x}_{1,k}) \\ &\quad - (\mathbf{C}_1\hat{\Phi}_{12})^{-1} s_{1,k} + (\mathbf{C}_1\hat{\Phi}_{12})^{-1} K_{1c} \text{sat} \left( \frac{s_{1,k}}{\psi_{1c}} \right). \end{aligned} \quad (48)$$

$\Delta\hat{\mathbf{x}}_{2,k}$  is viewed as the required change in the  $\mathbf{x}_{1,k}$  trajectory to confine  $\mathbf{e}_{1,k}$  to a tighter boundary layer defined by  $\psi_{1c}$ . **It should be noted that, approximation errors in differentiation are neglected and given the simplicity of  $\hat{\Phi}_{11}$ , uncertainties in  $\hat{\Phi}_{11}$  are assumed negligible such that  $\tilde{\Phi}_{11} = 0$ . This simplifies the discontinuous corrective action to a constant term, such that  $K_{1c} = \mathbf{C}_1 \mathbf{v}_{1,max} + 2\varepsilon \geq |\mathbf{C}_1 \mathbf{v}_{1,k}|$ .**

**Stage 2** In this stage the  $\Delta\hat{\mathbf{x}}_{2d,k}$  is transformed to an estimate of the change in the system input  $u_{SMC2} = \Delta u_k$ , which would allow for its addition to the main controller control input  $u_{SMC1}$ . Considering the lower system partition of equation (24), the required transformation is found as:

$$\Delta\hat{\mathbf{x}}_{2,k+1} = \bar{\mathbf{x}}_{2,k+1} - \mathbf{x}_{2,k+1} = \hat{\Phi}_{21}\mathbf{x}_{1,k} + \hat{\Phi}_{22}\mathbf{x}_{2,k} + \hat{G}_2\bar{u}_k - \hat{\Phi}_{21}\mathbf{x}_{1,k} - \hat{\Phi}_{22}\mathbf{x}_{2,k} - \hat{G}_2u_k. \quad (49)$$

Simplifying equation (49) yields:

$$\Delta\hat{\mathbf{x}}_{2,k+1} = \hat{G}_2(\bar{u}_k - u_k) = \hat{G}_2\Delta u_k. \quad (50)$$

Accordingly the mapping of the  $\mathbf{x}_{2,k+1}$  corrective action to the system input space is achieved using sliding mode with  $s_2 = C_2\Delta\hat{\mathbf{x}}_{2d,k}$  and a boundary layer  $\psi_{2c}$ :

$$u_{SMC2} = (C_2\hat{G}_2)^{-1} K_{2c} \text{sat} \left( \frac{C_2\Delta\hat{\mathbf{x}}_{2d,k}}{\psi_{2c}} \right). \quad (51)$$

**It should be noted that the uncertainty associated with equation (50) is assumed to be bounded, since it is a function of the system input, and the system input is bounded ( $\pm 10 \text{ volts}$  for the EHA system). Hence, a constant switching gain  $K_{2c}$  is used for stage 2 sliding mode controller. Furthermore, the use of a saturation function in this stage is necessary for the proof of stability. It provides the ability to increase the gain of the inner loop controller, which results in a high frequency switching action (a dither-like effect). This results in minimizing the effects of static friction on the system performance.**

The overall control input is established by combining the main outer-loop control element with the secondary inner-loop control as follows:

$$u_{MSMC,k} = u_{SMC1} + u_{SMC2} = \hat{u}_{eq,k} - (C\hat{G})^{-1} s_k + (C\hat{G})^{-1} K_c \text{sat} \left( \frac{s_k}{\psi_c} \right) + (C_2\hat{G}_2)^{-1} K_{2c} \text{sat} \left( \frac{\Delta\hat{\mathbf{x}}_{2d,k}}{\psi_{2c}} \right), \quad (52)$$

$$u_{MSMC,k} = \hat{u}_{eq,k} - (C\hat{G})^{-1} s_k + (C\hat{G})^{-1} K_c \text{sat} \left( \frac{s_k}{\psi_c} \right) + (C_2\hat{G}_2)^{-1} K_{2c} \text{sat} \left( \frac{(C_1\hat{\Phi}_{12})^{-1} C_1 (\mathbf{x}_{1d,k+1} - \hat{\Phi}_{11}\mathbf{x}_{1,k})}{\psi_{2c}} - \frac{(C_1\hat{\Phi}_{12})^{-1}}{\psi_{2c}} s_{1,k} + \frac{(C_1\hat{\Phi}_{12})^{-1} K_{1c}}{\psi_{2c}} \text{sat} \left( \frac{s_{1,k}}{\psi_{1c}} \right) \right). \quad (53)$$

## 5 COMBINED MIL/MSMC STRATEGY

Figure 8 shows the block diagram for the EHA system with the MIL feedback approach, similar to the basic EHA system, the input to the system is the demanded rotational speed of

the motor, and the output is the position of the hydraulic actuator. From the block-diagram, the transfer function relating the pump rotational speed is found as:

$$\begin{aligned} G_{MIL} &= \frac{G_{EHA}}{1 - G_{inner} + G_{EHA} \left( G_{inner} \frac{A}{D_p} + K_B \right) p}, \\ &= \frac{C_{MIL,num}}{p^3 + C_{MIL,den2} p^2 + C_{MIL,den1} p + C_{MIL,den0}}, \end{aligned} \quad (54)$$

where:

$$\begin{aligned} C_{MIL,num} &= \frac{AD_p \beta_e}{MV_o (1 - K_{inner})}, \\ C_{MIL,den2} &= \frac{BV_o + M\beta_e (L/2 + \zeta)}{MV_o} + \frac{P_{inner}}{1 - K_{inner}}, \\ C_{MIL,den1} &= \frac{B\beta_e (L/2 + \zeta)}{MV_o} + \frac{A^2 \beta_e + A\beta_e D_p K_B + P_{inner} (M\beta_e (L/2 + \zeta) + BV_o)}{MV_o (1 - K_{inner})}, \\ C_{MIL,den0} &= \frac{P_{inner} (MV_o + A^2 \beta_e)}{MV_o (1 - K_{inner})}. \end{aligned}$$

Further to the EHA parameters of Table. 1, the EHA/MIL subsystem transfer function could be found as:

$$G_{MIL} = \frac{637.7}{p^3 + 3085p^2 + 1.145 \times 10^{11}p + 1.74 \times 10^8}.$$

the EHA/MIL is converted to a discrete state space form for the application of the MSMC strategy as shown in Fig. 12. Using forward difference approximation and a sampling period of  $T_s = 0.0001 \text{ sec}$  the discrete state space model is given by:

$$\begin{aligned} x_{1,k+1} &= x_{1,k} + T_s x_{2,k}, \\ x_{2,k+1} &= x_{2,k} + T_s x_{3,k}, \\ x_{3,k+1} &= -T_s C_{MIL,den0} x_{1,k} - T_s C_{MIL,den1} x_{2,k} \\ &\quad + (1 - T_s C_{MIL,den2}) x_{3,k} + T_s C_{MIL,num} u_k. \end{aligned} \quad (55)$$

The discrete equation can now be represented in the state space form with parameter values listed in Table. 1:

$$\mathbf{x}_{k+1} = \Phi \mathbf{x}_k + \mathbf{G} u_k + \mathbf{w}_k, \quad (56)$$

where

$$\hat{\Phi} = \begin{pmatrix} 1 & T_s & 0 \\ 0 & 1 & T_s \\ -T_s C_{MIL,den0} & -T_s C_{MIL,den1} & (1 - T_s C_{MIL,den2}) \end{pmatrix}, \quad (57)$$

$$\hat{\Phi} = \begin{pmatrix} 1 & .0001 & 0 \\ 0 & 1 & .0001 \\ -1.7402 \times 10^4 & -1.1449 \times 10^7 & 0.6915 \end{pmatrix}, \quad (58)$$



**Table 1: Physical parameters of the EHA mathematical model, [6, 26]**

Symbol	Value	Unit
$a_1$	$1.419 \times 10^5$	$Ns^2/m^2$
$a_2$	$-12801$	$Ns/m$
$a_3$	$415.21$	$N$
$M$	$3.688$	$Kg$
$A$	$1.52 \times 10^{-3}$	$m^2$
$V_o$	$1.08 \times 10^{-3}$	$m^3$
$x_o$	$0.71$	$m$
$L$	$6.52 \times 10^{-12}$	$Nm/s$
$\beta_e$	$2.10 \times 10^8$	$Pa$
$\xi$	$3.26 \times 10^{-12}$	$Nm/s$
$D_p$	$5.57 \times 10^{-7}$	$m^3/rad$
$P_{pipe}$	$0$	
$R_c$	$1.04$	$\Omega$
$L_c$	$0.014$	$H$
$K_c$	$1.61$	$Nm/A$
$K_\omega$	$0.98$	$Vs/rad$
$K_{pvisc}$	$2 \times 10^{-4}$	$Nms/rad$
$K_{fric}$	$2 \times 10^{-4}$	$Nms/rad$
$J_{pm}$	$1.98 \times 10^{-3}$	$kgm^2$
$T_{DB}$	$0.001$	$Nm$

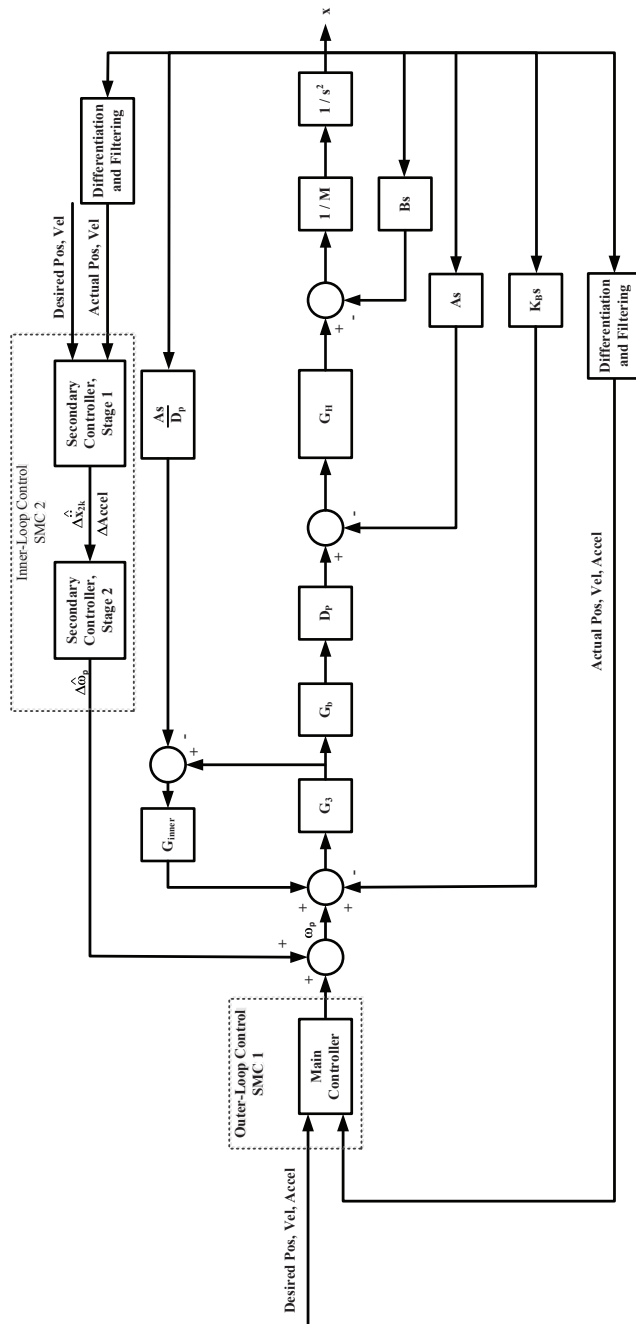


**Figure 12: Combined MIL/MSMC control strategy**

and

$$\hat{\mathbf{G}} = \begin{pmatrix} 0 \\ 0 \\ T_s MIL_n um \end{pmatrix} = \begin{pmatrix} 0 \\ 0 \\ 0.0638 \end{pmatrix}. \quad (59)$$

Accordingly the partitioned system matrices are found as:

$$\hat{\Phi}_{11} = \begin{pmatrix} 1 & .0001 \\ 0 & 1 \end{pmatrix}, \quad (60)$$

$$\hat{\Phi}_{12} = \begin{pmatrix} 0 \\ .0001 \end{pmatrix}, \quad (61)$$

$$\hat{\Phi}_{21} = \begin{pmatrix} -1.7402 \times 10^4 & -1.1449 \times 10^7 \end{pmatrix}, \quad (62)$$

$$\hat{\Phi}_{22} = \begin{pmatrix} 0.6915 \end{pmatrix}, \quad (63)$$

$$\hat{G}_2 = \begin{pmatrix} 0.0638 \end{pmatrix}. \quad (64)$$

The controller coefficients such as sliding gain, sliding surface, and boundary layer were estimated based on experimental tests on the EHA prototype. Similarly to section ??, using pole placement and by considering the system stability and experimental precision, the sliding surface was selected at:

$$s_k = \mathbf{C} \mathbf{e}_k = \begin{bmatrix} 10000 & 500 & 1 \end{bmatrix} \mathbf{e}_k. \quad (65)$$

The sliding gain and boundary layer were selected as:

$$\begin{aligned} K_c &= \mathbf{C} \tilde{\Phi}_{max} |\mathbf{e}_k| + \mathbf{C} \tilde{\Phi}_{max} |\mathbf{x}_{d,k}| + 100, \\ \psi_c &= \mathbf{C} \tilde{\Phi}_{max} |\mathbf{e}_k| + \mathbf{C} \tilde{\Phi}_{max} |\mathbf{x}_{d,k}| + 1000, \\ K_{1c} &= 50, \quad \psi_{1c} = 20, \\ K_{2c} &= 100, \quad \psi_{2c} = 1500. \end{aligned}$$

The overall control input was derived in Chapter 5 and is given by equations (45) to (53) as:

$$\hat{u}_{eq} = (\mathbf{C} \hat{\mathbf{G}})^{-1} \mathbf{C} (\mathbf{x}_{d,k+1} - \hat{\Phi} \mathbf{x}_k), \quad (66)$$

$$u_{SMC1} = \hat{u}_{eq} - (\mathbf{C} \hat{\mathbf{G}})^{-1} s_k + (\mathbf{C} \hat{\mathbf{G}})^{-1} K_c sat \left( \frac{s_k}{\psi_c} \right), \quad (67)$$

$$\begin{aligned} \hat{\mathbf{x}}_{2d,k} &= (\mathbf{C}_1 \hat{\Phi}_{12})^{-1} \mathbf{C}_1 (\mathbf{x}_{1d,k+1} - \hat{\Phi}_{11} \mathbf{x}_{1,k}) - (\mathbf{C}_1 \hat{\Phi}_{12})^{-1} s_{1,k} \\ &\quad + (\mathbf{C}_1 \hat{\Phi}_{12})^{-1} K_{1c} sat \left( \frac{s_{1,k}}{\psi_{1c}} \right), \end{aligned} \quad (68)$$

$$u_{SMC2} = (\mathbf{C}_2 \hat{G}_2)^{-1} K_{2c} sat \left( \frac{\mathbf{C}_2 \hat{\mathbf{x}}_{2d,k}}{\psi_{2c}} \right), \quad (69)$$

$$\begin{aligned} u_{MSMC,k} &= u_{SMC1} + u_{SMC2}, \\ &= \hat{u}_{eq} - (\mathbf{C} \hat{\mathbf{G}})^{-1} s_k + (\mathbf{C} \hat{\mathbf{G}})^{-1} K_c sat \left( \frac{s_k}{\psi_c} \right) \\ &\quad + (\mathbf{C}_2 \hat{G}_2)^{-1} K_{2c} sat \left( \frac{\hat{\mathbf{x}}_{2d,k}}{\psi_{2c}} \right). \end{aligned} \quad (70)$$

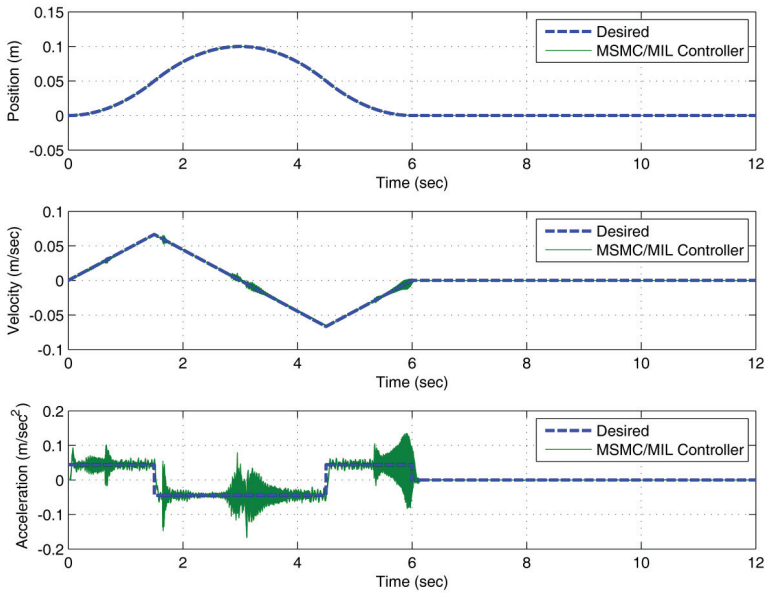


**Figure 13: MSMC/MIL Trajectory Experimental Results**

## 6 EXPERIMENTAL RESULTS

The combined MIL/MSMC experimental results are shown in figures. 13 and 14, it is clear that the added MIL feedback loop control action, is effective in further enhancing the positional accuracy at the expense of increased chatter at the zero velocity crossing regions. Those results confirms the hypotheses behind the MIL strategy, that the added differential velocity/position feedback loop is successful in overcoming the backlash/friction dead-band effect.

## 7 CONCLUSIONS

The work in this paper involves combining the Multiple Inner Loop (MIL) control strategy with the Multiple Sliding Mode Control (MSMC). The purpose of the combined method is to include additional feedback from the motor in the MSMC strategy to enhance its accuracy in trajectory tracking applications. A differential velocity/position feedback was added in an inner loop format. The added control input proved effective in further enhancing the trajectory tracking positional accuracy. However, an increased level of chatter was observed in the zero velocity crossing zones. As such, there is a trade off between the MSMC/MIL accuracy and chatter amplitude, and the choice between the MSMC and MSMC/MIL will depend on the application requirements.

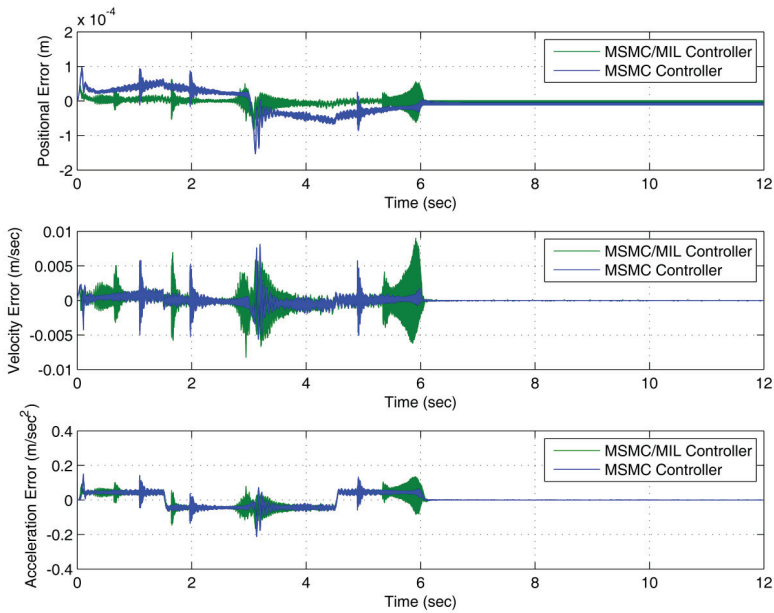


**Figure 14: MSMC/MIL Tracking Error Experimental Results**

## REFERENCES

- [1] J. Watton, *Fluid Power Systems*. Prentice-Hall Int. (UK), Hemel Hempstead, 1989.
- [2] S. Habibi and A. Goldenberg, "Design and analysis of a new symmetrical linear actuator for hydraulic and pneumatic systems," *Transactions of the Canadian Society for Mechanical Engineering*, vol. 23, no. 3-4, pp. 377 – 396, 1999.
- [3] W. Qian, "Neural network control of nonlinear hydraulic systems," Master's thesis, University of Saskatchewan, Saskatoon, Canada, 1999.
- [4] H. D. Tran and D. B. DeBra, "Design of a fast short-stroke hydraulic actuator," *CIRP Annals*, vol. 43, no. 1, pp. 469 – 472, 1994.
- [5] S. Habibi and A. Goldenberg, "Design of a new high-performance electrohydraulic actuator," *IEEE/ASME Transactions on Mechatronics*, vol. 5, no. 2, pp. 158 – 64, 2000.
- [6] S. Habibi, R. Burton, and E. Sampson, "High precision hydrostatic actuation systems for micro and nano manipulation of heavy loads," *Journal of Dynamic Systems, Measurement, and Control*, vol. 128, pp. 778–787, December 2006.

- [7] E. B. Sampson, "Fuzzy control of the electrohydraulic actuator," Master's thesis, University of Saskatchewan, Saskatoon, Canada, 2005.
- [8] S. Wang, S. Habibi, R. Burton, and E. Sampson, "Sliding mode control for a model of an electrohydraulic actuator system with discontinuous nonlinear friction," *2006 American Control Conference (IEEE Cat. No. 06CH37776C)*, p. 8 pp. 38, 2006.
- [9] F. Repoulas and E. Papadopoulos, "Dynamically feasible trajectory and open-loop control design for unmanned airships," *Mediterranean Conference on Control and Automation, Athens-Greece*, 2007.
- [10] H. Richter, "Hyperplane design in observer-based discrete-time sliding mode control," Master's thesis, School of Mechanical and Aerospace Engineering, Oklahoma State University, 1997.
- [11] K. J. Åström and R. M. Murray, *Feedback Systems, An Introduction for Scientists and Engineers*. 41 William Street, Princeton, New Jersey 08540: Princeton University Press, 3<sup>rd</sup> ed., 2008.
- [12] H.-J. Shieh and P.-K. Huang, "Trajectory tracking of piezoelectric positioning stages using a dynamic sliding-mode control," *IEEE Transactions on Ultrasonics, Ferroelectrics, and Frequency Control*, vol. 53, no. 10, pp. 1872–1882, 2006.
- [13] V. I. Utkin and H. Lee, "Chattering problem in sliding mode control systems," *2<sup>nd</sup> IFAC Conf. on Analysis and Design of Hybrid Systems, Alghero, Italy*, 2006.
- [14] H. Lee, V. I. Utkin, and A. Malinin, "Chattering reduction using multiphase sliding mode control," *International Journal of Control*, vol. 82, no. 9, pp. 1720–1737, 2009.
- [15] H. Lee and V. I. Utkin, "The chattering analysis," *Advances in Variable Structure and Sliding Mode Control, Lecture Notes in Control and Information Sciences*, eds. C. Edwards, E. Fossas Colet, and L. Fridman, Berlin: Springer, 2006.
- [16] H. Lee and V. I. Utkin, "Chattering suppression methods in sliding mode control systems," *Annual Reviews in Control*, vol. 31, pp. 179–188, 2007.
- [17] M. A. El Sayed and S. Habibi, "Multiple sliding mode control for an electrohydrostatic actuator system," *Proceedings of the Fluid Power and Motion Control Symposium 2010, FPMC 2010, Bath, UK*, vol. 1, pp. 353 – 364, 2010.
- [18] Y. A. Chinniah, *Fault Detection in the ElectroHydraulic Actuator using Extended Kalman Filter*. PhD thesis, University of Saskatchewan, Saskatoon, Canada, 2004.
- [19] V. Del Toro, *Basic Electric Machines*. Prentice Hall; England Cliffs, NJ, 1<sup>st</sup> ed., 1990.
- [20] J. Van de Vegte, *Feedback Control Systems*. Prentice Hall; England Cliffs, NJ, 1<sup>st</sup> ed., 1994.

- [21] S. Habibi and G. Singh, "Derivation of design requirements for optimization of a high performance hydrostatic actuation system," *International Journal of Fluid Power*, vol. 1, no. 2, pp. 11 – 29, 2000.
- [22] S. Habibi, J. Roach, and G. Luecke, "Inner-loop control for electromechanical (ema) flight surface actuation systems," *Journal of Dynamic Systems, Measurement and Control, Transactions of the ASME*, vol. 130, pp. 051002–1–13, 2008.
- [23] M. A. El Sayed and S. Habibi, "Inner-loop control for electro-hydraulic actuation (eha) systems," *Journal of Dynamic Systems, Measurement and Control, Transactions of the ASME. In Press*, 2010.
- [24] E. Misawa, "Discrete time sliding mode control for nonlinear systems with unmatched uncertainties and uncertain control vector," *Transactions of the ASME. Journal of Dynamic Systems, Measurement and Control*, vol. 119, no. 3, pp. 503 – 12, 1997.
- [25] E. Misawa, "Discrete-time sliding mode control: the linear case," *Transactions of the ASME. Journal of Dynamic Systems, Measurement and Control*, vol. 119, no. 4, pp. 819 – 21, 1997.
- [26] K. R. McCullough, "Design and characterization of a dual electro-hydrostatic actuator," Master's thesis, McMaster University, Hamilton, Ontario, Canada, 2011.

# The Fractional Order PID Control of Hydraulic Position System Based on Internet

**Shi Guanglin, Wang Ruigang, Xu Zhenyin**

School of Mechanical Engineering, Shanghai Jiao Tong University,  
P.R. China, 200240, Email: glshi@263.net

## ABSTRACT

The issue of stochastically varying network delays in Networked Control System (NCS) application, especially the Internet-based real-time control of a hydraulic position system, is addressed in this paper. In order to compensate the Internet-induced large delay effect, a fractional-order PID controller with derivative of reference signal forward feed (FO-PIDC) is proposed. A test bench platform which involves real Internet data transmission is built to compare the performance of FO-PID with that of traditional PID. A series of experiments based on three Internet data transmission channels with different delay distribution are carried out. The experimental results reveal that 1) if the round trip time (RTT) is under 70ms and period jitter is small, the FO-PID works better; 2) if the RTT is more than 160ms and period jitter is large, the FO-PID with compensation performs well.

**Keywords:** hydraulic position system; FO-PID; random delay; Internet-based real-time control

## 1 INTRODUCTION

An Internet-based control system is a typical network control system in which the control loops are closed over the Internet [1, 2]. Although position control loops would be generally closed locally and internet command would essentially be open control, there are still cases that we want to close the loop over internet to meet some particular requirements. For one thing, new complicated real-time control algorithm tends to have a large computational cost which probably exceeds the capability of a single local controller. A network based control methodology may provide a professional solution without computational constraints and worry about confidentiality and simultaneously simplifies the design of local controllers. Furthermore, applications like tele-medicine, tele-manipulation robot has presented a strong trend for a real-time control system closing loop over network. Due to its easy access to communication system, Internet-based control methodology has received increasing attention from both application engineers and theoretical researchers. Hydraulic components, typical actuators, are widely used in engineering. W.J.Book proposed an Internet-based hydraulic control education experiment schema [3]. Jie Huang designed a test bench of hydraulic system based on Internet [4].



Senchun Chai et al. realized an Internet-based servo position system by using general model predictive control method [5]. The main challenge of Internet-based control system is from the nature of Internet itself: Delay and packet dropouts, which not only degrades the performance but also make a control system unstable. In particular, delay introduced by the shared Internet is of prime concern when evaluating the control performance. Variety methods were developed to alleviate this problem [6]. However, these methods usually simplify the dynamic model of Internet-induced delay. Researchers have found that Internet induced delay is non-Gauss process according to plenty of experiments. It contains strong self similarity in the long range of observation which means its dynamic model is fractional order model [7]. Y.Q. Chen discussed basic problems and strategies in applying fractional calculus and FO-PID in networked control system [8].

The rest of this paper is organized as follows. Section 2 introduces the details of Internet based hydraulic position system including the control architecture, Internet delay feature and mathematical model of physical plant. Section 3 discusses the design of FO-PID and proposes a control algorithm FO-PID with forward compensation. Section 4 proposes a new schematic for Internet-based control experiments and carries out the experimental results for verifying the effectiveness of control algorithm. The paper ends with conclusion in section 5, followed by references.

## 2 SYSTEM DESCRIPTION

### 2.1 Architecture of Internet-based Control System

The structure of Internet-based control system is shown in Figure 1. This structure is known as a direct structure which is formed by a controller and a remote system including a physical plant, actuators and sensors. And the critical control information between the controller and the physical plant like sensor and control signals is transmitted by Internet.

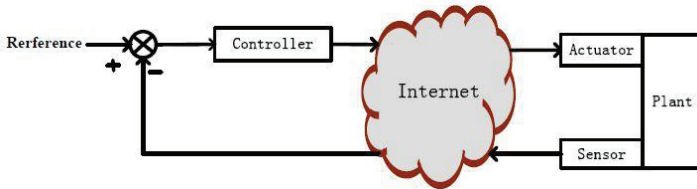


**Figure 1: Architecture of Internet-based Control System**

The basic features of Internet data transfer are delay effect, delay jitter, package disorder and package dropout. Inevitably, these features weaken the performance of control system. The Internet-induced delay between Shanghai Jiao Tong University ([www.sjtu.edu.cn](http://www.sjtu.edu.cn)) and Hong Kong University of Science and Technology ([www.ust.hk](http://www.ust.hk)) is shown in Figure 2. The RTT between these two sites is measured by PING (Packet Internet Grope).

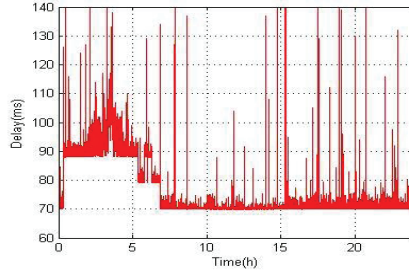


**Figure 2: RTT between SJTU and UST**

## 2.2 Plant Model

The schematic of the hydraulic position system is shown in Figure 3. It contains two valves (one of them is high speed on/off valve, the other is on/off valve) and one cylinder. There are three operation modes in this system: 1) forward mode, the cylinder moves forward when the high speed on/off valve driven by PWM wave provides a positive mean flow and on/off valve, meanwhile, is closed; 2) backward mode, the cylinder moves backward when the high speed on/off valve is closed and on/off valve is open; 3) stop mode, the cylinder stands still when both valves are closed.

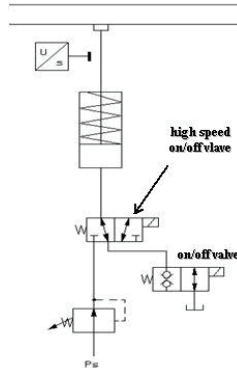


**Figure 3: Schematic of hydraulic system**

The plant's control unit automatically switches an operation mode due to the control input  $c$  ( $-1 \leq c \leq 1$ ). The switching rules can be expressed as

$$\text{operator}(c) = \begin{cases} \text{forward} & \text{if } c_0^+ < c \leq 1 \\ \text{stop} & \text{if } c_0^- \leq c \leq c_0^+ \\ \text{backward} & \text{if } -1 \leq c < c_0^- \end{cases} \quad (1)$$

where  $(c_0^-, c_0^+)$  is the dead zone of control input.

The experimental flow rate of high speed on/off valve is identified by RBF network as [9]

$$q_0 = \varphi(f, \alpha, \Delta p_0) \quad (2)$$

where  $f$  is switching frequency.  $\alpha$  is the ratio of PWM wave.  $\Delta p_0$  is the difference of

pressure at the inlet and outlet of valve during the identification experiment. So from Equation (2), one obtains the working flow rate as

$$q'_0 = \varphi(\alpha) \sqrt{\frac{\Delta p}{\Delta p_0}} \quad (3)$$

where  $\Delta p$  is the difference of working pressure at the inlet and outlet of valve. And the working flow rate of on/off valve can be expressed as

$$q'_1 = q_1 \sqrt{\frac{\Delta p}{\Delta p_1}} \quad (4)$$

where the flow rate of on/off valve is  $q_1$  when its difference of pressure is  $\Delta p_1$ . From Equation (1)—(4), the flow rate of plant's control unit can be written as

$$q(c) = \begin{cases} \varphi(c) \sqrt{\frac{p_s - p}{\Delta p_0}} & \text{if } c_0^+ < c \leq 1 \\ 0 & \text{if } c_0^- \leq c \leq c_0^+ \\ -q_1 \sqrt{\frac{p}{\Delta p_1}} & \text{if } -1 \leq c < c_0^- \end{cases} \quad (5)$$

where  $p_s$  is the pressure of system supply.  $p$  is the working pressure of non-rod chamber. According to the Newton's second law, one obtains

$$pA = m\ddot{y} + B_p\dot{y} + K_s y \quad (6)$$

where  $m(3\text{kg})$  is the mass of load.  $K_s(100\text{Nmm}^{-1})$  is rigidity of load.  $B_p(0.2\text{Nsm}^{-1})$  is the damping coefficient of load.  $y$  is the displacement of cylinder. According to the experiments,  $y, \dot{y}, \ddot{y}$  satisfy  $y \leq 60\text{mm}$ ,  $\dot{y} \leq 30\text{mms}^{-1}$ ,  $\ddot{y} \leq 60\text{mms}^{-2}$ . So  $m\ddot{y} \leq 0.18\text{N}$  and  $B_p\dot{y} \leq 6\text{N}$  are very small compared to the elastic force  $0\text{N} \leq K_s y \leq 6000\text{N}$ . Therefore, Equation (6) can be simplified as

$$pA = m\ddot{y} + B_p\dot{y} + K_s y \quad (7)$$

According to the continuity equation of fluid, one obtains

$$q = A\dot{y} + \frac{V_t}{\beta_e} \frac{dp}{dt} \quad (8)$$

where  $A$  is the area of non-rod chamber,  $V_t(V_t = V_0 + Ay)$  is the volume of control fluid,  $V_0(0\text{mL})$  is the initial volume. From Equation (7) and (8), one obtains

$$q = \left(A + \frac{K_s y}{\beta_e}\right) \frac{dy}{dt} \quad (9)$$

Equation (5), (7) and (9) show that the physical system contains a series of nonlinear features.

### 3 CONTROLLER DESIGN

#### 3.1 Conventional PID

The conventional PID control algorithm can be expressed in the time domain as:

$$u(t) = K_p e(t) + K_i \int_0^t e(t) dt + K_d \frac{de}{dt} \quad (10)$$

where  $e(t)$  is the error between the reference signal and system output,  $K_p$  is the proportional gain.  $K_i$  is the integral gain.  $K_d$  is the differential gain. In a digital system, the discrete form of PID controller is expressed as:

$$u(k) = K_p e(k) + K_i \sum_{i=1}^k e(i) + K_d \frac{e(k) - e(k-1)}{T} \quad (11)$$

#### 3.2 Fractional-order PID

Although the conventional PID is widely used in both academic research projects and industry applications, it is not robust in network situation due to the Internet-induced delay effect. The FO-PID is proposed by Podlubny [10]. The main benefits of FO-PID are that the designed controller can ensure to fulfill the given gain crossover frequency and phase margin, and further more the phase derivative over the frequency is zero at the gain crossover frequency [11].

Before the realization of FO-PID controller, a brief introduction to fractional order calculus needs to be presented first. Fractional order calculus is a generalization of integration and differentiation to any order operator  ${}_a D_t^\lambda$ , where  $a$  and  $t$  are the limits and  $\lambda$  ( $\lambda \in \mathbb{R}$ ) is the order of the operator. There are several definitions for fractional order derivate operator, such as Grunwald-Letnikov definition, Riemann-Liouville (RL) definition, the Caputo definition, etc. Among these definitions, the RL definition is the most frequently used definition. The RL fractional operator of function  $f(t)$  is defined as [12]

$${}_a D_t^\lambda f(t) \triangleq \frac{1}{\Gamma(n-\lambda)} \frac{d^n}{dt^n} \int_a^t \frac{f(\tau)}{(t-\tau)^{\lambda-n+1}} d\tau \quad (12)$$

where  $n-1 < \lambda \leq n$ ,  $\Gamma(\bullet)$  is the Gamma function.

The Laplace transform of the fractional operator is usually used in system modeling. And the transform of the Equation (12) under zero initial conditions for order  $\lambda$  ( $0 < \lambda < 1$ ) is given as [12]

$$\ell\{{}_a D_t^{\pm\lambda} f(t)\} = s^{\pm\lambda} F(s) \quad (13)$$

where  $0 < \lambda < 1$ ,  $\Gamma(\bullet)$  is the Gamma function.

The Laplace transform of FO-PID is expressed as

$$C(s) = K_p + K_i \frac{1}{s^\lambda} + K_d s^\mu \quad (14)$$

where  $0 < \lambda, \mu < 1$ . The design of FO-PID controller usually involves several principles such as phase margin and gain crossover frequency specifications, gain margin and phase crossover frequency specifications, robustness to variations in the gain of the plant, high

frequency noise rejection, good output disturbance rejection, and limitation of control effort [13]. And these principles work well when the plant model is linear. However, the Internet-based hydraulic position system contains complex nonlinear characters which are generated by high speed on/off valve and Internet-induced delay. So it calls for more research efforts on how to tuning or adjust the FO-PID parameters online.

The most important issue in the implementation of FO-PID is how to realize fractional order operator with numerical methods. Usually, signals do not have any exact expression so that the RL definition can work well in digital control practice. Instead, several filter approaching methods were developed to calculus the fractional order integration differential of a signal, such as Tustin, Al-Alaoui, and Oustaloup's recursion filter. Among these filters, the Oustaloup's recursion filter performs best [14-17]. It can approach the fractional order operator in a given frequency interval  $(\omega_b, \omega_h)$  with the expression as [15]

$$G(s) = K \prod_{k=-n}^n \frac{s + \omega_k^1}{s + \omega_k^2} \quad (15)$$

where  $n$  is the filter's order, and the gain  $K$ , zero  $\omega_k^1$  and pole  $\omega_k^2$  can be expressed as

$$K = (\omega_h)^\lambda, \omega_k^1 = \omega_b \left( \frac{\omega_h}{\omega_b} \right)^{\frac{k+n+0.5(1-\lambda)}{2n+1}}, \omega_k^2 = \omega_b \left( \frac{\omega_h}{\omega_b} \right)^{\frac{k+n+0.5(1+\lambda)}{2n+1}} \quad (16)$$

The Oustaloup's recursion filter has a pretty precise approximation to the FO-PID at given frequency range.[14]

Although we have obtained the structure of the FO-PID controller in a numerical way, it remains the question of how to optimize the parameters  $K_p, K_i, K_d, \lambda, \mu$ . Superficially, global optimization is a stronger version of local optimization, whose great usefulness in practice is undisputed. However, in many practical applications finding the globally best point, though desirable, is not essential, since any sufficiently good feasible point is useful and usually an improvement over what is available without optimization (this particular case). [13] In our application, we take the phase margin as the object function and tune the parameters  $\lambda, \mu$  heuristically around the initial value to maximize the object function locally. More efficient and intelligent searching algorithm like particle swarm optimization (PSO) or immune clone algorithm (ICA) can be further studied at next step.

### 3.3 Fractional-order PID with forward compensation

No matter PID or FO-PID, the basic concept is feedback control, which is a passive control method that acquire error first and then take control action. However, the error information in Internet-based control system cannot be acquired in time. In order to compensate the delay effect, the traditional method is to involve velocity or acceleration feedback in controller designed. The shortcoming is also obvious: velocity or acceleration feedback induce strong signal noise, especially when the jitter of Internet-induced delay is large. Forward feed is another way to improve the speed of control system response. A simple differentiator with a low pass filter can easily acquire the derivatives of the reference signal. The schematic of FP-PIDC is shown in Figure 4.

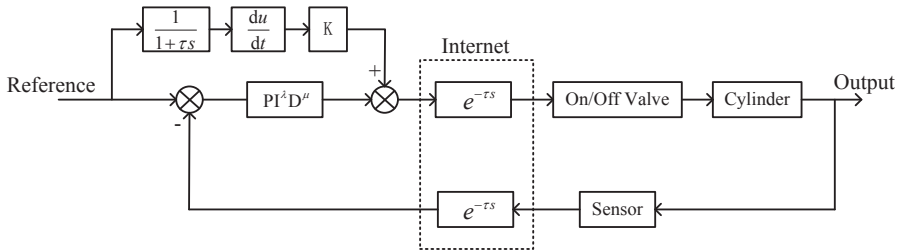


Figure 4: Schematic of fractional order PID with compensation

## 4 EXPERIMENTS

### 4.1 Test bench

Currently, the main architecture of Internet is based on IPv4, which is short for IP address. In order to solve this problem, computer scientists proposed a schematic – NAT (Network Address Translation). Although it release the IP address shortage, it builds a wall for P2P (peer-to-peer) communication. In the control experiment (seen in Figure 1), two computers in two different network (one acts as controller, the other acts as plant regulator) cannot communicate directly without a public P2P sever. Besides, it's not flexible to perform several control experiments with different delay feature. So the control experiment cannot choose P2P as its network protocol. The PING protocol, which is part of ICMP (Internet Control Message Protocol), can provide a solution to this problem. The basic function of PING is that a source host sends a PING package to another host and the target host sends back a package with the same payload.

The schematic of test bench is based on PING protocol, as seen in Figure 5. The computation of the controller and plant regulator is performed on one host computer. It sends a PING package with sensor data as its payload to a target network and carries out the control computation based on the sensor data from echo package. Meanwhile, the controller output is sent to the actuator in the same way. So the real Internet transmission is involved in the control experiment. Moreover, it is very easy to perform different delay feature experiment by changing the target network.

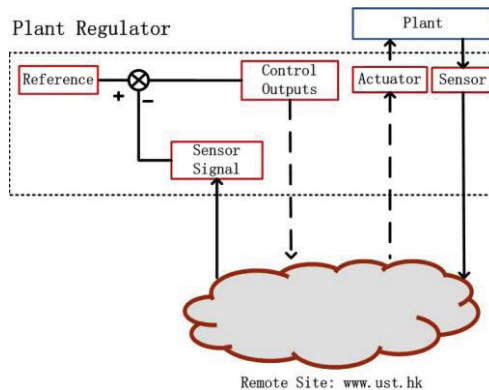


Figure 5: Schematic of test bench

4.2 Experimental results

A series of test experiments were carried out to prove the effectiveness of FO-PID over traditional PID. In these experiments, the plant regulator computer lies in www.sjtu.edu.cn (Shanghai) and three typical sites with different delay features, seen in Table 1, were selected as the PING sever. And three control algorithms (PID, FO-PID, FO-PIDC) were test on each Internet transmission channel.

Table 1: Three PING Severs

Site	City	Distance	Mean RTT	Jitter
www.sina.com.cn	Beijing	1100km	32ms	small
www.ust.hk	Hong Kong	1200km	78ms	large
www.u-tokyo.ac.jp	Tokyo	1500km	115ms	median

Experiment 1 contains three experiments with different control algorithms on the Internet channel between www.sjtu.edu.cn and www.sina.com.cn and its results are shown in Figure 6. Due to the variety load of Internet, there exists small difference in the delay feature of each experiment. However, the mean RTT of sensor to controller is around 30ms and delay jitter is small. Because the delay feature of controller to actuator is very similar to that of sensor to controller, so the total mean RTT is under 70ms and delay jitter is relative small. The controller parameters and performance measurements are shown in Table 2. Although the raise time of PID and FO-PID is around 1.3s which is smaller than that of FO-PIDC, the P.O. of these two is much larger than that of FO-PIDC. However, considering that the mean RTT and jitter of Internet delay in FO-PID is much larger than the others, the FO-PID performs better.

Table 2: Controller Parameters and Performance of Experiment 1

Algorithm	$K_p$	$K_i$	$K_d$	$\lambda$	$\mu$	feed gain	$T_r(s)$	P.O.(%)	ess(mm)
PID	50	10	1	-	-	-	1.31	0.52	-0.21
FO-PID	50	10	7	0.5	0.5	-	1.37	0.43	-0.17
FO-PIDC	45	8	4	0.5	0.5	5	1.57	-0.25	0.10

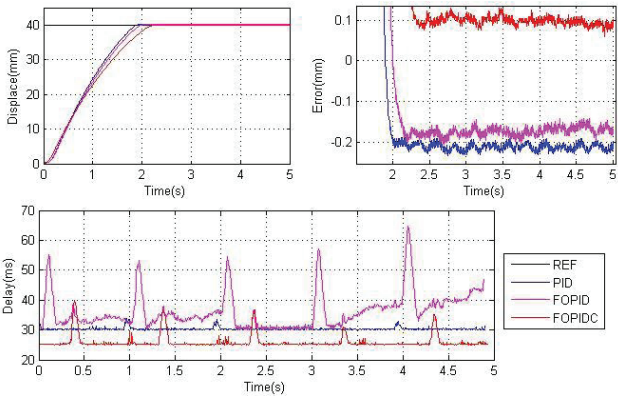
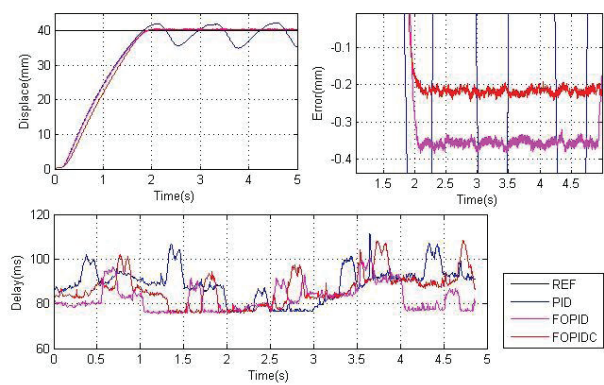


Figure 6: Results of Experiment 1

Experiment 2 was carried out on the Internet channel between [www.sjtu.edu.cn](http://www.sjtu.edu.cn) and [www.ust.hk](http://www.ust.hk) and its results are shown in Figure 7. There exists frequent Internet communication between the mainland of China and Hong Kong district, meanwhile the network architecture of these two areas is under a same system. Therefore, the mean RTT from sensor to controller is around 80ms and delay jitter is large, which is much larger than that of the Internet channel in Experiment 1. The controller parameters and performance measurements are shown in Table 3. The large delay and delay jitter make the PID control unstable. Although the raise time is nearly the same (about 1.25s), the P.O. of FO-PIDC is much smaller than that of FO-PID. Considering that the delay feature of these three is very close, so the FO-PIDC works better than the other two.

**Table 3: Controller Parameters and Performance of Experiment 2**

Algorithm	$K_p$	$K_i$	$K_d$	$\lambda$	$\mu$	feed gain	$T_r(s)$	P.O.(%)	ess(mm)
PID	45	6	1	-	-	-	1.25	-	-
FO-PID	45	6	4	0.5	0.5	-	1.27	0.89	-0.35
FO-PIDC	40	5	4	0.5	0.5	8	1.25	-0.54	0.21



**Figure 7: Results of Experiment 2**

Experiment 3 was carried out on the Internet channel between [www.sjtu.edu.cn](http://www.sjtu.edu.cn) and [www.u-tokyo.ac.jp](http://www.u-tokyo.ac.jp) and its results are shown in Figure 8. The Internet connection between these two sites is crossed over ocean. But the load of this connection is lighter than that of connection between Shanghai and Hong Kong. Therefore, the mean RTT of sensor to controller is much larger around 115ms and delay jitter is median. The controller parameters and performance measurements are shown in Table 4. The results are very similar to that of experiment 2. Therefore, it can be concluded that if the total RTT is more than 160ms and period jitter is large, the FO-PIDC performs well.



Table 4: Controller Parameters and Performance of Experiment 3

Algorithm	$K_p$	$K_i$	$K_d$	$\lambda$	$\mu$	feed gain	$T_r(s)$	P.O.(%)	ess(mm)
PID	40	4	0.5	-	-	-	1.19	-	-
FO-PID	40	4	3	0.5	0.5	-	1.48	0.79	-0.31
FO-PIDC	35	3	2	0.5	0.5	6	1.48	-0.46	0.18

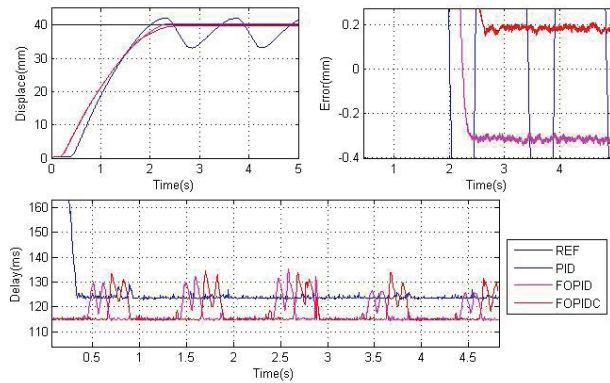


Figure 8: Results of Experiment 3

5 CONCLUSION

In this paper, FO-PID controller was applied to the Internet-based hydraulic position control system employing high speed on/off valves in order to solve the problem of stochastically varying network delays. In order to compensate the large Internet delay effect, FO-PID with derivative of reference signal forward feed was proposed. A flexible test bench which involved real Internet data transmission channel was built to perform control experiments. The experimental results of three Internet transmission channels with different delay feature revealed that 1) if the round trip time (RTT) is under 70ms and period jitter is small, the FO-PID works better; 2) if the RTT is more than 160ms and period jitter is large, the FO-PID with compensation performs well. Optimization of the parameters in FO-PID remains to be further studied in the future.

REFERENCES

[1] Murry R.M., Astrom K.J., Boyd S.P., et al. Future directions in control in an information-rich world. IEEE Control System Magazine, 2003, 23(2):20-33.

[2] Walsh G.C., Hong Ye, Bushnell L. Stability analysis of networked control systems. American Control Conference, 1999, 4:2876-2880.

[3] Wayne J. Book, Mathew D. Rouse, Kyle Koeppen. Internet Access to a Fluid Power Mechatronics Laboratory. IEEE/ASME International Conference on Advanced Intelligent Mechatronics Proceedings. Como, Italy, 2001:1112-1117.

- [4] Jie Huang, Jian Li, et al. Design for the Remote Control Hydraulic Servo Test Bed. Proceedings of the 8th World Congress on Intelligent Control and Automation. Jinan, China, 2010:927-932.
- [5] Senchun Chai, Guo Ping Liu, David Rees, Yuanqing Xia. Design and Practical Implementation of Internet-based Predictive Control of a Servo System. IEEE TRANSACTIONS ON CONTROL SYSTEMS TECHNOLOGY. 2008, 16(1):158-168.
- [6] Y. Tipsuwan, M.-Y. Chow. Control methodologies in networked control systems. Control Engineering Practice, 11, 2003.
- [7] Qiong Li, David L. Mills. Investigating the Scaling Behavior, Crossover and Anti-persistence of Internet Packet Delay Dynamics. Global Telecommunications Conference, 1999:1843-1852.
- [8] Y.Q. Chen. Fractional Calculus, Delay Dynamics and Networked Control Systems. 3rd International Symposium on Resilient Control Systems, 2010:58-63.
- [9] Jian Pan, Guanglin Shi, Peng Yang. Coordinated Position Control of Five Hydraulic Cylinders Based on High Speed On/Off Valves. Proc. of 6<sup>th</sup> FPNI-PhD Symp. West Lafayette 2010:115-125.
- [10] Podlubny I. Fractional-order systems and  $PI^{\lambda}D^{\mu}$  - controllers. IEEE Trans. on Automatic Control. 1999, 44(1):208-214.
- [11] Blas M.Vinagre, Concepcion A.Monje, Antonio J.Calderon, Jose I.Suarez. Fractional PID Controller for Industry Application - A Brief Introduction. Journal of Vibration and Control 2007 13:1419.
- [12] Podlubny I. Fractional Differential Equations. Academic Press, New York (1999).
- [13] Concepcion A.Monje, Blas M. Vinagre, Vicente Feliu, YangQuan Chen. Tuning and auto-tuning of fractional order controllers for industry applications. Control Engineering Practice, 2008, 16(7):798-812.
- [14] Oustaloup, A., Mathieu, B., Lanusse, P.: The CRONE control of resonant plants: application to a flexible transmission. Euro. J. Control, 1995,1(2):113-121.
- [15] Y. Q. Chen, Ivo, Petras, Dingyu Xue. Fractional Order Control - A Tutorial. American Control Conference, St. Louis, USA, 2009: 1397-1411.
- [16] Podlubny I. Numerical solution of initial value problems for ordinary fractional-order differential equations. Proceedings of the 14th world congress on computation and applied mathematics. Atlanta, Georgia, USA, 1994:107.
- [17] Podlubny I. Numerical methods of the fractional calculus. Trans Tech Univ Kosice, 1994, 4(3-4):200.



# Deterministic Control Strategy for a Hybrid Hydraulic System with Intermediate Pressure Line

**Dipl.-Ing. Peter Dengler**

Karlsruhe Institute of Technology (KIT), Chair of Mobile Machines, Karlsruhe, Germany

**Prof. Dr.-Ing. Marcus Geimer**

Karlsruhe Institute of Technology (KIT), Chair of Mobile Machines, Karlsruhe, Germany

**Dipl.-Ing. René von Dombrowski**

FLUIDON GmbH, Aachen, Germany

## ABSTRACT

The paper introduces a new hydraulic system for mobile machines based on a constant pressure system with the aim to increase the efficiency of actuation of hydraulic cylinders. Using a third pressure level located between high pressure and tank pressure called intermediate pressure the system enables additional pressure potentials from high pressure to intermediate pressure and from intermediate pressure to tank pressure. This reduces throttle losses at hydraulic cylinders when driven at low or medium loads. An accumulator connected to the intermediate pressure line is being charged or discharged in function of which pressure potential is currently used.

Due to the discrete pressure potentials of the system a control strategy is required which reduces throttle losses at the proportional valves and allows maximum recuperation of potential energy. Best results can be obtained if the future loads on the cylinders are predictable. For this reason a Model Predictive Control (MPC) was developed for a wheel loader which was used as a reference system. By using its specific geometric properties the MPC allows a precise load prediction as a function of the piston's position. Using the criteria of Bellman, an analytic online calculation of the optimum sequence of pressure potentials and their durations for one complete cylinder stroke can be effectuated using Dynamic Programming. This leads to a deterministic algorithm which is easy to handle and which can be implemented into an online control loop of the wheel loader. The paper furthermore shows how an optimal switching sequence and the optimal accumulator parameters can be found offline using multi objective optimization and closes with simulation results showing an increase of efficiency of 13% compared to a LS system at the example of a typical duty cycle of a wheel loader.

# 1 INTRODUCTION

Constant pressure (CP) systems are one of the simplest hydraulic systems. They are not very efficient as high pressure losses occur when lower loads are lifted. Advanced systems are equipped with a pressure controlled pump and a hydraulic accumulator connected to the main pressure line. In these “Advanced Constant Pressure Systems” /1/ secondary controlled hydraulic rotary drives can be operated without system-related losses /2/. Furthermore secondary controlled four quadrant drives can be operated in pump mode while braking which enables recovery of potential or braking energy which is stored in a hydraulic accumulator for later use. Both aspects, high system efficiency and energy recovery, make Advanced Constant Pressure Systems to a suitable drive system for hydraulic hybrid drives for mobile machines. These systems already exist at the market /3/, even though not in mobile applications yet. One inconvenient of a large scale application of this system is its incompatibility with linear actuators as the high pressure still needed to be throttled to adapt it to the actual load pressure. One concept of an efficient integration of hydraulic cylinders into a constant pressure system is the secondary controlled linear actuator which allows an at least discrete adaptation of the piston area to the present load /4/. Another way is the so called “hydraulic transformer” which consists of a constant flow pump connected to a secondary controlled drive /5/. Both systems have in common that they need components which are costly or which are simply not available at the market. Another approach for the efficient integration of linear actuators in a CP system by the use of standard components is shown in **Figure 1**.

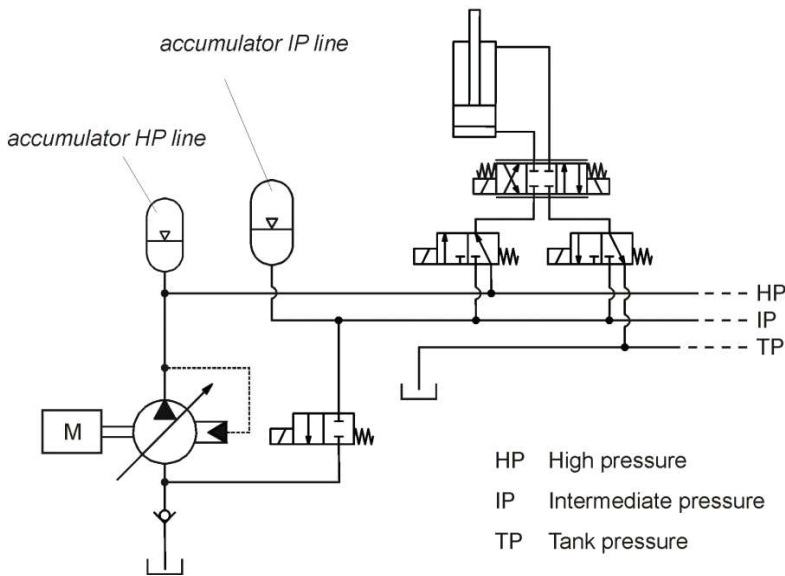


**Figure 1: Basic layout of a CPIP system**

In this system multiple discrete pressure potentials are used to reduce pressure losses at the proportional valves. These can be created if a supplementary pressure line is used. The

pressure level of the additional line is located between high pressure (HP) and tank pressure (TP) and is therefore called “intermediate pressure (IP) line” /6/ so the system is called “Constant Pressure System with Intermediate Pressure Line” (CPIP). A hydraulic accumulator is connected to the IP line to enable recovery of potential energy. A second accumulator is connected to the HP line to buffer pressure oscillations. Two switching valves for each actuator can change the pressure on the inlet and the outlet port of the proportional valve between high-, intermediate- and tank pressure. Losses can be reduced by adapting the applied pressure difference at the piston of the hydraulic cylinder to the actual load.

For very high loads, the switching valves connect the inlet port of the proportional valve to HP and the outlet port to TP and the system acts like a conventional constant pressure system. For lower loads the inlet port of the proportional valve is connected to the IP line and the accumulator is being discharged. The next lower switching state connects the inlet port of the proportional valve to the HP line and the outlet port to the IP line, the accumulator is being charged. For very low loads both ports of the proportional valve can be connected to the IP line. Due to energetic reasons the IP line can be connected to the suction side of the pump which results in lower energy demand of the system when using the pump. This results in six switching states with a different use of pump and accumulator energy. **Figure 2** illustrates the energies for a piston movement at constant speed and constant load when a switching sequence is used which contains all possible switching states. The displayed energies are accumulated input energies if above the x-axis and output energies if located below.

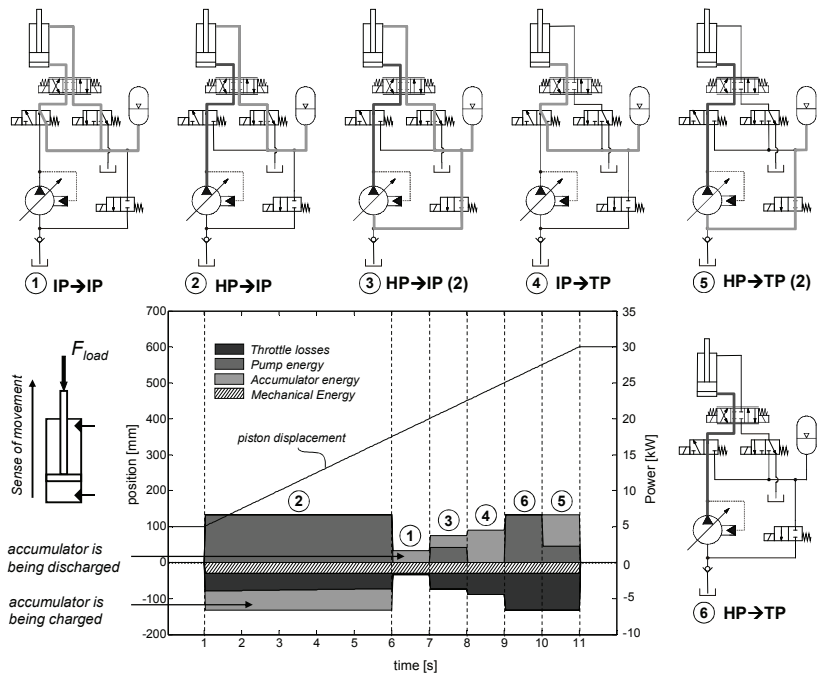


Figure 2: Possible switching states to effectuate a piston movement

Besides the hydraulic components the system needs a control algorithm to be operated. This control algorithm is programmed into a programmable logic controller (PLC) and determines the actual load at the cylinders by measuring the pressures in the chambers and the position of the piston and chooses the appropriate switching state by actuating the switching valves. Once the switching state is set, the fine control of the piston is enabled with the proportional valve according to the needed flow given by the operator. Furthermore, the algorithm has a switching strategy which performs actuation of the switching valves not only in terms of having enough force to move the piston but also in terms of the global efficiency of the system. It therefore allows switching states which may cause high throttle losses at the moment but allow charging or discharging the accumulator in order to reach a more advantageous state of charge for future energy demands. These control strategies for hybrid drives are subject of intensive research /7/ as they essentially influence the overall efficiency of the system and represent the most important part of the control architecture, also in this system.

## 2 SYSTEM IMPROVEMENT WITH MULTI OBJECTIVE OPTIMIZATION

To develop a switching strategy which is able to find an optimum switching sequence a duty cycle with cylinder strokes and loads is needed. For this reason, the CPIP system was analyzed for the working hydraulics of a 4.7 t wheel loader. The considered actuators of the working hydraulics are two hydraulic cylinders, one for lifting and one for tilting. A typical duty cycle for this application is the so called “Load & Carry” cycle. In this cycle the loader loads the bulk material into the bucket and carries it to a transport vehicle where it is dumped. It can be composed in five different stages as illustrated in **Figure 3**:

1. The wheel loader drives from the starting position (A) to the material (B). The bucket is lowered and aligned to the ground.
2. The machine drives into the material and loads the bucket. In the following the wheel loader transports the material to the transport vehicle at (C).
3. The machine drives to the transport vehicle and lifts the bucket when arriving.
4. When the bucket is above the bed of the transport vehicle the tilt cylinder is actuated and the bucket is dumped.
5. The loader backs off and the operator brings the bucket back into the starting position.

The described cycle was repeated during tests about 90 times at realistic digging conditions. For the system optimization one representative duty cycle was chosen and the load pressures were transformed into forces acting on the pistons of the cylinders. This allows identifying the needed forces and calculating the needed energies in the different stages with the aim to get an energy profile of the duty cycle as shown exemplarily in Figure 2. To obtain an efficient system a sequence of switching states must be found which allows performing the movements of the duty cycle but with a lower energy demand than the current LS system.

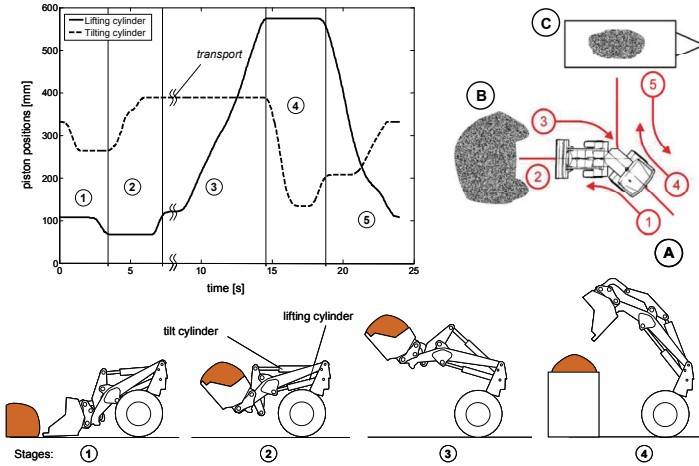


Figure 3: “Load and Carry” cycle of a wheel loader according to /8/

### 2.1 Optimal switching sequence

An optimum switching sequence for the given duty cycle is the one with the lowest use of energy delivered by the pump. As the pump directly feeds the high pressure line all switching states taking oil from the HP line like HP/IP, HP/IP (2), HP/TP and HP/TP (2) increase the energy demand of the system. These switching states have energy “costs” in form of the hydraulic energy  $E_{Pump}$  generated by the pump. Considering a switching sequence with  $n$  switching decisions the costs for HP/TP and HP/IP at decision  $i$  can be calculated (supposing  $1 \leq i \leq n$ ). Assuming a constant pressure  $p_{HP}$  in the HP line the costs for HP/TP and HP/IP can be calculated according to the oil volume  $\Delta V_{Cyl,HP,i}$  taken from the HP line at a cylinder stroke effectuated at  $i$ .

$$\Delta E_{Pump,i} = \Delta V_{Cyl,HP,i} \cdot p_{HP} \quad (1)$$

Considering the entire duty cycle the total energy demand of the system after  $n$  switching decisions can be described as

$$E_{Pump} = \sum_i^n \Delta E_{Pump,i} \quad (2)$$

The switching states IP/IP and IP/TP have no energy costs according to the definition given above as they only take energy from the accumulator. When used instead of HP/TP or HP/IP equation (2) is minimized as  $\Delta E_{Pump,i}$  becomes zero. However, IP/TP and IP/IP reduce the state of charge (SOC) of the accumulator by  $\Delta V_{Cyl,IP,i}$  so the used potential energy can be calculated as

$$\Delta E_{Acc,i} = \int_{V_{IP1}}^{V_{IP2}} p_{IP,i}(V_{IP}) dV_{IP} \quad (3)$$



$$\Delta V_{Cyl,IP,i} = V_{IP1} - V_{IP2} \quad (4)$$

$\Delta E_{Acc,i}$  is negative if the accumulator is being discharged and positive if the accumulator is being charged. This potential energy must be created by charging the accumulator using HP/IP or by lowering high loads with TP/IP (recuperation mode) or medium loads with HP/IP (2). The total accumulator energy after  $n$  switching decisions is therefore

$$E_{Acc} = \sum_i^n \Delta E_{Acc,i} \quad (5)$$

The switching states HP/IP (2) and HP/TP (2) combine pump energy and accumulator energy to reduce their costs as the accumulator of the IP line is connected to the suction side of the pump. The costs for HP/IP (2) and HP/TP (2) can be given as

$$\Delta E_{Pump,i} = \Delta V_{Cyl,out,i} \cdot p_{HP} + \int_{V_{IP1}}^{V_{IP2}} p_{IP,i}(V_{IP}) dV_{IP} \quad (6)$$

The optimum switching sequence balances switching states with high costs and high generation of potential energy and switching states with low or zero costs and high consumption of accumulator energy in a manner that the global costs, e.g. the total energy demand  $E_{Pump}$  for the given duty cycle, become minimal. This is an optimization problem which can be solved with a multi objective optimization considering both energy types  $E_{Pump}$  and  $E_{Acc}$  as equivalent. The optimal decision changes the current energy state into a Pareto optimum as shown in **Figure 4**.

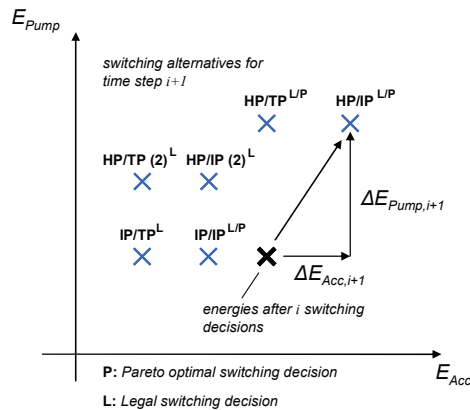


**Figure 4: Pareto optimal decisions**

To apply multi objective optimization the duty cycle is divided in  $n$  discrete time steps. At each time step  $i$  all “legal” switching states are identified. A switching state is legal if it generates a force which is high enough to move the piston in the current load situation.

Furthermore switching states which take oil from the accumulator can only be legal if the SOC is high enough to effectuate the cylinder stroke in the given time step. Starting from a state of total energy demand  $E_{Pump}$  and total accumulator energy  $E_{Acc}$  at a time step  $i$  the energies  $\Delta E_{Pump}$  and  $\Delta E_{Acc}$  for the next time step  $i+1$  are calculated for all legal switching alternatives and added to  $E_{Pump}$  and  $E_{Acc}$ . The optimal switching decisions are those which do not worsen one energy type without improving the other one and therefore called Pareto optimal (see Figure 4). They are added to the already existing sequence of Pareto optimal switching decisions. If there is more then one optimal switching alternative the existing sequence must be duplicated by the number of optimal alternatives. The calculated energies  $E_{Pump}$  and  $E_{Acc}$  are used as starting energies for the next time step and the procedure is repeated. At the end of the duty cycle a set of points is found with different energies  $E_{Pump}$  and  $E_{Acc}$  following a Pareto frontier which begins with very low values for  $E_{Pump}$  and  $E_{Acc}$  and ending with very high values for both energy types. The searched sequence of optimal decisions is the one which leads to the lowest pump energy demand and is shown in **Figure 5**.

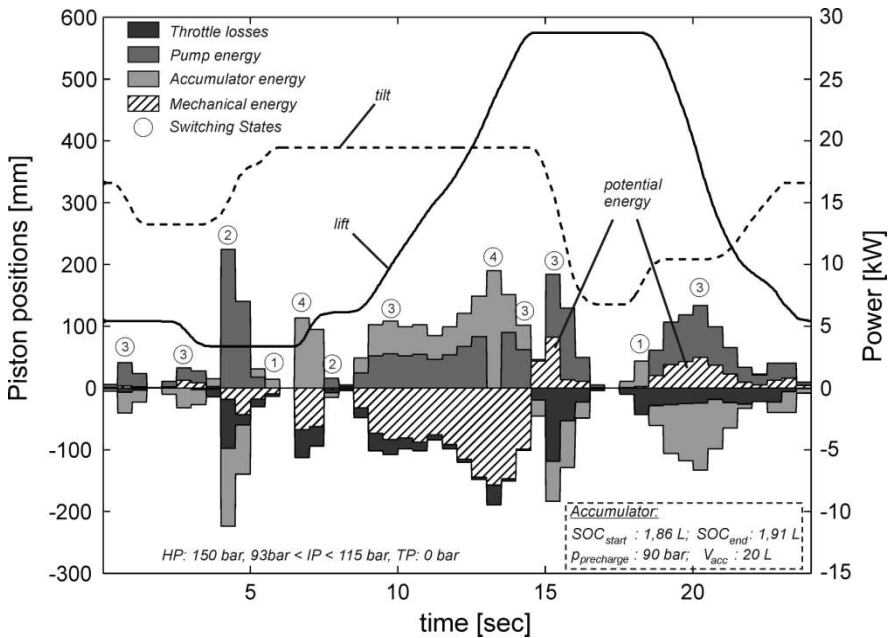


**Figure 5: Optimal switching sequence for the given duty cycle**

## 2.2 Optimal accumulator parameters

The described optimization method is done for a given duty cycle and fix accumulator parameters. In order to build up an optimized system the parameters *precharge pressure* and *accumulator size* can be found with the same method. Supposing a hydro-pneumatic accumulator with a polytropic gas behavior with the polytropic index  $\kappa$  the relation between gas volume and gas pressure can be given as

$$p \cdot V_{Acc}^{\kappa} = const. \quad (7)$$

Applying the multi objective optimization on the same duty cycle by gradually changing the values for precharge pressure and gas volume of the accumulator a characteristic correlation between those parameters and the total energy demand can be observed in **Figure 6**. A valley can be identified showing low energy demands for all tested accumulator sizes at a precharge pressure of 90 bar. This valley has a smooth slope and reaches the global minimum of hydraulic energy consumption at 20 L gas volume and 90 bar precharge pressure. An accumulator with these parameters enables therefore the highest efficiency improvement of the system and was chosen to be mounted on the wheel loader.

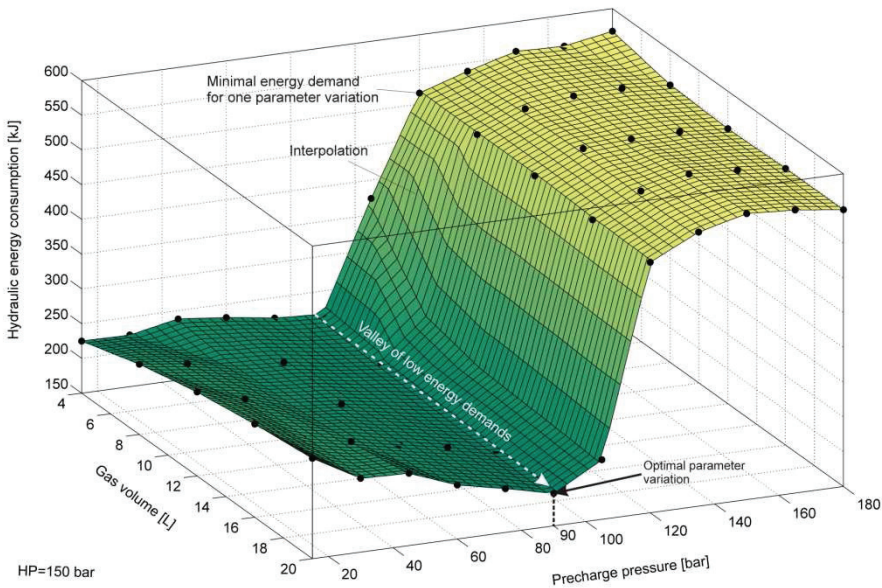


**Figure 6: Results of parameter variation reveal optimal accumulator settings**

### 3 MODEL PREDICTIVE CONTROL USING DYNAMIC PROGRAMMING

Besides an optimal switching sequence Figure 5 shows the mechanical energy which is needed in the hydraulic cylinders of the wheel loader. The working stages 1 and 2 (described in Figure 3) are characterized by load peaks which are relatively high but short so the needed energy is quite low. In these stages the switching valves must be fast enough to create the forces which are needed at the pistons but due to the spontaneous character of these peaks an optimization of the switching sequence can not really take place. At stage 4 potential energy occur at the tilting cylinder when the bucket is dumped and at the lifting cylinder when the arm is lowered. This energy must be recuperated in order to improve the energy demand of the system. At stage 3 it can be seen that most of the energy is needed for the lifting cylinder when the arm is lifted. Here the loads are high and the movement lasts long so an online optimization of the switching sequence can be effectuated. An

optimization algorithm must be found which can take an optimal switching decision at any instant of the piston movement. This algorithm must be flexible, fast and easy to handle to use it as an online control algorithm. The most promising approach can be created with Model Predictive Control (MPC) [9]. MPC implies a mathematical model of the system and extrapolates the present state of charge for a definite time step into the future, called prediction horizon. Using this model the controller can approximate the future response of the system to interactions of actuators at the present instant of time which allows a positive influence on the system behavior for the prediction horizon.

In general, the piston movements of a wheel loader are very quick (a couple of seconds to lift the bucket) and can furthermore be interrupted at any instant by the operator. At these conditions a time extrapolation of the present load would be quite difficult to carry out. Doing this, a time related MPC would not improve the system as the precision of prediction would be very poor. For this reason a position related MPC was created which predicts precisely the development of loads on the lifting cylinder according to the present position of the piston.

### 3.1 Modeling of loads and of the accumulator

Due to the geometric properties of the wheel loader the load at the lifting cylinder is a linear function of the piston's position. Once the arm is lifted and the present load and position are known the future evolution of loads is determined no matter which velocity will be chosen or whether the movement will be interrupted or not. Using this information the optimization problem is limited to the question at which positions the system needs to change from one switching state into another.

Another important aspect is the modeling of the accumulator. According to equation (7) it has a nonlinear behaviour which is difficult to handle. For this reason the accumulator behaviour needs to be linearized. One of the results of the multi objective optimization (shown in Figure 5) is that the accumulator is never charged with more than 5 L so a linear model represents a good approximation if compared to the real measured behaviour shown in Figure 7.

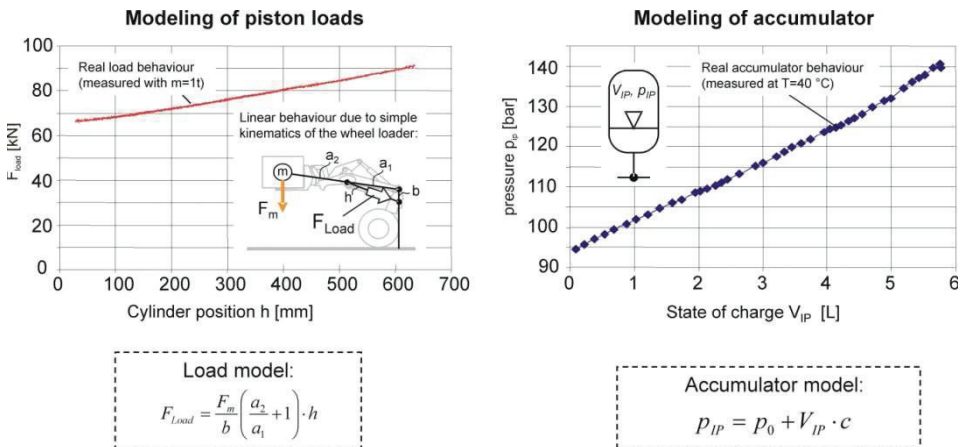


Figure 7: Modeling of loads and accumulator using measuring data

### 3.2 Online optimization algorithm with Dynamic Programming

Due to the linear correlation between load and piston position the loads on the lifting cylinder can be precisely predicted. The *prediction horizon* is therefore the cylinder stroke from the present position (which is measured) until its end position (which is estimated). A simplification of the optimization problem can be achieved if the variety of possibilities is limited by sorting the switching states in ascending order of maximal reachable force as shown in **Figure 8**. The switching sequence therefore consists of  $n=6$  periods with different switching states for each period. The sequence begins with period  $i=1$  and IP/IP as the switching state with the lowest force and finishes with  $i=6$  and HP/TP as the one with the highest force. For the given prediction horizon the duration of each period  $i$  can be described with the length  $s_i$  representing the cylinder stroke driven with the respective switching state. The prediction horizon is therefore the sum of all lengths  $s_1 \dots s_6$ . As almost all switching states influence the SOC of the accumulator, the choice of the length  $s_i$  at the period  $i$  is called *policy* as it influences all switching decisions in the succeeding periods and therefore the efficiency of the whole movement. When driving the piston at HP/IP for example, the accumulator is being charged and therefore the maximum possible force is continuously lowered due to the increasing pressure in the accumulator (which is considered as a linear function of the SOC). Simultaneously the maximum force of IP/TP will increase as well as its possible duration because of the simple fact that there is more oil in the accumulator to effectuate the movement. The online optimization algorithm must therefore determine the optimal policy  $s_{opt,i}$  for each period  $i$  in a way that the throttle losses, which are described by the *objective function*  $E_{Loss}$  are as low as possible. The Dynamic Programming optimization method /10/ supposes the criteria of Bellman describing a policy in a period  $i$  as optimal if it minimizes the objective function of the same period  $i$  and the one of the succeeding period  $i+1$ .

$$E_{Loss,min,i}(h_i, V_{IP,i}) = \min \left\{ E_{Loss,i}(h_i, V_{IP,i}) + E_{Loss,min,i+1}[T(h_i, V_{IP,i})] \right\} \quad (8)$$

$s_{opt,i}$  is the solution for equation (8) and minimizes  $E_{Loss,i}$  which are throttle losses and result from the difference of maximal forces of the states and the load at each period. Due to the dependence of the maximal force on the SOC  $V_{IP,i}$  and the dependence of the load on the position  $h_i$  of the piston the objective function  $E_{Loss,i}$  depends on both parameters which are variables describing the *states* at the beginning and end of each period. The throttle losses  $E_{Loss}$  at the stage  $i$  and the throttle losses at the succeeding stage  $i+1$  need to be linked to calculate the minimum at  $i$ . This link is done here with the *transition functions*  $T[h_i, V_{IP,i}]$  which describe the linking of the SOC  $V_{IP}$  and the piston position  $h$  of two periods:

$$h_{i+1} = h_i + s_i \quad (9)$$

$$V_{IP,i+1} = V_{IP,i} + s_i \cdot A_{Piston,i} \quad (10)$$

As the accumulator is being charged or discharged in dependency of which switching state is presently used, the piston surface  $A_{Piston}$  and its sign depend on the present stage  $i$ .

With the easy initial calculation of the optimum length of the switching state at the last stage using the estimated final position  $h_7$

$$s_{opt,6} = h_7 - h_6 \quad (11)$$

equation (8) can be solved top down calculating  $s_{opt,i}$  for each period until arriving at index 1 with the initial state variables  $h_1$  and  $V_{IP,1}$  which are measured and therefore known. The results for  $s_{opt,i}$  are functions which depend on the state variables  $h_i$  and  $V_{IP,i}$  of each period. They are created offline and stored in a table. If the initial state variables  $h_1$  and  $V_{IP,1}$  change, the optimum switching sequence is adapted immediately by recalculating bottom up all values  $s_i$  which makes this optimization algorithm very fast and deterministic as it does not approach iteratively the optimum but it calculates it analytically in a single run. However, the quality of the optimization depends on how the prediction horizon is chosen. For better results the maximum stroke at  $h_7$  need to be as close as possible to the real stroke used in practice.

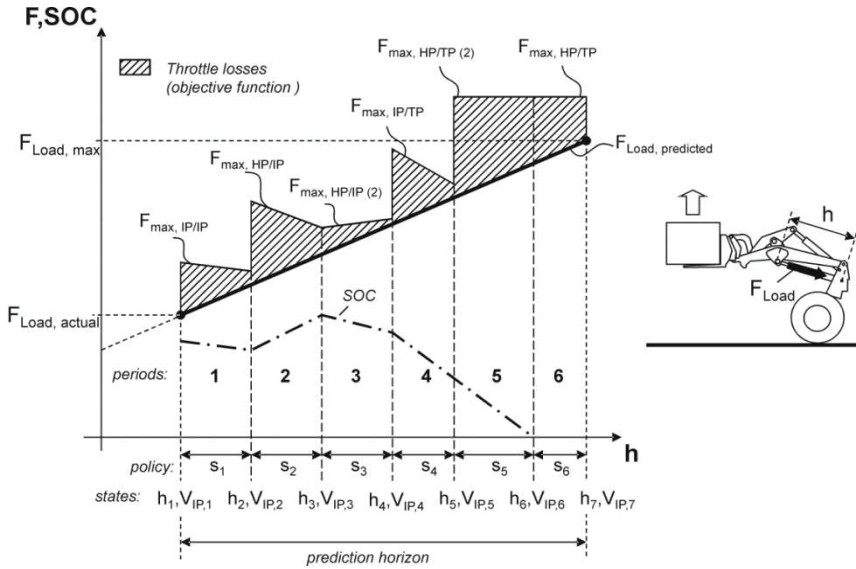


**Figure 8: Principle of online optimization with Dynamic Programming**

### 3.3 Simulation results

A big advantage of the online optimization algorithm is the deterministic calculation of global minima. The equations are simple as the used mathematical models to describe load and accumulator behaviour are linear. For each switching state of the lifting cylinder exists one equation which is stored in the controller of the system. At each calculation cycle of the controller the input data like piston loads, piston positions and intermediate pressure are transformed into loads, forces and SOC and the equations are solved. This very simple and fast online optimization algorithm is programmed into a Programmable Logic Controller (PLC) which will pilot the system of the experimental vehicle. Before being applied on the machine, the program code is tested in a simulation environment first. For this purpose a simulation model was created and validated with measuring data from the wheel loader. In order to make the virtual test environment as realistic as possible and to have an efficient tool to improve the program code of the PLC, the simulation model was connected directly



to the program code via an Object Linking and Embedding for Process Control (OPC) interface as described in [11]. This enables an interchange of data between program algorithm of the PLC and the simulation model. A realistic system behaviour can be achieved allowing a first validation if the online optimization is working and how the system does improve the efficiency of the system. **Figure 9** shows the simulation results of four succeeding Load & Carry cycles. In this simulation the duty cycle is not known by the control algorithm, the controller need to find the optimal switching decision at any instant. Thanks to the online optimization algorithm the switching sequence is very close to the one found with the offline optimization method and an improvement of efficiency of 13% compared to a LS system could be determined. The energy trajectory shown in Figure 9 represents not the global optimum as only the extending lifting cylinder is considered with the optimization method.

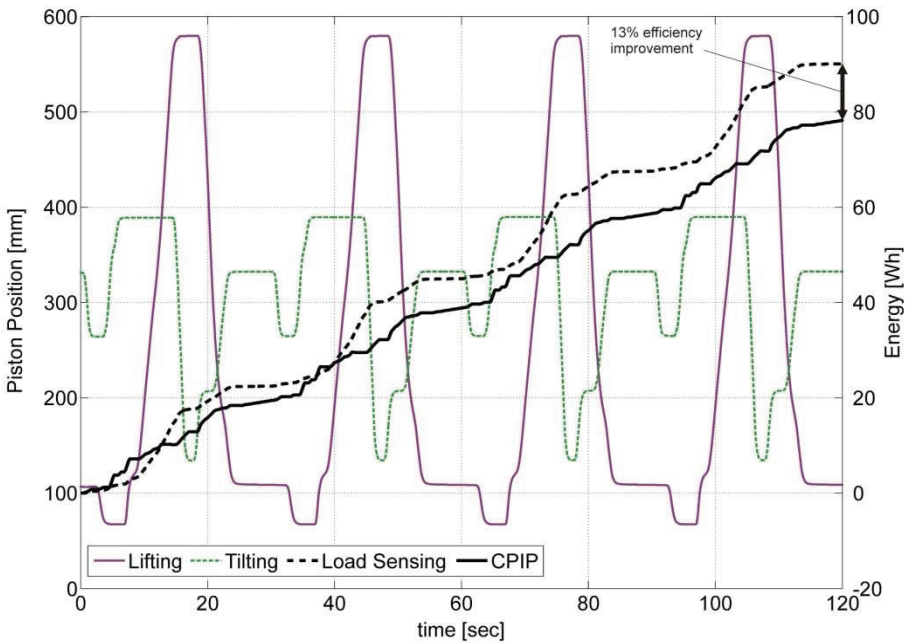


**Figure 9: Results of simulation run of four cycles showing efficiency improvement**

#### 4 SUMMARY AND OUTLOOK

The paper presents the idea of an energy efficient actuation of hydraulic cylinders in a constant pressure system when another line with intermediate pressure is used. This allows an integrated hybrid hydraulic system with secondary controlled hydraulic rotary drives and standard hydraulic cylinders which are operated at different pressure potentials between high pressure, intermediate pressure and tank pressure. An optimum sequence for a chosen specific duty cycle is determined by the use of a multi objective optimization. An online

control algorithm was developed using the Dynamic Programming method and tested in simulation showing an efficiency improvement of 13% compared to LS.

The control algorithm which will be used for the logic controller will be tested and improved by the help of software-in-the-loop simulations [11]. The wheel loader is equipped with valve blocks and accumulators for HP line and IP line as shown in **Figure 10**. The fuel consumption of the new system will be compared to the one of the LS system to prove the overall efficiency.



**Figure 10: Results Test machine with mounted valve blocks and accumulators**

## 5 ACKNOWLEDGEMENTS

The project was performed by the Chair of Mobile Machines (Mobima) at the Karlsruhe Institute of Technology (KIT) in cooperation with ARGO-HYTOS GmbH, FLUIDON GmbH and Hermann Paus Maschinenfabrik GmbH. The project is financed by the Federal Ministry of Education and Research (BMBF) and supervised by the German Aerospace Center (DLR). The authors thank the BMBF and the DLR for the support of this project.



## 6 REFERENCES

- /1/ Dreher, T.: *The Capability of Hydraulic Constant Pressure Systems with a Focus on Mobile Machines*, 6<sup>th</sup> FPNI – PhD Symposium, West Lafayette 2010, proceedings p. 579-588.
- /2/ Haas, H.-J.: Sekundärgeregelte hydrostatische Antriebe im Drehzahl- und Drehwinkelregelkreis, PhD thesis, RWTH Aachen, 1989
- /3/ Fischer, H. Steigerwald, T. & Godzig, M.: Hydraulic Systems for Deep-Sea Applications, 7<sup>th</sup> International Fluid Power Conference, Aachen, 2010.
- /4/ Linjama et. al.: Secondary Controlled Multi Chamber Cylinder, 11<sup>th</sup> Scandinavian International Conference on Fluid Power, Linköping, 2009.
- /5/ Bishop, E. D.: Digital Hydraulic Transformer – Approaching theoretical Perfection in Hydraulic Drive Efficiency, 11<sup>th</sup> Scandinavian International Conference on Fluid Power, Linköping, 2009.
- /6/ Dengler P. et. al.: Efficiency Improvement of a Constant Pressure System Using an Intermediate Pressure Line, 8<sup>th</sup> International Fluid Power Conference, Dresden, Germany, 2012.
- /7/ Böckl, M.: Adaptives und prädiktives Energiemanagement zur Verbesserung der Effizienz von Hybridfahrzeugen, PhD Thesis, University of Vienna, Austria, 2008.
- /8/ Kohmäscher, T, Jähne, H., Deiters, H.: Moderne voll- und teilhydrostatische Fahrtriebe – Untersuchung und Weiterentwicklung von Antriebsstrangkzepten mobiler Arbeitsmaschinen, O+P 5, 2006.
- /9/ Back, M.: Prädiktive Antriebsregelung zum energieoptimalen Betrieb von Hybridfahrzeugen, PhD Thesis, University of Stuttgart, Germany, 2005.
- /10/ Sniedovich, M.: Dynamic Programming: Foundations and Principles, CRC Press, 2011.
- /11/ von Dombrowski R., Dengler P.: KonZwi – Effizienzsteigerung durch eine Zwischendruckleitung, SIMPEP – Kongress für Simulation im Produktentstehungsprozess, Veitshöchheim, Germany, 2011.

# Proportional control system design and probability of stability for a pilot operated proportional valve with parametric uncertainty

**Richard Carpenter** (racf8f@mail.missouri.edu)

**Roger Fales** (falesr@missouri.edu)

Mechanical and Aerospace Engineering Department

Rolf Fluid Power Lab

University of Missouri

Columbia, Missouri

## ABSTRACT

The stability and performance of hydraulic components is critical to ensure the reliable and robust operation of the entire system. Parametric uncertainties within the system, i.e. spring rates and part geometry, can contribute to variations in performance and can affect the overall stability of the system. The focus of this work is first to show that analytical models can be used to predict variations in frequency responses, given known variations of the system parameters. Feedback control system gains can then be found that increase system performance while maintaining the stability of a large fraction of the plants. This methodology is verified by modeling and testing of a pilot operated proportional valve. Thirty replications of the pilot stage of the valve were tested for performance and stability along with one main stage. An analytical model of the system was developed and simulated with known physical parameter distributions. An uncertainty model is formed based on experimentally determined parameters and used for robustness analysis of the system. It is shown that an increase in performance can be realized with a tradeoff in possible instability of a small and predictable fraction of the plants.

## 1. INTRODUCTION AND BACKGROUND

The goal of this work is to provide a method to account for the effects of parametric uncertainty in dynamic systems when designing closed-loop controllers. Uncertainties in parameters such as spring rates, masses, and geometrical properties can lead to variations in system stability and performance. This research is focused on constructing error (uncertainty) models that account for a certain fraction of total error within the system and utilizing the error model to design reliable and robust controllers.

An uncertainty model can be used to predict stability and performance of a valve control system with consideration of uncertain parameters within the model. A typical conservative approach would be one that bounds all possible error within the system. Generally, the higher the plant model uncertainty, the lower performance of a feedback control system must be to ensure robustness, Skogestad and Postlethwaite [1]. In classical control terms, more plant model uncertainty means that a controller applied to create a closed loop system must have a greater gain margin. Greater gain margin typically is obtained at the expense of performance.

In this work, statistical data about parameters systems are used to predict the probability of failure due to not achieving performance and stability requirements expressed in the frequency domain. A Monte Carlo method will be used to build an error model based on parameters that can be modeled as random numbers. The error model can be used to determine whether a system is stable or meets performance specifications with a given probability. The Monte Carlo approach used in this work provides a convenient way to solve a problem that is a function of potentially numerous random variables, Rubinstein [2].

For a long time, manufactures have predicted the number of assembly failures due to the interference fit between parts that experience tolerance stack up, Stoll [3]. Some research has focused on probabilistic control design which seeks to design controls such that success would be most likely given the statistical distribution of plant dynamics, Crespo [4]. This method is similar to what is presented here but does not provide for predictions of failure rates. There is also active research in the area of Probability Stability where one can predict the probability of stability based on the statistical distribution of dynamic equation parameters, Jovanovic and Dankovic [5]. However, these methods tend to be cumbersome for all but the simplest low order systems.

Further research has focused on determining bounds on parametric uncertainties which would lead to instability, Jang [6]. This work has shown that Monte Carlo methods can be used to accurately simulate perturbed frequency responses given uncertain parameters within a system. However, these methods tend to focus on determining acceptable uncertainty bounds from Eigen-value analysis. This work does not consider the use of the uncertainty bounds in developing robust control systems. Other research has focused on the stochastic nature of plant uncertainty (i.e. uncertain parameters) which can be used to determine the stochastic root locus and probability of instability, Stengel [7]. In addition, this work has been extended to determining the probability of achieving performance requirements and to nonlinear systems by developing indicator functions that are examined statistically to determine the probability of achieving specified behavior, Stengel and Wang [8].

## 2. FREQUENCY DOMAIN ERROR MODELING

A frequency domain error (uncertainty) model can be used to analyze the robust performance and stability of closed-loop control systems, Skogestad and Postlethwaite [1]. Let a plant transfer function,  $G(j\omega)$ , represent all possible perturbations of the plant due to model uncertainty. Model uncertainty could take the form of uncertain parameters modeled as random numbers or experimental data describing the physical components of a system. A

nominal plant transfer function,  $G_{nom}(j\omega)$ , can be chosen as an average or typical plant. At each frequency, the frequency response of a set of  $G_p(j\omega)$  can be calculated and the frequency response of the multiplicative model error,

$$l(\omega) = \frac{G_{nom}(j\omega) - G_p(j\omega)}{G_{nom}(j\omega)}, \quad (1)$$

can also be calculated.  $l(\omega)$  comprises a set of multiplicative errors generated using (1) and a set of perturbed plants  $G_p(j\omega)$ . It should be noted that multiplicative error is not the only type of error that could be used in this procedure. The uncertainty model could also be generated using for example, additive, relative, or inverse multiplicative error.

If the plant response is uncertain, due to random uncertain parameters, then the frequency response of the multiplicative error magnitude will also have a random distribution at each frequency with probability density function,  $f_{l\omega}(\Theta)$ . Uncertainty can be modeled to account for a specified fraction of all possible error if the distributions of the plant frequency responses are known.

With an uncertainty model that describes the uncertainty for a large fraction of the possible error, control design and robustness analysis can then be carried out. Note that bounding a certain fraction of possible error within the system does not necessarily mean that the same fraction of perturbed plants are bounded. If 90% of error is bounded at each frequency, then the resulting number of plants bounded by the error model could be less than or equal to 90%. This is due to possible overlapping of frequency responses which is inherent in any randomly generated set of plant errors due to uncertain parameters.

Robustness analysis on a controller designed using the new uncertainty model would then only apply to the fraction of plants bounded by the uncertainty model. This creates a way to avoid the typically conservative control design that results from considering all possible plants in stability and performance analysis. Of course, the drawback is that control design using the new uncertainty model can only guarantee results for a portion of possible plants. Rather than finding a transfer function that bounds all  $l(\omega)$  at each frequency, we want to find a transfer function,  $w_x(j\omega)$ , with a magnitude frequency response that bounds a given fraction,  $x$ , of error at each frequency. If  $l(\omega)$  has a random magnitude at each frequency,  $\omega$ , then

$$P_{\omega}(|w_x(j\omega)| \geq |l(j\omega)|) = x \quad \forall \omega. \quad (2)$$

If  $w_x(j\omega)$  satisfies (2), then  $w_x(j\omega)$  is a model of the multiplicative uncertainty for a fraction,  $x$ , of the error associated with  $G(j\omega)$ . To satisfy Equation (2),  $w_x(j\omega)$  can be satisfied by first finding a magnitude,  $l^*(\omega)$  for each frequency in the following equation:

$$\int_0^{l^*(\omega)} f_{l\omega}(\Theta) d\Theta = x \quad \forall \omega \quad (3)$$

The magnitude,  $l^*(\omega)$ , is the explicit error magnitude that bounds the desired percentage of error at a particular frequency. The symbol  $f_{l\omega}(\Theta)$  stands for the probability density function

of the error magnitudes at a particular frequency. Note that the lower limit of the integral can be zero since the error magnitude is always greater than or equal to zero. A  $w_x(j\omega)$  must then be found that satisfies the above criteria.

The fraction of error,  $x$ , to be bounded by the error model is also determined. This value should be established by the designer based on experience with the system and the potential for uncertainty within the parameters. For this work  $x = 0.90 - 0.95$  is typically used, however,  $x$  could take on any value from zero to one. In terms of the probability of stability or performance, this means that bounding zero percent ( $x = 0$ ) of the error will result in an analysis that will not be able to guarantee that any plants meet the desired performance specifications and the analysis is therefore meaningless. Similarly, if 100% ( $x = 1$ ) of the error is chosen, all plant error is included in the uncertainty model and resulting analysis would be used to form conclusions on 100% of possible plants.

The model of the plant accounting for error is then given in the multiplicative form as

$$G(j\omega) = (w_x(j\omega)\Delta(j\omega) + 1)G_{nom}(j\omega). \quad (4)$$

The symbol  $\Delta(j\omega)$  stands for the set of all stable rational transfer functions with magnitude less than or equal to one. A block diagram describing the plant model including the nominal plant with the error model applied is given in Figure 1. In this case,  $w_x(j\omega)$  takes the form of a transfer function,  $w_x(s)$ , which can be found using standard transfer function fitting techniques. In this work,  $w_x(s)$  will be determined using Matlab's "fitmag" command.

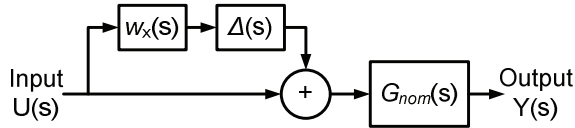


**Figure 1. Plant model including an error model where  $G_{nom}(s)$  is the nominal plant model**

### 3. OPEN-LOOP EXPERIMENTAL SETUP AND RESULTS

Pilot operated proportional control valves are electro-hydraulic systems that control the motion of actuators by regulating hydraulic pressure and flow to the actuator. In large valve systems a substantial amount of force is necessary to move the main valve due to large flow forces that need to be overcome. Typically in applications such as off highway machinery, two stage proportional valves are implemented that use pilot pressure in the first stage to shift the main valve in the second stage. The performance and stability of the entire hydraulic system is largely dependent on the characteristics of the pilot stage. In this work, uncertainty modeling and stability analysis are considered for a three-way electric pilot valve. The purpose of this study is to determine if uncertainty modeling and control design of an open-loop system, based on simulations of an analytical model, can accurately predict the stability of a closed-loop system.

Thirty replications of the electro-hydraulic pilot valve shown in Figure 2 were obtained and tested in an open-loop system using one main valve. Sinusoidal inputs were given to the valves via MATLAB SIMULINK and a Copley Controls current driver (Model #421CE). Each pilot stage valve was tested individually with the main valve. The three-way pilot stage is connected to the four-way main valve. The solenoid creates a force on the pilot spool which compresses a spring and opens the control pressure port to supply pilot control pressure. The control pressure is sent to one side of the main valve which displaces the main spool, opening Port A to supply pressure. Flow is then sent through port A and returns through port B. To depressurize the system, the current command to the solenoid is decreased which allows the pilot spool to return to a position such that there is a flow path to tank. For the experimental work presented here, ports A and B of the main valve were connected together and flow allowed to pass between the two ports.

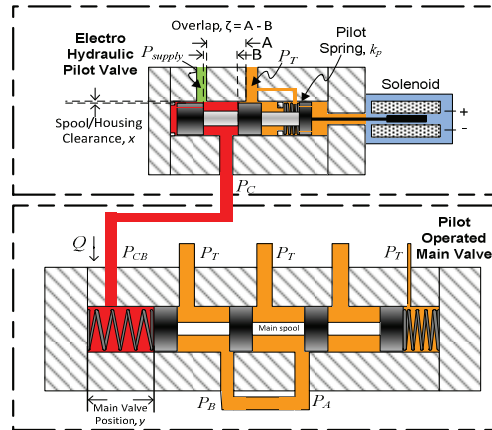


**Figure 2: Pilot operated proportional control valve used for experiments.**

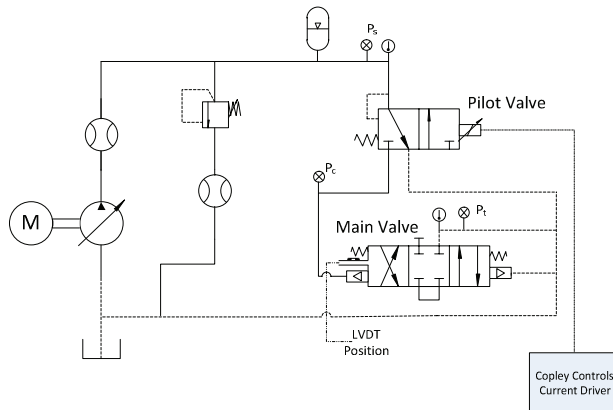


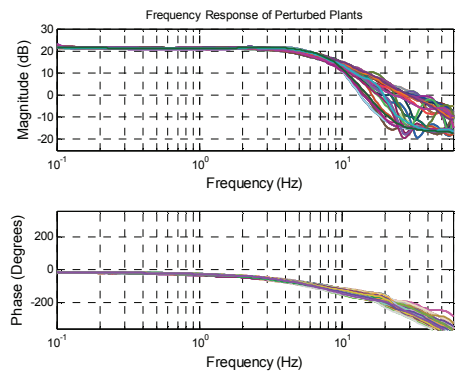
**Figure 3: Hydraulic circuit used for valve testing.**

The hydraulic circuit shown in **Figure 3** is used for experimental testing. A pilot supply pressure of 31 bar was supplied by a hydraulic power unit (HPU) and regulated using a pressure relief valve. A flow of 15 lpm over the relief valve was kept constant during the

tests and measured using a flow meter. An LVDT was used to measure the position of the main valve. Inlet temperature to the system was maintained within a range of 30° C and 40° C for all valve testing.

Sinusoidal inputs to the valves were given to show variability in the frequency responses between the valves. A current offset of 0.8 Amps was supplied to the valve to move the main valve to the center of the main spool range of operation at 5 mm. Sinusoidal inputs were then superimposed, one with an amplitude of 0.25 Amps (~25% of full range). The sinusoid frequency was increased logarithmically over 30 frequencies from 0.1 Hz to 60 Hz. At each frequency the amplitude was held steady for 20-30 seconds for small frequencies and 5-10 seconds for large frequencies to ensure that multiple periods of the response were captured.

A frequency response was formed from each valve response using a Fast Fourier Transform (FFT) algorithm in MATLAB. At each frequency the magnitude and phase of the response at that frequency was determined and plotted in a Bode diagram. The results are based on the current to the pilot valve solenoid taken as the input and the main valve position taken as the output. The resulting Bode diagrams from all of the valves are shown in Figure 4. Little error between the responses is shown at low frequency. However, at higher frequencies, above 10 Hz, the error becomes significantly greater.

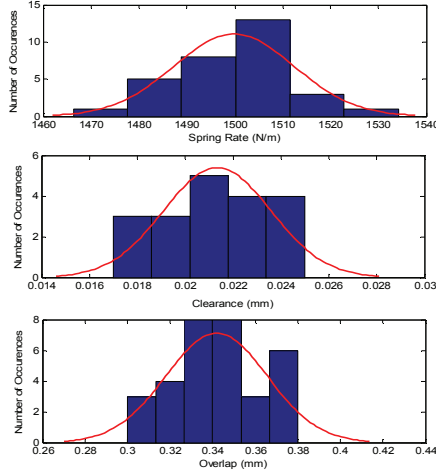


**Figure 4. Bode plots of the frequency responses of all valves using data from frequency grid inputs.**

After open-loop testing was completed, each valve was disassembled and spring rates and geometrical properties were measured. Figure 5 shows histograms of the pilot spring rates, spool/housing clearance, and pilot overlap. A fair amount of variations in the physical parameters is shown. The mean and standard deviations of these distributions, shown in Table 1, will be used in a later section to perform Monte Carlo simulations of a linearized model.

**Table 1. Summarization of parameter measurement results.**

	Spring Rates (N/m)	Overlap (microns)	Clearance (microns)
<b>Mean</b>	1500	340	21
<b>Standard Deviation</b>	12.6	23.9	2.2
<b>95% Confidence Interval</b>	$\pm 4.7$	$\pm 8.9$	$\pm 0.9$

**Figure 5: Histograms of pilot valve physical parameters with over-plot of normal distribution.**

## 5. MATHEMATICAL MODEL OF THE POPCV

In this section, a mathematical model of the pilot operated proportional control valve is presented. The analytical model is primarily based on work by Manring [9]. The model is constructed with regards to the experimental setup presented in Section 3. Equations for the pilot stage and the main stage are presented and include pressure rise rate and flow equations. The mass spring damper system for the pilot spool valve is shown in Eq. (5) and includes flow forces. A second mass spring damper equation for the main spool is shown in Eq. (6). Due to the A and B output ports of the main spool being connected together and held at tank pressure, flow forces into and out of these ports could be neglected.

$$m\ddot{x} = F - b_x\dot{x} - k_x x - F_{px} - (P_B - P_T)A_p - (P_B - P_T)2C_d^2 A_1(x)\cos(\theta) + (P_S - P_B)2C_d^2 A_2(x)\cos(\theta) \quad (5)$$

$$M\ddot{y} = (P_B - P_A)A_y - b_y\dot{y} - k_y y - F_{py} \quad (6)$$

A pressure rise rate equation for the pilot control pressure is shown in Eq. (7).



$$\dot{P}_{CB} = \frac{\beta}{V_{c0} + A_y y - A_p x} (-Q_1 + Q_2 - A_y \dot{y}) \quad (7)$$

The flow rates  $Q_1$  and  $Q_2$  are given in Eq. (8) and Eq. (9).  $Q_1$  is dependent on the pilot tank orifice area which is a function of the position of the pilot spool.  $Q_2$  is dependent on the pilot supply orifice area which again is a function of the position of the pilot spool.

$$Q_1 = A_1(x) C_d \sqrt{\frac{2}{\rho} (P_B - P_T) + (P_B - P_T) C_{IL}} \quad (8)$$

$$Q_2 = A_2(x) C_d \sqrt{\frac{2}{\rho} (P_S - P_B) + (P_S - P_B) C_{SL}} \quad (9)$$

The nonlinear model of the valve system was constructed in Simulink. Parameters of the nonlinear model were either found by measurement of the physical system or optimized to provide similar results to the experimental data.

Step inputs were also given to the nonlinear model and comparisons of those are shown in Figure 6 and compare well with the experimental data. A frequency response of the model is shown in Figure 7. The magnitude of the nonlinear model is shown to compare well to experimental data at frequencies below 10 Hz, with little to no error. Above 10 Hz, the magnitude error grows and reached a maximum of approximately 50%.

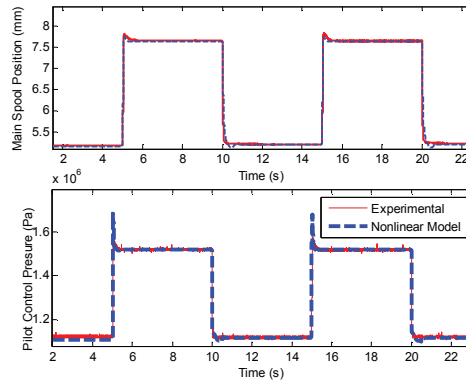


**Figure 6. Step responses of experimental versus nonlinear model of the main spool position and control pressure.**

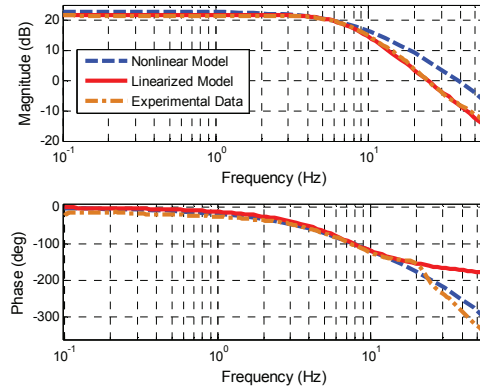


**Figure 7. Experimental versus simulated results of frequency response with experimental data from 50% nominal 25% amplitude grid input.**

## 6. UNCERTAINTY MODEL OF THE POPCV

The nonlinear model was linearized about a nominal operating condition of 50% of the metering range. Monte Carlo simulations were performed on the linearized model with the physical parameters found in Section considered to be random variables with normal distributions. Parameters including pilot/housing clearance, pilot spring rate, and the pilot metering area were chosen as the random variables. Other parameters within the model could be chosen, such as damping coefficients and oil bulk modulus. However, the distribution of these parameters is not easily determined. Therefore, it was decided to only use parameters that could be directly measured, i.e. spring rate and geometry. Pilot valve overlap does not appear directly in the linearized valve model; however it is used in the calculation of the pilot metering area Manring [9]. Clearance also does not directly appear in the model. However, it is used in calculation of the supply and tank leakage coefficients which directly affects valve performance.

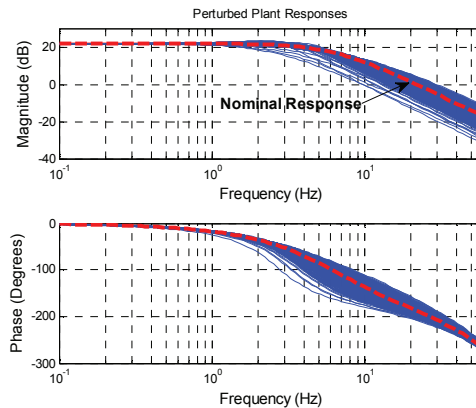


**Figure 8. Frequency responses of perturbed plants**

An  $N = 1000$ , number of perturbed plants were simulated using the linearized valve model. Frequency responses of the perturbed plants are shown in Figure 8. A significant amount of variability is shown at higher frequencies, although less than that of the experimental data. The bounded fraction of error,  $x = 0.90$ , was used to construct an uncertainty model based on the simulated responses. The error bounds along with the multiplicative error magnitudes are shown in Figure 9.

**Table 2. Experimental and simulated error magnitudes at high and low frequency.**

Error Bound	Experimental		Simulated	
	90% , $w_x(s)$	100 %	90% , $w_x(s)$	100 %
Low Frequency Error, (0.1 Hz)	5%	10%	1.4%	1.8%
High Frequency Error, (60 Hz)	84%	100%	34%	81%

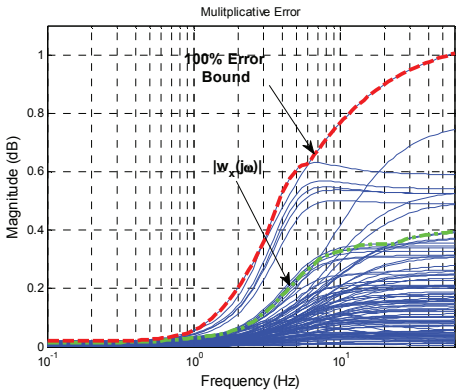


**Figure 9. Multiplicative error magnitudes of simulated frequency responses.**

**7. PROPORTIONAL CONTROLLER DESIGN**

A proportional control design for the pilot operated proportional valve system is presented in this section. The same control structure as that shown in Figure 1 will be used, with  $K(s) = K_p(s)$ . The proportional controller takes the form of a simple feedback gain applied to the main valve position error. The controller is designed through analysis of the open-loop stability margins.

Stability margins can be utilized as a way of characterizing closed-loop performance and stability using an open-loop frequency response. Gain margins can be calculated from a frequency response and used as a measure of how close a closed-loop system is to instability (Skogestad 1996). Gain margin is defined as:

$$GM = \frac{1}{|L(j\omega_{180})|} \tag{10}$$

Where the phase crossover frequency,  $\omega_{180}$ , is the frequency at the point where the phase of  $L(s) = K(s)G(s)$ , crosses  $-180^\circ$ , i.e.

$$\angle L(j\omega) = -180^\circ \quad (11)$$

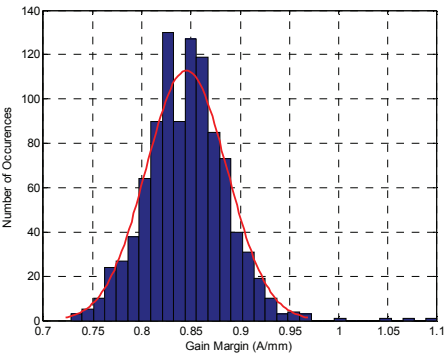


**Figure 10. Simulated gain margins of valve model with over plot of normal distribution.**

The frequency responses of the linearized valve model were also used to determine a distribution of gain margins of the valve system. A histogram of the gain margins of the frequency responses shown is shown in Figure 10, with an over plot of the normal distribution associated with the data. A mean gain margin of 0.84 A/mm was found with a standard deviation of 0.04 A/mm. A few outliers are present in the data, showing a very small percentage of systems being stable at unity gain.

From uncertainty modeling of the analytical model, it was determined that 80% of plants were bounded when accounting for 90% of the total error within the system. Therefore, a proportional control gain that ensures stability for 80% of the plants can be found. Using the normal distribution of the simulated gain margins, it was determined that a proportional control gain of  $K(s) = 0.80$ , should ensure stability for the fraction of plants bounded by the model, the same fraction of plants bounded by the error model.

Robustness analysis is completed using the error model,  $w_x(j\omega)$ , the tracking performance weight transfer function,  $w_p(j\omega)$  and the control effort weight  $w_u$ . The block diagram of the system including the uncertainty model and performance inputs and outputs is given in Figure 11. The critical signals are labeled on the diagram.

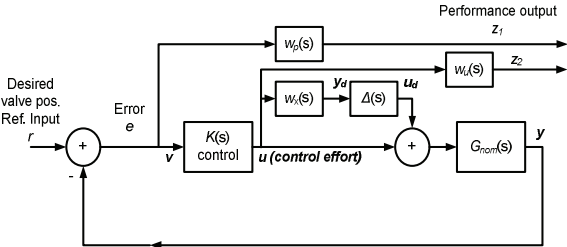


**Figure 11. Control system with performance weights and error transfer functions.**

**Table 3: Proportional Control Design Parameters**

Low Frequency Error, $a$	0.1
High Frequency Error, $M_p$	1.5
Bandwidth, $\omega_b$	10
Weight on Input (mm), $w_u$	0.01

A rearrangement of the block diagram in

FIGURE 11 is a convenient way to look at a system with many of the blocks combined into a generalized plant,  $P$  (Skogestad, 1996). The system in terms of the generalized plant is given as follows with  $P$  partitioned into four parts:

$$\begin{aligned}
 \begin{Bmatrix} y_d \\ z \\ v \end{Bmatrix} &= \begin{bmatrix} P_{11} & P_{12} \\ P_{21} & P_{22} \end{bmatrix} \begin{Bmatrix} u_d \\ r \\ u \end{Bmatrix} \\
 P_{11} &= \begin{bmatrix} 0 & 0 \\ -w_p G_{nom} & w_p \\ 0 & 0 \end{bmatrix} & P_{12} &= \begin{bmatrix} w_x \\ -w_p G_{nom} \\ w_u \end{bmatrix} \\
 P_{21} &= [-G_{nom} \quad 1] & P_{22} &= [-G_{nom}] \\
 z &= [z_1 \quad z_2]^T
 \end{aligned} \tag{12}$$

Once a system can be expressed in the standard form in (12) and the system can be transformed into a new transfer function matrix,  $N(s)$ , which includes the controller,  $K(s)$ , using a linear fractional transformation (LFT) with  $N = P_{11} + P_{12}K(I - P_{22}K)^{-1}P_{21}$ . After  $N$  is computed and partitioned, standard robustness analysis becomes a simple task using the following conditions on  $N$  for Nominal Stability (NS), Nominal Performance (NP), Robust Stability (RS), and Robust Performance (RP):

NS  $\leftrightarrow N$  is stable

NP  $\leftrightarrow \bar{\sigma}(N_{22}) = \mu_{\Delta p} < 1 \quad \forall \omega$

RS  $\leftrightarrow \mu_{\Delta}(N_{11}) < 1 \quad \forall \omega$

RP  $\leftrightarrow \mu_{\Delta}(N(j\omega)) < 1 \quad \forall \omega$ .

Also, note that RP implies NS, NP, and RS.

The Structured Singular Values for the 100% error bounds and the  $w_x(s)$  error bound are shown in Figure 12. The SSV's are shown to rise above one at some frequencies, for both error bounds. Therefore, it is not expected that the proportional controller will be able to ensure the performance parameters will be met. Results from robust stability test, shown in Table 4, confirm that with the control gain  $K(s) = 0.80$ , the system should ensure stability for the fraction of plants bounded by the error model,  $w_x(s)$ , given in Figure 9.

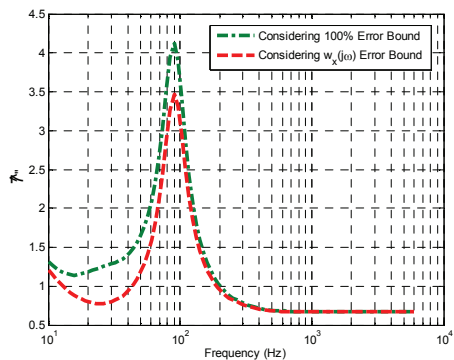


**Figure 12. Structured Singular Value of the robust performance norm of valve model with proportional gain  $K(s) = 0.80$ .**

**Table 4. Robustness analysis results for the two control schemes with uncertainty model bounding 100% of plants and 90% of plants.**

		Nominal Performance $\bar{\sigma}(N_{22})$	Robust Stability $\mu_{\Delta}(N_{11})$	Robust Performance $\mu_{\Delta}(N(j\omega))$
% of Error Bounded	90%	17.67	0.89	3.46
	100%	17.67	1.56	4.11

### 8. CLOSED-LOOP EXPERIMENTAL RESULTS

The testing circuit used for closed-loop testing of the POPCV was identical to that shown in Figure 3. The same testing procedure outlined for open-loop testing was also followed for closed-loop testing of all 30 pilot valves. Step input responses were used to determine stability of the closed-loop system with a proportional gain. Instead of testing the single proportional gain found in Chapter 6, a large range of proportional gains were tested to determine the gain at which instability occurs. A step input of 5 mm to 7.5 mm was repeatedly given to the valve while increasing the gain from 0.1 to 1, in steps of 0.01. An example of the step responses is shown in Figure 13. It is clearly shown the point at which instability in the valve occurs. A sustained oscillation (stable limit cycle) is produced at a gain of  $K_p = 0.88$  for the valve response shown. The limit cycle typically appears in the 7.5 mm step range before occurring in the 5 mm range. The gain which first causes a limit cycle in either step range is taken for consideration in the analysis. The set of proportional gains which caused a stable limit cycle for each valve are shown in the histogram in Figure 14. Note also the large amount of steady state error associated with the proportional control gains. At low gains the steady state error is as large as 200% and only decreases to approximately 15% at higher gains. The low frequency error performance objective for the proportional controller was given as 1% in Table 3. This confirms the robustness analysis discussed in Chapter 6, which showed robust performance could not be achieved with proportional feedback.

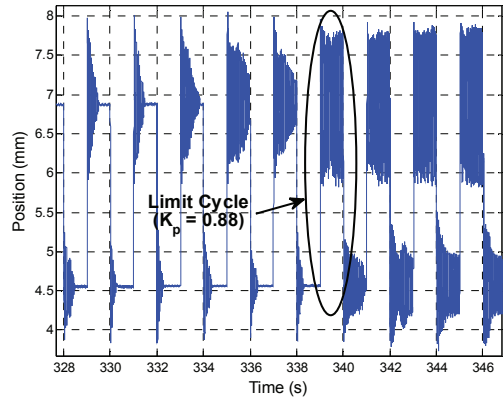


**Figure 13. Zoomed in step responses with increasing gain.**

The distribution of the proportional gains is comparable to the distribution of the gain margins found from simulations of the analytical model. A comparison is made in Table 5 of the, analytical gain margins and the proportional gains which caused instability. The mean, standard deviation and confidence bounds of the analytical model are similar to the experimental proportional gains. It could therefore be considered that simulated frequency responses of the linearized analytical modeling, given varying parameters, provided a good indication of the actual distribution of proportional gains which would cause instability. It was determined in Section 7, that a proportional gain of  $K_p = 0.80$ , would cause instability in no more than 20% of possible plants. The actual number of plants found with a proportional gain less than or equal to 0.80 was 4 out of 30 (13%).

The fraction of plants bounded by the error model (20%) and the fraction that was found to be unstable (13%) given the desired proportional gain are not an exact match. Although this may be true, given the small sample size ( $N = 30$ ) it would not be expected that these ratios would match perfectly. Control design using the error model,  $w_x(s)$ , does however ensure that *at least* the fraction of plants bounded by the model achieve stability. Taking into account the normal distribution shown with the proportional gains, it can be concluded that in order to achieve stability for near 100% of plants, a gain of  $K_p = 0.70$  would be needed.

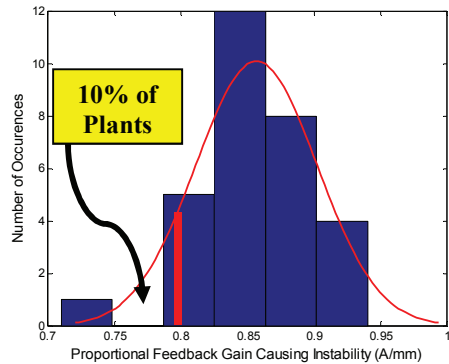


**Figure 14. Histogram of proportional gains causing a limit cycle in the valve system.**

**Table 5. Comparison of predicted control gains to actual.**

	Analytical Model Gain Margins	Proportional Gain Causing Limit Cycle
<b>Mean</b>	0.84	0.85
<b>Standard Deviation</b>	0.04	0.05
<b>95% Confidence Bounds</b>	$\pm 0.018$	$\pm 0.020$

## 9. CONCLUSIONS

The frequency domain uncertainty modeling technique presented in this work was used to design a proportional controller for a pilot operated proportional control valve. The uncertainty modeling was based on simulations of a linearized model using known distributions of physical parameters and open-loop responses of the valve. A controller was synthesized based on an error model that only bounded 90% of the perturbed plants. Robustness analysis showed that the controller would only guarantee stability for the fraction of plants that were bounded. Closed-loop experimental results showed that when the controller was implemented only 86% of the valves would remain stable. It can be concluded that this technique would allow for the development of closed-loop control systems that account for uncertainty within a system while increasing the performance of the system. However, this would come at a trade off that only the fraction of the plants bounded by the model would be guaranteed stability.

## NOMENCLATURE

Pilot Spool Displacement	$x$	Main Spool Mass	$M$
Main Spool Displacement	$y$	Solenoid Force	$F$
Pilot Spring Rate	$k_x$	Pilot Spring Pre-Load	$F_{px}$
Pilot Damping Coefficient	$b_x$	Main Spring Pre-Load	$F_{py}$
Pilot Spool Diameter	$d$	Control B Pressure	$P_{CB}$
Pilot Spool Mass	$m$	Tank Pressure	$P_T$
Main Spool Damping Coefficient	$b_y$	Supply Pressure	$P_S$
Pilot Metering Port Diameter	$D$	Area of Pilot Tank Orifice	$A_1(x)$
Discharge Coefficient	$C_d$	Area of Pilot Supply Orifice	$A_2(x)$
Fluid Density	$\rho$	Main Spool Area	$A_y$
Fluid Bulk Modulus	$\beta$	Pilot Spool Area	$A_p$
Discharge Angle	$\Theta$	Initial Control Volume	$V_{c0}$
Pilot Housing Radius	$R$	CB Supply Flow	$Q_1$
Pilot Spool Radius	$r$	CB Tank Flow	$Q_2$
Absolute viscosity	$\mu$	Coefficient of Leakage	$C.L$



## REFERENCES

1. Skogestad, S. and I. Postlethwaite, *Multivariable Feedback Control: Analysis and Design*. 1996, New York: John Wiley and Sons.
2. Rubinstein, R.Y., *Simulation and the Monte Carlo Method*. 1981, Hoboken, New Jersey: John Wiley and Sons.
3. Stoll, H.W., *Product Design Methods and Practices*. 1999, New York: Marcel Dekker.
4. Crespo, L. and S. Kenny, *Reliability-Based Control Design for Uncertain Systems*, in *AIAA Guidance, Navigation, and Control Conference* 2005: San Francisco, California.
5. Jovanovic, A. and B. Dankovic, *On the Probability Stability of Discrete-Time Control Systems*. FACTA UNIVERSITATIS. SERIES: ELECTRONICS AND ENERGETICS, 2004. **17**.
6. Jang, J.W., C.V. Tassell, and N. Bedrossian, *Evaluation of Ares I Control System Robustness to Uncertain Aerodynamics and Flex Dynamics*. AIAA Guidance, Navigation, and Control Conference, 2008.
7. Stengel, R.F. and L.R. Ray, *Stochastic Robustness of Linear Time-Invariant Control Systems*, "IEEE Transactions, Automatic Control, 1991. **36**(1).
8. Wang, Q. and R.F. Stengel, *Robust control of nonlinear systems with parametric uncertainty*. Automatica, 2002. **39**(9): p. 1591-1599.
9. Manring, N.D., *Hydraulic Control Systems*. 2005, Hoboken, New Jersey: John Wiley and Sons.

# Control and Modelling



# Optimizing Dynamic Properties of Hydraulic Actuator for Hardware-in-the-Loop Damper Testing

**T. Saarikoski, J. Kajaste, M. Pietola**

Aalto University School of Science and Technology  
Department of Engineering Design and Production  
P.O.Box 14400  
02150 Espoo  
Email: [tuomas.saarikoski@aalto.fi](mailto:tuomas.saarikoski@aalto.fi)

## ABSTRACT

In Hardware-in-the-Loop (HIL) damper testing a physical damper is embedded in a virtual operational environment, or ‘plant model’. Hydraulic actuation is a common choice for this type of application for generating plant model motion to the damper rod. It has been found in previous studies, that actuator dynamics is the major source of simulation error in a real-time HIL damper testing environment. Actuator lag causes measured damping force in the system to lag behind the virtual plant model, which causes error in the simulation increasing with frequency. While the issue is often acknowledged, its effect in final simulation error is dependent on various system parameters and not easily analyzed.

In this paper the effect of actuator dynamics in HIL simulation accuracy was studied using an example plant model and simulated actuator dynamics. This allows estimation of HIL simulation error when reference data from the original system is not available.

To improve the system’s high frequency performance predictive control was implemented for the actuator. Inverted model of the actuator and its control valve were used to compensate for valve-actuator dynamics. It was found with this setup that HIL simulation error could be greatly reduced with the predictive control.

**Keywords:** Hydraulic actuator, control, Hardware-in-the-Loop, damper, real-time

## 1. INTRODUCTION

Hardware-in-the-Loop (HIL) method in damper testing means that a physical damper is embedded in a virtual operational environment called the ‘plant model’. A real-time interface is used to connect the hardware to the plant model. An actuator is needed to generate plant model motion to the damper rod. It was found in a previous study that the hydraulic actuator used was the single most significant source of simulation error and was

limiting system's usable frequency range.[1] Traditional PID controller gave good amplitude response but introduced significant phase lag. Measured actuator movement was found to be 6 ms behind plant simulation target. This causes the damping force to arrive 6 ms late to the plant model.

The usable frequency range in HIL damper testing usually extends to 10-20 Hz depending on system setup. However it is mentioned in many sources [2, 3, 4] that accuracy starts to suffer after 8-10 Hz. This is because of the 6-8 ms response time of the hydraulic system, when using PID control. The main problem with PID is that it requires either a significant amount of error variable or gain to react quickly. Using higher feedback loop gain reduces lag but causes overshoot and instability due to fluid compressibility and moving mass inertia.

Not a lot of information about HIL simulation accuracy can be found with mechanical systems testing, although possible instability issues are often mentioned as a result of interface delays. In [5] a method for evaluating interface 'transparency' was introduced. However, it only addresses the interface error, not the HIL system as a whole. To predict HIL result error it is necessary to model the whole system, because HIL simulation is a closed loop system. [6] proposes a method for evaluating accuracy of high power electrical HIL simulations. The method was found fairly accurate compared to a 'pseudo-HIL' with modelled interface dynamics, and a real HIL setup. In this paper a similar approach 'pseudo-HIL' is used to evaluate the simulation. It was also investigated how different types of actuator error affect the HIL simulation results. Simulation's sensitivity to both amplitude and phase error was investigated by software simulations, where the error was advisedly added to the system.

To improve HIL accuracy predictive velocity feedforward and acceleration feedforward loops are implemented to compensate for actuator phase lag. Improved actuator tracking capability in the system improves the dynamic performance of the HIL method in damper testing providing more accurate results especially in higher frequencies.

## 2. HIL TEST SETUP

The plant was modelled with MATLAB/Simulink software. The model was then uploaded to a real-time computer running xPC Target operating system. The plant model describes inertia of the mass, spring forces and excitation forces affecting the mass and calculates position of mass that is used as a target value for a position controlled hydraulic actuator. The actuator produces the movement to the physical damper under test. A load sensor is used to measure the damping force created in the system. Measured damping force is fed back into the plant simulation that calculates new mass position in real-time. The model also includes a software controller that is used to drive the directional valves directly. Layout of the test system including the hydraulic position servo, real-time simulation hardware and the damper being tested can be seen in Fig.1.

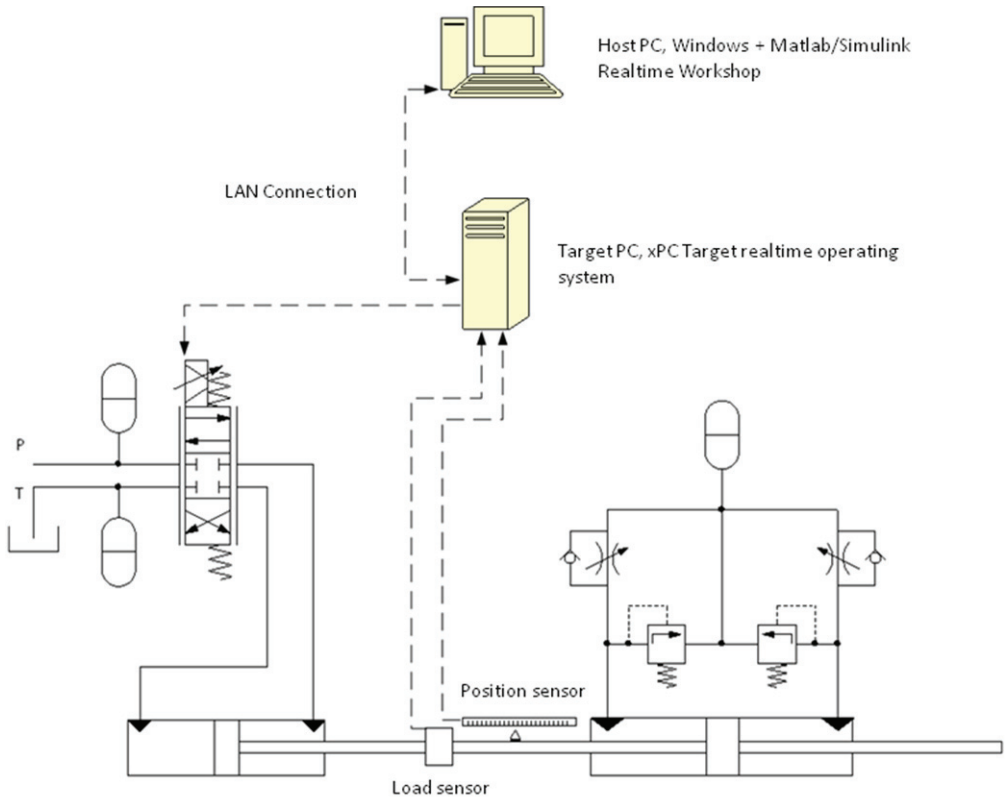


**Figure 1: HIL system layout**

Two Parker DFplus directional valves were used in parallel configuration to allow more fluid flow for better dynamics. The specification for a single valve is 40 l/min with 35 bar pressure difference per metering edge. Inlet pressure was 100 bar measured at the valve block. The actuator was a differential hydraulic cylinder with 63 mm bore diameter, 45 mm piston rod and 230 mm stroke. Damping force measurement was done with a 50 kN HBM U2B load sensor.

The damper used in the system was built around a symmetric hydraulic cylinder with two needle valves to control fluid flow in both directions. An accumulator was used to pressurise the damper for reduced cavitation.

As the system has a physical damper embedded in a virtual simulation environment the simulation must be real-time. This sets certain requirements for the hardware and software used in the test setup. Possible sources of error in the simulation are

- Plant model (model inaccuracy, integration error)
- Actuator (amplitude, phase response)
- Load and position sensor (error, sampling time)

The solver used was ode8 (Dormand-Prince) which is one of the explicit fixed step solvers provided within MABLAB. In this context it is important to notice that not all solvers are equally suitable for real-time simulation.[7] Integration error with different fixed step integration algorithms and step sizes was studied by Besinger et.al.[3] The results show that error stays sufficiently low as long as the suitable solver is 2<sup>nd</sup> order or higher and simulation step is small enough. Gomez suggests that sampling frequency should be at least 5 to 10 times higher than frequencies of interest in the system.[8] This is also consistent with Besinger's results. Processing power was not a limiting factor in this case thus a relatively high sampling frequency of 5 kHz was used in the real-time simulation. One should also pay special attention to critical measurement sensors and equipment to make sure their dynamics are sufficient. For example, filtering measured signals can cause phase shift in the feedback signal and increase error in the simulation.

## 2.1 Plant model

The plant model consist of a spring-mass system with a mass of  $m_1 = 1000$  kg and a spring constant of  $k_1 = 1 \times 10^6$  N/m (Fig.2). The damping term  $B_1 = 1265$  Ns/m is added to describe mechanical friction in the system. This is only equal to 2% of critical damping as the plant is to be damped with the external HIL damper. The plant model also includes an excitation force  $F(t)$ .

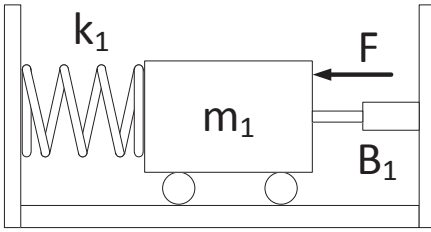


**Figure 2: Plant model used in the HIL simulations**

Differential equation for the system can be written as

$$m_1 \ddot{x}(t) + b_1 \dot{x}(t) + k_1 x(t) = F(t) \quad (1)$$

With Laplace transformation the plant model transfer function becomes

$$G(s)_{plant} = \frac{X(s)}{F(s)} = \frac{1}{m_1 s^2 + b_1 s + k_1} \quad (2)$$

## 2.2 Software simulation model of the HIL system

Verification of HIL simulation is difficult without having a reference system to compare simulation results to. This would require the real plant for the damper to be installed in, because the original system is the only one able to generate correct response. The original plant, however, is often not available, and could be the reason HIL simulation was chosen in the first place. Another way get a reference would be to build a simulation model of the HIL system with an ideal actuator, but for a direct comparison with the HIL system a perfect model of the system under test (the damper in this case) would be needed in the

reference simulation model. Again, this usually not a practical method, since having a perfect model of the damper would render HIL simulation useless.

An approach to estimate HIL simulation error with the information that we have available is clearly needed. In this study a full software model of the HIL system was constructed in Matlab Simulink (Fig.3). This model includes the hydraulic servo used in the HIL system. By modelling the actuator dynamics we can compare these simulations to ones with an ‘ideal actuator’ to see the effect on simulation results. The damper model used in the simulations was an ideal viscous damper, which should be sufficient, as we are just interested about the effect of the interface non-idealities on the simulation.

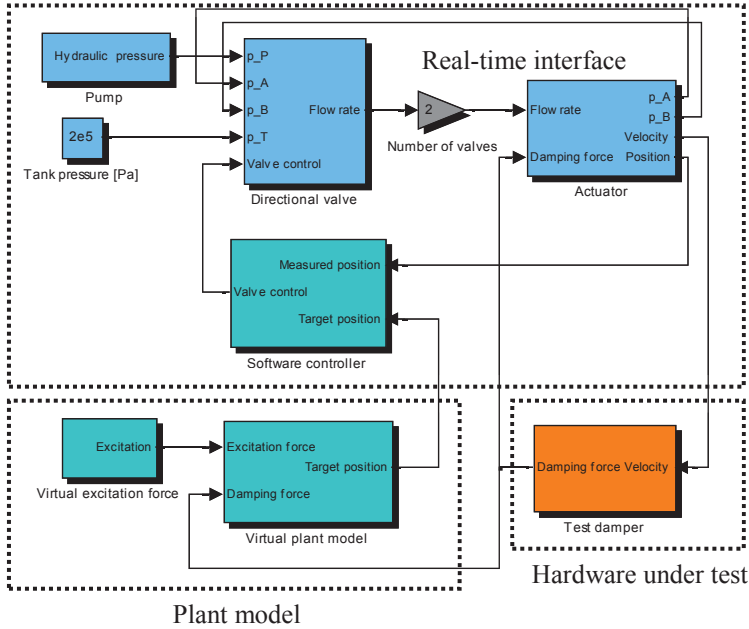


**Figure 3: Simulink software model of the of the HIL system**

The hydraulic position servo system with a four-way critical center spool valve can be described as shown in Fig.4. Because in simulations  $x_p \ll x_{pmax}$ , both chamber volumes were assumed constants. This makes it possible to use a linear model and greatly simplify the problem. Because of the discontinuity of the flow equations (3) and (4), two linear models are needed. The flow equations for  $x_v > 0$  can be written as,

$$Q_A = C_q w x_v \sqrt{\frac{2}{\rho} (p_s - p_A)} \quad \text{and} \quad Q_B = C_q w x_v \sqrt{\frac{2}{\rho} p_B} \quad (3)$$

Where  $w$  is the gradient of the valve,  $p_s$  is the supply pressure and tank pressure is assumed zero.



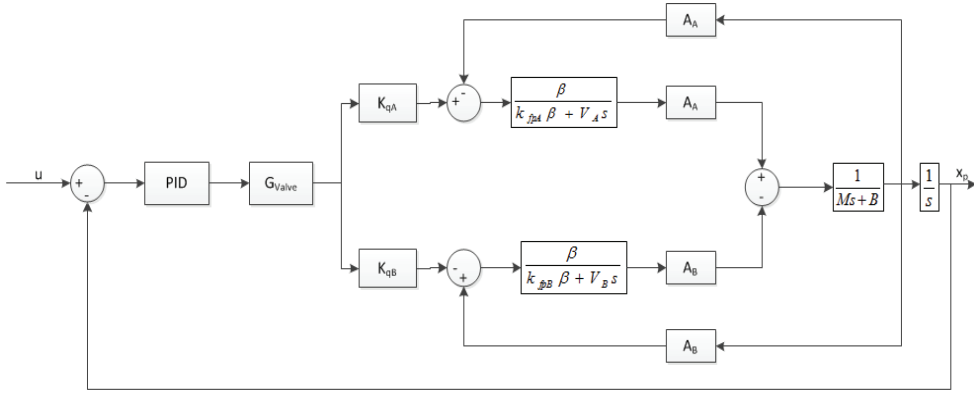


**Figure 4: Hydraulic system block diagram ( $x_v > 0$ )**

Coefficients for the linearised system are

$$K_{qA} = K_u C_q w \sqrt{\frac{2}{\rho} (p_s - p_{A0})} \quad K_{qB} = K_u C_q w \sqrt{\frac{2}{\rho} p_{B0}} \quad (5), \quad (6)$$

$$K_{fpA} = \frac{K_u C_q w u_{v0}}{\sqrt{2\rho(p_s - p_{A0})}} \quad K_{fpB} = \frac{K_u C_q w u_{v0}}{\sqrt{2\rho \cdot p_{B0}}} \quad (7), \quad (8)$$

The valve spool is modeled as a second order system:

$$G_{valve}(s) = \frac{X_{valve}(s)}{U(s)} = \frac{\omega_{valve}^2}{s^2 + 2\zeta_{valve}\omega_{valve}s + \omega_{valve}^2} \quad (9)$$

Parameters used were:  $A_A = 3.1 \times 10^{-3} \text{ m}^2$ ,  $A_B = 1.5 \times 10^{-3} \text{ m}^2$ ,  $\beta = 1.0 \times 10^9 \text{ Pa}$ ,  $K_{qA} = 1.88 \times 10^{-4} \text{ m}^3/\text{Vs}$ ,  $K_{qB} = 8.37 \times 10^{-5} \text{ m}^3/\text{Vs}$ ,  $K_{fpA} = 1.03 \times 10^{-11} \text{ m}^5/\text{Ns}$ ,  $K_{fpB} = 2.32 \times 10^{-11} \text{ m}^5/\text{Ns}$ ,  $M = 15 \text{ kg}$ ,  $V_A = 4.78 \times 10^{-4} \text{ m}^3$ ,  $V_B = 2.78 \times 10^{-4} \text{ m}^3$ ,  $\omega_{valve} = 1.26 \times 10^3 \text{ rad/s}$ ,  $\zeta_{valve} = 1$ .

### 2.3 HIL interface influence

Ideally an actuator would produce the movement described by the plant model with correct amplitude and phase response to the damper rod. In this case the damping force generated in the system would also be accurate. Of course this is not the case in the real world as actuator delay causes phase shift in the measured damping force that is used to damp the plant model. Because dynamics of sensors and control hardware is far superior, the actuator is what effectively determines the dynamic performance of the HIL system.

The HIL interface non-idealities can be divided roughly in two different types of error. One is the transfer function containing dynamics of the hydraulic actuator. The other one is noise and error caused by the sensors and their electronics used to measure position and

damping force in this case. In mechanically coupled HIL systems, like this one, delays introduced by the electronics are usually insignificant compared to those of the mechanical system as frequency range of electrical systems is decades higher. As we are only studying frequencies up to 30 Hz, sensor delays are assumed negligible.

Measured frequency response of the PID controlled position servo described in section 2 can be seen in Fig.5. The magnitude response of the servo is good but there is some delay in the response as can be seen from the phase plot. The average time delay was measured to be 5 ms. This was found to be true as long as the system was operated within limits of the hydraulic system.

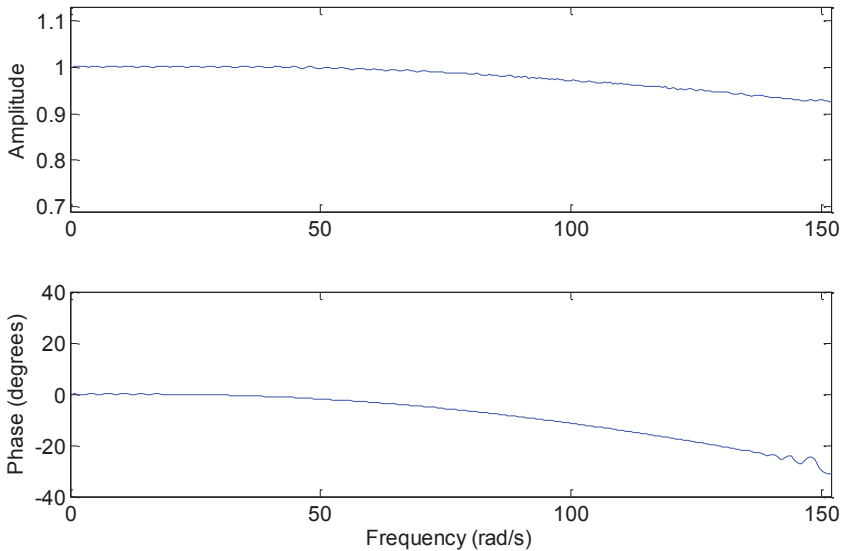


**Figure 5: Measured frequency response of the HIL interface position servo**

Before we can start optimizing the actuator response, we must know the effects of different types of actuator tracking error on HIL simulation error. This is not trivial task because of the fact that HIL is a closed loop system. Viscous damper's damping force is generally velocity dependent and so the error in prevailing actuator velocity causes interference in the measured damping force. The interference is fed back into the process as the damping force is used to calculate new system position.

For the purpose of studying effects of actuator error on the HIL simulation, two different kinds of error were artificially created in simulated environment. In this case simple errors were used instead of the actuator model to better identify different sources of error. First a pure time delay of 5 ms was added to HIL interface (Fig.6). To simulate actuator magnitude error 10% of excessive gain was added to HIL interface (Fig.7). Plant model was same as described in section 2.1. Ideal viscous damper model was used to damp the plant model.

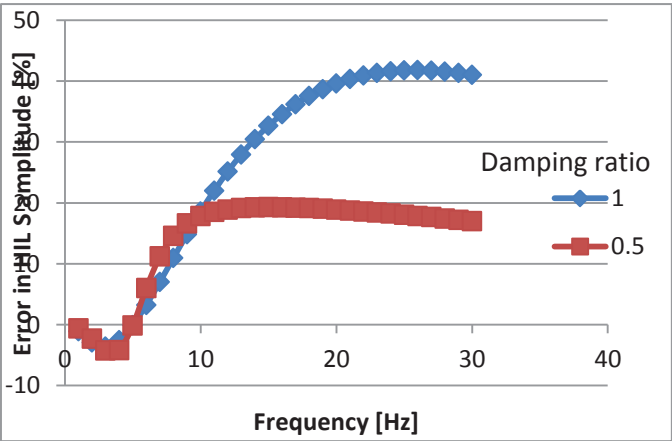


Figure 6: Corresponding magnitude error in HIL simulation result with 5 ms of added time delay in HIL interface. Sinusoidal force excitation signal.

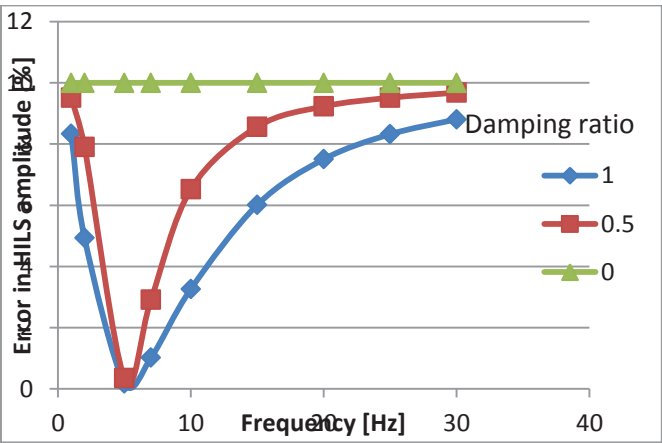
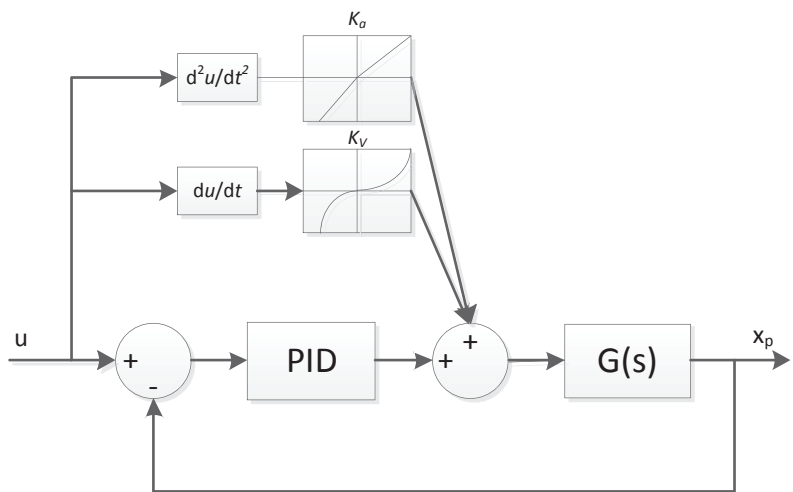


Figure 7: Corresponding magnitude error in HIL simulation result with 10% excessive magnitude in HIL interface. Sinusoidal force excitation.

#### 2.4 Control methods

As shown in Fig.6, delay introduced by the hydraulic position servo induces significant amounts of error in HIL output. To combat this, a feedforward controller was added beside the PID feedback controller. The feedforward controller was developed by measuring system response with a series of excitation signals. The result is a feedforward gain schedule for both velocity and acceleration request. The velocity feedforward loop is capable of compensating asymmetric flow gains, asymmetric cylinder areas and valve deadband. The acceleration feedforward compensates for moving mass dynamics in the system. PID feedback loop will correct position tracking error left by the open loop system. Fig.10 shows the measured frequency response of the actuator with the feedforward loops added to the system.



**Figure 8:** Block diagram of the velocity-acceleration feedforward controller with PID (FFPID).  $K_a = 0.020 \text{ Vs}^2/\text{m}$  when  $\ddot{u} \geq 0$  and  $0.031 \text{ Vs}^2/\text{m}$  when  $\ddot{u} < 0$ .

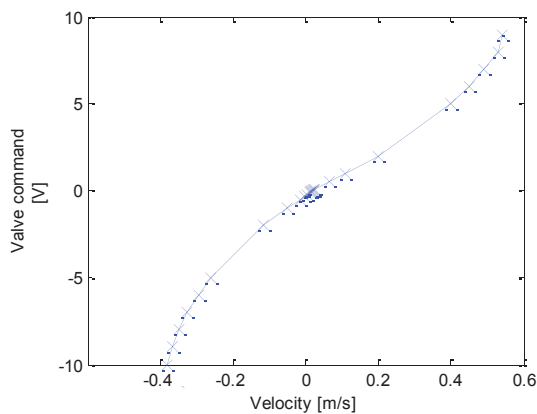


**Figure 9:** Velocity feedforward gain table  $K_v$ .

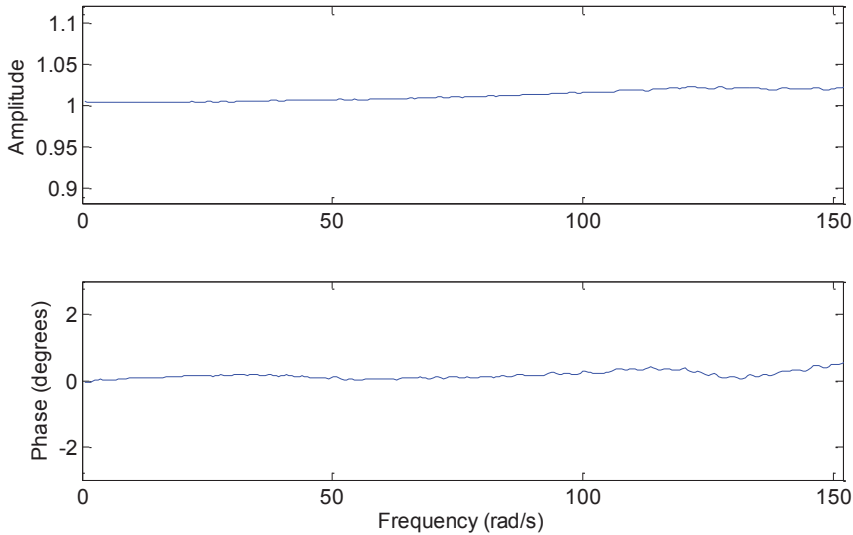


**Figure 10: Measured actuator response with FFPID controller.**

### 3. COMPARISON BETWEEN PID AND FFPID PERFORMANCE

The software model of the hydraulic servo system introduced in section 2.2 was validated comparing it against measured data from the real system. Fig.11 shows the simulated and measured responses with a 10 Hz sine excitation with both PID and FFPID controllers.

The HIL simulation error (Fig.12) was estimated using the simulated hydraulic system embedded in the HIL interface and comparing the results against simulations done with an ‘ideal actuator’. Both control methods were simulated using a viscous damper ( $\zeta = 0.5$  and  $\zeta = 1$ ) that damps the plant model and also acts as a load for the actuator. Sinusoidal force of 5 kN amplitude varied from 1 Hz to 25 Hz was used as plant excitation.

During testing plant model was excited with different types of signals to study system performance. Fig.13 shows system position tracking performance during an example HIL simulation with random force impulses as input. A hardware fluid damper was used to damp the plant.

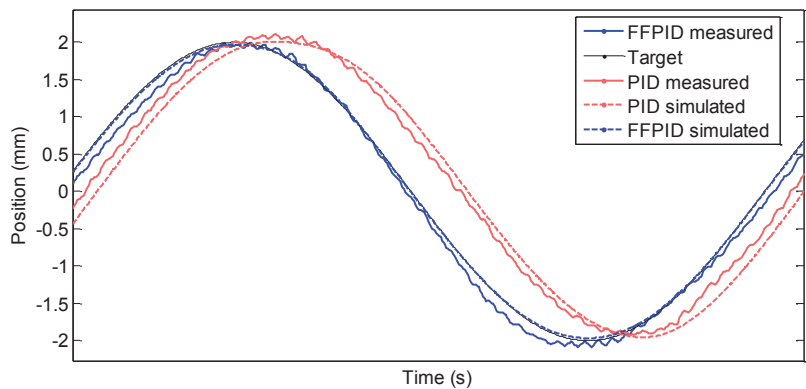


Figure 11: Measured actuator position tracking, 10 Hz sinusoidal signal.

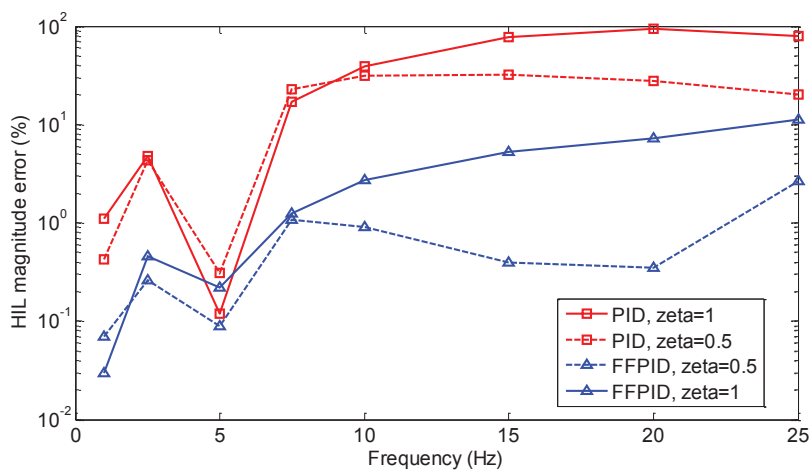


Figure 12: Estimated HIL simulation magnitude error with PID and FFPID.

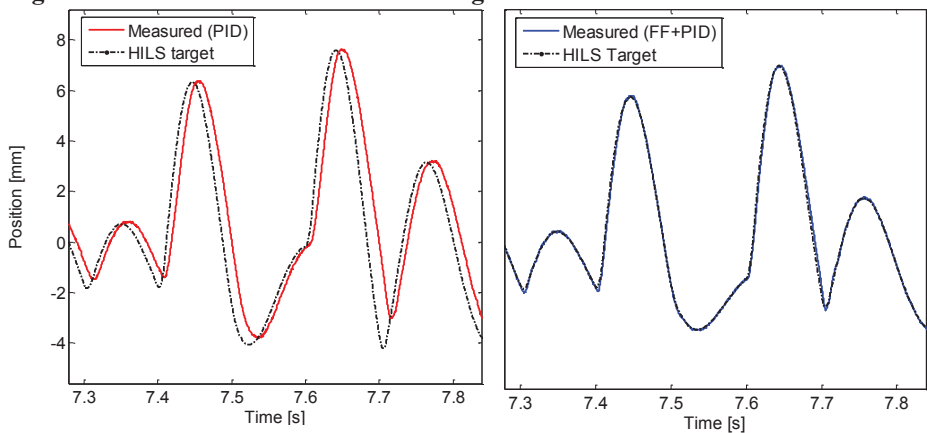


Figure 13: Measured actuator position tracking during actual HIL simulation with a hardware damper. Plant model was excited with random force impulses up to 40kN.

#### 4. CONCLUSION

Validation of HIL simulation is not an easy task without original system reference data. Because HIL is a closed loop system, accuracy of HIL simulation results cannot be directly deduced from the interface transfer function and disturbances. Parameters of the plant model and properties of the damper hardware can have a big significance in simulation outcome in terms of accuracy.

In this paper HIL accuracy was validated for a given plant model using a simulation model of the hydraulic actuator and assuming the damping is viscous type. Using this method we were able to estimate error in the HIL simulation magnitude without data from the original system.

It was found that traditional hydraulic servo using PID control was introducing a lot of error in the simulation, especially with excitations above the plant resonance frequency (5 Hz). A predictive feedforward control method based on measured data was implemented to improve actuator tracking performance. Using predetermined control values the controller does not require the computation power of some model based controllers, but still makes a significant improvement over traditional PID. While the PID system showed estimated maximum magnitude errors of 32.4% and 94.4% with damping ratios  $\zeta = 0.5$  and  $\zeta = 1$ , errors for FFPID system were 2.7% and 11.3% respectively. Poor performance of the PID system is partly explained by the differential actuator having asymmetric velocity characteristics in proportion to valve flow. The FFPID was designed to compensate for this as well as other characteristics of the system. FFPID was able to compensate for actuator dynamics very effectively near the operating point it was optimized for. In this case optimization was done at halfway point of actuator stroke and for light load. It was found that that a large damper loads can distract actuator tracking. As the differential actuator is by nature stiffest near its end positions, better results could be obtained by operating near those points, if full stroke it not needed.

#### NOMENCLATURE

$A_{A,B}$	piston area [ $\text{m}^2$ ]
$b_1$	plant model viscous damping coefficient [ $\text{Ns/m}$ ]
$B$	viscous damping coefficient [ $\text{Ns/m}$ ]
$C_q$	flow coefficient [-]
$F$	plant model excitation force [ $\text{N}$ ]
$k_1$	plant model spring constant [ $\text{N/m}$ ]
$K_{fp}$	flow-pressure coefficient [ $\text{m}^3/\text{Ns}$ ]
$K_{qu}$	flow gain [ $\text{m}^3/\text{Vs}$ ]
$K_u$	valve spool gain [ $\text{m/V}$ ]
$m_1$	plant model mass [ $\text{kg}$ ]
$M$	actuator moving mass [ $\text{kg}$ ]
$Q$	flow [ $\text{m}^3/\text{s}$ ]
$p$	pressure [ $\text{Pa}$ ]
$u_v$	valve command signal [ $\text{V}$ ]
$V_{A,B}$	fluid volume [ $\text{m}^3$ ]

$x_v$	valve spool displacement [m]
$x_p$	piston displacement [m]
$w$	valve area gradient [m]
$\zeta$	damping ratio [-]
$\beta$	bulk modulus [Pa]
$\omega$	angular frequency [rad/s]
$\rho$	fluid density [kg/m <sup>3</sup> ]

## REFERENCES

- [1] Saarikoski, T., Kajaste, J., and Pietola, M. Hardware-in-the-loop simulation as test method for hydraulic dampers. Aalto University School of Science and Technology. SICFP'11. Tampere, Finland. 2011.
- [2] D C Batterbee and N D Sims, Hardware-in-the-loop simulation of magnetorheological dampers for vehicle suspension systems. Department of Mechanical Engineering, The University of Sheffield, Sheffield, UK. Proc. IMechE vol.221 part I: J. Systems and Control Engineering. 2007.
- [3] Besinger, F.H., Cebon, D. & Cole, D.J. 1995. Damper Models for Heavy Vehicle Ride Dynamics. Vehicle System Dynamics, Volume 24 : 35-64
- [4] Hwang, S., Heo, S., Kim, H. & Lee, K. 1997. Vehicle Dynamic Analysis and Evaluation of Continuously Controlled Semi-Active Suspensions Using Hardware-in-the-Loop Simulation. Vehicle System Dynamics, Volume 27: 423 - 434.
- [5] Bacic, M. On hardware-in-the-loop simulation. 44<sup>th</sup> IEEE Conference on Decision and Control / European Control Conference, Seville, Spain. 2005.
- [6] Ren, W., Steurer, M. and Baldwin, T. An effective method for evaluating the accuracy of power hardware-in-the-loop simulations. IEEE Transactions on industry applications, vol.45, no.4, July/August 2009.
- [7] Jim A. Ledin. Hardware-in-the-Loop Simulation. February 1999. Embedded System Programming.
- [8] Gomez, M. Hardware-in-the-loop simulation. Electronic Engineering Times-India. December 2001.





# Dynamic Modelling of a Linear Friction Welding Machine actuation system

**D.T. Williams**

The University of Bath, Bath, BA2 7AY, UK

**P. Wilson**

Rolls-Royce plc. CRF, 5 LittleOak Drive, Sherwood Enterprise Park, Annesley, Nottinghamshire, NG15 0GP

**A. R. Plummer**

Centre for Power Transmission and Motion Control  
University of Bath

## ABSTRACT

This paper presents the modelling and model validation of the in-plane axis control and actuation system for a Linear Friction Welding (LFW) machine in Rolls-Royce. The LFW machine is a complex 11 actuator machine which has 6 degrees of freedom. The in-plane axis is the most complex axis due to the high power and high dynamic response requirements, necessitating the use of two four-stage servo valves. Amplitude and Phase control (APC) outer loop control, and Proportional, Integral, and Derivative (PID) closed-loop compensation methods are used to control the in-plane system to allow an accurate system response during welding. The servo hydraulic actuation system is complemented by a 'resonator' which provides some of the required acceleration forces at normal operating frequencies. Both the control and hydraulic systems are included in the model described in this paper, together with an empirical model for the welding force. The model is being used to help diagnose faults and performance issues with the machine, and the intention is to run the model alongside the machine for real-time or near real-time condition monitoring. The models are implemented using Simulink®, and the validation contained within the paper shows the model to have a good match to the actual system.

## 1 INTRODUCTION

Linear Friction Welding (LFW) has been a key technology in recent years for aircraft engine manufacture in both commercial and military market sectors. For joining Blades to Discs (Blisks), LFW is the ideal process for the following reasons:

- LFW is a solid state process which gives reproducibility, and high quality bonds therefore improving performance
- More cost effective than machining Blisks from solid billets
- Blisks enable up to 30% weight saving over conventional rotors
- LFW enables hollow bladed Blisks
- Dissimilar materials can be joined for optimised blade and disc properties
- Enables blade replacement

The process can be divided into six phases: *contact* - initial advancement of actuators seating the blade onto the disc stub and applying a seating force, *ramp up* - blade oscillations start to occur, *conditioning* - maintaining the oscillations to enable frictional heat to build up, *burn-off* - material deforming plastically under compression, *ramp down* - blade decelerated to a static position, and *forging* - allowing the weld to complete under a constant pressure. Figure 1 outlines the process phases.

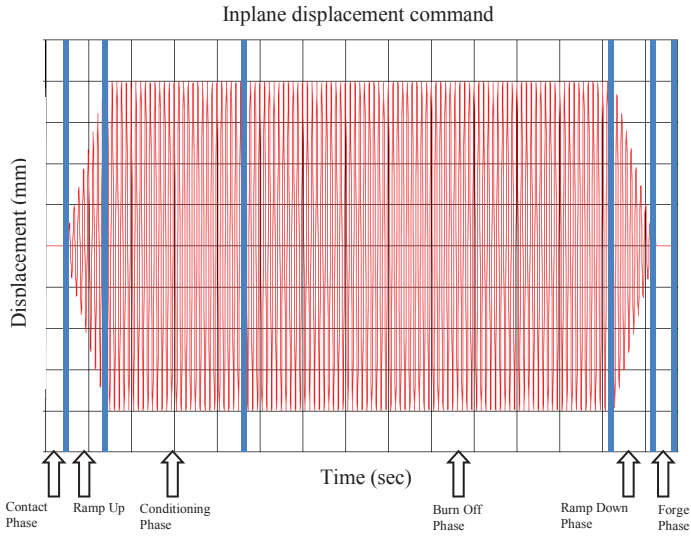


**Figure 1 - LFW Process phases**

Rolls-Royce's LF60 is a linear friction welding system that is designed to weld Blisks in a production environment. The system uses a combination of high performance, high accuracy servo-hydraulics to produce oscillatory motion between the components which creates frictional heating, and a forging force sufficient to produce a high strength and geometrically precise bond.

No full system dynamic modelling of linear friction welders has previously been done. Similar multi-axis machinery has been modelled such as Stewart-Gough platforms [1] which are mainly used in aerospace and automotive simulators, and shaking tables [2] used for earthquake simulations. Models of these systems are developed to enable detailed understanding of the dynamic characteristics therefore allowing control algorithms to be optimised and the systems limitations to be assessed. Modelling in this case will be done to enable detailed understanding of the systems dynamics, and for fault diagnosis, including real-time simulations in order to detect faults before they cause production problems.

The modelling of hydraulic systems has been widely covered in the literature [3-6]. Important modelling factors are outlined in [2], and include fluid compressibility, variable cylinder oil volumes, internal cylinder leakage, cylinder cross-port bleed, valve orifice pressure-flow characteristic, valve overlap, valve body pressure drop, manifold pressure drop and oil volume, valve spool dynamics, maximum valve opening, valve spool slew rate limit, friction, and geometric properties.

Only the in-plane axis is considered in this paper. Section 2 introduces the LFW machine. Section 3 reviews the replication of the in-plane controller, and the following section outlines the modelling of the hydraulic and mechanical components. Validation of the models can be found in section 5.

## 2 THE LF60 LINEAR FRICTION WELDING MACHINE

Each machine axis is independently controlled using a combination of PID and Amplitude and Phase control (APC). The six main degrees of freedom are referred to as in-plane, forge, hade, roll, pitch and yaw. The in-plane actuator, which is driven by two four stage valves, oscillates the blade tangentially to the disk. Forging pressure is obtained by a combination of four PID controlled hydrostatic actuators. The six hade actuators restrain the unwanted movement in the other degrees of freedom[7].

A CAD picture of the Inner cage showing the actuator attachments can be seen in figure 2.

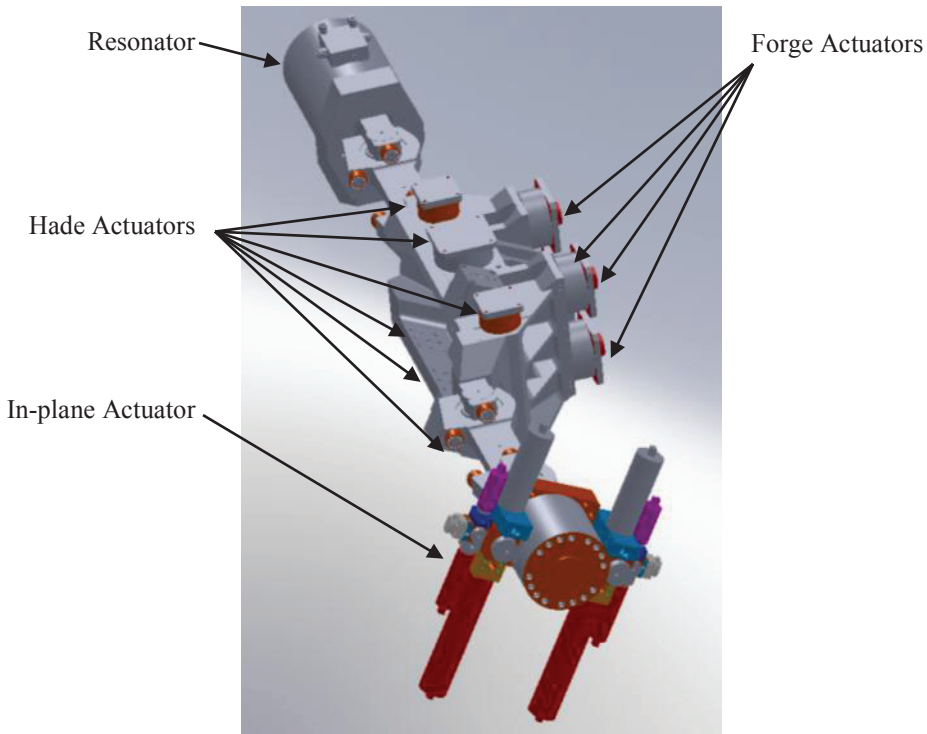


Figure 2 - Picture of the Inner cage with actuators attached

## 3 MODELLING LFW INPLANE CONTROLLER

The LF60s inplane system needs a fast and accurate position response for the production components to be of the required quality. For this reason two methods of controlling the

inplane system are used: Proportional, Integral, and Derivative (PID), and Amplitude and Phase control (APC).  
 PID control is used for the inner loop, and the APC is used for the outer loop. Detailed PID operation can be found [8]. This section covers APC only.

Modelling of the APC was done in Simulink®, from the original Patent developed by MTS Systems Corporation, [9]. The APC modifies the control system’s command signal using an inverse model of the PID-controlled in-plane actuator which is found via a Least Mean Squares (LMS) estimation method.  
 A detailed description of the APC algorithm can be found in [9]. For the removal of any amplitude or phase errors the algorithm needs to determine the closed loop system’s amplitude and phase so that suitable corrections can be made to the reference signal. This is done by an on-line estimated inverse model as shown in Figure 3.

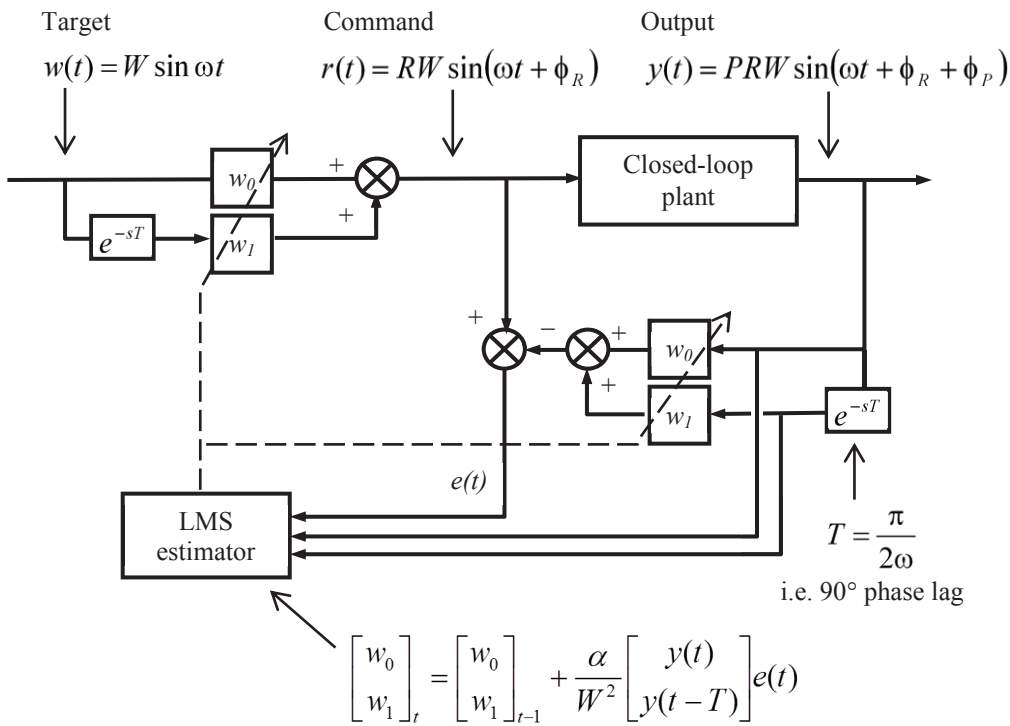


**Figure 3 - APC schematic**

The LMS Algorithm drives the error  $e(t)$  to zero by calculating weights  $w_0$  and  $w_1$ . The error signal is the difference signal generated from a comparison of the sinusoidal component of the reference input signal and a phase and amplitude shifted signal derived from processing the feedback signal. The error is given by:

$$e(t) = r(t) - (\omega_0 y(t) + \omega_1 y(t - T)) \tag{1}$$

Or

$$e(t) = RW[\sin(\omega t + \varphi_r) - \omega_0 P \sin(\omega t + \varphi_r + \varphi_p) + \omega_1 P \cos(\omega t + \varphi_r + \varphi_p)] \quad (2)$$

Given a perfect inverse model to remove the error:

$$\omega_0 = \frac{1}{P} \cos \varphi_p \text{ and } \omega_1 = \frac{1}{P} \sin \varphi_p \quad (3)$$

Applying equation 3 to the command signal gives:

$$R = \frac{1}{P} \text{ and } \varphi_r = -\varphi_p \quad (4)$$

Therefore the plant output becomes the same as the original command (the target signal in Figure 3).

Simulation of the APC controller can be seen in section 5.1 of this paper.

## 4 MODELLING IN-PLANE SERVO VALVE AND ACTUATOR

### 4.1 The 4Stage Servo Valve Model

The in-plane actuator is driven by two 4 stage servo valves<sup>1</sup>. Each one has a pilot two stage valve rated at 1 GPM (gallon per minute); this drives the 3rd stage 40 GPM spool which in turn drives the 4th stage 400 GPM spool. Figure 4 shows a front view of the in-plane servo valves.

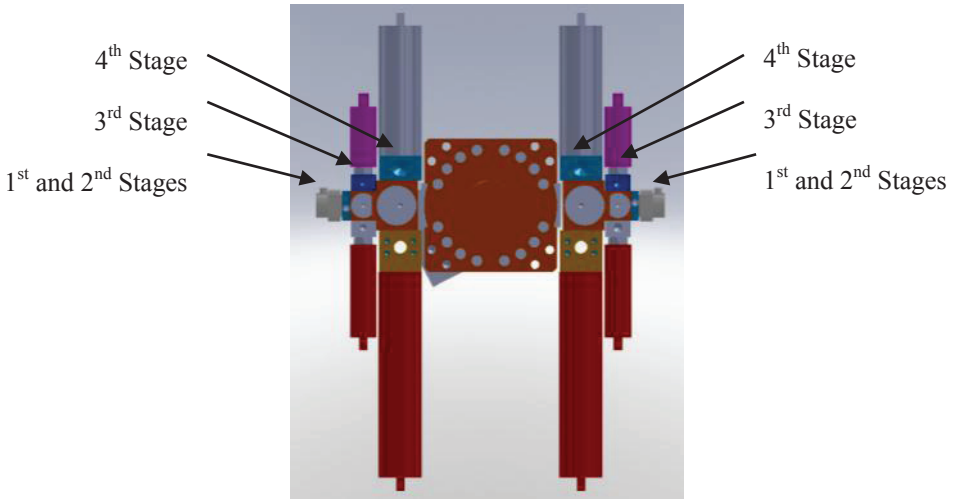


**Figure 4 - LF60 4 stage in-plane Valves arrangement: front view**

<sup>1</sup> The valve rating in Litres per minute (LPM) are as follows: pilot stage 3.79LPM, 3rd stage 151.42LPM, 4th stage 1514.17LPM.

The in-plane system is driven from a command signal which initially starts in position control at zero displacement, ramps up to the required maximum sinusoidal amplitude which is held for the required time, ramped down and then held at nominally zero displacement in load control. The 4 stage valve construction can be seen in figure 5.

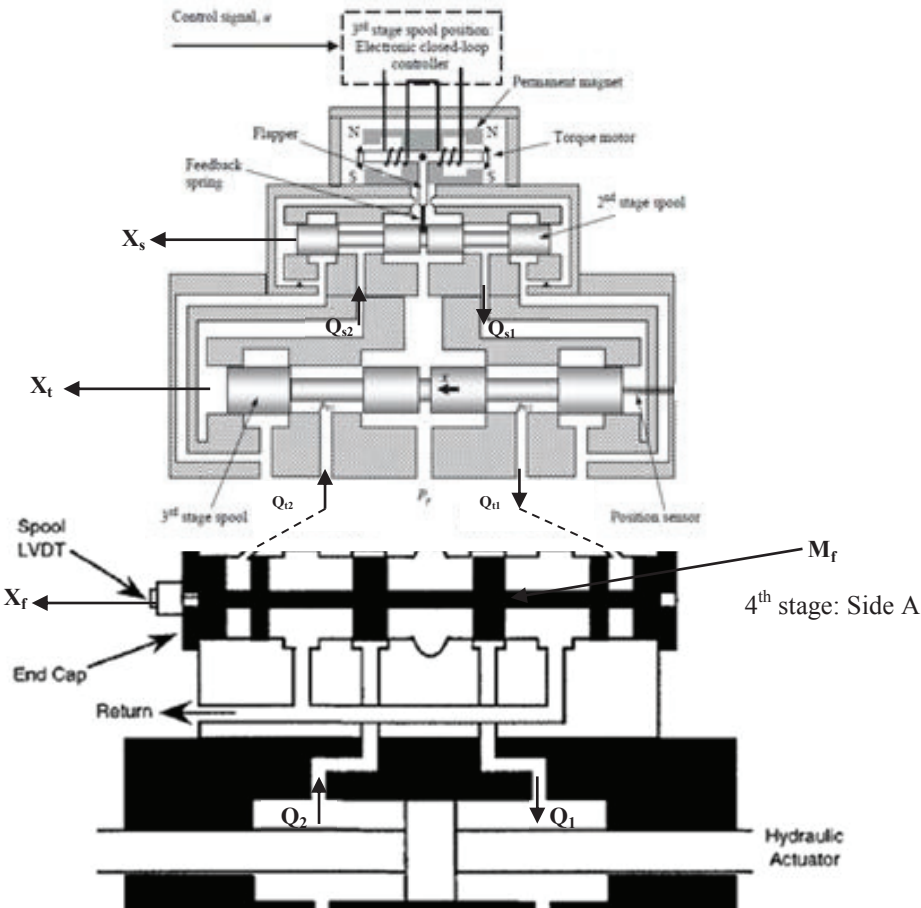


Figure 5 - Construction of one side of the LF60 4 stage valves

The 4 stage servo valve works by the initial first stage torque motor controlling flow via a nozzle-flapper arrangement, the 2<sup>nd</sup> stage has a mechanically feedback spool linked to the first stage by the feedback spring. The 3<sup>rd</sup> stage spool, with electronic position feedback, acts as a flow amplifier to the 4<sup>th</sup> stage, which also has electronic closed-loop control of the spool position.

**Two-stage valve model[10]**

The spool dynamics are modelled as a delay and a second order transfer function:

$$\tilde{X}_s = \frac{e^{-sD}}{V(s)} \tilde{U} \quad (5)$$

Where,

$$V(s) = \left(\frac{s}{\omega_{ns}}\right)^2 + 2\delta_s \left(\frac{s}{\omega_{ns}}\right) + 1 \quad (6)$$

and where  $\tilde{X}_s$  and  $\tilde{U}$  is the spool movement and valve drive signal respectively, both normalised to  $\pm 1$ .  $\delta_s$  represents the valve damping and  $\omega_{ns}$  the natural frequency.

Second stage valve orifice equations:

For positive  $\tilde{X}_s$ :

$$Q_{s1} = k_{vs} \tilde{X}_s \sqrt{P_s - P_1} \quad (7)$$

$$Q_{s2} = k_{vs} \tilde{X}_s \sqrt{P_{s2} - P_r} \quad (8)$$

For negative  $\tilde{X}_s$ :

$$Q_{s1} = k_{vs} \tilde{X}_s \sqrt{P_1 - P_s} \quad (9)$$

$$Q_{s2} = k_{vs} \tilde{X}_s \sqrt{P_r - P_2} \quad (10)$$

### Third stage model<sup>2</sup>

The third stage spool motion is described by:

$$Q_{s1} = A_t \dot{X}_t + \frac{P_{t1}}{k_{t1}} + (P_{t1} - P_{t2})c_t \quad (11)$$

$$Q_{s2} = A_t \dot{X}_t + \frac{P_{t2}}{k_{t2}} + (P_{t1} - P_{t2})c_t \quad (12)$$

Where  $A_t$  is spool area,  $c_t$  is a leakage coefficient, and the fluid stiffness on each side of the spool is represented by:

$$k_{t1} = \frac{B}{V_{t1}} \text{ and } k_{t2} = \frac{B}{V_{t2}} \quad (13)$$

And where  $B$  is the bulk modulus and  $V_{t1}$  and  $V_{t2}$  are fluid volumes which equal  $v_{t1}$  and  $v_{t2}$  when the spool is at mid position:

$$V_{t1} = v_{t1} + A_t X_t \text{ and } V_{t2} = v_{t2} - A_t X_t \quad (14)$$

Spool force balance:

$$(P_{t1} - P_{t2})A_t = M_t \ddot{X}_t \quad (15)$$

Normalisation of spool movement:

$$\tilde{X}_t = \frac{X_t}{S_t} \quad (16)$$

Where  $S_t$  is half the stroke of the spool (i.e. the maximum value of  $X_t$ ).

---

<sup>2</sup> Viscous friction has been ignored throughout the valve modelling stages



Third stage valve orifice equations:

For positive  $\tilde{X}_t$ :

$$Q_{t1} = k_{vt} \tilde{X}_t \sqrt{P_s - P_{t1}} \quad (17)$$

$$Q_{t2} = k_{vt} \tilde{X}_t \sqrt{P_{t2} - P_r} \quad (18)$$

For negative  $\tilde{X}_t$ :

$$Q_{t1} = k_{vt} \tilde{X}_t \sqrt{P_{t1} - P_r} \quad (19)$$

$$Q_{t2} = k_{vt} \tilde{X}_t \sqrt{P_s - P_{t2}} \quad (20)$$

Where  $k_{vt}$  is the third stage valve flow constant.

### Fourth stage<sup>3</sup>

Fourth stage spool motion:

$$Q_{t1} = A_f \dot{X}_f + \frac{\dot{P}_{f1}}{k_{f1}} + (P_{f1} - P_{f2}) c_f \quad (21)$$

$$Q_{t2} = A_f \dot{X}_f + \frac{\dot{P}_{f2}}{k_{f2}} + (P_{f1} - P_{f2}) c_f \quad (22)$$

$c_f$  is a leakage coefficient, and the fluid stiffness on each side of the spool is represented by:

$$k_{f1} = \frac{B}{V_{f1}} \text{ and } k_{f2} = \frac{B}{V_{f2}} \quad (23)$$

$V_{f1}$  and  $V_{f2}$  are fluid volumes:

$$V_{f1} = v_{f1} + A_f X_f \text{ and } V_{f2} = v_{f2} - A_f X_f \quad (24)$$

Spool force balance:

$$(P_{f1} - P_{f2}) A_f = M_f \ddot{X}_f \quad (25)$$

Normalisation of spool movement:

$$\ddot{X}_f = \frac{x_f}{s_f} \quad (26)$$

Where  $S_f$  is half the stroke of the spool.

Fourth stage valve orifice equations:

$$Q_1 = k_{vf} \tilde{X}_f \sqrt{P_a - P_1} \quad (27)$$

$$Q_2 = k_{vf} \tilde{X}_f \sqrt{P_2 - P_r} \quad (28)$$

---

<sup>3</sup> Viscous friction has been ignored throughout the valve modelling stages

$\ddot{X}_f$  is always positive and  $P_a$  is the main system pressure, as the modelling assumes accurate accumulator sizing and therefore very small pressure drop during welding. The servo valve simulation and validation can be found in section 5.2.

#### 4.2 Actuator Model

The dynamic characteristics of the hydraulic actuator are modelled in this section.

The hydraulic actuator is a double ended equal area actuator. The model includes fluid compressibility, internal cylinder leakage, cylinder cross-port bleed, and coulomb friction. The hydraulic actuator model does not include viscous friction. The actuator is modelled driving a mass  $M$ , with the welding load considered as an external force  $F$ .

Piston force balance:

$$(P_1 - P_2)A - F = M\ddot{Y} \quad (29)$$

Cylinder flow equations:

$$Q_1 = A\dot{Y} + \frac{P_1}{k_1} + (P_1 - P_2)c + c_1\sqrt{P_1 - P_2} \quad (30)$$

$$Q_2 = A\dot{Y} + \frac{P_2}{k_2} + (P_1 - P_2)c + c_1\sqrt{P_1 - P_2} \quad (31)$$

Where the fluid stiffness on each side of the cylinder is represented by:

$$k_1 = \frac{B}{V_1} \text{ and } k_2 = \frac{B}{V_2} \quad (32\&33)$$

The validation of the servo valve and actuator can be seen in section 5.2.

#### 4.3 Load dynamics and resonator

The load on the actuator is made up of the following loads:

- Weld Load (an empirical model)
- Resonator force (acts like a spring)
- Inertial force
- Friction

Giving:

$$F_{ACTUATOR\ LOAD} = F_{WELD} + F_{RESONATOR} + F_{INERTIA} + F_{FRICTION} \quad (34)$$

Each of the loads are discussed in the following sections.

##### 4.3.1 Weld force Modelling

An example of two test pieces, with the main welding forces outlined can be seen in figure 6. Analytical and numerical models of the linear friction welding process studying the impact and contact dynamics have been investigated mainly by [11-14], describing the process, its variables, and validation of the models using software packages such as Forge2007. Analytic and numerical contact modelling of LFW aims to improve understanding of the physics and mechanics involved in objects which are moving and touching. Friction between the objects is the main factor involved in the process, and this can be described as static friction or dynamic friction [15]. Research from [16] showed that

the instantaneous friction coefficient measured varied approximately linearly with blade velocity within certain boundaries, producing the empirical relationship as seen in figure 7. The empirical relationship determines the force at the weld given the in-plane position, velocity, maximum amplitude, and the total forging force.

$$F_{WELD} = F_z f(A(t), v(t)) \quad (35)$$

Where  $F_{WELD}$  is the force at the weld,  $F_z$  is the forge force,  $A(t)$  is the oscillation amplitude, and  $v(t)$  is the oscillation velocity. The empirical function  $f$  can be found in [16].

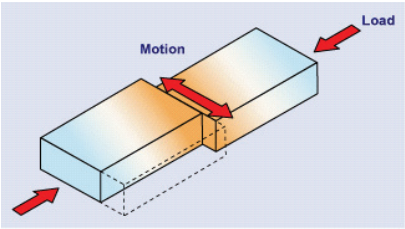


Figure 6 - Oscillating Weld Pieces[17]

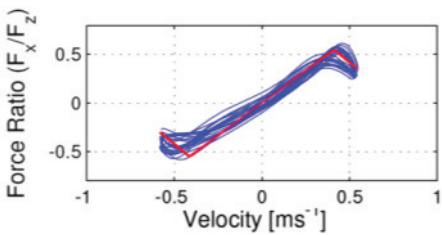


Figure 7 - Empirical relationship for weld force [16]

### 4.3.2 Resonator Model

The resonator is made up of three pistons, the main resonator piston, and two smaller ones forming piston accumulators on each side of the resonator. A diagram can be seen in figure 8.

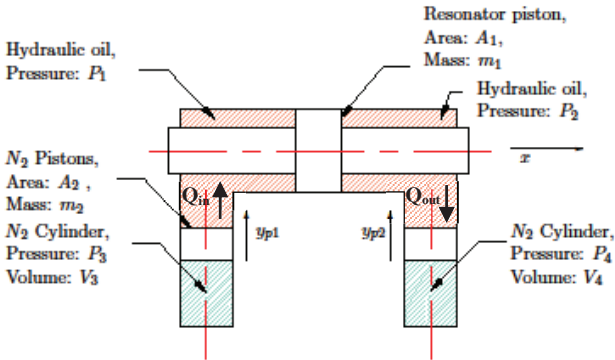


Figure 8 - Simplified Resonator diagram[16]

The resonator enables the in-plane actuator load requirement to be reduced by acting as a hydraulic spring to assist the acceleration of the inner cage at the operating frequency. Assuming that the main piston of the resonator is rigidly fixed to the inner cage, the resulting flow into the hydraulic oil volume on the left side of the piston is given by:

$$Q_{in} = -\frac{dx}{dt} A_1 + k(P_1 - P_2) \quad (36)$$

Where,  $k$  is a leakage coefficient accounting for the flow past the piston due to clearances. The flow out of this volume, determined by the movement of the left side resonator piston, where leakage is assumed zero (due to the need to keep the nitrogen and oil separate), is:

$$Q_{out} = -\frac{dy_{p1}}{dt} A_{p2} \quad (37)$$

To account for the hydraulic oil stiffness, the pressure in the oil volume ( $P_1$ ) on the left side of the piston, is related to the net sum of flows by the following expression:

$$\frac{dP_1}{dt} = \frac{B}{V} \sum Q \quad (38)$$

Where  $B$  is the oil bulk modulus and  $V$  is the initial volume of oil. The motion of the nitrogen pistons is given by Newton's second law as:

$$m_2 \frac{dy_1}{dt^2} = A_2(P_3 - P_1) \quad (39)$$

And the compression of the nitrogen gas is assumed to be a polytropic process governed by the expression:

$$P_3 = P_0 \left( \frac{V_3}{V_3 + A_2 y_{p1}} \right)^n \quad (40)$$

Where  $n$  is the polytropic index and  $V_3$  is the original volume of the nitrogen cylinder. Similar equations were developed for the right side of the resonator. The force applied to the in-plane system can then be found from the pressure differential across the resonator piston:

$$F_{RESONATOR} = A_1(P_1 - P_2) \quad (41)$$

This is a simplified model therefore it doesn't include friction between either the main resonator piston or the smaller nitrogen pistons against their bores.

#### 4.3.3 Inertia and friction force

The machine tooling connecting the inner cage to the in-plane actuator and resonator are assumed to be rigid and have been modelled as a mass along with that of the inner cage and the tooling suite. Therefore this added force is calculated from Newton's second law:

$$F_{INERTIA} = (m_{cage} + m_{tooling})\ddot{x} \quad (42)$$

Where,  $m_{cage}$  is the mass of the inner cage including the connecting rods,  $m_{tooling}$  is the mass of the tooling suite.

The net friction force is approximated by.

$$F_{FRICTION} = F_C \tanh(\dot{x}) \quad (43)$$

Where  $F_C$  is a friction constant. Validation of the in-plane dynamics can be found in section 5.3.

5 VALIDATION OF IN-PLANE MODEL

5.1 Validation of In-plane APC Controller Model

Due to the dynamic nature of the system<sup>4</sup> the APC gain and phase signals do not exactly match the machine’s signals, so APC validation will be done by using three simulations of actual welds to check how adjusting the gain and start-up cycle affects the ramp up response of the in-plane system as these are the most frequently adjusted parameters. The aim is to see similar changes occur in the modelled and actual in-plane position response. As the APC mainly affects the ramp up, the focus will be on this part of the weld cycle.

Figure 9 shows a good APC machine response (upper) where the in-plane feedback signal closely matches the in-plane command signal. The simulated response (Figure 9: lower) shows an accurate modelled response of the real system. Figure 10 show a poor ramp up response, where the initial APC gain is too high therefore the feedback of the in-plane position greatly overshoots the command signal. The model response is similar. Figure 11 shows an OK in-plane system response with a modified start-up delay enabling the APC to start sooner. These three examples show that changes to the modelled APC give similar effects to those seen in the actual data.

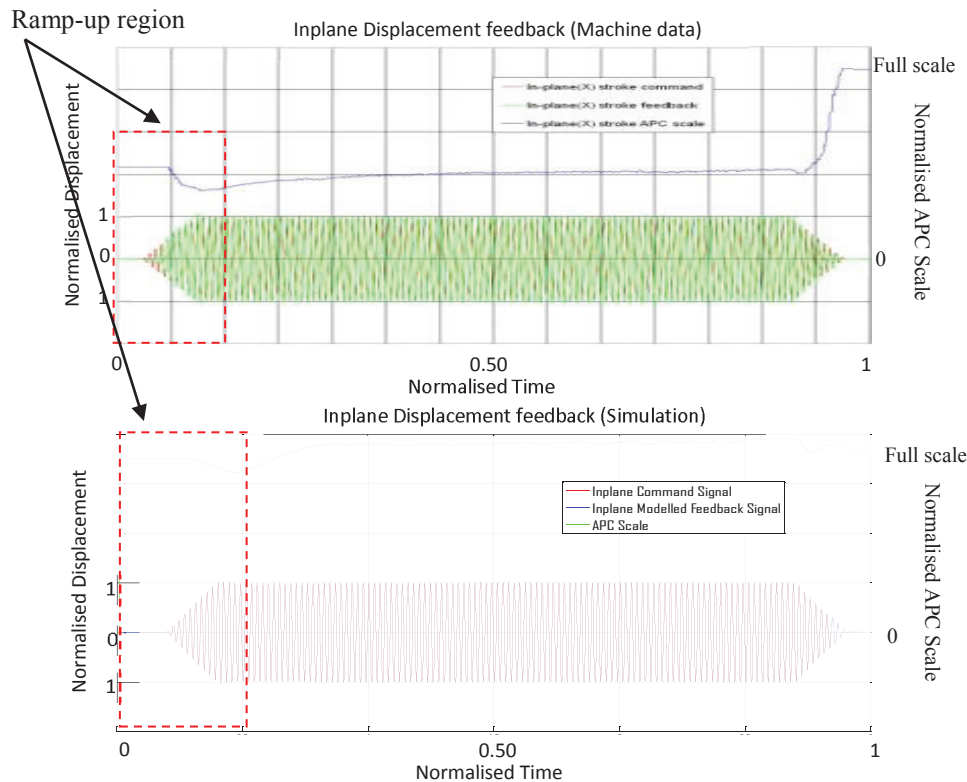
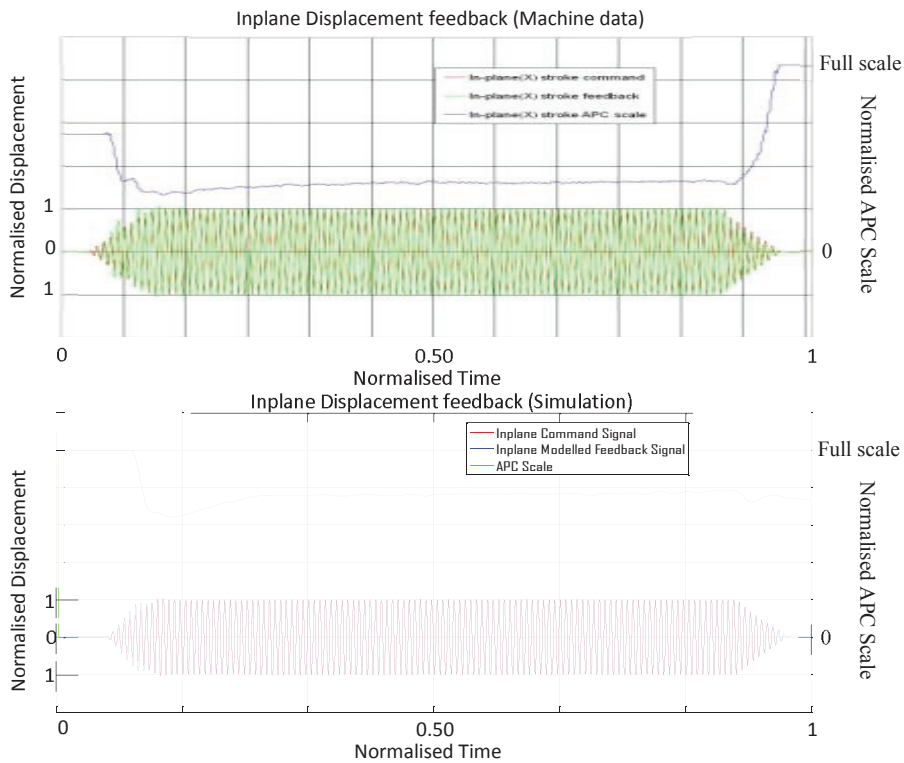
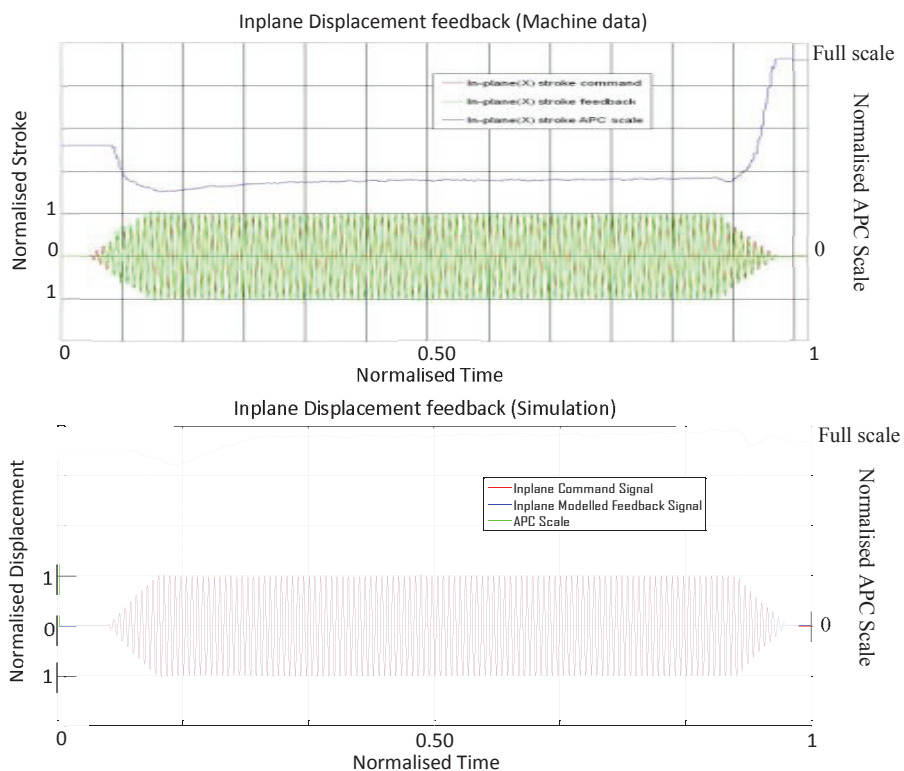


Figure 9 - Measured (upper), and simulated (lower): ‘good’ ramp up responses

<sup>4</sup> The axis of the welds have been normalised due to Roll-Royce PLC confidentiality. For an appreciation of the machines dynamics to understand the complexity of the modelling approach, the typical weld length is a few seconds and generally has over 100 cycles.



**Figure 10 - Measured (upper), and simulated (lower): Initial APC gain too high**



**Figure 11—Measured (upper), and simulated (lower): APC initialised earlier**

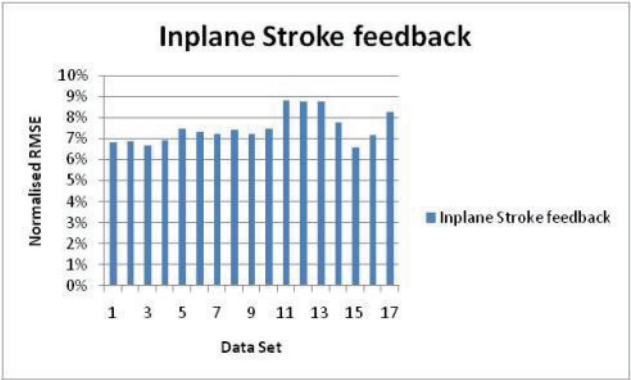
**5.2 Validation of in-plane Servo valve and Actuator Models**

An overview of the validation of the in-plane and APC models can be seen in this section; only the main signals will be reviewed, the full validation analysis can be found in [18]. The model fit is quantified using the Normalised Root Mean Square Error (NRMSE) between the actual and modelled output signals:

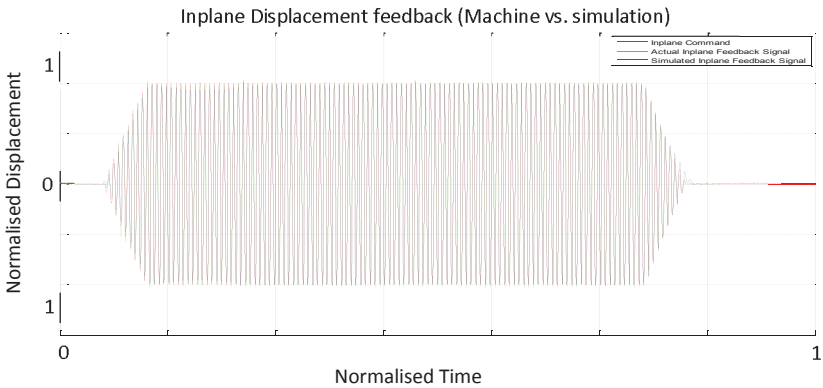
$$NRMSE = \frac{\sqrt{\frac{\sum_{i=1}^n (x_{1,i} - x_{2,i})^2}{n}}}{\sqrt{\frac{\sum_{i=1}^n (x_{1,i})^2}{n}}} \tag{44}$$

A sample interval of 1ms is used throughout.

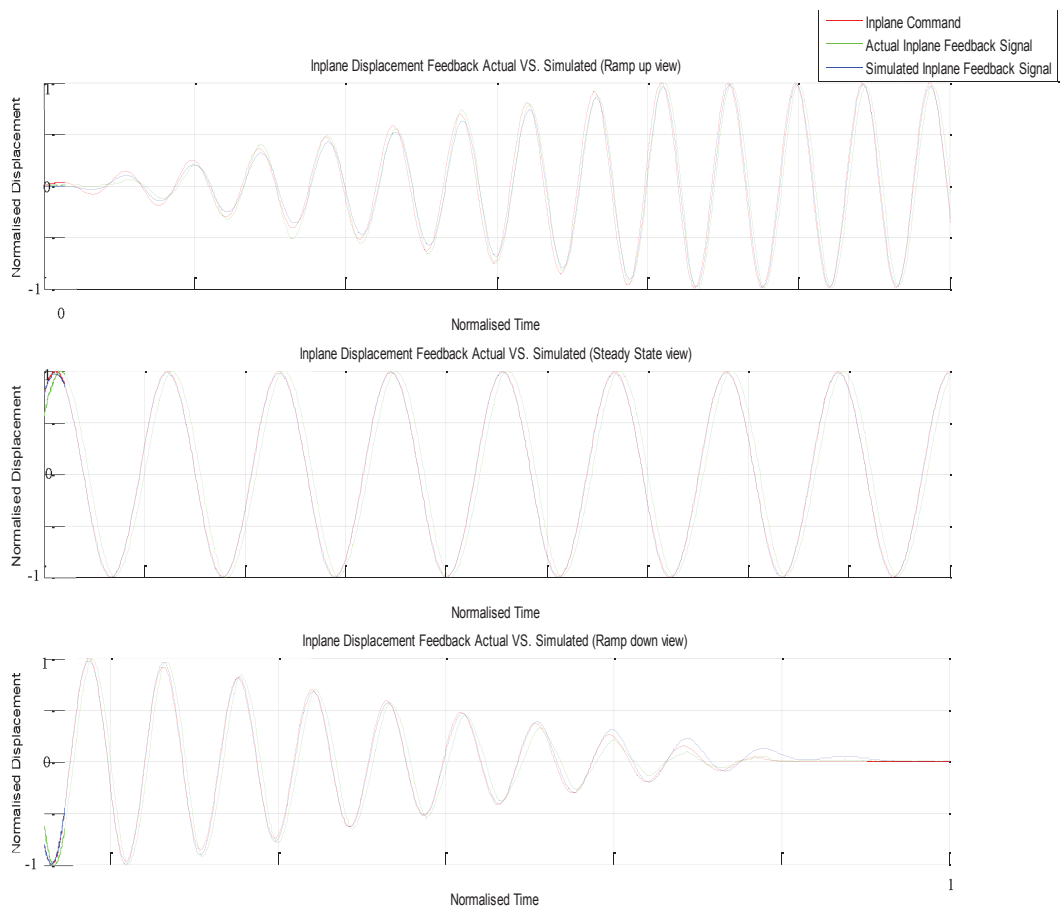
Figure 12 shows the in-plane position NRMSE values across 17 data sets. The worst of these is data set 11, and the fit for this data set can be seen in figure 13 and 14. The slightly higher NRMSE values are due to small ramp up, and steady state errors. The model performs very well, with an average NRMSE of 7%.



**Figure 12 - Normalised RMSE for the Modelled Vs. Actual in-plane position.**



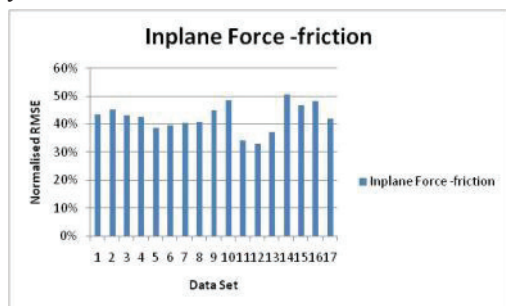
**Figure 13—Modelled Vs. Actual Inplane displacement for data set 11**



**Figure 14—Modelled Vs. Actual Inplane displacement for data set 11 zoomed in**

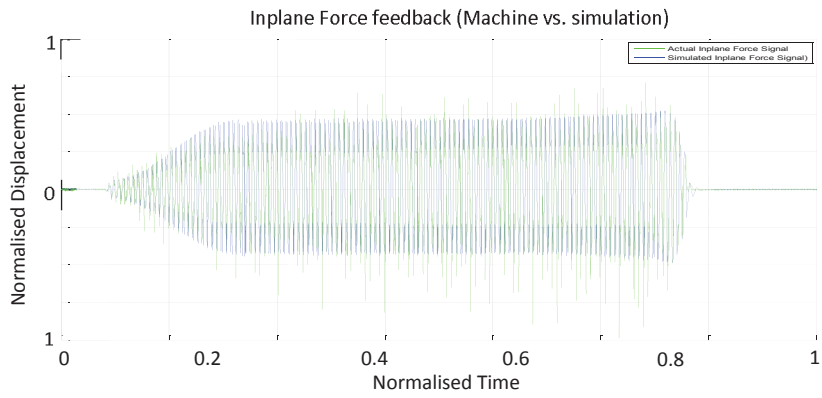
### 5.3 Validation of in-plane Dynamics

Figure 15 shows the in-plane–weld force, estimated from cylinder pressures, corrected for inertia force and estimated friction. The worst fit data set is the 14<sup>th</sup>, time series data can be seen in figure 16 and 17. The simulation does not exhibit the spikes seen in the real signal, but the lower frequency characteristics are modelled well.



**Figure 15 - Normalised RMSE for the Inplane Force**





**Figure 16–Modelled Vs. Actual Inplane Force for data set 14**

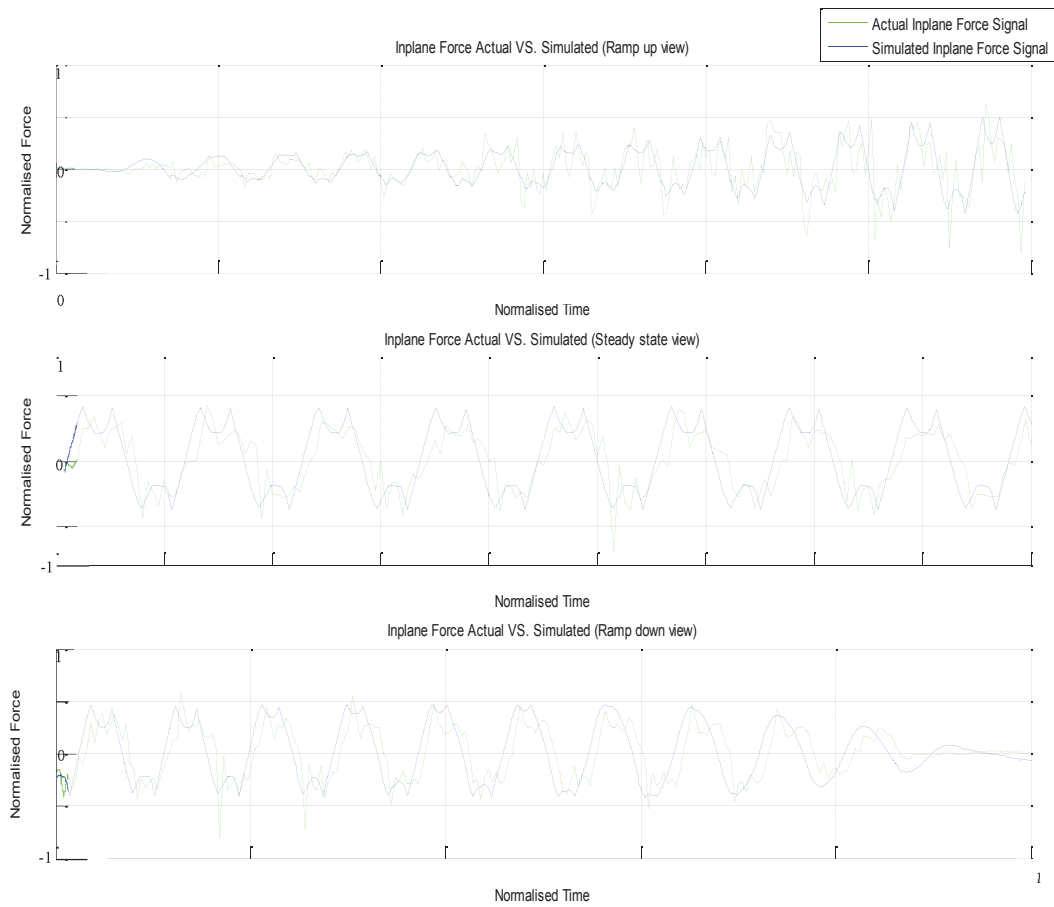


**Figure 17–Modelled Vs. Actual Inplane Force for data set 14 zoomed in**

## 6 CONCLUSION

A model of the LF60s in-plane controller, servo valve, actuator and weld characteristic has been developed in this paper. Simulink® has been used as the numerical simulation package. Validation of the developed models showed accurate results in the majority of cases, owing to good parameter estimation and modelling of the system. Therefore fault diagnosis methods will be placed on some of the more accurately represented signals.

The modelled APC behaviour showed the same trends as those seen on the actual machine. In-plane servo valve and actuator simulations show <10% position NRMSE, with all modelled signals having an accurate phase relationship with the actual signals.

Noise-like spikes were seen on the actual weld force signal which was not captured in simulation, therefore these results were not as accurate.

Given the good signal reproducibility over the validation data set, future work will investigate the models' sensitivity to faults, so that it can be used for fault diagnosis. Once complete and given a positive outcome the model will be used alongside the machine to enable the models predictive capabilities to be used in detecting and diagnosing faults.

## NOMENCLATURE

$Q_1$  = Flow out of port 1 into cylinder  $m^3/s$

$Q_2$  = Flow into port 2 from cylinder  $m^3/s$

$X$  = Spool movement mm

$U$  = Valve drive  $v$

$k_v$  = Constant for a given valve and a given fluid GPa

$X$  = Normalised spool position

$P_1$  = Pressure at port 1  $N/m^2$

$P_2$  = Pressure at port 2  $N/m^2$

$P_s$  = Supply pressure  $N/m^2$

$P_a$  = Main system pressure  $N/m^2$

$P_r$  = Return pressure  $N/m^2$

$Q_R$  = Manufacturer's rated flow  $m^3/s$

$Q_B$  = Body flow  $m^3/s$

$A$  = Piston Area  $cm^2$

$K_1, K_2$  = fluid stiffness GPa

$V_{t1}, V_{t2}$  = fluid volume  $m^3$

$M$  = Mass kg

$F$  = Force N

$c_l$  = Cross piston leakage coefficient  $m^5/Ns$

$c_b$  = Cross port bleed coefficient  $m^5/Ns$

$c_t$  = leakage coefficient  $m^5/Ns$

$B$  = Bulk Modulus  $GN/m^2$

$W_{ns}$  = Natural frequency rad/s

$n$  = Polytropic index

## REFERENCES

1. I. Davliakos and E. Papadopoulos, *Model-based control of a 6-dof electrohydraulic Stewart-Gough platform*. 2008, Mechanism and Machine Theory 43 1385-1400.
2. Plummer, A.R., *A Detailed Dynamic Model of a Six-Axis Shaking Table*, in Centre for Power Transmission and Motion Control. 2008, University of Bath: Bath. p. Journal of Earthquake Engineering, 12:4, 631 - 662.
3. O. Hancu, V. Maties, and R. Balan, *Modeling, simulation and control a hydraulic servo system*, in Department of Mechanisms. 2007, Technical University of Cluj-Napoca.
4. A. Akers, M. Gassman, and R.J. Smith, *Hydraulic Power Systems Analysis*. 2006: New York: 0-8247-9956-9.
5. B. Ayalew and B.T. Kulakowski, *Modeling supply and return line dynamics for an electrohydraulic actuation system*. 2004, ISA Transactions 44 329-343.
6. F. Rovira-Mas, Q. Zhang, and A.H. Hansen, *Dynamic behavior of an electrohydraulic valve: Typology of characteristic curves*. 2007, Mechatronics 17 (2007) 551-561.
7. MTS, *LF60 Operation Manual*. Internal Rolls-Royce documentation. 2000.
8. K.J. Astrom and T. Hagglund, *PID Controllers: Theory, Design and Tuning*, in ISA; 2nd Revised edition (15 June 1995): 1556175167. 1995.
9. Thoen, B.K., *Sinusoidal signal amplitude and phase control for an adaptive feedback control system*. 1992, Patent: MTS Systems Corporation, Eden Prairie, Minn.
10. J. Will M Bertrand and J.C. Fransoo, *Operations management research methodologies using quantitative modeling*. Operations Management Research, 22, (2), pp. 241 - 264, 2002.
11. A. Vairis and M. Frost, *Modelling the linear friction welding of titanium blocks*, in Department of Mechanical Engineering. 2000, University of Bristol: Bristol.
12. Vairis, A.F., M., *Recent Advances on Friction Modelling Within a Computational Mechanics Framework* in Department of Mechanical Engineering 2005, University of Crete
13. Turner, R., *EngD Technical Report: 2nd year*, in University of Birmingham - Rolls-Royce. 2008.
14. Stevens, P., *EngD Technical Report: 2nd year*, in University of Birmingham - Rolls-Royce. 2009.
15. N. Christakis and A. Vairis, *A Study of the Frictional Behaviour of A Titanium Alloy with the use of an Analytic Contact Model*, in Department of Applied Mathematics. 2007, University of Crete.
16. A.R. Plummer and C. Lamming, *Simulink Modelling of the MTS LF60 Linear Friction Welder*, in The Centre for Power Transmission and Motion Control. 2007, The University of Bath.
17. P. Threadgill, *Linear Friction Welding*. Copyright 2001, TWI Ltd <http://materialteknologi.hig.no/Lettvekttdesign/joining%20methods/joining-welding-linear%20friction%20welding.htm>.
18. D.T. Williams, *Validation Report*, in Rolls-Royce and Bath University. 2009.

# Multivariable Backstepping Controls of a High Bandwidth Electro-hydraulic Actuator

Yaozhong XU, Lilia SIDHOM, Eric BIDEAUX, and Mohamed SMAOUI

Université de Lyon, Institut National des Sciences Appliquées de LYON

Laboratoire Ampère, UMR CNRS 5005

Villeurbanne, France

## ABSTRACT

Electro-hydraulic actuators have been widely applied in industry for position or pressure control. However, conventional linear control is still satisfying for many applications, due to hydraulic system nonlinearities, linear approaches are not able to satisfy high performance related to new control requirements as precision, energy efficiency and bandwidth. The test bench, on which this work is based on, consists in a hydraulic actuator equipped with 2 servovalves. This architecture allows high performance to be achieved and multiple-objective control to be developed. This paper presents two control strategies (denoted P-Y and Y- $\lambda$ ) based on the backstepping approach, which enable the tracking of two trajectories simultaneously: piston position and chamber pressures. Firstly, the synthesis of the P-Y and P- $\lambda$  control laws is introduced. Then the proposed controls are validated experimentally. Results show better performances than conventional control techniques.

**Keywords:** Backstepping, Multivariable control, Electro-hydraulic system, High performance.

## 1. INTRODUCTION

For some operating ranges, position control of electro-hydraulic actuators is widely used without any problem. However, the accurate position tracking on a large frequency domain can be a difficult target to achieve with only a linear control strategy. This is due to the nonlinearities of this system, such as friction force, servovalve dynamic and flow rate characteristics [1]. Some previous research works [2, 3] have used high-order linear models for control system design by reformulating the problem with its nonlinear state equations. Nevertheless, this kind of linear model is valid only on the neighbourhood of an operating point and not suitable for certain applications where high performance and large frequency response ranges are required.

To ensure the system has an asymptotical global stability on a whole operating domain, nonlinear robust control design has been extensively studied during the last decade [4, 5, 6, 7, 8]. Among the applied methods, backstepping is one of the most interesting techniques.

This approach gives a powerful design methodology for stabilizing controls for nonlinear systems. It provides a recursive control design, which begins with the simplest known-stable subsystem to build a series of virtual feedback controllers to stabilize progressively each subsystem till reaches to the ultimate external control [9, 10]. While dealing with the stability of the subsystems, the backstepping approach constructs systematically a number of Lyapunov functions to guarantee their asymptotical stability. Because of its robustness and ease of implantation, the backstepping-based design has been successfully applied for accurate position tracking or regulation purpose in many domains, including hydraulics [11], pneumatics [4], electrics [12], and robotics [13, 14].

In this paper, we focus on the implementation of a multivariable nonlinear control, which is based on backstepping theory. The electro-hydraulic system under study is equipped with two servovalves and has therefore two control inputs. This enables multivariable control [15, 16] laws to be developed. Then the control could aimed at tracking two trajectories simultaneously: the first one is naturally the position and the second one can be defined according to other requirements on the system performance such as actuator stiffness, energy, bandwidth, etc.. We propose here two types of control laws based on the backstepping method. For the first one, called P-Y control, the tracking trajectories are the piston displacement and the pressure in one chamber of the cylinder. For the second one, called Y- $\lambda$  control, the tracking trajectories are the piston displacement and a dynamic weight on the pressure in each cylinder chamber. This last control law enables the accuracy of the piston position tracking to be improved. In both case, the backstepping based control design guarantee the asymptotical stability of the system except in some singular points.

Following this introduction, the second section gives an overview on the modeling of the studied electro-hydraulic system. The P-Y and Y- $\lambda$  control design are presented in the third section. Experimental validation and results are given in section four before concluding on the control performance and possible uses of such approaches.

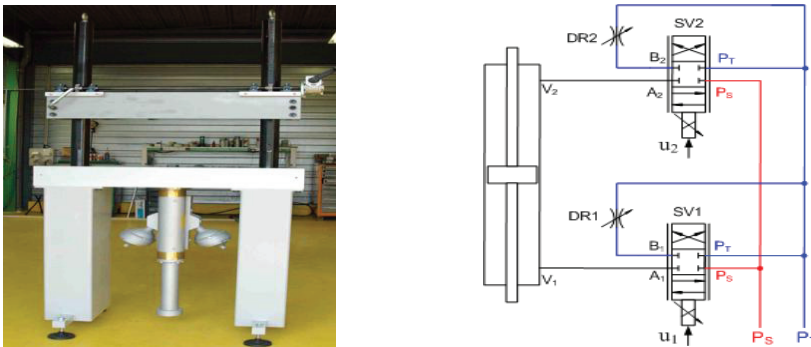


**Figure 1 The electro-hydraulic test bench**

## 2. MODELLING OF ELECTRO-HYDRAULIC SYSTEM

As shown in Figure 1, the developed electro-hydraulic test rig has two high bandwidth servovalves (MOOG D765) used as a 3-ways component for driving each actuator chamber. They are both implanted on an intermediate block equipped with accumulators and solenoid

valves, which enable several modes by connecting the servovalve's ports to the actuator installed vertically.

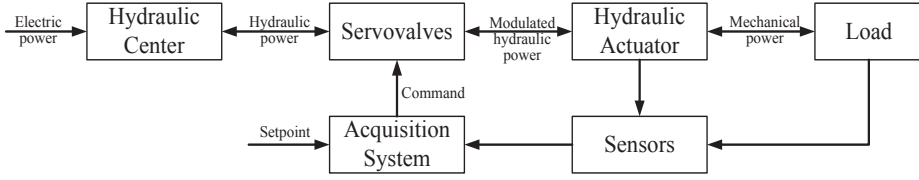


**Figure 2 Overview of the electro-hydraulic system**

Figure 2 shows an overview of the electro-hydraulic system. The actuator used here is symmetrical with two rods. The piston stroke can reach up to 300 mm with an active section area of 945 mm<sup>2</sup> and a movable load of 5.9 Kg. A LVDT transducer enables the measurement of the piston displacement. The bandwidth of the actuator is about 250 Hz with the piston at mid-stroke. The servovalves (MOOG D765) have a high response time of 2 ms and a nominal flow rate of 19 L/min. While considering the dynamic model for the control design, the dynamic of the servovalves is neglect due to its high response time. The servovalve model adopted accordingly, consists only in a static characteristic with respect to the supply pressure  $P_S$ , tank pressure  $P_T$ , actuator chamber pressure  $P_1$  or  $P_2$ , and input command  $u_1$  or  $u_2$ . While handling the control of this system, the focus is given on the dynamic of the actuator.

The compressibility of the fluid gives the pressure dynamic in each actuator chamber according to the piston velocity and the flow provided by each servovalve ( $\phi_1$  and  $\phi_2$ ), internal and external leakages being here neglected. The Newton's law gives the dynamics of the moving load. Dry friction  $F_{fs}$  (2), as well as the viscous friction term and gravity, are taken into account. The dynamic model of the actuator is then as follows:

$$\begin{cases} \frac{dy}{dt} = v \\ \frac{dv}{dt} = \frac{A}{M} (P_1 - P_2) - g - \frac{b}{M} v - \frac{F_{fs}(v)}{M} - \frac{F_{ext}}{M} \\ \frac{dP_1}{dt} = -\frac{\beta}{v_1(y)} \cdot A \cdot v + \frac{\beta}{v_1(y)} \cdot \phi_1(P_1, P_S, P_T, \text{sign}(u_1)) \cdot u_1 \\ \frac{dP_2}{dt} = \frac{\beta}{v_2(y)} \cdot A \cdot v + \frac{\beta}{v_2(y)} \cdot \phi_2(P_2, P_S, P_T, \text{sign}(u_2)) \cdot u_2 \end{cases} \quad (1)$$

where  $\phi_i = \frac{Q_n}{u_n} \cdot \sqrt{\frac{|P_S - P_i|}{\Delta P_n}} \cdot \frac{\text{sign}(u_i) + 1}{2} + \frac{Q_n}{u_n} \cdot \sqrt{\frac{|P_i - P_T|}{\Delta P_n}} \cdot \frac{\text{sign}(u_i) - 1}{2}$ ,  $i = 1, 2$ .

$$F_{fs}(v) = (F_{s\text{dyn}} + (F_{s\text{dyn}} - F_C)e^{-C|v|})\tanh(v) \quad (2)$$

### 3. CONTROL DESIGN

The system two inputs enable a multiple-objective control to be implemented. Namely, we can develop a control strategy to track different trajectories corresponding to different requirements. The following control designs mainly focus on tracking the piston position

and chamber pressures. These control strategies, based on the backstepping method, follow the general control scheme given in figure 3.

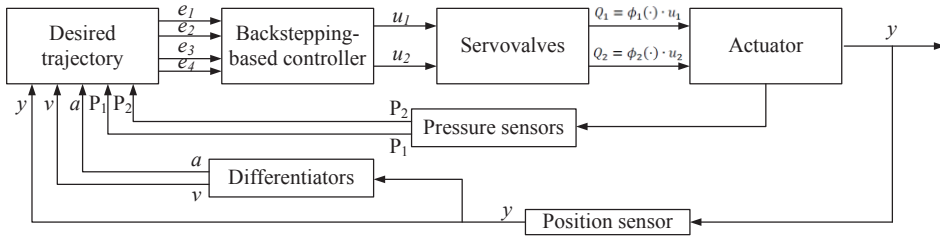


**Figure 3 General control scheme based on backstepping technique**

As shown on Figure 3, to apply the backstepping technique, several state variables have to be determined. Here position and chamber pressures are obtained from sensors, but for cost reasons, high-order sliding modes differentiators [17, 18] have been implemented to obtain velocity and acceleration from the position measurement.

### 3.1 Y-λ control strategy

Firstly, a backstepping-based method is adopted to synthesize the Y-λ control. It can be decomposed in 3 steps:

**Step 1:** The position tracking error  $e_1$  is defined by (3) as the difference between the measured ( $y$ ) and the desired ( $y^d$ ) piston position.

$$e_1 = y - y^d \quad (3)$$

$$\Rightarrow \dot{e}_1 = \dot{y} - \dot{y}^d = v - v^d \quad (4)$$

The piston velocity is considered as a virtual command for the above subsystem and a first Lyapunov function is chosen as follows:

$$V_1(e_1) = \frac{1}{2} e_1^2 \quad (5)$$

To ensure stability, its derivative (6) has to be negative. A first feedback function  $v = \alpha_0(e_1, v^d)$  is therefore defined by (7) with  $c_1$  a positive constant, which is satisfying the asymptotical stability condition from  $e_1 = 0$ .

$$\dot{V}_1(e_1) = e_1 \dot{e}_1 \quad (6)$$

$$v = \alpha_0(e_1, v^d) = v^d - c_1 e_1 \quad (7)$$

$$\Rightarrow \dot{V}_1 = -c_1 e_1^2 \leq 0 \quad (8)$$

**Step 2:** A new error variable  $e_2$  between the measured value  $v$  and the defined function  $\alpha_0(e_1, v^d)$  is now defined (9), however  $v$  is not exactly an real control but a system state.

$$e_2 = v - \alpha_0(e_1, v^d) = v - v^d + c_1 e_1 = \dot{e}_1 + c_1 e_1 \quad (9)$$

$$\Rightarrow \begin{cases} \dot{e}_1 = e_2 - c_1 e_1 \\ \dot{e}_2 = a - \dot{\alpha}_0(e_1, v^d) \end{cases} \quad (10)$$

A new Lyapunov function is defined for this new subsystem as:

$$V_2(e_1, e_2) = V_1(e_1) + \frac{1}{2} e_2^2 = \frac{1}{2} e_1^2 + \frac{1}{2} e_2^2 \quad (11)$$

$$\begin{aligned} \Rightarrow \dot{V}_2(e_1, e_2) &= e_1 \dot{e}_1 + e_2 \dot{e}_2 \\ &= -c_1 e_1^2 + e_2 \left( e_1 + \frac{A}{M} (P_1 - P_2) - g - \frac{b}{M} v - \frac{F_{fs}(v)}{M} - \frac{F_{ext}}{M} - \dot{\alpha}_0(e_1, v^d) \right) \end{aligned} \quad (12)$$

To verify the stability condition,  $\dot{V}_2(e_1, e_2)$  has to be negative and the pressure difference  $\Delta P = P_1 - P_2$  is chosen as a new virtual control defined by (13). This ensures the subsystem asymptotical stability from  $e_1 = e_2 = 0$  with  $c_2$  a positive constant (14).

$$\begin{aligned} \Delta P &= P_1 - P_2 = \alpha_1(e_1, e_2, v^d, a^d) \\ &= \frac{M}{A} \left( a^d + \frac{b}{M} v + \frac{F_{fs}(v)}{M} + \frac{F_{ext}}{M} + g + (c_1^2 - 1)e_1 - (c_1 + c_2)e_2 \right) \end{aligned} \quad (13)$$

$$\Rightarrow \dot{V}_2(e_1, e_2) = -c_1 e_1^2 - c_2 e_2^2 \leq 0 \quad (14)$$

**Step 3:** The two estimated pressures values in the cylinder chambers are given by (15) where  $\lambda$  is the dynamic weight of the chamber pressures and  $P_0$  is a reference pressure.

$$\begin{cases} P_1 = \alpha_2(e_1, e_2, v^d, a^d) = P_0 + \lambda \cdot \alpha_1(e_1, e_2, v^d, a^d) \\ P_2 = \alpha_3(e_1, e_2, v^d, a^d) = P_0 + (\lambda - 1) \cdot \alpha_1(e_1, e_2, v^d, a^d) \end{cases} \quad (15)$$

As  $P_1$  and  $P_2$  are not real commands, the differences between the measured pressures and estimated ones exist and are given by equation (16). This leads to a formulation, which differs from the conventional backstepping technique.

$$\begin{cases} e_3 = P_1 - \alpha_2(e_1, e_2, v^d, a^d) = P_1 - P_0 - \lambda \cdot \alpha_1(e_1, e_2, v^d, a^d) \\ e_4 = P_2 - \alpha_3(e_1, e_2, v^d, a^d) = P_2 - P_0 - (\lambda - 1) \cdot \alpha_1(e_1, e_2, v^d, a^d) \end{cases} \quad (16)$$

Then the new system coordinates are given by (17):

$$\begin{cases} \dot{e}_1 = e_2 - c_1 e_1 \\ \dot{e}_2 = \frac{A}{M} (e_3 - e_4) - c_2 e_2 - e_1 \\ \dot{e}_3 = \dot{P}_1 - \dot{\alpha}_2(\cdot) = f_1 + g_1 \cdot u_1 - \dot{P}_0 - \lambda \cdot \dot{\alpha}_1(\cdot) - \dot{\lambda} \cdot \alpha_1(\cdot) \\ \dot{e}_4 = \dot{P}_2 - \dot{\alpha}_3(\cdot) = f_2 + g_2 \cdot u_2 - \dot{P}_0 - (\lambda - 1) \cdot \dot{\alpha}_1(\cdot) - \dot{\lambda} \cdot \alpha_1(\cdot) \end{cases} \quad (17)$$

$$\text{with } f_1 = -\frac{\beta}{v_1(y)} \cdot A \cdot v, f_2 = \frac{\beta}{v_2(y)} \cdot A \cdot v, g_1 = \frac{\beta}{v_1(y)} \cdot \phi_1(\cdot) \text{ and } g_2 = \frac{\beta}{v_2(y)} \cdot \phi_2(\cdot)$$



$$\text{and } \dot{\alpha}_1(\cdot) = \frac{M}{A} \left( \dot{a}^d + \frac{b}{M} a + \frac{\partial F_{fs}(v)}{\partial v} \cdot \frac{a}{M} - (c_1^3 - 2c_1 - c_2)e_1 + (c_1^2 + c_1c_2 + c_2^2 - 1)e_2 - \frac{A}{M}(c_1 + c_2)(e_3 - e_4) \right)$$

A final Lyapunov function is defined as follows:

$$V_3(e_1, e_2, e_3) = V_2(e_1, e_2) + \frac{1}{2}e_3^2 + \frac{1}{2}e_4^2 = \frac{1}{2}e_1^2 + \frac{1}{2}e_2^2 + \frac{1}{2}e_3^2 + \frac{1}{2}e_4^2 \quad (18)$$

$$\begin{aligned} \Rightarrow \dot{V}_3(e_1, e_2, e_3) &= e_1\dot{e}_1 + e_2\dot{e}_2 + e_3\dot{e}_3 + e_4\dot{e}_4 \\ &= -c_1e_1^2 - c_2e_2^2 + e_3\left(\frac{A}{M}e_2 + \dot{e}_3\right) + e_4\left(-\frac{A}{M}e_2 + \dot{e}_4\right) \end{aligned} \quad (19)$$

In order to guarantee the stability of the system, a series of command combinations which solve the following system of equations (20) are required.

$$\begin{cases} f_1 + g_1 \cdot u_1 - \dot{P}_0 - \lambda \cdot \dot{\alpha}_1(\cdot) - \dot{\lambda} \cdot \alpha_1(\cdot) + \frac{A}{M}e_2 = -c_3e_3 \\ f_2 + g_2 \cdot u_2 - \dot{P}_0 - (\lambda - 1) \cdot \dot{\alpha}_1(\cdot) - \dot{\lambda} \cdot \alpha_1(\cdot) - \frac{A}{M}e_2 = -c_4e_4 \end{cases} \quad (20)$$

$$\Rightarrow \begin{cases} u_1 = \frac{1}{g_1} \left( -f_1 - c_3e_3 + \lambda \cdot \dot{\alpha}_1(\cdot) + \dot{\lambda} \cdot \alpha_1(\cdot) + \dot{P}_0 - \frac{A}{M}e_2 \right) \\ u_2 = \frac{1}{g_2} \left( -f_2 - c_4e_4 + (\lambda - 1) \cdot \dot{\alpha}_1(\cdot) + \dot{\lambda} \cdot \alpha_1(\cdot) + \dot{P}_0 + \frac{A}{M}e_2 \right) \end{cases} \quad (21)$$

According the above commands, the whole system has an asymptotical stability from  $e_1 = e_2 = e_3 = e_4 = 0$  with  $c_3$  and  $c_4$  two positive constants.

$$\dot{V}_3(e_1, e_2, e_3) = -c_1e_1^2 - c_2e_2^2 - c_3e_3^2 - c_4e_4^2 \leq 0 \quad (22)$$

In the case of Y- $\lambda$  control, the two pressures  $P_1$  and  $P_2$  can be controlled according to the reference pressure  $P_0$  and the dynamic weight  $\lambda$ .

### 3.2 P-Y control strategy

For the P-Y control strategy, a diffeomorphism is firstly applied to the initial system coordinates (1). With these new coordinates  $(y, v, a, P_1)$ , the system equations are now:

$$\begin{cases} \frac{dy}{dt} = v \\ \frac{dv}{dt} = a \\ \frac{da}{dt} = \frac{1}{M} \left( -b \cdot a - \frac{\partial F_{fs}(v)}{\partial v} \cdot a - A^2\beta \left( \frac{1}{v_1(y)} + \frac{1}{v_2(y)} \right) \cdot v \right. \\ \quad \left. + A\beta \left( \frac{\phi_1(\cdot)}{v_1(y)} \cdot u_1 - \frac{\phi_2(\cdot)}{v_2(y)} \cdot u_2 \right) \right) \\ \frac{dP_1}{dt} = -\frac{\beta}{v_1(y)} \cdot A \cdot v + \frac{\beta}{v_1(y)} \cdot \phi_1(P_1, P_S, P_T, \text{sign}(u_1)) \cdot u_1 \end{cases} \quad (23)$$

The backstepping method is now applied to the above system to synthesize the P-Y control.

**Step 1:** We consider a pressure control in chamber  $V_1$  using an error  $e_4$  between the measured and the desired pressure  $P_1$ .

$$e_4 = P_1 - P_1^d \quad (24)$$

$$\Rightarrow \dot{e}_4 = \dot{P}_1 - \dot{P}_1^d \quad (25)$$

The Lyapunov function selected for this subsystem is written as:

$$V_4(e_4) = \frac{1}{2} e_4^2 \quad (26)$$

$$\Rightarrow \dot{V}_4(e_4) = e_4 \dot{e}_4 = e_4 \left( -\frac{\beta}{V_1(y)} \cdot A \cdot v + \frac{\beta}{V_1(y)} \cdot \phi_1(\cdot) \cdot u_1 - \dot{P}_1^d \right) \quad (27)$$

$$u_1 = \frac{1}{g_1} \left( \frac{\beta}{V_1(y)} \cdot A \cdot v + \dot{P}_1^d - c_4 e_4 \right) \text{ where } g_1 = \frac{\beta}{V_1(y)} \cdot \phi_1(\cdot) \quad (28)$$

In order to make sure that  $V_4(e_4) \leq 0$ , we define the control  $u_1$  by (28). This leads to have  $\dot{V}_4(e_4) = -c_4 e_4^2 \leq 0$ , i.e., the subsystem is asymptotically stable from  $e_4 = 0$  with  $c_4$  a positive constant.

While working on the position control for this new model (23), the same steps as previously (for the P- $\lambda$  control) are done.

**Step 2:** Using the position tracking error  $e_1$  defined by (29), the control law is given by (31). With the Lyapunov function (32), it ensures the subsystem asymptotical stability from  $e_1 = 0$  with  $c_1 > 0$ .

$$e_1 = y - y^d \quad (29)$$

$$\Rightarrow \dot{e}_1 = v - v^d \quad (30)$$

$$v = \alpha_0(e_1, v^d) = v^d - c_1 e_1 \quad (31)$$

$$V_1(e_1) = \frac{1}{2} e_1^2 \quad (32)$$

$$\Rightarrow \dot{V}_1(e_1) = -c_1 e_1^2 \leq 0 \quad (33)$$

**Step 3:** Using the error  $e_2$  (34) between the measured velocity and  $\alpha_0(e_1, v^d)$  and the Lyapunov function defined by (36), the control law (38) is applied for stabilizing the subsystem (35) for  $c_2 > 0$ .

$$e_2 = v - \alpha_0(e_1, v^d) \quad (34)$$

$$\Rightarrow \begin{cases} \dot{e}_1 = e_2 - c_1 e_1 \\ \dot{e}_2 = a - a^d + c_1(e_2 - c_1 e_1) \end{cases} \quad (35)$$

$$V_2(e_1, e_2) = V_1(e_1) + \frac{1}{2} e_2^2 = \frac{1}{2} e_1^2 + \frac{1}{2} e_2^2 \quad (36)$$

$$\Rightarrow \dot{V}_2(e_1, e_2) = e_1 \dot{e}_1 + e_2 \dot{e}_2 = -c_1 e_1^2 + e_2(e_1 + a - a^d + c_1(e_2 - c_1 e_1)) \quad (37)$$

$$a = \alpha_1(e_1, e_2, v^d, a^d) = a^d + (c_1^2 - 1)e_1 - (c_1 + c_2)e_2 \quad (38)$$

$$\Rightarrow \dot{V}_2(e_1, e_2) = -c_1 e_1^2 - c_2 e_2^2 \leq 0 \quad (39)$$

**Step 4:** Considering finally the whole system (23), we introduce a new error  $e_3$  between the measured acceleration and  $\alpha_1(e_1, e_2, v^d, a^d)$ .

$$e_3 = a - \alpha_1(e_1, e_2, v^d, a^d) = a - a^d - (c_1^2 - 1)e_1 + (c_1 + c_2)e_2 \quad (40)$$

The error variables lead to the following formulation:

$$\begin{cases} \dot{e}_1 = e_2 - c_1 e_1 \\ \dot{e}_2 = e_3 - c_2 e_2 - e_1 \\ \dot{e}_3 = \dot{a} - \dot{\alpha}_1(e_1, e_2, v^d, a^d) \\ \dot{e}_4 = \dot{P}_1 - \dot{P}_1^d \end{cases} \quad (41)$$

where  $\dot{\alpha}_1(e_1, e_2, v^d, a^d) = \dot{a}^d - (c_1^3 - 2c_1c_2 - c_2)e_1 + (c_1^2 + c_1c_2 + c_2^2 - 1)e_2 - (c_1 + c_2)e_3$ .

The Lypunov function selected for the whole system is then as follows:

$$V_3(e_1, e_2, e_3) = V_2(e_1, e_2) + \frac{1}{2}e_3^2 + V_4(e_4) = \frac{1}{2}e_1^2 + \frac{1}{2}e_2^2 + \frac{1}{2}e_3^2 + \frac{1}{2}e_4^2 \quad (42)$$

$$\begin{aligned} \Rightarrow \dot{V}_3(e_1, e_2, e_3) &= e_1 \dot{e}_1 + e_2 \dot{e}_2 + e_3 \dot{e}_3 + e_4 \dot{e}_4 \\ &= -c_1 e_1^2 - c_2 e_2^2 - c_4 e_4^2 + e_3(e_2 + \dot{a} - \dot{\alpha}_1(e_1, e_2, v^d, a^d)) \end{aligned} \quad (43)$$

The command  $u_2$  is then defined as:

$$u_2 = -\frac{M}{A \cdot g_2} \left( -f - \frac{A \cdot g_1}{M} \cdot u_1 + \dot{a}^d + K_1 e_1 + K_2 e_2 + K_3 e_3 \right) \quad (44)$$

$$\text{where } \begin{cases} K_1 = 2c_1 + c_2 - c_1^3 \\ K_2 = c_1^2 + c_1c_2 + c_2^2 - 2 \text{ with } c_3 > 0 \\ K_3 = -(c_1 + c_2 + c_3) \end{cases}$$

$$\text{and } \begin{cases} f = -\frac{b}{M} \cdot a - \frac{\partial F_{fs}(v)}{\partial v} \cdot \frac{a}{M} - \frac{A^2 \beta}{M} \left( \frac{1}{V_1(y)} + \frac{1}{V_2(y)} \right) \cdot v \\ g_2 = \frac{\beta}{V_2(y)} \cdot \phi_2(\cdot) \end{cases}$$

According to the control law defined by equations (28) and (44), the whole system asymptotical stability is verified from  $e_1 = e_2 = e_3 = e_4 = 0$ .

#### 4. EXPERIMENTAL VALIDATION AND RESULTS

The proposed control strategies have been implemented on the hydraulic test bench (figure 1). The position is given by a LVDT sensor installed on the actuator rod. The sensor linearity is less than 0.1% and its sensibility is 4mV/V/mm. The pressures in actuator

chambers are measured from pressure sensors with a precision of  $\pm 0.1\%$ . All these signals are collected on an analog conditioning unit, and then digitalized at a sampling rate of 1 KHz with 16 bits precision on dSPACE acquisition board (DS1104). Velocity and acceleration are calculated from online 2nd-order adaptive differentiators [17, 18].

The presented experimental results focus on the validation of the proposed control strategies and on the analysis of the observed tracking performance. The desired trajectory which is applied here, is a step signal defined by a 7th-order polynomial function that enables a smooth velocity, acceleration, and jerk trajectory, namely, the 1st, 2nd, and 3th derivative of position respectively.

Firstly, we apply low gain values to the both backstepping-based controls:

- Y- $\lambda$  control:  $c_1 = 600, c_2 = 500, c_3 = 500, c_4 = 500, \lambda = 0.5, P_0 = 80 \text{ bar}$ ;
- P-Y control:  $c_1 = 600, c_2 = 500, c_3 = 500, c_4 = 500, P_1^d = 80 \text{ bar}$ .

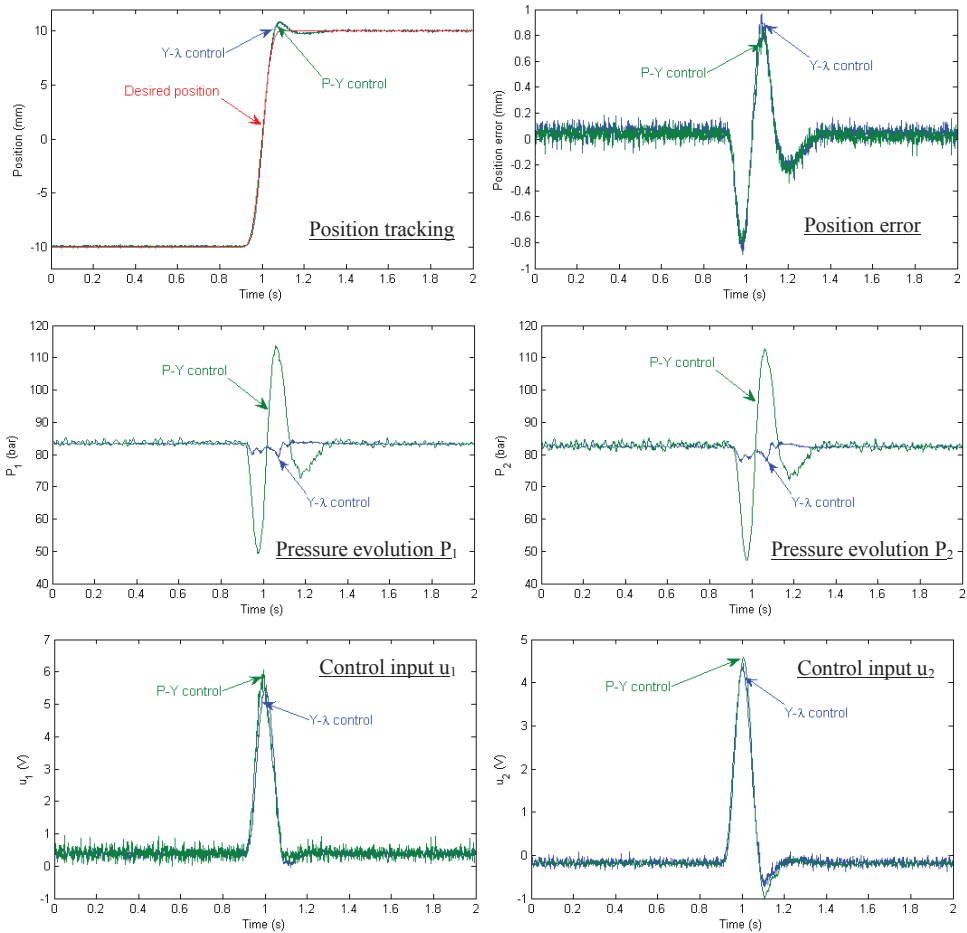
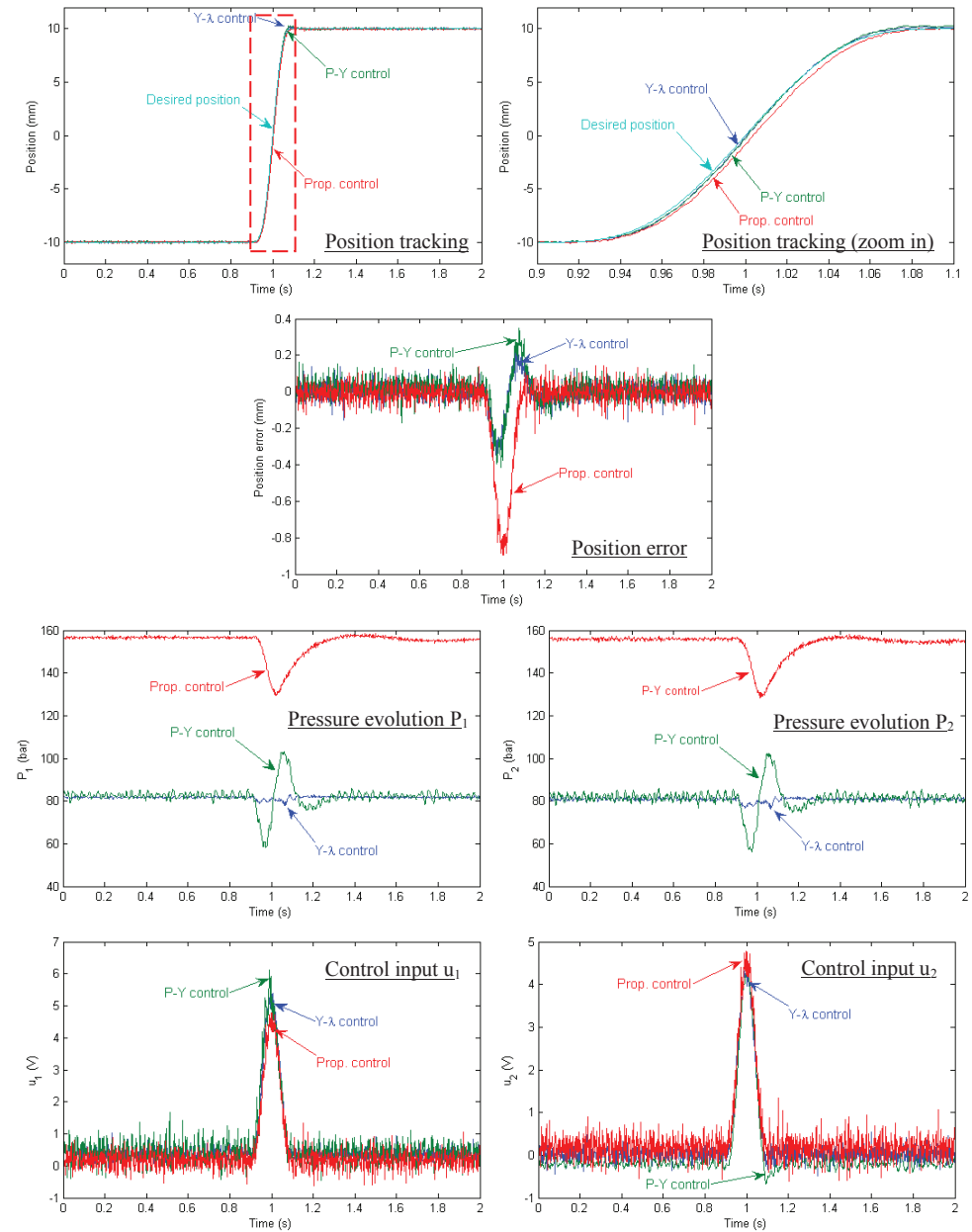


Figure 4 Experimental results with low gain values



**Figure 5 Experimental results with high gain values; comparison with proportional control**

The experimental results (Figure 4) show that there is a bit of overshoot and the position exceeds the desired trajectory final value. The mean position error in steady state condition is respectively about 64 $\mu$ m for Y- $\lambda$  and 37 $\mu$ m for P-Y control, while the maximum position error in the transient part of the trajectory is nearly 0.968mm for Y- $\lambda$  and 0.868mm for P-Y

control. Besides, we can notice that the commands are smooth, which leads to a good energy efficiency. Similarly, the pressure varies smoothly without any sharp impulsion.

Low gain values do not enable best performance to be achieved. Let us use higher gain values now:

- a) Y- $\lambda$  control:  $c_1 = 700, c_2 = 600, c_3 = 700, c_4 = 700, \lambda = 0.5, P_0 = 80 \text{ bar}$ ;
- b) P-Y control:  $c_1 = 700, c_2 = 600, c_3 = 600, c_4 = 700, P_1^d = 80 \text{ bar}$ .

As is shown in the Figure 5, the tracking performance has significantly been improved. Increasing the gains limits the position overshoot and reduces the tracking errors. The mean steady state error is now about  $6\mu\text{m}$  for the Y- $\lambda$  and  $25\mu\text{m}$  for P-Y control. The maximum position error in the transient part is less than  $350\mu\text{m}$  for the Y- $\lambda$  and  $415\mu\text{m}$  for P-Y control. Compared with the previous results (Figure 4), it can be observed that the position error decreases more rapidly for Y- $\lambda$  control than that for P-Y control as the gains increase. It implies that the Y- $\lambda$  control is more sensitive to the gain values. Besides, we note that as the gain values increase, the SNR (Signal-to-Noise Ratio) of the commands decreases slightly.

For comparison, a proportional control has also been implemented with the highest possible gain value until no significant performance improvement is observed. Compared with the results obtained using a conventional linear controller, the backstepping based controls achieve better tracking performances with a higher response speed (Figure 5). Beside, the conventional linear control focuses only on one control objective, namely the position control, and do not enable any other requirement to be fulfilled such as pressures value.

A comparative summary is given in the Table 1. Clearly, the Y- $\lambda$  control shows better performances than the other methods, not only in steady state condition but also in transient phases. However, both proposed backstepping-based controls show good performances.

**Table 1: Position errors in backstepping-based controls and proportional control**

Control strategy	Steady state		Transient phase	
	Mean ( $\mu\text{m}$ )	STD <sup>1</sup> ( $\mu\text{m}$ )	Max. ( $\mu\text{m}$ )	STD <sup>1</sup> ( $\mu\text{m}$ )
Y- $\lambda$ control	6	36	350	158
P-Y control	25	42	415	191
Prop. control	-4	41	894	321

1. STD: Standard deviation

Instead of using a constant pressure set value as shown previously, the pressure can also be defined as a trajectory which can corresponds to the application requirements. Figure 6 shows the experimental results obtained when the desired pressure is a sinusoidal function at 0.5Hz and 10 bar amplitude with an offset of 80 bar.

Along with the evolution of the reference pressure  $P_0$ , the pressures  $P_1$  and  $P_2$  follow the desired profiles. However, the position step can clearly be seen around 1s on the P-Y control. The dynamic weight  $\lambda$  of the Y- $\lambda$  control algorithm can precisely adjust the pressure distribution in two chambers and attenuates the pressure changes when the position step occurs.

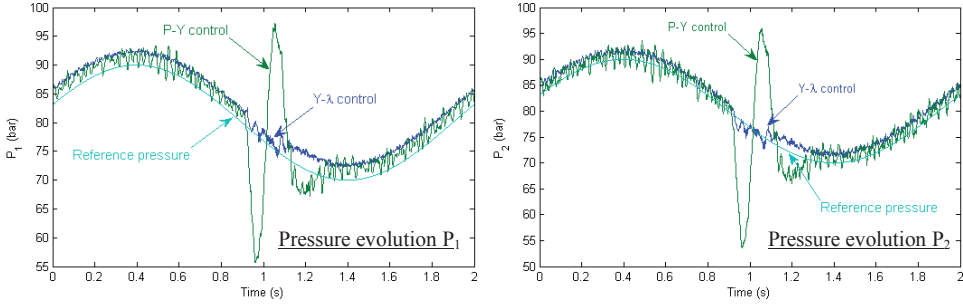


**Figure 6 Pressure trajectory: 1) Y- $\lambda$  control:  $\lambda = 0.5$ ,  $P_0 = 80 + 10\sin(\pi t)$ ; 2) P-Y control  $P_1^d = 80 + 10\sin(\pi t)$ .**

Finally, let us remark that when  $\lambda$  equals to 1, the trajectory of pressure in chamber  $P_2$  is directly  $P_0$ , while it is the pressure trajectory  $P_1$  which is equal to  $P_0$  when  $\lambda$  equals to 0. In this last case ( $\lambda = 0$ ), the Y- $\lambda$  Control is equivalent to the P-Y control.

## 5. CONCLUSIONS

The electro-hydraulic system presents nonlinearities, which make difficult to implement controls with high accuracy by conventional linear method. This paper proposes two nonlinear control strategies based on backstepping. These two strategies can achieve multiple-objective controls on a specific test bench on which the hydraulic actuator is equipped with 2 servovalves. The proposed controls are validated experimentally and have shown good steady state and dynamic performances with a very short response time. Besides, according to those controls, the pressures can easily be modulated according to the application requirements (dynamic stiffness, efficiency etc.). Compared to conventional linear control, the proposed controls are more suitable for position tracking tasks. The Y- $\lambda$  control algorithm shows better performances than the P-Y control, the weight  $\lambda$  allowing a better tracking of pressures.

Further prospects should now study and analyse more precisely the control parameters. Experiments have to be carried out with different values for  $\lambda$  in order to evaluate the influence of this parameter. Finally time depending values for  $\lambda$  instead of constant ones have to be defined according to control design requirements and experimentally tested.

## NOMENCLATURE

$y$	Piston position [m]	$P_1$	Pressure in chamber 1 [Pa]
$v$	Actuator velocity [m/s]	$P_2$	Pressure in chamber 2 [Pa]
$a$	Actuator acceleration [m/s <sup>2</sup> ]	$P_1^d$	Desired pressure of $P_1$ [Pa]
$y^d$	Desired position [m]	$P_T$	Tank pressure [Pa]
$v^d$	Desired velocity [m/s]	$P_S$	Supply pressure [Pa]
$a^d$	Desired acceleration [m/ s <sup>2</sup> ]	$\Delta P_n$	Rated valve pressure drop [Pa]
$P_0$	Reference pressure [Pa]		

$u_{1,2}$	Control inputs [V]	$V_1$	Volume in chamber 1 [m <sup>3</sup> ]
$u_n$	Rated control input [V]	$V_2$	Volume in chamber 2 [m <sup>3</sup> ]
$Q_n$	Rated flow [m <sup>3</sup> /s]	$F_{ext}$	External force [N]
$A$	Piston active area [m <sup>2</sup> ]	$F_{fs}$	sec friction [N]
$b$	Viscous coefficient [N/(m/s)]	$F_{sdyn}$	Dynamic sec friction [N]
$\beta$	Bulk modulus [Pa]	$F_C$	Coulomb friction [N]
$M$	Mass of the moving part [Kg]	$C$	Friction index
$g$	Gravity [m/s <sup>2</sup> ]		

## REFERENCES

- [1] Merritt H. E., Hydraulic Control Systems. John Wiley & Sons, New York, 1967.
- [2] Kim D.H., and Tsao T.-C., "A Linearized Electrohydraulic Servovalve Model for Valve Dynamics Sensitivity Analysis and Control System Design". Journal of Dynamic Systems, Measurement, and Control, Vol. 122, pp. 179-187, March 2000.
- [3] Watton J., "The Effect of Drain Orifice Damping on the Performance Characteristics of a Servovalve Flapper /Nozzle Stage". Journal of Dynamic Systems, Measurement, and Control, Vol. 109, pp. 19-23, 1987.
- [4] Smaoui M., Brun X., and Thomasset D., "A Study on Tracking Position Control of Electropneumatic System Using Backstepping Design". Control Engineering Practice, Vol. 14, n° 8, pp. 923-933, August 2006.
- [5] Fridman L., "Singularity Perturbed Analysis of Chattering in Relay Control Systems". IEEE Transaction on Automatic Control, Vol. 47, n° 12, pp. 2079-2084, December 2002.
- [6] Bartolini G., Pisano A., and Usai E., "A Survey Applications of Second-Order Sliding Mode Control to Mechanical Systems". International Journal of Control, Vol. 76, n° 9, pp. 875-892, June 2003.
- [7] Precup R.-E., Hellendoorn S. H., "A Survey on Industrial Applications of Fuzzy Control". Computer in Industry, Vol. 62, pp. 213-226, October 2011.
- [8] Leandro dos Santos Coelho, and Mauro André Barbosa Cunha, "Adaptive Cascade Control of a Hydraulic Actuator with an Adaptive Dead-Zone Compensation and Optimization Based on Evolutionary Algorithms". Vol. 38, n° 10, pp. 12262-12269, September 2011.
- [9] Krstic M., Kanellakopoulos I., and Kokotovic P., Nonlinear and Adaptive Control Design. John Wiley & Sons, New York, 1995.
- [10] Khalil K., Nonlinear Systems, third edition, Prentice-Hall, New Jersey, 2001.
- [11] Alleyne A., and Liu R., "Systematic Control of a Class of Nonlinear Systems with Application to Electrohydraulic Cylinder Pressure Control". IEEE Transaction on Control Systems Technologies, Vol. 8, n° 4, pp. 623-634, July 2000.



- [12] Lin F.J., and Lee C.C., "Adaptive Backstepping Control for Linear Induction Motor Drive to Track Periodic References". IEE Proceedings - Electric Power Applications, Vol. 147, pp. 449-458, November 2000.
- [13] Jiang Z.P., Jiang E., and Nijmeijer H., "Saturated Stabilization and Track Control of a Nonholonomic Mobile Robot". Systems and Control Letters, Vol. 42, pp. 327-332, 2001.
- [14] Lee T.C., Song K.T., Lee C.H., and Teng C.C., "Tracking Control of Unicycle-modeled Mobile Robots Using a Saturation Feedback Controller". IEEE Transactions on Control Systems Technology, Vol. 9, pp. 305-318, March 2001.
- [15] Wang L., Maré J.C., Fu Y., and Qi H., "Force Equalization for Redundant Active/Active Position Control System Involving Dissimilar Technology Actuators". Proc. of the 8th JFPS International Symposium on fluid Power, Okinawa, Japan, pp. 136-143, October 2011.
- [16] Bai Y. and Quan L., "Principle and Method to Improve the Dynamic Stiffness of the Electro-Hydraulic Servo System". Proc. of the 8th JFPS International Symposium on fluid Power, Okinawa, Japan, pp. 163-170, October 2011.
- [17] Sidhom L., Smaoui M., Thomasset D., Brun X., Bideaux E., "Adaptive Higher Order Sliding Modes for Two-dimensional Derivative Estimation". 18th World Congress of the International Federation of Automatic Control (IFAC), Milano, 28 Août - 2 Septembre, 2011.
- [18] Sidhom L., Pham M.T., Thévenoux F., Gautier M., "Identification of a robot manipulator based on an adaptive higher order sliding modes differentiator". IEEE/ASME International Conference on Advanced Intelligent Mechatronics, Montreal, 6-9 Juillet, 2010.

# Analysis of Two Typical Thrust Electro-hydraulic Control Systems for Shield Tunneling Machine

**Weiqiang Wu, Guofang Gong, Hu Shi**

Zhejiang University, State Key Laboratory of Fluid Power Transmission and Control, Hangzhou, Zheda Road No. 38, 310027, China  
wuwq33@zju.edu.cn

## ABSTRACT

This research is in an attempt to make a comparison between two typical thrust hydraulic control systems applied in shield machine. The shield manufacture corporations mostly equip their shields with this two thrust control systems. Firstly, the mathematical model of two thrust systems is built up based on the flow laws and dynamic theoretics. Then the characteristics in pressure and speed regulation of two thrust hydraulic systems are revealed by a simulation in AMESIM environment. Finally, experiments are conducted on the shield test rig. Within the pressure and speed regulating progress, the results verify the simulation well. It is shown that both two control systems are capable to reach the control demand, while the thrust hydraulic system adopting proportional flow control valve shows a more excellent performance in the field of tunneling.

**Keywords:** shield thrust systems, electro-hydraulic control, pressure and speed regulation

## 1 INTRODUCTION

With rapid development of big cities and the sustaining expansion of transport systems and the existing infrastructure, demands of underground space exploration and utilization have been reasonably growing. In order to satisfy the updating demands, it is significantly necessary to develop the safe, inexpensive and highly efficient technology for tunneling [1]. More and more tunnels are employed to accommodate transportation systems, electricity and communication constructions nowadays.

Shield tunneling machine (shield for short) is a modern construction machine dominating the tunneling field [2]. At present, the shield tunneling machine becomes to be the most promising and competitive equipment, for which gains superiority on quick and safe construction, high automation and environmental friendliness.

The shield thrust system plays an important role in the shield. By means of its large force, the thrust system is commonly driven by a hydraulic system. It accomplishes the task of driving shield ahead while tunneling, and rectifies the attitude of shield, which ensures

the shield to march along the expected path consequently, at the same time. Face stabilization appears to be another kernel technique while tunneling [3]. The thrust hydraulic cylinders push shield forward, meanwhile, the cutter head at the front of shield revolves and cuts the earth. As a result of that, the earth chamber will be full of pressurized earth, which sustains the excavating face during the whole excavation process [4]. To maintain the face stability, the earth pressure in the chamber has to be kept in a reasonable region [5]. Otherwise, the ground will heave while the earth pressure is too high or settle while it's too low. The thrusting force and velocity that depend on the pressure and flow control of the hydraulic system, which determine the earth pressure, play a vital role in shield tunneling. Fig. 1 shows the most important parts of the shield machine.

This paper presents two typical electro-thrust hydraulic control systems most widely used in the shield machine. The two thrust control systems comprise a cartridge valve and a pressure relief proportional valve. The mainly difference between them is the valve selected for the pressure and flow control. One chooses a flow control proportional valve to achieve the goal. The other makes it to be a pressure reducing proportional valve. By the diverse valves of the pressure and flow control, the response to the sudden load and the capability of speed accommodation of the thrust systems are destined to be quite unlike.

In this project, experiments are conducted with an earth pressure balance (EPB) simulation test rig consisting of shield machine, earth box filled with pressurized earth of different characteristics for test, and PLC control system.

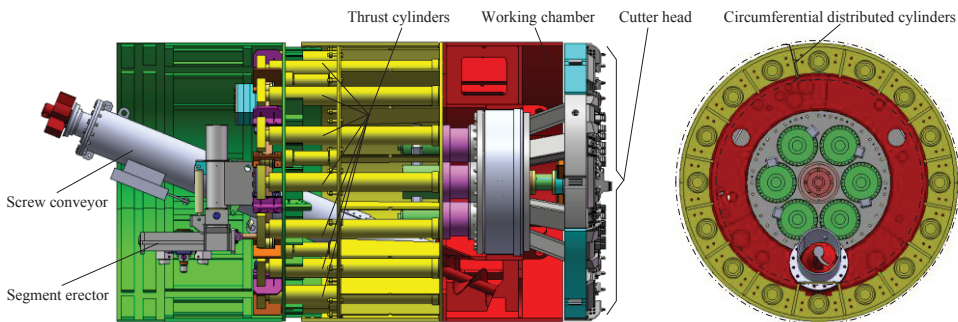


**Figure 1: Structure of the shield machine**

## 2 THRUST HYDRAULIC CONTROL SYSTEM

During tunneling process, the regulation of pressure and speed is a key part with high difficulty on account of complexity of soil environment. Achieving smooth and stepless regulation becomes an ideal target [6]. Two typical electro-hydraulic control systems are adopted in the tunneling field. Major shield manufacture corporations such as Herrenknecht, select proportional flow control valves and pressure relief valves into their products, while NFM, Kawasaki, Kamatsu and other manufacturer equip their shields with proportional pressure reducing valves in thrust systems. The thrust system falls into six identical groups for the sake of reducing the complexity and the cost of the control system. Each group follows the same control principle, which is illustrated in Fig. 2.

As shown in Fig. 2, for each group, the thrust system can switch the control modes freely by directional valve 2. Before the thrust progress, the cylinder piston rod must move forwards quickly to reach the goal position. That's what the cartridge valve 6 set for. While the right position of valve 1 is actuated, the oil goes through valve 6 to the cylinder with a large flow rate, which cuts down on the time of the whole tunneling circle. When valve 1 is on left, with valve 2 working at right position, thrust mode 1 with flow control valve takes the thrust task in hand. The oil flows through valve 3, whose flow rate can be regulated by adjusting the electric current through the coils of valve 3. Besides, the pressure relief valve maintains the system pressure at a constant level. When thrust is applied, the cylinder piston rod moves forward, the pressure and displacement of which are measured by pressure sensor 11 and displacement sensor 10 real-timely. With the control closed-loop, the pressure and speed of the system can be obtained with anticipated efficiency. To attain the control performance of another mode, valve 2 shifts to the left position. The pressure reducing valve comes to work to meet the pressure and speed requirements. Similar to mode 1, adjusting the electric current through the coils of valve 5 can reach the goal. To move the cylinder backwards, the pressure line and tank line are exchanged by switching the three position four way directional control valve (not shown here) connected the hydraulic source and the thrust systems.

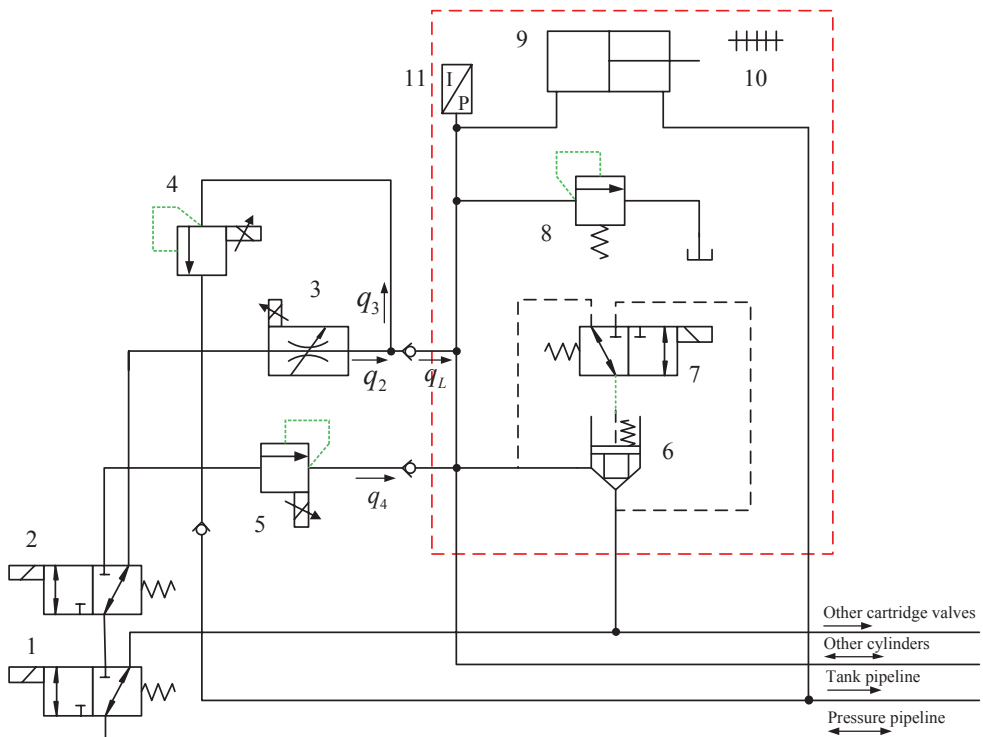


**Figure 2: Schematic diagram of the thrust hydraulic system**

### 3 SYSTEM MODELING

#### 3.1 Mathematical model

Within the system modeling process, we just give attention to the major elements, such as flow control valve, pressure relief valve, pressure reducing valve, cylinders, and so on. We may go to the thrust mode 1 with proportional flow control valve first.

In the tunneling process, the output flow of the proportional flow control valve, which is just the oil flow through the orifice of the throttle valve inside valve 3, can be revealed as

$$q_2 = K_{q2}y + K_{p2}(P_2 - P_L) \quad (1)$$

where  $K_{q2}$  denotes the valve flow gain,  $y$  the spool displacement,  $K_{p2}$  the valve flow-pressure coefficient,  $P_2$  the output pressure of the fixed difference pressure reducing valve,  $P_L$  the load pressure. By Newton's laws of motion, we can find the dynamics equation of the spool as

$$F_{M1} = m_1 \frac{d^2 y}{dt^2} + D_1 \frac{dy}{dt} + K_1 y \quad (2)$$

where  $F_{M1}$  is the output force of the solenoid of valve 3,  $m_1$  the mass of the spool,  $D_1$  the coefficient of viscous friction,  $K_1$  the stiffness of spring. The current characteristic equation of the proportional solenoid coil can be written as

$$u(t) = L \frac{di}{dt} + iR + K_v \frac{dy}{dt} \quad (3)$$

where  $u$  denotes the output voltage of the solenoid coil,  $L$  the inductance,  $i$  the current,  $R$  the resistances of coils and amplifier,  $K_v$  the coefficient of velocity back electromotive force induced by armature displacement. Moreover, taken the current-force characteristics of the proportional solenoid being approximately linear into account, the output electromagnetic force can be derived as

$$F_M = K_F i \quad (4)$$

where  $F_M$  is the electromagnetic force,  $K_F$  the current force gain. Given that the outlet pressure is zero, for the outline of the pressure relieve valve connected to the oil tank directly, then the oil flow through the valve 4 can be shown as

$$q_3 = \alpha_D A(y) \sqrt{\frac{2}{\rho} p_L} \quad (5)$$

where  $q_3$  is the flow rate,  $\alpha_D$  the flow rate coefficient,  $A(y)$  the effective flow area.  $A(y)$  of the valve can be derived as

$$A(y) = \pi y \sin \beta \left( d - \frac{1}{2} y \sin 2\beta \right) \quad (6)$$

where  $y$  denotes the spool displacement,  $\beta$  the half cone angle of the cone valve,  $d$  the diameter of the orifice.

Substituting Eq. (6) into Eq. (5), there will be:

$$q_3 = \alpha_D \pi \sin \beta \left( d - \frac{1}{2} y \sin 2\beta \right) y \sqrt{\frac{2 p_L}{\rho}} \quad (7)$$

The dynamics equation of the spool can be revealed as

$$p_L A_0 - F_{M2} - F_f + K_3(y_0 - y) = m_2 \frac{d^2 y}{dt^2} + D_2 \frac{dy}{dt} \quad (8)$$

where  $A_0$  is the effect acting area of the poppet,  $F_{M2}$  the output force of the solenoid of valve 4,  $F_f$  the steady-state fluid dynamic force,  $K_3$  the total stiffness of the spring,  $y_0$  the pre-compressed displacement of the spring,  $m_2$  the mass of the moving body,  $D_2$  the coefficient of viscous friction. The flow equation of the cylinder is conducted as

$$q_L = q_2 - q_3 = A \frac{dx}{dt} + C_{ic} p_L + \frac{V}{E} \frac{dp_L}{dt} \quad (9)$$

where  $q_L$  is the cylinder flow (load flow),  $A$  the effective working area,  $x$  the displacement of cylinder,  $C_{ic}$  the coefficient of leakage,  $V$  the total actuating volume,  $E$  the effective bulk modulus. The dynamics equation of the cylinder is carried out as

$$A p_L - F_L = M \frac{d^2 x}{dt^2} + B_v \frac{dx}{dt} + Kx \quad (10)$$

where  $F_L$  is the load force,  $M$  the total mass of the moving parts,  $B_v$  the viscous damping coefficient,  $K$  the stiffness of the load.

To the pressure reducing valve control mode, the pressure reducing valve make the outlet pressure be nearly stable, which can be regulated to accommodate different soil layers when tunneling.

The oil flow through the valve 5 can be shown as

$$q_4 = K_{q4} y_4 - K_{c4} P_L \quad (11)$$

where  $q_4$  is the flow rate,  $K_{q4}$  the valve flow gain,  $y_4$  the spool displacement,  $K_{c4}$  the valve flow-pressure coefficient. The dynamics equation of the spool is

$$A_4 p_c(s) - K_c y_4(s) - A_{m4} p_4(s) = (m_4 s^2 + B_4 s - K_{s4}) y_4(s) \quad (12)$$

where  $A_4$  is the area of the spool connected the control pipeline,  $A_{m4}$  the area of the spool linked to the load, while  $p_c$  and  $p_4$  are the pressure corresponding to the area respectively.  $K_c$  denotes the stiffness of the spring,  $m_4$  the mass of the moving body,  $B_4$  the viscous damping coefficient,  $K_{s4}$  the equivalent stiffness for steady-state fluid dynamic force of the spool.

### 3.2 Control design

In the practical tunneling process, the interaction between the shield and complex soil layer determines the successful grade of the tunneling project, which makes it a significant work to cope with different soil ahead the shield [7]. The thrust system should attain the control parameters of the thrust speed on one hand, and do the pressure regulation to maintain the face stability on the other hand. To achieve a preferable performance in the pressure and speed control system, which comprises controllers, amplifiers, valves, cylinders and sensors, there's no doubt to adopt the pressure and flow compound control technique [8]. In this paper, to clearly distinguish two different thrust control systems, we just observe the pressure and speed control characteristics under two different control systems respectively.

Pressure regulation is under the control of proportional pressure valve (a pressure relief valve or pressure reducing valve). The signal of the working pressure of cylinders in each

group detected by pressure sensors is delivered back to the control units, which constitutes the closed-loop control system, as shown in Fig. 3. PID controller is most adopted here to guarantee the control quality, while an open-loop control system directly adjusted by the proportional valves is also acceptable when the precision of the thrust pressure control system is not so strict.

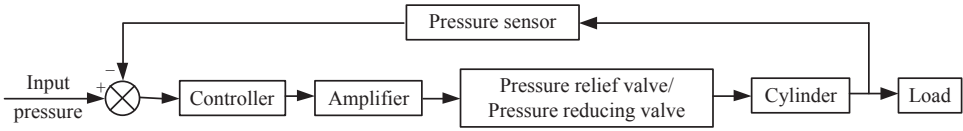


**Figure 3: Block diagram of the thrust pressure control system**

Similar to the thrust pressure control, the speed control is carried out by proportional flow control valve or pressure reducing valve. The displacement of cylinders is detected by displacement sensors, whose signal will be fed back to the control units after that. And then the displacement signal will be differentiated to velocity signal to accomplish the closed-loop control, as illustrated in Fig. 4. As like the pressure control, general PID controllers are widely used. However, setting the proportional valve straightly can yet be regarded as one correct solution in a precision reducing circumstance.

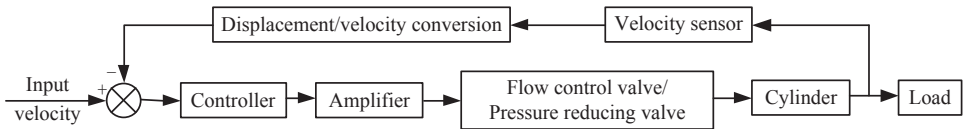


**Figure 4: Block diagram of the thrust speed control system**

## 4 SIMULATION

The simulation is carried out in AMESim environment, as shown in Fig. 5. The models of the proportional flow control valve, pressure relief valve and pressure reducing valve are conducted with the tool of HCD in the software. The components not so closely related to the simulation performance, such as directional valves and cartridge valves, are omitted in the simulation. According to soil mechanics, the load of the thrust system is composed of three parts: passive earth pressure, friction force and active pressure [9]. The parameters in this simulation are set in accordance with the thrust system of a  $\Phi 3\text{m}$  shield. The models of thrust control mode 1 with flow control valve and mode 2 with pressure reducing valve are illustrated in Figs. 5a and Fig. 5b respectively.

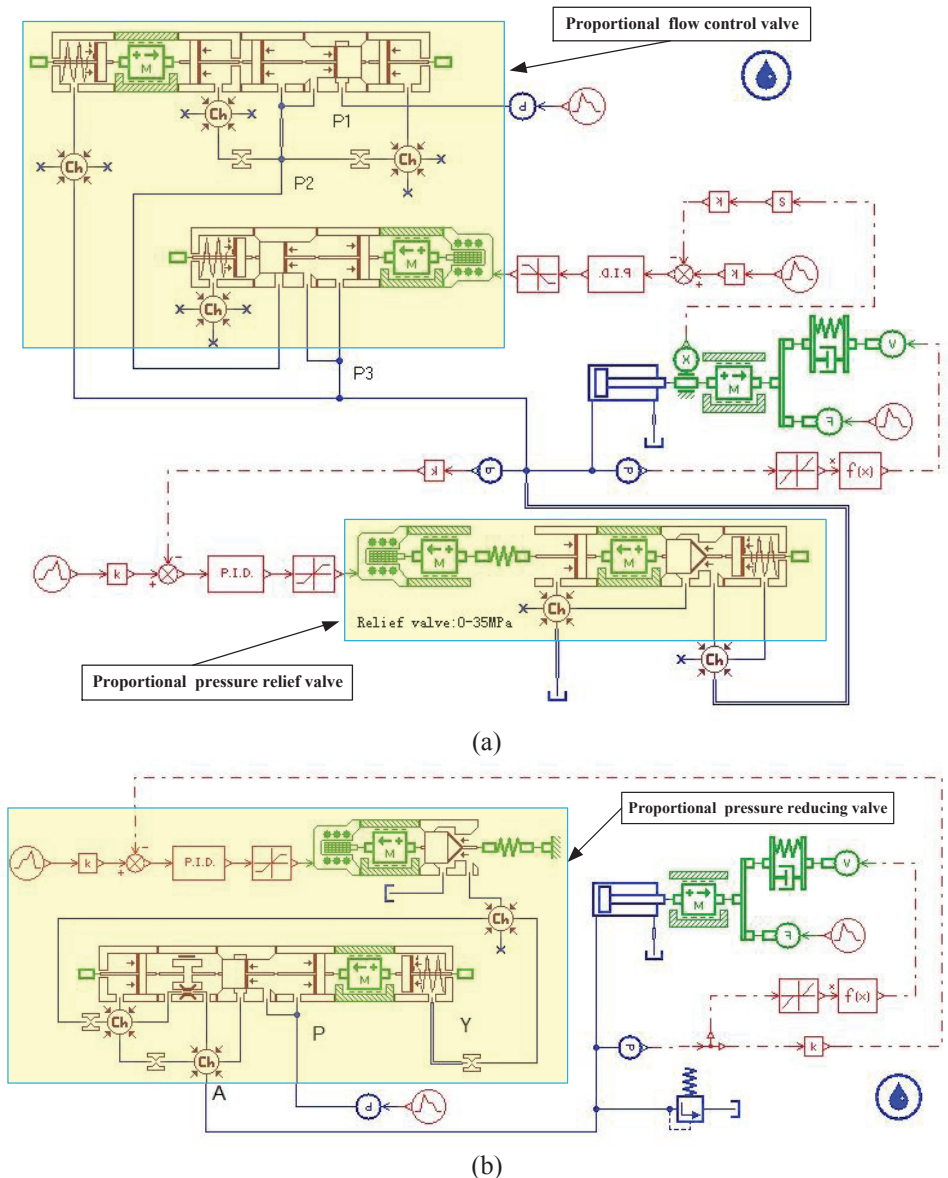


**Figure 5: Simulation model in AMESim**

In the simulation, the performance of pressure and speed regulation under two different control models is clearly represented, which enlightens us to compare the two models in multi-aspects explicitly. Fig. 6 shows the simulation results of pressure regulation for the thrust system under two different control models. The working pressure varies from 6.5MPa to 9.5MPa. Thrust velocity changes at the regulating moment by load disturbance. As the curves reveal, there is no obvious diversity within the pressure responding process but back to a stable state after vibrating by the great inertia of load (Fig. 6a). The fluctuation of velocity under the control of pressure relief valve is smaller by comparisons



(Fig. 6b), for the working flow rate of pressure relief valve needed to adapt to the pressure regulation is very small thanks to the flow control valve. To the pressure reducing valve control system, the open of the spool moves when accommodating thrust pressure, which disturbs the flow through the pressure reducing valve. That is to say, it affects the thrust velocity accordingly.

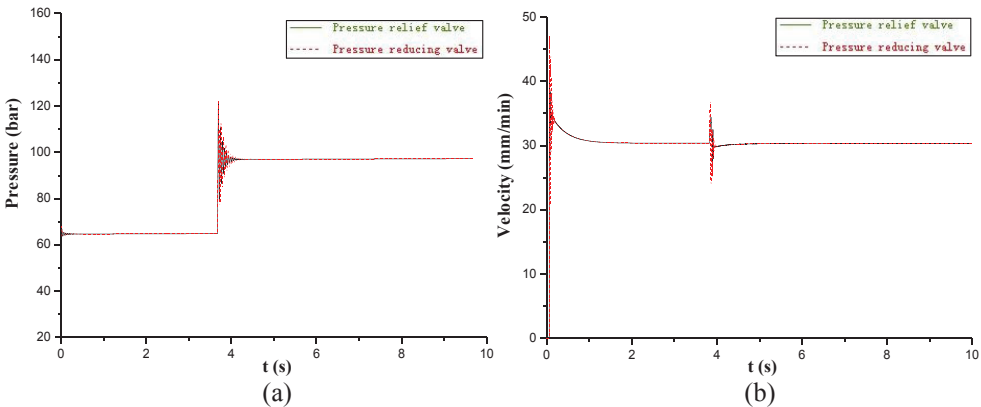


**Figure 6: Simulation results of pressure regulation of thrust system**

As to the speed control, the results are illustrated in Fig. 7, while the thrust velocity ranges from 35mm/min to 63mm/min. At the moment of speed regulating, working pressure is disturbed and fluctuates. It is explicit from Fig. 7 that because of the huge mass of the load, there both exists velocity vibration under two control systems. System under flow control valve appears smoother to the velocity inflection after further comparison. The flow control valve is composed of throttle valve and pressure reducing valve. The differential pressure between the input and output port of the valve nearly stays constant in spite of the open rate of the spool change. Under the control of pressure reducing valve, the opening ratio and differential pressure of the pressure reducing valve are shifted simultaneously. Both two control systems are capable to reach the control demand. The system adopted pressure reducing valve lies a bigger vibration nevertheless.

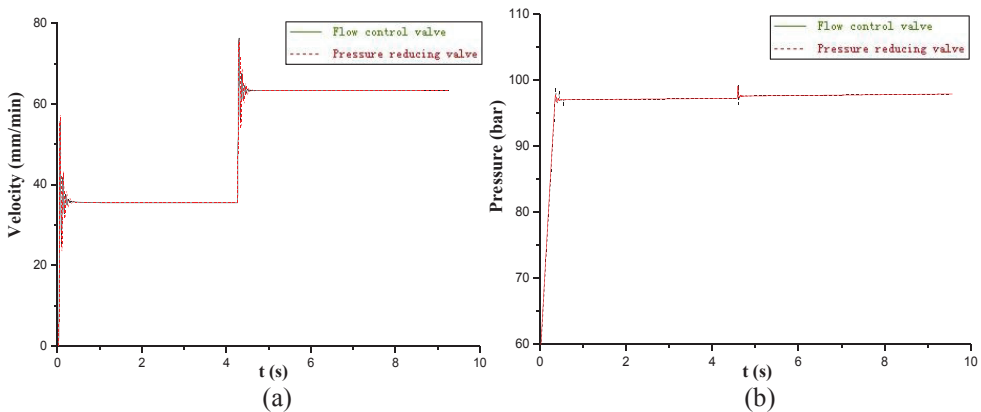


**Figure 7: Simulation results of speed regulation of thrust system**

5 EXPERIMENTAL RESULTS

The experiments are carried out under the pressure control mode to thrust forward firstly, switching from proportional pressure relief valve to pressure reducing valve. Then the velocity control mode switches from proportional flow control valve to pressure reducing valve. Results are shown in Fig. 8 and Fig. 9. The uncertainty of the viscous feature of the soil brings out oscillation in the whole test process. The regulation is performed around 300s with a steady thrust circumstance.

According to the experiments, we can conclude as follows:

1) Within the pressure regulating progress, the pressure compensation of the proportional flow control valve makes it simple to stabilize the thrust velocity. Correspondingly to the proportional pressure reducing valve, the flow rate is influenced by the pressure, which means the velocity will be disturbed significantly in a short time while pressure regulates.

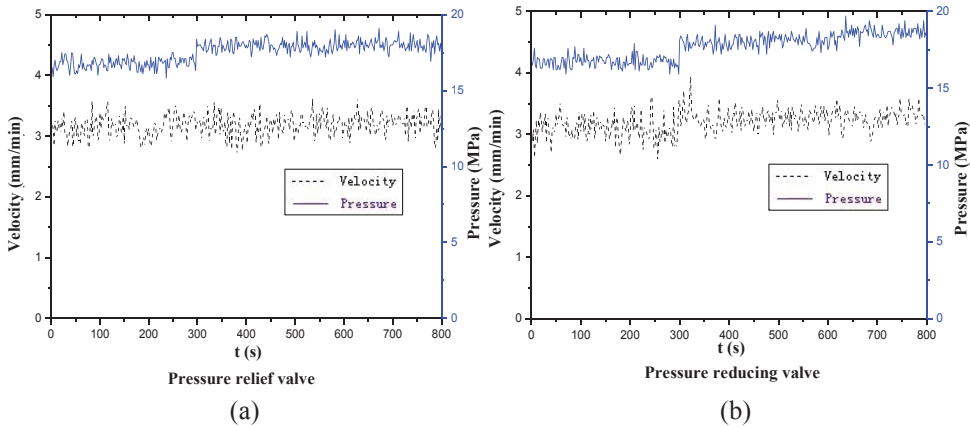


Figure 8: Experimental results of pressure regulation of thrust system

2) Under the speed control mode, proportional pressure relief valve is set at the maximum safe pressure, and the flow control valve dominates the thrust speed. The results show a close control quality by both control systems. They can fulfill the thrust demand.

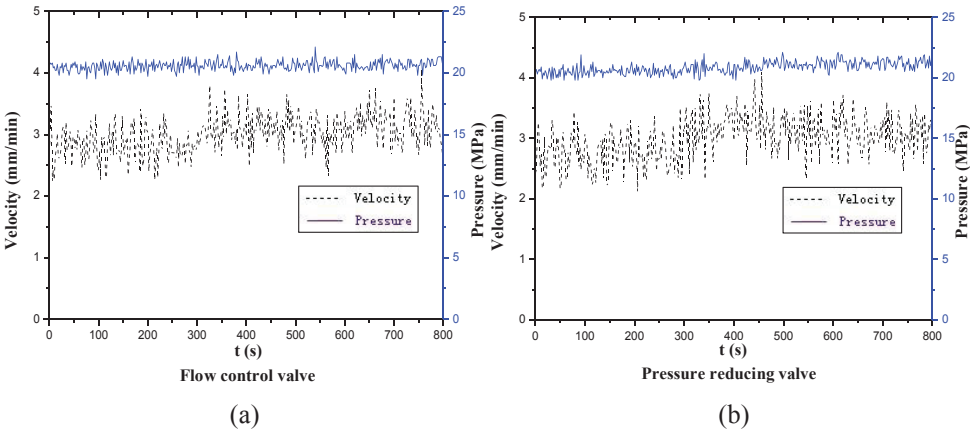


Figure 9: Experimental results of speed regulation of thrust system

## 6 CONCLUSION

This paper represents the similarities and differences between two different kinds of hydraulic thrust control system for a shield. The closed-loop control scheme of both control systems proved to be an effective technique to achieve a desired thrust performance. As a whole, the thrust control of proportional flow control valve appears to be better at a smaller vibration of pressure and speed regulation by comparisons. The control configuration of the combination of flow control valve and pressure relief valve brings two preferences in the control dimension, which makes the control more flexible and reduces disturbance during the pressure and speed regulation. In the meantime, complexity becomes its disadvantage. These conclusions will definitely provide some positive guidelines to select the proper hydraulic thrust system to attain the control characteristics.

## ACKNOWLEDGEMENTS

This project is supported by National Basic Research Program (973 Program) of China (No. 2007CB714004). The support is gratefully appreciated.

## REFERENCES

- [1] H. Yang, H. Shi, G. Gong, Electro-hydraulic proportional control of thrust system for shield tunneling machine, *Automation in Construction*, vol. 18(7), pp.950–956 (2009)
- [2] H. Yang, G. Gong, Shield TBM and its applications of hydraulic technology, *Hydraulics Pneumatics & Seals*, vol. 1, pp.27--29 (2004)
- [3] G. Anagnostou, K. Kovari, Face stability conditions with earth-pressure-balanced shields, *Tunnelling and Underground Space Technology*, vol. 11(2), pp.165--173 (1996)
- [4] R. Vinai, C. Oggeri, D. Peila, Soil conditioning of sand for EPB applications: a laboratory research, *Tunnelling and Underground Space Technology*, vol. 23(3), pp.308--317 (2008)
- [5] K. Deng, X. Tang, Research on characteristics of deformation in thrust system for EPB shield machines, *Tunnelling and Underground Space Technology*, vol. 26(1), pp.15--21 (2011)
- [6] M. Bernhard, H. Martin, A. Lothar, *Mechanised Shield Tunnelling*, Erbst & Sohn, Berlin, (1996)
- [7] M. Hisakazu, Earth pressure balanced shield method, *Tunnels & Tunnelling*, vol. 12(1), pp.47--49 (1980)
- [8] G. Hu, G. Gong, H. Yang, Thrust hydraulic system of shield tunnel boring machine with pressure and flow compound control, *Chinese Journal of Mechanical Engineering*, vol. 42(6), pp.124--127 (2006)
- [9] S. Bernat, B. Cambou, Soil-structure interaction in shield tunnelling in soft soil, *Computers and Geotechnics*, vol. 22(3), pp.221--242 (1998)

# **Modelling and Simulation**



# System Modelling and Bulk Modulus Estimation of an Electrohydrostatic Actuator

Y. Song, S. A. Gadsden, S. A. El Delbari, and S. R. Habibi

Centre for Mechatronics and Hybrid Technology Research

Department of Mechanical Engineering, McMaster University, Canada

songy@mcmaster.ca, gadsden@mcmaster.ca, delbarsa@mcmaster.ca,  
and habibi@mcmaster.ca

## ABSTRACT

An electrohydrostatic actuator (EHA) is an emerging type of actuator typically used in the aerospace industry. EHAs are self-contained units comprised of their own pump, hydraulic circuit, and actuating cylinder. The main components of an EHA include a variable speed motor, an external gear pump, an accumulator, inner circuitry check valves, and a cylinder (or actuator). This article presents the system modelling of an EHA built for experimentation. The system has been built to study a variety of different faults (friction, leakage, and bulk modulus); and models were obtained mathematically, and through system identification. Furthermore, using these system models, this article studies the results of estimating the bulk modulus by implementing the extended Kalman filter (EKF) algorithm.

## 1 BRIEF INTRODUCTION

Hydraulic actuation techniques have been developed and well-studied for decades [1,2,3]. Despite its high power-to-weight ratio, the demand of conventional hydraulics has fallen due to its limitations of control precision, energy efficiency, leakage, and noise [4,5,6]. A new pump controlled, hydraulic actuating technique referred to as an electrohydrostatic actuator (EHA) has been developed since 1990 [4,6]. Compared to conventional valve controlled hydraulic systems; advantages of the EHA system include more precise controllability and higher energy efficiency [7]. A model library that is able to describe the EHA dynamics is required for fault detection and control purposes. In this paper, models are obtained by implementing two modeling techniques: mathematical modelling and system identification. Mathematical models were generated based on a system model in which the parameters have physical meanings. An advantage of this modelling method is that it helps users understand the dynamic effect of each physical parameter in the system. By performing system identification modelling, an empirical black box model is extracted statistically [8]. It does not require full knowledge of the target system; however, the resulting system transfer function has no physical meaning [9].

In this paper, an EHA built for experimentation is studied. Models are generated based on mathematical equations and system identification. Section 2 describes the EHA in more detail, followed by a section on the classification of working and fault conditions. Section 4 provides EHA modelling based on system identification. Mathematical models of the EHA are created in Section 5. These models are validated in Section 6. The EHA bulk modulus is estimated using the extended Kalman filter (EKF), and the results are shown in Section 7. The main findings of the paper are then summarized in the conclusion.

## 2 ELECTROHYDROSTATIC ACTUATOR

An EHA is an emerging type of actuator typically used in the aerospace industry. EHAs are self-contained units comprised of their own pump, hydraulic circuit, and actuating cylinder [10]. The main components of an EHA include a variable speed motor, an external gear pump, an accumulator, inner circuitry check valves, a cylinder (or actuator), and a bi-directional pressure relief mechanism. The schematic of the EHA circuitry is shown in the Figure 1, as presented in [11]. The EHA can be divided into two subsystems. The first is the inner circuit that includes the accumulator and its surrounding check valves. The second is the high pressure outer circuit which performs the actuation. The inner circuit prevents cavitation which occurs when the inlet pressure reaches near vacuum pressures and provides make-up fluid for any dynamic leakage [10].

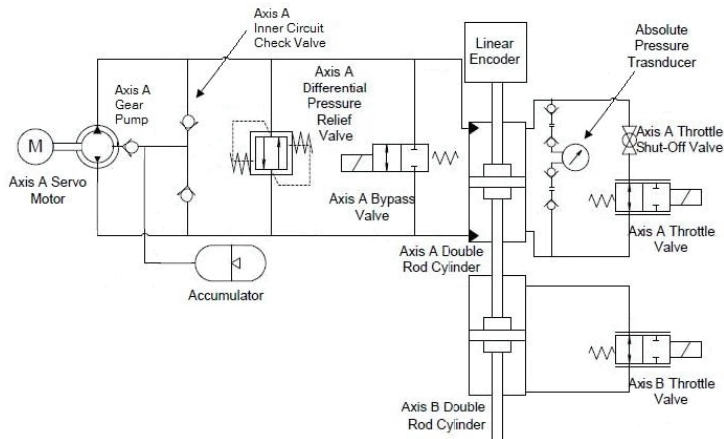


**Figure 1. EHA circuit diagram**

In Axis A, a bi-directional gear pump driven by a servo motor forces fluid to flow from one chamber of the cylinder to the other. The pressure difference generated between chambers starts the actuator movement which is captured by the linear encoder. Besides the position, the pressure difference between chambers is also be measured by the absolute pressure transducer. An inner circuit consists of three check valves, and an accumulator collects the leakage from the gear pump case strain and prevents cavitation of the system by maintaining the system pressure above 40 *Psi*. A differential pressure relief valve was installed to prevent the system pressure from exceeding 500 *Psi*, and a bypass valve was set up as a pump fail safe [12].

The EHA experimental setup is shown in the Figure 2. The cylinder on the right (foreground) is referred to as Axis A and the cylinder connected to it on the left (foreground) is referred to as Axis B. An optical linear encoder attached to Axis A is used to obtain position measurements (which are differentiated to obtain velocity measurements). The gear pump and electric motor are located in the rear (middle) of the table. The electric motor drives the gear pump, which moves the hydraulic fluid throughout the circuit. A voltage input controls the direction and speed of the pump which affects the velocity of the cylinders (or actuators). This setup is a closed hydrostatic circuit [13]. More details on the design and setup of the EHA may be found in [14,11,12,13]. The computer and electrical cabinet are located off-camera to the right of the setup. The software used to communicate with the EHA setup is MATLAB's Real-Time Windows Target environment.

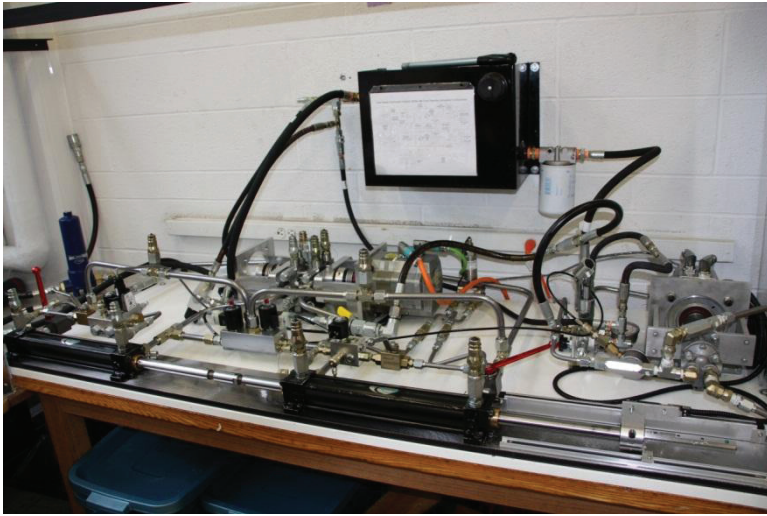


**Figure 2. EHA experimental setup**

### **3 CLASSIFICATION OF WORKING AND FAULT CONDITIONS**

In this section, the working and fault conditions of the EHA are classified. Two faults (friction and internal leakage) are simulated by connecting chambers of cylinders through throttle valves. The throttle valve selected is the SP08-25 2-way proportional valve from Hydraforce. The SP08-25 valve has its open area controlled by the input voltage. With a maximum 10 V input, the valve is fully closed. In contrast, the valve has the largest flow rate ( $2.57 \times 10^{-3} \text{ m}^3/\text{s}$ ) with a minimum 0 V input. When the Axis A motor drives the actuator to move, the fluid in the Axis B cylinder flows from one chamber to the other through the Axis B throttle valve freely if the valve is set as fully open. In this scenario, a negligible load is generated in Axis B and the system is considered as working normally. As the input converges to 10 V, the throttle valve is partially closed and starts to block the flow. The additional load increases in Axis B and resists the driving axis until the throttle valve is fully closed which leads the system to stall. This additional load is considered as the simulated friction in the EHA system.



A throttle valve connects chambers of the Axis A cylinder in order to simulate internal cross port leakage. When the throttle valve is fully closed, a negligible amount of flow is able to move from one chamber to the other, and the system is considered as working normally. However, when fluid flows cross those chambers while the throttle valve is partially open, one has the internal cross port leakage case. The amount of internal leakage and friction force can be modified and controlled by the throttle valves in Axis A and Axis B, respectively.

Since the EHA system has different dynamic performances with different levels of faults involved, the EHA system working conditions are classified into nine categories: normal, minor leakage, major leakage, minor friction, major friction, and four combined faults conditions; such as minor leakage plus minor friction, major leakage plus minor friction and so forth. The increase of leakage flow causes less flow rate on the main circuit and results in a decrease of actuator velocity. Therefore, the actuator velocity is used to define the level of leakage fault. The system is run under different levels of leakage by keeping the Axis B throttle valve fully open, as shown in the Figure 3. The x-axis refers to the throttle valve designed flow rate which corresponds to the throttle valve control input, while the y-axis refers to the actuator velocity. The minor and major leakage conditions are defined as when the system has nearly 75% and 50% of its normal performance, respectively. Based on Figure 3, the minor leakage fault condition is chosen with a throttle valve input of 2.1 V. The major leakage fault condition is chosen with a throttle valve input of 1.9 V.

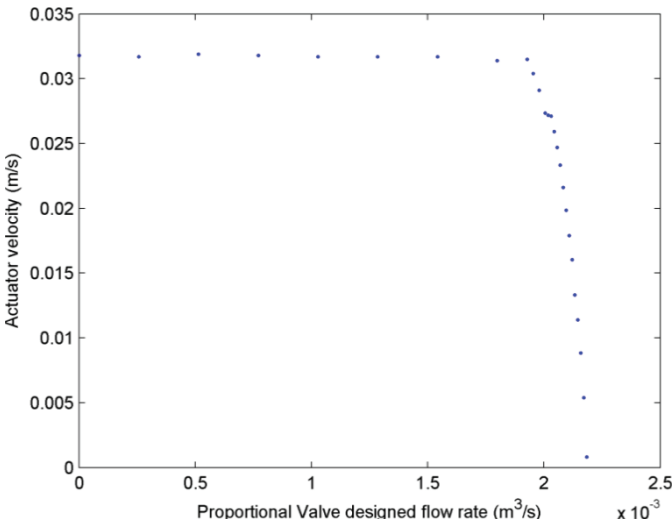


**Figure 3. Methodology for defining the leakage levels**

The decrease of Axis B throttle valve open area causes higher viscosity friction in the flow line and generates a higher pressure difference between the chambers in both cylinder A and B. In order to involve the overall friction force, the pressure difference in cylinder A is used to define the friction fault level.

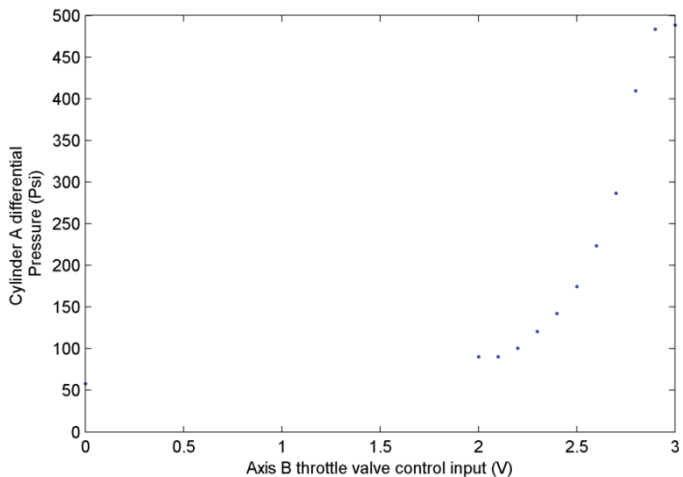


**Figure 4. Methodology for defining the friction levels**

As demonstrated in the Figure 4, the Axis A cylinder differential pressure increases from 58 *Psi* (399.91 *kPa*) as the Axis B throttle valve control input increases until it is saturated at the pressure relief valve activated pressure of 500 *Psi* (3,447.5 *kPa*). Similar to the definition of the leakage fault level, the minor and major friction fault condition are defined as 200% and 300% of the differential pressure at normal case. All of the working conditions that are studied in this paper and their corresponding throttle vale inputs are summarized in the following table.

**Table 1. Summary of Working Conditions and Inputs**

Working Condition	Axis A Input (V)	Axis B Input (V)
Normal Operation	10	0
Minor Leakage	2	0
Major Leakage	1.75	0
Minor Friction	10	2.3
Major Friction	10	2.5
Minor Leakage and Minor Friction	2	2.3
Major Leakage and Minor Friction	1.75	2.3
Minor Leakage and Major Friction	2	2.5
Major Leakage and Major Friction	1.75	2.5

#### 4 EHA MODELLING BY SYSTEM IDENTIFICATION

A complete system identification process involves three main stages. In the first tests stage, the target system is tested to obtain prior knowledge including the system delay, steady state gain, break frequency, system piece-wise linearity, and system order. In the second stage, data collection, the most crucial element is the test signal designed based on the prior

knowledge. A well-designed test signal would help to collect data in the system linear region with proper frequency range. After signal processing, the noisy collected data is filtered and ready to be used in the third stage, model fitting and validation. In the model fitting stage, four model structures are fitted and validated to obtain the most accurate model. The root mean square error (RMSE) is calculated to validate the accuracy of the models. A similar system identification process has been completed with the EHA system by Kevin McCullough in [12]. A third order model was obtained for the system working normally. In this paper, the system identification process is repeated and extended to obtain a model library for the EHA system working under the various conditions defined in Table 1. The results in the latest first tests generally agree with the findings in [12], except for the system piece-wise linearity and order of the model.

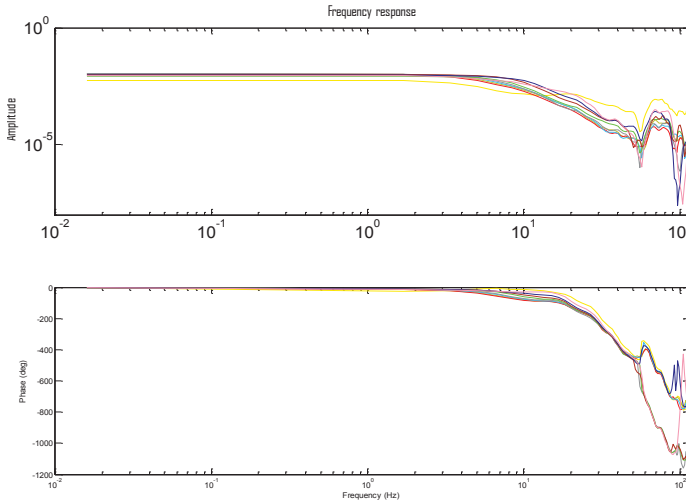


**Figure 5. Frequency response curves (amplitude and phase)**

The above figure demonstrates the updated test result of the system piece-wise linearity about various input means for systems working under the normal scenario. The coloured curves are smoothed empirical transfer function estimate (ETF) curves of the system working with motor voltage input means from 0 V to 8 V. Both of the curves result from the actuator velocity over the motor voltage. These curves generally share the same shape which indicates that the system performs linearly with changing input mean. The test is repeated again for systems operated with various input amplitudes and the results are plotted in Fig. 6. The results indicate that the system has different dynamic performances with low input amplitudes (below 1 V) and high amplitudes. Realizing that the dead zone of the system is larger than 1 V under the major leakage condition, the system is operated with amplitude higher than 1 V in the later tests.

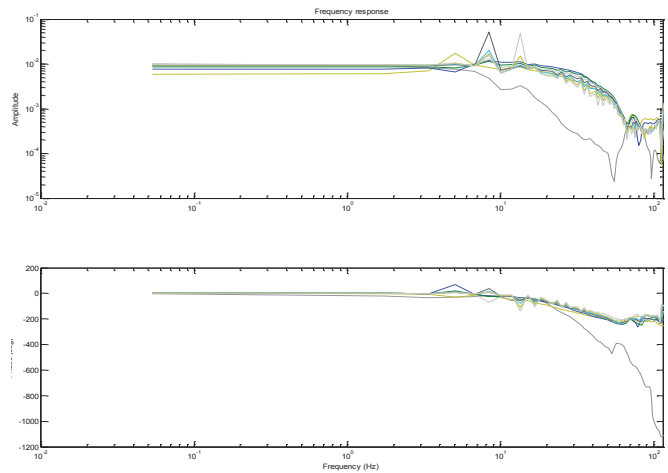


**Figure 6. Frequency response curves (amplitude and phase)**

The EHA system was found in [12] to be a third order system with an actuator velocity as an output. In this paper, the latest single value decomposition experiment results demonstrate that the system is a second order system with minor higher order dynamics, as shown in Fig. 7. Based on the prior knowledge obtained, a test input signal for data collection is designed as a 5 Hz pseudo random binary signal (PRBS) with zero mean and amplitude 4 V. The experimental output is filtered by a zero phase filter with 12<sup>th</sup>-order 30 Hz Butterworth low pass filter. Black box models are estimated with an output error model structure based on collected data for each working condition, as defined in Table 1. The system identification models are listed in the Appendix, and the performances of these models are validated in the model validation section.

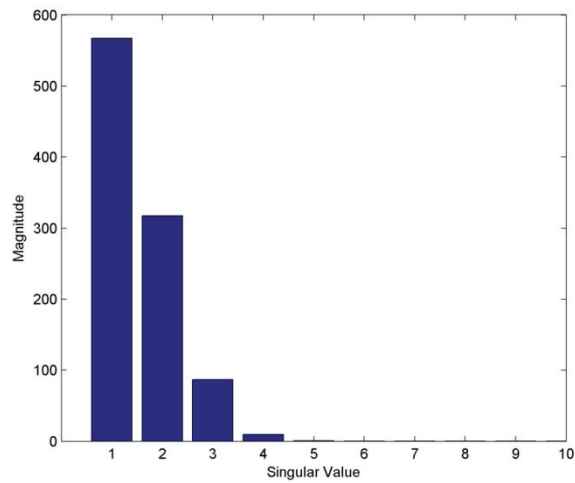


**Figure 7. Single value decomposition experiment results**

## 5 EHA MATHEMATICAL MODELLING

In the previous section, linear models were obtained by implementing system identification techniques. However, these models are not able to capture the nonlinear system dynamics accurately. For comparison purposes, traditional mathematical modelling processes are implemented in this section. A mathematical model was developed and demonstrated for the EHA system in [4]. The mathematical model was then simplified further in [13]. The EHA pump flow is modeled as follows [13]:

$$Q_a = D_p \omega_p - \xi(P_a - P_b) - \frac{V_a}{\beta} \frac{dP_a}{dt} - C_{ep}(P_a - P_r) \quad (5.1)$$

$$Q_b = D_p \omega_p - \xi(P_a - P_b) + \frac{V_b}{\beta} \frac{dP_b}{dt} + C_{ep}(P_a - P_r) \quad (5.2)$$

In the equations above,  $Q_a, Q_b, P_a, P_b, V_a, V_b$  are: the pump flow rate, pressure and section volume associated with the inlet and outlet, respectively.  $\omega_p$  is the motor angular velocity.  $\xi$  is the pump cross-port leakage coefficient and  $C_{ep}$  is the pump external leakage coefficient.  $\beta$  stands for the effective bulk modulus of the working fluid while  $P_r$  is the accumulator pressure.  $V_a, V_b$  are assumed to be identical because the symmetrical design of the gear pumped in this study. The actuator flow is modeled by [13]:

$$Q_1 = A\dot{x} + \frac{A(x_0 + x)}{\beta} \frac{dP_1}{dt} + L_{in}(P_1 - P_2) + L_{out}(P_1) \quad (5.3)$$

$$Q_2 = A\dot{x} - \frac{A(x_0 - x)}{\beta} \frac{dP_2}{dt} + L_{in}(P_1 - P_2) - L_{out}(P_2) \quad (5.4)$$

where  $Q_1, Q_2, P_1, P_2$  are the actuator flow rate and pressure associated with the inlet and outlet, respectively.  $A$  is the effective piston area and  $x$  stands for the actuator displacement.  $L_{in}$  and  $L_{out}$  are the internal and external leakage coefficient. Since a steal pipeline is implemented in the prototype, the pressure loss and leakage due to the pipeline is assumed to be negligible. Therefore:

$$Q_a + Q_b = Q_1 + Q_2; P_1 = P_a, P_2 = P_b$$

Since the actuator is symmetrical,  $\frac{dP_1}{dt} = -\frac{dP_2}{dt}$ .  $V_0$  is the total mean volume given by  $V_0 = V_a + Ax_0$ . By substituting and simplifying, the flow rate model of the EHA is obtained as follows:

$$D_p \omega_p = A\dot{x} + \frac{V_0}{\beta} \left( \frac{dP_1}{dt} - \frac{dP_2}{dt} \right) + \left( L_{in} + \frac{L_{out}}{2} + \xi + \frac{C_{ep}}{2} \right) (P_1 - P_2) \quad (5.5)$$

Using a lump sum leakage coefficient  $L_t = L_{in} + \frac{L_{out}}{2} + \xi + \frac{C_{ep}}{2}$ , the model can be further simplified as follows:

$$D_p \omega_p = A\dot{x} + \frac{V_0}{\beta} \left( \frac{dP_1}{dt} - \frac{dP_2}{dt} \right) + L_t(P_1 - P_2) \quad (5.6)$$

According to the model, the ideal pump flow  $D_p \omega_p$  contributes to the actuator motion  $A\dot{x}$ , fluid volume change  $\frac{V_0}{2\beta} \left( \frac{dP_1}{dt} - \frac{dP_2}{dt} \right)$ , and leakage  $L_t(P_1 - P_2)$ . At steady state one has  $\frac{dP_1}{dt} = \frac{dP_2}{dt} = 0$ , and the model can be transformed as follows:

$$L_t = \frac{D_p \omega_p - A\dot{x}}{P_1 - P_2} \tag{5.7}$$

According to the design of the EHA in [12], the values of the EHA parameters are listed in the following table.

**Table 2. EHA parameters and their values**

EHA Parameter	Description	Value
$D_p$	Gear pump volumetric displacement	$5.57 \times 10^{-7} \text{ m}^3/\text{s}$
$A$	Piston surface area	$1.52 \times 10^{-3} \text{ m}^2$
$V_0$	Nominal volume of each EHA chamber	$1.08 \times 10^{-3} \text{ m}^3$

In order to determine the leakage coefficient  $L_t$ , the EHA system is run with a constant velocity under different levels of differential pressure. The differential pressure is modified by changing the Axis B throttle valve input. Both the differential pressure and the actuator velocity are measured at steady state. The system leakage flow rate can be calculated by using (5.7). The experimental results regarding previously defined leakage conditions are plotted in Fig. 8.

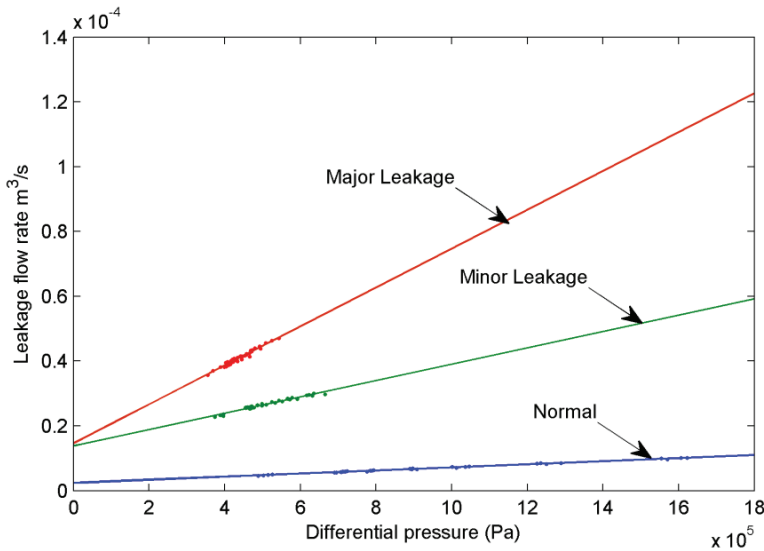


**Figure 8. Various leakage flow rates based on condition**

The leakage flow rate has a linear relationship with differential pressure which agrees with the mathematical model. However, a significant bias caused by the static friction of the system is also shown (with zero differential pressure). In order to calibrate the bias, the system model is modified as follows:

$$D_p \omega_p = A \dot{x} + \frac{V_0}{\beta} \left( \frac{dP_1}{dt} - \frac{dP_2}{dt} \right) + L_t (P_1 - P_2) + \text{sign}(\omega_p) Q_b \quad (5.8)$$

With  $L_t$  and  $Q_b$  calculated as per the following table.

**Table 3. Leakage coefficients and flow rates**

Condition	Leakage Coefficient	Flow Rate
Normal	$4.784 \times 10^{-12} \text{ Pa m}^3/\text{s}$	$2.413 \times 10^{-6} \text{ m}^3/\text{s}$
Minor Leakage	$2.523 \times 10^{-11} \text{ Pa m}^3/\text{s}$	$1.382 \times 10^{-5} \text{ m}^3/\text{s}$
Major Leakage	$6.006 \times 10^{-11} \text{ Pa m}^3/\text{s}$	$1.465 \times 10^{-5} \text{ m}^3/\text{s}$

In this paper, the EHA is not connected to any external load. The displacement of the actuator is related with the output force by the following equation:

$$F = (P_1 - P_2)A = M\ddot{x} + F_f \quad (5.9)$$

where  $M$  is the actuating mass which equals to  $7.376 \text{ kg}$  according to [12] and  $F_f$  is the actuator friction which can be described by a second order quadratic function related to the actuating velocity, as defined in [13]:

$$F_f = a_2 \dot{x} + (a_1 \dot{x}^2 + a_3) \text{sign}(\dot{x}) \quad (5.10)$$

At steady state, the acceleration of the actuator becomes zero and the force model can be modified as follows:

$$(P_1 - P_2)A = a_2 \dot{x} + (a_1 \dot{x}^2 + a_3) \text{sign}(\dot{x}) \quad (5.11)$$

To determine the friction coefficients  $a_1, a_2, a_3$ , experiments were performed with various randomly step inputs from  $0.5 \text{ V}$  to  $3.5 \text{ V}$ . Steady state velocity and differential pressures were measured and plotted regarding three previously defined friction conditions, as shown in Fig. 9. By best fitting the parabola curves into the data points, three friction models are extracted and are listed in the following table.

**Table 4. Leakage coefficients and flow rates**

Condition	$a_1$	$a_2$	$a_3$
Normal	$6.589 \times 10^4$	$2.144 \times 10^3$	436
Minor Friction	$1.162 \times 10^6$	$-7.440 \times 10^3$	500
Major Friction	$4.462 \times 10^6$	$1.863 \times 10^4$	551

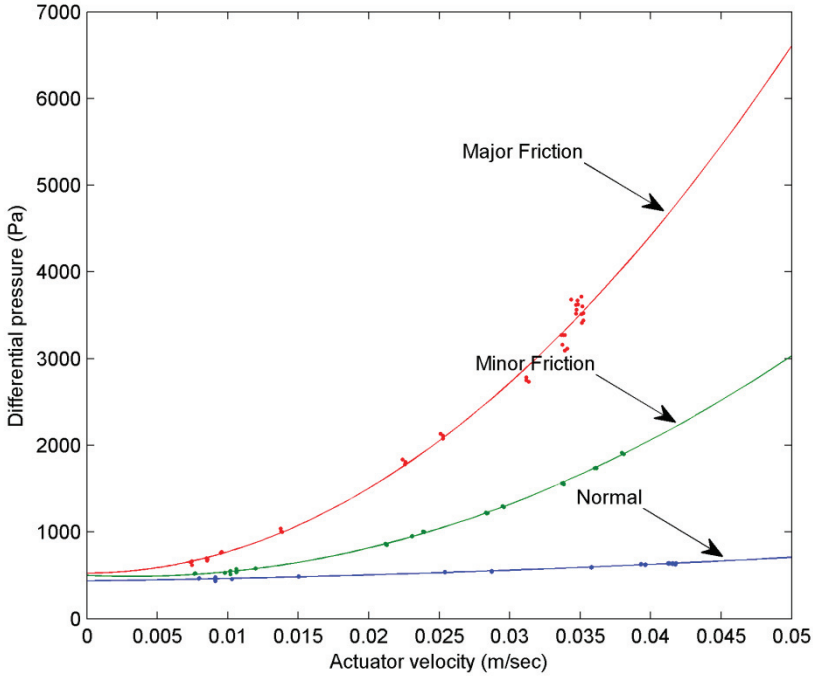


**Figure 9. Various friction rates based on condition**

Rearrange the force equation as follows:

$$P_1 - P_2 = \frac{M}{A} \ddot{x} + \frac{a_2}{A} \dot{x} + \frac{a_1 \dot{x}^2 + a_3}{A} \text{sign}(\dot{x}) \quad (5.12)$$

By assuming  $\text{sign}(\dot{x})$  as a constant then (5.12) becomes:

$$\frac{dP_1}{dt} - \frac{dP_2}{dt} = \frac{M}{A} \ddot{x} + \frac{a_2}{A} \dot{x} + \frac{2a_1 \dot{x} \ddot{x}}{A} \text{sign}(\dot{x}) \quad (5.13)$$

Substitution and rearranging yields the following:

$$\begin{aligned} D_p \omega_p - Q_b = & \frac{MV_0}{A\beta} \ddot{x} + \frac{a_2 V_0 + M\beta L_t}{A\beta} \dot{x} + \frac{A^2 + a_2 L_t}{A} \dot{x} \\ & + \frac{2a_1 V_0 \dot{x} \ddot{x} + \beta L_t (a_1 \dot{x}^2 + a_3)}{A\beta} \text{sign}(\dot{x}) \end{aligned} \quad (5.14)$$



6 MODEL VALIDATION

The validation test input consists of nine sequential steps. The absolute amplitude of each step is a random number between 2.5 V to 4 V. Since the stroke of the actuator is limited, the actuating direction is switched after each step. The corresponding motor angular velocity is plotted as follows. The RMSE for each model is calculated based on the velocity measurement.

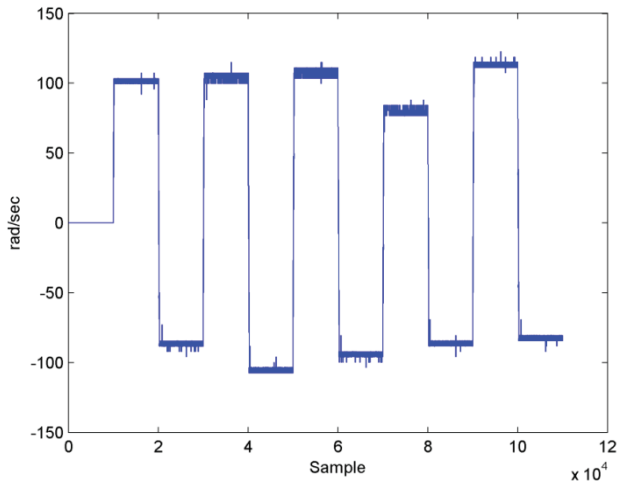


Figure 10. System input used for model validation

The following table lists the RMSE values for the models obtained mathematically and through system identification, as applied to the above signal under various conditions.

Table 5. Model validation

Model / Condition	RMSE (System ID)	RMSE (Mathematical)
Normal	0.0023	0.0015
Minor Friction	0.0023	0.0018
Major Friction	0.0035	0.0014
Minor Leakage	0.0027	0.0011
Major Leakage	0.0044	0.0013
Min. L & Min. F	0.0018	0.0013
Min. L & Maj. F	0.0012	0.0011
Maj. L & Min. F	0.0032	0.0007
Maj. L & Maj. F	0.0029	0.0011

As demonstrated in the above table, the models obtained mathematically yielded the best fit to the measurements. This is expected since the models from the system ID are linear, whereas the mathematical models better capture the nonlinearities present in the system.

## 7 BULK MODULUS ESTIMATION

Hydraulic fluid is incompressible when it is considered as ideal (i.e., no air bubbles present). With the presence of air, the fluid become compressible and causes slower response of the system and losses of energy. The parameter effective bulk modulus  $\beta$  is a measure of the fluid resistance to compression. It is difficult to determine the effective bulk modulus experimentally since the volume of air trapped in the system is unpredictable. In such cases, the popular extend Kalman filter may be used with the mathematical model to estimate the effective bulk modulus [13]. In an effort to implement the EKF, the system model is transformed into the following state space equations. Note however that the EKF equations may be found in [13,15], and were omitted due to space constraints.

$$x_{1,k+1} = x_{1,k} + T x_{2,k} \quad (7.1)$$

$$x_{2,k+1} = x_{2,k} + T x_{3,k} \quad (7.2)$$

$$x_{3,k+1} = \left[ 1 - T \frac{a_2 V_0 + M L_t x_{4,k}}{M V_0} \right] x_{3,k} - T \frac{A^2 + a_2 L_t}{M V_0} x_{4,k} x_{2,k} - T \left[ \frac{2 a_1 x_{2,k} x_{3,k}}{M V_0} + \frac{(a_1 x_{2,k}^2 + a_3) L_t}{M V_0} x_{4,k} \right] \text{sign}(x_{2,k}) \quad (7.3)$$

$$+ T \left[ \frac{A(D_p \omega_p - \text{sign}(\omega_p) Q_b)}{M V_0} x_{4,k} \right] \quad (7.4)$$

$$x_{4,k+1} = x_{4,k}$$

Note that the linearized system matrix is defined as follows:

$$\varphi(k) = \frac{\partial f(x(k))}{x(k)} = \begin{bmatrix} \varphi_{11}(k) & \varphi_{12}(k) & \varphi_{13}(k) & \varphi_{14}(k) \\ \varphi_{21}(k) & \varphi_{22}(k) & \varphi_{23}(k) & \varphi_{24}(k) \\ \varphi_{31}(k) & \varphi_{32}(k) & \varphi_{33}(k) & \varphi_{34}(k) \\ \varphi_{41}(k) & \varphi_{42}(k) & \varphi_{43}(k) & \varphi_{44}(k) \end{bmatrix} \quad (7.5)$$

where the parameters of (7.5) are defined by:

$$\begin{aligned} \varphi_{11}(k) &= 1; \varphi_{21}(k) = T; \varphi_{31}(k) = 0; \varphi_{41}(k) = 0; \varphi_{22}(k) = 0; \varphi_{23}(k) = 1; \\ \varphi_{24}(k) &= T; \varphi_{32}(k) = 0; \varphi_{33}(k) = 0; \\ \varphi_{32}(k) &= -T \text{sign}(x_{2,k}) \left( \frac{2 a_1 x_{3,k}}{M} + \frac{2 a_1 L_t x_{2,k} x_{4,k}}{M V_0} \right) - T \frac{A^2 + a_2 L_t}{M V_0} x_{4,k}; \\ \varphi_{33}(k) &= 1 - T \frac{2 a_1}{M} x_{2,k} \text{sign}(x_{2,k}) - T \frac{a_2 V_0 + L_t M x_{4,k}}{M V_0}; \\ \varphi_{34}(k) &= T \frac{A u_k}{M V_0} - T \frac{x_{2,k} (A^2 + a_2 L_t)}{M V_0} - T \frac{L_t}{V_0} x_{3,k} - T \frac{L_t (a_1 x_{2,k}^2 + a_3)}{M V_0} \text{sign}(x_{2,k}); \\ \varphi_{41}(k) &= 0; \varphi_{42}(k) = 0; \varphi_{43}(k) = 0; \varphi_{44}(k) = 1; \\ u_k &= D_p \omega_p(k) - \text{sign}(\omega_p) Q_b; \end{aligned}$$

Furthermore,  $T$  is the sampling time used in this paper, and was set to 0.1 ms. Note that the system and measurement noise covariance matrices were defined respectively as follows:

$$Q = \text{diag}(1 \times 10^{-12} \ 1 \times 10^{-8} \ 1 \times 10^{-6} \ 1 \times 10^{-12}) \quad (7.6)$$

$$R = \text{diag}(1 \times 10^{-12} \ 1 \times 10^{-4}) \quad (7.7)$$

The input with the higher frequency can excite the system better for more accurate bulk modulus estimation [13]. However, based on the experiments performed in system identification, the bandwidth of the EHA is around 25 Hz. The EHA system dynamics change significantly at a higher frequency region due to the dead-band and nonlinear friction. The testing input is chosen as a sinusoidal wave with 4 V amplitude and 10 Hz frequency. The corresponding motor angular velocity range is  $\pm 1200$  RPM. Note that the two measurements include piston displacement and velocity. The bulk modulus estimation process is executed with initial bulk modulus values from 0 Pa to  $5 \times 10^8$  Pa, and the result is plotted in Fig. 11. The bulk modulus values converge to the same value  $2.07 \times 10^8$  Pa which agrees with the bulk modulus value  $2.1 \times 10^8$  Pa obtained in [13].

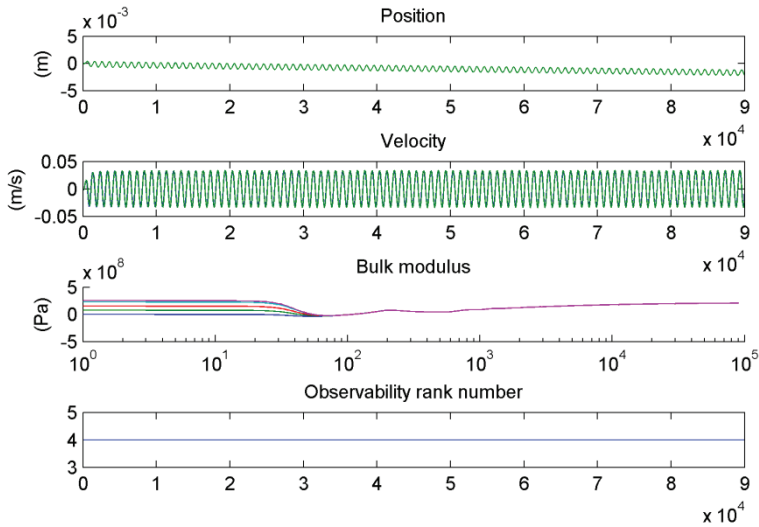


**Figure 11. Effective bulk modulus estimation of the EHA using the EKF**

## 8 CONCLUSION

In this paper, an EHA built for experimentation is studied. System models based on a number of conditions were generated mathematically as well as through system identification. It was found that the mathematical models were better able to capture the nonlinearity of the EHA system. These models were validated based on experimental results obtained from the EHA setup. The effective bulk modulus of the system was estimated using the EKF, and the results confirmed the values obtained in earlier studies.

## 9 REFERENCES

- [1] J. F. Blackburn, G. Reethof, and J. L. Shearer, *Fluid Power Control*. Boston, U.S.A.: MIT Press, 1960.
- [2] H. E. Merritt, *Hydraulic Control Systems*. New York, U.S.A.: John Wiley & Sons, Inc., 1967.
- [3] T. J. Viersma, *Analysis, Synthesis, and Design of Hydraulic Servo-Systems and Pipelines*.: Elsevier Scientific Publishing Company, 1980.
- [4] S. R. Habibi and A. Goldenberg, "Design of a New High-Performance Electrohydrostatic Actuator," *IEEE/ASME Transactions on Mechatronics*, vol. 5, no. 2, pp. 158-164, June 2000.
- [5] S. R. Habibi, R. Richards, and A. Goldenberg, "Hydraulic Actuator Analysis for Industrial Robot Multivariable Control," in *American Control Conference*, 1994, pp. 1003-1007.
- [6] S. R. Habibi and R. Richards, "Computed-Torque and Variable-Structure Multivariable Control of a Hydraulic Industrial Robot," in *Inst. Mechanical Engineering*, 1991, pp. 123-140.
- [7] S. R. Habibi, "High Precision Hydrostatic Actuation Systems for Micro and Nano Manipulation of Heavy Loads," *ASME Journal of Dynamic Systems, Measurement and Control*, vol. 128, December 2006.
- [8] L. Ljung, *System Identification: Wiley Encyclopedia of Electrical and Electronics Engineering*. New York, U.S.A.: Wiley & Sons, Inc., 1999.
- [9] S. R. Habibi, "System Identification: Part 1," McMaster University, Hamilton, Ontario, Graduate Mechatronics Course Lecture 2010.
- [10] S. R. Habibi, "The Smooth Variable Structure Filter," *Proceedings of the IEEE*, vol. 95, no. 5, pp. 1026-1059, 2007.
- [11] M. El Sayed, "Multiple Sliding Mode Control for Electro-Hydraulic Actuation (EHA) Systems," *Article Under Preparation*, 2011.
- [12] K. McCullough, "Design and Characterization of a Dual Electro-Hydrostatic Actuator," Department of Mechanical Engineering, McMaster University, Hamilton, Ontario, M.A.Sc. Thesis 2011.
- [13] Y. A. Chinniah, "Fault Detection in the Electrohydraulic Actuator Using the Extended Kalman Filter," Department of Mechanical Engineering, University of Saskatchewan, Saskatoon, Saskatchewan, Ph.D. Thesis 2004.
- [14] S. R. Habibi and R. Burton, "Parameter Identification for a High Performance Hydrostatic Actuation System using the Variable Structure Filter Concept," *ASME Journal of Dynamic Systems, Measurement, and Control*, 2007.
- [15] S. A. Gadsden, "Smooth Variable Structure Filtering: Theory and Applications," Department of Mechanical Engineering, McMaster University, Hamilton, Ontario, Ph.D. Thesis 2011.

# APPENDIX

The following is a list of the EHA models obtained through system identification.

**Table 6. Models Obtained by System Identification**

Operating Condition	System ID Model
Normal	$\frac{0.0001977z^2 - 0.000361z + 0.0001635}{z^2 - 1.893z + 0.894}$
Minor Friction	$\frac{0.0003197z^2 - 0.0006023z + 0.0002867}{z^2 - 1.747z + 0.7646}$
Major Friction	$\frac{0.0003089z^2 - 0.0005827z + 0.0002763}{z^2 - 1.675z + 0.6906}$
Minor Leakage	$\frac{4.137e - 6z^2 + 5.574e - 5z - 5.912e - 5}{z^2 - 1.755z + 0.7577}$
Major Leakage	$\frac{0.0002287z^2 - 0.0004551z + 0.0002331}{z^2 - 1.883z + 0.9092}$
Min. L & Min. F	$\frac{0.000208z^2 - 0.0004107z + 0.0002086}{z^2 - 1.905z + 0.9356}$
Min. L & Maj. F	$\frac{0.0001352z^2 - 0.0002643z + 0.0001323}{z^2 - 1.943z + 0.9619}$
Maj. L & Min. F	$\frac{(0.0001897z^2 - 0.0003723z + 0.0001877)}{z^2 - 1.933z + 0.9738}$
Maj. L & Maj. F	$\frac{(0.0001016z^2 - 0.0001982z + 9.692e - 5)}{z^2 - 1.959z + 0.9621}$

# Modeling of a Proportional Valve by MCMC Method

**Junhong Liu\*, Huapeng Wu, Heikki Handroos and Heikki Haario**

Faculty of Technology, Lappeenranta University of Technology

53851, Lappeenranta, Finland

E-mail:firstname.lastname@lut.fi

## ABSTRACT

This paper presents the modeling of a proportional valve using a Markov chain Monte Carlo (MCMC) method. We first observe that the MCMC method reveals if a first order model of valve has appropriate parameterization. To be exact, the obtained 2-dimensional MCMC chain revealed the correlation between the two parameters of this model. Based on the results, a fine parameterization of the first order model is formed. This first order model of valve is then compared with a second order model of the valve, and the coming out results show that the second order model better fits the valve's dynamics. This outcome was further verified with three new independent physical experiments. Based on the obtained results, the conclusion is made as: this modeling approach has the advantages of offering correlation information between the system parameters, using the noise-corrupted original physical data, and optimizing the model structure.

## 1. INTRODUCTION

Modeling and control of hydraulic-driven mechatronic systems have been studied earlier [1]. System identification is a prerequisite for the analysis of a dynamic system. Systems are normally nonlinear. Optimization methods have been used to find the system parameters.

The Markov chain Monte Carlo (MCMC) approach provides a powerful statistical tool to analyze the nonlinear models [2, 3]. The approach is different from the traditional least squares (LSQ) method: it does not seek for only one best fitting point estimate of the unknown model parameter vector, but all solutions to the parameter estimation problem given as the statistical distribution that contains “all” the possible parameter combinations: they statistically fit the data equally well within the limits of measurement error. The reliability of parameters and model predictions are quantified as probability distributions. Via evaluating the model predictions by the ensembles of parameter values, we can concretely see how reliably the model is in simulating various situations. The results of analyses can be used to optimize the model structures and design experiments. The MCMC approach also allows great flexibility in the definition of noise covariance structure of data.

In this study, the basic principles of the MCMC approach are first presented in Section 2. The mathematical description of models is in Section 3. Section 4 contains the physical experiments, the estimation results, and the analyses. Finally Section 5 holds conclusion.

## 2. THE MCMC METHOD

### 2.1 General form of a model

Statistical analysis studies the uncertainties in scientific inference by probabilistic reasoning. For the statistical treatment of uncertainties, we assume that all the unknown quantities can be described by statistical distribution, whether they are the model parameters, the unknown states of system, the model predictions, or the prior information of solutions.

Observations of system state are direct or indirect. A model is the mathematical description of a process generating states and observations. It can depend on a set of model parameters and be driven externally by control parameters. A separate error model accounts for the unsystematic variation in observations not covered by the systematic part of model. Statistically we estimate the unknown parameters with the help of physical data and a priori information about unknown parameters.

We represent the model of a system in the following form:

$$\mathbf{s} = f(\mathbf{x}, \boldsymbol{\theta}, \mathbf{c}), \quad (1-1)$$

$$\mathbf{y} = g(\mathbf{x}, \boldsymbol{\theta}) + \boldsymbol{\varepsilon}, \quad (1-2)$$

being  $\mathbf{s}$  the state vector,  $\mathbf{y}$  the observed variables,  $\mathbf{x}$  the experimental variables,  $\mathbf{c}$  constants,  $\boldsymbol{\varepsilon}$  the unsystematic observation errors, and  $\boldsymbol{\theta} = [\theta_1 \dots \theta_n]^T$  the estimated parameters with term  $n$  the number of identified parameters. Function  $f$  explains the model in terms of  $\mathbf{x}$ ,  $\boldsymbol{\theta}$ , and  $\mathbf{c}$ ; and  $g$  represents the response behavior predicted by the model (in terms of  $\mathbf{x}$  and  $\boldsymbol{\theta}$ ). A phenomenon can be static or dynamic, so a model may consist of algebraic or ordinary differential equations (ODEs).

The objective of model estimation is to minimize the sum of squared residuals:

$$\ell = \sum_{i=1}^N (y_i - \hat{y}_i)^2, \quad (2)$$

with  $N$  the number of observed data points,  $y_i$  the observed response ( $i = 1, 2, \dots, N$ ), and  $\hat{y}_i$  the model predicted response of  $y_i$ .

### 2.2 Approximative error analysis

Function  $\ell$  can be seen as a function of  $\boldsymbol{\theta}$ . Let  $\nabla \ell$  denote the gradient of  $\ell$ ,  $\mathbf{H}$  the Hessian matrix of the second derivatives of  $\ell$ , and  $\mathbf{J}$  the Jacobian matrix of the first derivatives. Assume small residual terms  $y_i - \hat{y}_i$ .  $\ell(\boldsymbol{\theta})$  can be approximated by the Taylor series expansion:

$$\ell(\boldsymbol{\theta}) = \ell(\hat{\boldsymbol{\theta}}) + (\boldsymbol{\theta} - \hat{\boldsymbol{\theta}})^T \nabla \ell(\hat{\boldsymbol{\theta}}) + \frac{1}{2!} (\boldsymbol{\theta} - \hat{\boldsymbol{\theta}})^T \mathbf{H} (\boldsymbol{\theta} - \hat{\boldsymbol{\theta}}) + \dots \cong \ell(\hat{\boldsymbol{\theta}}) + (\boldsymbol{\theta} - \hat{\boldsymbol{\theta}})^T \mathbf{J}^T \mathbf{J} (\boldsymbol{\theta} - \hat{\boldsymbol{\theta}}), \quad (3)$$

at point  $\hat{\boldsymbol{\theta}}$ . The covariance matrix of the LSQ estimators is given by  $\text{cov}(\hat{\boldsymbol{\theta}}) \approx \sigma^2 (\mathbf{J}^T \mathbf{J})^{-1}$ , where  $\sigma$  is the estimated standard deviation (STD) of the measurement error.

### 2.3 Bayes formula

Vector  $\boldsymbol{\theta}$  is interpreted as random variable. The aim of analysis is to find its distribution. Given the model, observations  $\mathbf{y}$  update the prior distribution  $p(\boldsymbol{\theta})$  to the posterior distribution  $\pi(\boldsymbol{\theta})=p(\boldsymbol{\theta}|\mathbf{y})$ , the conditional distribution of parameters. The Bayes formula is given by:

$$\pi(\boldsymbol{\theta}) = \frac{p(\mathbf{y} | \boldsymbol{\theta}) p(\boldsymbol{\theta})}{p(\mathbf{y})}. \quad (4)$$

When data  $\mathbf{y}$  is fixed, denominator  $p(\mathbf{y})$  is a single number. In principle, it can be calculated by integrating product  $p(\mathbf{y}|\boldsymbol{\theta}) p(\boldsymbol{\theta})$  over all values of  $\boldsymbol{\theta}$ . Term  $p(\mathbf{y}|\boldsymbol{\theta})$  is the probability distribution of observations  $\mathbf{y}$  given  $\boldsymbol{\theta}$  — the likelihood function. The most ‘likely’ values of parameters are those that give high values for  $\pi(\boldsymbol{\theta})$ . Assuming independent and identically distributed Gaussian errors for observations  $y_i$ , we have

$$p(\mathbf{y} | \boldsymbol{\theta}) = \prod_{i=1}^N p(y_i | \boldsymbol{\theta}) = \left(1/(2\pi\sigma^2)^{n/2}\right) \cdot \exp\left(-\frac{1}{2\sigma^2} \sum_{i=1}^N (y_i - g(f(\mathbf{x}_i)))^2\right). \quad (5)$$

### 2.4 Markov chain Monte Carlo algorithms

The original idea of the MCMC method was introduced in statistical physics [2], and the proposed Metropolis algorithm is the base of the Metropolis-Hastings algorithm founding the MCMC algorithm variants. Utilization of the algorithms for posterior inference in statistics was realized [3]. The algorithms take into account noise in measurement data and have commonly been used to approximate posterior distributions in different applications.

A MCMC algorithm generates a sequence of parameter values,  $\boldsymbol{\theta}_1, \boldsymbol{\theta}_2, \dots$ , with empirical distribution asymptotically converging to the posterior distribution  $\pi(\boldsymbol{\theta})$  [4]. The chain vectors are generated by random numbers; *Monte Carlo* generally refers to the methods based on the random number generation. Each new point of chain may only depend on the previous point, which is the *Markov property*. Intuitively, a correct distribution of parameters is generated by favouring points with the high values of  $\pi(\boldsymbol{\theta})$ . The basic Metropolis MCMC algorithm can be formulated in five steps (Table 1).



**Table 1: Metropolis MCMC algorithm**

Step	Explanation
1	$i = 1$ ; initialize $\theta_i$ , define the length of chain $n_{\text{simu}}$ , and select a <i>proposal distribution</i> $q$
2	$i = i + 1$ ; at the current point $\theta_{i-1}$ , propose candidate $\theta^*$ from distribution $q(\cdot \theta_{i-1})$ . Candidate depends on the previous point of the chain.
3	Accept the candidate with probability $\alpha(\theta_{i-1}, \theta^*) = \min(1, \pi(\theta^*)/\pi(\theta_{i-1}))$
4	If $\theta^*$ is not accepted, the chain stays at the current value, i.e., set $\theta_i = \theta_{i-1}$ .
5	Repeat simulation from Step 2 if $i < n_{\text{simu}}$ .

If  $\pi(\theta^*) > \pi(\theta_{i-1})$ , then  $\theta^*$  is better than  $\theta_{i-1}$ , the proposed candidate is accepted,  $\theta_i = \theta^*$ ; if not,  $\theta^*$  is accepted with probability set by the ratio of posterior values. In other words, points with high probability are favoured, reasonable but less probable points are allowed; while impossible parameters, those generating model values far from the observed data, are rejected. Only the *ratio* of the likelihood values is needed, the normalizing constant in (4) is cancelled. The delayed rejection adaptive metropolis [4] method is used in this study.

The MCMC algorithm finds all the parameter values that can be statistically considered as solutions to the parameter estimation problem. A standard procedure is: first use any usual optimizer to find the minimum of squared sum with respect to  $\theta$ ; then start the MCMC sampling algorithm, by using the LSQ fit as the first parameter value for the chain, and the approximative covariance as the covariance of a Gaussian proposal distribution. The choice of prior distribution is a topic that is much discussed in the literature. We use the *noninformative (flat)* priors by excluding physically impossible parameter values with simple lower and upper bounds. Values between bounds are considered a prior equally possible.

A chain produced after the optimization process is a matrix of samples from the posterior distribution of parameters. The statistical reasoning on model and parameters can be based on this matrix, for example, calculating the posterior means and illustrating correlation plots. Any model-derived values are given by calculating the respective values using the parameter samples from the chain. The posterior correlations and two-dimensional (2-D) marginal posterior plots of the parameter combinations can be used as diagnostics of parameter identifiability. The variance of the predictive distribution reflects the predictive power of model. A large variance may be due to the uncertainty or untaken effects in model.

### 3. SYSTEM DESCRIPTION

The experimental system (Fig. 1) comprises a directly operated proportional servo solenoid valve with position control, cylinder, and power unit. Voltage  $u$  ( $\pm 10\text{V}$ ) is the valve input. When the input is applied to the valve, spool is shifted and openings are produced. The spool shift  $x_s$  (mm) is small in two directions, and its maximum is not available. The spool is connected to the linear variable differential transformer (LVDT) that gives a testable voltage output  $u_s$  ( $\pm 10\text{ V}$ ) proportional to  $x_s$ .  $u_s$  is used as the information of spool displacement.

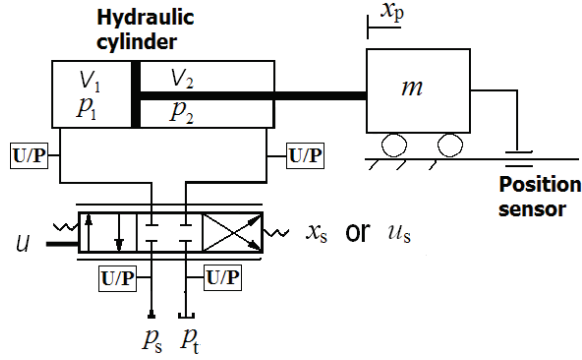


Figure 1: Schematic diagram of experimental configuration

### 3.1 First order model

Let  $t_1$  be the gain ( $s^{-1}$ ) and  $t_2$  the time constant ( $s^{-1}$ ). The valve's dynamics is [5]:

$$\dot{u}_s = t_1 u - t_2 u_s. \quad (6-1)$$

Set  $K$  the gain (no physical unit) and  $T$  the time constant (s). The model of valve can also be given as follows [1]:

$$\dot{u}_s = (K \cdot u - u_s) / T, \quad (6-2)$$

### 3.2 Second order model

Let  $k$  be the gain (no physical unit),  $\zeta$  the damping ratio (no physical unit), and  $\omega_n$  the natural angular frequency ( $\text{rad} \cdot \text{s}^{-1}$ ). A second order model describes the valve's dynamics as [1]:

$$\ddot{u}_s = k \omega_n^2 u - 2 \zeta \omega_n \dot{u}_s - \omega_n^2 u_s, \quad (6-3)$$

### 3.3 Ordinary differential equations (ODE)

The MCMC approach requires the ODEs of studied system. Based on (6), three models are obtained and represented in ODEs as the following:

$$\frac{du_s}{dt} = t_1 u - t_2 u_s, \quad (7-1)$$

$$\frac{du_s}{dt} = (K u - u_s) / T, \quad (7-2)$$

$$\begin{cases} \frac{du_s}{dt} = \dot{u}_s, \\ \frac{d\dot{u}_s}{dt} = k \omega_n^2 u - 2 \zeta \omega_n \dot{u}_s - \omega_n^2 u_s. \end{cases} \quad (7-3)$$

The state of (7-1) and (7-2) is  $u_s$  with the initial state  $s_0 = u_{s0}$ , and the state of (7-3) is  $[u_s \ du_s/dt]$  with  $s_0 = [u_{s0} \ 0]$ . Each has the control variable  $x = u$  and the observation variable  $y = u_s$ .

#### 4. EXPERIMENTS AND ANALYSIS

The valve under study is a Bosch Rexroth servo solenoid valve with on-board electronics (OBE) (4WRPET 6), having a nominal flow rate of  $0.00067 \text{ (m}^3 \cdot \text{s}^{-1}\text{)}$ . The data acquisition system was a dSPACE digital signal processor. The sampling frequency was 1000 (Hz). The control program was the c/c++ language program [6]. The input voltage  $u$  was fed to the valve using a DS 1103 I/O card;  $u_s$  was collected from the LVDT. Experiments were independently carried out, while  $u$  and  $u_s$  were directly collected along with time. Each model in (7) is optimized by the MCMC algorithm [7] with the same physical data, which has valve input in Fig. 2, pressure supply of  $12 \times 10^6 \text{ Pa}$  and mass of 210 kg. The obtained chain is used for statistical reasoning.

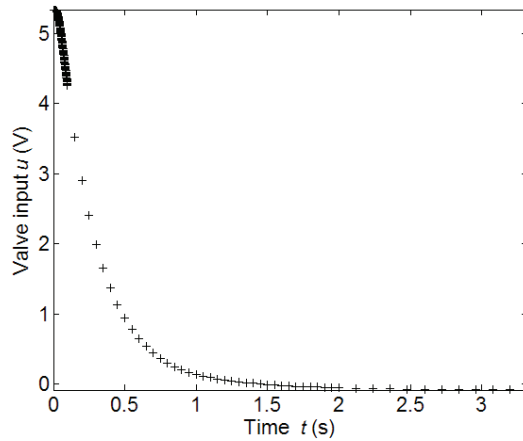
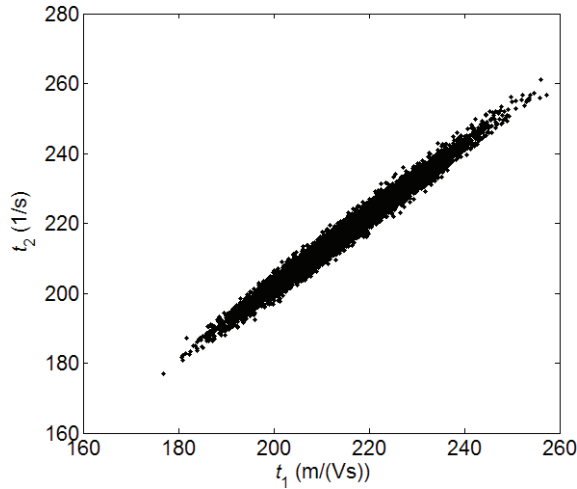


Figure 2: Valve input

##### 4.1 Model (7-1)

Seeing from (7-1), we notice that: (i) the valve's model has two parameters,  $t_1$  and  $t_2$ ; and (ii) terms  $t_1 u$  and  $t_2 u_s$  appear additively with opposite sign. An increase of any constant to both terms does not change  $du_s/dt$  at all. This effect is revealed by examining optimization results.

Figure 3 shows the posterior distribution of parameters  $t_1$  and  $t_2$ . As expected, there is clearly a strong correlation between them — the increasing linear relationship: the values of both each vary in quite large sections; a value-pair at one point on the line forms a model, which has the modelled responses agreeing with the real physical observations as well as a model formed by any other value-pair from the chain.



**Figure 3: 2-D MCMC chain of parameters  $t_1$  and  $t_2$  (Figure legends: “.” chain points)**

**4.2 Model (7-2)**

Based on the MCMC chain from the optimization process, the 2-D marginal distribution of parameters  $K$  and  $T$  is obtained (Fig. 4). This figure noticeably illustrates that there is no heavy linear dependency of them. Figure 5 shows the data and the model predicted responses by model (7-2). The posterior means and the standard deviations of the estimated parameters are listed in Table 2.

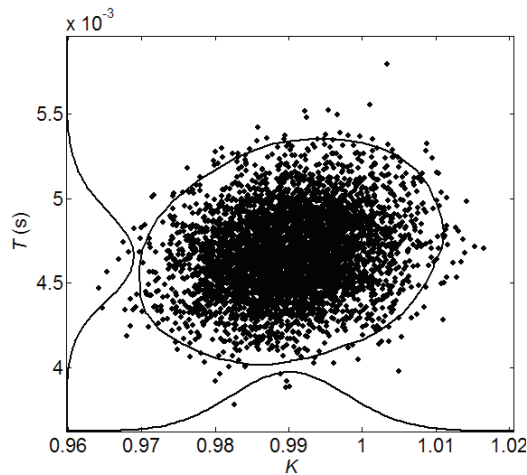


**Figure 4: 2-D marginal posterior distribution of parameters  $K$  and  $T$ . (Figure legends: Dots show the points in the related MCMC chain from which the density contour lines corresponding to 50% and 95% levels are constructed using the statistical kernel density estimation method [8]; distributions drawn along the  $x$  and  $y$  axes are the corresponding one-dimensional marginal densities)**

Given observation  $\mathbf{y}$  and model  $p(\mathbf{y}|\boldsymbol{\theta})$ , predictions are naturally based on the posterior distributions of  $\boldsymbol{\theta}$ . (i) The model response by the solid line in Fig. 5 is first represented by

the most probable response curve simulated with the sampled parameters  $\theta$  by (1-2). (ii) A confidence interval (95%) for the response at certain points in the x-axis is formed and plotted in dark gray color. This dark gray area represents where the model prediction curve lies with this probability. (iii) The estimate of measurement error is then added to the simulated responses to produce “noisy responses”. The measurement error with the standard deviation  $\sigma$  is normally thought to be fixed during the MCMC run and estimated from the residuals as in (2). However in our estimation this error was treated as a random variable and sampled along with the parameters. We add the estimate of the measurement error  $\varepsilon$  to the simulated response  $\hat{y}_i$  to produce “noisy response” according to (1-2). Similarly, a confidence interval (95%) for the response at certain points in the x-axis is formed and plotted in lighter gray color. This lighter gray area represents from where the observations (current and forthcoming) can be found with this probability. The lighter gray areas contain the parameter uncertainty, the uncertainties due to model “lack of fit” (the misspecification of model), and the noise of model.

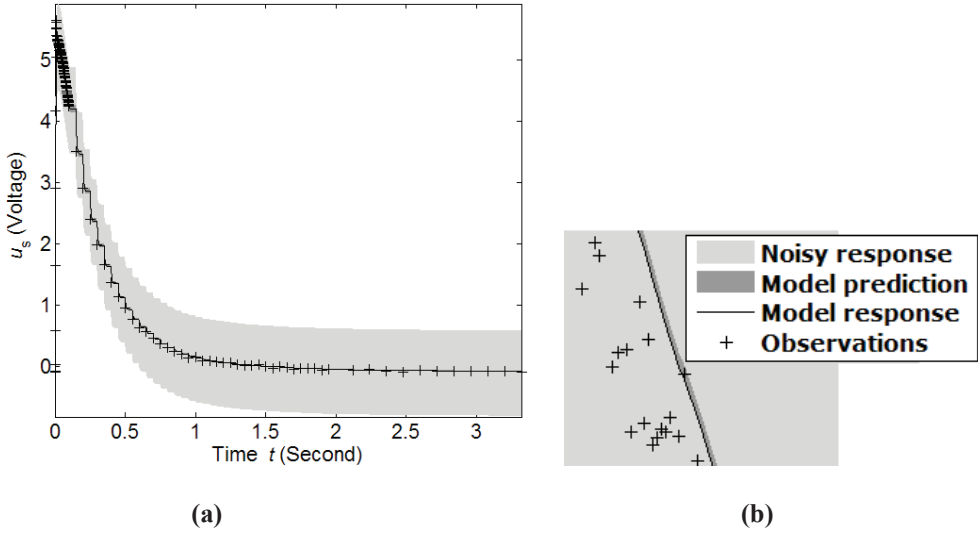


**Figure 5: Plots of the found model (7-2) and uncertainties. (a) Output signal of the LVDT; (b) Figure legends (The solid line shows the median fit obtained by the MCMC method; the darker area corresponds to the 95% posterior limits of model uncertainty; the lighter area illustrates the 95% bounds of uncertainty in predicting new observations; and plus-signs present observations)**

In Table 2, the standard deviations of parameters  $K$  and  $T$  are  $7.44 \times 10^{-3}$  and  $2.43 \times 10^{-4}$  s; the small values mean that the two parameters are appropriately found.

**Table 2: Characteristics of the estimated parameters**

Parameter	Posterior mean	Posterior standard deviation
$K(s)$	$9.90 \times 10^{-1}$	$7.44 \times 10^{-3}$
$T$	$4.68 \times 10^{-3}$	$2.43 \times 10^{-4}$
$k$	$9.91 \times 10^{-1}$	$6.90 \times 10^{-3}$
$\zeta$	$5.56 \times 10^{-1}$	$2.10 \times 10^{-2}$
$\omega_n \text{ (rad/s)}$	$4.81 \times 10^{+2}$	$8.94 \times 10^0$

Comparing the results from the above two optimization processes, we conclude: regarding the MCMC method, (7-2) appears to be well-defined as the first order model but (7-1).

**4.3 Model (7-3)**

The 2-D marginal distribution of the parameters noticeably illustrates that there is no heavy linear dependency of them (Fig. 6). Fig. 7 shows the data and the model predicted responses. From the 95% predictive intervals of the fitted models and the 95% predictive limits for observations (Figs. 5 and. 7), we see that this model gives better agreement to observations.

Based on the optimization results, we have observed that while the 1-D marginal posteriors are informative, they can only give a partial truth of a multidimensional problem. The inspection of the mutual correlations of parameters in a MCMC chain can reveal the identifiability and uncertainty in the estimated values of model parameters, which may result from the parameter correlations, the characteristics of experimental data, and the mathematical structure of model equations (non-linearity of model) as (7-1) where the varying cause of correlation makes it difficult to differentiate the individual effects of the two terms in the model. The posterior correlations and the 2-D marginal posterior plots of the parameter combinations can be used as diagnostics of parameter identifiability (Fig. 4).

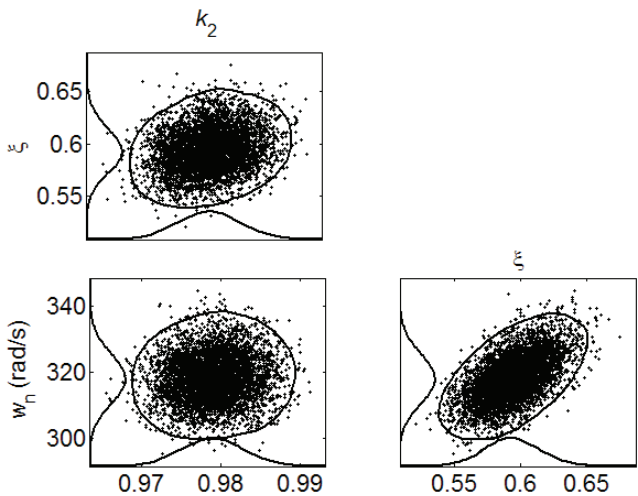


**Figure 6: 2-D marginal distribution of parameters in (7-3).  
(Figure legends as in Fig. 4)**

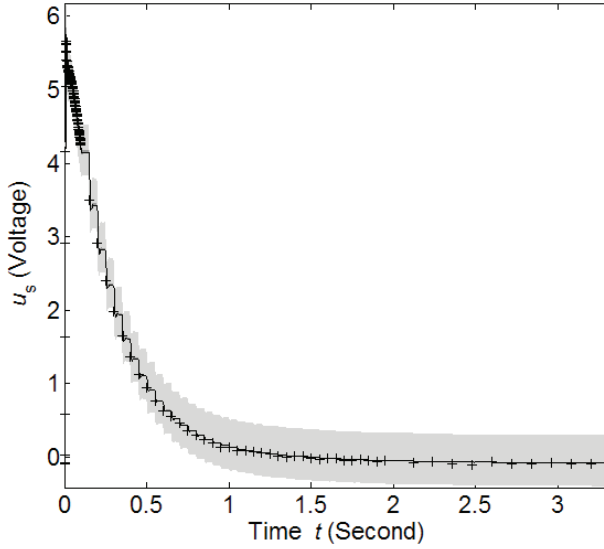


**Figure 7: Plots of the found model (7-3) and uncertainties.**  
(Figure legends as in Fig. 5b)

The found models (Table 2) are verified with independent physical experiments (Table 3) and the standard variations of errors show that the second order model is more accurate.

## 5. CONCLUSION

The MCMC method was applied to the estimation and analysis of modeling of the servo valve. The model predictions are confidential since the Bayes computations take the full multidimensional distribution of parameters into account without any approximation. Different models of the dynamics systems, namely the valve's dynamics, have been studied. Independent experiments were used for verification. The obtained results have demonstrated the outcome of study:

- The first order model (7-1) has linearly correlated parameters  $t_1$  and  $t_2$ .
- The first order model (7-2) in [1] was approved to have fine parameterization.
- The comparison between the two models (7-2) and (7-3) illustrates in two ways that the second order model better fits the valve's dynamics: (i) in estimation (Fig. 5 and Fig. 7) by the differences in the model responses, the model predictions and the noisy responses; and (ii) in verification (Table 3) by errors applying different inputs and loads to the studied system.
- The performance of the parameter estimation cannot be affected by, for example, the size of the physical input to the studied system, the complexity of the studied system or model or the linearity of the operation region. The system and the model structures used for estimation were simple, but the results from estimation and verification have clearly revealed the power of this estimation method. As can be seen from Figs. 3, 5 & 7 and Table 3, the errors between the observed responses and the modeled responses evidently show if a model is fine parameterized, which

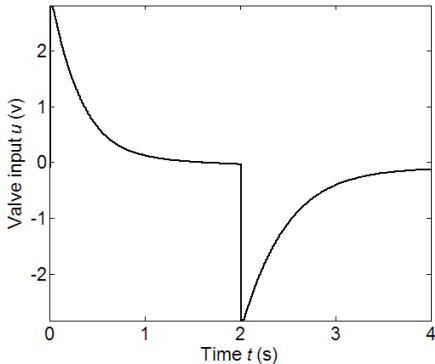
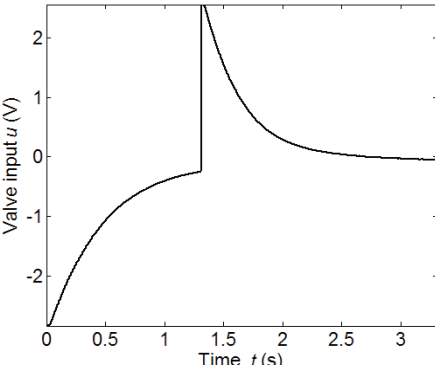
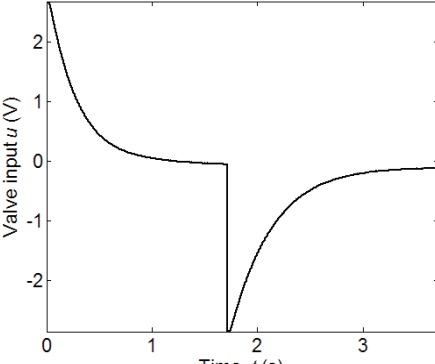
model better fits the dynamics of the studied system or which part of the operation region is not well described by a model.

## REFERENCES

1. Jelali, M. and Kroll, A. (2003). *Hydraulic servo-systems — modelling, identification and control*. Springer, London.
2. Metropolis, N., Rosenbluth, A.W., Rosenbruth, M.N., Teller, A.H., and Teller, E. (1953). Equations of state calculations by fast computing machine. *J CHEM PHYS*, **21**, pp. 1087-1091.
3. Gelfand, A.E. and Smith, A.F.M. (1990). Sampling-based approaches to calculate marginal densities. *Journal of the American Statistical Association*, **85**, pp. 853-409.
4. Haario, H., Laine, M., Mira, A., and Saksman, E. (2006). DRAM: Efficient adaptive MCMC. *Stat. Comput*, **16**, pp. 339-354.
5. Yousefi, H., Handroos, H., and Soleymani, A. (2008). Application of differential evolution in system identification of a servo-hydraulic system with a flexible load. *Mechatronics*, **18**(9), pp. 513-528.
6. Mathworks Inc. (2005). Users guide of real time workshop.
7. Haario, H. (1995). *MODEST user guide*. ProfMath Company.
8. Silverman, B.W. (1986). *Density estimation for statistics and data analysis*. Chapman & Hall, London.



Table 3: Verification of models

Experiment		STD of errors	
Mass	Valve input $u$ (V)	Model (7-2)	Model (7-3)
210 (kg)		$5.57 \times 10^{-2}$	$1.21 \times 10^{-2}$
238.46 (kg)		$5.63 \times 10^{-2}$	$4.02 \times 10^{-2}$
238.46 (kg)		$5.29 \times 10^{-2}$	$2.99 \times 10^{-2}$

# Steady and Unsteady Flow Force acting on a Spool Valve

Kazuhiro TANAKA<sup>1)</sup>, Keitaro KAMATA<sup>1)</sup>, Kouki TOMIOKA<sup>2)</sup>, and Takeshi YAMAGUCHI<sup>3)</sup>

1) Dept. of Mechanical Information Science and Technology, Kyushu Institute of Technology,  
680-4 Kawazu Iizuka, Fukuoka, 820-8502, Japan.

2) NITTO DENKO Co., Ltd. Engineering Center,  
18 Hirayama Nakahara-cho Toyohashi Aichi, 441-3194, Japan.

3) Aisin AW Co., Ltd. Engineering Division,  
10 Takane Fujii-cho Anjyo Aichi, 444-1192, Japan.

## ABSTRACT

A spool valve is an indispensable component to control flow direction as well as flow rate in an oil-hydraulic system. Because an axial flow force sometimes causes an oscillation of the valve, it is important to predict the axial flow force precisely at the design stage. Many studies on the axial flow force acting on a spool valve have been conducted by deriving mathematical models based on the theory of conservation of momentum as well as by CFD numerical method. As the spool valve really has three-dimensionally complicated configurations, it is interesting to study effectiveness of the above mathematical models against three-dimensional influences. This paper describes the influences of three-dimensionality and unsteadiness for the spool valve through CFD (Computational Fluid Dynamics) three-dimensional numerical precise simulations, compared with the mathematical models.

**Key Words:** Flow force, Spool valve, Oil-hydraulics, CFD, Momentum theory

## 1 INTRODUCTION

Recent trend of high-pressure and quick-response in hydraulic systems needs to comprehend precisely dynamic characteristics of a hydraulic control valve, which is a key component in a hydraulic circuit. A flow force acting on a valve body is an important factor for dynamic characteristics of the hydraulic control valve. The flow force is caused by imbalance between static and dynamic pressure when working oil flows into/out of a valve chamber and often causes control precision to deteriorate.

A spool valve is widely used in a hydraulic circuit to control flow direction as well as flow rate of working oil. Axial direction flow force (hereafter, axial force) acting on a spool itself often causes vibration of the spool valve. Many studies have been performed and they

are based on the momentum theory. Lee and Blackburn proposed the mathematical model to predict a flow force [1] [2]. The prediction method was built on the hypothesis of two-dimensional flow in a spool chamber and they are widely used and are known as the effective formula. In the model 69 deg. is considered as standard angle for the flow leaving/entering a control volume in a right-angled spool, as shown in Fig.1. And then, Ikebe and Ohuchi also proposed another model based on the same hypothesis [3]. Though the predicting mathematical model is very useful for design of a right-angled spool [4], many kinds of spool with complicated configuration such as notches and taper angle have recently been manufactured to materialize higher controllability and the applicability of the mathematical model to a tapered spool has not been studied. It seems to be interesting to study the applicability of the mathematical model to a tapered spool with notches.

On the other hand, CFD (Computational Fluid Dynamics) methods have been much developed recently [5, 6, 7] and commercial CFD codes begin to be applied to develop industry products for high-performance and high-reliability in the preliminary design stage. Nowadays, 3D unsteady numerical analyses have been much developed to analyze the flow forces in hydraulic valves and to improve their response characteristics. Two-dimensional numerical simulations were performed for predicting the globe control valve performance [8, 9]. Krishnaswamy and Li found that unstable valves had faster responses than their stable counterparts when the stroking force was limited [10]. Yuan and Li investigated the effects on the steady flow force of various material properties, such as the fluid viscosity and the momentum flux at the nonmetering surface [11]. However, these numerical studies were limited to hydraulic valves, which have geometries that are relatively axisymmetric and simple. Since the test spool valve in the present study have geometrically circumferential notches, their flows are comparatively complicated and fully three dimensional. Amirante et al. performed three dimensional numerical simulations and experimental analyses of a open center directional control valve [12, 13] and of a proportional control valve [14]. Furthermore, the effects of notch shape on the flow force were scrutinized. As a result, they were able to minimize the flow force of the spool for a compensated spool notch, which means that the geometry of a notch has a significant impact on a flow force. Though Valdes et al. developed a reduced-order model for estimating the fluid flow and flow force of a hydraulic proportional valve for use in antilock braking systems [15], the geometry of the valve is much different from a spool valve. And though Lee et al. analyzed a flow force on a variable force solenoid valve using 3D CFD simulations, the geometry of the spool is different from that in the present study and the detailed geometry of the notches are not described [16]. As stated above, because the geometry of a spool and a notch, including on/off, is different in the literatures, it is not easy to compare the characteristics of a flow force on a spool valve.

In the present study, the applicability of the mathematical formulae for predicting an axial flow force on a spool valve is studied by comparing numerical results obtained by 3D unsteady incompressible viscous flow analysis through commercial CFD codes. In order to confirm the reliability of the numerical results, they are compared firstly with the theory of conservation of momentum and secondly with the experimental results on the test spool valve. Then, in order to study the applicability of the above-mentioned mathematical formulae, they are compared with an axial flow force calculated by the mathematical formulae in case that the valve opening displacement is kept constant as well as that the valve is forced to move sinusoidally.



where  $Q$  indicates volumetric flow rate,  $L_s$  special distance of configuration,  $V$  mean velocity at inlet/outlet of the flow field,  $\phi$  inlet/outlet flow angle,  $x_s$  valve-opening displacement, and  $A_s$  effective cross-sectional area of land, respectively. Suffix 1 indicates the location of the spool chamber inlet.

In the right hand side of Eq. (4), the first term indicates steady term and the second damping term. Similarly in Eq. (5), the first indicates steady term, the second damping term, the third inertial term, and the fourth velocity term.

In this study, four kinds of results on the axial flow force are considered. First of which is the experimental results, the second the numerical results, and the third the calculated results from Eq. (4) and (5) with flow rate-weighted mean velocity and inlet/outlet flow angle on the control surface through numerical results. In order to study the applicability of the above-mentioned mathematical formulae, in which 69 deg. is considered as standard angle for the flow leaving/entering a control volume in a right-angled spool, as shown in Fig.1, the last results on the axial flow force is the calculated data as the inlet/outlet flow angle is given as 69 deg..

### 3 ANALYSIS TARGET AND CONDITIONS

The numerical studies have been performed in case that the spool valve displacement is fixed (hereafter, steady axial flow force) and that the spool is moved by sinusoidal forced oscillation (hereafter, unsteady axial flow force). The test spool valve is shown in Fig. 2, where the dimensions are indicated using the represented dimension  $D$ , which is the diameter of the spool. The signs, CH1, CH2 and CH3, indicate the respective spool chamber. This spool has 4 notches which are located every 90-degree circumferentially on the spool edge. By adjusting configuration of the notches, the eccentricity of the spool becomes negligible in the experiment.

An example of numerical grid is shown in Fig. 3. The numerical domain consists of the spool, the sleeve, the chambers, and three kinds of port. Considering the case of sinusoidal forced oscillation of the spool, the numerical grid is preliminarily separated inside into two

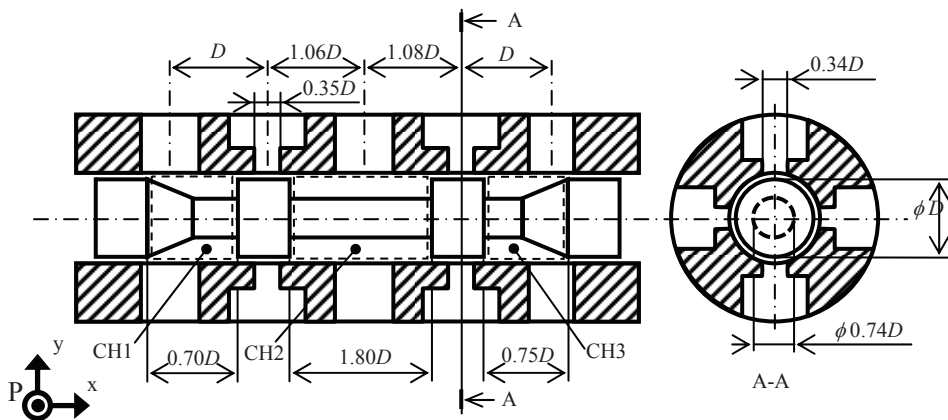


**Figure 2: Dimensions of test spool valve**

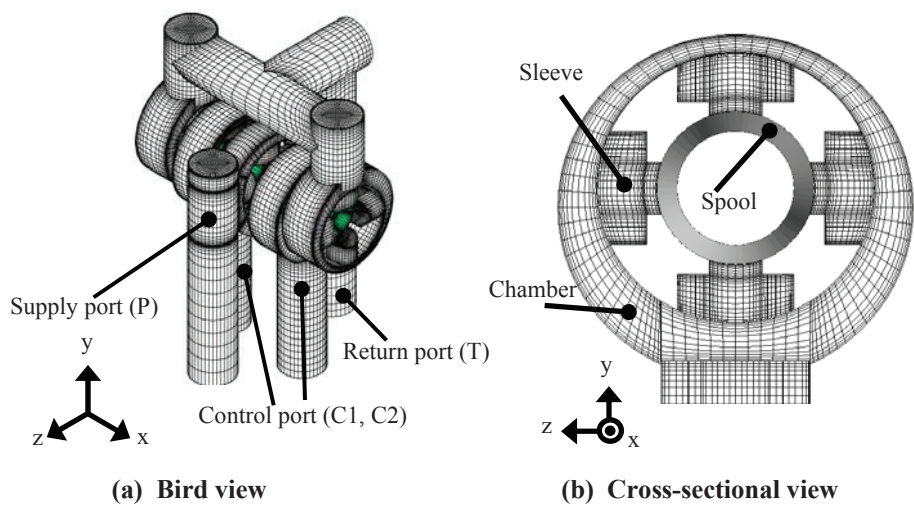


Figure 3: Computational grids

Table 1: Parameters for numerical simulation

Density ( $\rho$ )	849 [kg/m <sup>3</sup> ]
Viscosity ( $\mu$ )	0.027 [Pa s]
Valve Opening ( $x_s$ )	-100~100 [%]
Supply Port Pressure	7.0 [MPa]
Return Port Pressure	0.2 [MPa]
Control Port Pressure	3.5 [MPa]
Turbulence Model	SST k- $\omega$ model
Gird number	2,000,000

Table 2: X-directional flow force

	$F_x$ [N]
6 D	8.596
10 D	8.606
20 D	8.572

parts, the spool and the sleeve, and the numerical grid correspondent to the spool part can move independently of the sleeve part. The slide-interface condition is applied between the spool and the sleeve and the mass as well as the momentum are conserved between the neighboring grids. This means that the leakage flow through the gap between the spool and the sleeve are not considered in the present study.

As the pressure boundary condition, 7.0 MPa is given at the pressure supply port, 3.5 MPa at the control port and 0.2 MPa at the return port. The spool valve opening displacement is represented by the ratio against the full-opening, which means 100 %. In case of calculating steady axial flow force, calculations have been performed at 16 cases from + 100 % to -100 % valve opening displacement. In case of unsteady axial flow force,

any condition but the valve motion is the same as that in case of the steady axial flow force. The oscillation amplitude is  $\pm 100\%$  of the valve opening and the frequency is 100 Hz which is the maximum frequency to control the test valve.

The SST  $k-\omega$  turbulence model is used in the present study. The SST  $k-\omega$  turbulence model is a two-equation eddy-viscosity model which has become very popular. The shear stress transport (SST) formulation combines the best of two worlds. The use of a  $k-\omega$  formulation in the inner parts of the boundary layer makes the model directly usable all the way down to the wall through the viscous sub-layer, hence the SST  $k-\omega$  model can be used as a Low-Re turbulence model without any extra damping functions. The SST formulation also switches to a  $k-\epsilon$  behaviour in the free-stream and thereby avoids the common  $k-\omega$  problem that the model is too sensitive to the inlet free-stream turbulence properties. Total number of the numerical grid is 2.0 million. Table 1 shows calculating conditions.

The location of the outlet boundary may have considerable effect on the precision of numerical results and preliminary calculations were performed to determine the optimal location of the outlet boundary. The diameter of the pressure supply pipe is defined as  $D$  and the location of the inlet boundary is located at  $2D$  distant from the inlet port. When the distance from the outlet port to the outlet boundary is set  $6D$ ,  $10D$  and  $20D$ , the axial flow force was calculated and the calculated results, shown in Table 2, show that the axial flow force is almost same if the distance is more than  $6D$ . Consequently the distance from the outlet port to the outlet boundary is set  $6D$  in this study.

#### 4 EXPERIMENTATION ON AXIAL FLOW FORCE

In order to verify the precision of numerical results, the axial flow force was measured in the test valve. Figure 4 shows a schematic diagram of the experimental test circuit. The test spool valve is a solenoid proportional valve. The spool can move because it is directly connected with the plunger and can switch over the hydraulic circuit. The neutral position of the spool is adjusted by adding spring force. The solenoid proportional valve, in which the relationship between current and force is already known, is used in this experiment. The applied current of the solenoid ( $I$ ) and the spool displacement ( $D$ ) are always measured. The axial flow force acting on the spool is calculated by the difference between the solenoid-coil force and the spring force by the following.

$$\text{Axial flow force} = \text{Electro-magnetic force} - \text{Spring force} - \text{Friction force} \quad (6)$$

The above Electro-magnetic force and Friction force are calibrated by measuring one at a time as follows. The static characteristics of an electro-magnetic force are measured by a load cell, which is serially-cascaded between an armature and external forces. Its dynamic characteristics are measured by the load cell, which is serially-cascaded to an armature, a spring and external forces with a sinusoidal function while the frequency is varied.

A friction force is measured by the load cell which is serially-cascaded to the spool and an actuator like a piston for exclusive use. The static characteristics of the friction force are measured when the actuator moves very slowly, and its dynamic characteristics are measured by the way as same as the above-mentioned one by varying the frequency of the actuator motion. As the friction force may varies according to the inside pressure, the friction forces are measured under the condition that the inside pressure are kept low or high constantly to confirm the effect of seal part and fluid lubrication.

The axial flow force calculated from the current data is shown in Fig. 5, where the spring force is calculated by the product of measured data of the valve displacement with the spring constant. This result shows that the electro-magnetic force is linearly proportional to the spool displacement and there is hysteresis characteristics based on the influence of friction between the spool and the sleeve.

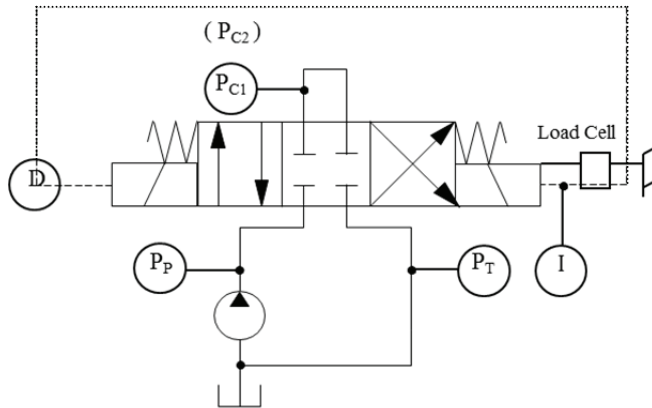


**Figure 4: Experimental test circuit**

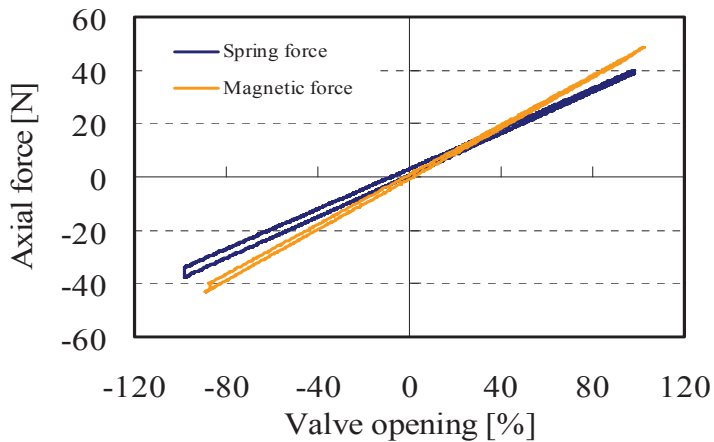


**Figure 5: Axial flow force calculated from current in a solenoid valve**



## 5 VERIFICATION OF THIS ANALYSIS METHOD

First, the validity of this numerical result is discussed by verifying whether the momentum is conserved or not according to Eq. (3), which is the physical law. Figure 6 shows comparison between the axial flow forces calculated according to Eq. (3) and the numerical results. In the figure, “Cal.” indicates the numerical data and “Momentum theory” the axial flow force calculated according to Eq. (3). The difference between both data is up to 0.4 % and the numerical result clears the momentum theory sufficiently.

Next, the numerical data are compared with the experimental data on the flow rate. Figure 7 shows both data at each valve opening displacement. The mean value of the difference between both data is up to 7 % and the both are almost coincident. Figure 8 shows another comparison on the axial flow force. As the valve opening displacement becomes larger, the difference between both data increases similarly. The reason of the difference is not solved yet. In the experiment, the eccentricity of the spool becomes negligible by adjusting configuration of the notches. The reason may be the number of numerical grids, the grid shape, or neglect of the gap between the spool and the sleeve. So, the numerical result satisfies the momentum theory from a big standpoint though there is a little difference between the numerical and experimental data near at full valve-opening displacement. It is verified that the numerical result is reasonable and reliable.

## 6 RESULTS AND DISCUSSIONS ON STEADY FLOW FORCE

Comparison on the steady flow force at each valve opening displacement between the numerical result and the result based on Eq. (4) and Eq. (5) is shown in Fig. 9, in which the sign, Eq. (4) and Eq. (5), indicates the data calculated by Eq. (4) and Eq. (5) using numerical data on inlet/outlet flow angle directly. In order to study the applicability of Eq. (4) and Eq. (5) to the test valve with the tapered geometry, the axial flow forces are calculated according to Eq. (4) and Eq. (5) supposing that the inlet/outlet flow angle would be 69 deg, which is considered as standard angle in a right-angled spool, as shown in Fig.1. The sign, Eq. (4)\_const or Eq. (5)\_const, indicates the axial flow force by Eq. (4) or Eq. (5) with  $\phi_1 = 69$  deg. Here because steady flow condition is considered, the result between from Eq. (4) and Eq. (5) becomes the same.

All data including the experimental result are almost same around the neutral position within the limits of  $\pm 40$  % valve-opening displacement. Consequently, it is clear that the conventional formula, Eq. (4), can predict precisely the axial flow force in case of small valve-opening displacement. However, their difference increases as the valve-opening becomes larger. The reason is thought as follows. Comparison of the numerical data and the calculated data by the conventional prediction formula is shown in Fig. 10 when return flow from CH2 chamber to the tank or inflow from the pressure supply source to CH1/CH3 chamber exists. The difference on the axial flow force is small in CH2 chamber and increases in CH1 and CH3 chamber as the valve opening becomes larger. This is because inlet velocity is supposed to be much higher than outlet velocity in case of inflow in a right-angled spool. Figure 11(a) and (b) show the situation of the return flow from CH2 and inflow to CH1, respectively. In the figures the arrow indicates flow direction. In case of the return flow from CH2, the inlet flow velocity can be negligible and the above-mentioned supposition is reasonable. However, CH1/CH3 chamber has tapered land in this test valve. As a result, the inflow jet collides against the spool shaft and flows out along the wall.

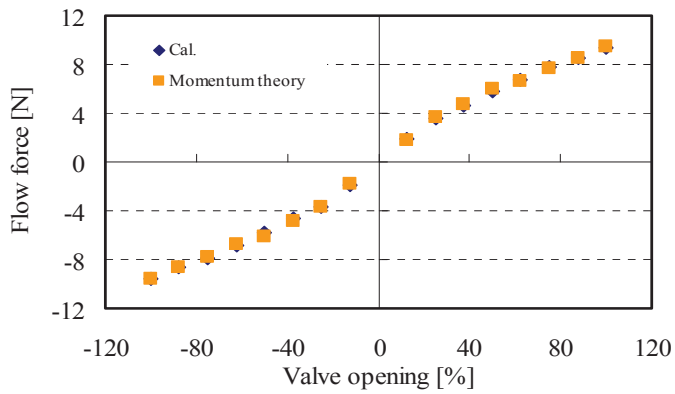


Figure 6: Steady flow force comparison of numerical result with momentum theory

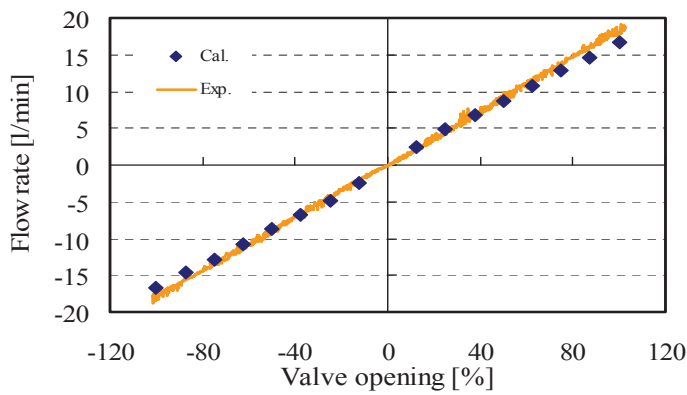


Figure 7: Experimental and numerical results on flow rate

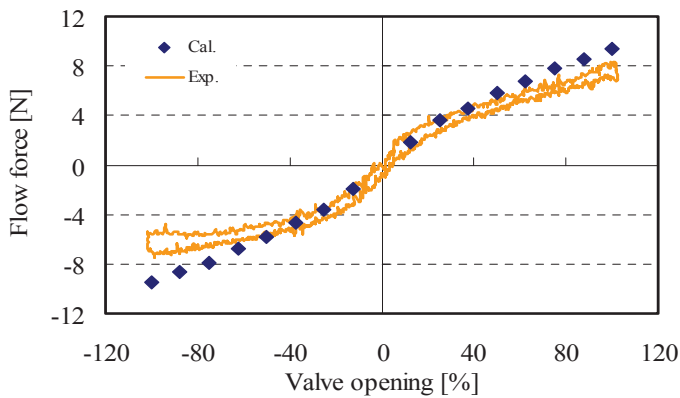
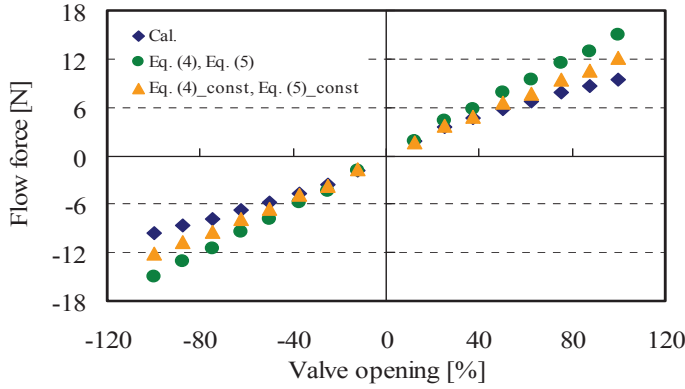


Figure 8: Experimental and numerical results on steady flow force



**Figure 9: Comparison of steady flow force**

Consequently, neglect of the momentum at the outlet side causes deterioration of the applicability in case of inflow. Inversely, the above-mentioned consequence would be verified by considering the momentum at the outlet side. Equations (4-2) and (5-2) are derived by adding the momentum at the outlet side to Eq. (4) and Eq. (5).

$$F(4-2) = F(4) + \rho Q V_2 \cos \phi_2 \quad (4-2)$$

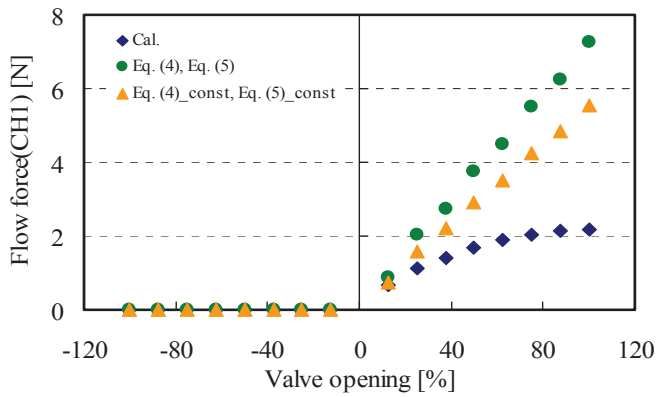
$$F(5-2) = F(5) + \rho Q V_2 \cos \phi_2 \quad (5-2)$$

Here, suffix 2 indicates location of the spool chamber outlet. Figure 12 shows the data on steady axial flow force calculated by these equations. In this figure, the sign, Eq. (4-2)\_const or Eq. (5-2)\_const, indicates the axial flow force in case of considering the momentum at the outlet side when the inlet/outlet flow angle is supposed to be 69 deg. Compared with the results by Eq. (4) and Eq.(5), the results by Eq. (4-2) and Eq. (5-2) are improved up to 11 % difference from the numerical results.

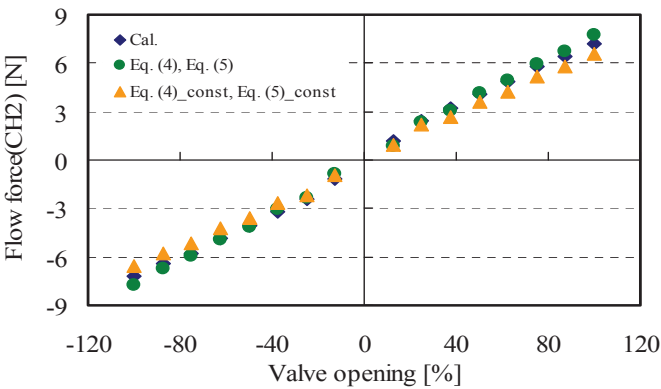
In addition, the data calculated by the conventional formula with 69 deg. leaving/entering flow angle are smaller than the numerical results. This is because the inlet/outlet flow angle in the numerical analysis is generally less than 69 deg. and the axial flow force becomes smaller than that predicted in case that the inlet/outlet flow angle is supposed as 69 deg.

## 7 RESULTS AND DISCUSSIONS ON UNSTEADY FLOW FORCE

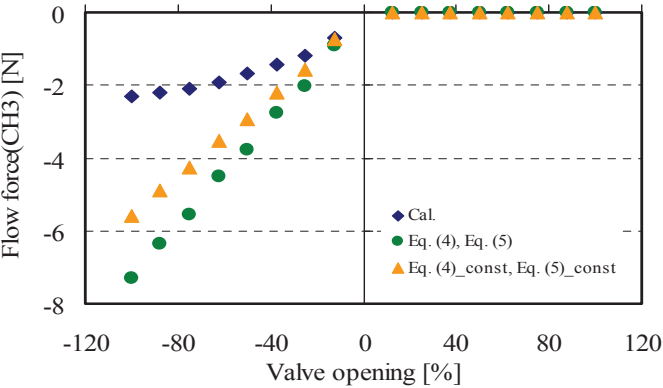
Figure 13 shows fluctuation of the unsteady flow force for one cycle when the spool moves along sinusoidal oscillation, of which the frequency is 100 Hz. Though this frequency is not realistic, it is set to compare the magnitude of the unsteady terms in an extreme case. The data is averaged for five cycles. Here in the figure, 'Cal.' indicates the axial flow force calculated by integrating pressure and shear stress distributed on the spool wall surface, 'Momentum theory' the axial flow force calculated by the difference of momentum between at the inlet and outlet, 'Mom\_steady' the axial flow force based on the steady term in Eq. (4), and 'Mom\_transient' the axial flow force based on the steady as well as unsteady term, respectively. Because the flow forces represented by 'Cal.' and 'Momentum theory'



(a) Flow force acting on CH1 chamber



(b) Flow force acting on CH2 chamber



(c) Flow force acting on CH3 chamber

Figure 10: Flow force acting on chambers, CH1, CH2 and CH3

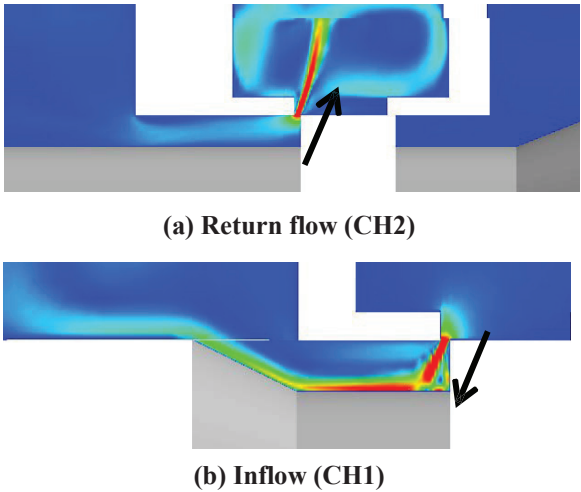


Figure 11: Flow patterns in valve chambers, CH1 and CH2

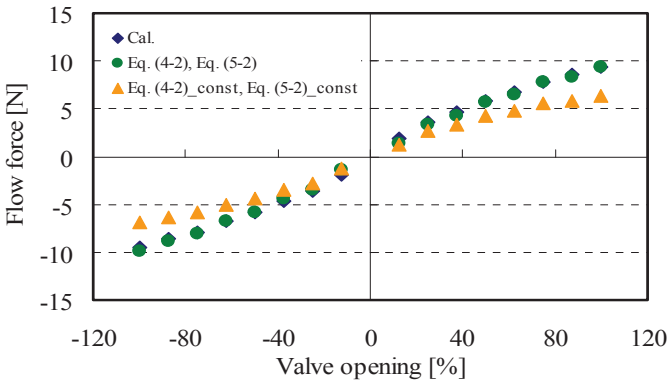


Figure 12: Steady flow force including outlet momentum

are well coincident in the amplitude and the phase, it is verified that the numerical analysis on the unsteady flow force also satisfies the law of conservation of momentum.

Compared with the value of the steady term in Eq. (4), the value of the unsteady term is very small. Consequently, it is verified that the influence of unsteadiness is very small in this study and the main factor of the axial flow force is the steady flow force.

Next, the characteristics of Eq. (5) are discussed. The difference between Eq. (4) and Eq. (5) is the existence of velocity term and inertia term. And it is already known that the influence of momentum at the outlet side is strong in case of inflow in a chamber with tapered land. Here the numerical result is compared with the axial flow force calculated by Eq. (5-2) under condition that the momentums at inlet/outlet side are considered exactly. Figure 14 shows fluctuations of the unsteady flow force for one cycle at 100 Hz. Because the numerical result is very close to the result calculated from Eq. (5-2), it is verified that Eq. (5-2) modified by adding momentum at the outlet side can predict the unsteady flow force precisely. In addition, the result calculated by Eq. (5-2)\_const is quite different from

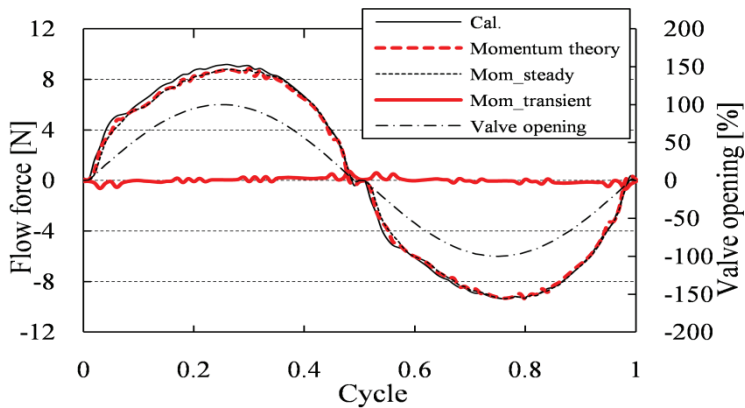


Figure 13: Unsteady flow force comparison with momentum theory

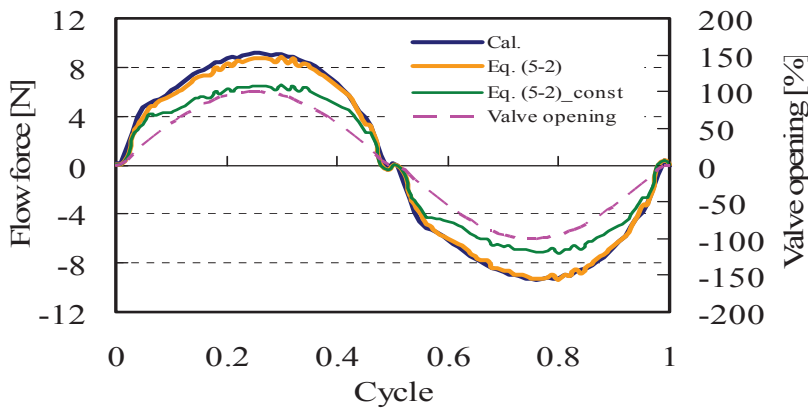


Figure 14: Time history of unsteady flow force

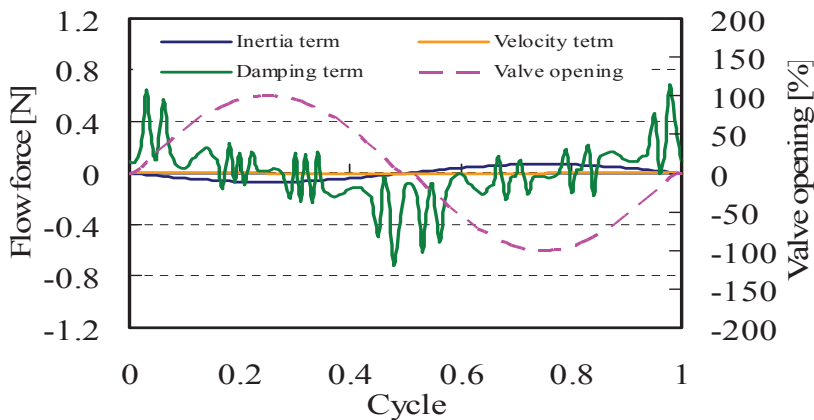


Figure 15: Transient terms of unsteady flow force

the other results. This means that the predicting precision deteriorates somewhat in case that the outlet flow angle is supposed to be 69 deg.

Figure 15 shows fluctuating results of the damping term, inertia term and velocity term, which is represented as the second, the third and the fourth term in Eq. (5), for one cycle. The velocity term and inertia term are always almost zero and their influence on the axial flow force can be neglected in this test valve. The damping term varies largely at the instant of valve opening/closing, however, the amplitude is at most  $\pm 0.7$  N., which sometimes occupies 40 % of the axial flow force.

## 8 CONCLUDING REMARKS

3D unsteady incompressible viscous turbulent flow analysis was performed against the internal flow with strong three-dimensionality in a chamber inside the spool valve, and the unsteady flow force as well as the steady flow force acting on the spool valve was calculated by a CFD code. In addition, the numerical result was compared with the result calculated by the conventional prediction formulae as well as with the experimental result.

As a result, the followings were verified.

1. 3D numerical analysis gives precisely the axial flow force acting on the spool valve with complicated configuration.
2. It is possible to predict precisely the steady axial flow force by use of the conventional prediction formula based on the momentum theory when the valve displacement is around the neutral position within the limits of  $\pm 40$  % valve-opening displacement.
3. In a valve chamber with tapered land, the inflow has significant momentum at the outlet and the precision of the axial flow force calculated by the conventional formulae deteriorates without considering momentum at the outlet.
4. Even in an extreme frequency case of 100 Hz in the test spool, the velocity term and inertia term are always almost zero and their influence on the axial flow force can be neglected compared with the damping term in the unsteady flow force terms.

## REFERENCES

- [1] Lee, S. Y. and Blackburn, J. F. "Contributions to Hydraulic Control, 1 Steady State Axial Forces on Control-Valve Pistons", Trans. ASME, Vol. 74, pp.1005-1011, 1952
- [2] Lee, S. Y. and Blackburn, J. F. "Contributions to Hydraulic Control, 2 Transient-Flow Forces and Valve Instability", Trans. ASME, Vol. 74, pp.1013-1016, 1952
- [3] Y. Ikebe and H. Ohuchi "Generalised Formulation of Momentum Theory", Fluidic Quarterly No.10 pp.27-46, 1978
- [4] Merritt, H. E. "Hydraulic Control Systems", Wiley, New York, 1967
- [5] Ferziger, J. H. and Peric, M. "Computational Methods for Fluid Dynamics," Springer Verlag, ISBN: 3540653732, 1999
- [6] Anderson, J. D. "Computational Fluid Dynamics: The Basics with Applications", McGraw Hill, ISBN: 0070016852, 1995
- [7] Wesseling, P. "An Introduction to Multigrid Methods", R.T. Edwards, Inc., ISBN: 1930217080, 2004

- [8] Davis, J. A. and Stewart, M. "Predicting Globe Control Valve Performance-Part I: CFD Modeling," ASME J. Fluids Eng., 124, pp. 772–777, 2002
- [9] Davis, J. A. and Stewart, M. "Predicting Globe Control Valve Performance-Part II: Experimental Verification," ASME J. Fluids Eng., 124, pp. 778–783, 2002
- [10] Krishnaswamy, K. and Li, P. Y. "On Using Unstable Electrohydraulic Valves for Control," ASME J. Dyn. Syst., Meas., Control, 124, pp. 183–190, 2002
- [11] Yuan, Q. and Li, P. Y. "Using Steady Flow Force for Unstable Valve Design: Modeling and Experiments," ASME J. Dyn. Syst., Meas., Control, 127, pp. 451–462, 2005
- [12] Amirante, R., Del Vescovo, G., and Lippolis, A. "Flow Force Analysis of an Open Center Hydraulic Directional Control Valve Sliding Spool," Energy Convers. Manage., 47, pp. 114–131, 2006
- [13] Amirante, R., Del Vescovo, G., and Lippolis, A. "Evaluation of the Flow Forces on an Open Centre Directional Control Valve by Means of a Computational Fluid Dynamic Analysis," Energy Convers. Manage., 47, pp. 1748–1760, 2006
- [14] Amirante, R., Moscatelli, P. G., and Catalano, L. A. "Evaluation of the Flow Forces on a Direct Single Stage Proportional Valve by Means of a Computational Fluid Dynamic Analysis," Energy Convers. Manage., 48, pp. 942–953, 2007
- [15] Valdes, J. R., Miana, M. J., Nunez, J. L., and Putz, T. "Reduced Order Model for Estimation of Fluid Flow and Flow Forces in Hydraulic Proportional Valves," Energy Convers. Manage., 49, pp. 1517–1529, 2008
- [16] Lee, G. S., Sung, H. J., Kim, H.C., and Lee, H. W. "Flow Forces Analysis of a Variable Force Solenoid Valve for Automatic Transmissions", ASME J. Fluids Eng., 132, 031103-1–7, 2010
- [17] ANSYS CFX-Solver, Release 10.0 Theory, 2005





# Effective Bulk Modulus Model Verification for the Mixture of Air/Gas and Oil

**H.Gholizadeh, D. Bitner, R.Burton, G.Schoenau**

Department of Mechanical Engineering, University of Saskatchewan  
Saskatoon, Saskatchewan, Canada

Contact: [h.gholizadeh@usask.ca](mailto:h.gholizadeh@usask.ca)

## ABSTRACT

The effective bulk modulus of oil inside a chamber is affected by the air content of oil, oil pressure, oil temperature, pipe rigidity and interface conditions between the oil and the air. Assuming the oil is inside a rigid container, the theoretical relationship to find the oil effective bulk modulus in the presence of the mixture of oil and air/gas, has been derived by various researchers. A commonly used model which reflects both compression and dissolving of air/gas in the oil is a model which is used in AMESim simulation software and in this paper is called the LMS model [1]. At the critical pressure point where the air/gas is fully dissolved, a discontinuity appears. This discontinuity is related to the first derivative in Henry's law equation. The derivative is not continuous at the critical pressure and to compensate for this, Henry's law was adjusted mathematically, to smooth out the transition through the critical pressure region. However, this modified Henry's law is not based on the true physics of what is really happening when the air/gas is both compressed and dissolved. Thus, this discontinuity issue was the motivation behind the development of a new model based on sound physical principles which would address the critical transition pressure region.

The purpose of this paper is to present and validate a new model for the effective bulk modulus of the mixture of the air/gas and oil where air/gas is assumed to be both compressed and dissolved in the oil. Whilst the model reflects the true physics of an assumed set of conditions, experimental differences in some regions to model predictions indicate that some challenges still exist for future model development.

## 1 INTRODUCTION

The effective bulk modulus of oil inside a chamber is affected by the air content, pressure, temperature, pipe rigidity and interface conditions between the oil and the air [2]. Assuming the oil is inside a rigid container, the theoretical relationship to find the oil effective bulk modulus in the presence of the mixture of oil and air/gas, has been derived by various researchers. In Gholizadeh et al. [3], these relationships were examined and two different models of effective bulk modulus of oil were investigated based on the air volumetric variation assumption. These two models were categorized as:

- 1) Models which just consider the volumetric compression of air
- 2) Models which consider both the volumetric compression of air and the volumetric reduction of air due to air dissolving into solution

A general model of the oil effective bulk modulus for the first group of models was recommended based on the standard definition of the “volumetric fraction of air/gas at atmospheric pressure” and using the tangent bulk modulus definition [3]. Experimental verification of these groups of models was presented by Kajaste et al. [4] and recently by Kim and Murrenhoff [5]. In [4], the air was added as a free pocket at the top of the test cylinder and the maximum amount of air added was 1%. In [5], the air content was varied in a range up to 0.5%. The air was injected through a valve, but the air distribution was unknown or at least not mentioned in the paper. Both studies successfully verified the effective bulk modulus model in the range of their experimental limitations. However, the applicability of the model for higher percentages of air content (for example 5% which is common in mobile hydraulic systems [6]) and different types of distribution of air bubbles in oil needs to be studied both theoretically and experimentally.

For the second groups of models in which the effect of dissolution of the entrained air in oil according to Henry’s law has been also included, a common problem was found in which the effective bulk modulus model experienced a discontinuity at some “critical” pressure. A commonly used model of this type is the LMS model (modified Henry’s law) [1]. At the critical pressure point where the air/gas is fully dissolved, a discontinuity appears. This discontinuity is related to the first derivative in Henry’s law equation. The derivative is not continuous at the critical pressure and to compensate for this, Henry’s law is adjusted mathematically, to smooth out the transition through the critical pressure region. However, this modified Henry’s law is not based on the true “physics” of what is really happening when the air/gas is both compressed and dissolved.

In this paper, the reason for the discontinuity is discussed and a new model is proposed in which the discontinuity problem no longer exists. Experimental verification of the new model and suggestions for model improvements are considered.

## 2 VOLUMETRIC VARIATION OF AIR/GAS CONTENT IN OIL

The main problem in estimating the effective bulk modulus of a mixture of oil and air is to determine the volumetric variation of entrained air/gas under different pressures and temperatures. Before discussing the problems of the LMS model (both simple and modified Henry’s law), an analytical description of the change in volume of entrained air/gas as a function of pressure is given. As pressure increases, the amount of entrained air/gas in a hydraulic system decreases due to the fact that air/gas is compressed via the ideal gas law and at the same time, starts to be dissolved into solution as dictated by Henry’s law. Henry’s law for a mixture of gas-liquid can be written as:

$$P = H \frac{N_{dg}}{N_{dg} + N_l} \quad (1)$$

This law assumes that the liquid is in a thermodynamic equilibrium with air/gas at absolute pressure  $P$ . Since usually  $N_l \gg N_{dg}$ , this equation simplifies to

$$P = H \frac{N_{dg}}{N_l} \quad (2)$$

It is important to realize that this law refers to the thermodynamic equilibrium state; therefore it is assumed that enough time is allowed for the mixture to reach an equilibrium state. As pressure increases, more of the air/gas is compressed and dissolved in the oil until the system pressure reaches a “critical pressure”. At this point it is assumed that all of the air/gas is dissolved in the oil. Since it is well known that the dissolved air/gas has no effect on the bulk modulus of the oil, the fluid effective bulk modulus approaches that of the pure oil once critical pressure has been reached.

If it is assumed that the process is isothermal and under equilibrium conditions, according to the conservation of mass, the total moles of entrained and dissolved air /gas are conserved. Therefore the sum of entrained and dissolved air/gas at pressure  $P$  and temperature  $T$  is equal to the sum of entrained and dissolved air/gas at pressure  $P+dP$  and temperature  $T$ . That is

$$N_g(P, T) + N_{dg}(P, T) = N_g(P + dP, T) + N_{dg}(P + dP, T) \quad (3)$$

Therefore using the ideal gas law and Henry’s law, Equation (3) can be written as

$$\frac{PV_{gcd}}{RT} + \frac{PN_L}{H} = \frac{(P + dP)(V_{gcd} + dV_{gcd})}{RT} + \frac{(P + dP)N_L}{H} \quad (4)$$

Assuming higher order differential products are negligible, Equation (4) can be re-written as:

$$\frac{-dV_{gcd}}{dP} = \frac{V_{gcd} + \frac{N_L RT}{H}}{P} \quad (5)$$

Assuming that Henry’s law constant ( $H$ ) does not change with temperature, it can be shown

that  $\frac{N_L R}{H}$  will always be a constant value  $C$ . Thus equation (5) becomes

$$\frac{-dV_{gcd}}{V_{gcd} + CT} = \frac{dP}{P} \quad (6)$$

It should be noted that the initial volume of entrained air/gas is assumed to be measured at pressure  $P_0$  and temperature  $T_0$ . However, before starting compression it is possible for the working temperature to be set at any temperature  $T$ . Therefore in defining the initial condition for Equation (6), the effect of temperature  $T$  on the volume of entrained air/gas needs to be considered according to the ideal gas law. It means that when  $P=P_0$ , the volume of entrained air/gas at temperature  $T$  is

$$V_{gcd}(P_0, T) = V_{g0} \frac{T}{T_0} \quad (7)$$

By solving the differential equation and applying the above initial condition ( $P_0, V_{g0}(P_0, T)$ ) the relationship between the volume of entrained air/gas as a function of absolute pressure and temperature is obtained as

$$V_{\text{gcd}}(P, T) = \frac{P_0 V_{g0}}{P} \frac{T}{T_0} + \left( \frac{P_0 - P}{P} \right) CT \quad (8)$$

From Equation (8), it can be observed that the volume of entrained air/gas changes with the isothermal pressure compression according to the expression  $P_0 V_{g0} T / PT_0$ . However, since the air/gas is also being dissolved into solution, an additional volume reduction of  $((P_0 - P)/P)CT$  will occur. In this later term,  $C$  depends on the number of moles of oil, ideal air/gas constant and Henry's law constant. As pressure increases, more air/gas is dissolved into the oil, until the pressure reaches a critical pressure,  $P = P_C$ , in which all the air/gas becomes completely dissolved; at this point, the volume of entrained air/gas equals to zero. Therefore, the critical pressure can be described as

$$P_C = P_0 + \frac{P_0 V_{g0}}{T_0} \frac{1}{C} \quad (9)$$

From Equation (10), the value of  $C$  can be also expressed in terms of  $P_C$ , that is

$$C = \frac{N_L R}{H} = \frac{P_0 V_{g0}}{(P_C - P_0) T_0} \quad (10)$$

Substituting Equation (10) in Equation (8), the volumetric change of entrained air/gas mixed in oil when pressure is less than the critical pressure ( $P < P_C$ ) is found to be:

$$V_{\text{gcd}}(P, T) = \frac{P_0 V_{g0}}{P} \frac{T}{T_0} \left( \frac{P_C - P}{P_C - P_0} \right) \quad P < P_C \quad (11)$$

For pressures equal to or higher than the critical pressure, all the air/gas will dissolve into the oil and the volume of entrained air/gas will be zero. That is:

$$V_{\text{gcd}}(P, T) = 0 \quad P \geq P_C \quad (12)$$

In Equation (11), the term  $P_0 V_{g0} T / PT_0$  is due to the compression of air/gas at pressure  $P$  and temperature  $T$  and the term  $(P_C - P) / (P_C - P_0)$  is due to the effect of air/gas dissolving into the oil which is now defined as  $\theta$ . Therefore

$$V_{\text{gcd}}(P, T) = \frac{P_0 V_{g0}}{P} \frac{T}{T_0} \theta \quad (13)$$

where

$$\theta = \left( \frac{P_C - P}{P_C - P_0} \right) \quad (14)$$

Equations (13) and (14) represent the volumetric variation of air/gas in the oil when both the compression and dissolving effect of the air/gas under isothermal condition is considered. These relations will be used later to derive the effective bulk modulus of the mixture of oil and air/gas.

### 3 EFFECTIVE BULK MODULUS OF THE MIXTURE OF THE OIL AND AIR/GAS

In the introduction, it was mentioned that a discontinuity existed in some models at the critical pressure point. This section will demonstrate how this discontinuity arises and how it can be changed to more closely represent the physical behavior of the effective bulk modulus of the mixture of oil and air/gas. The theoretical model representing the effective bulk modulus of the mixture of oil and air/gas developed by LMS [1], is given by

$$K_{LMS} = \frac{V_{l0} + V_{g0} \left( \frac{P_0}{P} \right)^{\frac{1}{n}} \frac{T}{T_0} \theta}{\frac{V_{l0}}{K_l} + \frac{T}{T_0} \left( \frac{P_0}{P} \right)^{\frac{1}{n}} \left( \frac{\theta V_{g0}}{nP} - V_{g0} \frac{d\theta}{dP} \right)} \quad (15)$$

In this study, isothermal conditions are considered and hence  $n = 1$ . The term  $(d\theta/dP)$  in Equation (15) is not continuous at the critical pressure point and introduces a discontinuity in the LMS model (simple Henry's law). In order to obtain a continuous derivative function, LMS has changed the underlying mathematical model (Henry's law) near the critical pressure point by proposing a new  $\theta$  which is smoother than the previous real  $\theta$  and hence does not display a discontinuity in the term  $(d\theta/dP)$ .

$$\theta_{modified} = (1 - y)^5 (1 + 5y + 15y^2 + 35y^3 + 70y^4) \quad (16)$$

$$y = \frac{P - P_0}{P_c - P_0}$$

This smoothing function is a mathematical convenience and is not based on any physical property. To try to understand physically what is happening was one of the motivations for this study.

Figure 1 compares the LMS (simple and modified Henry's law) with the first group of models in which only the compression of air/gas is considered. The LMS model with the simple Henry's law is approximately the same as the  $K_{ec}$  model up to the critical pressure. This behavior is inconsistent with the physical behavior of bulk modulus in that by increasing the density, the bulk modulus should also increase. As pressure increases, more of the air/gas is dissolved in the liquid and therefore it is expected that the LMS model should give a bulk modulus value which is greater than the  $K_{ec}$ .

After investigating the LMS model, it was found that the reason for the term  $(d\theta/dP)$  appearing in the LMS model is due to the way that the effective bulk modulus was derived. The LMS model was developed based on this definition of fluid bulk modulus given by

$$\frac{1}{K_{LMS}} = - \frac{1}{V_l + V_{gcd}} \left( \frac{dV_l + dV_{gcd}}{dP} \right) \quad (17)$$

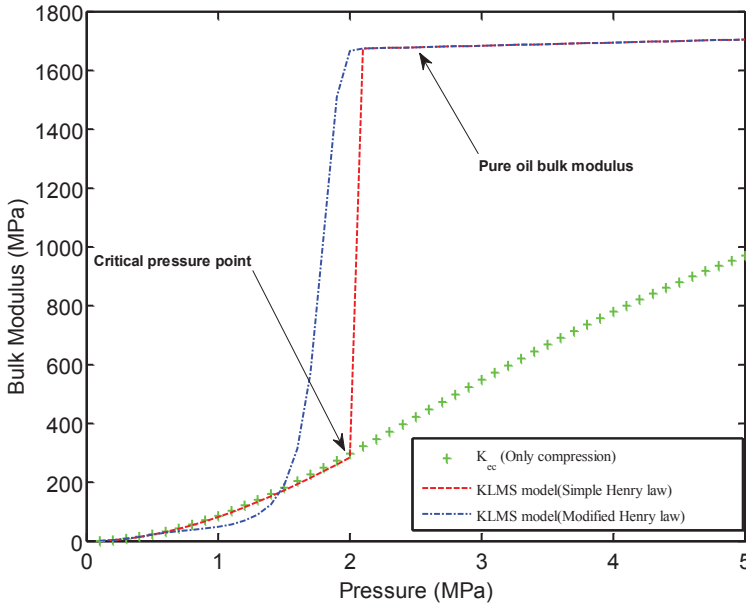


**Figure 1: Comparison of the LMS model with  $K_{ec}$ (only compression) model, when  $P_c=2$  MPa ,  $X_\theta=10\%$  and  $K_f=1700$  MPa**

Equation (17) must be examined more closely. The bulk modulus definition should only be applied to a fluid with a constant composition. For example, in order to find the bulk modulus of air/gas, the definition that should be used is

$$K_g = -V_{gc} \frac{dP}{dV_{gc}} \quad (18)$$

This equation implies that, when air/gas is compressed in a confined container ( $V_{gc}$ ) the mass of air/gas remains constant. In another words, this definition of bulk modulus should only applied when a change in the volume occurs solely due to compression. This definition does not hold when the change in the volume occurs due to the other factors like leakage. Thus, writing the bulk modulus as

$$K_g = -V_{gcd} \frac{dP}{dV_{gcd}} \quad (19)$$

is a poor approximation (remembering that  $V_{gcd}$  is the combined volume of air/gas which is being compressed and being dissolved).  $V_{gcd}$  shows that the volume of air/gas changes because of both compression and dissolving (here dissolving can be thought as leakage, in which as pressure increases some of the air/gas “leaks” out).

It is well established that the isothermal bulk modulus of air/gas using the form of equation (18) is

$$K_g = P \quad (20)$$

But substituting  $V_{gcd} = V_{gc}\theta$  into equation (19), then

$$K_g = \frac{1}{\frac{1}{P} - \frac{d\theta}{dP} \frac{1}{\theta}} \quad (21)$$

It is quite apparent that equation (21) does not converge to equation (20); thus problems will arise if equation (19) is used.

Using the fundamental definition of bulk modulus, the true effective bulk modulus equation for the mixture of air/gas and oil would be

$$K_e = -(V_{gc} + V_l) \left( \frac{dP}{dV_l + dV_{gc}} \right) \quad (22)$$

Equation (22) is the true definition, because the change in the volume of both the oil and air/gas is only due to compression. Thus in equation (22),  $V_{gc}$  should be used rather than  $V_{gcd}$  to account for the effect of air/gas dissolving into the oil.

Based on this discussion, it is apparent that equation (17), which was used by LMS to find the effective bulk modulus of the mixture of oil and air/gas, is an approximation only. In equation (17),  $V_{gcd}$  was used instead of  $V_{gc}$ . This conflicts with the basic definition of bulk modulus.

It is interesting to note that the additional  $V_{gcd}$  term in equation (17) results in the term  $d\theta/dP$  appearing in the bulk modulus equation. This produces the discontinuity shown in Figure 1.

The challenge then becomes one of how the effective bulk modulus of the mixture of oil and air/gas can be modeled when the volume of air/gas decreases, not only because of compression, but also because of air/gas dissolving into the oil. To answer this question, equation (22) can be written in another mathematical form as:

$$\frac{1}{K_e} = -\frac{1}{V_l + V_{gc}} \left( \frac{dV_l}{dP} \frac{V_l}{V_l} + \frac{dV_{gc}}{dP} \frac{V_{gc}}{V_{gc}} \right) \quad (23)$$

Using oil and air/gas bulk modulus definitions, equation (23) simplifies to

$$\frac{1}{K_e} = \frac{1}{V_l + V_{gc}} \left( \frac{V_l}{K_l} + \frac{V_{gc}}{K_g} \right) \quad (24)$$

Equation (24) is a useful equation to find the effective bulk modulus when it is desired to consider both the effect of compression and dissolving; however, some approximations are necessary which is now discussed.

Consider Figure 2. For very small changes in pressure, the corresponding change in the volume of air/gas is shown.  $V_{g0}$  shows the initial volume of air/gas at pressure  $P_0$ . When the pressure increases from  $P_0$  to  $P_1$ , the volume of entrained air/gas decreases according to the ideal gas law and reduces to  $V_{gc1}$ . As soon as pressure reaches  $P_1$ , some of the air/gas is dissolved into the oil and the volume of air/gas decreases to  $V_{gcd1}$ . The bulk modulus of air/gas at exactly pressure  $P_1$  is not defined, but is slightly above and below that point. If it



is assumed that the change in pressure from  $P_0$  to  $P_l$  is small enough, the effective bulk modulus at pressure  $P_l$  could be approximated as:

$$\frac{1}{K_e} = \frac{1}{V_l + V_{gcdl}} \left( \frac{V_l}{K_l} + \frac{V_{gcdl}}{K_g} \right) \quad (25)$$

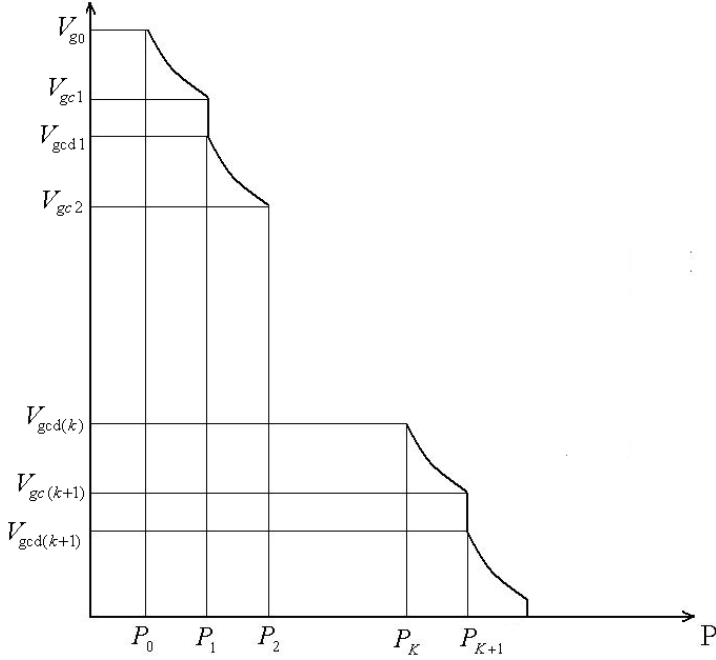


**Figure 2: Volume change of air/gas due to compression and the dissolving effect**

$V_{gcdl}$  can be found according to Henry's law.

$$V_{gcdl} = V_{gc1} \theta_1 = \frac{P_0 V_{g0}}{P_1} \theta_1 \quad (26)$$

$$\theta_1 = \frac{N_{g1}}{N_{g0}} = \frac{V_{g1}}{V_{g0}} \quad (27)$$

Now at pressure  $P_{k+1}$

$$\frac{1}{K_e} = \frac{1}{V_l + V_{gcd(k+1)}} \left( \frac{V_l}{K_l} + \frac{V_{gcd(k+1)}}{K_g} \right) \quad (28)$$

$$\theta_{K+1} = \frac{N_{g(K+1)}}{N_{g(K)}} = \frac{V_{g(K+1)}}{V_{g(K)}} \quad (29)$$

$$V_{\text{gcd}(K+1)} = \frac{P_0 V_{g_0} \theta_1 \theta_2 \dots \theta_{K+1}}{P_{K+1}} = \left( \frac{P_0 V_{g_0}}{P_{K+1}} \right) \frac{N_{g(K+1)}}{N_{g_0}} \quad (30)$$

Theoretically, this process can be continued until the pressure reaches the critical pressure in which there will be no entrained air/gas. Therefore on the pressure versus volume plot of Figure 2 and at each pressure, a series of bulk modulus points can be estimated. Each point can be estimated by

$$\frac{1}{K_{ecd}} = \frac{V_{gc} \theta}{V} \frac{1}{K_g} + \frac{V_l}{V} \frac{1}{K_l} \quad (31)$$

From the previous sections

$$V_{\text{gcd}} = V_{gc} \theta = \frac{P_0 V_{g_0}}{P} \frac{T}{T_0} \theta \quad (32)$$

$$\theta = \left( \frac{P_C - P}{P_C - P_0} \right) \quad (33)$$

$$V = V_{gc} \theta + V_l \quad (34)$$

$$K_g = P \text{ (For isothermal compression)} \quad (35)$$

Therefore, a theoretical model which relates the effective bulk modulus to the volumetric variations of air/gas due to both compression and the dissolving of air/gas in the oil, and also due to the change in volume and bulk modulus of the pure oil as a function of pressure and temperature is given by

$$\left\{ \begin{array}{l} K_{ecd} = \frac{V_l(P, T) + V_{\text{gcd}}(P, T)}{\frac{V_l(P, T)}{K_l(P, T)} + \frac{1}{P} V_{\text{gcd}}(P, T)} \quad \text{For } P < P_C \\ K_e = K_l(P, T) \quad \text{For } P \geq P_C \end{array} \right. \quad (36)$$

where

$$V_{\text{gcd}}(P, T) = V_{gc}(P, T) \theta = \frac{P_0 V_{g_0}}{P} \frac{T}{T_0} \left( \frac{P_C - P}{P_C - P_0} \right) \quad (37)$$

$$V_l(P, T) = V_l(P_0, T) e^{\int_{P_0}^P \frac{dP}{K_l(P, T)}} \quad (38)$$

$$K_l(P, T) = K_l(0, T) + m(P - P_0) \quad (39)$$

$$V_l(P_0, T) = V_l(P_0, T_0) e^{\alpha(T - T_0)} \quad (40)$$

This model was derived based on the assumption of an **isothermal compression** process and that an equilibrium condition between the air/gas bubbles and oil was reached.

Equations (36-40) can be considered to be a model of the effective bulk modulus of the mixture of the air/gas and oil which in addition to considering both the compression and the dissolving of air/gas in the oil, assumes that the volume and bulk modulus of the pure oil is a function of pressure and temperature. In order to consider the effect of pressure and temperature on the pure oil volume and bulk modulus, the equations developed by Song et al. [9] which predicts the isothermal secant bulk modulus of mineral oils and polymer solutions with hydrocarbon bases and non-hydrocarbon based oils, is used here. Since the tangent bulk modulus value is required in the model, these predicted equations for the secant bulk modulus will be converted to the tangent bulk modulus values.

The dissolving effect of air/gas in the oil introduces new variables like the Henry's law constant and the critical pressure term which makes the model more complicated. In applications where the effect of air/gas dissolving in oil can be neglected, the model can be simplified by just considering the compression of air/gas. To do this, Equation 36 is modified by replacing  $V_{gcd}(P, T)$  with  $V_{gc}(P, T)$  and  $P_c$  is assumed to be infinity which means that there is a permanent presence of air/gas in the oil. The effective bulk modulus for the mixture of oil and air/gas when only the compression of air/gas is considered is given by:

$$K_{ec} = \frac{V_l(P, T) + V_{gc}(P, T)}{\frac{V_l(P, T)}{K_l(P, T)} + \frac{1}{P} V_{gc}(P, T)} \quad (41)$$

where

$$V_{gc}(P, T) = \frac{P_0 V_{g0}}{P} \frac{T}{T_0} \quad (42)$$

In Figure 3, the proposed model, Equations (36) to (40), is compared with the LMS model (using both the simple and modified Henry's law). For comparison purpose,  $P_c=5\text{MPa}$  and  $X_0=3\%$  were chosen. It was also assumed that liquid bulk modulus changes with pressure according to Equation (44). The plot representing the LMS model using the simple Henry's law, clearly shows the large jump in discontinuity at the critical pressure point. With the modified Henry's law, the plot has improved, but still significant deviations from the proposed model ( $K_{ecd}$ ) are observed. This is especially true in the lower pressure range from 0-1.5 MPa, in which the  $K_{LMS}$  (modified Henry law) predicts less bulk modulus values than those predicted by the  $K_{ec}$  model. This means, this model predicts that instead of air/gas dissolving in the oil, some more air/gas is added to the oil and decreases the effective bulk modulus. This trend cannot happen physically.

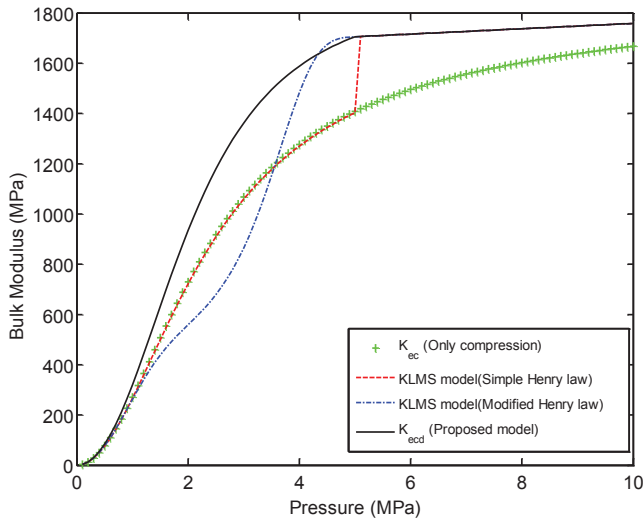


**Figure3: Comparison between LMS models and the new proposed model ( $K_{ecd}$ ), when  $X_{\theta}=3\%$ ,  $P_C=5$  MPa and Liquid bulk modulus changes with pressure according to Equation (44)**

## 4 EXPERIMENTAL RESULTS

In the previous sections, the theoretical models to find the effective bulk modulus of the mixture of oil and air were presented. An experimental system was built in order to investigate and compare the bulk modulus versus pressure behavior of the mixture of oil and air/gas at a constant temperature with those predicted by the models. In this section, the experimental set up and some of the results will be presented.

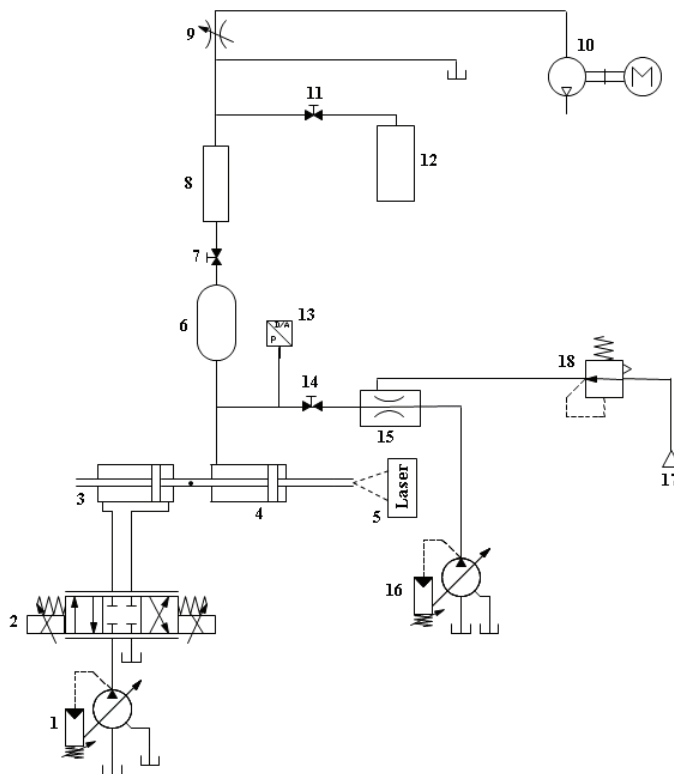
### 4.1 Experimental Apparatus

A schematic diagram of the apparatus used for measuring the effective bulk modulus of the mixture of oil and air/gas is shown in Fig. 4. Greater details of the experimental systems can be found in Gholizadeh et al. [7]. For the test, the oil is fed to the testing volume (6) and the end of the cylinder (4) by a hydraulic pump (16) and circulated for a specified period of time. A venturi orifice (15) is used to mix the oil and the air. After the air is distributed in the circuit, the needle valve (11) is opened to collect the sample of aerated oil to be used by the pycnometer (12). By measuring the specific weight of the collected sample with the pycnometer, the approximate volumetric fraction of air at atmospheric pressure could be found. During all of the tests, the throttle valve (9) was closed except for the calibration test where it was used to control the amount of vacuum pressure for degassing the oil. The transparent tube (8) is used to visually view the size of the bubbles and their distribution.

The transparent tube also facilitates a location for a high speed camera to be used in measuring the approximate size and distribution of the bubbles. After aerating the oil, the needle valves (14) and (7) are closed and the confined aerated oil in the testing vessel (6) and the cylinder end (4) is compressed by actuating the hydraulic cylinder (3) which is

mechanically linked to the hydraulic cylinder (4). The speed that the aerated oil is compressed is controlled by servo valve (2). At the same time that the aerated oil is compressed, the pressure reading of pressure transducer (13) is taken and the change in the volume of aerated oil is measured by displacement sensor (5). A pressure versus volume curve is plotted and used for calculating the tangent bulk modulus. The specification of the pressure and displacement sensors is given in table 1.

The volume of the testing vessel including extra volume added due to the fittings is 2133695 mm<sup>3</sup>. All the measurements were taken at a temperature of 23±1 °C. Isothermal curves were obtained by applying the load very slowly. It took about 3.5 minutes for each test to increase the pressure from 0-6.9 MPa.



(1) Pressure compensated variable displacement pump, (2) Pressure control servo valve, (3) Double acting double rod end hydraulic cylinder, (4) Double acting double rod end hydraulic cylinder, (5) Displacement sensor (MicroTrak II-SA), (6) Testing vessel, (7) Needle valve, (8) Transparent tube, (9) Variable throttle valve, (10) Vacuum pump, (11) Needle valve, (12) Pycnometer, (13) Pressure transducer, (14) Needle valve, (15) Venturi orifice, (16) Pressure compensated variable displacement pump, (17) Compressed air source, (18) Pressure regulator

**Figure 4: Schematic diagram of the bulk modulus tester**

A couple of lip type piston seals were used in the hydraulic test cylinder (4) in order to

prevent the leakage from the test chamber to the cylinder. Leakage test were performed at the maximum pressure of 6.9 MPa in 3.5 minutes and a negligible amount of leakage during this period of time was observed. The errors in estimating the bulk modulus caused by the deformation of the testing vessel, cylinder and seals as well as the error due to the small amount of leakage can be removed from the final test results by the calibration method which will be explained later. The errors due to the sensors were estimated and it was found that the calculated error in estimating the bulk modulus using this method is as low as 3%.

#### 4.2 Calibration

Errors due to the deformation of the testing vessel, cylinder and especially lip seals need to be estimated and removed from the final results. Some theoretical relations exist which estimate the deformation of testing vessel and cylinders, but estimating the lip seal deformation using theoretical relations was found to be impractical. In order to remove the deformation effects, before adding air to the system, the calibration procedure was followed in which steps were taken to ensure that the apparatus interior was entrained of any trapped air. Vacuum was also applied to the system to remove any residual air bubbles. In order to make sure that the results of the calibration test were repeatable, the oil was completely removed from the testing vessel and cylinder and a second test was performed. The results of these two tests were highly repeatable. Isothermal curves were obtained by applying the load very slowly at the same rate which was later applied to the final tests. Figure 5 shows the results of pressure versus the change in the volume and also the effective bulk modulus versus pressure of the system. The change in volume due to the expansion of the testing vessel and compression of the piston lip seals can be found using this relationship:

$$\Delta V_{def} = V_{Cal} - V_0 + \Delta V_l \quad (43)$$

**Table 1: Specifications of sensors**

Sensor Type	Range	Linearity ( % of full scale)
Validyne DP15TL Pressure transducer	$\pm 6.9$ MPa ( $\pm 1000$ Psi)	$\pm 0.5$
Microtrak II stand-alone laser sensor	$\pm 100$ mm	$\pm 0.03$

$V_{cal}$  and  $V_0$  are known by measurements, but  $\Delta V_l$  is unknown and needs to be accurately measured or estimated by knowing the bulk modulus of pure oil. Using semi-empirical relations provided by Song et al. [9] for mineral oils, the bulk modulus of the test oil (Esso Nuto H68) was predicted within  $\pm 3.7$  percent by measuring its viscosity and density at atmospheric pressure and a temperature of 23 °C. The predicted secant and tangent bulk modulus at this temperature and pressure range of 0-15 MPa are given respectively by

$$\bar{K}_l(P, 23^\circ C) = 1652 + 5.53(P - P_0) \quad (44)$$

$$K_l(P, 23^\circ C) = 1652 + 10.64(P - P_0)$$

The change in volume due to the deformation of the apparatus was estimated and subtracted off from all subsequent measurements.

#### 4.3 Experimental results with entrained air

Using the test rig and procedure explained in section 4.1, a series of tests were carried out using different amounts of air. Air was continuously added and circulated throughout the system for a short period of time. For longer periods of time, a higher percentage of air could be accumulated in the oil. The maximum amount of entrained air obtained using this method was limited to  $X_0=6\%$ . This method of adding air to the bulk modulus tester is different from others [4,5,8,10] in which air is added locally to a part of a bulk modulus tester resulting in one large pocket of air. This contrasts our method where a mixture of air/gas and oil with different air bubble sizes are created, which more closely represents a hydraulic system in practice.

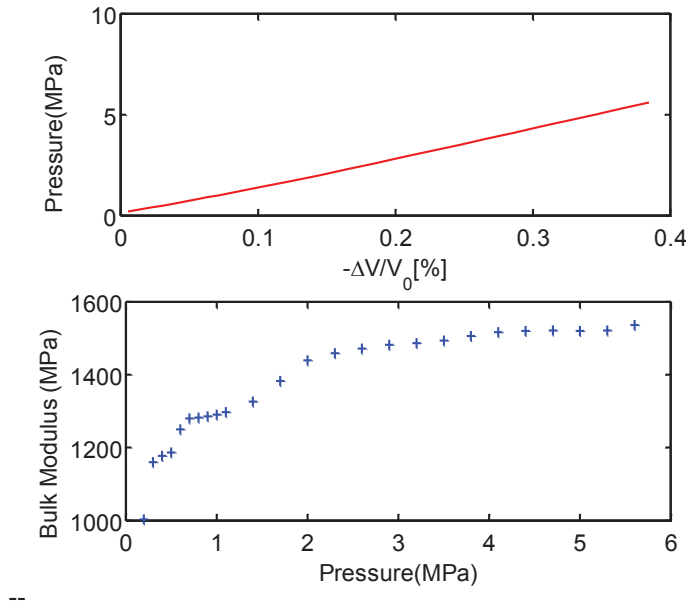


**Figure 5: Pressure versus change in volume and effective bulk modulus versus pressure curves for the calibration test**

$X_0$  which is the volumetric fraction of entrained air/gas at atmospheric pressure ( $P_0$ ) and temperature  $T_0$  is defined as

$$X_0 = \frac{V_{g_0}}{V_{g_0} + V_{l_0}} \quad (45)$$

If it is assumed that a unit volume of fluid is taken; then

$$\begin{aligned}
 V_{g_0} + V_{l_0} &= 1 \\
 X_0 &= V_{g_0} \\
 1 - X_0 &= V_{l_0}
 \end{aligned}
 \tag{46}$$

$X_0$  and  $P_C$  can be estimated by plotting the  $(\Delta V/V_0)$  curve versus pressure as shown in Figure 6. By drawing an asymptotic line from the maximum slope to the abscissa,  $X_0$  can be determined.  $P_C$  is determined as the pressure where the slope of the curve approaches that of pure oil. These techniques have been used and explained by Kajaste et al. [4] and Ruan and Burton [10].

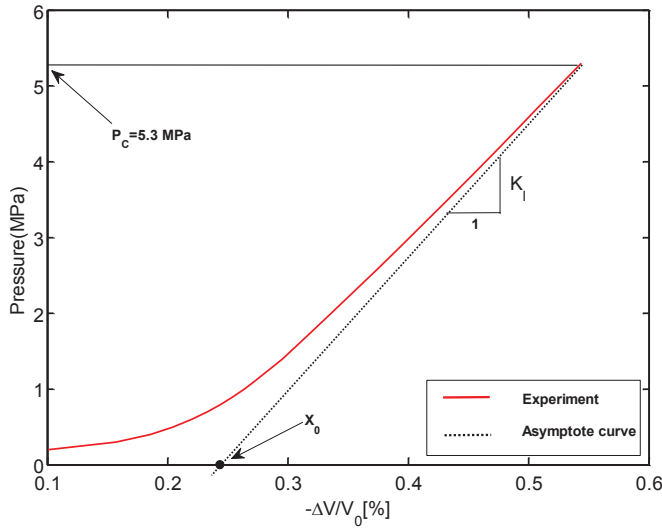


**Figure 6: A representative diagram which shows how  $X_0$  can be calculated using measured data**

Figures 7-9 show how the experimental and theoretical tangent bulk modulus changes as a function of pressure, when  $X_0$  is 0.23%, 1.15% and 3.32% respectively. All the measurements were taken at a temperature of  $23 \pm 1$  °C. The experimental bulk modulus values were determined by taking the slopes at locations along the pressure versus volume curve of each set of experimental results.

The experimental bulk modulus results for  $X_0 = 0.23\%$  and  $1.15\%$  cases (Figures 7 and 8) were divided into three phases for comparison purposes with the theoretical models. It remains an immediate challenge to verify the following statements but based on what has been observed and indeed, derived, the observations appear to be consistent.

Phase 1 ( $0 < P < 1$  MPa): The measured values follow the  $(K_{ec})$  model quite closely, which suggests that the air bubbles are only being compressed and no dissolving occurs.



Phase 2 ( $1 < P < 1.7$  MPa): The bulk modulus values start to increase more than the value predicted by the ( $K_{ec}$ ) model and follows closely with the ( $K_{ecd}$ ) model, which shows that in this region the air bubbles are dissolving.

Phase 3 ( $1.7 < P < 6$  MPa): The bulk modulus no longer increases with the same rate as in the second phase, but follows the ( $K_{ec}$ ) model quite closely. This indicates that the air bubbles may have stopped dissolving and are only being compressed as pressure increases.

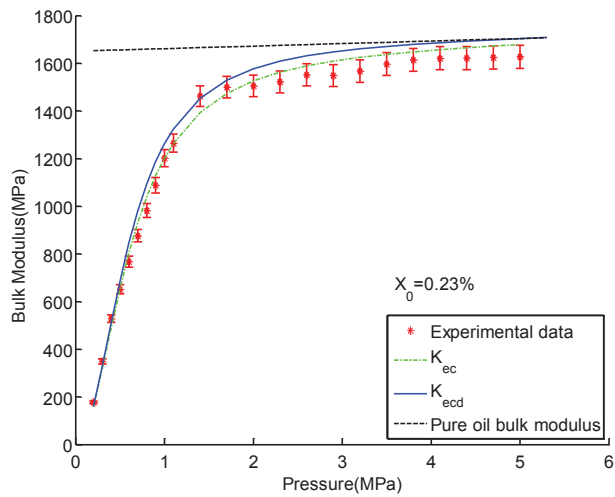


**Figure 7: Comparison of the experimental and theoretical bulk modulus ( $X_0=0.23\%$ ,  $P_C=5$ MPa)**

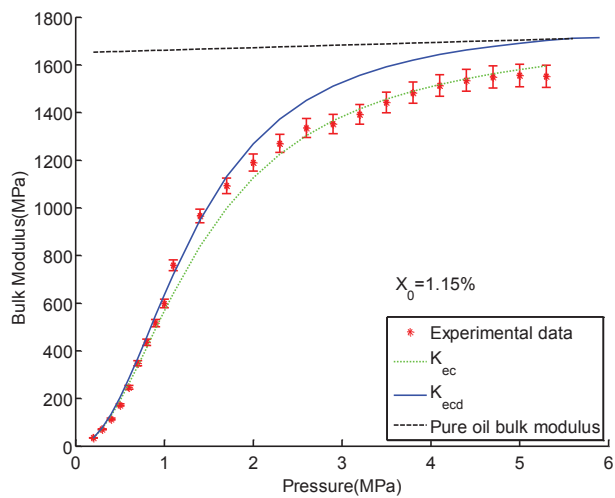


**Figure 8: Comparison of the experimental and theoretical bulk modulus ( $X_0=1.15\%$ ,  $P_C=5$  MPa)**

In Figure 9, as the amount of air/gas increases ( $X_0=3.32\%$ ), the measured values initially follow the ( $K_{ec}$ ) model. After  $P=0.5$  MPa, the bulk modulus values follow the ( $K_{ecd}$ ) model quite closely suggesting that air bubbles are being dissolved. Between the region of  $1 < P < 3.2$  MPa, there is a significant deviation between the model and the experimental results. This indicates that the amount of dissolved air is greater than that predicted by the ( $K_{ecd}$ ) model.

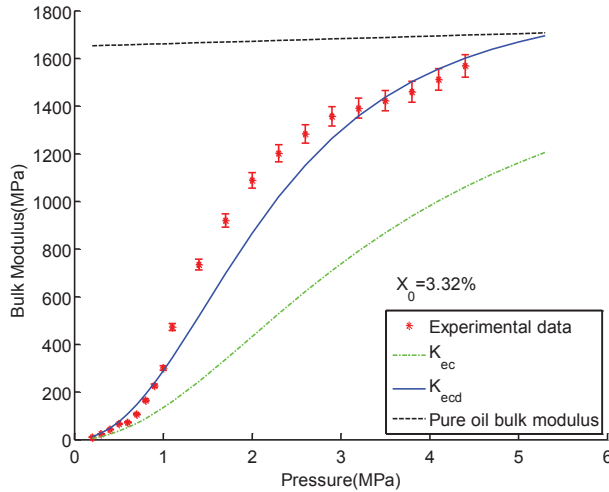


**Figure 9: Comparison of the experimental and theoretical bulk modulus ( $X_0=3.32\%$ ,  $P_c=5.5$ MPa)**

## 5 CONCLUSION

Theoretical models to find the effective bulk modulus of a mixture of oil and air/gas were presented and the discontinuity problem associated with the LMS model was discussed and its limitations were presented. A new model which accounts for the effect of dissolution of the entrained air/gas in oil according to Henry's law was developed. An experimental system was introduced to investigate and compare it to the bulk modulus versus pressure behavior of the mixture of oil and air/gas at a constant temperature with those predicted by the models.

Tests were carried out by adding different amounts of air to the oil and distributing it in the oil. The results of the pressure versus bulk modulus curve showed that for the  $X_0=0.23\%$  and  $1.15\%$  cases, the agreement between the  $K_{ecd}$  model and the measured values is good up to  $1.7$  MPa. After this pressure it appears that the  $K_{ec}$  model follows the experimental results more closely suggesting that the mechanism for dissolution is not fully accounted for and leads to deviation from the experimental results. However, by increasing the amount of air to  $X_0=3.32\%$ , it was observed that none of the models agreed well with the experimental values, but the results of  $K_{ecd}$  were closer to the experimental values than the  $K_{ec}$  model. This difference may be related to the distribution and size of the air bubbles and is an area where more research will be conducted in the future.

## NOMENCLATURE

$H$	Henry's constant	[MPa]
$K_e$	Tangent effective bulk modulus	[MPa]
$K_g$	Tangent bulk modulus of the air/gas	[MPa]
$K_l$	Tangent bulk modulus of the liquid	[MPa]
$K_{LMS}$	Effective bulk modulus model of the mixture of oil and air/gas provided by LMS	[MPa]
$N_{dg}$	Number of moles of dissolved air/gas at pressure $P$	[mole]
$N_g(P, T)$	Number of moles of entrained air/gas at pressure $P$ and temperature $T$	[mole]
$N_{dg}(P, T)$	Number of moles of dissolved air/gas at pressure $P$ and temperature $T$	[mole]
$N_{dg}(P+dP, T)$	Number of moles of dissolved air/gas at pressure $P+dP$ and temperature $T$	[mole]
$Ng(P+dP, T)$	Number of moles of dissolved air/gas at pressure $P+dP$ and temperature $T$	[mole]
$N_l$	Number of moles of oil	[mole]
$P$	Instantaneous pressure (absolute)	[MPa]
$P_0$	Atmospheric pressure (absolute)	[MPa]
$P_C$	Critical pressure (absolute)	[MPa]
$P_g$	Instantaneous gauge pressure	[MPa]
$R$	Ideal gas constant	[m <sup>3</sup> PaK <sup>-1</sup> mol <sup>-1</sup> ]
$T$	Instantaneous temperature	[°K]
$T_0$	Initial Temperature	[°K]
$V_0$	Volume of fluid (entrained air/gas+liquid) at $P_0$ and $T_0$	[m <sup>3</sup> ]
$V$	Volume of fluid (entrained air/gas+liquid) at $P$ and $T$	[m <sup>3</sup> ]
$V_{g0}$	Volume of entrained air/gas at $P_0$ and $T_0$	[m <sup>3</sup> ]
$V_{gc}$	Instantaneous volume of gas due to compression	[m <sup>3</sup> ]
$V_{gcd}$	Instantaneous volume of gas due to both compression and dissolve	[m <sup>3</sup> ]
$V_g$	Volume of entrained air/gas at $P$ and $T$	[m <sup>3</sup> ]
$V_{l0}$	Volume of liquid at $P_0$ and $T_0$	[m <sup>3</sup> ]
$V_l$	Volume of liquid at $P$ and $T$	[m <sup>3</sup> ]
$n$	Polytropic index for air/gas content	[-]
$m$	Slope of the pure oil bulk modulus versus pressure curve	[-]
$X_0$	Volumetric fraction of entrained air/gas at $P_0$ and $T_0$	[-]

$\theta$       The ratio of the number of moles of entrained air/gas at pressure P to the number of moles of entrained air/gas at pressure  $P_0$       [-]

## REFERENCES

- (1) LMS IMAGINE, S.A., 2008, HYD Advanced Fluid Properties, *LMS Imagine, S.A.*, Technical Bulletin n° 117, Rev 8B.
- (2) Yu, J., Chen, Z. and Lu, Y. 1994. Variation of Oil Effective Bulk Modulus with Pressure in Hydraulic Systems. *Journal of dynamic systems, measurement, and control*, Vol. 116 (1), pp. 146-150.
- (3) Gholizadeh, H., Burton, R. and Schoenau, G. 2012. Fluid Bulk Modulus: Comparison of Low Pressure Models, *International Journal of Fluid Power*, Vol. 13(1), pp. 7-16.
- (4) Kajaste, J., Kauranne, H., Ellman, A. and Pietola, M. 2005. Experimental Validation of Different Models for Bulk Modulus of Hydraulic Fluid. *The Ninth Scandinavian International Conference on Fluid Power*, SICFP'05, Linköping, Sweden.
- (5) Kim, S., and Murrenhoff, H. 2012. Measurement of Effective Bulk Modulus for Hydraulic Oil at Low Pressure. *Journal of Fluids Engineering, Transactions of the ASME*, Vol. 134 (2).
- (6) Bock, W., Braun, J., Puhl, N. and Heinemann, H. 2010. Air Release Properties of Hydraulic Fluids, Dynamic Air Release *7th International Fluid Power Conference, IFK2010*, Aachen, Germany.
- (7) Gholizadeh, H., Bitner, D., Burton and D., Schoenau, G., 2012. Experimental Investigation of measuring Fluid Bulk Modulus in low pressure regions, *7th FPNI PhD Symposium on Fluid Power*, Reggio Emilia, Italy.
- (8) Huayong, Y., Bin, F. and Guofang, G. 2011. Measurement of Effective Fluid Bulk Modulus in Hydraulic System. *Journal of dynamic systems, measurement, and control*, Vol. 133 (6).
- (9) Song, H. S., Klaus, E. E. and Duda, J. L. 1991. Prediction of Bulk Moduli for Mineral Oil Based Lubricants, Polymer Solutions, and several Classes of Synthetic Fluids. *Journal of Tribology*, 113 (4), pp. 675-680.
- (10) Ruan, J. and Burton, R. 2006. Bulk Modulus of Air Content Oil in a Hydraulic Cylinder. *Proceedings of 2006 ASME International Mechanical Engineering Congress and Exposition, IMECE2006 - Fluid Power Systems and Technology Division*, pp. 259-269.



# **Automotive and Aerospace Applications**



# Optimal Sizing of Pipe Networks in Aircraft Hydraulic System Preliminary Design

C. Dunker<sup>1</sup>, F. Thielecke<sup>1</sup>, T. Homann<sup>2</sup>

<sup>1</sup> Hamburg University of Technology, Institute of Aircraft Systems Engineering,  
Hamburg, Germany

<sup>2</sup> Airbus Operations GmbH, Hydraulic Performance & Integrity, Bremen, Germany

## ABSTRACT

A method for optimal sizing of pipe networks in aircraft hydraulic system preliminary design is presented. This method sizes the hydraulic system's pipe diameters for a defined architecture in order to meet maximum fluid velocity and consumer delta pressure constraints with a minimum pipe network mass. The optimization function uses evolutionary algorithms and implements techniques developed for pipe size optimization of water distribution networks, like scaled fitness or Gray code representation of discrete pipe diameters. Additionally, an advanced problem formulation is determined, which decreases solution space and computation time by taking advantage of the network characteristics. Furthermore, a dynamic penalty function for infeasible solutions is designed. The method is implemented in the preliminary architecting and sizing tool AROLAB via the EVA2 optimization framework. The performance is tested on an aircraft hydraulic system supplied by an electric motor pump. The results show that the system mass could be reduced up to 22% in comparison to a former manual sizing. Much more important during this design phase, however, also the sizing time is reduced significantly.

**Keywords:** Aircraft hydraulic systems, preliminary design, pipe networks, optimization

## 1. INTRODUCTION

During aircraft preliminary design different architectures of hydraulic systems are generated, analyzed, sized, and compared regarding key performance indicators, such as mass, costs or reliability [1]. As the pipe networks mass is the main contribution to the system related aircraft fuel consumption, a low mass network is the best way to design an efficient hydraulic system. On the other hand, the tubing has a major influence on the systems' performance and low mass networks may be infeasible. Thus the sizing of pipe networks is one of the main tasks during this design phase. It is conducted to generate objective key performance data for concept benchmarks and fundamental parameters for detailed design [2]. Due to up to 100 system states, 40 consumers and multiple redundant systems, the architecting and sizing of aircraft hydraulic systems (AHS) is rather complex and can hardly be done without computer-aided methods. Today a MICROSOFT EXCEL-based tool is used for network sizing. Since this assistance was insufficient, the tool AROLAB (Architecture Optimization Laboratory) was developed to support the whole preliminary design process [1].



The sizing of AHS pipe networks is undertaken according to fluid velocity constraints in the pipes themselves and delta pressure constraints for hydraulic consumers. In the EXCEL-based tool this step is done by the designer, who is manually setting the pipe diameters to meet both constraints with an acceptable system mass. This trial-and-error sizing process is very time consuming and can create suboptimal solutions. Thus for AROLAB the implementation of an automatic and optimal sizing function for AHS pipe networks in addition to the manual sizing option seems to be promising.

The optimal sizing of pipe networks is widely spread through different engineering topics, such as water distribution, chemical industry and gas distribution. The problems, especially in water distribution network sizing, are very similar to the AHS pipe network sizing problem. Instead of a least-mass network, a least-cost network is aimed with similar constraints. This least cost design can initially be divided into two groups regarding the pipe diameter modeling. Lansey and Mays [3] modeled the pipe diameter as continuous variables. Although this approach has some advantages considering possible algorithms, it does not seem to be suitable for the AHS pipe network sizing problem, since rounding errors may be quite significant. Other research work treats the problem as a discrete optimization problem, where there is a limited set of available pipe sizes. For this problem many different optimization algorithms have been developed. Cheng and Mah [4] used dynamic programming, Dandy et. al. [5] and Savic and Walters [6] genetic algorithms and Maier et al. [7] ant colony optimization. In AROLAB it was decided to use the EVA2 optimization package of the University of Tübingen [8]. This framework offers a wide set of evolutionary algorithms and the possibility to define individual problem formulations. For the pipe network sizing problem a genetic algorithm was chosen. The reasons for this were the promising results shown by Dandy et. al. for water distribution networks and the simple implementation of improvements and adaptations. The optimization is directly implemented via the EVA2 package into the Java-based preliminary architecting and sizing tool AROLAB.

## **2. AIRCRAFT HYDRAULIC SYSTEMS PRELIMINARY DESIGN IN AROLAB**

In this section the basics of AHSs are explained with special regard to their preliminary design. First, the general architecture of these systems is discussed. In the second section it is shown why preliminary design is necessary and what is undertaken in the corresponding process. In the third section the modeling used for aircraft hydraulic system preliminary design in the AROLAB tool is explained.

### **2.1 General aircraft hydraulic system architecture**

AHS are closed center, constant pressure regulated systems. They are normally supplied by variable displacement axial-piston pumps, which are driven by the aircraft engines or electric motors. The systems are multiple redundant with two to four AHS per aircraft. In Figure 1 a sheet for the triple redundant AIRBUS A320 hydraulic system is shown. It can be seen that there are multiple consumers located all over the aircraft. Due to low temperatures and long distances, the tubing has a major influence on the systems performance and mass. Thus, in order to achieve objective benchmarks between different system concepts, the sizing of hydraulic pipe networks is a key factor in preliminary design.

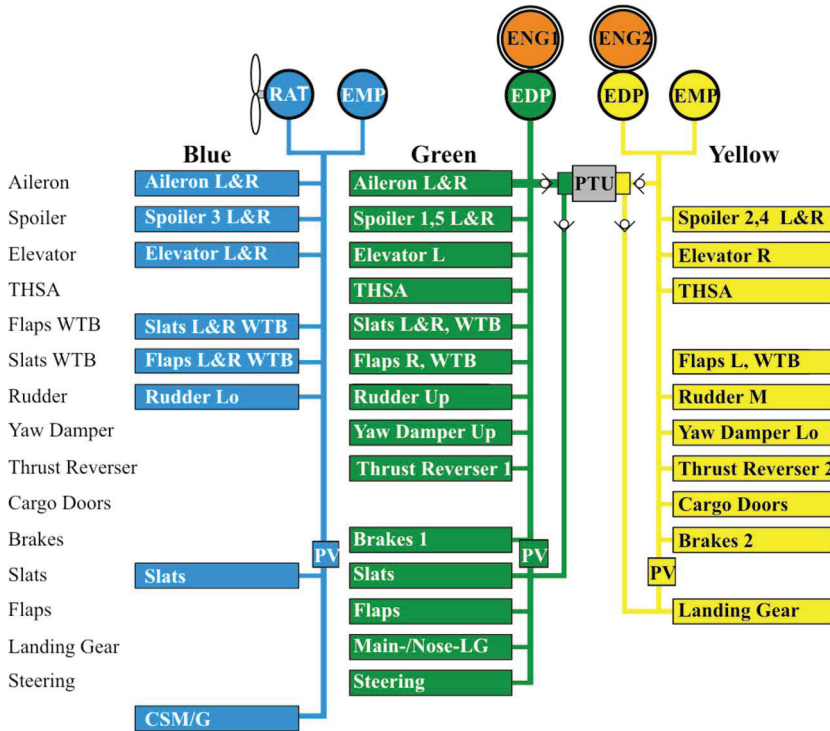


Figure 1: Hydraulic sheet of an Airbus A320

## 2.2 Aircraft hydraulic system preliminary design process

The preliminary design process of AHS can be grouped into the phases *requirements definition*, *architecting*, *sizing* and *benchmark*. A main task during the first phase is the definition of system states and failure cases. For all these states the required system in- and outputs, like consumer deflection rates or engine speeds, have to be defined. In the next phase different system architecture concepts are generated, by varying the number of independent systems, the number and type of pumps and the allocation of consumers. These system concepts are sized, regarding pipe diameters, pumps and reservoirs. On the basis of this sizing, key performance indicators like mass, power consumption and costs are calculated and used for a concept benchmark in the next phase. The most suitable concept is selected and analyzed further in detailed design with thermal, dynamic and realtime simulation.

## 2.3 Preliminary architecting and sizing tool ArOLab

Since the decisions made at the preliminary design stage are essential to subsequent system performance, and the assistance from the EXCEL-based tool was insufficient for this purpose, the sizing tool ArOLab has been developed [9]. The tool uses a model-based system design approach, which is supported by knowledge-based methods. It has a graphical user interface, a model library and various functions and features for requirements import, data visualization and project comparison. The user interface is depicted in Figure 2. The tool implements steady-state flow and pressure calculation. These methods are briefly described in the next sections.

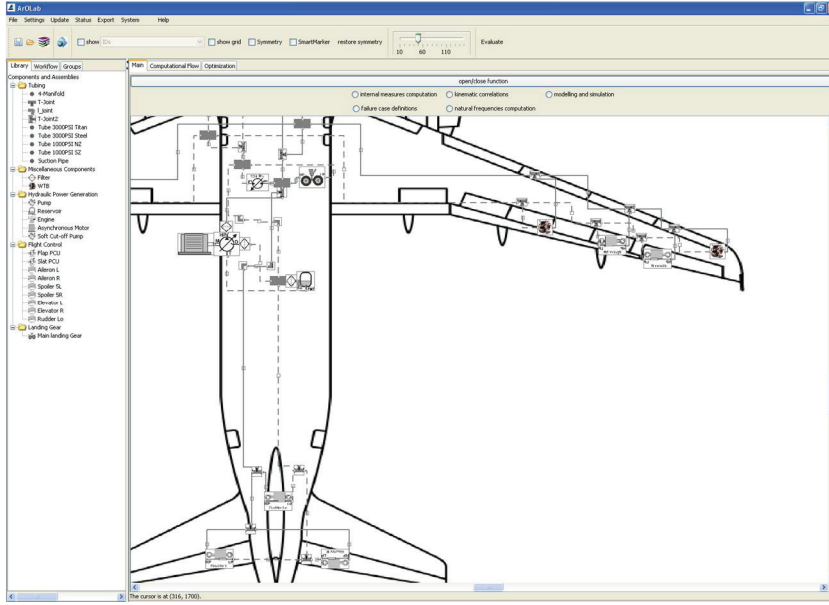


**Figure 2: AROLAB user interface**

### 2.3.1 Steady-State flow and pressure modeling in ArOLab

AROLAB uses a steady-state flow and pressure calculation. This seems to be accurate enough for a preliminary sizing and has advantages in comparison to dynamic modeling regarding calculation time and necessary parameter input. By using the required consumer deflection rates  $\dot{\delta}$  and assuming a linear relation between deflection rate and flow with an empirical flow factor  $k_{flow}$

$$Q = k_{flow} \cdot \dot{\delta} \quad (1)$$

the demanded consumer flows can be calculated for all system states. Next, a flow vector  $q$ , which implements the flow variables at the component ports, is defined. This vector can be calculated by solving the equation system

$$A \cdot q = b \quad (2)$$

with an interconnection matrix  $A$  and the vector  $b$  incorporating all demanded consumer flows. Having determined the flows at all ports and all system states the pump can be sized by calculating with

$$V_{P,dem} = \frac{Q_P}{n \cdot \eta_{vol}} \quad (3)$$

the demanded pump displacement  $V_{P,dem}$  regarding flow demand  $Q_P$  and rotational speed  $n$  in each state and the volumetric efficiency  $\eta_{vol}$ . The maximum demanded displacement is used for pump mass estimation. The pump discharge port pressure can be determined on

the basis of the pump characteristic line. Knowing all flows in the pipes, the pressure loss in each pipe can be determined by

$$p_l = \frac{\rho}{2} \cdot v^2 \cdot \left( \lambda \frac{l}{d_{in}} + \zeta \right), \quad (4)$$

regarding fluid density  $\rho$ , fluid velocity  $v$ , the Reynolds number dependent linear pressure drop coefficient  $\lambda$ , the inner pipe diameter  $d_{in}$  and the singular pressure drop coefficient  $\zeta$ , which is derived per pipe length  $l$  from statistical data. Temperature effects are taken into account by modeling a temperature depended viscosity. The pressure losses can be listed into a pressure loss vector  $d(q)$ , the reference pressures at pump and reservoir are incorporated in a reference pressure vector  $h$  and the general pressures at each port of each component are listed in the vector  $p$ . With these vectors and the equation system

$$B \cdot p = d(q) + h \quad (5)$$

with the interconnection Matrix  $B$ , the pressure at each port in the system can be calculated. By subtracting the pressures at the high and low pressure port of the consumers, the delta pressure  $p_\Delta$  is determined for each consumer and state.

### 2.3.2 Mass Modeling in ArOLab

The mass of components is either modeled by known discrete table values, physical relations or by statistical data. The masses of pipes are determined with

$$m_t(d) = m_{t,dry}(d) + m_{fl}(d) + m_{cl,ft}(d) \quad (6)$$

regarding the pipe's mass itself  $m_{t,dry}(d)$ , the fluid mass in the pipe  $m_{fl}(d)$  and the mass of clamps and fittings  $m_{cl,ft}(d)$ . The pipe and fluid mass can be calculated by geometrical data, like pipe length, material, fluid densities, wall thicknesses and inner diameters. The clamp and fitting mass is determined by statistic data for the specific pipe length and diameter [1].

## 3. GENERAL PIPE NETWORK SIZING PROBLEM

The basic goal of the pipe network optimization is the sizing of diameters for defined network architectures, so that the network meets fluid velocity and consumer delta pressure constraints with the lowest possible mass. The problem can be formulated as: Finding a set of diameters  $D$ , in which all elements  $d_i$  are part of a set of available pipe sizes  $S$

$$d_i \in S, \quad (7)$$

which minimizes the overall pipe network mass

$$f(D) = \sum_{i=0}^n m_{t,i}(d_i), \quad (8)$$

meeting fluid velocity constraints in all pipes  $i = 0$  to  $n$

$$v_i \leq v_{max,i}, \quad (9)$$

and consumer delta pressure constraints

$$p_{\Delta,k} \geq p_{\Delta,k,min} \quad (10)$$

for all consumers  $k = 0$  to  $m$ .

#### 4. FUNDAMENTALS OF GENETIC ALGORITHMS

Genetic algorithms are heuristic optimization methods and are based on artificial evolution [10]. They simulate the theory of natural selection, genetic recombination and implement the natural rules of survival in pursuit of the ideas of adaption. Especially the good results of Dandy et. al. using this algorithm type for water distribution network sizing have led to its selection. Genetic algorithms are widely used throughout different disciplines. Their main strength is the flexibility of problem formulation and the robustness regarding different problem types [11].

The optimization process can be described by the phases:

1. Initializing (Generation of initial population of solutions)
2. Evaluation (Determination of the fitness of the solutions)
3. Selection (Selection of solutions due to particular rules)
4. Recombination (Recombination of the selected solutions)
5. Mutation (Arbitrary changes in solutions)
6. Reproduction (Reproduction of new generation according to particular rules)
7. Termination (After e.g. populations, function calls...)

The simplest problem formulation for genetic algorithms, which is also used for the present problem, is the representation of a solution by a binary string, where recombination means interchanges in bit sequences and mutation means arbitrary flipping of bits.

#### 5. ADVANCED PROBLEM FORMULATION

The main difficulties during the sizing of pipe networks are the vast number of possible solutions and the time consuming and often repeated calculation of hydraulic equations. In this section an advanced problem formulation of the pipe network sizing problem is shown. It explains an attempt to overcome these problems for AHS pipe networks by taking advantage of the present problem characteristic and the general AHS architecture.

##### 5.1 Reduction of solution space

One key factor for a fast and well converging optimization is a small solution space. For its reduction advantage is taken of the architecture of AHS. Most AHS have a tree-like

structure for high and low pressure pipe networks, or can be reduced to such. In these networks the steady-state flow and pressure loss in one pipe is independent from the other pipes. By choosing the next available discrete pipe diameter according to the fluid velocity constraint in Equation (9) with

$$d_i \geq d_{min,i} = \sqrt{\frac{4 \cdot Q_i}{\pi \cdot v_{max,i}}} \quad (11)$$

all pipes  $i$  can be analyzed and pre-sized separately. So, the fluid velocity criterion is generally met after this step and does not have to be checked again during optimization. As described in section 4, a binary code can be used for representing solutions in genetic algorithms. The number of bits needed for one pipe depends on the number of available pipe sizes. Eight different diameters and therefore three bits for each pipe are needed. Due to the pre-sizing, diameters smaller than the pre-sized diameter are not feasible. It is as well known that realistic diameters are in the range of the pre-sized solution. Therefore two bits, starting with the lowest bit at the pre-sized diameter, seem to be sufficient. By taking only the pipes into account that have direct influence on consumers with insufficient delta pressure, the solution space can be reduced further. With this approach, the solution space of a 50 pipe network sizing problem can be reduced from  $8^{50}$  to less than  $4^{50}$  solutions. This represents a factor of  $2^{50}$  and so the space is decreased to about  $1/10^{15}$  of the initial solution space.

## 5.2 Predetermination of parameters

The main computation effort during optimization is the calculation of hydraulic equations and masses for each solution. Due to the large numbers of evaluated solutions these calculations have to be as fast as possible. So, generally a predetermination of parameters is favorable, if it is practicable. In this case the masses of each individual pipe for all possible diameters are predetermined. During evaluations the particular masses can be read from a look-up-table, summed up and represent the pipe network mass of the solution.

Also, the pressure loss can be computed separately for each pipe and a calculation can be undertaken prior to the optimization. The pressure losses are saved in an array for each pipe, possible pipe diameter and system state. During optimization these predetermined pressure losses are used for the consumer delta pressure calculation. Due to the large number of system states examined during preliminary design, this approach reduces the computation time significantly. This method is only possible for tree-like networks, for other network types, pressure and flow equations have to be solved during optimization.

## 5.3 Problem transformation

In section 3 a general problem formulation for the AHS pipe network sizing problem is defined. Due to the fluid velocity pre-sizing, the consumer delta pressure criterion is the only constraint. To work effectively with the predetermined pressure losses, the delta pressure constraint is transformed. Combining the pump outlet pressure  $p_p$ , the reservoir pressure  $p_{res}$  and the minimum consumer delta pressure  $p_{\Delta,k,min}$  with

$$p_{al} = p_p - p_{res} - p_{\Delta,k,min} , \quad (12)$$

it is possible to determine the total allowable pipe pressure losses  $p_{at}$  for each consumer  $k$ . If the sum of the pressure losses of the pipes supplying the consumer is higher than the consumer's allowable pressure loss, the constraint is not met. The allowable pressure losses are written into an array for each consumer and state prior to the optimization.

## 6. PROPOSED OPTIMAL SIZING OF AIRCRAFT HYDRAULIC SYSTEM PIPE NETWORKS USING GENETIC ALGORITHMS

In this section the proposed AHS pipe network optimization algorithm is described. The optimization uses a genetic algorithm and techniques derived from Dandy et. al. [5]. The section starts with the de/encoding of solutions, before showing the evaluation as a main part of the algorithm and describing the general process in the EvA2 framework.

### 6.1 De- and encoding of solutions

As discussed in section 4, a common way to treat combinatorial problems, like the pipe network sizing problem, is the representation of solutions by a binary coded string. The value of a design variable is defined by a specific substring of the solution. Often common binary coding is used for representation. When using two bit coding a solution "00000000" would represent a problem with four pipes, all sized to the lowest available diameter.

The usage of common binary code in genetic algorithms has one major disadvantage. The mutation operator used in genetic algorithms flips bits arbitrary according to a predefined probability. So, in common binary code very large jumps in the represented diameter may occur. This may decrease convergence and increase optimization time. Dandy et. al. proposed the usage of Gray code instead of common binary code. An example is given in Table 1. In Gray code there is only a change in one bit for neighbouring pipe sizes. This increases the convergence, especially when handling larger bit strings.

**Table 1: Example for an encoding of pipe diameter sizes as binary and Gray code**

Diameter in 1/16 inch	Binary Code	Gray Code
6	00	00
8	01	01
10	10	11
12	11	10

### 6.2 Evaluation of solutions

When evaluating a solution  $D$ , first the coded bit string is encoded to derive the particular pipe diameter sizes  $d_i$ . With these sizes it is possible to determine the solution's pipe network mass according to Equation (8). Next, it is checked whether the solution is feasible. Due to the pre-sizing of pipe diameters, the fluid velocity constraint in Equation (9) is generally met. The delta pressure constraint is checked by using the predetermined pressure loss and the allowable pressure loss look-up-tables. For each consumer the pressure loss in the lines supplying the consumer is read from the table and is summed up. If in each system state the overall pressure loss in the lines to the consumer is smaller than the allowable pressure loss, the supply is sufficient. If this is the case for all consumers, the



solution  $D$  is feasible and the fitness  $f_f(D)$  can be described as the mass of the pipe network and is returned by:

$$f(D) = f_f(D) = \sum_{i=0}^n m_{t,i}(d_i) . \quad (13)$$

If one or more consumers are not supplied sufficiently, the solution is infeasible. One major difficulty when using genetic algorithms for constrained problems is the handling of infeasible solutions. There is no general methodology for the development of constraint handling functions [12]. Therefore, many different approaches for this problem, like specialised operators, repair algorithms, penalty functions etc., were developed. An overview is given in [13]. Penalty methods are the most widespread form of constraint handling for pipe network optimization and are also used for the present problem.

Generally, genetic algorithms are very sensitive to penalty functions. If the penalty is too high, infeasible solutions that carry valuable genetic information are eliminated and the algorithm tends to local minima. If the penalty is too low, there is a high probability that the convergence is poor and that infeasible solutions are dominating the result. This shows why such functions are often designed by tuning a general method. For the hydraulic pipe size optimization problem the approach of Joines and Houck [14] was chosen:

$$f(D) = f_f(D) + (C \times t)^\alpha \sum_{j=1}^m f_j^\beta(D) . \quad (14)$$

The result of an evaluation at a time  $t$  is the sum of the feasible fitness  $f_f(D)$ , which represents the pipe network mass, and a penalty function. The penalty function is computed with the constants  $C, \alpha$  and  $\beta$  and sums the extend of constraint violation for the constraints  $j$  to  $m$ . The variable  $t$  describes the function calls in the optimization. Thus, this method is a dynamic penalty that increases the amount of penalty for a violation along the optimization. This concept allows relatively high violations in early optimization and works as a death penalty in later optimization. It is realized by the term  $(C \times t)^\alpha$ , with  $\alpha > 1$ . The constraint functional  $f_j(D)$  can be chosen in different ways. The decision was made to use the maximum missing delta pressure in one system state for each consumer for the penalty function. The parameters  $C, \alpha$  and  $\beta$  were tuned on reference systems. The parameter  $C$  can be adjusted by the user in order to allow slightly infeasible, low mass solutions.

Dandy et. al. proposed the usage of variable fitness scaling for increased competition between solution during the optimization process. For that task often a power law with the raw fitness  $f(D)$  and the scaled fitness  $f(D)'$ , like

$$f(D)' = f(D)^n , \quad (15)$$

is used. The exponent  $n$  is increased from 1 at the beginning of the optimization to values like 3 or 4 at the end. This preserves the diversity of the population at the beginning, but also increases the competition at the end to accentuate small differences in raw fitness. The fitness value  $f(D)'$  is returned by the evaluation function to the algorithm. In the next section it is described how the evaluation function is embedded into the algorithm, by showing the general optimization process.



### 6.3 General optimization process using the EvA2 framework

The general process for AHS pipe network optimization uses a common genetic algorithm described in section 4, offered by the EvA2 framework. In the next paragraph this process is described briefly.

**Initializing:** During this phase bit strings are generated. The size of the pipes is randomly set to the initial value from the available four diameter values.

**Evaluation:** For each solution the fitness and the feasibility regarding the consumer delta pressures is computed. The methods used for evaluation were described in detail in the previous section. The evaluation is implemented in the generic problem formulation of the EvA2 framework.

**Selection:** After the fitness of each solution is determined, the solutions used as a parent generation for recombination are selected. The type of selection method can be chosen by the engineer in the user interface, as shown in Figure 3. The default selection method is the roulette wheel selection.

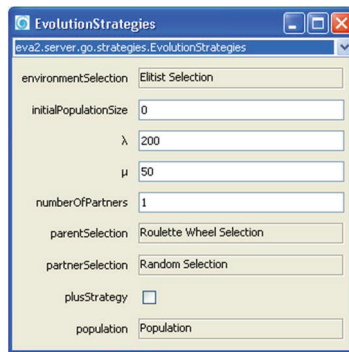


Figure 3: Settings interface for pipe network optimization

**Recombination:** After selection the solutions are recombined to generate the children generation. Like in the selection phase it is possible to use different methods, which choose the partner combinations. The default setting is random combination. The number of partners and the number of children from the partners can be adjusted by the user.

**Mutation:** During the mutation phase the solutions are randomly changed in one bit. The probability of a mutation is set to 10% in default settings.

**Reproduction:** The new generation is used as a new population of solutions. For this generation the process starts back in the evaluation phase, where the fitness of all solutions is determined.

**Termination:** There are several methods for setting the termination point of the optimization, like termination after a certain number of generations or evaluations. The default settings are to terminate the optimization after 20000 function calls.

**Number of Runs:** Experience has shown that the number of runs has a major impact on the quality of the optimization. Since the algorithm is sometimes locked in local minima, the probability to find the global minimum rises with the number of runs. Normally a minimum number of 20 runs should be undertaken.

The optimization user interface is depicted in Figure 4. In the main panel curves of the current optimization run are depicted, showing the fitness over the number of function calls. In the interface the problem can be loaded, different algorithms can be selected and optimization parameters, like population size, can be set. The parameters were varied and tuned for different pipe networks. It was found that the optimization quality is relatively insensitive to these parameters. In contrast to this the results were quite sensitive to the penalty function, as described in section 6.2. By slightly reducing the penalty function parameter  $C$ , a certain state of infeasible, low mass solutions can be allowed, which may be acceptable and have to be judged by the engineer. A basic optimization with 20 runs, 20000 function calls, a parent population of 50 and a children population of 200 takes about 5 minutes computation time on a standard desktop PC. Often this setting is already suitable to find an optimal or near optimal solution.

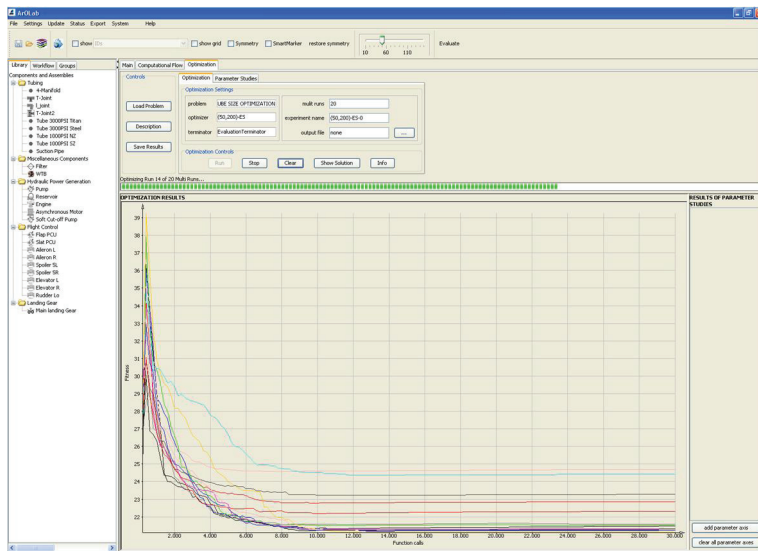


Figure 4: Optimization user interface in ArOLab implementing the EVA2 package

## 7. CASE STUDY: HYDRAULIC SYSTEM FOR A SHORT RANGE AIRCRAFT

In this section a case study for demonstrating the pipe network optimization algorithm's performance and capabilities is described. The test case is a conventional hydraulic system for a short range aircraft. The test network is sized with the tool AROLAB. The optimization function is implemented via the EVA2 framework.

**7.1 The test case aircraft hydraulic system**

In Figure 5 the test case AHS schematic is shown. It can be seen, that the system is powered by one pressure regulated variable displacement pump driven by an electric motor, which is a common design in AHS. The system supplies a pair of spoilers, ailerons and elevator actuators. Also the rudder actuator, landing gear actuator, brakes and secondary flight control devices, like flap and slat power control unit (PCU) and the corresponding wing tip brakes (WTB), are supplied. The pipe network is depicted by solid lines for the high pressure and dotted lines for the low pressure network. The pump's case drain and suction line is shown in dash-dot lines. The pipe network consists out of 56 pipe elements.

For the particular system all pipe lengths, available diameters and corresponding pipe masses per length were given. Also all system states and the corresponding demanded consumer deflection rates are known. Additionally, the minimum consumer delta pressures, the pump's characteristic line and reservoir pressure were defined prior to pipe network sizing. These values were used in AROLAB parameterization of the system model. Two system sizing cases were checked. In the first case a fluid temperature of  $-15^{\circ}\text{C}$  is assumed. This sizing case represents the minimum temperature, in which the system has to have full performance. In the second case an active temperature control is assumed, which ensures a minimum fluid temperature of  $20^{\circ}\text{C}$  during system operation. For both cases the pipe network was sized by an experienced engineer in the EXCEL-based tool, which takes about one hour per case, excluding the modeling effort. These manually sized systems are used as a benchmark for the optimization.

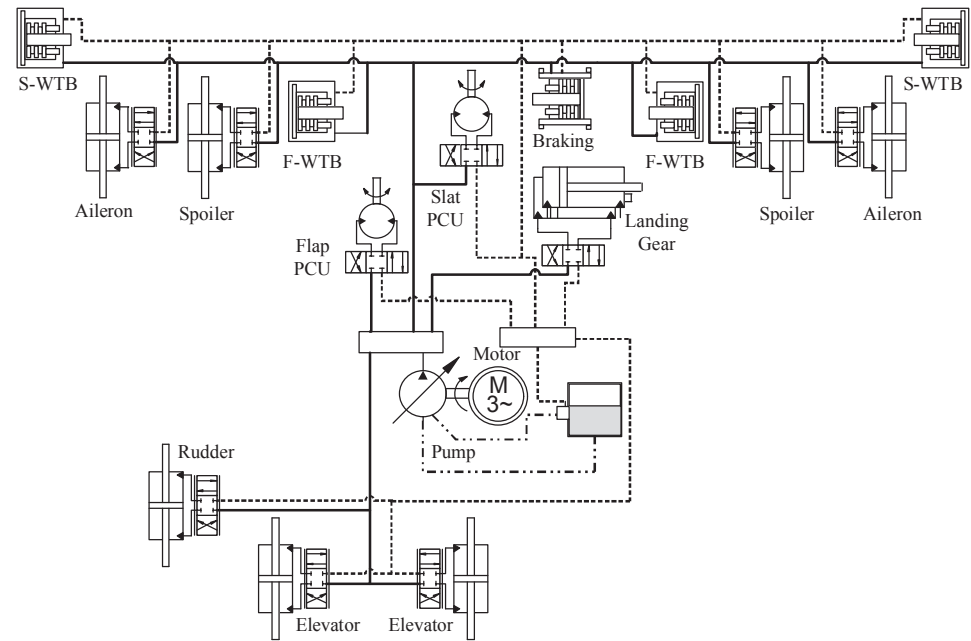


**Figure 5: Schematic of the test case aircraft hydraulic system**

## 7.2 Optimization of the test case aircraft hydraulic system's pipe network

After modeling the system with the described data, an optimization was undertaken. The optimization problem is formulated automatically and is loaded into the implemented EvA2 framework. The optimization results are normalized according to the mass of the manually sized benchmark systems for 20° and -15°C sizing cases, respectively. The benchmark system represents the normalized fitness of one. Figure 6 shows five optimization runs for the test case systems. In the left part the 20°C fluid temperature system is shown; in the right part the -15°C test case is depicted. The x-axis describes the number of evaluations; the y-axis shows the normed fitness of the best solution in each generation. In both test cases the algorithm converges well and is very fast, with about 15 seconds per run.

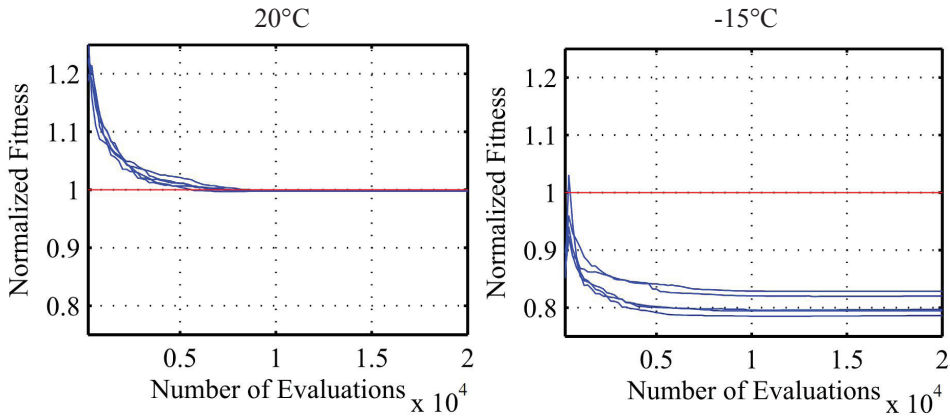


**Figure 6: Best of generation diagram left 20°C, right -15°C for 5 runs**

For the 20°C sizing case depicted in the left it can be seen that the best solution has a normed fitness of about 0.99 and thus is nearly equal to the benchmark system. In the sizing case the algorithm converges to this solution in every run. This result was also found in optimizations with much more runs and function calls. Thus, there is a very high probability, that the best solution found is also the global minimum for this sizing case. In the best solution only a combination of three pipes was chosen differently from the manually sized benchmark system. In the whole pipe network only eight pipes were resized in comparison to the pre-sized system by the fluid velocity criterion. So, the sizing effort is low and finding a global minimum manually is still possible for an experienced engineer.

For the -15°C sizing case the best optimization result has a normed fitness of about 0.78 and thus is about 22% lighter than the benchmark system. The algorithm converges to different solutions during the five runs, which represents the convergence into local minima and explains why there should be a minimum amount of runs undertaken. In this example nearly all pipes had to be resized in comparison to the fluid velocity criterion. The low temperature increases pressure losses significantly, and the consumer delta pressure criterion has a larger influence than the fluid velocity criterion. This makes manual sizing much harder, which explains the 22% lighter system found during optimization.

This test case shows two main aspects. First, the algorithm finds the possible global minimum in only a few minutes. This reduction of development time is one key advantage

of the optimal network sizing function for AHS preliminary design. Second, the algorithm finds solutions, which are equal or lighter than the benchmark networks. This is especially the case, if there is a big manual sizing effort to fulfill the consumer delta pressure criterion, like in the  $-15^{\circ}\text{C}$  sizing case. In these sizing cases it is more difficult for the engineer to generate feasible and light solutions. It has to be said, that a more intensive sizing action in the EXCEL-based tool, which is normally undertaken in AHS preliminary design, would most likely have resulted in a lighter benchmark system. So the test case shows that the goals of decreasing sizing time and pipe network mass are both achieved. The scale of improvement, however, depends on the network and environmental conditions.

## 8. CONCLUSIONS AND OUTLOOK

A method for the optimal sizing of pipe networks in aircraft hydraulic systems has been described in this paper. The method is implemented into the preliminary architecting and sizing tool AROLAB. After introducing aircraft hydraulic systems preliminary design and sizing, the general aircraft hydraulic pipe network sizing problem is shown. The problem can be explained as a search for the lowest mass network, which fulfills fluid velocity and consumer delta pressure constraints with a limited set of available pipe sizes. The fundamentals of genetic algorithms are introduced and the advanced formulation of the optimization problem is described. This formulation reduces solution space and computation effort considerably and is one key factor for a fast and high quality optimization. Next, the algorithm itself and its implementation into the EVA2 framework are explained. Finally, a test case aircraft hydraulic system is shown. This is used for a benchmark test of the algorithms performance by comparing the optimization results with a manually sized benchmark system in the cases of  $-15^{\circ}\text{C}$  and  $20^{\circ}\text{C}$  fluid temperature. It is made clear that the network solutions found were in both conditions lighter than the benchmark network. A real improvement in system mass was achieved for the  $-15^{\circ}\text{C}$  test case. Here a feasible and 22% lighter network was found. The key advantage, however, is the short sizing time. In comparison to the one hour manual sizing work in the EXCEL-based tool in use today, the optimization takes about 5 minutes for a multi run optimization. This is even more relevant, if design trades, like in this case a  $20^{\circ}\text{C}$  or  $-15^{\circ}\text{C}$  trade, and parameter changes are regarded. These trades occur constantly in preliminary design and normally need a complete resize. Thus the method reduces preliminary development time and increases quality considerably. Additionally, the method is more robust in comparison to manual sizing, since problems with data handling and transcription errors do not occur. Also a benchmark between different concepts is more objective.

Future work will be needed for enabling an optimization for other than tree-like systems. Such systems with e.g. cyclic structures cannot be handled with the present problem formulation. Here, a separation of the problem, taking advantage of the large tree-like areas and treating cyclic structures separately with other methods, is being developed. This method still has the advantage of a short optimization time and is more flexible. In the AROLAB tool itself an export interface for aircraft hydraulic system models into dynamic and thermal simulation tools is planned. This approach would enable a complete tool-chain from requirements definition to complex simulations and virtual integration analysis.

## ACKNOWLEDGEMENTS

The author would like to thank the German Federal Ministry of Economics and Technology for supporting this work in the scope of the aeronautical research program LuFo IV and the project ArOSoft. Also the University of Tübingen is acknowledged for their EvA2 optimization framework and the Airbus Hydraulic Performance and Integrity department for their support in the test case system.

## REFERENCES

- [1] Dunker, C., Thielecke, F. and Homann, T., *New Computer-Aided Methods for Preliminary Architecting and Sizing of Aircraft Hydraulic Systems*, Deutscher Luft- und Raumfahrtkongress, Bremen, 2011
- [2] Scholz, D., *Computer Aided Engineering for the Design of Flight Control and Hydraulic Systems*, 20th Congress of the International Council of the Aeronautical Sciences, Sorrento, 1996,
- [3] Lansey, K. E. and Mays, L. W., *Optimization Model for Water Distribution System Design*, Journal of Hydraulic Engineering, 115, No. 10, 1989
- [4] Cheng, W. B. and Mah, R.S. H., *Interactive Synthesis of Pipeline Networks Using Pigraph*, Computers and Chemical Engineering, 2, 1987
- [5] Dandy, G. C., Simpson, A. R. and Murphy, L. J., *An Improved Genetic Algorithm for Pipe Network Optimization*, Water Resource Research, 32, No. 2, 1996
- [6] Savic, D. A. and Walters, G. A., *Genetic Algorithms for Least-Cost Design of Water Distribution Networks*, Journal of Water Resources Planning and Management, 123, No. 2, 1997
- [7] Maier, H.R., A.R. Simpson, W.K. Foong, K.Y. Phang, H.Y. Seah and C.L. Tan, *Ant colony optimization for the design of water distribution systems*, World Water and Environmental Resources Congress, Orlando, Florida, 2001
- [8] Kronfeld, M., Planatscher, H. and Zell, A., *The EvA2 Optimization Framework*, Learning and Intelligent Optimization Conference, Venice 2010
- [9] Pfennig, M., Carl, U.B., Thielecke, F., *Recent Advances Towards an Integrated and Optimized Design of High Lift Actuation Systems*, SAE International Journal of Aerospace, 2010
- [10] Holland, J.H., *Adaption in Natural and Artificial Systems*, University of Michigan Press, Ann Arbor, 1975
- [11] Goldberg, D.E., and C.H. Kuo, *Genetic Algorithms in Search, Optimization and Machine Learning*, 412pp., Addison-Wesley, Reading, Mass., 1989
- [12] Michalewicz, Z. and Janikow, C.Z., *Handling Constraints in Genetic Algorithms*, Technical-Report, Department of Computer Science, University of North Carolina, Charlotte, 1993
- [13] Michalewicz, Z., *A Survey of Constraint handling Techniques in Evolutionary Computation Methods*, Proceedings of the 4<sup>th</sup> Annual Conference of Evolutionary Programming, MIT press, Cambridge, Massachusetts, 1995
- [14] Joins, J.A. and Houck, C.R., *On the Use of Non-Stationary Penalty Functions to Solve Nonlinear Constrained Optimization Problems With GSs*, Proceedings of the IEEE ICEC, 1994



# Coupling Displacement Controlled Actuation with Power Split Transmissions in Hydraulic Hybrid Systems for Off-Highway Vehicles

**Michael Sprengel and Dr. Monika Ivantysynova**

Department of Agricultural and Biological Engineering & School of Mechanical Engineering, Purdue University, USA

## ABSTRACT

Displacement controlled (DC) actuation and hydraulic power split transmissions (PST) have both shown large improvements in efficiency for mobile machinery. DC actuation eliminates metering losses present in current valve controlled systems, which can account for 35% of total energy demand [1]. Further hydraulic power split transmissions decouple the engine and the wheels allowing for efficient engine operation [2]. Both of these technologies also allow for recovering of energy normally dissipated as heat. DC actuation permits conversion of potential energy of a lowering load into torque, which is placed back upon a common drive shaft. Kinetic energy is also captured during braking events and can be placed on the same common shaft by means of the PST. For certain working machines the level of recovered energy far exceeds demand and thus those machines are prime candidates for hybridization.

In this paper the authors will present a novel system configuration for a combined DC/ PST machine. A reach stacker, chosen as a reference machine, has been modeled and simulated in both the baseline LS/ power shift transmission configuration and the proposed DC/ PST architecture. An energetic comparison will be presented which shows reduced energy consumption of up to 73% and an estimated lifetime savings of 1,250 barrels of diesel fuel equating to an overall savings of \$195,000 (USD).

**Keywords:** displacement control, power split transmission, energy recovery, reach stacker

## 1. INTRODUCTION

In a world becoming more aware of pollution and diminishing fuel reserves, increasing vehicle efficiency is becoming more of a priority than ever. To date much work has focused on improving fuel economy in on-highway vehicles; however less effort has been directed at



large off-highway vehicles. These working machines are characterized by high power working hydraulics and powerful drive trains, along with proportionally high losses. While small improvement can be made by increasing individual component efficiency, large improvements are possible by capturing energy normally dissipated as heat. In these machines two types of energy can be recovered, kinetic and potential. Kinetic energy is found in the vehicles inertia while potential energy is present in elevated loads.

Two novel technologies can be combined to achieve significantly increased efficiencies in working machines. First conventional valve controlled hydraulics can be replaced with displacement controlled actuation eliminating metering losses and allowing for energy recovery. Second a standard power shift transmission with torque converter can be substituted with an infinitely variable hydraulic power split transmission, increasing engine efficiency while facilitating energy recovery.

## 2. INVESTIGATED MACHINE

Many working machines would benefit from the reduction of metering losses and potential of energy recovery afforded by switching from valve control to displacement control. Likewise machines with high transmission power requirements would benefit from reduced fuel consumption by moving to a power split transmission. Machine architecture has a significant impact on the benefits received from moving to these new technologies. The greatest improvements will be found on machines which possess the following qualities:

- Heavy load lowering (DC energy recovery)
- Large braking events (transmission energy recovery)
- Rapid cycle times (energy storage)
- Multiple actuators coupled to a single LS pump (reduction in metering losses)

One machine that meets most of these requirements quite well is a reach stacker. Reach stackers are commonly used in ports and rail yards to transport shipping containers short distances. These containers are then stacked by the reach stacker up to 5 containers high before being retrieved. Standard loaded shipping containers can have a mass up to 45 tones. This, coupled with the mass of the reach stacker's boom, represents a tremendous quantity of potential and kinetic energy.

Figure 1 shows a typical reach stacker along with its maximum lifting capacity in each position. A reach stacker's working group consists of a primary boom, which is elevated using two single acting hydraulic lift cylinders. A secondary boom extends from boom 1 by means of a single double acting boom cylinder. Finally an end effector known as a spreader interfaces with the container. Select machine parameters are located in Table 1.

The chosen reach stacker will serve as the representative machine for comparing a machine with combined DC/ PST architecture possessing large levels of recoverable energy against a conventional machine. The following two sections will describe the hydraulic and mechanical configurations of the conventional and proposed machine.

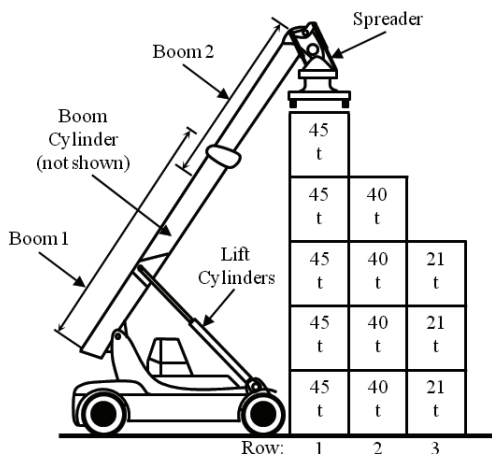


Figure 1 Reach stacker

Table 1 Reach stacker parameters

Vehicle (curb weight)	77 t
Boom 1	9 t
Boom 2	6 t
Spreader	9.5 t
Container (height, width)	2.9, 2.4 m
Top speed (loaded, unloaded)	23, 25 km/h
Engine power	280 kW
Rated speed	2100 rpm
Raising speed (loaded, unloaded)	0.28, 0.39 m/s

### 2.1. Conventional architecture

Both machine architectures have been condensed down into the components required for an energetic analysis. Reach stackers have a number of auxiliary hydraulic functions, including steering, which were not considered. These subsystems do not consume large quantities of energy and their load on the engine remains consistent between both machines. As such these simplifications should not have a large impact on relative energy consumption between the two architectures.

System parameters were selected for a typical reach stacker based on published data from several manufactures. Kinematics, hydraulic pressures, cylinder dimensions, and performance requirements were based on published information along with experience and intuition. A summary of key parameters can be found in Table 2. These core parameters were used to simulate both machines so variance in their approximation from an actual machine is acceptable though undesired.

A simplified schematic of a conventional reach stacker is shown in Figure 2. Note that each actuator has its own load sensing pump. This configuration reduces metering losses to that of the 10 bar marginal pressure, lessening that advantage of DC. Instead of a significant reduction in metering losses, DC's main advantage for the reach stacker is energy recovery.

Table 2 Baseline machine parameters

Lift circuit		Boom circuit	
pump displacement	135 cc/rev	pump displacement	70 cc/rev
max pressure	380 bar	max pressure	380 bar
cylinder bore diameter (x2)	0.2246 m	cylinder bore diameter	0.1374 m
cylinder rod diameter	N/A	cylinder rod diameter	0.0795 m
cylinder stroke	3.037 m	cylinder stroke	5.549 m

**Low pressure system**

pump displacement	20 cc/rev
set pressure	15 bar
accumulator volume	30 l

**LS system**

marginal pressure	10 bar
lift control valve flow (@ 10 bar)	284 lpm
boom control valve flow (@ 10 bar)	147 lpm

**Power shift transmission**

gear 1 ratio	4.10
gear 2 ratio	2.78
gear 3 ratio	1.65
gear 4 ratio	0.85
axle/ final drive ratio	32
tire rolling radius	0.85 m

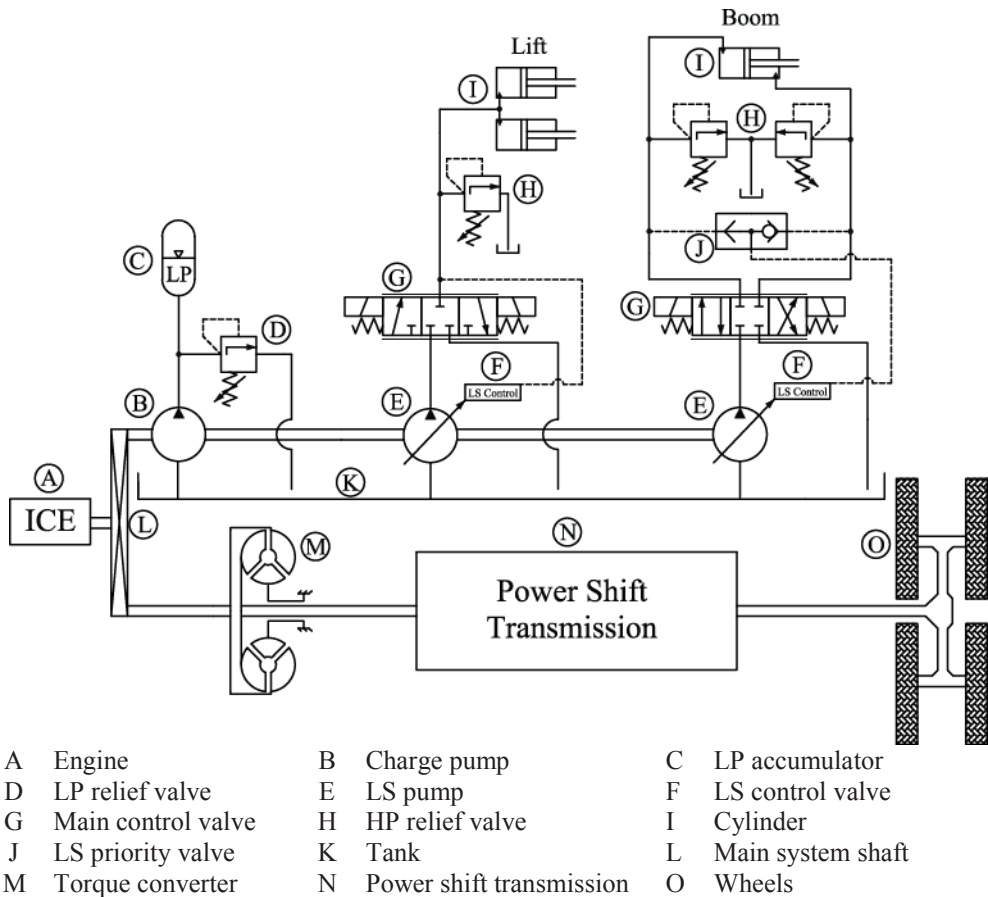


**Figure 2 Conventional reach stacker architecture**

**2.2. DC PST architecture**

A novel circuit (Figure 3) is proposed in this paper, which combines DC actuation and a power split transmission into a single integrated system. Two variations of DC actuation, first proposed by Rahmfeld and Ivantysynova [3], are used for the reach stacker. First the boom cylinder (Q) uses a conventional closed circuit approach by connecting each side of the cylinder directly to a port in the pump (P). Pilot operated check valves (L) compensate for varying flow rates generated by differences in area between the bore and rod sides of the cylinder. The lift cylinders (K) on the other hand use a less common open circuit DC

approach where only the high pressure port of pump (G) is connected with the lift cylinders. Both DC circuits require a low pressure supply provided by charge pump (C) and low pressure accumulator (E). This same low pressure system is used to supply the hydrostatic transmission.

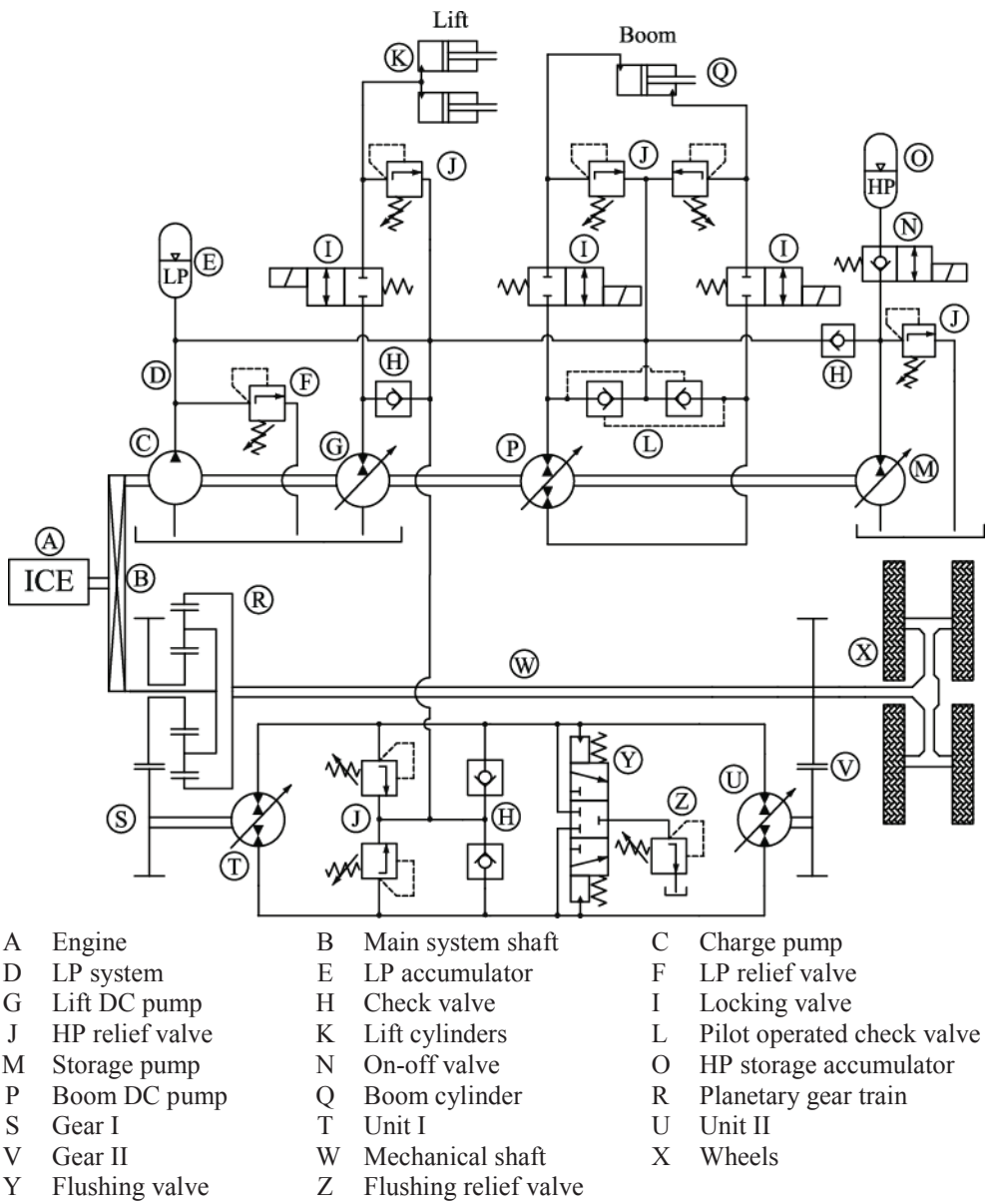


**Figure 3** Proposed reach stacker architecture

The torque converter and power shift transmission have been replaced with an output coupled power split transmission. Power enters the transmission from the main system shaft (B) and passes first through the PGT (R). The PGT serves to split power between the efficient mechanical path (W) and the flexible hydrostatic path. Power is then recombined at the junction of (V) and (W). At low speed all of the transmission power is transmitted through the hydrostatic path. However as vehicle speed increase a greater percentage of power transverse the mechanical path up until all of the power is transmitted in this manner at this vehicle's top speed. Vehicle speed is controlled by adjusting Unit I and II's (T and U's) displacement. An in-depth discussion of power split transmission control and power flow can be found in [6].

A principle concept of this circuit is that recovered energy flows freely between both subsystems. Recovered kinetic energy from the transmission can be used to power the working hydraulics and likewise, recovered potential energy from an aiding load can be sent to the transmission. When recovered energy exceeds current system demand, storage pump (M) is used to store this excess energy in accumulator (O).

Properly sizing the storage system requires a deep understanding of power flows within the system. Of importance is not only the magnitude of energy recovered and subsequently required by each subsystem, but also when each of these events occurs in relationship to one another. Thus optimal sizing is only possible by dynamically considering a given working cycle.

In this paper a systematic approach was taken in which a reference cycle consisting of lowering a 45 t container stacked 5 high was simulated. During this cycle a maximum overrunning torque of 765 Nm was observed. This torque, combined with a 240 bar minimum working pressure, leads to a 200 cc storage pump insuring sufficient resistive torque is always available from the storage pump. The reference cycle was again simulated now with storage pump inline and the accumulator size iteratively increased until all of the system's excess energy was captured. Sizing in this manner led to a 200 l accumulator and ensured all excess recovered energy was captured.

One of the energy storage system's key features is the on-off valve (N). The integrated check valve in the on-off valve's non-energized position allows charging of the accumulator at any time. However when no fluid is being pumped this valve limits the pressure seen by the storage pump to that of the low pressure system. This low differential pressure significantly reduces parasitic losses caused by exposure to the high pressure accumulator. When stored energy is required, valve (N) is energized connecting the accumulator to the storage pump (M), which acts as a motor placing torque back on the main system shaft. The proposed architecture uses the same size hydraulic component as the baseline machine (located in Table 2). Parameters for the power split transmission and energy storage system can be found in Table 3.

**Table 3 Proposed machine parameters**

<b>Power split transmission</b>		<b>Energy storage system</b>	
$i_0, i_1, i_2$	-2.2, 3.5, 1.25	pump displacement	200 cc/rev
Unit I displacement	300 cc/rev	precharge pressure	200 bar
Unit II displacement	300 cc/rev	min working pressure	225 bar
max pressure	380 bar	max pressure	450 bar
axle/ final drive ratio	32	accumulator volume	200 l

### 3. MATHEMATICAL MODEL

A dynamic multi-domain mathematical model was developed in order to compare energy consumption between a conventional machine and a machine outfitted with the new architecture. All modeling and simulation work has been completed in the Matlab Simulink environment allowing for the development of high fidelity machine models. For this study models developed by previous researchers of the author's research group have been used for the LS system [4], the DC system [5], and the PST system [6] and integrated into the two models for the baseline reach stacker and the new proposed system architecture. Due to length restriction of this paper the complete models are not included here.

New in this study is the addition of a model of the power shift transmission. The baseline machine's transmission is composed of two primary components, the torque converter and the transmission gear ratios. Torque converters consist of four main elements; an impeller coupled to the engine, a turbine connected to the transmission, a stator which helps to redirect spent fluid, and a lock up clutch. Torque transmitted through the torque converter is a function of the speed ratio between impeller and turbine. When a high speed ratio exists within the torque converter a torque multiplication occurs due to the stator recycling fluid still possessing kinetic energy. As the turbine speed increase less fluid is recycled through the stator and the torque ratio approaches one. A simplified approach has been chosen to model the torque converter based on empirical data. Known as the K Factor approach, measured speed ratio and resulting torques have been placed in a look up table. This method allows engine and transmission torque to be calculated when both speeds are known.

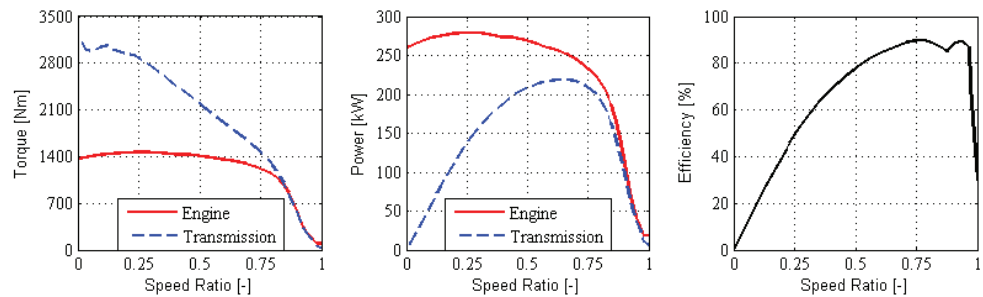


Figure 4 Torque converter performance curves

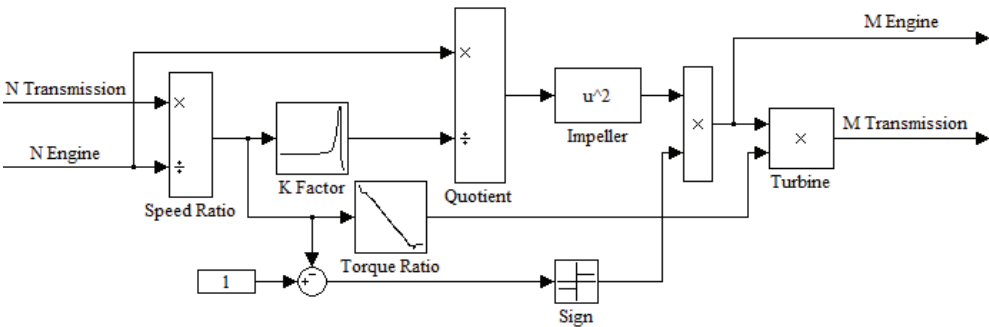


Figure 5 Torque converter model

The fourth major component found in many torque converters is a lock up clutch. When engaged this hydraulically actuated clutch rigidly connects the engine and transmission and allows power to be transmitted mechanically greatly improving efficiency. A more important function exists for this clutch in that while decelerating the torque converter is able to place torque back on the main system shaft. Due to the modeling approach taken (speeds are input, torques are output) a rigid coupling presents difficulties. However if a small level of slip between the clutch plates is allowed ( $< 15$  rpm), torque transmitted through the clutch can be modeled as a function of this slip. Whenever the turbine begins to rotate faster than the impeller, torque is placed back on the engine shaft. Artificial points (above a 1:1 speed ratio) included in the K factor and torque ratio lookup tables along with a sign function were used to represent this function.

The second major component of the reach stacker's driveline is the power shift transmission. This automatic transmission features 4 gear ratios, which can be shifted with minimal loss in power. For this simulation gear up shifts occur when the engine reaches high idle and downshifts when the engine drops below low idle.

#### 4. SIMULATED WORKING CYCLE

Reach stackers operate in varied environments but their typical working cycle can be condensed down into one of two varieties: unloading a truck and stacking the container, or unstacking the container and transferring it to a truck. For both working cycles a standard driving cycle is used. This drive cycle (Figure 6) covers a 100 m path and is indicative of a typical working environment.

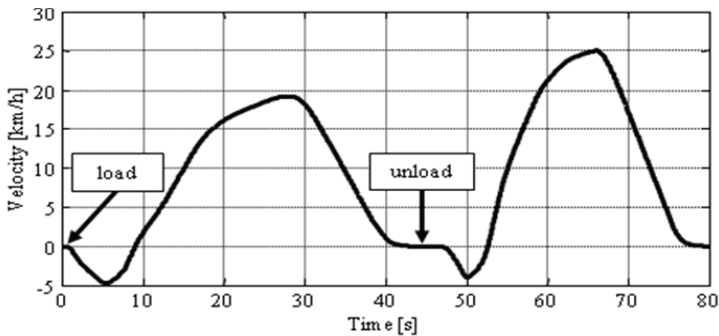


**Figure 6** Standard driving cycle

Reach stackers store and retrieve containers of various weights from numerous distinct stacked positions resulting in a wide range of energy consumption rates. In order to accurately compare the proposed and baseline machines, 12 cycles were chosen based on the maximum permissible container mass at each stacked position (Figure 1). These 12 cycles were simulated for both stacking and unstacking operations. While stacking the cycle begins and ends at a truck (1.2 m high), whereas for the unstacking cycle the operation began and ended at a given container stack position. 24 cycles were thus simulated for both machines resulting in a total of 48 simulations.

Engine speed, and consequently maximum pump flow rate, is continuously changing in the baseline machine due to the power shift transmission. However in the proposed machine, engine and wheel speeds are decoupled thanks to the power split transmission which allows the engine to run at a constant efficient speed. This results in very different maximum pump flow rates in both machines for a given cycle. Instead of determining an actuator position cycle that both machines could meet, a final actuator position was given and the system allowed to reach that point as power and flow permitted.

Properly accounting for differences in the accumulator's state of charge at the beginning and end of the cycle is critical. In order to accurately determine fuel consumption each working cycle was repeated three times. Fuel consumption has stabilized by this point so only results of the final cycle were recorded.



5. RESULTS

Simulation results yield a depended understanding of the differences between both machine configurations. Insight into these differences can be gained by analyzing energy consumption and dissipation within subsystems and individual components. In this paper energy distribution has been visualized using Sankey diagrams. To aid comparison, energy consumption in each machine had been normalized to the energy provided by that machines engine.

An average stacking cycle (stacked three high in the second row) with a mass of 40 tones was selected as a reference cycle for the following discussion. In this cycle the reach stacker moves the container from a truck to the stack using the drive cycle in Figure 6 before returning to the truck. A stacking cycle was selected for clarity even though the proposed machine’s benefits are more pronounced in the unstacking cycle. In an unstacking cycle energy enters the system not only from the engine but also from the potential energy contained in the already elevated container, muddying energy flow. A stacking cycle, while possessing fewer benefits for the proposed machine, only uses energy from the engine.

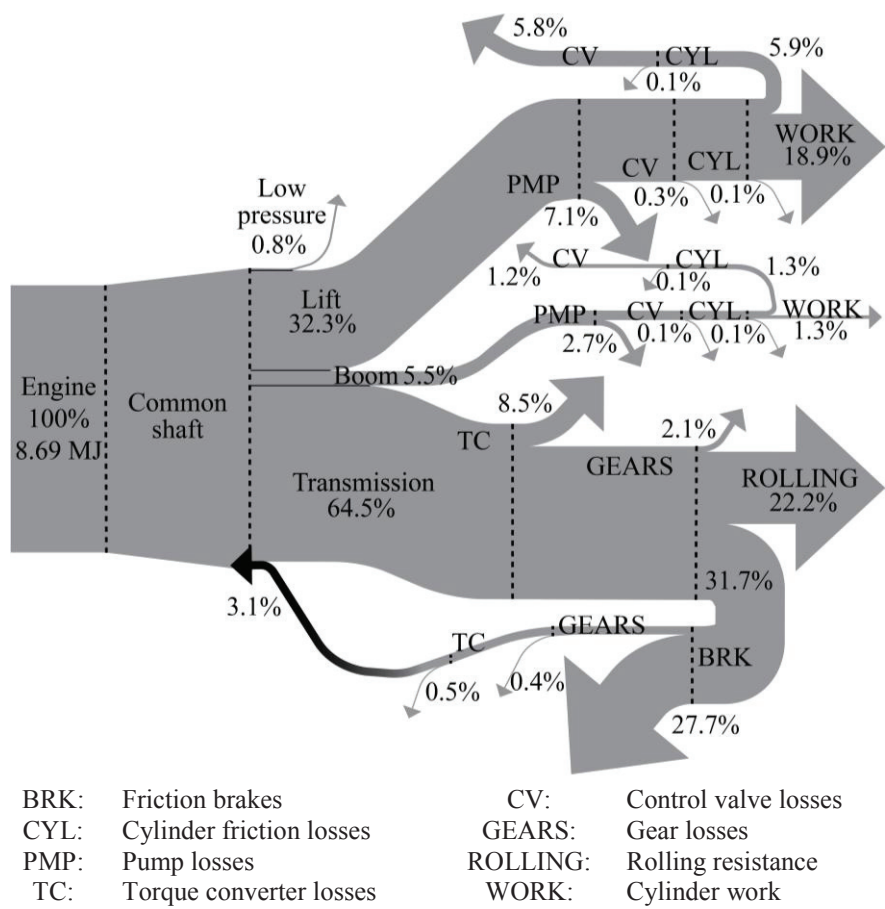


Figure 7 Baseline machine energy distribution

Figure 7 shows the energy distribution during the reference cycle for the baseline machine. It can be seen that all of the 0.63 MJ of energy recovered from lowering loads is dissipated through the control valves and converted into heat. A wasteful process that also requires additional energy to cool, a subsystem not simulated. Also of interest is the 2.41 MJ of energy dissipated through the transmission's friction brakes. The transmission is capable of transferring a larger percentage of this energy back to the common shaft. However as this energy was not immediately required it had to be dissipated.

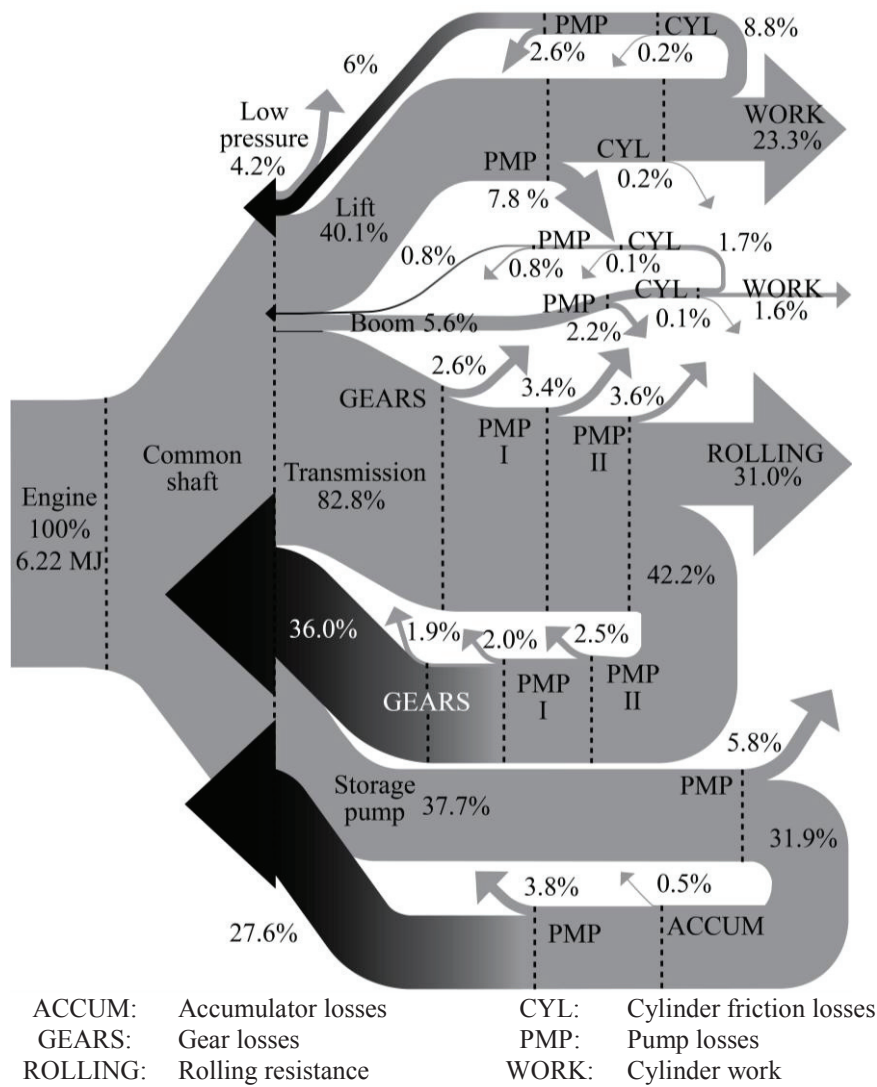


Figure 8 Proposed machine energy distribution

A similar Sankey diagram for the modified machine is shown in Figure 8. Energy consumption for the proposed machine has decreased 28.7% to 6.22 MJ down from 8.69 MJ in the baseline machine. This can be attributed to several factors including 0.42 MJ of energy recovered from lowering loads and 2.24 MJ recovered through regenerative braking. These high levels of recovered energy are possible because the storage pump absorbs 2.34 MJ and release 1.72 MJ of energy back into the system. Further efficiency improvements can be found in the transmission where 35.2% less energy is dissipated while driving. However lower losses are not the main benefit of power split transmissions. PST's decouple the engine and wheel speeds permitting more efficient engine operation and allowing the same quantity of energy to be produced with less fuel. In this paper only the brake energy produced by the engine is considered and thus this advantage of PST's is not investigated.

While Sankey diagrams provide insight into the machine's inner workings, overall energy consumption illustrates the ultimate benefits of these new technologies. Located in Figure 9 is the simulated energy consumption during all 24 cycles for both machines. While unstacking the proposed machine exhibits a significant reduction in energy consumption, up to 72.9%. Additionally during stacking the proposed machine reduces energy consumption by 29.7% on average (down from 47.9% found on average in the unstacking cycle). Over all cycles energy consumed is reduced by 38.0% equating to a 2.89 MJ savings per cycle.

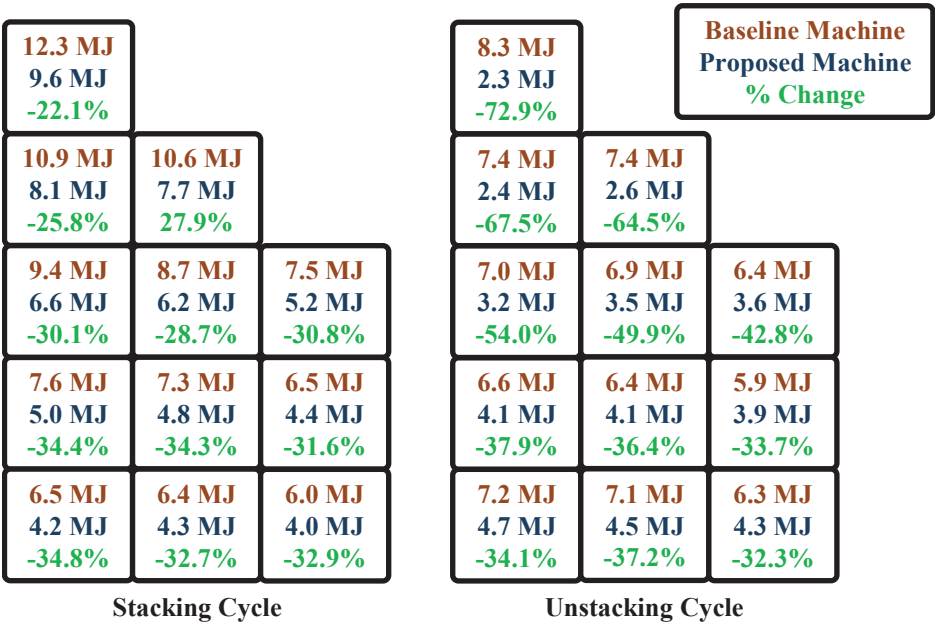


Figure 9 Simulated energy consumption

Over a reach stacker's 1,000,000 cycle life, significant energy and fuel savings are expected. Assuming an average savings of 2.89 MJ/cycle, a 36.4 MJ/l energy density for diesel fuel, and a 40% thermal efficiency for the diesel engine, a lifetime savings of 1,250 barrels of diesel fuel is estimated. At a cost of \$0.99 (USD) per liter this equates to an overall lifetime savings of \$195,000. Any costs incurred by transitioning to the new system architecture will be small in comparison with the estimated fuel savings.

## 6. CONCLUSIONS

This paper investigates a new energy saving hydraulic hybrid architecture for high power mobile machines. To study this new system configuration a reach stacker was chosen as a reference machine. Baseline energy consumption was determined by modeling and simulating a conventional reach stacker with load sensing hydraulics and a power shift transmission. Then a reach stacker outfitted with displacement controlled actuation and a power split transmission was modeled and simulated. An energetic analysis showed the new architecture achieved a significantly decreased energy consumption of up to 73% (38% on average) when compared against a conventional machine. Improvements which result in a lifetime savings of 1,250 barrels of diesel fuel equating to \$195,000 (USD).

Much work still exists which should show increased savings for the new architecture. First an engine model will be included to show the benefits of flexible engine operation afforded by the power split transmission. Future work will include a power management strategy designed to operate the engine in the most efficient manner possible. Further hybridization allows for engine downsizing though load leveling and will be explored. Finally the DC architecture significantly decreases cooling requirements compared to LS. A thermal model of both machines is planned which will show the differences in cooling power.

## 7. LIST OF NOTATIONS

$M$	torque	[Nm]
$N$	angular velocity	[rpm]

## 8. REFERENCES

- [1] **Zimmerman, J., Busquets, E. and Ivantysynova, M.** 2011. 40% Fuel Savings by Displacement Control Leads to Lower Working Temperatures – A Simulation Study and Measurements. *Proceedings of the 52<sup>nd</sup> National Conference on Fluid Power (NCFP)*, Las Vegas, NV.
- [2] **Renius, K. and Resch, R.** 2005. Continuously Variable Tractor Transmissions. *ASAE Distinguished Lecture Series*.
- [3] **Rahmfeld, R. and Ivantysynova, M.** 1998. Energy Saving Hydraulic Actuators for Mobile Machines. *Proceedings of 1st Bratislavian Fluid Power Symposium*, pp. 47-57. Častá – Píla, Slovakia.
- [4] **Zimmerman, J., Pelosi, M., Williamson, C. and Ivantysynova, M.** 2007. Energy Consumption of an LS Excavator Hydraulic System, *Proceedings of 2007 ASME International Mechanical Engineering Congress & Exposition (IMECE2007)*, Seattle, Washington, USA.
- [5] **Williamson, C., Zimmerman, J. and Ivantysynova, M.** 2008. Efficiency Study of an Excavator Hydraulic System Based on Displacement-Controlled Actuators. *ASME/Bath Workshop on Fluid Power and Motion Control (FPMC08)*. Bath, UK.
- [6] **Carl, B., Williams, K. and Ivantysynova, M.** 2006. Comparison of Operational Characteristics in Power Split Continuously Variable Transmissions. SAE Paper 2006-01-3468.



# Fault-tolerant steer-by-wire valve for agricultural tractors based on independent metering with on/off valves

**Dipl.-Ing. David Schmitz and Prof. Dr.-Ing. Marcus Geimer**

Chair of Mobile Machines, Karlsruhe Institute of Technology (KIT), Germany

## ABSTRACT

Nowadays the field of agriculture is driven by a rising demand regarding productivity and turnover, but also regarding driver's comfort, driver assistance and driving safety. One component which contributes to both requirements is the steering system. Whereas the potential of conventional hydrostatic steering systems is nearly exploited electro-hydraulic steering systems are emerging. Especially with existing steer-by-wire systems, to meet the European regulations for on-road steering systems and functional safety regarding fault-tolerance, the system complexity tends to get high.

Based on an analysis of requirements for steer-by-wire systems in tractors this paper presents a novel concept of a hydraulic circuit which satisfies the conflicting requirements of fault-tolerance and low complexity at the same time. In this concept, the principle of independent metering is utilized to provide the steering capability even in the case of hydraulic faults. The independent metering is realized with pulse-width-modulation controlled on/off-valves. For the presented circuit a self-test routine is developed to detect faults in time before hazardous situations evolve. Based on measurements of a hardware-in-the-loop test bench it is shown that faults can be tolerated without additional safety-shut-off valves and even without reconfiguration of the closed-loop controller. Although some faults can reduce the performance of the steering system, the driving safety is always maintained.

**Keywords:** fault-tolerance, independent metering, steering system, steer-by-wire, agricultural tractor, switching valves

## 1 INTRODUCTION

With the improvement of the accuracy of GPS positioning for civilian use in the year 2000, a revolution in the field of agriculture started: Precision farming. To fulfil the need of increased productivity and turnover it is now possible to assist or even automate the guidance of agricultural machinery in order to improve the process of cultivation and thereby save resources and time. Apart from this, a rising demand regarding driver's comfort and driving safety is noticeable, as tractors are used in combination with huge trailers for transportation jobs at higher velocities than decades ago. When it comes to driver's comfort, the optimal design and positioning of all user interfaces inside the cabin as well as a good visibility onto the implements and the land is of great importance (1).

One component which contributes to the above mentioned requirements is the steering system. The hydraulic circuit of a conventional steering system of an agricultural tractor is shown in Figure 1. It is classified as a hydraulic power-assisted steering system with a purely hydraulic transmission of the steering forces at a certain point in the energy transmission. This means, in contrast to passenger and commercial vehicles, that there is no mechanical linkage between the steering wheel and the steered wheels. Apart from the hydraulic power supply, the hydrostatic steering valve is the main component inside this steering system. An integrated user-driven fixed-displacement pump ensures that the flow rate to the steering cylinder is proportional to the angular velocity of the steering wheel during normal operation and that the driver can use his muscular force to pump oil and steer the vehicle in case the power supply is out of order (2). The long-time usage of such steering systems shows that it can be considered as fault-tolerant and safe enough to steer vehicles with a maximum velocity of up to 60 km/h.

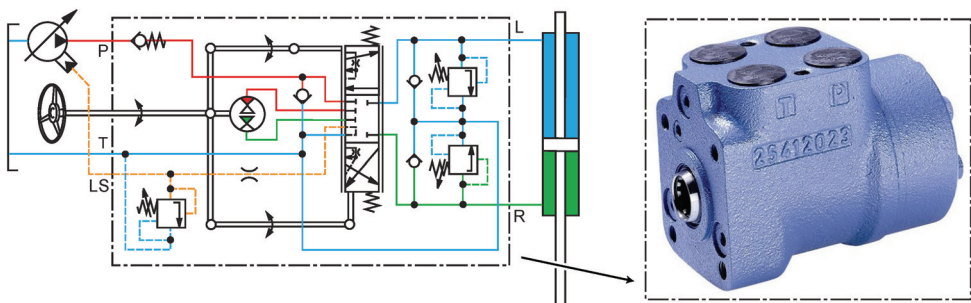


**Figure 1: Hydraulic circuit of a conventional steering system for tractors (2)**

As this steering system is not electrified, the degree of power-assistance is defined during construction and cannot be changed by the driver manually or the vehicle automatically. The steering ratio is determined by the relation between the displacement of the user-driven pump, the size of the steering cylinder and the kinematics of the steering linkage. Thus, a tradeoff has to be achieved between a direct steering for maneuverability at low velocities, an indirect steering for stability at high velocities and low steering control effort in case the vehicle is steered with muscular force. The steering valve itself has to be positioned inside or at the cabin and has to be connected to the steering wheel by a mechanical linkage reducing the degree of freedoms for a modular and flexible cabin design.

To overcome these drawbacks and to be able to implement automatic guidance functionality electro-hydraulic steering systems are emerging, see (3) and (4). The increasing complexity of the steering system and their electronics is the challenging task as the requirements of the customer regarding functionality and of the legislative regarding safety are sometimes contrary to each other. Especially with steer-by-wire systems, to meet the European regulations for on-road steering systems and for functional safety, the system complexity and thereby the costs tends to get high, as in these kinds of steering systems the user request is transmitted purely electronically without any mechanical or hydraulic connection between the steering wheel and the steered wheels. Hence, the power supply of such systems needs to be fault-tolerant and thereby redundant too as the muscular force of the driver cannot be used to steer the wheels<sup>1</sup>.

Goal of this work is to design an electro-hydraulic steer-by-wire system which is fault-tolerant and safe enough on the one hand but which has a low complexity on the other hand. Such a solution improves the relationship between cost and functional benefit and leads to an increased market share of steer-by-wire systems. In addition to this, systems with a lower complexity in hardware and software are less susceptible to systematic faults. This paper deals with the core component of such a steering system: the fault-tolerant hydraulic valve and the steering cylinder. Other important components like the electric and hydraulic power supply, the electronic control unit or the sensors are not addressed here.

## 2 REQUIREMENTS FOR STEER-BY-WIRE SYSTEMS

The requirements for steering systems are mainly based on legislative regulations on the one hand and the functional requirements of the customers on the other hand. The basic legislative requirements are defined in different national and international regulations like the ISO 10998 for agricultural tractors or the ECE-R 79 for vehicles of different kinds in general, see (5) and (6). For steering systems which include electronics additional regulations apply, especially regarding functional safety. Since the second revision of the ECE-R 79 in April 2005, steer-by-wire system with a purely electronic signal transmission of the user request are covered for on-road use. In the following paragraphs only some of the most important requirements for steering systems are mentioned. At the end of each paragraph the requirements for the steering system are transferred down to the hydraulic steering valve and the steering cylinder.

One basic requirement is that steering has to be **easy** and **safe** up to the maximum velocity of the vehicle. During steering there shall be **no vibrations** and **no high steering control effort**<sup>2</sup>. Steering the vehicle in the test manoeuvres defined in ISO 10998 has to be possible without exceeding predefined forces and within a certain time period at a given vehicle

---

<sup>1</sup> Steer-by-wire systems are generally classified as full-power steering systems. In vehicles with full-power steering systems, the vehicle cannot be steered with muscular force according to the requirements pointed out in section 2, because there is no or only little energy transmission between the steering wheel and the steered wheel possible.

<sup>2</sup> According to (5) the steering control effort is the force the driver needs to turn the steering wheel. In contrast to this, the steering force is the force in the energy transmission necessary to steer the wheels.



velocity (5). To fulfil these requirements, the steering cylinder has to be controlled with at least a certain **velocity** and **precision**.

For safety reasons, hydraulic steering systems have to be equipped with pressure limiting valves at the steering cylinder to prevent damage to hydraulic components. As the integrity of the two hoses connecting the steering cylinder to the steering valve is of vital importance these and all other hoses have to be dimensioned to a pressure four times higher than the maximum possible system pressure. It is necessary that even in the event of a single fault the above mentioned steering requirements have to be fulfilled. Thereby all faults in non-mechanical components have to be detectable in order to alarm the driver in time. Additionally to these requirements ISO 25119 defines requirements for the development process of such a system concerning functional safety (7). Particularly with regard to the steering valve it has to be analyzed which kinds of faults can occur and how they can be detected. If fault-tolerance can be guaranteed for a certain period of time it is not compulsory to detect every fault immediately but within an appropriate time interval which has to be much shorter than the time period of fault-tolerance. Further it is specified that after the occurrence of faults, changes in steering ratio are acceptable but abrupt changes in steering angle are not.

Apart from these basic steering requirements additional requirements regarding the functionality of the steering system come along by the customers. These requirements are very specific for agricultural tractors. Reasonably, the functionality of **automatic guidance** is most important to relieve the driver and improve the process quality during cultivation. In some cases it is also beneficial if the tractor is used in reverse to enhance the manoeuvrability and visibility onto the implements. In these vehicles, the driver has the possibility to **turn the seat** or even the complete **cabin** to drive backwards for a long time comfortably. In addition to this, the steering control effort at low velocities and the driving stability at high velocities of the tractor can be improved by implementing an **adaptive steering ratio** or even an **adaptive steering control effort** (8). Furthermore, the electronification of the steering system can be used to implement **automatic stability systems** or **different input devices** (f.e. joystick instead of steering wheel). All these requirements are a motivation to implement a closed-loop position controller for the steering cylinder in which the reference value is calculated to meet the above mentioned functionality. Benefits of such a closed-loop control are the inherent **compensation of nonlinearities** and **disturbances**<sup>3</sup>.

In general, the necessary velocity of the steering cylinder to carry out fast headland-turns or to manoeuvre at low speeds is higher than the requirements from ISO 10998. This leads to the fact that degradations in steering performance after the occurrence of faults are acceptable as long as the legislative requirements are fulfilled and the vehicle can be steered safely. While the maximum velocity of the steering cylinder can be specified for a certain type of machinery quite easily, the required precision that results in an easy and safe steering feel is subjective and hard to define. It has to be considered that in both of the

---

<sup>3</sup> In the conventional steering system described in section 1, there is no fixed relation between the angle of the steering wheel and the steering angle of the steered wheels. The main reasons for this are the internal hydraulic leakages in combination with the missing mechanical connection between both elements.

steering modes, “automatic guidance” and “manual operation”, an overlaying trajectory controller is active. In case of the automatic guidance, it is an electronic trajectory controller, based on GPS for example, and in case of the manual operation it is the driver of the vehicle himself. Obviously the steering comfort decreases with a decreasing precision. If the precision gets too low the requirement of an easy and safe steering cannot be fulfilled anymore. Apart from this, the manoeuvrability is also influenced by properties of the closed-loop control like overshoot, time delay, etc. (9).

### 3 FAULT-TOLERANT STEER-BY-WIRE VALVE

When designing a fault-tolerant steering valve it has to be considered that every component can fail, even if the residual probability of failure is quite small. Regarding hydraulic valves, the two following worst-case faults are dominating: the valve is closed and cannot be opened anymore (**fault type A**) or the valve is opened and cannot be closed anymore (**fault type B**). An exemplary cause for fault type A can be a cable break while a cause for fault type B can be a particle contamination or a permanent actuation because of an error in the electronics. The threat of fault type A in combination with the requirement of manoeuvrability even in the case of any single fault leads to a redundant architecture with two independent channels, for example. Faults of this type can be compensated with a robust controller in a two-channel-architecture very easily. To account for faults of type B, existing concepts use an active fault-tolerant controller architecture in which the system is reconfigured to guarantee the manoeuvrability. In contrast to this, the novel concept proposes a passive fault-tolerant controller which is able to ensure the manoeuvrability inherently without fault-detection and reconfiguration.

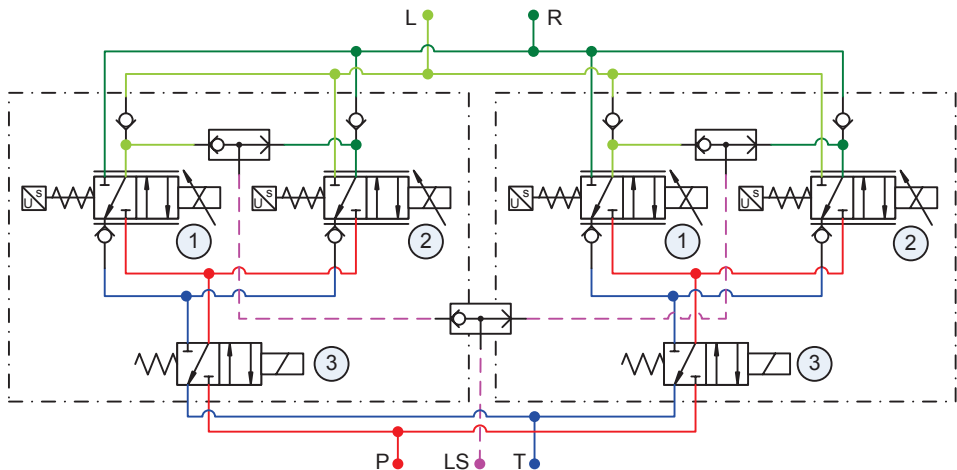


**Figure 2: Main part of the hydraulic circuit of a state of the art steer-by-wire valve for agricultural tractors (10)**

#### 3.1 State of the art concept

In (4) and (10) a fault-tolerant steer-by-wire system is presented. The main part of the hydraulic circuit of the steering valve is shown in Figure 2. It is composed out of two

independent and identical channels. Each of them mainly consists of two directional valves for steering to the left ① and to the right ② and one safety-shut-off valve ③. This shut-off valve ③ is used in case of fault type A or B to completely deactivate the faulty channel. In order to deactivate the faulty channel each of the four directional valves ① and ② have to be monitored by position sensors to isolate the fault and determine the faulty of the two channels. This fault-detection, fault-isolation and reconfiguration has to be reliable and finished in time before hazardous steering cylinder movements can occur. In this concept six 4/2-directional valves (18 metering edges) with six coils, four spool position sensors, eight high-flow check-valves and three shuttle valves are necessary in total.

### 3.2 Novel concept

The goal of the novel concept for a fault-tolerant steering valve is to reduce the complexity and thereby the costs without losing the manoeuvrability after faults of type A and B. To accomplish this, a passive fault-tolerant controller instead of an active fault-tolerant one shall be used. A passive fault-tolerant controller compensates faults inherently by its robustness. Thus no immediate fault-detection, fault-isolation and reconfiguration is necessary. Speaking in terms of components, the spool position sensors and safety-shut-off valves might be obsolete. To design a closed-loop controller which is robust enough to compensate faults of type B, the effect of such a fault has to be kept as low as possible. In the above mentioned concept one fault of type B in the main directional valves leads to an unintended movement of the steering cylinder as the pressure supply is connected to one chamber and the tank reservoir to the other one. The hydraulic circuit of the novel concept, which is shown in Figure 3, makes use of the concept of independent metering to achieve fault-tolerance with a robust controller without reconfiguration. Even in the case of fault type B at one single valve the steering cylinder does not move when the other valves are de-energized.

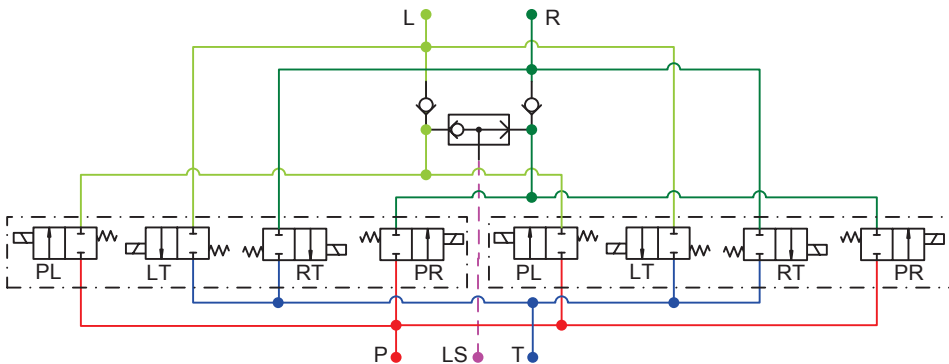


Figure 3: Main part of the hydraulic circuit of the novel steer-by-wire valve

The valve consists of two identical and independent channels with one valve per metering edge each. Thus, with one individual channel the steering cylinder can be moved in both directions. For each of the eight valves, one with a very low complexity is chosen: A 2/2 directional on/off-valve in poppet style. Using this valve type, because of the low complexity and the poppet style, the robustness against particle contamination is higher compared to spool-type valves. To be able to move the cylinder continuously with a certain velocity requested by the driver, the on/off-valves are “proportionalized” using the pulse-

width-modulated control scheme according to (11) and (12). In contrast to this, using the PCM control theory only four ( $2^2$ ) different cylinder velocities would be realizable using two valves per metering edge<sup>4</sup>. As the controller is supposed to be robust enough to compensate one fault of type A or B inherently without reconfiguration, position sensors at each valve and safety-shut-off valves can be omitted, as no immediate fault-detection, fault-isolation and reconfiguration is necessary. This is true under the assumption that faults can be detected during initialisation and periodically using an active self-test routine. After the detection of faults the driver should be alarmed and the vehicle should be forced to reach a safe state automatically<sup>5</sup>. In total this concept uses eight 2/2-directional on/off-valves (8 metering edges) with eight coils, two high-flow check valves and one shuttle valve.

To summarize two main assumptions regarding the novel concept are specified, which will be evaluated in the following section:

1. Fault-tolerance: Single faults of type A and B can be compensated by a robust controller inherently without losing the safe manoeuvrability
2. Fault-detection: Faults of type A and B can be detected without position sensors at each individual valve

#### 4 PROOF OF CONCEPT

In this section, the two assumptions regarding fault-tolerance and fault-detection are evaluated. For this purpose, a hardware-in-the-loop test bench is used. It is built up of a variable pressure LS-pump for the steering valve, the fault-tolerant steering valve itself and a steering cylinder. The pressure drop over the inlet valves is kept constant using a pressure compensator. An additional load cylinder, which is connected by a load cell to the steering cylinder, is used to induce external forces. These forces represent the steering forces of the real vehicle.

To control the steering valve and the load cylinder, a real-time electronic control unit is used. For the closed-loop position control of the steering cylinder the actual position is measured and compared to the reference value, which can be generated automatically or manually by the user with an electronic steering wheel. Based on this information, the controller calculates and outputs the necessary control signal for each valve. To control the external force, the measured signal of the load cell is evaluated and compared to the corresponding reference value, in order to control the pressure in the two chambers of the load cylinder. A simplified load model is implemented in the electronic control unit to calculate the reference value of the external force. The parameters of this model can be adjusted to account for different driving conditions like manoeuvring with a low velocity or

---

<sup>4</sup> For more information on the control of on/off-valves using PWM and the PCM control scheme used in the so-called Digital Flow Control Units see (13).

<sup>5</sup> The vehicle is considered to be in a safe state as soon as the velocity of the vehicle is smaller than a certain limit. For a given vehicle this limit is defined as the velocity at which the vehicle can be brought safely to standstill by braking in the case of a complete loss of manoeuvrability.

driving on the street with a high velocity. Because of the coupling between the tires of the vehicle and the ground, the steering forces are the highest if the vehicle is at standstill.

#### 4.1 Closed-loop control using on/off-valves

The on/off-valves in the novel concept are controlled with the PWM control scheme described in (12). Using this control technique, it is possible to adjust the flow rate through an on/off-valve very precisely and without hysteresis within the so-called “ballistic” operation mode. In this mode the piston of the on/off-valve starts to move whenever the PWM actuation signal is rising but does not reach the upper end stop because the impulse length is chosen to be small. Doing this, the volume flow can be adjusted by changing the duty cycle and thereby the impulse length. An exemplary characteristic curve of an on/off-valve using this control technique is shown in Figure 4 (ballistic mode between  $g = 0.19$  and  $g = 0.27$ ). In this figure, the relationship between the duty cycle of the control signal and the normalized flow rate is shown. It is noticeable that only the proportional part in the ballistic operation mode is suitable for a precise closed-loop control.

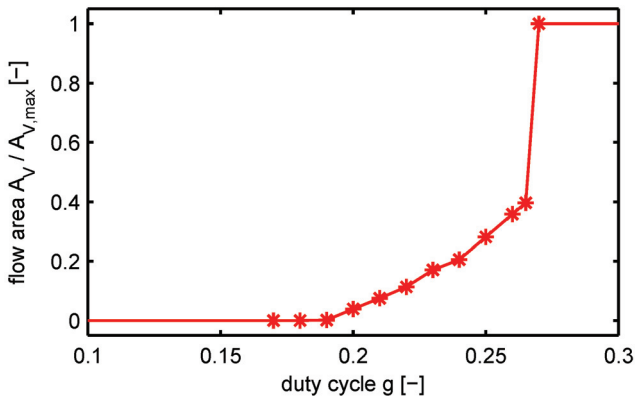


**Figure 4: Measured characteristic curve of an on/off-valve with a volume flow of 14 l/min at a pressure drop of 10 bar using PWM control (12)**

In order to evaluate the two assumptions a simple proportional controller is used, as the plant is characterized by an integral behaviour. It must be said that finding optimal control parameters in order to optimize the characteristic curve and the closed-loop position control is not part of this article. Inside the controller the characteristic curve of the on/off-valve is used to calculate the optimal control signal for a given output signal of the controller. Depending on the desired direction of motion the corresponding inlet and outlet valves are actuated. For reasons of simplicity the inlet and outlet valves are not controlled individually but in a certain relationship.

Figure 5 shows experimental results of the closed-loop controller in nominal conditions with high steering forces (representing a vehicle at standstill). In the first row the actual and the reference value of the steering cylinder and the control error is shown, in the second row the supply pressure and the pressures in both cylinder chambers are compared. The supply pressure is shown unfiltered to see the pressure oscillations, the two chamber pressure are filtered in order to see the mean value. On the one hand, it is obvious that the position of the steering cylinder can be controlled continuously by using on/off-valves with

PWM-control. On the other hand, the measurements of the pressure signals show pressure oscillations corresponding to the frequency of the PWM-control signal. Along with these pressure oscillations noises occur, which might have to be damped by an optimal integration of the valve block into the machine. As the pressure oscillations also occur in the power supply, other hydraulic systems connected to this power supply have to tolerate these too. For the on/off-valves each pressure pulse is the result of one switching cycle. Even though switching cycles in the ballistic operation mode are not that stressful compared to complete switching cycles the fatigue life of the on/off-valves has to be very high to withstand this stress.

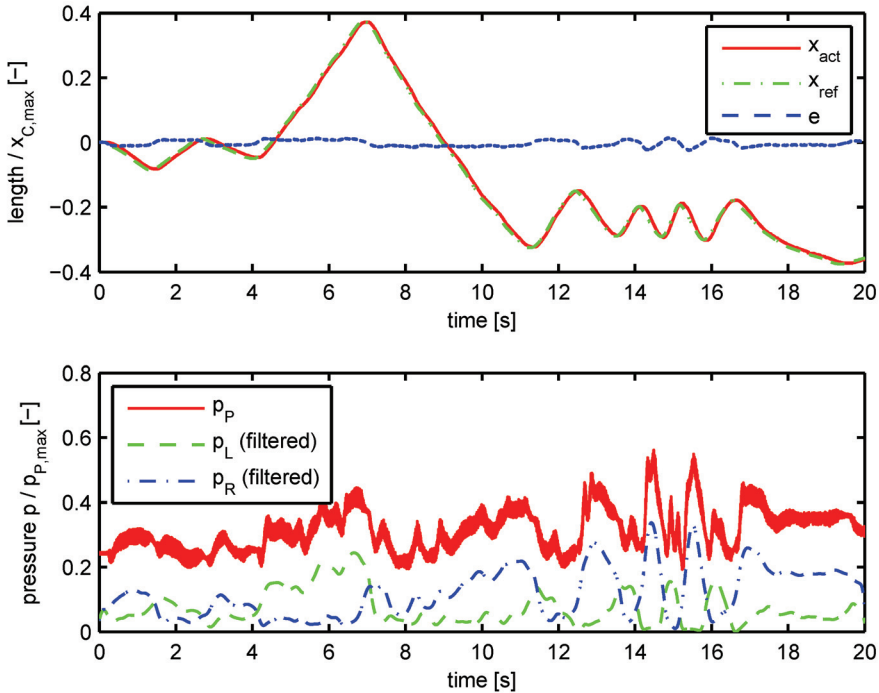


**Figure 5: Experimental closed-loop control of steering cylinder and corresponding system pressures using a user-defined reference signal with high steering forces representing a vehicle at standstill**

## 4.2 Fault-tolerance

In the following evaluation of assumption 1, “fault-tolerance” faults of type A are neglected. The reason for this is the fact, that valves which cannot be opened anymore influence the performance of the steering valve only very little. Whereas faults of type A at outlet valves only lead to increased system pressures, faults of this type at inlet valves result in a reduction of system amplification of only 50%<sup>6</sup>. Generally a closed-loop controller can compensate such a reduction using higher control signals without any problems. As the requirements from the tractor manufacturer regarding volume flow are higher than the

<sup>6</sup> A reduction of system amplification of 50% means, that the volume flow at a certain control signal is reduced from  $Q$  to  $Q/2$ .

legislative requirements a reduction of the maximum steering velocity of 50% is not safety-relevant. Depending on the controller type, faults of type A may result in an increased tracking error or static control error.

Considering faults of type B at outlet and inlet valves, the two load cases I and II in Figure 6 illustrate the worst-case effects of both faults under the assumption of static conditions in an open-loop control. The annotation “1x” and “2x” at each valve in Figure 6 indicates that two fault-free valves per metering edge can be opened while only one valve is faulty at the same time. In load case I, the incoming oil flow from the pump and the pressure  $p_L$  is reduced because of the faulty opened outlet valve at the inlet. The higher the external force, the higher the pressure  $p_L$  and the higher the pressure difference at the faulty outlet valve. This increase of the pressure difference results in a higher flow rate, thus reducing the maximum velocity of the steering cylinder. In contrast to this the faulty opened inlet valve in case II has no influence on the maximum speed of the cylinder for low external forces. The faulty valve requests an additional oil flow from the power supply leading to a higher pressure  $p_R$ , compared to case I. With an increasing force, the maximum velocity of the steering cylinder in case II is reduced as soon as the pressure or flow rate limitation of the pressure supply is reached.

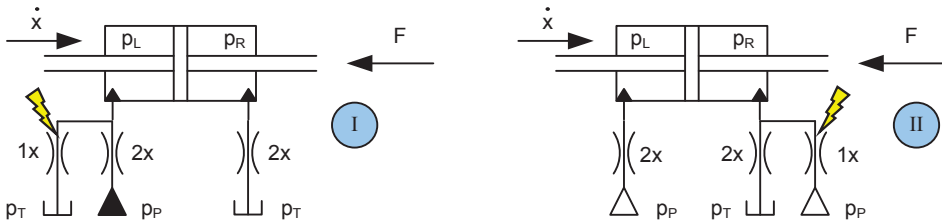


**Figure 6: Schematic representation of fault type B at outlet valve (case I) and at inlet valve (case II) with external forces counteracting the movement of the cylinder**

With the assumption of static conditions and friction-less movement using the equation of force equilibrium at the steering cylinder [1], the equation for the flow rate through the valves [2] and the equilibrium of flow rates at port L and R, the maximum velocity of the steering cylinder in both cases can be calculated analytically with respect to the steering force.

$$p_L = p_R + \frac{F}{A_C} \quad [1]$$

$$Q = c \cdot A_v \cdot \sqrt{\Delta p} \quad [2]$$

In Figure 7 the solution for this nonlinear system of equations for both cases is shown for typical parameters of a steering system. All pressures are normalized with the maximum pump pressure  $p_{P,max}$  while all flow rates are normalized with the maximum inlet flow rate of the steering cylinder in a fault-free situation  $Q_{C,max}$ . The external force is normalized with the maximum force  $F_{max}$  which the steering cylinder can apply without any faults. An additional horizontal line indicates the minimum flow rate necessary to fulfil the legislative



regulations. At any point where the curve of  $Q_C$  is below this dotted line the wheels cannot be moved fast enough. The results shown in Figure 7 represent the main effects explained at the beginning of this section: In case I the constant flow rate of the pump is split into a part flowing into the cylinder and one flowing back to the tank; in case II the flow rate into the cylinder is constant until the pressure or flow rate limitation of the pump is reached. The oil flow through the inlet valves in case I is constant because their pressure drop is kept constant by a pressure compensator.

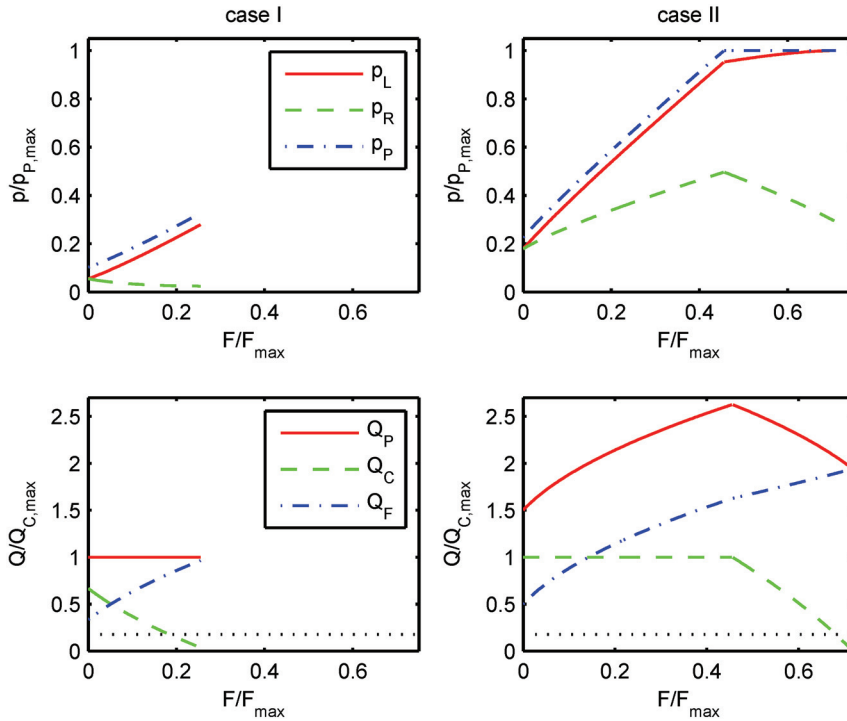


**Figure 7: Effect of fault type B in case I and II calculated analytically**

To interpret these results it is necessary to know that the steering forces  $F/F_{\max}$  are below 0.2 for a slalom maneuver at a velocity of about 25 km/h, for example. A maneuver like this would still be possible with a fault of type B. Otherwise, if the steering forces are higher because the velocity of the vehicle is very low, the risk potential of a steering cylinder that moves not fast enough is not that high. Comparing case I and II, the results show that case II is less critical, if the pump is capable of supplying higher flow rates than the maximum flow rate  $Q_{C,\max}$ . In vehicles where the steering and other consumers are supplied by the same hydraulic pump, these flow rates are tolerable in the very rare event of fault type B. The measurement of case I shown in Figure 8 provide equivalent results than the analytical one shown above.

Beside the analysis of the maximum steering cylinder velocity in case of fault type B in static conditions and open-loop control, these faults are also evaluated on the test bench during closed-loop position control. The faults are applied by a manual activation of the corresponding valve to a full open position and excluding it from the closed-loop control.



As an example for the other measurements, Figure 9 shows the experimental results of fault type B in case I and II without steering forces. The reference curve for the cylinder position represents a slalom maneuver. It is shown by the measurements that even in the rare event of a fault of type B the steering cylinder can be moved in both directions without reconfiguration. In case I, resulting from the steep part of the characteristic curve of the on/off-valves, a small and stable oscillation occurs whenever the position of the steering cylinder is increasing. Because of the elasticity of the tire and the inertia of the vehicle these steering cylinder oscillations should not influence the safe maneuverability of the vehicle.

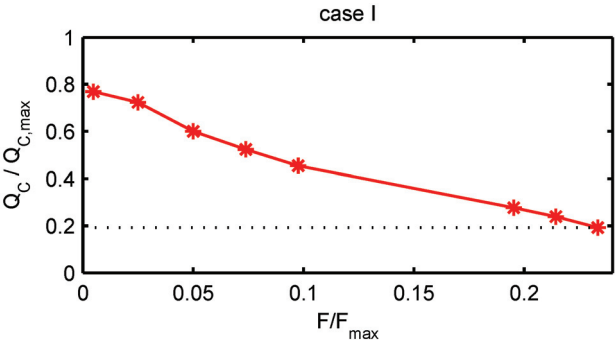


Figure 8: Effect of fault type B in case I measured on test bench

Referring to assumption 1 “fault-tolerance”, the analytical and experimental results indicate that the steering cylinder can be moved in both directions with an adequate speed even in the rare event of faulty opened valves (fault type B). Depending on the control strategy of the on/off-valves, the control performance is reduced but still good enough to bring the vehicle to a safe stop or to drive the vehicle to a workshop with a reduced and thereby safe vehicle velocity. It is important to point out that in every fault case the fault compensation is done by the closed loop controller itself without an increase of the steering control effort for the driver. In future work vehicle tests are essential to finally prove assumption 1.

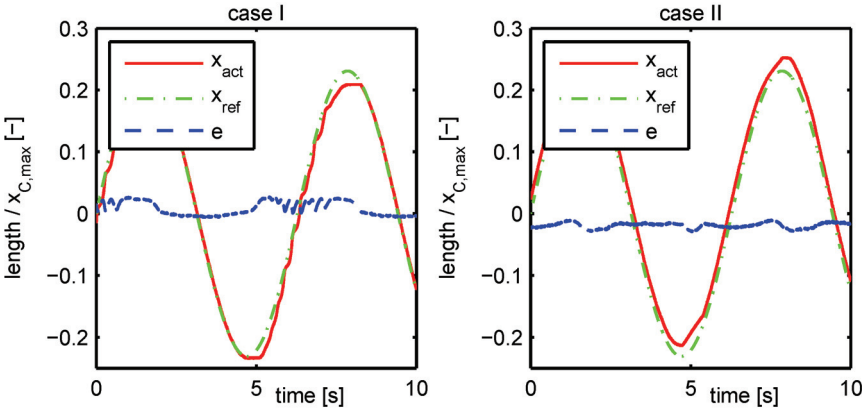
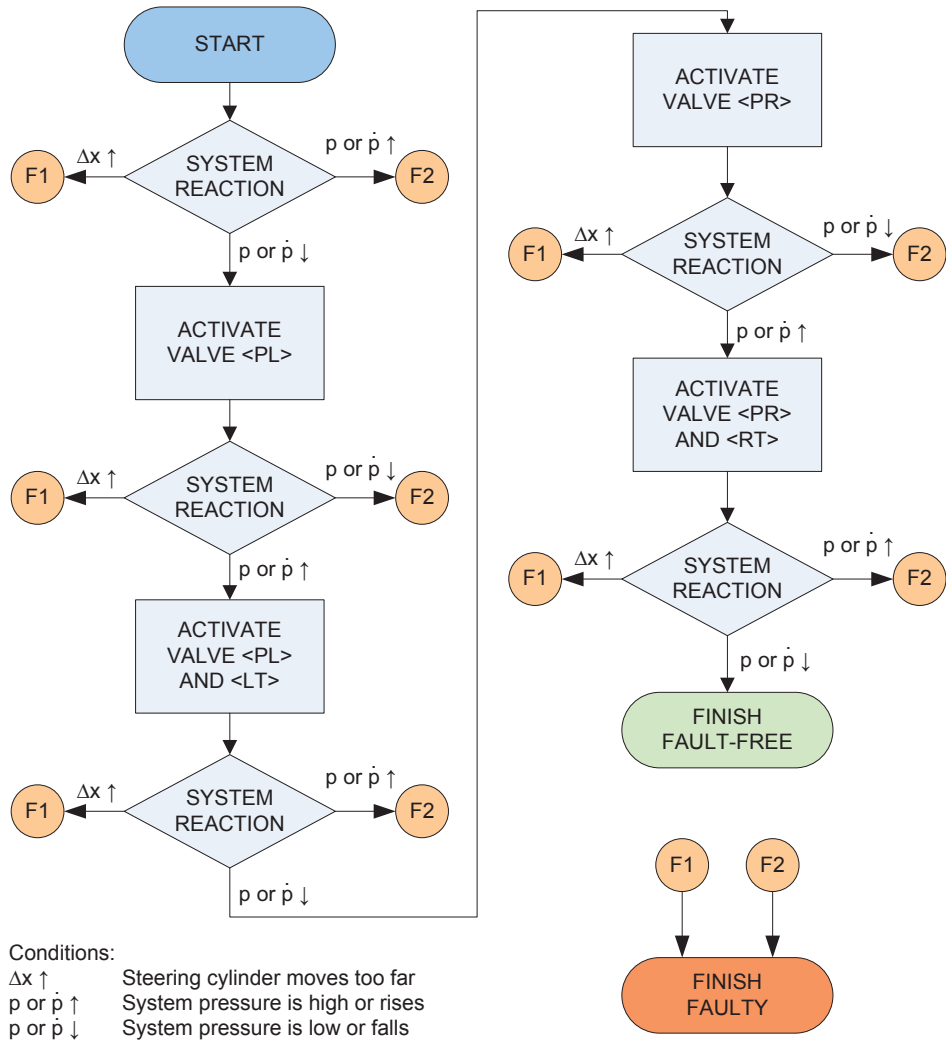


Figure 9: Experimental result of fault type B in case I and II without steering forces

### 4.3 Fault-detection

Beside the fault-tolerance, the evaluation of assumption 2 “fault-detection” is of great importance. Undetected faults within the steering could lead to an accumulation of additional faults during the usage of the vehicle, which may result in hazardous situations.



**Figure 10: Flow-chart for a self-test routine for one single channel of a steer-by-wire valve with independent metering**

To detect faults of type A and B in the novel concept a self-test routine is proposed which can be started during the initialisation of the steering system and periodically from time to time when the vehicle is at standstill. Priority for the self-test is a robust detection whether the steering system is faulty or not, in order to alarm the driver and force the vehicle into a safe state. Less important is the isolation of each fault down to an individual valve, as the controller is fault-tolerant without reconfiguration. Important for a self-test routine is the

requirement that no hazardous situations are caused by the test itself. Applied to the steering system this means that the self-test must not cause hazardous movements of the steering cylinder.

In (14) a self-test routine for a digital hydraulic system using individual pressure sensors at the cylinder ports is presented. The self-test routine proposed in this paper uses the characteristic of a variable pressure supply system that the pressure in the supply line changes whenever the pressure at one of the ports L or R changes because of incoming or outgoing oil flow. As all metering edges can be actuated individually, the steering cylinder does not move significantly while oil is flowing in or out at only one port while the valves connected to the other port are de-energized. Just in the rare case of fault type B a cylinder movement is possible. The beginning of the movement can be detected immediately using the position sensor at the steering cylinder to initiate a shut-down of the remaining valves. Doing this, a hazardous movement is successfully prevented. The flow-chart shown in Figure 10 illustrates one variant for such a self-test routine.

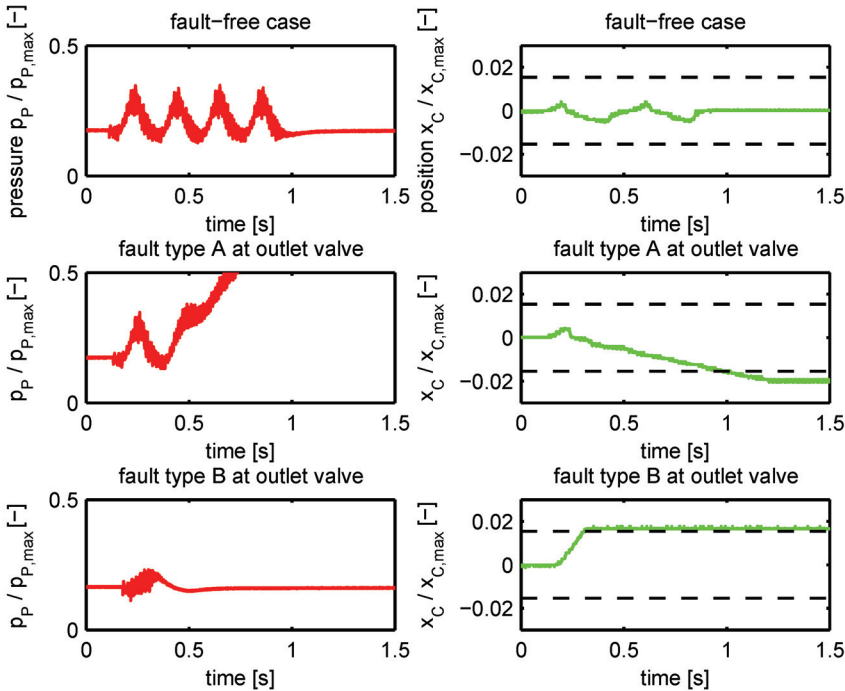


**Figure 11: Experimental results of system pressures and cylinder position during the self-test routine (row 1: fault-free system; row 2: fault type A at outlet valve; row 3: fault type B at outlet valve)**

After the specification of the test, the flow-chart was implemented into the electronic control unit of the test bench and evaluated under realistic conditions. The measurement results of the fault-free and two faulty cases are shown in Figure 11. Corresponding to the different steps in the flow-chart the system pressure rises and falls consecutively. During

the test, the position of the steering cylinder shows only little movement, which is caused by the compressibility of the fluid. In case of fault type A at an outlet valve, the pressure will not fall when the corresponding valve is activated, thus indicating that a fault is present. Opposite to this, fault type B at an outlet valve prevents a rise of the system pressure and leads to a cylinder movement when an inlet valve on the opposite cylinder chamber is activated. The movement is detected fast enough and can thus be stopped by closing the inlet valve instantly.

Because of the experimental results of the self-test, it can be stated that valve faults can be detected in the given hydraulic system without position sensors at each valve (assumption 2 “fault-detection”). When transferring this test on a real vehicle it has to be optimized to find a trade-off between robustness and runtime of the self-test routine

## 5 SUMMARY AND OUTLOOK

In this paper a novel concept for a fault-tolerant electro-hydraulic steer-by-wire valve is presented. To reduce the system complexity, a concept with independent metering edges is chosen. The experimental results show that it is possible to tolerate faults with a robust closed loop controller inherently and without reconfiguration and that fault-detection with a self-test routine works. Because of this, safety-shut-off valves and position sensors at each control valve are dispensable.

To keep the complexity as low as possible, 2/2-directional poppet-type on/off-valves are used and controlled with a PWM signal. Because of the switching of the poppet, pressure pulses and thereby noises occur in the hydraulic system, which might have to be damped. Additionally, the fatigue life of each on/off-valve has to be very high in order to withstand the stress of the continuous switching. Although on/off-valves are used, because of the PWM control scheme, the average movement of the steering cylinder can be controlled continuously. As one of the two individual channels of the steering valve is not shutdown in the case of a fault type B, the steering performance is reduced in such situations, depending on the level of the steering forces.

Future work will deal with the quantitative and qualitative safety requirements of the overall steering system. Of particular importance is the question, how frequently the proposed self-test has to be initiated to reduce the risk of an accumulation of faults to an acceptable limit.

## NOMENCLATURE

A	$\text{m}^2$	area
c	$\frac{\text{m}^2}{\text{s} \cdot \sqrt{N}}$	proportional factor in equation [2]
e	m	control error
F	N	force
g	-	duty cycle
p	bar	pressure
Q	l/min	flow rate
t	s	time
x	m	steering cylinder position

## INDICES

act	actual value
max	maximum value
ref	reference value
C	cylinder
F	faulty losses
L	left chamber
P	pump
R	right chamber
T	tank
V	valve

## ABBREVIATIONS

GPS	global positioning system
LS	load-sensing
PCM	pulse-code-modulation
PWM	pulse-width-modulation

## REFERENCES

- (1) **Kleffmann, B.:** *Development of a Modular Cabin Concept for Selfpropelled Machines*, in: LAND. TECHNIK Agricultural Engineering, 2007
- (2) **Bosch Rexroth AG:** *Load-Sensing Lenkaggregat*, poster from <http://www.boschrexroth.com/various/utilities/mediadirectory>, 2000
- (3) **Pudszuhn, R.:** *Elektrohydraulische Lenksysteme*, in: Elektronisch-hydraulische Systeme, Ed. Bartz, W.; Mesenholl, J. and Wippler, E., Kontakt & Studium, volume 683, 2008
- (4) **Schick, T. and Kearney, J.:** *“Steer-by-Wire” for Large Row Crop Tractors - John Deere 8R Series Tractors*, in: 68. Internationale Landtechnik Tagung, 2010
- (5) **International Organization for Standardization:** *ISO 10998 - Agricultural tractors - Requirements for steering*, second edition 2008-06-01
- (6) **United Nations:** *ECE Regulation No. 79 – Uniform provisions concerning the approval of vehicles with regard to steering equipment*, revision 2 2005-04-21
- (7) **International Organization for Standardization:** *ISO 25119 - Tractors and machinery for agriculture and forestry - Safety-related parts of control systems*, first edition 2010-06-01
- (8) **Crow, S.:** *Steer-by-Wire: A technology for tomorrow, or today?*, in: Proceedings of the 51st National Conference on Fluid Power (NCFP I08-8.3), 2008
- (9) **Koch, T.:** *Untersuchungen zum Lenkgefühl von Steer-by-Wire Lenksystemen*, PHD-Thesis, Technische Universität München, 2010
- (10) **Schick, T.; Wallestad S.; Herbst B.; Becker M. and Müller B.:** *Hydraulic circuit for a steer-by-wire steering system*, United States Patent Application Publication US 2008/0087014, 2008
- (11) **Wennmacher, G.:** *Untersuchung und Anwendung schnellschaltender elektrohydraulischer Ventile für den Einsatz in Kraftfahrzeugen*, in: Aachener Beiträge zum Kraftfahr- und Maschinenwesen, Verlag der Augustinus Buchhandlung, volume 9, 1996
- (12) **Schepers, I.; Schmitz, D.; Weiler, D.; Cochoy, O. and Neumann, U.:** *A novel nodel for optimized development and application of switching valves in closed loop control*, in: International Journal of Fluid Power, Volume 12 Number 3, 2011
- (13) **Linjama, M.:** *Digital Fluid Power – State of the Art*, in: The Twelfth Scandinavian International Conference on Fluid Power, May 18-20, 2001, Tampere, Finland
- (14) **Siivonen, L.; Linjama, M.; Huova, M. and Vilenius, M.:** *Pressure Based Fault Detection and Diagnosis of a Digital Valve System*, in: Power Transmission and Motion Control, 2007



# Generation of power transmission architectures for redundant actuators

**Amine FRAJ, Jean-Charles MARE and Marc BUDINGER**

Université de Toulouse; INSA, UPS, Institut Clément Ader

135, avenue de Rangueil, F-31077 Toulouse, France

Corresponding author: fraj@insa-toulouse.fr

Phone +33 (0)5 6155 9704, fax +33 (0)5 6155 9700

## ABSTRACT

The design of actuation systems faces the problem of the definition and selection of the power transmission architecture in the very early stages of the project. This is emphasized when redundancy requirements apply, extending as a consequence variety of the candidate concepts. Up to now, this task was based on the experience and expertise of the designers: candidate architectures were proposed on basis former projects, including recombination of concepts or technologies. When multiple requirements are to be met, especially for embedded applications such as aerospace, this "bottom-up" approach may undergo large loop validation and generates minor innovation. On the opposite side, a "top-down" approach is more opened but must consider with care the maturity of the concepts and technologies that are involved by the proposed power architectures.

The research reported in this paper deals with a method for automatic generation and selection of candidate solutions in the presence of specific requirements. It particularly applies to redundant power architectures for electromechanical and electro-hydraulic actuators, depending on the desired response to failure (passive, neutral, freeze). The communication will begin with the presentation of the issue for decision making, regarding the architecture of an aerospace actuator power transmission under reliability, security, mass, integration and power capability constraints. The second part will focus on the proposed practical methodology for identifying the candidate architectures and its implementation as an automated tool. The interest of the proposed approach will be finally illustrated using a typical application that relates to position actuation with fail neutral capability.

**Keywords:** actuator, architecture, reliability, systematic.

## 1 INTRODUCTION

The study presented in this paper has been conducted in the frame of the project SYRENA (Système de regulation nouvelle architecture). The aim of this project is to develop and test a hydraulic and an electrically powered actuator system allowing air flow regulation in a helicopter turbine. This offers significant operation gains and increases the turbine



efficiency. The reported work focuses on the design of the EMA and EHA to be embedded into a new generation of turbines. Towards the more efficient regulation system in helicopter turbine, this challenging project must provide a technology step change, improving the system safety and reliability to allow airflow regulation by limiting the weight impact. Such a critical embedded actuation system is very complex to design and to optimize, especially because of its multidisciplinary characteristic. The design of the power transmission, modulation and transformation must cope with multiple and antagonist constraints when considering as a whole mass, reliability, safety, integration, and so on.

## **1.2 Decision making of actuator under design constraints**

In [1] the design is defined as an iterative decision making process. These decisions happen at all stages and all levels of the design process [2] [3]. The designer must make choices on the specifications, constraints, and relative importance of the dependent variables; the best among alternate configurations for the overall design; he/she must select the suppliers and the technologies for major components. Most of these decisions come from intention. Some will be qualitatively logical and some will be based on specific laws. To make the decisions the designer must predict the results of more than one possible course of action. It is important to realize that all decisions are made in presence of uncertainties. Generally this is done by selecting the outcome with the greatest value. In practical terms, value must be identified directly with dependent variables that are considered. However, it is not as simple as it sometimes appears. In this work, the decision making relates to the design or selection of an actuator architecture adapted to a particular application. This activity is quite important when the designer is currently designing an actuator that was not a usual object of study before. Help in decision making is also useful particularly in preliminary design phases.

## **1.3 Redundant power architectures**

To meet the reliability requirements of a system, two solutions are commonly used: oversizing or redundancy. Redundancy consists in multiplying the functions and defining a combination of these in order to reduce the overall probability of failure of a given system. The arrangement of these functions depends on the nature of possible faults in the considered system. In this paper the study will be restricted to dual power paths with two variants:

- Using paralleling and averaging when the failed channel can be forced to passive. The fail operative capacity is achieved by doubling the function in a parallel architecture.
- The detection-correction, design also involves only two identical channels. In normal operation, one of the two channels is active while the second is set on passive. A function switch selects the active channel according to the diagnostic report.

Summing up, the process of creating architectures is given central activity for creating working systems that meet needs under constraints.

As mentioned at the functional level, a multitude of combinations of actuator architectures can be considered for each sub-function.

The Figure 1 summarizes the different type of generic blocs that are proposed to define the power architecture of redundant system, so as represent the functions involved by redundancy.

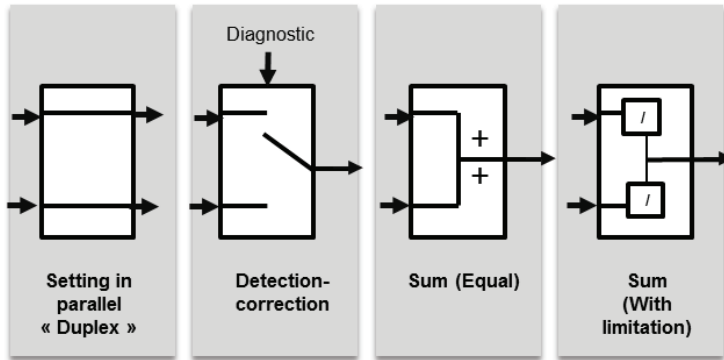


**Figure 1: Elementary types of redundancy blocs**

#### **1.4 Nature and scope of design constraints for systematic approach**

By clearly defining the objectives for the design project, the designer makes a proper framework for decisions making. The constraints provide a framework and boundaries for the solution. Narrowing the project from an ill-defined, unstructured problem into a well-ordered, defined solution is a major activity. The first task of a systematic design method is establishing the criteria before any decisions are made. Objective evaluation techniques based on predefined requirements are used to select between design variants. Systematic design processes seek optimal solutions. Assuming enough variants have been created, objective decision processes are important for selecting optimal solutions with the minimum effort. By using the requirements and objectives defined at the beginning of the process, the designer can overcome inherent biases and properly select good alternatives, even if they are counter-intuitive. Systematic decision processes ensure that all alternatives have been considered in a fair and consistent manner.

## **2 PROPOSED METHODOLOGY WITH TEST CASE: FAIL NEUTRAL CAPABILITY POSITION ACTUATION**

### **2.1 Actuator structure**

For the purpose of this method, it is essential to consider a structure that enables choosing the different architectures based on the identified actuator functions and constraints. For many reasons, as integration or safety, an actuator can consist of multiple power paths (limited in this study to two). This allows redundancy without impacting weight too much.

As shown in Figure 2, the architecture is considered an association of components that are arranged in couple for calculation needs. They are connected through a link / transition block. Six varieties of links can be defined to cover most of the association schemes of the transition block corresponding to the type of redundancy.

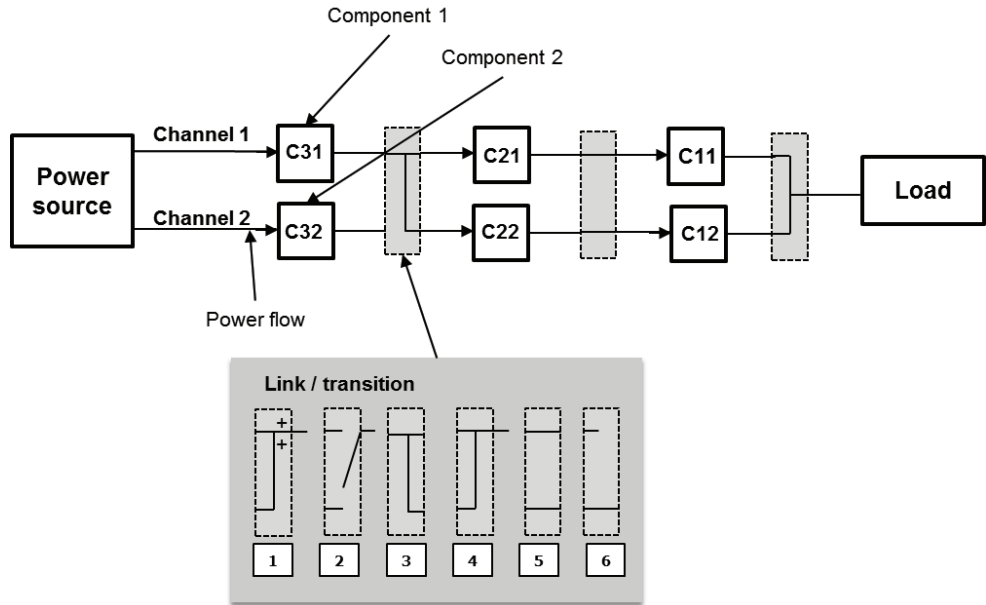


Figure 2: Actuator architecture structure

This approach provides the set of candidate architectures for the first step evaluation (see 2.4)

## 2.2 Presentation

As a test case, an actuator with fail-neutral position capability for aeronautical applications will be considered. After detection of a failure, the actuator must position the driver bad in an intermediate position called backup-position (fail-neutral). The actuator requirements mention a reduced space for integration (lengths  $L_1$ ,  $L_2$ , and  $L_3$ ), an allocated mass  $M_I$  and a reliability objective  $R$ .

## 2.3 Specification as a function of requirements and mission profile

A mission profile was set up in order to represent the actual operation. The mission profile is defined as the time history of the load position and force as a function of time.

## 2.4 Architecture generation and evaluation

The process of generating and evaluating the actuator power architecture is summarized in Figure 3. The proposed approach is structured into two main phases:

- The first phase corresponds to the generation of candidate architectures and preliminary screening. All the candidate architectures are generated automatically using a step-by-step approach from the load to the power source. For screening, the set of candidate architectures is filtered using qualitative criteria that are related to the consistency of the technological choices with respect to requirements.
- The second phase is a more accurate filtering process. It is based on expert knowledge in actuators sizing and allowances of existing reliability rates. This operation quantitatively compares the remaining set of architectures from phase 1. It finally outputs the most relevant architecture.

This systematic process enables generating a limited number of actuator architectures that comply with the system requirements in general, and the safety requirements in particular.

#### 2.4.1 First phase

Starting from the structure described in 2.1 the components are interconnected one after another to create the power network. Some combination are eliminated directly when found non coherent. For this trial version of the process, the listed components are identified considering only with their type of power transmission (e.g. rotational to translational reducer).

The evaluation criteria are calculated from the weighted contribution of each item to the overall value of the system. The first filtering is based on the criteria presented on table 1. The weights are firstly chosen to facilitate the comparison between design options (e.g. “geared” against “direct-drive”) with another equivalent system and this is intended to test the method.

Evaluation criteria are derived directly from the objectives, in which the individual objectives are arranged in hierarchical order. The sub-objectives are arranged into levels of decreasing complexity. The Figure 3 gives an example where the geometric integration is a main objective while volume and weight are considered as sub-objectives.

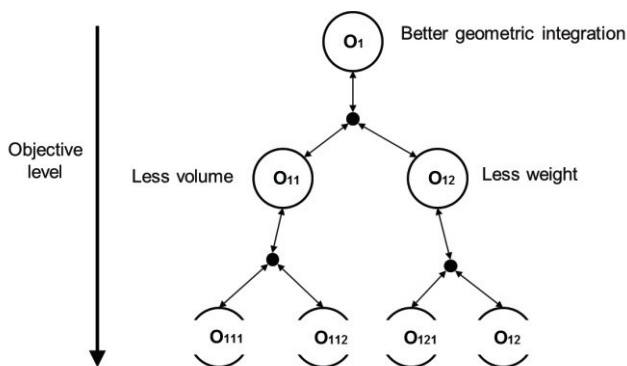


Figure 3: An example of objective and sub-objectives

Criteria	Symbol	Importance factor (/5)
Maturity of the solution	$w_1$	3
Geometric integration	$w_2$	2
System complexity	$w_3$	3
Levels of reliability and system security	$w_4$	4

**Table 1: weighted filtering criteria of phase 1**

Once generated the set of architectures, each candidate is ranked, calculating an evaluation coefficient  $K_j$  as follows:

$$K_j = \sum_i^n v_{ij} w_i \quad (1)$$

where  $v_{ij}$  is the weight of the criteria  $i$  related to actuator design  $j$  and  $w_i$  is the importance factor of the criteria  $i$ .

The best candidate architectures are extracted if their criteria are greater than a defined threshold.

#### 2.4.2 Second phase

The second phase of the filtering process addresses the geometric integration and the reliability. It involves a sizing process that is based on scaling laws [4] in order to generate the dimensions and the weight of the actuator. The reliability is calculated as follows.

Assuming the failure rate  $\lambda$  does not depend on time, the reliability  $R$  over a period of time  $T$  is given by:

$$R = e^{-\lambda T/t} \quad (2)$$

For  $n$  components associated in series, the overall reliability is

$$R = \prod_{i=1}^n R_i \quad (3)$$

while for  $n$  components associated in parallel, it becomes

$$R = 1 - \prod_{i=1}^n (1 - R_i) \quad (4)$$

## 2.5 Software implementation

The overall process is displayed by Figure 4.

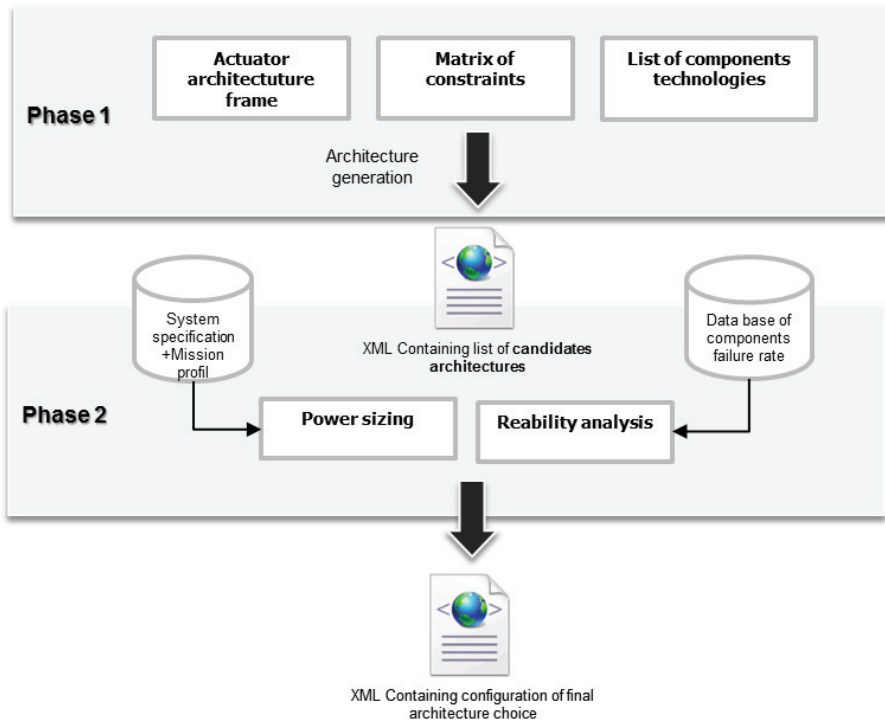


**Figure 4: Architecture of the developed tool**

The *actuator architecture frame* comes from the architecture generation algorithm detailed at paragraph 2.6. The *matrix of constraints* summarises the criteria levels (Table 1) of each type of component of the *list of component technologies*. The first step of the process is implanted to generate an *XML* file containing the  $N$  candidate architectures.

The second step involves two independent activities to be run for each candidate architecture. The preliminary *power sizing* is performed knowing the *system specification* and the *mission profile*. The *preliminary reliability analysis* is run using typical values for each technology coming from a *database of the components failure rates*. Combining the outputs of these activities enables extracting the best architecture.

## 2.6 Generation architecture algorithm

Figure 5 shows the process used to generate the actuator architecture list. The process starts from the load (power stage number 1) and propagates in the opposite direction of functional power flow. Each block  $b$  is associated with one design decision.

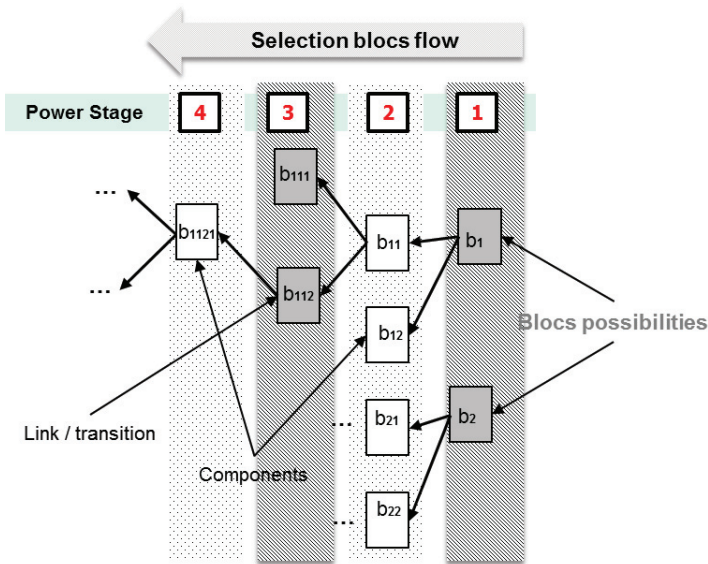


Figure 6: Architecture generation process

3 CASE STUDY

The proposed approach has been applied to the design of an EMA meeting the following requirements:

- The actuator shall have a *fail-neutral* response to failure,
- The actuator shall not exceed the limit value  $M$ ,
- The actuator shall be integrated within a cubic volume defined by lengths  $L_1$ ,  $L_2$  and  $L_3$ ,
- The actuator shall develop a maximal force  $F_{max}$ .

Consequently the remaining degree of freedom concerns the combination of these three types of components to make redundant power paths. Firstly, 26 architectures were generated to make the actuator architecture frame. The matrix of constraints was defined as given on table 2. It is created with relative comparison between each technology and it is built collecting information and expert reviews for a limited number of components.

In order to simplify the study, some technological choices were frozen:

- For the motor, permanent magnet synchronous machine
- For the rotational to translational transformation, ball screw
- For the prime reducer, spur gear

Finally, 3 candidate architectures were output by step one, as illustrated by Figure 6. The radar chart of the Figure 7 facilitates the identification of the most interesting architectures and the definition of the criteria threshold (set to 85%).

Criteria weight (/5)\Components	Motor	Ball screw	Spur gear
Maturity of the solution	3.5	3	3
Geometric integration	2	2.5	2.5
Complexity	2.5	2.5	3
Reliability and security	2.5	3	2.5

Table 2: Case matrix of constraints

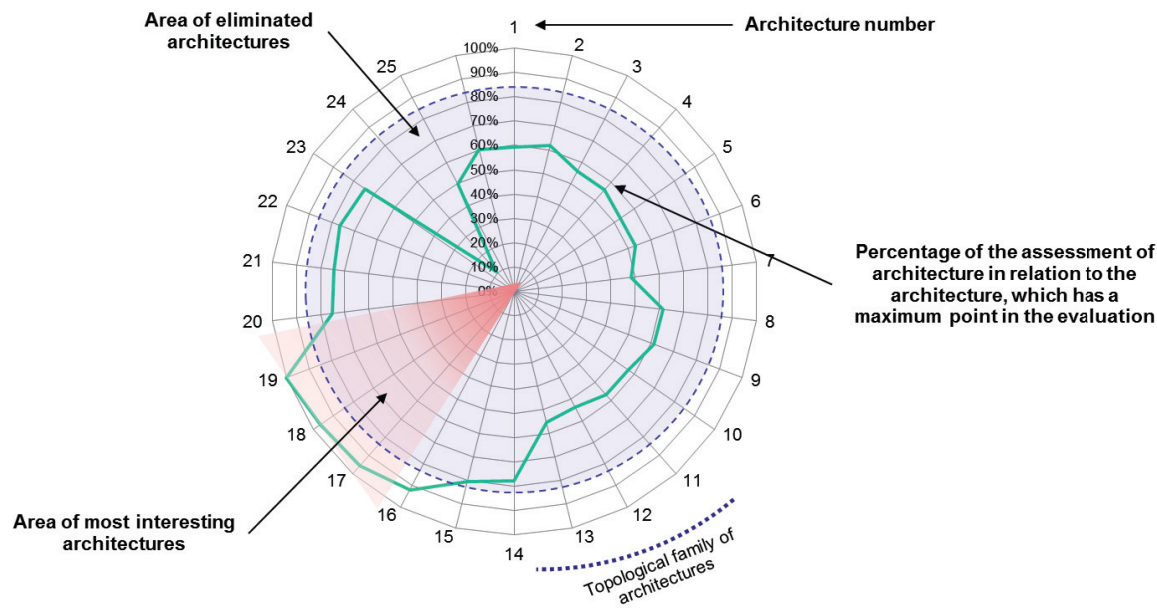
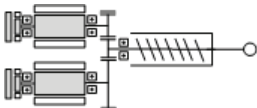
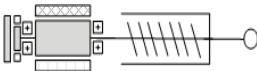
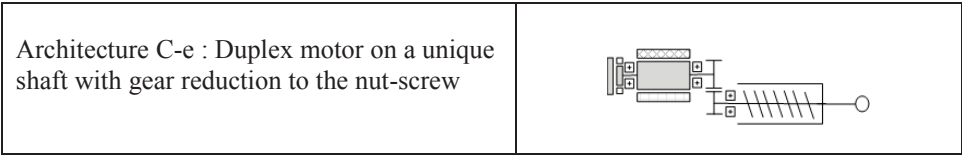


Figure 6: Architecture evaluation result

Figure 7 shows the three architectures selected after the first phase.

Architecture A-e : Duplex motor with torque summing to single nut-screw	
Architecture B-e : Duplex motor on a unique shaft with direct drive to the nut-screw	





**Figure 7: Architecture selected after the first phase**

Starting from these 3 architectures, two independent calculations are launched. On one side the reliability calculation using the components standard failure rate database [5][6], on the other side a sizing-to-power calculation is launched using the actuator specification and the mission profile. The actuator sizing process was performed with the in-house preliminary design tool [4] [7] to meet the power needs and the required service life. The main results presented on table 3 summarize the main results that are related to mass, geometrical envelope and reliability. They are expressed as a percentage of the target values coming from the specification. It can be seen that the difference between the three candidate solutions is minor for this case study. However it must be kept in mind that the proposed process addresses very preliminary design. In particular, a more detailed pass should address in addition:

- The estimation of the mass of the actuator housing,
- The link between sizing and reliability (sizing for power and reliability),
- The consistency of the architecture with control performance objectives,
- The segregation between the two power paths,
- The cost of the candidate solution.

The first four topics are currently (or have already been) addressed in the lab in the frame of more electrical actuation projects for future aircrafts.

	Architecture A-e	Architecture B-e	Architecture C-e
Mass m1	93,30%	80%	87%
Length l1	90%	88%	91%
Length l2	92,40%	94%	87%
Length l3	93,80%	94%	87%
Reliability R	98%	95%	94%

**Table 3: Results of actor sizing and reliability calculation in phase 2**

### 3 CONCLUSION

The presented approach was motivated by the need to offer more automated process for the preliminary design of embedded actuation systems. A mixed top-down and bottom-up approach has been introduced that generates, reduces and evaluates all the acceptable architectures in an automated process. It has been proposed to start with the full enumeration of candidate solutions meeting the functional requirements. In order to save time, a first step consists in ranking the candidate solutions using qualitative criteria (mass,

integration and safety) in order to point out the most attractive ones. The second step proceeds with a preliminary sizing and reliability calculation to compare the solutions that came out the first step.

In a future work, the proposed process must be followed by a more detailed assessment of the candidate solutions considering additional criteria and performing in-depth sizing. In order to take advantage of this approach for even more complex multi-domain system designs, it would be interesting to extend the developed software tool to the multi-objective exploration and optimization versus the key design parameters.

## 4 REFERENCES

- [1] Pahl G., Beitz W., Feldhusen J., Grote K.H. Engineering Design, a Systematic Approach. Third edition, Springer, 2007.
- [2] VDI 2206, Design methodology for mechatronic systems. Beuth Verlag, Düsseldorf, Germany, 2004.
- [3] Budynas R., Nisbett J. K. Mechanical Engineering Design. Height edition, Mc Graw Hill, 2008.
- [4] M. Budinger, J. Liscouët, S. Orioux, J-C. Maré Automated Preliminary Sizing of Electromechanical Actuator Architectures. Proceedings of the ELECTRIMACS 2008 Conference, Québec, Canada, June 2008.
- [5] Reliability Information Analysis Center (RIAC), RIAC Automated Databook v2.20.
- [6] Dhillon B. S. Mechanical reliability: Theory, models and applications. American Institute of Aeronautics and Astronautics Inc., 1988.
- [7] M. Budinger, J. Liscouët, F. Hospital, J-C Maré. Estimation Models for the Preliminary Design of Electro-Mechanical Actuators, Proceedings of ImechE, Part G: Journal of Aerospace Engineering 19 Oct. 2011

## 5 NOMENCLATURE

$L$	Length	(m)
$M$	Weight	(kg)
$T$	Time	(sec)
$R$	Reliability	(-)
$F$	Effort	(N)
$\lambda$	Failure rate	(h)

## 6 NOTATION

EMA: Electromechanical actuator  
EHA: Electro-hydraulic actuator



# Renewable Energy



# Design and Control of Full Scale Wave Energy Simulator System

Henrik C. Pedersen, Anders H. Hansen, Rico H. Hansen<sup>1</sup>, Torben O. Andersen & Michael M. Bech

Department of Energy Technology, Aalborg University, 9220 Aalborg East, Denmark

<sup>1</sup>Wave Star A/S, 2605 Brøndby, Denmark

## ABSTRACT

For wave energy to become feasible it is a requirement that the efficiency and reliability of the power take-off (PTO) systems are significantly improved. The cost of installing and testing PTO-systems at sea are however very high, and the focus of the current paper is therefore on the design of a full scale wave simulator for testing PTO-systems for point absorbers. The main challenge is here to design a system, which mimics the behavior of a wave when interacting with a given PTO-system.

The paper includes a description of the developed system, located at Aalborg University, and the considerations behind the design. Based on the description a model of the system is presented, which, along with a description of the wave theory applied, makes the foundation for the control strategy. The objective of the control strategy is to emulate not only the wave behavior, but also the dynamic wave-float interaction, the inertia of the float and the added inertia of the water. Based on this simulation results are presented, which show that the system is able to emulate waves more than three meters in height and with a resulting force of more than 800 kN, while interacting with a general PTO-system.

## 1 INTRODUCTION

Wave energy is today at a stage, where several concepts have reached proof-of-concept, showing it is possible to produce electricity. Despite this achievement, an even larger technology push remains to achieve a commercial breakthrough, as the produced electricity is far from price competitive compared to e.g. wind turbines. This is to a large extent due to the low efficiency of the Power Take-Off (PTO) systems. There are several reasons for this low efficiency and the non-competitive prices. Cruz et al. [2] describes several of these and Salter, [17], has made a good overview of the different control strategies normally considered. Based on these the main challenges for the low PTO-efficiency may be outlined as:

- The wave motions result in slow irregular oscillating movements with varying frequency and amplitude and extreme high torques/forces, where the available components have extremely poor efficiency and durability.

- The PTO system deals with large power scales combined with a very high ratio between peak and mean power. The peaks may, however, contain up to 40% of the available energy.
- Due to the large variations in wave power (both frequency and amplitude), a big challenge for the PTO design is to smooth the power to grid, while maintaining a high efficiency.
- Advanced control strategies and high dynamic performance of the PTO are required to optimize the amount of energy extracted from the waves.
- Reliability and lifespan is of crucial importance.

Two main barriers exist for solving these challenges. Firstly, there are no components available that has a high efficiency in the whole operating range required for wave energy converters. Secondly, the research activities regarding wave energy have almost entirely disregarded the PTO system or assumed ideal PTO-systems, see e.g. [18, 5, 4, 9, 3]. Others have considered components, see [16], where Salter describes the potential in using digital hydraulics, including the Artemis Ltd digital displacement pump technology, which is also described in Payne et al., [15, 14]. It is not until recently that the PTO-system efficiency has been taken into account, see [8, 7, 6], but this has primarily been based on simulation results. Hence, there is a major need for starting to address the PTO-system design and efficiency, and to have the promising simulation results experimentally validated. The focus of the current paper is therefore on the design of a full scale wave simulator to be used for testing and validating different PTO concepts including development of control strategies. Two other test benches exist, see [10, 12], both of these are however “small scale” versions, by which it is not possible to test PTO systems under full load operating conditions. The key element is in this regard to be able to test full scale, as it is not possible to obtain valid data based on scaled versions. The two existing test benches are in this regard either not designed for testing full scale PTO-systems, but instead for testing control strategies [10] and for testing with limited power capabilities [12]. The challenge in designing a full scale test bench is, however, far from trivial and much more complicated due to the forces and power involved. Furthermore, the wave simulator is not only to mimic the behaviour of the waves, but also to represent the remaining dynamics of the wave energy converter float connected to the PTO-system. Based on this, the focus in this paper is on the designed wave simulator set-up, see [13], and the control strategy devised for this.

## 2 DESCRIPTION OF THE WAVE SIMULATOR SYSTEM

The background for the design of the wave simulator test bench is to be able to test PTO-systems at full scale operation for Wave Energy Converters (WECs) of the point absorber type. The requirements are derived with basis in a single float of the Wavestar C5 600kW prototype WEC, see Fig. 1, although the test bench may be used to test general PTO-systems within the design limitations.

### 2.1 The Design Considerations

One of the main challenges in the design of the test bench is to be able to emulate the behaviour of a wave and the float, when interacting with the PTO-cylinder. The challenge here

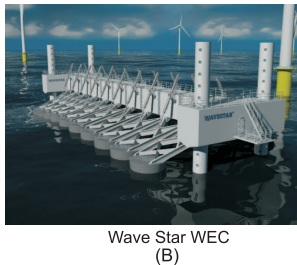
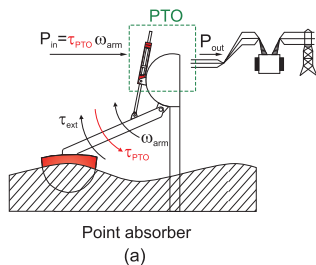


**Figure 1: To the left the working principle behind each of the floats. To the right an illustration of the Wavestar C5 600kW converter.**

lies in the added inertia, damping and spring effect, which the waves represent. Combined with the requirement that it should be possible to test reactive control strategies, a solution with cylinders mounted back-to-back is the preferred solution. This has lead to the design shown in Fig. 2, where the force between the two cylinders is transferred through the force sensor. The force sensor is mounted in the sleigh, which runs on a set of low friction guide rails. The whole assembly is mounted within the tube, which are designed to withstand the extensive forces in the system, but with easy access to the system.

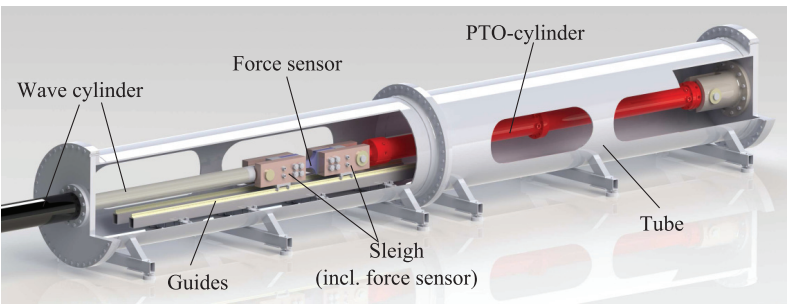


**Figure 2: The wave simulator, with parts of the tube cut away. The main data for the system are given in Table 1.**

A key element in the design of the test bench was the requirement to test full scale, as it is not possible to do scaled tests and get coherent data for all the parameters to analyse under the same conditions, due to the highly non-linear correlations in the hydraulic systems to test. Based on the requirements from the C5 machine, the wave simulator should be able to simulate waves with a significant wave height,  $H_s$ , of up to 3 [m] (6 meters peak-to-peak at the float), and should be able to resist a PTO torque,  $\tau_{PTO}$ , of approximately 1 [MNm]. As reactive control strategies will be applied by the PTO, the wave simulator should also be able to both deliver and dissipate power, i.e. four-quadrant behaviour. Finally the system should be able to emulate the behaviour of both the float and water, when also interacting with different PTO systems. This includes emulating the mass inertia of the float, arm and added inertia from the radiated waves. Realising this mechanically is not realistic, as the mass of the float itself is more than 15 ton, not even taking the gearing into account. The system was therefore designed to be able to realise this by means of the force transferred from the wave cylinder,



which also set part of the dynamic requirements for the system. Based on these requirements the system has been designed with the specifications given in Table 1.

Max. force:	827 [kN]	Max. system pressure:	350 [Bar]
Max. velocity:	> 0.5 [m/s]	Max. continuous flow:	~ 550 [l/min]
Max. stroke:	3 [m]	Max. continuous (hyd.) power:	~ 320 [kW]
Total length:	> 15 [m]	Installed accumulator capacity:	2 x 28 [l]

**Table 1: Main system specifications.**

### 2.2 The Fluid Power system

To fulfil system specifications the system should be able to deliver sufficient power to simulate all sea states. However, in a large part of the time, the system will not have to operate at full power. For this reason the system has been designed as a two pump system, which may run in either parallel or independently of each other. Both pumps are of the Bosch-Rexroth A4VSO type, with displacements of 250 [cm<sup>3</sup>/rev] and 125 [cm<sup>3</sup>/rev] respectively and both run at 1500 rpm. To drive the pumps two electric motors of respectively 250 and 110 [kW] are utilised. The pumps are electronically controlled, with possibility of direct swivel angle control, hereby enabling the system to be run as a LS-system to minimise power consumption. By default both pumps are, however, run as pressure controlled pumps to obtain the highest possible valve gain and hence stiffness and controllability in the system, to enable the system to counteract disturbances from the PTO-system. For the same reason two 28 litre accumulators, are placed next to the control valve to stabilize the system pressure, account for peak power requirements and minimise transmission line effects. To control the wave cylinder, which is a custom made 250/180-3000 [mm] symmetric cylinder, a Parker D111FP NG32 pilot operated servo proportional valve is used, which has a nominal flow of 1000 [l/min] at  $\Delta p = 5$  [Bar], a small signal bandwidth of 40 [Hz] and a full stroke time of 45 [ms]. The high bandwidth is required, as the wave side system is not only to emulate the low frequency wave but also be able to counteract the disturbances from the PTO-system. The system has furthermore been designed to minimise the distance between the accumulators, control valve and cylinder to obtain the highest possible bandwidth in the system. The system has furthermore been fitted with pressure sensors at all ports at both the valve and cylinder to be able to monitor pressure pulsations, and for control purposes. Two sensors may be connected at each port if required to separate the control and monitoring system.

### 3 MODELLING THE SYSTEM

To describe and test the control strategy of the wave simulator, the model is made with basis in the simplified system shown in Fig. 3. The system is considered as consisting of three parts, namely the wave side, the PTO-side and the mechanical interaction between the two sides, as described in the following.

Notice the sign convention used in Fig. 3, which is used to represents a positive wave motion being upwards and a positive PTO-cylinder movement when extending. This sign convention is used throughout the article.

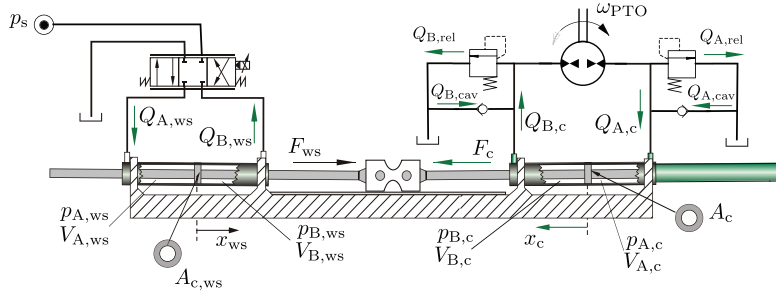


**Figure 3: Sketch of wave simulator. A simplified “standard” PTO-system is considered.**

### 3.1 Wave side

As described in the system description the wave side power supply is by default run as a constant pressure system, where the two accumulators are placed next to the control valve to maintain the constant system pressure at the valve and dampen pressure fluctuations. In the model the system pressure is therefore considered constant and with a set value of  $p_s = 350 \text{ [Bar]}$ . Considering first the continuity equations for the two cylinder chambers these may be described as:

$$\begin{aligned}\dot{V}_{A,ws} &= \frac{\beta_{A,ws}}{V_{A,ws}(x_{ws})} (Q_{A,ws} - A_{c,ws}\dot{x}_{ws}) \\ \dot{V}_{B,ws} &= \frac{\beta_{B,ws}}{V_{B,ws} - A_{c,ws}x_{ws}} (A_{c,ws}\dot{x}_{ws} - Q_{B,ws})\end{aligned}\quad (1)$$

where  $V_{A,ws}(x_{ws}) = V_{A,ws,0} + A_{c,ws}x_{ws}$  and  $V_{B,ws}(x_{ws}) = V_{B,ws,0} - A_{c,ws}x_{ws}$ , with  $V_{A,ws,0}$  and  $V_{B,ws,0}$  being the two volumes when the cylinder is in the middle position.  $\beta_{i,ws}$  is the effective bulk modulus in the  $i$ 'th cylinder chamber, which is modelled as:

$$\beta = \frac{1}{\frac{1}{\beta_{oil}} + \frac{V_{\%air}}{\beta_{air}}}\quad (2)$$

With the volume content of air being determined as:  $V_{\%air} = (p_0 V_{\%air,0}^\kappa / p)^\frac{1}{\kappa}$ , where  $p_0$  is atmospheric pressure,  $\kappa = 1.4$  for an adiabatic process,  $\beta_{oil} = 14.000 \text{ bar}$  (oil bulk modulus) and  $\beta_{air} = 1.4p$ . From the two cylinder pressures the stationary cylinder force is described as:

$$F_{ws,s} = (p_{A,ws} - p_{B,ws})A_{c,ws} - F_{fric,ws} = F_{\Delta p,ws} - F_{fric,ws}\quad (3)$$

With the friction force being modelled as:

$$F_{fric,ws} = B_{ws}\dot{x}_{ws} + F_{cou,ws} \tanh(\dot{x}_{ws}/\gamma)\quad (4)$$

Which also accounts for the friction part resulting from the left part of the sleigh, which is considered included in the cylinder friction. The slope of the friction curve is here controlled via  $\gamma$ , which is set to  $\gamma = 0.0001 \text{ [m/s]}$  to avoid numerical switching problems. The viscous and coulomb friction coefficients are unknown, but estimated low. A detailed friction mapping/investigation will be made, when the experimental set-up is running, as the friction force also influences the control strategy, as described below. For the testing of the control strategy the above friction model is sufficient. Considering the proportional valve, the flows through this are modelled by the orifice equation, whereas the dynamics is modelled by a critically damped second order system, with a slew rate limitation:

$$Q_{A,ws} = \begin{cases} K_v u_{ws} \sqrt{p_s - p_{A,ws}} & , \quad u_{ws} \geq 0 \\ K_v u_{ws} \sqrt{p_{A,ws} - p_t} & , \quad u_{ws} < 0 \end{cases} \quad (5)$$

$$Q_{B,ws} = \begin{cases} K_v u_{ws} \sqrt{p_{B,ws} - p_t} & , \quad u_{ws} \geq 0 \\ K_v u_{ws} \sqrt{p_s - p_{B,ws}} & , \quad u_{ws} < 0 \end{cases} \quad (6)$$

$$u_{ws} = \frac{\omega_{n,ws}^2}{s^2 + 2\zeta \omega_{n,ws}s + \omega_{n,ws}^2} u_{ref,ws} \quad (7)$$

Where  $K_v = 2.35 \cdot 10^{-5} [m^4 / \sqrt{kg \cdot m}]$  is the valve coefficient,  $u_{ref,ws}$  is the valve reference and  $u_{ws}$  is the normalized valve opening. The slew rate limitation is implemented as a velocity limit on the valve spool. Both the valve coefficient, valve eigenfrequency and slew rate limitation is determined from the data sheet of the valve. The valve eigenfrequency is determined to  $\omega_{n,ws} = 80\pi [rad/s]$  and the slew rate limitation is set to  $\dot{u}_{ws,max} \approx 22 [s^{-1}]$ , where the latter yields a stroke time of 45 [ms].

### 3.2 Power Take-Off side

The objective of the wave simulator is to be able to test various configurations and components of the Power Take-Off (PTO) system, and as such the system is not limited to a specific PTO-design. In the present paper and for testing the control strategy for the wave simulator, a simplified standard PTO-system is assumed and modelled, as shown in Fig. 3. Boost circuitry etc. is neglected in the modelling, as this has no influence when considering control of the wave side. The component data used are based on the data for components in the Wavestar C5 prototype machine, cf. Fig. 1. The pressure build up in the two cylinder chambers are:

$$\begin{aligned} \dot{p}_{A,c} &= \frac{\beta_{A,c}}{V_{A,c} + A_c x_c} (Q_{A,c} - A_c \dot{x}_c - Q_{A,rel} + Q_{A,cav}) \\ \dot{p}_{B,c} &= \frac{\beta_{B,c}}{V_{B,c} - A_c x_c} (A_c \dot{x}_c - Q_{B,c} - Q_{B,rel} + Q_{B,cav}) \end{aligned} \quad (8)$$

The two volumes are defined for the cylinder in the middle position. The effective bulk modulus in each chamber is calculated according to Eq. (2). The flows  $Q_{i,rel}$  and  $Q_{i,cav}$  are the flows across the  $i$ 'th pressure relief valve and anti-cavitation valve respectively, cf. Eq. (11). For the simple model used here, the motor is considered leak free, why the two flows  $Q_{A,c} = Q_{B,c} = Q_m$ , where the flow across the motor is modelled as:

$$Q_m = D_m \alpha \omega_m \quad (9)$$

Here  $D_m = 250 [cm^3/rev]$  is the motor displacement and  $\omega_m$  is the motor speed. As the motor drives a generator, which is connected to grid via a frequency inverter, the motor speed is considered constant to  $\omega_m = 50\pi [rad/s]$ , regardless of whether the motor is running in motor or pump operation.  $\alpha$  is the relative pump displacement, where the pump dynamics is simply described as a second order system as:

$$\alpha = \frac{\omega_{n,m}^2}{s^2 + 2\zeta_m \omega_{n,m}s + \omega_{n,m}^2} \alpha_{ref} \quad (10)$$

Assuming primarily small signal variations the motor eigenfrequency is approximated to  $\omega_{n,m} = 16\pi [rad/s]$  and the damping is assumed to unity. The reference displacement,  $\alpha_{ref}$ , is determined via the PTO control, which is described in section 4. Finally the flows across the pressure relief valves and the anti-cavitation valves should be considered. These valves

are normally intended as emergency features, but may for the modelled PTO-system come into play, if the PTO-system is not properly tracking the reference, like e.g. if the wave is reversing direction too fast. The flows are, for the  $i$ 'th chamber, described as:

$$Q_{i,rel} = \begin{cases} 0 & , \quad p_{i,c} < p_{cr} \\ c_1 (p_{i,c} - p_{cr}) & , \quad p_{i,c} \geq p_{cr} \end{cases} \quad Q_{i,cav} = \begin{cases} 0 & , \quad p_{i,c} > p_{cav} \\ c_2 (p_t - p_{i,c}) & , \quad p_{i,c} \leq p_{cav} \end{cases} \quad (11)$$

Here  $p_{cr} = 250 [Bar]$ ,  $p_{cav} = 2 [Bar]$ , whereas  $c_1$  and  $c_2$  are approximated valve coefficients, which are set to  $c_1 = 8.33 \cdot 10^{-9} [m^4 s/kg]$  and  $c_2 = 3.3 \cdot 10^{-8} [m^4 s/kg]$ . Finally the stationary cylinder force from the PTO-cylinder is described as:

$$F_{c,s} = (p_{A,c} - p_{B,c})A_c - F_{fric,c} = F_{\Delta p,c} - F_{fric,c} \quad (12)$$

The cylinder friction is modelled similar to the wave side cylinder, see Eq. 4, taking into account the friction from the right part of the sleigh.

### 3.3 Mechanical Link & Force Sensor

The mechanical system is modelled by Newton's second law of motion as:

$$(m_{ws} + m_c + m_s) \ddot{x}_c = F_{c,s} - F_{ws,s} \quad (13)$$

where  $m_{ws}$ ,  $m_c$  and  $m_s$  are the masses related to the wave side cylinder rod, PTO cylinder rod and the force sensor respectively. To describe the force measured by the sensor, a cut through the force sensor may be made as illustrated in Fig. 4.

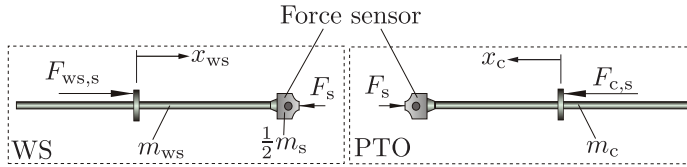


**Figure 4: Free-body diagram pistons and force sensor cut.**

From the free-body diagrams in Fig. 4, the equation of motion for the PTO cylinder may be manipulated to yield the measured force as:

$$F_s = F_{c,s} - \ddot{x}_c \left( m_c + \frac{1}{2} m_s \right) = F_c - \ddot{x}_c \frac{1}{2} m_s \quad (14)$$

with  $F_s$  being the measured force.  $F_c$  is here defined as the dynamic PTO cylinder force,  $F_c = F_{c,s} - \ddot{x}_c m_c$ , where the acceleration of the piston mass has been accounted for. From Eq. (14) it may be seen that the force sensor output is approximately equal to the cylinder force except for the contribution of the inertia term  $\frac{1}{2} m_s \ddot{x}_c$ . In the control strategy the approximation  $F_s \approx F_c$  may however be utilised, which is valid considering the inertia, which the system is to emulate. The latter yields that  $|F_{ws}| \gg |m_s \ddot{x}_c|$ , where  $F_{ws} = F_{ws,s} - \ddot{x}_{ws} m_{ws}$ . Combining this with  $F_c - F_{ws} = m_s \ddot{x}_c$  it follows that  $|F_c| \gg |m_s \ddot{x}_c|$ , and hence the approximation is valid. Similarly the sensor force may be described as:

$$F_s = F_{ws,s} + \ddot{x}_c \left( m_{ws} + \frac{1}{2} m_s \right) = F_{ws} + \ddot{x}_c \frac{1}{2} m_s \quad (15)$$

which is utilised in the control strategy.

## 4 DEVELOPMENT OF CONTROL STRATEGY

To describe the interaction between the float and the wave, linear wave theory is applied, as it gives an adequate description in the conditions in which a WEC is producing energy, [5]. Before describing the interaction, an example of a used wave spectrum is presented, which is used for testing the control strategy.

### 4.1 Wave Spectrum

To describe the ocean waves a stochastic model based on a digitally filtered white noise signal is used, see [11], utilising the wave spectrum shown in Fig. 5. The spectrum  $S_A(f)$  is usually represented in terms of the significant wave height  $H_{m,0}$  and the peak wave period  $T_p$ . The significant wave height  $H_{m,0}$  is the average wave height of the one-third highest waves and  $T_p$  is the wave period where most energy is concentrated. For the simulation presented in subsequent sections, the wave example shown in Fig. 5 is one of the waves used.

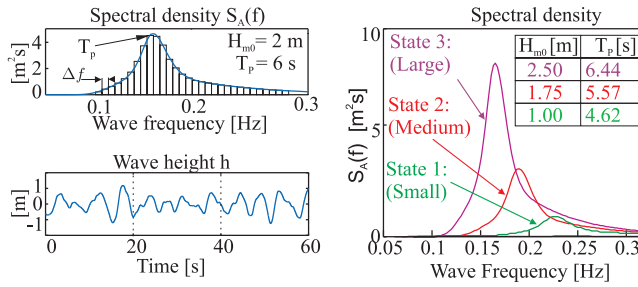


Figure 5: Example of wave and wave spectrum for different sea states.

### 4.2 Wave-Float Interaction

To develop the control strategy, the system wave side cylinder and sensor (sleigh) is to mimic the behaviour of the wave, float and arm connected to the PTO-cylinder as shown in Fig. 1. The description of the wave-float interaction is made with basis in the geometry of the Wavestar machine. The equation of motion of the float is here given as:

$$J_{\text{mech}} \ddot{\theta}_{\text{arm}} = \tau_{\text{wave}} - \tau_{\text{G}} - \tau_{\text{PTO}} \quad (16)$$

where  $J_{\text{mech}}$  is the inertia of float and arm,  $\tau_{\text{wave}}$  is the torque due to wave-float interaction,  $\tau_{\text{G}}$  is the torque due to gravity and  $\tau_{\text{PTO}}$  is the torque applied by the PTO system to the float arm. Using linear wave theory,  $\tau_{\text{wave}}$ , may be described as, cf. [8]:

$$\tau_{\text{wave}} = \tau_{\text{rad}} + \tau_{\text{Arch}} + \tau_{\text{ext}} \quad (17)$$

where  $\tau_{\text{ext}}$  is the excitation torque an incoming regular wave applies to a float held fixed.  $\tau_{\text{rad}}$  is the radiation torque experienced from oscillating the float in otherwise still water, and  $\tau_{\text{Arch}}$  is the torque due to the Archimedes force, i.e. buoyancy. The torque due to the radiated wave is described as:

$$\tau_{\text{rad}} = -J_{\infty} \dot{\omega}_{\text{arm}} - h_{\text{rad}} * \omega_{\text{arm}} \quad (18)$$

where  $h_{\text{rad}}$  is the (time dependent) impulse response function from float velocity to torque, describing the hydrodynamic damping. The impulse response function  $h_{\text{rad}}$  may be viewed as

a high order damping term. The inertia term  $J_\infty$  represents the "added mass", which represents the effect, that when oscillating a float, it will appear to have a greater mass due to the water being displaced along with the float. The coefficients of Eq. (18) are identified via the numerical tool WAMIT, which also outputs a force filter, which may be applied to the wave function,  $\eta_w(t)$ , to find  $\tau_{\text{ext}}$ . Inserting (17) and (18) into (16) gives the equation of motion for the float:

$$\dot{\omega}_{\text{arm}} = \frac{-k_{\text{res}}\theta_{\text{arm}} - h_{\text{rad}} * \omega_{\text{arm}} + \tau_{\text{ext}} - \tau_{\text{PTO}}}{J_{\text{mech}} + J_\infty} \quad (19)$$

where the sum of gravity and Archimedes term has been linearized around the draft of the float,  $\tau_{\text{res}} = \tau_G - \tau_{\text{Arch}} \approx \theta_{\text{arm}} k_{\text{res}}$ . The float-arm subsystem are thus subject to the torques  $\tau_{\text{ext}}$  and  $\tau_{\text{PTO}}$ , and the output is the angular position and velocity of the arm. To avoid the convolution term  $h_{\text{arm}}(t) * \omega_{\text{arm}}(t)$ , the impulse response has been fitted with a fifth-order system in the Laplace domain, see [8], using Prony's methods [1]:

$$\tau_{\text{rad}}(s) = \frac{a_5 s^5 + \dots + a_1 s + a_0}{b_5 s^5 + \dots + b_1 s + b_0} \omega_{\text{arm}}(s) = H_{\text{rad}}(s) \omega_{\text{arm}}(s) \quad (20)$$

The wave-float dynamics, which the wave simulator is to emulate is hereby described. The float and arm system with hydrodynamics included is shown in Fig. 6(a). Figure 6(b) illustrates the torque arm  $d_c$  and 6(c) shows the torque arm as a function of the arm angle.

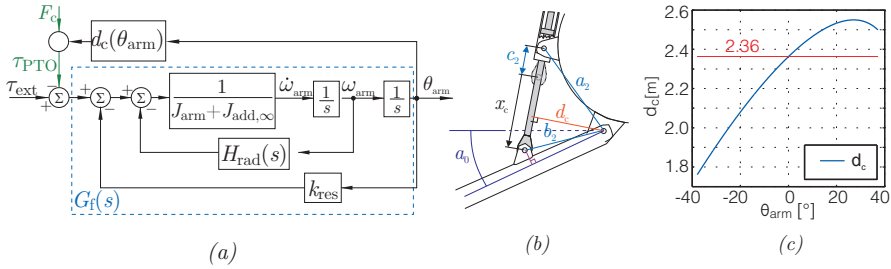


**Figure 6: Model of the float and arm dynamics.**  $\theta_{\text{arm}} = 0$ , when the float is resting in shallow water.

### 4.3 Control Strategy

The objective of the control is to make  $x_c$  track the "real" cylinder position  $x_{c,\text{ref}}$ , predicted in terms of  $\theta_{\text{arm}}$  by the float model in Fig. 6(a), i.e.:

$$\theta_{\text{arm}} = (\tau_{\text{ext}} - \tau_{\text{PTO}}) G_f(s) \quad (21)$$

$$\begin{aligned} x_{c,\text{ref}} &= \sqrt{a_2^2 + b_2^2 - 2a_2b_2 \cos(\theta_{\text{arm}} - \theta_{\text{arm},0})} - c_2 \\ &\approx -\theta_{\text{arm}} d_{c,0} + x_{c,\theta_0} \end{aligned} \quad (22)$$

where the distances  $a_2, b_2, c_2$  are shown in Fig. 6(b), and the  $d_{c,0}$  in part (c) of the figure. By differentiation it follows directly that:

$$v_{c,\text{ref}} = -\frac{a_2 b_2 \sin(\theta_{\text{arm}} - \theta_{\text{arm},0})}{\sqrt{a_2^2 + b_2^2 - 2a_2b_2 \cos(\theta_{\text{arm}} - \theta_{\text{arm},0})}} \omega_{\text{arm}} \quad (23)$$

The position and velocity references are now available, both of which may also be measured at the test set-up. A state feedback controller is hence possible, giving the effect of a PD-controller, when considering the system as a position servo. However, the wave cylinder is not to directly follow the wave motion, but instead to emulate the behaviour of the wave on the float. Hence, the system is to transfer the correct force from the wave side to the PTO-cylinder, hereby also influencing the float position. The manipulating input to make  $x_c$  track  $x_{c,\text{ref}}$  is therefore the wave cylinder force, which is utilised in what may be considered a feedforward term. The wave motion may from linear wave theory be expressed in terms of  $\tau_{\text{ext}}$ . Utilising the approximation  $\tau_{\text{PTO}} \approx F_{\text{PTO}} d_{c,0}$  Eqs. (22) and (21) may be rearranged to express  $x_{c,\text{ref}}$  as a function of  $\tau_{\text{ext}}$ :

$$x_{c,\text{ref}} = \left( \frac{1}{d_{c,0}} \tau_{\text{ext}} - F_{\text{PTO}} \right) G_f(s) d_{c,0}^2 + x_{c,\theta_0} \quad (24)$$

Here  $F_{\text{PTO}}$  is the reference force from the PTO-side, which practically may be considered as:  $F_{\text{PTO}} \approx F_{c,s}$ . The wave side cylinder force may be controlled in terms of  $F_s$ , which is measured directly at the force sensor, or via  $F_{\Delta p,ws}$ , which is measured in terms of the differential pressure in the wave cylinder. Both the two signals may be used, and which to choose will therefore be dependent on the quality of the measurement signals. In the following it is assumed that the control is made in terms of  $F_s$ , whereby friction effects in both the sleigh and the wave side cylinder are accounted for. The control strategy may however easily be modified to be based on  $F_{\Delta p,ws}$  instead. Utilising the above approximation and Eq. (15) to describe the sensor force, Eq. (13) may be rearranged as:

$$\left( m_c + \frac{1}{2} m_s \right) \ddot{x}_c = F_{\text{PTO}} - F_s \quad (25)$$

which, assuming  $x_c(0) = x_{c,\theta_0} = 0$  and  $\dot{x}_c(0) = 0$ , gives the following transfer function:

$$G_s(s) = \frac{x_c}{F_{\text{PTO}} - F_s} = \frac{1}{\left( m_c + \frac{1}{2} m_s \right) s^2} \quad (26)$$

For a given  $F_{\text{PTO}}$  and  $\tau_{\text{ext}}$  the output  $x_c$  of the system and the reference cylinder position  $x_{c,\text{ref}}$  should be equivalent. Hence, the wave cylinder force, expressed in terms of  $F_s$ , is given by using that  $x_{c,\theta_0} = 0$  and rearranging (24) and (26) to:

$$F_s = F_{\text{PTO}} - \left( \frac{1}{d_{c,0}} \tau_{\text{ext}} - F_{\text{PTO}} \right) \frac{G_f(s)}{G_s(s)} d_{c,0}^2 \quad (27)$$

The control structure is shown in Fig. 7. In the controller an integral part may be included to remove small drift offset in the practical setup. It should further be noted that  $G_f(s)$  is part of the feedforward term. Here  $H_{\text{rad}}(s)$  and  $J_{\text{add}}$  are evaluated at a given frequency, based on the given sea state and wave spectrum, to avoid implementing the high frequency filter effects. The latter approximation is justified in the term being a feedforward term, where the controller will still ensure the tracking.

For the force controller in the wave side, a PI-controller is utilised, which is sufficient to ensure proper tracking. The controller is tuned somewhat aggressively, with a break-frequency set to  $15\pi$  [rad/s], in order to obtain sufficient dynamic disturbance rejection from the PTO-side.

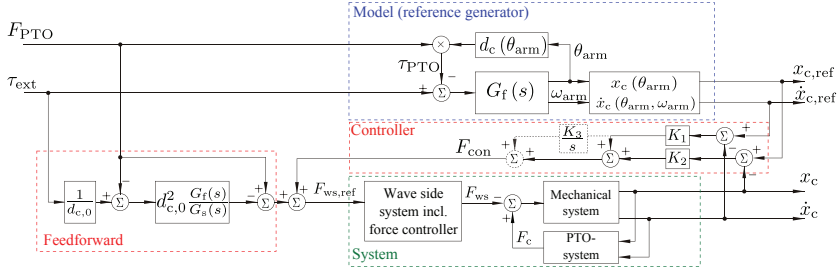


**Figure 7: The control structure for the wave simulator.**

#### 4.3.1 PTO-side control

For testing the wave simulator a controller for the PTO-cylinder has to be utilised. As described in the modelling section, the PTO-motor is considered as running at fixed speed. The objective of the pump displacement is therefore to control the PTO cylinder force. Here a reactive control scheme is utilised, where the force reference is generated as:

$$F_{c,ref} = B_{PTO}\dot{x}_c + K_{PTO}(x_c - x_{c,0}) \quad (28)$$

The reactive force coefficients,  $B_{PTO}$  and  $K_{PTO}$ , are the ones used by Wave Star for the C5 machine, and are adjusted according to the sea state. To ensure the system is tracking the reference in steady state a simple PI-controller is utilised, which is tuned approximately a factor of ten slower than the PTO side dynamics. The integral term is included to account for friction etc. It may be noted that the PTO-side is of minor interest, why the system not tracking perfectly is not a problem for validating the control strategy of the wave side. In fact this tests whether the controller for the wave side will still be able to track the reference, even though the feedforward term is wrongly estimated.

## 5 SIMULATION RESULTS

To test the described control strategy, simulations have been made for each of the three sea states. In the following, results for the first and third sea state are presented. The results from sea state two show similar tendencies. Starting with sea state one, the results are shown in Fig. 8, with zoomed graphs to the right in the figure.

From the graphs it may be seen that the wave cylinder nicely tracks the reference position generated by the model of the wave-float dynamics of the system to emulate. The errors are here below 11 [mm], which is considered within acceptable limits. Similarly it is seen in the lower graphs that the force reference is tracked fairly nicely, with a maximum error of 48 [kN], but where the error for the most part is well below 10 [kN], which is within acceptable limits. The latter should also be seen in relation to that the wave system is to simulate a wave, and not tracking this perfectly, basically just represents a wave which is slightly different than the one simulated. This is therefore only a problem, if different systems are to be compared exactly against each other. Considering the PTO force this is not following the reference particularly well in parts of the period. This is however not considered a problem for the



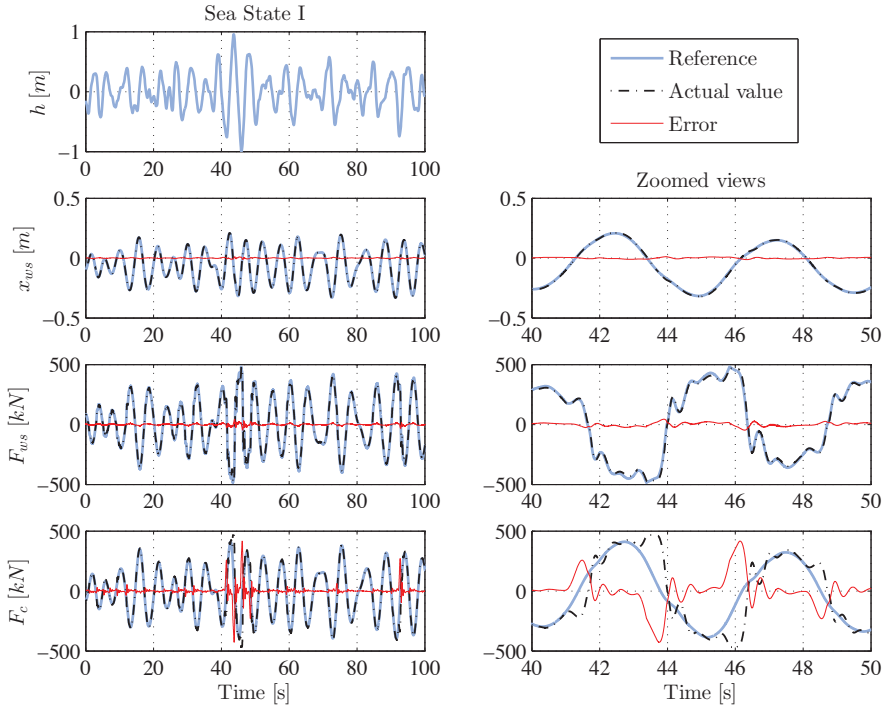


**Figure 8: Results for sea state I.**

wave simulator, which just shows that even if the PTO-system is not tracking the reference, the system is still able to track the reference fairly well, despite the feedforward term being off. The PTO-system not tracking the reference is therefore not addressed further, as this is outside the scope of the present article. The results for sea state two and three show similar results, with the results for sea state three given in Fig. 9

As for sea state one, both the position and force is here tracked fairly well, but with short periods with larger deviations. The maximum errors are here 20 [mm] and 80 [kN] respectively. Although in the high end, this is still considered acceptable, as these deviations correspond to the points where the PTO-system hits the pressure limitation, hereby effectively impressing a step disturbance on the wave side system. The latter may indirectly be seen via the PTO-force, which is limited at approximately 500 [kN] due to the pressure limitations - hence the large errors in the PTO force. Based on these findings it is therefore also found that the control strategy and system is able to emulate the wave behaviour and that the control strategy may be implemented on the real system.

## 6 CONCLUSION

The focus of the current paper has been on the development of a full scale wave simulator for testing Power Take-Off (PTO) systems for wave energy converters. A description of the

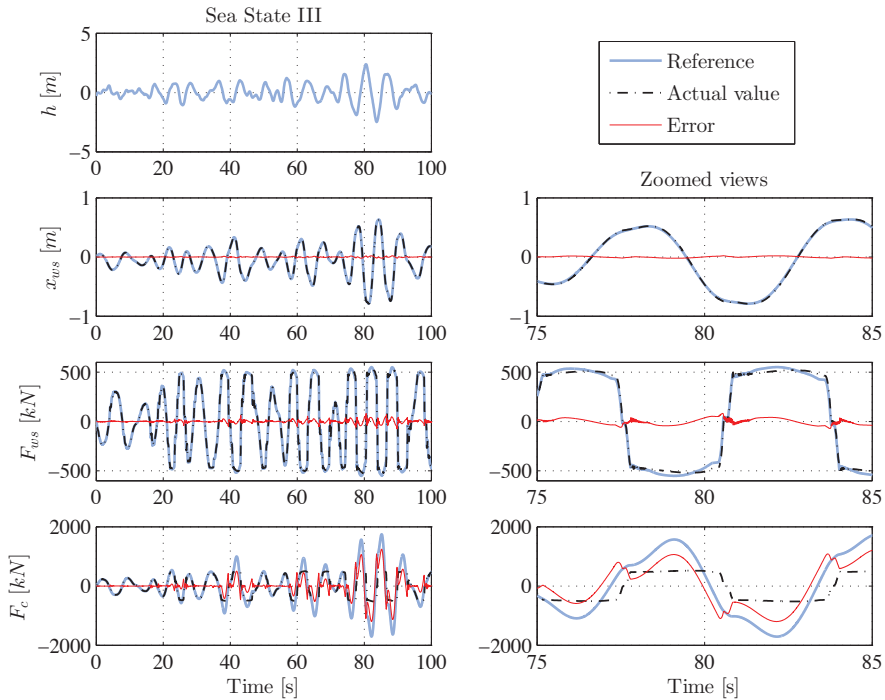


**Figure 9: Results for sea state III.**

system was first presented along with a model of the system. Based on the model of the system a control strategy for the wave side was presented, by which the system is able to emulate real wave behaviour and the effects of wave-float interaction. The control strategy was based on linear wave theory being applied to generate the references to the system, and a state feedback controller was developed, which also include a feedforward term. Based on the developed model and control strategy, simulation results were presented, showing the validity of the control strategy. From the simulation results it was found that the system behaves as expected, and that the control strategy is expected to work when implemented on the real test set-up at AAU, [13].

## REFERENCES

- [1] Griet De Backer. *Hydrodynamic Design Optimization of Wave Energy Converters Consisting of Heaving Point Absorbers*. PhD thesis, Coastal Engineering Division & Maritime Technology Division Department of Civil Engineering Faculty of Engineering Ghent University, 2009. WE0, WE2, WE3.3, WE5.0.
- [2] J. Cruz. *Ocean Wave Energy - Current Status and Future Perspectives.*, volume XII. Green Energy and Technology, 2008.
- [3] Antonio F. de O. Falcao. Modelling and control of oscillating-body wave energy

- converters with hydraulic power take-off and gas accumulator. *Ocean Engineering*, 34:2021–2032, 2007. WE2.3, WE3.1.2.
- [4] Antonio F. de O. Falcao. Phase control through load control of oscillating-body wave energy converters with hydraulic PTO system. *Ocean Engineering*, 35(3-4):358 – 366, 2007. WE2.3, WE3.1.2.
- [5] J. Falnes. *Ocean Waves and Oscillating Systems*. Cambridge University Press, 2002. ISBN: 978-0521782111.
- [6] R.H. Hansen, T.O. Andersen, and H.C. Pedersen. Analysis of discrete pressure level systems for wave energy converters. In *2011 International Conference on Fluid Power and Mechatronics*, pages 552–558, Beijing, China, 2011. IEEE Press.
- [7] R.H. Hansen, T.O. Andersen, and H.C. Pedersen. Model based design of efficient power take-off systems for wave energy converters. In *12th Scandinavian International Conference on Fluid Power, SICFP 2011*, pages 35–49, Tampere University of Technology, Finland, 2011.
- [8] Rico H. Hansen and Morten M. Kramer. Modelling and control of the Wavestar prototype. In *EWTEC 2011*, 2011. WE2.1, WE5, WE6.1.
- [9] Ross Henderson. Design, simulation, and testing of a novel hydraulic power take-off system for the pelamis wave energy converter. *Renewable Energy*, 31(2):271 – 283, 2006. WE3.1.3.1, WE6.2.
- [10] Y. Kamizuru. Wave energy converter PTO Test Bench. [http://www.ifas.rwth-aachen.de/Main/Kontakt/Handouts/KA\\_Handout\\_WEC%20test%20bench\\_en.pdf](http://www.ifas.rwth-aachen.de/Main/Kontakt/Handouts/KA_Handout_WEC%20test%20bench_en.pdf), April 2012.
- [11] M.J. Ketabdari and A. Ranginkaman. Simulation of random irregular sea waves for numerical and physical models using digital filters. *Transaction B: Mechanical Engineering*, 16(3):240–247, 2009. WE5.
- [12] Ocean Navitas. Hydraulic linear wave simulator. [http://www.oceannavitas.com/technology/wave\\_simulator.html](http://www.oceannavitas.com/technology/wave_simulator.html), April 2012.
- [13] Department of Energy Technology. Full scale wave simulator at AAU. <http://www.et.aau.dk/research-programmes/fluid-power-in-wind-and-wave-energy/laboratory-facilities/>, July 2012.
- [14] G. S. Payne, A. Kiprakis, M. Ehsan, W. H. S. Rampen, J. P. Chick, and R. Wallace. Efficiency and dynamic performance of digital displacement hydraulic transmission in tidal current energy converters. In *Journal of Power and Energy, Part A : In Proceedings of IMechE.*, volume 221, pages 207–217, May 2007. ME1.2.2.1, WE3.1.3.
- [15] Gregory S. Payne, Uwe B.P. Stein, Mohammad Ehsan, Niall J. Caldwell, and W H.S. Rampen. Potential of digital displacement hydraulics for wave energy conversion. In *In proc. of the 6th European Wave and Tidal Energy Conference, Glasgow, UK*, August 29th - September 2nd 2005. ME1.2.2.1, WE3.1.3, WE6.2.
- [16] S. H. Salter. Digital hydraulics for renewable energy. In *World Renewable Energy Conference Aberdeen*, 2005. WE3.4.
- [17] S. H. Salter, J. R. M. Taylor, and N. J. Caldwell. Power conversion mechanisms for wave energy. In *Proceedings of the Institution of Mechanical Engineers, Part M: Journal of Engineering for the Maritime Environment*, 2002. WE3.4, WE2.1, WE2.2, WE2.3, WE2.4, WE2.5, WE3.1.3, WE4, WE0.
- [18] A. Weinstein, G. Fredrikson, M.J. Parks, and K. Nielsen. Aquabuoy - the offshore wave energy converter numerical modeling and simulation. In *OCEANS '04. MTT/IEEE TECHNO-OCEAN '04*, volume 4, pages 1854 –1859 Vol.4, 2004. WE4.1.

# Determining Required Valve Performance for Discrete Control of PTO Cylinders for Wave Energy

**Rico H. Hansen, Torben O. Andersen and Henrik C. Pedersen**

Aalborg University, Department of Energy Technology, DK-9220 Aalborg East, Denmark

## ABSTRACT

Within wave energy a large challenge remains in designing a Power Take-Off (PTO) system capable of converting the slow oscillations induced by waves into electricity. Fluid power is an essential part of most PTO-concepts. To implement an efficient control of the load force produced by a cylinder on a floating body, throttle-less force control by discrete variation of the effective cylinder area has been investigated and found feasible for the Wavestar wave energy concept. However, the feasibility study assumes adequate valve performance, such that only the compression loss remains. This paper investigates the required valve performance to achieve this energy efficient operation, while meeting basic dynamic requirements. The components making up the total energy loss during shifting is identified by analytically expressing the losses from the governing differential equations. From the analysis a framework for evaluating the adequacy of a valve's response is established, and the analysis shows the results may be normalised for a wider range of systems. Finally, the framework is successfully applied to the Wavestar converter.

**Keywords:** Hydraulics, Fluid Power, PTO, Wave energy, Discrete Displacement, Secondary Controlled System, Wavestar

## 1. INTRODUCTION

Numerous Wave Energy Converters (WEC) concepts are being developed for harvesting the energy of ocean waves, where the forerunners are passing the proof-of-concept stage and entering a pre-commercialisation phase. A survey of WEC concepts is given in (1) and (2). One of the main challenges for a large group of WECs is implementing an efficient Power Take-off (PTO) system for converting the mechanical energy of oscillating floating bodies into electricity.

Waves induce a very slow and irregular oscillation of the bodies, requiring the PTO system to possess high force densities (3) for generating the large bidirectional load forces required to perform energy extraction. Resultantly, fluid power is essential for implementing the transmission required for making the irregular oscillations of the body power a conventional high-speed generator. Unfortunately, fluid power systems are characterized by poor efficiencies, especially at part load which is required in wave power.

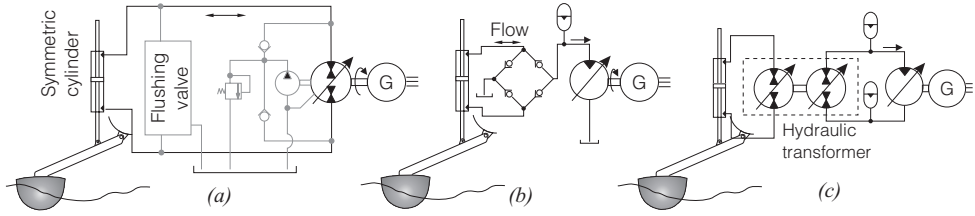


**Figure 1: Hydraulic transmissions for PTO systems.**

A conventional hydraulic transmission as seen in Fig. 1a would become very inefficient due to the varying load. An optimisation of such a PTO from wave-to-grid is performed in (4) for the Wavestar converter, showing an overall PTO efficiency of only 65% at the optimum point, quickly dropping to 45% in smaller waves. The system in Fig. 1a also has the weakness of not allowing to smooth the generator load. More simple PTOs as in Fig. 1b is used in (5) and (6), where energy smoothing can be performed using accumulators. These allow the hydraulic motors to work at a steady load and good efficiency. However, these PTOs may only deliver a fixed force, reducing the energy extraction from the waves (3).

It would be desirable to combine the above system characteristics, thereby having a PTO with a “constant” pressure line, while performing throttle-less force control of the cylinders. Hence, an efficient secondary controlled system is sought. In (7) a hydraulic transformer as in Fig. 1c is suggested. However, compared to Fig. 1a, two extra variable displacement units are used, reducing the benefit due to their negative impact on the efficiency.

In (8) a PTO system for the Wavestar is investigated, where the force control of a hydraulic cylinder is based on switching between fixed system pressures using an arrangement of on/off valves, see Fig. 2. The resulting PTO force  $F_{PTO}$  is generated as the sum of forces produced by the different cylinder areas.

In (8) it was shown that despite assuming infinite fast and large switching valves, a certain amount of energy will always be lost when shifting force due to the compressibility of the fluid. When shifting pressure of a fixed chamber of volume  $V$  from  $p_0$  to  $p_1$ , the amount of energy lost due to the compressibility of the fluid is (8),

$$E_{\beta\text{-loss}} = \frac{1}{2}(p_1 - p_0)^2 \frac{V}{\beta} \quad (1)$$

where  $\beta$  is the bulk modulus of the fluid. To assess whether a PTO system may be feasible with this unavoidable compression loss, a PTO efficiency was calculated for the Wavestar WEC based on assuming the minimum compression loss when shifting. This was performed for different wave conditions, showing that an efficiency above 90% was reachable for the discrete force control of the cylinder, making the system feasible. However, assuming only the minimum compression loss is equal to assuming infinite fast valves.

Discrete control of a hydraulic cylinder has also been investigated in (9), showing promising energy saving compared to e.g. load sensing systems. A similar PTO system utilising a system structure with two asymmetric cylinders has also previously been discussed in (10). The efficiency of controlling the force of the cylinders by pressure shifting was found to be between 88% and 94%, excluding the friction of the cylinder. However, none of these papers contained information on determining required valve performance.

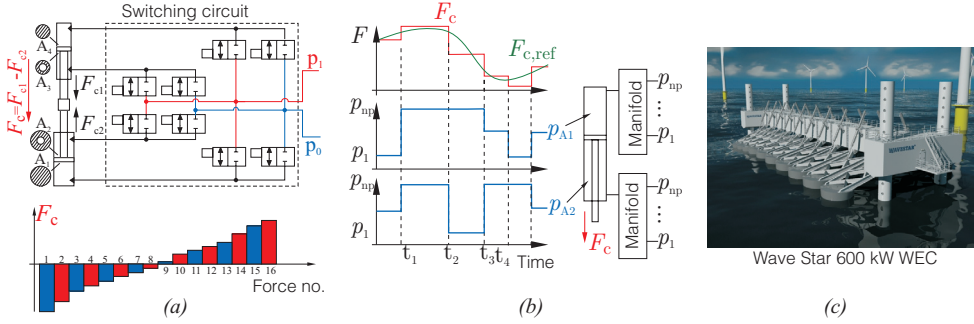


**Figure 2: Discrete force control using multiple areas and/or multiple pressure levels.**

The focus of this paper is to develop a framework for determining the required valve size and response time in order to maintain the desired efficiency of the system. The investigation is based on a single float and arm for the Wavestar 600kW WEC seen in Fig. 2c, consisting of 20 hemisphere shaped floats, each 5m in diameter.

## 2. Methods

The task is to analyse how the on/off valves' response time and size influence the energy loss present when operating with discrete force control of a cylinder. As discrete force control is basically to shift pressure in one or more chambers, and then have a longer "steady-state" period before the next shift, great benefit may be obtained by analysing the pressure shift within just a single generic cylinder chamber. The generic chamber may then be used for analysing different piston velocities, initial volumes, pressure shift combinations and valve opening characteristics.

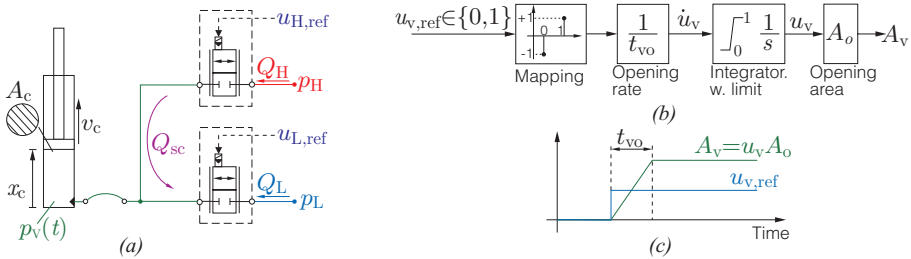


**Figure 3: (a) is the system model for analysis and (b),(c) are the valve model.**

An illustration of the model setup is seen in Fig. 3. In Fig. 3a a simple volume is shown, connected to two pressure lines using on/off valves. The valves may be actuated independently. When shifting from  $p_H$  to  $p_L$  and vice versa, problems arise when the displacement flow is non-zero, i.e.  $v_v \neq 0$ . In this case, the shifting might result in pressure peaks due to temporary restriction of fluid passage of the displacement flow when one valve is closing and the other is opening. This is especially the case if the opening and closing time of the valves  $t_v$  is slow compared to the pressure gradient in the volume. This is illustrated in

Fig. 4. Consequently, it may be necessary to open the second valve before the first valve has closed. This may result in a temporary short circuiting of the pressure lines with the risk of a severe energy loss, as the fluid will flow directly from high to low pressure.

The applied method is overall to have a simple model of a volume as in Fig. 3a, simulate it for different valve response times,  $t_v$ , and then calculated the energy loss due to pressure shifting. To generate and assess these results, the following is performed first:

- Define a generic model for the valves and establish the governing system equations.
- Basic analysis of the energy loss present when shifting pressure on a volume experiencing non-zero displacement flow. The analysis is based on analytical treatment of the differential system equations.
- Define a base for assessing the valve's performance in the system and a method for normalising the results.
- Identify the operating region of a cylinder for a Wavestar WEC in operation for determination of valve requirements.

## 2.1 System Model

Transmission phenomena within the connection from cylinder to valve is neglected. Instead the cylinder and the connection is modelled as one volume. The system pressure  $p_H$  and  $p_L$  are assumed constant, which may be obtained with adequate accumulator capacity. Thus, the pressure dynamics of the volume or cylinder pressure  $p_V$  in Fig. 3a is described by the continuity equation and the valve flows are described by the orifice equation,

$$\dot{p}_V(t) = \frac{\beta_{\text{eff}}}{V_0 + A_c x_c} (Q_H(t) + Q_L(t) - \dot{V}(t)) \quad (2a)$$

$$Q_H = \text{sign}(p_H - p_V(t)) C_d A_H(t) \sqrt{\frac{2}{\rho} |p_H - p_V(t)|} \quad (2b)$$

$$Q_L = \text{sign}(p_L - p_V(t)) C_d A_L(t) \sqrt{\frac{2}{\rho} |p_L - p_V(t)|} \quad (2c)$$

where  $\beta_{\text{eff}}$  is the bulk modulus of the fluid and  $C_d = 0.6$  is the discharge coefficient. A constant bulk modulus of 7000 bar is used, as the lowest pressure is 20 bar.

The transient behaviour of the valve is modelled as a ramp function in order to have a very generic valve, see Fig. 3c. This model is preferred compared to e.g. a linear first order model, as on/off valves do not tend to slow down near their set point, confer a seat valve. A linear second order model could also have been utilized, however, the response of a on/off valve also tends to saturate quite fast, making the ramp model more representative. The ramp model is also assumed to be the most conservative definition of a valve's opening time. In this study the valve is assumed to be equally fast at opening and closing.

The model is shown in Fig. 3b, and stated below:

$$A_v(t) = A_0 u_v(t) \quad (3)$$

$$\dot{u}_v(t) = \begin{cases} \frac{1}{t_v} + u_v & ; u_v < 1 \wedge u_{v,\text{ref}} = 1 \\ \frac{-1}{t_v} + u_v & ; u_v > 0 \wedge u_{v,\text{ref}} = 0 \\ 0 & ; u_v = u_{v,\text{ref}} \end{cases} \quad (4)$$

Any energy loss during and after the shift will be dissipated across the on/off valves, hence the power loss is,

$$P_{\text{loss}} = Q_L(t)(p_L - p_V(t)) + Q_H(t)(p_H - p_V(t)) \quad (5)$$

which may be integrated to yield the total energy loss. Having obtained the system model, the following section derives how the shifting loss may be calculated and how the valve performance may be assessed.

## 2.2 Energy Loss During Pressure Shift

In the work in (8), the energy loss during a pressure shift was investigated for a chamber assuming a fixed volume and zero displacement-flow. In this analysis, the investigation is performed including the displacement flow, i.e. non-zero cylinder velocity.

The procedure of shifting pressure involves closing one valve and opening a second valve to the desired new pressure. The basis of the analysis is to describe the minimum energy loss for such a procedure, i.e. no restriction on the valves. The first assumption is, that it will always be most efficient to close the first valve instantly instead of introducing throttling by closing it slowly. The argument is that if the pressure build up caused by the displacement flow is in agreement with the desired pressure change, as in case 3 and 4 in Fig. 4, it would be most efficient to shut-off the first valve, as no throttling is performed, and then the second valve may be opened with no extra throttling loss when the pressure has balanced. For case 1 and 2 the desired pressure change can only be performed by opening the second valve. Consequently, the first valve needs to be closed immediately, otherwise either a pressure peak in the wrong direction will occur or there will be a short-circuit flow.

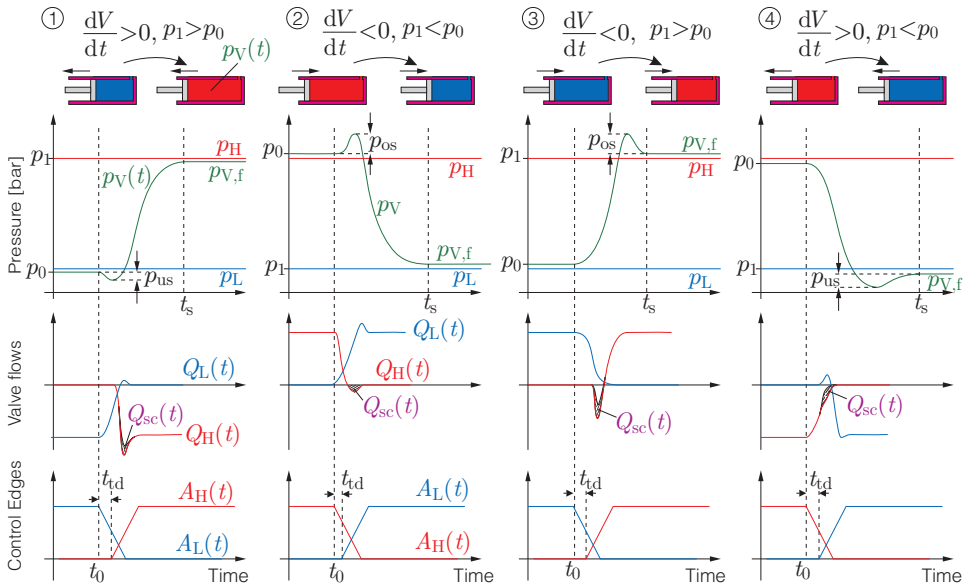
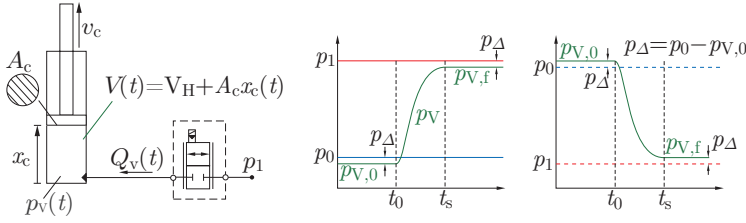


Figure 4: The four shift cases.





**Figure 5: System for analytical analysing pressure shift in a cylinder chamber.**

Thus, the problem reduces to analysing a chamber of an initial pressure  $p_{V,0}$  and initial volume size  $V_{t_0} = V_0$ , which needs to be connected to a pressure line with pressure  $p_1$  under a given displacement flow  $\dot{V}(t) = A_v v_c$ . This is illustrated in Fig. 5. The quantity  $p_\Delta$  denotes the steady state pressure drop across the valve for a given displacement flow, thus when steady-state pressure  $p_{V,f}$  is reached, then  $p_\Delta = p_1 - p_{V,f}$ .

The flow continuity equation describes the dynamics of the volume pressure  $p_v(t)$ ,

$$\dot{p}_v(t) = \frac{\beta}{\int \dot{V}(t)dt + V_0} (Q_v(t) - \dot{V}(t)) \Rightarrow p_v(t) \approx \frac{\beta}{V_0} \int (Q_v(t) - \dot{V}(t)) dt + p_{V,0} \quad (6)$$

where the change of volume during the shifting period is assumed to be small compared to the initial volume, i.e.  $|\int \dot{V}(t)dt| \ll |V_0|$ .

At some point  $t_f$  the pressure  $p_v$  will have increased to  $p_{V,f} = p_1 - p_\Delta$ ,

$$p_v(t_f) = p_{V,f} = \frac{\beta}{V_0} \int_0^{t_f} Q_v(t) - \dot{V}(t) dt + p_{V,0} \Rightarrow \int_0^{t_f} Q_\beta(t) dt = \frac{V_0}{\beta} (p_{V,f} - p_{V,0}) \quad (7)$$

where  $Q_v(t)$  has been substituted with:

$$Q_v(t) = \dot{V}(t) + Q_\beta(t) \quad (8)$$

Note that the above substitution of  $Q_v$  is without loss of generality, as no assumptions are made on  $Q_\beta$ . From Eq.7 it is seen that only the term  $Q_\beta$  of  $Q_v$  contributes to the pressure change as expected, as the term  $\dot{V}(t)$  only balance the displacement flow.

If the energy out of the pressure supply  $p_1$  is denoted  $E_{p,1}$ , and the energy received by the volume is denoted  $E_v$ , the energy loss at time  $t$  is given as:

$$E_{\text{loss}}(t) = E_{p,1}(t) - E_v(t) = \int_{t_0}^t p_1 Q_v(t) dt - \int_{t_0}^t p_v(t) Q_v(t) dt \quad (9)$$

$$\begin{aligned} &= \int_{t_0}^t p_1 (Q_\beta(t) + \dot{V}(t)) dt - \int_{t_0}^t p_v(t) (Q_\beta(t) + \dot{V}(t)) dt \\ &= p_1 \int_{t_0}^{t_f} Q_\beta(t) dt + \int_{t_0}^{t_f} \underbrace{(p_1 - p_v(t))}_{=p_{V,f}+p_\Delta} \dot{V}(t) dt - \int_{t_0}^{t_f} p_v(t) Q_\beta(t) dt \\ &\quad + p_1 \underbrace{\int_{t_f}^t Q_\beta(t) dt}_{=0} + \int_{t_f}^t \underbrace{(p_1 - p_v(t))}_{=p_1 - p_{V,f}=p_\Delta} \dot{V}(t) dt - \underbrace{\int_{t_f}^t p_v(t) Q_\beta(t) dt}_{=0} \\ &= p_1 \int_{t_0}^{t_f} Q_\beta(t) dt + \int_{t_0}^{t_f} (p_{V,f} - p_v(t)) \dot{V}(t) dt - \int_{t_0}^{t_f} p_v(t) Q_\beta(t) dt + \int_{t_0}^t p_\Delta \dot{V}(t) dt \quad (10) \end{aligned}$$

By denoting the flow integral  $\int_{t_0}^{t_f} Q_\beta(t)dt$  as the volume  $V_Q(t)$ , the pressure  $p_V(t)$  may according to Eq.7 be expressed as:

$$p_V(t) = \frac{\beta}{V_0} V_Q(t) + p_{V,0} \Rightarrow V_Q(t_f) = \int_{t_0}^{t_f} Q_\beta(t)dt = \frac{V_0}{\beta} (p_{V,f} - p_{V,0}) \quad (11)$$

Inserting into Eq.10 gives:

$$\begin{aligned} E_{\text{loss}} &= p_1 V_Q(t_f) + \int_{t_0}^{t_f} (p_{V,f} - p_V(t)) \dot{V}(t)dt - \int_{t_0}^{t_f} \left( \frac{\beta}{V_0} V_Q(t) + p_{V,0} \right) Q_\beta(t) dt + \int_{t_0}^t p_\Delta \dot{V}(t)dt \\ &= p_1 V_Q(t_f) - p_{V,0} V_Q(t_f) - \frac{\beta}{V_0} \int_{t_0}^{t_f} V_Q(t) Q_\beta(t)dt + \int_{t_0}^{t_f} (p_{V,f} - p_V(t)) \dot{V}(t)dt + \int_{t_0}^t p_\Delta \dot{V}(t)dt \end{aligned} \quad (12)$$

By noting that  $\frac{dV_Q}{dt} = Q_\beta(t)$ , the first integral in Eq.12 may be solved:

$$\begin{aligned} \frac{\beta}{V_0} \int_{t_0}^{t_f} V_Q(t) Q_\beta(t)dt &= \int_{t_0}^{t_f} \frac{\beta}{V_0} V_Q(t) \frac{dV_Q}{dt} dt = \frac{\beta}{V_0} \left[ \frac{1}{2} V_Q(t)^2 \right]_{t_0}^{t_f} = \frac{\beta}{V_0} \frac{1}{2} V_Q(t_f)^2 \\ &= \frac{1}{2} \frac{V_0}{\beta} (p_{V,f} - p_{V,0})^2 = \frac{1}{2} \frac{V_0}{\beta} (p_{V,f} - p_{V,0})(p_1 - p_{V,0} - p_\Delta) \end{aligned} \quad (13)$$

Inserting Eq.11 and Eq.13 into Eq.12 yields:

$$\begin{aligned} E_{\text{loss}} &= \frac{V_0}{\beta} (p_1 - p_{V,0})(p_{V,f} - p_{V,0}) - \frac{1}{2} \frac{V_0}{\beta} (p_{V,f} - p_{V,0})(p_1 - p_{V,0} - p_\Delta) + \int_0^{t_f} (p_{V,f} - p_V(t)) \dot{V}(t)dt + \int_0^t p_\Delta \dot{V}(t)dt \\ &= \frac{1}{2} \frac{V_0}{\beta} (p_1 - p_{V,0})^2 - \frac{1}{2} \frac{V_0}{\beta} p_\Delta^2 + \int_0^{t_f} (p_{V,f} - p_V(t)) \dot{V}(t)dt + \int_0^t p_\Delta \dot{V}(t)dt \end{aligned} \quad (14)$$

There are four shifting case as defined in Fig. 4. These are treated in pairs in the following.

### 2.3 Active Shift: Case 1 and 2

For case 1 and 2, where the desired pressure shift is opposite the pressure build up caused by displacement, Eq.14 states that:

$$E_{\text{loss}}(t) = \underbrace{\frac{1}{2} \frac{V_0}{\beta} (p_1 - p_{V,0})^2 - \frac{1}{2} \frac{V_0}{\beta} p_\Delta^2}_{>0} + \underbrace{\int_{t_0}^{t_f} (p_{V,f} - p_V(t)) \dot{V}(t) dt}_{\text{Case 1 \& 2: } >0} + \underbrace{\int_{t_0}^t p_\Delta \dot{V}(t) dt}_{>0} \quad (15)$$

The first term cannot be manipulated by control of the valve flow  $Q_\beta(t)$ , hence the first term constitutes an inevitable energy loss under the given assumption of the system. The second term is the extra loss from throttling the displacement flow until steady state has been reached, and the third term is the steady state throttling. As the integrand of the second term is bounded and non-negative, this loss will go towards zero for the shifting time  $t_s = t_f - t_0$  going to zero, i.e. for case 1 and 2, term 1 is the minimum shifting loss:

$$E_B = \min_{0 \leq t_s} E_{\text{loss}}(t) = \lim_{t_s \rightarrow 0} E_{\text{loss}}(t) = \frac{1}{2} \frac{V_0}{\beta} (p_1 - p_{V,0})^2 - \frac{1}{2} \frac{V_0}{\beta} p_\Delta^2 \quad (16)$$

However,  $t_s \rightarrow 0$  infers that  $Q_v \rightarrow \infty$  as the pressure increase occurs instantaneously. Hence for a real system and non-zero displacement flow, the minimum loss can only be approached.

After the system has settled, only the steady throttling loss  $\int_{t_0}^t p_{\Delta} \dot{V}(t) dt$  will remain as  $(p_{V,f} - p_V(t)) = 0$  for  $t > t_f$ . As this term is always present in Eq.14, the shifting loss for the active shifting cases 1 and 2 is defined as the loss subtracted the steady-state loss:

$$E_{\text{shift,A}} = E_{\text{loss}}(t) - \int_{t_0}^t p_{\Delta} \dot{V}(t) dt = \frac{1}{2} \frac{V_0}{\beta} (p_1 - p_{V,0})^2 - \frac{1}{2} \frac{V_0}{\beta} p_{\Delta}^2 + \int_{t_0}^{t_f} (p_{V,f} - p_V(t)) \dot{V}(t) dt \quad (17)$$

Resultantly, the exact time of steady state  $t_f$  is not required identified for evaluating the loss, just that  $t > t_f$ . With this definition  $E_{\text{shift,A}}$  also equals  $E_{\beta}$  for  $t_s \rightarrow 0$  as desired. The loss  $E_{\text{shift,A}}$  for the active shifting case may thereby be measured or calculated during simulation as the loss across the valves  $P_{\text{loss}}$  minus the steady state loss:

$$E_{\text{shift,A}} = \int_{t_0}^t P_{\text{loss}} - \dot{V}(t) p_{\Delta} dt \quad (18)$$

## 2.4 Passive Shift: Case 3 and 4

For case 3 and 4 the displacement flow aids the desired pressure change, see Fig. 4. Thus, if the flow out of the volume is set to zero until the steady-state pressure  $p_{V,f}$  is reached, and afterwards equated to the displacement flow, the shifting loss may be reduced to zero. This is shown using the established equations by setting the flow into the volume  $Q_v$  to zero until the steady state pressure is reach at  $t_f$ , and afterwards equating the valve flow to the displacement flow  $\dot{V}(t)$ :

$$Q_v(t) = \begin{cases} 0 & ; 0 \leq t \leq t_f \\ \dot{V}(t) & ; t > t_f \end{cases} \quad (19)$$

Inserting Eq.19 into Eq.9 yields:

$$E_{\text{loss}}(t_f) = \int_{t_f}^t p_1 \dot{V}(t) dt - \int_{t_f}^t p_{V,f} \dot{V}(t) dt = \int_{t_f}^t p_{\Delta} \dot{V}(t) dt = 0 \quad (20)$$

Hence, by using the displacement flow for pressure build up, a “passive shift” is obtained, and the shifting loss is zero as expected.

Like for case 1 and 2 it is desirable to have a definition allowing the calculation of the shifting loss without knowing the exact settling time  $t_f$ . If the loss across the valve is measured, the shifting loss for the passive shifting cases 3 and 4 may be calculated as:

$$E_{\text{shift,P}} = \int_{t_0}^t Q_v (p_1 - p_V(t)) - \dot{V}(t) p_{\Delta} dt + p_{\Delta} \int_{t_0}^{t_0+t_{s,\text{opt}}} \dot{V}(t) dt \quad (21)$$

The last term is added as the flow  $\dot{V}(t)$  does not exist during the optimal shifting time  $t_{s,\text{opt}}$ . Thus, the above expression will become negative if this term was not added. By inserting the optimal control law in Eq.19 into Eq.6, the last integral can be calculated as:

$$p_{V,f} = \frac{\beta}{V_0} \int_{t_0}^{t_0+t_{s,\text{opt}}} (0 - \dot{V}(t)) dt + p_{V,0} \Leftrightarrow \int_{t_0}^{t_0+t_{s,\text{opt}}} \dot{V}(t) dt = -\frac{V_0}{\beta} (p_{V,f} - p_{V,0}) \quad (22)$$

Inserting into Eq.18 yields the expression for calculating the passive shifting loss:

$$E_{\text{shift,P}} = \int_{t_0}^t P_{\text{loss}} - \dot{V}(t) p_{\Delta} dt - p_{\Delta} \frac{V_0}{\beta} (p_{V,f} - p_{V,0}) \quad (23)$$

## 2.5 Assessment and Normalisation of Results

To assess the size of the shifting loss, a loss ratio  $\gamma$  is defined, which expresses the extra loss beside the minimum compression loss, as a ratio of the minimum compression loss:

$$\gamma(t_v, t_{ld}, x_o) = \begin{cases} \frac{E_{\text{shift,A}}}{E_\beta} - 1 & : \text{Active case (case 1 \& 2)} \\ \frac{E_{\text{shift,P}}}{E_\beta} & : \text{Passive case (case 3 \& 4)} \end{cases} \quad (24)$$

For the passive case, the shifting loss is ideally zero. Consequently, the extra shifting loss for the passive case is compared to  $E_\beta$  to have a indicative ratio of the loss size.

To avoid performing the evaluation of required valve response time for all different area sizes of a cylinder, the results may be normalised by proper definition of the valve opening area, and if the stroke length  $x_c$  is kept constant. The latter is a reasonable assumption, e.g. using a cylinder with multiple chambers or using pair of cylinders of equal length. In this case the velocity  $v_c$  is also the same for all areas.

Assume a chamber has a cylinder area of  $kA_{c,0}$ , where  $k$  is a positive coefficient. Then for a selected cylinder velocity  $v_{c,0}$ , define the valves' opening area  $A_o$  such that a desired steady state pressure drop  $p_{\Delta x}$  is obtained:

$$A_o = \frac{kA_{c,0}v_{v,0}}{C_d\sqrt{\frac{2}{\rho}p_{\Delta x}}} \quad (25)$$

The next step is now to prove that the loss ratio in Eq.24 remains constant. First it may be shown, that the pressure dynamics of  $p_v(t)$  is unchanged for a given control input to the system  $u_L$  and  $u_H$ . Inserting Eq.25 into the system equations in Eq.2 yields:

$$Q_H = k \frac{A_{c,0}v_{v,0}}{\sqrt{p_{\Delta x}}} u_H(t) \sqrt{|p_H - \dot{p}_v(t)|} \text{sign}(p_H - p_v(t)) \quad (26)$$

$$Q_L = k \frac{A_{c,0}v_{v,0}}{\sqrt{p_{\Delta x}}} u_L(t) \sqrt{|p_L - \dot{p}_v(t)|} \text{sign}(p_L - p_v(t)) \quad (27)$$

$$\dot{p}_v(t) = \frac{\beta}{kx_c A_{c,0}} (Q_H(t) + Q_L(t) - kv_v A_{c,0}) \quad (28)$$

Hence, by inserting the two flow expressions Eq.26 and Eq.27 into Eq.28,  $k$  will be cancelled in the differential equation of  $p_v(t)$ . Thus, the time development of  $p_v(t)$  is independent of the cylinder area. The above also shows, that the flows scale linearly with  $k$ . As  $p_v(t)$  is unchanged, this means that the valve losses will be scaled with  $k$ . Performing the same analysis of  $E_\beta$  in Eq.16 shows that it also scales linearly with  $k$ . Thus the defined loss ratio in Eq.24 remains constant. The result states that given a set of operating points, where the operating points are:

- Sets of cylinder velocities and cylinder positions  $\{(v_{c,1}, x_{c,1}), (v_{c,2}, x_{c,2}), \dots\}$
- Sets of pressure shift combinations  $p_0 \rightarrow p_1: \{(p_{01}, p_{02}), (p_{02}, p_{01}), (p_{01}, p_{03}), \dots\}$

Then if the steady state pressure drop  $p_{\Delta x}$  across the on/off valves at a given cylinder velocity  $v_c$  is kept constant, the required response time  $t_v$  for the valves and the corresponding control inputs  $u_{\text{ref}}(t)$  to meet the loss ratios requirement will be equal for all cylinder area sizes with equal total stroke length.

## 2.6 Requirement Specification and Optimisation of Control Inputs

The requirement of the valve's response time  $t_v$  is a trade-off between accepted energy loss and allowed pressure peaks. Thus, the requirement specification consists of:

- Allowed pressure overshoot  $p_{os}$  and  $p_{us}$  as defined in Fig. 4.
- Allowed loss ratio for  $\gamma$  in Eq.24 .
- Operating points and pressure shift combination, at which the above should be met.

The pressure overshoot may be specified as absolute values or relative sizes. To find the optimal shifting procedure for a given valve response, operating point  $x_o$ , and overshoot requirement, the optimal time delay  $t_{td,opt}$  is found as:

$$t_{td,opt} = \operatorname{argmin} \gamma(t_v, t_{td}, x_o) \quad \text{s.t.} \quad \begin{aligned} p_{os} &\leq p_{os,req} \\ t_{rd} &\geq 0 \\ p_{us} &\leq p_{us,req} \end{aligned} \quad (29)$$

The value  $E_{shift}(t_{td})$  is found by simulation, and a simple search function with initial guess  $t_{td} = 0$  is used to find the optimum. Next, to find the slowest valve response time  $t_v$  meeting the requirement, a search is performed on  $t_v$  with Eq.29 as an inner loop to find the optimum of  $t_{td,opt}$  for each iteration.

## 3. Operating Points of the Wavestar Converter

A model describing the dynamics of a single Wavestar float with a cylinder is given in (11) based on linear wave theory (12). Using the model a realisation of e.g. time signals of cylinder position and velocity may be obtained for a given sea condition or sea state. The system is simulated for 30min in one of the largest production sea states for the Wavestar C5, see (11) and (4). The sea state has a significant wave height of 2.50m and a mean wave period of 5.5s. A view of the simulation results is seen in Fig. 6a. To describe the cylinders operating region, a density function  $f(x_c, v_c)$  is calculated from the cylinder movement, showing how often the cylinder is in different position and velocity combinations. From the density function  $f(x_c, v_c)$ , the percentage  $F_{op}$  of time spend in a given region  $R_{op}$  may be found as:

$$F_{op}(R_{op}) = \iint_{R_{op}} f(x_c, v_c) dx_c dv_c \quad (30)$$

By dividing the cylinder position and velocities into discrete intervals, and integrating the time spend in each interval, the time trajectory in Fig. 6a is transformed into the density function in Fig. 6b. As expected, high velocities near the cylinder ends never occurs, thus choosing the valves according to the worst case velocity and position would be over-conservative. Instead the worst-case points are selected as the red trajectory in Fig. 6, as the cylinder is within this area more than 99% of the time.

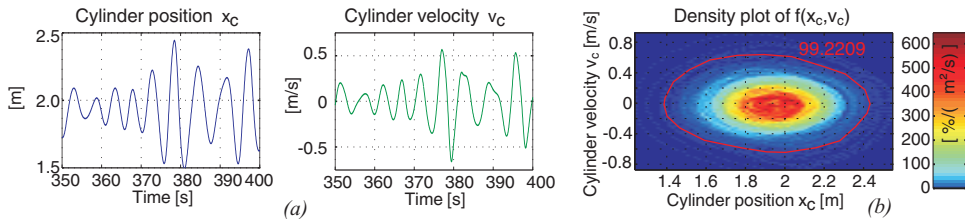


Figure 6: Cylinder movement for the Wavestar WEC and its density function.

#### 4. Results

To investigate how the shifting loss depends on the valve response time, the following results are presented and briefly discussed:

- 1) The shifting loss as a function of valve response time at a pressure change of 20 bar to 120 bar, initial position  $x_c = 0.5$  m and velocity in both directions  $\pm 0.5$  m/s.
- 2) The shifting loss as a function of valve response time for three different valve sizes  $p_{\Delta x}$  is evaluated for shift from 20 bar to 120 bar,  $x_c = 0.5$  m and  $v_c = 0.35$  m/s. This will show how much is gained by selecting larger valves.
- 3) The shifting loss is evaluated as a function of initial positions  $x_c$  and velocities  $v_c$  for a fixed valve response time  $t_v = 15$  ms, opening valve area  $p_{\Delta x} = 5$  bar and pressure shift 20 bar to 120 bar.
- 4) The shifting loss evaluated along the worst-case operating points of the Wavestar cylinder shown in Fig. 6 for four different valve response times, and for two pressure shifts, 20 bar to 120 bar and vice versa, .

The maximum allowed undershoot and overshoot  $p_{us}$  and  $p_{os}$  is set to 7 bar in all cases. The results are for a cylinder area of  $A_c = 210 \text{ cm}^2$ .

##### 4.1 Shifting Loss as a Function of Valve Response Time $t_v$

For positive velocity, the displacement flow counteracts the desired pressure shift and results in a non-zero loss. With the given cylinder area, the minimum loss  $E_\beta$  is 0.75 kJ for the initial conditions in Tab. 1. However, for infinite fast valves  $t_v = 0$  ms, the results in Tab. 1 show that an extra loss still exists. This is due to the fact that the valve opening area  $A_o$  is finite, resulting in a non-instant pressure build up. Thus, for non-zero displacement, the extra loss is due to the extra throttling of the displacement flow as expressed in Eq.15:

$$E_{\dot{V}} = \int_{t_0}^{t_f} (p_{v,f} - p_v(t)) \dot{V}(t) dt \quad (31)$$

If the desire is to evaluate if the valve is fast enough, this loss  $E_{\dot{V}}$  for  $t_v \rightarrow 0$  should be neglected. Thus a new loss ratio  $\gamma_{A_o}$  is defined for the active shift case as,

$$\gamma_{A_o} = \frac{E_{\text{shift}}}{E_{\text{shift},\infty}} - 1 \quad (32)$$

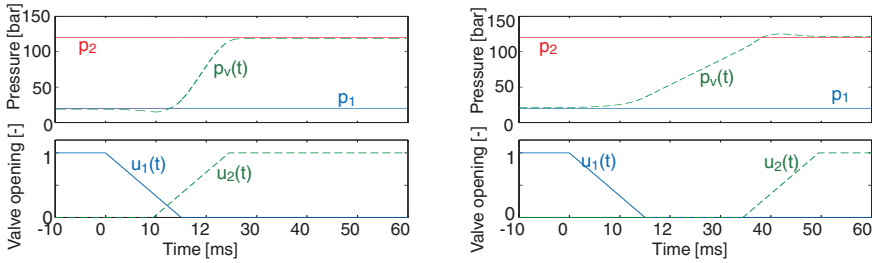
where  $E_{\text{shift},\infty}$  is the shifting loss for  $t_v \rightarrow 0$ .

For the results in Tab. 1,  $E_{\text{shift},\infty} = 0.15$  kJ. The results show, that the requirement of the valve is much higher for the active shifting case. The optimisation also shows that having a bit of overlap of the valve openings is more efficient than having the allowed pressure peaks. The allowed overshoot first becomes an active constraint at  $t_v > 30$  ms. Another characteristic is that as the valve gets slower, there is only a steady increase in loss.

An example of the optimisation results for  $t_v = 15$  ms is given in Fig. 7, showing the overlap for the active case, and non-overlapping behaviour for the passive case.

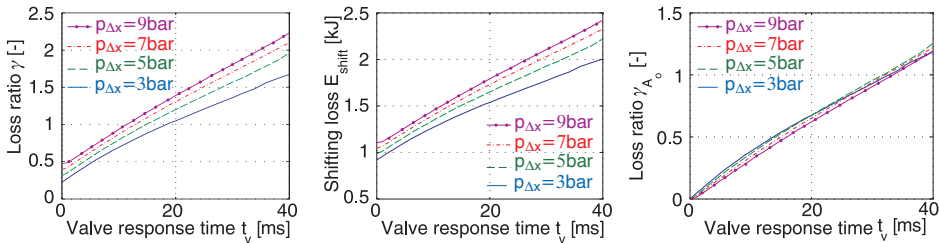
**Table 1: Shifting results for two cases as a function of valve response time.**

Case: $p_1 = 20 \text{ bar}$ , $p_2 = 120 \text{ bar}$ $v_c = 0.25 \text{ m/s}$ , $x_c = 0.5 \text{ m}$ $E_\beta = 0.75 \text{ kJ}$						Case: $p_1 = 20 \text{ bar}$ , $p_2 = 120 \text{ bar}$ $v_c = -0.25 \text{ m/s}$ , $x_c = 0.5 \text{ m}$ $E_\beta = 0.75 \text{ kJ}$				
$t_v$ [ms]	$p_{us}$ [bar]	$t_{td}$ [ms]	$E_{shift}$ [kJ]	$\gamma$ [-]	$\gamma_{A_o}$ [-]	$p_{os}$ [bar]	$t_{td}$ [ms]	$E_{shift}$ [kJ]	$\gamma$ [-]	$\gamma_{A_o}$ [-]
0.0	0.00	0.0	0.90	0.20	0.00	0.00	28.0	0.00	0.00	0.00
5.0	1.29	2.5	1.04	0.39	0.15	1.23	29.5	0.00	0.01	0.01
10.0	2.72	6.0	1.16	0.55	0.29	1.71	31.5	0.01	0.02	0.02
15.0	3.70	9.5	1.27	0.69	0.41	2.96	34.5	0.03	0.04	0.04
20.0	4.44	13.0	1.36	0.82	0.51	4.44	38.0	0.05	0.06	0.06
30.0	5.53	20.0	1.54	1.05	0.71	5.45	44.0	0.09	0.12	0.12
50.0	6.87	34.0	1.85	1.47	1.05	6.62	51.0	0.23	0.31	0.31
100	6.96	65.0	2.71	2.61	2.01	6.99	68.0	1.25	1.67	1.67
200	6.91	126.0	4.59	5.12	4.10	5.96	128.0	3.10	4.13	4.13


**Figure 7: Optimal shifting for  $t_v = 15 \text{ ms}$  for positive and negative cylinder velocity.**

#### 4.2 The Shifting Loss as a Function of Valve Size $A_o$

In Fig. 8 the shifting performance is shown for four different valve sizes. Compared to the minimum shifting loss  $E_\beta$ , increasing the valve size relaxes the valve response requirement. Looking at the energy cost in the second graph, the energy saving between two valve sizes is almost constant, inferring that the gained energy-saving is lowering the extra throttling of the displacement flow expressed in Eq.31. This is evident, as the ratio  $\gamma_{A_o}$  is near identical for all valve sizes. Thus, increased valve size reduces the energy loss by reducing throttling of the displacement flow during shifting, but does help at avoiding e.g. short circuit flow.


**Figure 8: The shifting performance for four different valve sizes.**

### 4.3 The Shifting Loss as a Function of Initial Piston Position $x_c$ and Velocity $v_c$ .

The results in Fig. 9 shows, as expected, that the most critical points are for high velocities and small volumes, both for passive and active shifting. I.e. a high amount of opening overlap between the valves is required for avoiding pressure peaks above 7 bar. However, the actual shifting cost in the second graph shows that despite this extra energy loss, these shifting costs are actually still inexpensive compared to shifting at larger cylinder volumes.

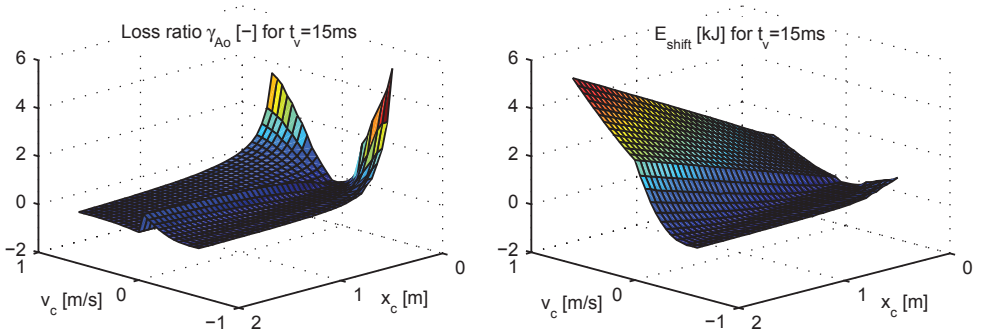


Figure 9: Shifting performance as a function of  $x_c$  and  $v_c$  for  $t_v = 15$  ms.

### 4.4 Shifting Loss Evaluated along the Wavestar Operating Points

The results in Fig. 9 showed that the highest demands are at high velocities and non-centre piston positions. Hence to evaluate valve performance, the loss ratio is evaluated along the red trajectory in Fig. 6 for different valve response times. The trajectory and shifting performance results are seen in Fig. 10. Due to the symmetric characteristics of the operating points, the results from shifting pressure both up and down becomes symmetric.

If  $t_v \leq 15$  ms, then an extra shifting loss of only 20% is present at the worst case point, i.e. the benefit of increasing the valve's response time beyond this point will be reduced. To further reduce the energy loss, the valve opening area should be increased.

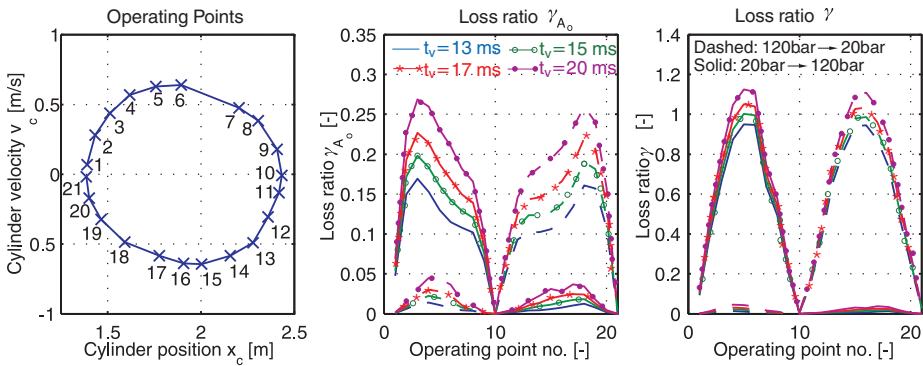


Figure 10: Performance of four valve response times evaluated along operating region.



## 5. Conclusion

Throttle-less force control of cylinders by discrete variation of the effective cylinder area is a technology very suitable for PTO systems for wave energy converters. It has the potential of an efficient force control, while implementing energy storage using accumulators and operating generators at a steady speed and load. The discrete force is obtained by shifting between system pressures within cylinder chambers using on/off valves.

However, the system is only feasible given adequate performance of the valves for pressure shifting. A framework for assessing and calculating the required valve response time is suggested, which is based on a generic valve model and analysing the pressure shift within just a single generic cylinder chamber. Based on a treatment of the governing equation an expression for the shifting losses for a chamber undergoing displacement is found.

A robust shifting loss definition was suggested, allowing normalisation of the results by defining a loss ratio and a valve size as a function of cylinder area. The normalisation allowed identifying valve requirements for a complete system by evaluating a single chamber.

The operating conditions of a discrete displacement cylinder for the Wavestar converter was established by calculating a density function of the cylinder movement. This finally lead to an evaluation of the required valve performance for the Wavestar converter, showing that a valve opening and closing time of 15ms would make the system feasible.

## References

- (1) B. Drew and A. Plummer and M.N. Sahinkaya. A review of wave energy converter technology. *Proceedings of the Institution of Mechanical Engineers, Part A: Journal of Power and Energy*, 223 (8), 2009.
- (2) J Cruz. *Ocean Wave Energy: Current Status and Future Perspectives*, 2008, Green Energy and Technology Series, ISBN:978-3-540-74894-6.
- (3) S.H. Salter, J.R.M. Taylor and N.J. Caldwell. Power conversion mechanisms for wave energy. *Proceedings of the Institution of Mechanical Engineers, Part M: Journal of Engineering for the Maritime Environment*, 2002.
- (4) R.H. Hansen, T.O. Andersen and H.C. Pedersen. Model based design of efficient power take-off. *The 12th Scandinavian International Conference on Fluid Power*, 2011.
- (5) A.F. de O. Falcao. Modelling and control of oscillating-body wave energy converters with hydraulic power take-off. *Ocean Engineering*, vol. 35, 2008.
- (6) A. Babarit, M. Guglielmi and A.H. Clement. Declutching control of a wave energy converter. *Journal of Ocean Engineering*, vol. 36, 2009,
- (7) N. Skinner. Wave energy converter device. Patent application EP2284386A2, 2009.
- (8) R.H. Hansen, T.O. Andersen and H.C. Pedersen. Analysis of discrete pressure level systems for wave energy converters. *Proc. of the 2011 International Conference on Fluid Power and Mechatronics*, IEEE Press, ISBN 978-1-4244-8449-2, 2011.
- (9) M. Linjama, H-P. Vihtanen, A. Sipola and M. Vilenius. Secondary controlled multi-chamber hydraulic cylinder. *SICFP'11*, 2009.
- (10) R. Henderson. Design, simulation, and testing of a novel hydraulic power take-off system for the Pelamis wave energy converter. *Renewable Energy*, vol.31,271-283,2006.
- (11) R.H. Hansen and M.M. Kramer. Modelling and Control of the Wavestar Prototype. *The 9th European Wave and Tidal Energy Conference (EWTEC)*, 2011.
- (12) J. Falness. *Ocean Waves and Oscillating Systems*. ISBN: 0-521-78211-2

# Wind turbines with variable hydraulic transmissions and electrically excited synchronous generators directly connected to the grid.

**Peter Chapple, Michael Niss and Knud Erik Thomsen**  
ChapDrive AS, Trondheim, Norway

## ABSTRACT

ChapDrive AS has developed hydrostatic power transmission systems to replace the mechanical transmission in wind turbines and currently have two turbines with ground based motor/generators. These have been operational during the last three years and use conventional Bosch Rexroth motors and Hagglund low speed units as pumps with power ratings of 225 and 900 kW respectively. During this time ChapDrive have evolved the required control strategies and for the future are looking at nacelle based solutions with an integrated hydraulic power transmission system. The major advantages of this type of drive are that it enables the use of synchronous generators, eliminates the need for frequency converters and power transformers as are required in mechanical transmissions and has lower weight and maintenance cost.

The use of variable motor displacement provides the transmission with a variable turbine speed control which allows the turbine to operate at optimum efficiency. It is intended to use digital control valves for the motor which together with a fixed displacement valve operated pump provides high hydraulic transmission operating efficiencies. This technology is ideally suited to the ChapDrive Control System which can also control the activation of the motor valves in order to provide the displacement control function. The paper describes the background to this development in the use of hydrostatic drives for wind turbine technology.

## 1 INTRODUCTION

Chapdrive AS was set up in 2007 in order obtain funding for trials of turbines in which the mechanical transmission has been replaced by a hydrostatic drive system. There has been relatively little published work on the use of hydrostatic transmissions for wind turbines whereas in contrast there are a considerable number of related patents on the subject (1). Consequently during the first stage of the project the work was concentrated on selecting the most appropriate components for the circuit. On the face of it the transmission gives the appearance of being one that would be classed as a secondary control where the motor is variable displacement but in this system a fixed displacement pump is driven by the load

and the output from the generator is also connected to a load that is essentially at fixed speed. The system pressure therefore varies with the torque load from the turbine rotor.

The main benefits of hydrostatic transmissions over most of the mechanical drives can be summarised as they:

- Have a relatively higher power to weight ratio
- Allow variable speed control of the turbine
- Avoid the requirement for a frequency converter and power amplifier
- Can be used directly connected to a synchronous generator.

The main difference in the requirements of a hydrostatic transmission for use in wind turbines is reflected mostly by the large rotary inertia of the turbine rotor which could be expected to have a considerable effect on the dynamic performance of the application.

## 2 CIRCUIT DESIGN AND COMPONENT SELECTION

Hydrostatic transmissions were installed in place of the gearboxes in two existing wind turbines; these being a 225kW Vestas V27 and a 900kW fixed pitch Micon units. In both of the systems Hagglunds pumps are mounted directly onto the rotor shafts with Bosch Rexroth type A4 motors mounted on the ground to drive the existing induction generators.

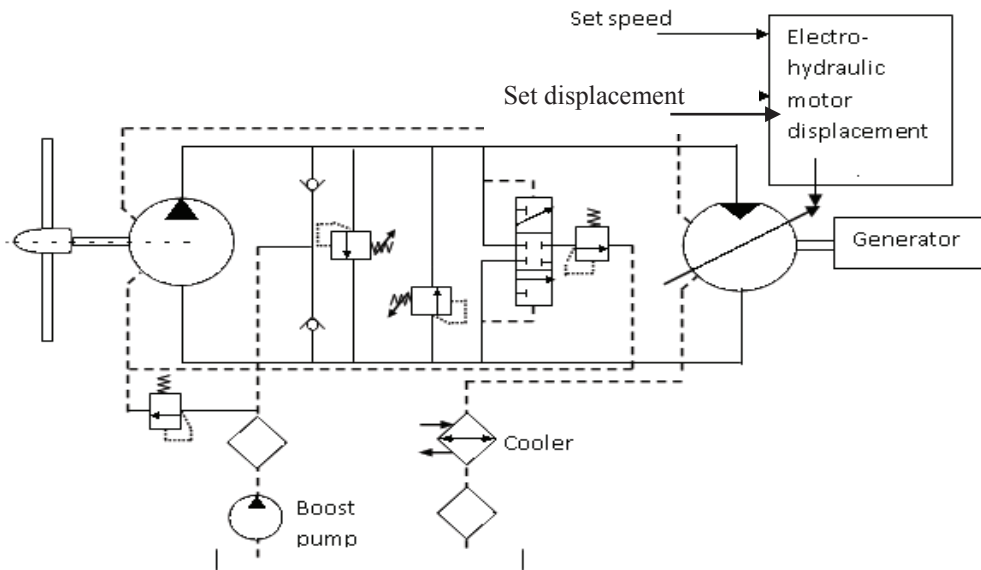


**Figure 1 Circuit diagram for the wind turbine hydrostatic transmission systems**

The pipes from the nacelle are connected to the tower using rotating couplings which allow the use of the normal yaw drive systems. For the 900kW machine two motors of 1L/rev capacity are used in series connection whilst in the smaller machine a single motor of 500cm<sup>3</sup>/rev capacity was installed. For both of these applications the circuits are essentially the same and that for the smaller turbine is shown in Fig 1.

The circuit caters for the normal functions that are required but in addition it is necessary to provide controls that act when there is an emergency stop which can arise from a number of events. These would include an emergency stop when the generator becomes disconnected from the grid and maintaining the turbine speed during the condition known as Low Voltage Ride Through (LVRT) when there is a transient change in the grid voltage.

### 2.1 Data for the 225 kW turbine

For the 225kW turbine the pump and motor sizes were selected as shown in Table 1.

**Table 1**

Maximum turbine speed rev/min	Pump displacement L/rev	Generator speed rev/min	Motor displacement L/rev	Maximum output power kW
45	11.3	1000	0.5	225

### 2.2 Control system

The turbine has a hydraulically operated variable pitch control from a separate hydraulic system in the nacelle (not shown in Fig1). During start up the turbine pitch is changed from the non-operating position which causes the turbine, and consequently the motor/generator to rotate. When the induction generator speed is 1000 rev/min the turbine pitch is operated in closed loop to keep the generator speed constant so that it can be connected to the grid. For a synchronous generator it is also necessary to create a minimal phase difference between the generator output and that of the grid in order to prevent excessive torque shocks when connecting to the grid. This aspect is described later in the paper.

This closed loop pitch control uses a PID the original setting of which needed to be modified because the dynamic characteristics of the hydrostatic transmission are considerably different to those having a gearbox. The pitch system is also used in closed loop to limit the maximum power output when the wind speed exceeds 15m/s.

For the hydrostatic transmission the motor displacement can be set at a fixed value to achieve the desired rotor speed with the original induction generator operating at 1000rev/min. For a synchronous generator the operating speed is 1500rpm. However the problem with this is that as the wind speed increases and hence the system pressure, the overall internal leakage causes the rotor speed to increase in order to provide sufficient flow to the motor. To avoid this situation the motor displacement can be controlled in closed loop to maintain a set turbine speed. This control has the following advantages:

- Increased damping of the hydraulic system
- Provides a variable speed controller that enables the operating speed of the turbine to be varied in order to obtain maximum efficiency over a range of wind speeds.
- Provides active damping of loads by reducing power and torque fluctuations

### 2.3 System dynamics

Clearly a major feature that has to be evaluated is that of the dynamics of the complete system particularly as an essential aspect involves different closed loop control functions. Consequently the first process involves obtaining the characteristics of the hydrostatic transmission in response to:

1. Changes in the turbine operating conditions which are a function of the wind speed, the turbine speed and pitch. These are contained in the overall power characteristics which are obtained from the turbine manufacturers literature (2). A typical variation of torque with turbine speed is shown in Fig 2 where rated conditions are 43rpm at 8m/s.
2. The response of the pitch control system
3. The response of the hydrostatic transmission system to changes in motor displacement.

The paper is initially concerned with item 3 that is required for the closed loop control of the turbine speed. The system is non-linear mostly because of the turbine characteristics but linearization of the system enables a transfer function to be obtained for the response of the hydrostatic system.

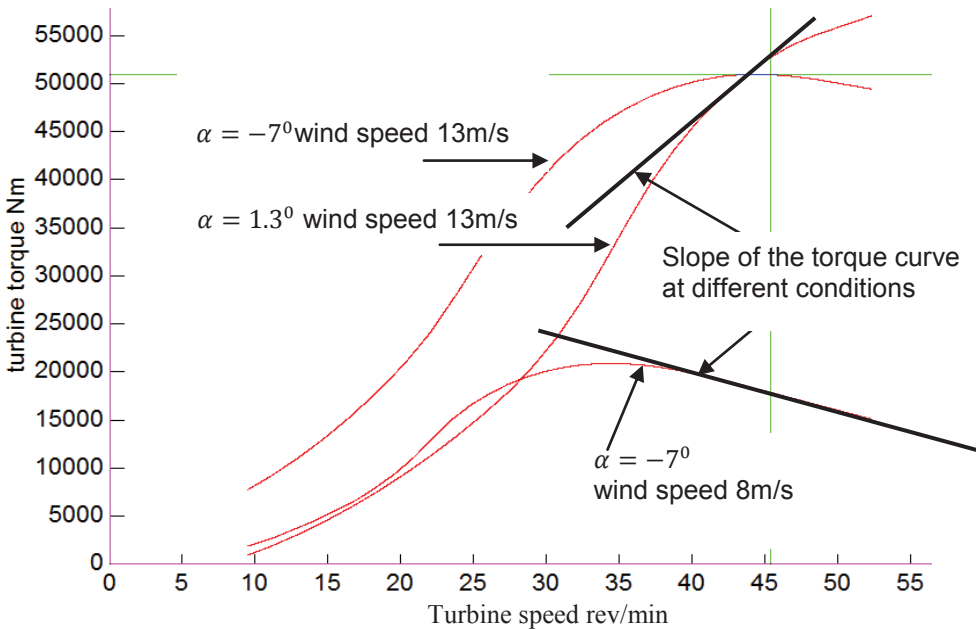


**Figure 2** Variation of turbine torque with turbine speed, wind speed and pitch angle  $\alpha$

#### 2.4 System transfer functions

The block diagram in Fig 3 shows the dynamic relationships of the parameters in the turbine power transmission system. In order to determine the overall response we can initially consider the relationship between turbine speed and motor displacement. Continuity of the flow in the high pressure system gives:

Motor flow + compressibility flow = pump outlet flow – leakage flow

$$D_m \Omega_m + \frac{V}{\beta} \frac{dP}{dt} = D_p \Omega_p - C_p P \quad (1)$$

Here  $C_p$  is the leakage coefficient for variations in pressure.

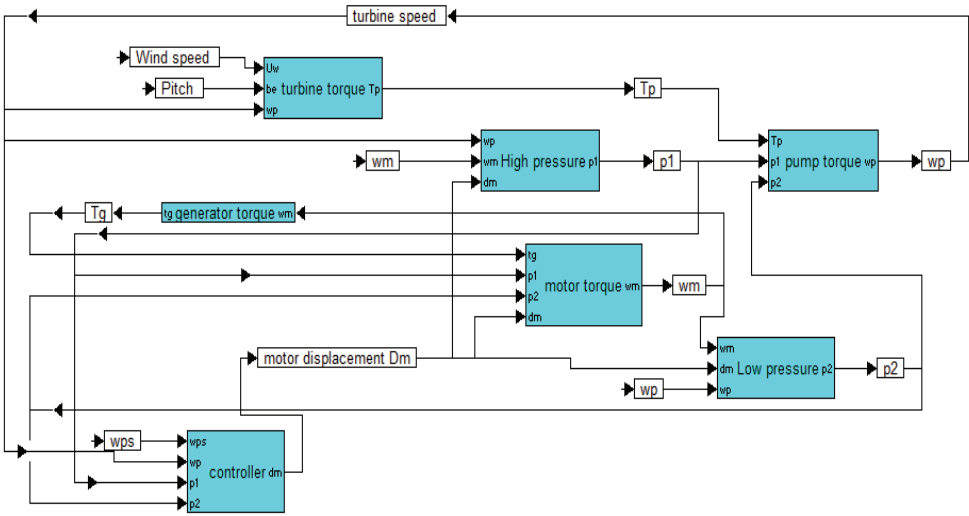


**Figure 3 Block diagram showing the hydraulic transmission installed in the wind turbine**

The low pressure  $P_2$  is controlled by the boost system so that the pressure can be assumed to be constant. Eqn. 1, can be linearised (3) where  $P$  is the high pressure. Thus:

$$p = \frac{(D_p \omega_p - D_m \omega_m - \Omega_p d_m)}{(C_p + \frac{V}{\beta} s)} \quad (2)$$

Here lower case letters are used to denote small changes in system variables where  $p$  is the change in the high pressure  $P$ ,  $\omega_p$  is the change in turbine speed and  $d_m$  a change in motor displacement. The letter  $s$  is the Laplace operator.

At a given wind speed, neglecting losses in the drive shaft the ideal turbine torque  $T_w$  is given by:

$$T_w = f(\Omega_p) = P D_p + J_p \frac{d\Omega_p}{dt} \quad (3)$$

The turbine torque,  $T_w$  is a function of the turbine speed and pitch angle. Eqn. 3 can be linearised by taking the slope of the torque/turbine, speed line,  $K_T$  for given values of the pitch angle and wind speed as shown in Fig 2 .

Thus linearising eqn. 3 gives:

$$\Delta T_w = p D_p = \Delta f(\Omega_p) - J_p s \omega_p = \frac{\partial T_w}{\partial \Omega_p} \omega_p - J_p s \omega_p.$$

Substituting  $C_T = \frac{\partial T_w}{\partial \Omega_p}$  and rearranging gives:

$$p = \frac{(C_T - J_p s) \omega_p}{D_p} \quad (4)$$

Combining eqns. 2 and 4 gives:

$$\omega_p = \frac{1}{D_p} \frac{(D_m \omega_m + \Omega_m d_m)}{((1-a) + (b-c)s + ds^2)} \quad (5)$$

Where:

$$a = \frac{C_p C_T}{D_p^2}; b = \frac{C_p J_p}{D_p^2}; c = \frac{V C_T}{\beta D_p^2}; d = \frac{J_p V}{\beta D_p^2} = \frac{1}{\omega_n^2} \quad (\omega_n = \text{hydraulic natural frequency})$$

The induction generator is directly driven by the motor and its torque,  $T_G$ , is created by the difference between the shaft speed and the grid synchronous speed. The relationship between the ideal motor torque,  $T_m$ , the motor speed and the pressure is:

$$T_m = P D_m = (J_m + J_G) \frac{d\Omega_m}{dt} + C_m \Omega_m + T_G \quad \text{and} \quad T_G = K_{mg} (\Omega_m - \Omega_{ms}) \quad (6)$$

where  $\Omega_{ms}$  = synchronous frequency.

Linearising eqn. 6 gives the relationship between the pressure and changes in motor speed and displacement as follows:

$$\therefore p = \left( \frac{J_m}{D_m} s + \frac{C_m + K_{mg}}{D_m} \right) \omega_m - \frac{P}{D_m} d_m;$$

Using typical values it is found that because the generator gain  $K_{mg}$  is relatively high, for changes in the operating conditions changes in the motor speed are small enough to be neglected in eqn. 5 (the generator always operates at near synchronous speed). Also the value of 'a' in eqn. 5 is found to be  $\ll 1$  so that the variation in turbine speed with changes in motor displacement is a second order equation which has a damping factor (3):

$$\zeta = \frac{1}{2} \left( \frac{C_p J_p}{D_p^2} - \frac{V C_T}{\beta D_p^2} \right) \omega_n = \frac{1}{2 D_p} \left[ C_p \sqrt{\frac{J_p \beta}{V}} - C_T \sqrt{\frac{V}{J_p \beta}} \right] \quad (7)$$

This is the normal hydraulic damping factor modified by the coefficient  $C_T$ . It is necessary for stability that  $\zeta$  is positive and for this to be so we get:

$$C_T \leq C_p \left[ \frac{J_p \beta}{V} \right] \quad (8)$$

From Fig 2 for speeds greater than rated,  $\Omega_{pm}$  the value of  $C_T$  is negative which increases the value of the damping factor. However for turbine speeds less than  $\Omega_{pm}$ ,  $C_T$  is positive which will reduce the damping factor with increasing wind speed so that excessive speed oscillations could occur.

## 2.5 Turbine speed control

The use of a proportional closed loop turbine speed control, for which there is a patent as described in (4), can be applied by reducing the motor displacement for speeds greater than the set value  $\omega_{ps}$  as shown by the control line in Fig 4

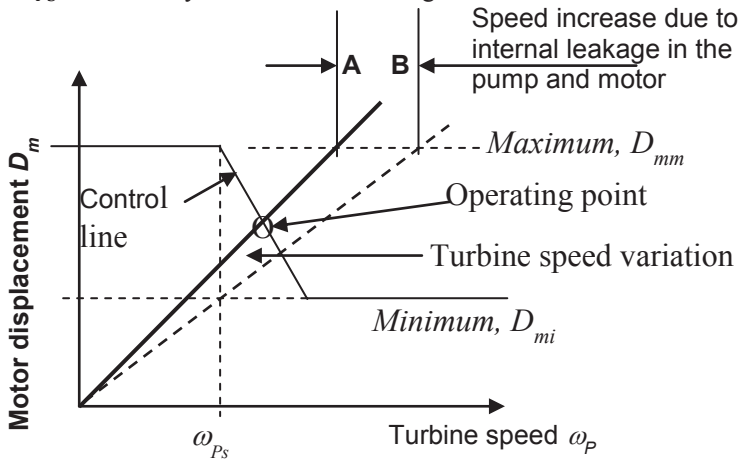


Figure 4 Relationship between motor displacement and turbine speed and closed loop control for a fixed speed of the motor.

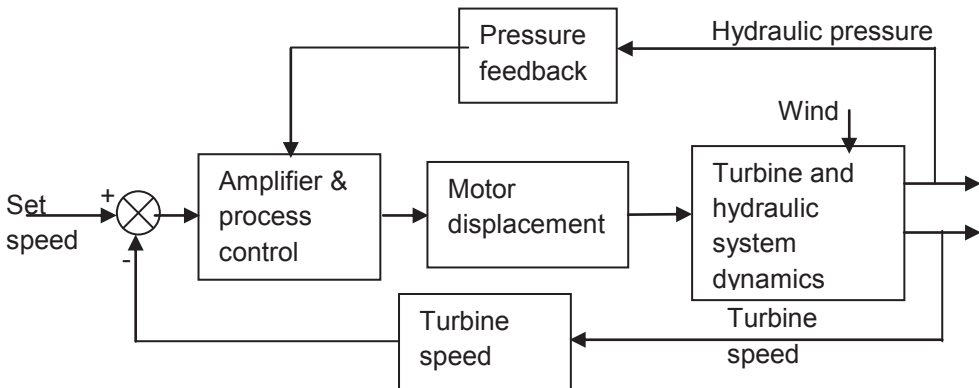
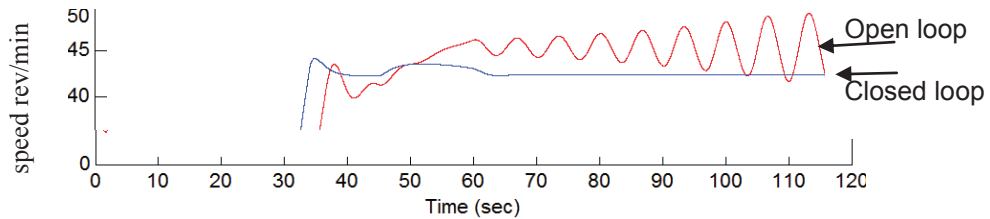


Figure 5 Turbine speed control system block diagram



Also seen in Fig 4 is the relationship between motor displacement and turbine speed for a fixed motor speed. The dotted line shows the speed increase due to increased leakage with pressure hence with the wind speed. The closed loop condition arises at the intersection of the two lines. Stabilisation of this control system shown in Fig 5 can be achieved by the use of pressure feedback and/or PID compensation which can be set to provide a performance having sufficient damping to minimise unwanted oscillations in speed.



**Figure 6 Non-linear simulation of turbine speed to change of wind speed at 50s**

Fig 6 shows the simulated response of turbine speed to a change in wind speed where it can be seen that the closed loop control has eliminated the speed oscillations that arise in open loop with fixed motor displacement. Thus the development of an effective control of turbine speed has made it possible to consider the approach that can be taken for varying the turbine speed so as to obtain optimum performance over the full range of operating conditions.

**3        CHAPDRIVE CONTROL SYSTEM AND SIMULATIONS OF WIND TURBINE OPERATION**

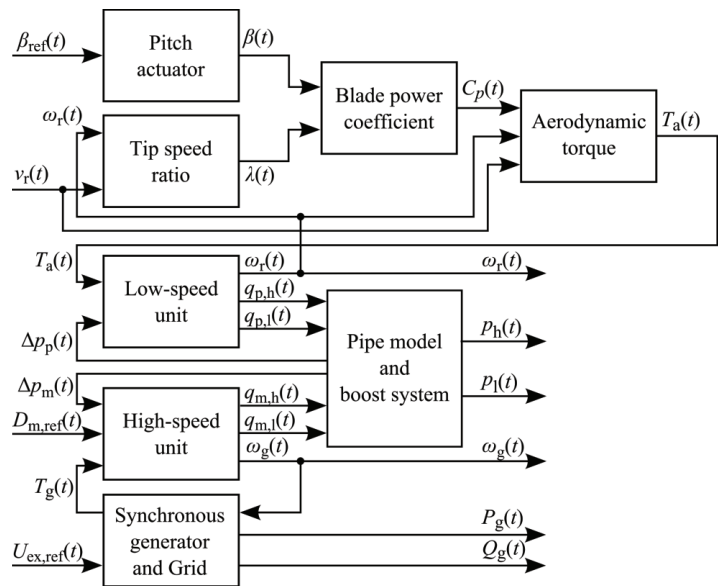


**Figure 7 - Overview of the simulation mode**

In the development of the ChapDrive Control System an analytic model of the system has been developed. An illustration of the simulation model is shown in Fig 7. The input variables to the model are the mean wind speed over the rotor swept area,  $v_r(t)$ , pitch angle reference,  $\beta_{\text{ref}}(t)$ , motor displacement reference,  $D_{\text{m,ref}}(t)$ , and generator excitation voltage reference,  $U_{\text{ex,ref}}(t)$ , while the output variables which can be measured are the rotor speed,  $\omega_r(t)$ , generator speed,  $\omega_g(t)$ , pressure in the high pressure side of the circuit,  $p_h(t)$ , pressure on the low pressure side of the circuit,  $p_l(t)$ , generator active power,  $P_g(t)$ , generator reactive power,  $Q_g(t)$ , and pitch angle,  $\beta(t)$ . The remaining variables shown in the figure are intermediate variables used in the model calculations, and are not expected to be available as measurements.

The model is developed in Matlab Simulink. It is used in a simplified form for controller design, while the full dynamic non-linear continuous time model is used for controller performance evaluation. Furthermore, the model of the hydraulics and the generator is also exported to GH Bladed (7) for detailed investigation and verification of the performance of the controller with the full dynamics of the wind turbine.

The control system is based on a wind speed estimator, a full state estimator and state feedback with integral action. An overview of the ChapDrive Control System is shown in Fig 8. The input vector  $\bar{x}_{\text{meas}}(t)$ , consists of the measurements available from the simulation/prototype turbine. The reference inputs to the control system are the rotor speed,  $\omega_{r,\text{ref}}(t)$ , generated active power,  $P_{g,\text{ref}}(t)$ , and generated reactive power,  $Q_{g,\text{ref}}(t)$ .

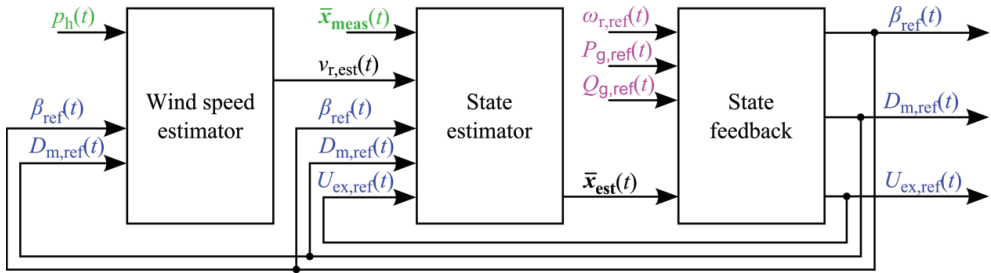


**Figure 8 - Overview of the ChapDrive Control System. Input measurements are written in green, reference inputs in magenta, and controller outputs in blue.**

The wind speed estimator is based on the principle described in (5), where a Kalman estimator is used to estimate the system states based on the pressure measurement  $p_h(t)$ , and having a PI-controller for approximating the torque input to the model, based on the error between the measured and the estimated system pressure, and finally a table lookup to determine the wind speed based on the estimated torque, pitch angle and rotor speed.

In order to control the turbine in the most optimal way at all times, the state estimator and state feedback is designed separately for different operating ranges with different control demands. This ensures that the controller can be designed specifically for a situation and does not need to take other conditions into account and hence perform less optimally. Most of the controllers for the individual control regions are designed based on the same overall principle. The design of each of the controllers is a combination of a full order Kalman estimator and full state feedback design using an LQR (Linear Quadratic Regulator)

approach, which is a feedback controller that is designed from a set of linear differential equations describing the system and a cost function specified as a quadratic function.

Since there are multiple sub-controllers it is necessary to switch between these at some pre-defined conditions. These switches are handled by an internal state machine which monitors the operation of the wind turbine at all times and chooses the most optimal controller.

An illustration of the performance of the controller is shown using measurements on a 225 kW wind turbine with a power reference of 200 kW, shown in Fig 9. As the measurements are performed above rated wind speed of the turbine, the rotor speed reference is constant at 45 rpm, and therefore not shown in the plot.

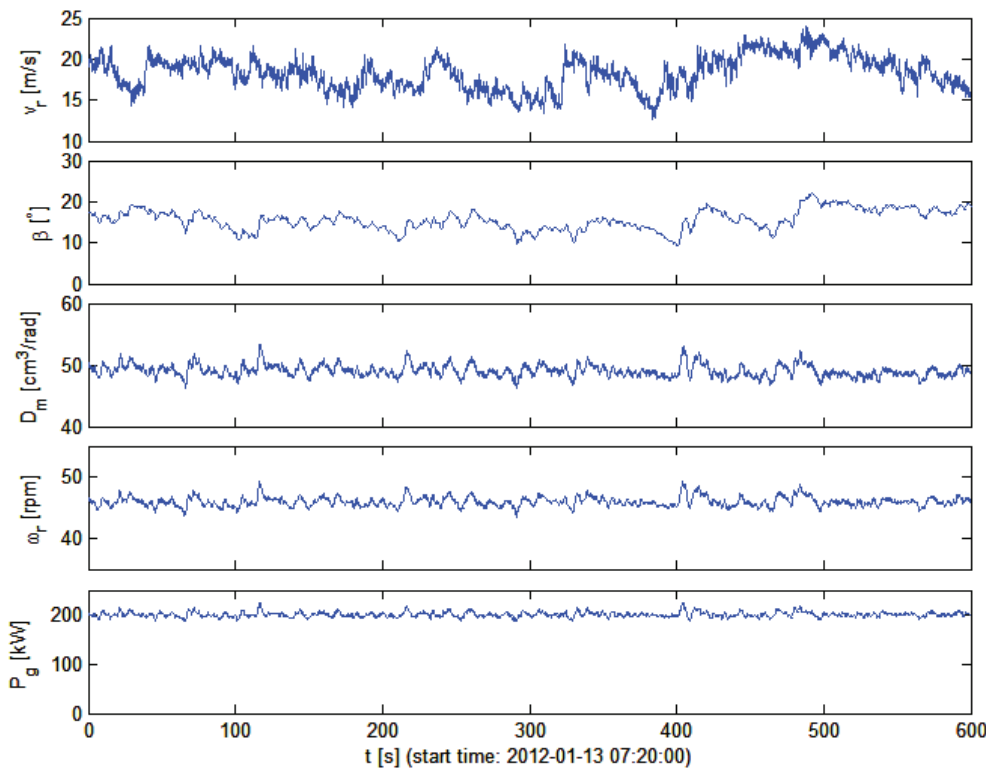


**Figure 9 - Measurements from 225 kW wind turbine with power reference at 200 kW.**

#### 4 SYNCHRONIZATION OF THE SYNCHRONOUS GENERATOR

One of the most challenging aspects of introducing a synchronous generator directly connected to the grid in a wind turbine is to obtain the correct conditions to get onto the grid.

The requirements to the synchronization are based upon the size of the generator; for which the given boundaries are shown in Table 2.

**Table 2 - Maximum limit values when synchronizing with a live grid (6).**

<i>Power rating [kVA]</i>	<i>Frequency deviation [Hz]</i>	<i>Voltage deviation [%]</i>	<i>Phase angle deviation [deg]</i>
0 – 500	0.3	10	20
500 – 1500	0.2	5	15
1500 – 10000	0.1	5	10

The simulation results and measurements that are presented here are from a 225 kW wind turbine, which means that the applicable boundaries are those in the first row. In order to get within the frequency range specified it is necessary to be able to control the generator speed very accurately. Given that the phase angle should also be within the specified limits at the same time as the frequency, it is necessary to control the generator speed so that it stays within the frequency range for some amount of time until the phase angle difference gets low enough to connect the generator to the grid.

This precision in generator speed is obtained by combined use of pitch and displacement control in a controller designed using the above described approach.

To illustrate how the ChapDrive Control System performs the results of a simulation with a mean wind speed of 7 m/s, is shown in Fig. 10.

In Fig 11 the measurement results from a physical 225 kW wind turbine are shown. For easy comparison the measurements are conducted with a mean wind speed of approximately 7 m/s. The objective of the simulation and measurements is to see that the controller can keep the generator speed (represented by frequency in the plots) within the specified limits. When the frequency is kept within the limits but not entirely constant, the phase angle will vary and within a short time be small enough to connect to the grid. The generator voltage (not shown in the plots) is controlled to match the grid voltage, using the generator excitation, independently of the speed of the generator.

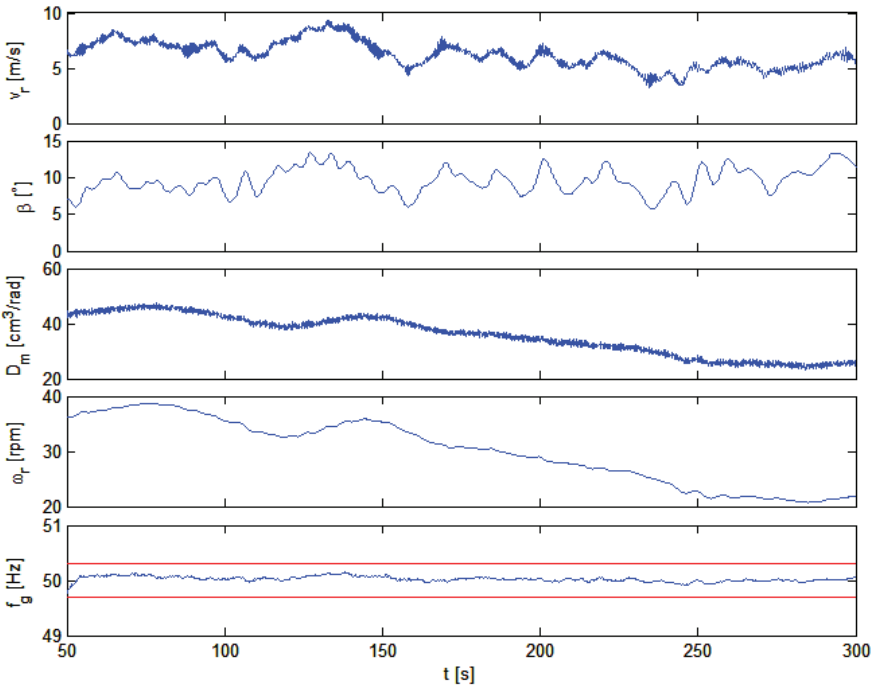


Figure 10 - Simulation at mean wind speed of 7 m/s.

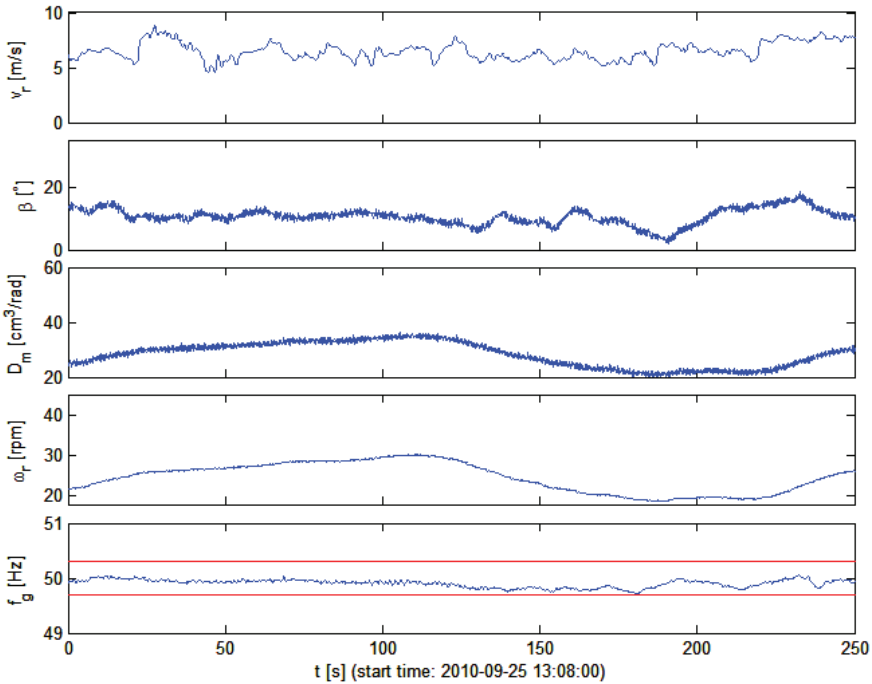


Figure 11 – Measured data from the 225 kW wind turbine ChapDrive 1 of a synchronization around 7 m/s.

## 5 CONCLUSIONS

The paper has described the hydraulic circuit and types of pumps and motors that have been installed by ChapDrive into two wind turbines in place of the original gearboxes by installing the motor/generator and hydraulic system on the ground. For the wind turbine torque to speed characteristics it is seen from the linearised system equations that the damping ratio of the hydraulic system is reduced as the wind speed increases above the rated value because of the increasing positive slope of the torque curve.

Proportional closed loop control of the turbine rotor speed acting on the motor displacement is shown to provide a system that increases the level of damping in the hydrostatic circuit using pressure feedback. This system provides the means to obtain variable speed control of the turbine which in combination with variations of the turbine pitch ultimately provides a system for controlling the turbine so as to obtain optimum performance.

It is shown that the ChapDrive Control System can control the rotor speed and use the rotor to absorb high frequency wind turbulence creating constant power output above rated wind speed, using combined pitch, displacement, and excitation control, thus enabling the use of a synchronous generator directly connected to the grid without the use of frequency converters.

It has also been shown that the behaviour of a wind turbine with ChapDrive hydraulic transmission can be modelled analytically and that simulations using this analytic model correspond to the measured behaviour of the system.

The unique advantages that are obtained from a hydrostatic power transmission system having a variable motor displacement enables the procedure for connecting the synchronous generator to the grid to be carried out and also allows the original objectives of being able to directly drive a synchronous generator without having to install either a frequency converter or a power transformer to be achieved.

## NOMENCLATURE

$D_m$	Motor displacement	$J_m$	Motor inertia
$D_p$	Pump displacement	$J_G$	Generator inertia
$\beta$	Oil bulk modulus	$C_p$	Leakage coefficient
$P_1$	High pressure	$T_p$	Turbine torque
$P_2$	Low pressure	$T_G$	Generator torque
$\Omega_m$	Motor speed	$v_r$	Wind speed
$\Omega_p$	Turbine speed	$U_{ex}$	Excitation voltage
$V$	System high pressure volume	$\omega_r$	Rotor speed
$C_m$	Speed dependent friction	$\omega_g$	Generator speed
$J_p$	Turbine inertia	$P_g$	Generator active power
$Q_g$	Generator reactive power		

## REFERENCES

- 1 Patents on hydrostatic transmissions for wind turbines. US-A-4503673 and JP 11287178
- 2 Vestas datasheet for V 27 turbine.
- 3 P J Chapple, Principles of hydraulic system design, Coxmoor Publishing Co., ISBN 1 901892 15 8
- 4 UK Patent, Turbine speed stabilisation control system, GB 2463647
- 5 Østergaard, K., Brath, P., and Stoustrup, J. (2007). *Estimation of effective wind speed*. Journal of Physics: Conference Series <http://dx.doi.org/10.1088/1742-6596/75/1/012082>
- 6 Petterteig, A., Mogstad, O., Henriksen, T., and Håland, Ø. (2006). SINTEF Energiforskning AS. *Tekniske retningslinjer for tilknytning av produksjonsenheter, med maksimum aktiv effektproduksjon mindre enn 10 MW, til distribusjonsnettet*. Tabell D1
- 7 GL Garrad Hassan Bladed – Wind turbine design and certification software. <http://www.gl-garradhassan.com/en/GHBladed.php>

# **Pneumatics II**





# Design of a Figure-Eight free-liquid-piston engine compressor for compact robot power

**Mark E Hofacker, Mengze Sun and Eric J Barth**  
Vanderbilt University

## ABSTRACT

This paper describes the design and control of a free-piston engine compressor. By combining the engine and compressor, the device is capable of efficiently producing low temperature air at high pressures. This in turns translates into a high-energy density power supply with an energy density three to five times greater than that of a battery/motor combination. By injecting compressed air and exploiting the dynamic loading of a high inertance, low mass liquid piston, this device is capable of an inject-and-fire operation that avoids traditional intake and compression strokes. The engine-compressor is capable of self balancing with a single cylinder due to the figure eight arrangement of the liquid piston. Due to an integrated, low weight, low stiffness check valve, air is compressed into a high pressure reservoir with low amounts of blow back. The design along with experimental and theoretical results are shown for the engine compressor.

## 1 INTRODUCTION

One major factor limiting the usefulness of human scale robotics is the lack of a light weight, compact power source and accompanying actuators. This paper describes the operation of a propane-powered free piston compressor that is meant to provide pneumatic power to a dog sized rescue crawler robot such as the device jointly developed by Vanderbilt University and Georgia Tech.

Current state of the art robots often utilize batteries and electric motors, but this combination does not have a sufficiently high power or energy density and so untethered robots tend to be limited in the amount of useful work they can perform before requiring recharging. (Dunn-Rankin, et al 2005).

Hydraulic actuation is an option that has shown to be useful for robots such as Boston Dynamics big dog. Scaling down this solution is difficult because the valving, hosing, and associated overhead from the return lines begin to dominate as the pistons reduce in size.

The goal for the untethered robots such as the rescue crawler is to provide a high system power density in terms of power per total weight.

Pneumatic power is therefore an attractive option because of the low weight of the actuators and the ability to exhaust the working fluid to the environment eliminates the need for return lines. However, compressed air has such a low energy density that powering a pneumatic robot solely by means of an onboard compressed air reservoir would be impractical. If pneumatic actuation were to be pursued, a more desirable option would be to equip the robot with an onboard compressor.

Monopropellants are an attractive energy source to such a compressor, but their energy density is lower than hydrocarbons, so an internal combustion solution was pursued. Propane has a high vapor pressure which eliminates the need of a fuel pump and was therefore chosen as the fuel source.

Ongoing research with hydrocarbon powered pneumatic power at Minnesota has produced a powerful, compact engine compressor that differs from the device described in this paper in that it is smaller in scale and requires an idle cycle. The design described herein eliminates the idle cycle which would waste fuel during periods of inactivity (Aichlmayr, 2002).

The engine described in this paper is a continuation of work done by Wilhite (2010), Yong (2011), and Riofrio (2008) in creating an internal combustion, single cylinder, free-piston engine compressor. New developments described in this paper include a self balancing figure-8 configuration, a high efficiency compressor head, and on board control and electronics.

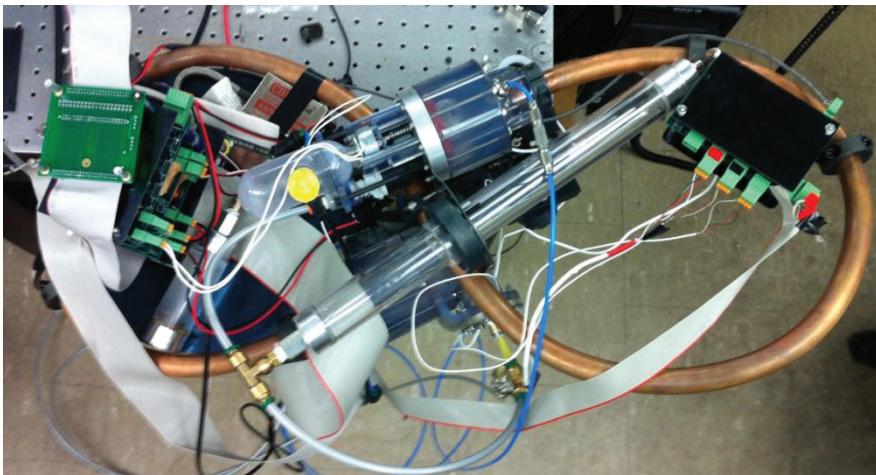


**Figure 1: Picture of Free Piston Compressor Engine**

## 2 OVERVIEW OF OPERATION

The engine compressor operates on what could be called an “inject and fire” cycle that differs from the 2-stroke and 4-stroke cycles used by many internal combustion engines. Although there are only 2 strokes in the cycle, intake, compression, and expansion are combined into one stroke while the second stroke is used only for exhaust. This operation is made possible by the inclusion of a pressure reservoir to provide compressed air, a compressed fuel source, and a free-piston with significant inertia. The free piston in this engine is comprised of water trapped between two elastic membranes. The term “free-piston” refers to an engine in which the piston is not kinematically constrained and can therefore respond dynamically to pressure forces.

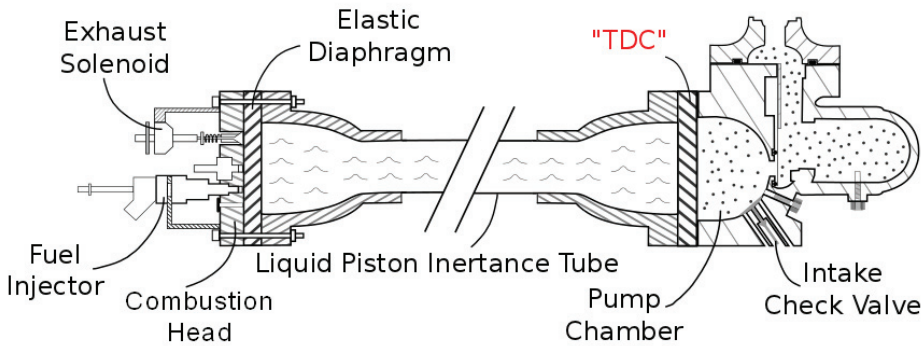


**Figure 2(a): Schematic of Free Piston Compressor at effective Top Dead Center**

In the first stroke, compressed air from the reservoir and propane from the buffer tank are injected into the combustion chamber. The combustion chamber is the volume that is bound on one side by a face of the free piston and on the other side by the aluminum combustion head. As shown in Figure 2, the “piston” consists of a section of water trapped between elastic diaphragms. Compression is dynamically maintained during injection because the inertia of the piston prevents the piston from moving quickly when the combustion chamber is pressurized. Immediately following injection, a spark plug ignites the air/fuel combination. Combustion forces the piston to move which in turn forces the air contained in the compressor head into the reservoir chamber.

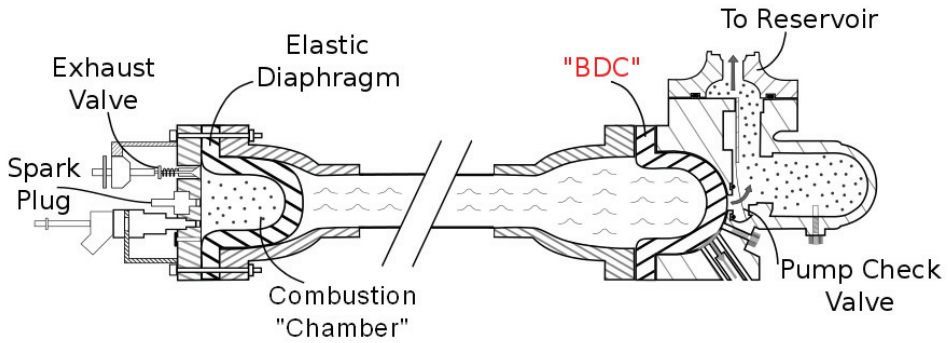


**Figure 2(b): Schematic of Free Piston Compressor at effective Bottom Dead Center**

When the combustion products are fully expanded, an exhaust valve on the combustion head opens, and the second stroke begins as the elasticity of the membranes returns the piston back to its original location. The compressor head's check valve to the reservoir closes, and atmospheric air breathes in through another check valve to refill the chamber. The combustion products are expelled from the combustion head through the open exhaust valve and the second stroke concludes with the closing of the exhaust valve.

**3 FIGURE-8 HIGH INERTANCE LIQUID PISTON**

It has been shown that piston inertia could be increased while reducing piston mass through the use of a variable cross sectional area liquid piston (Barth, 2010). A schematic of this concept is shown below in Figure 3.

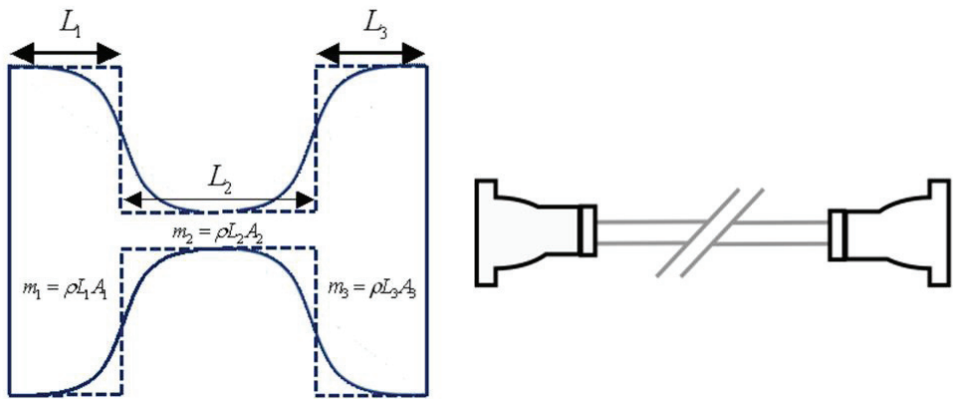


**Figure 3: Schematic of liquid piston with converging and diverging nozzles and diaphragms on both ends**

In this work, it was demonstrated that the inertia contained in such a liquid piston could be described as follows:

$$I = \left[ \frac{\rho L_1}{A_1} + \frac{\rho L_2}{A_2} + \frac{\rho L_3}{A_3} \right] \quad (1)$$

To maintain compression while injecting against the piston, the piston must be very stiff or possess a great quantity of inertia. Neither increasing the mass of the piston nor increasing the stiffness of the elastic membrane is a desirable option. Increasing the stiffness of the membranes reduces the efficiency of the engine because the energy spent stretching the membranes is not recovered. Increasing the mass of the piston is undesirable because any additional weight added to the engine would reduce the system's energy density.

For this scale of engine, the needed inertia was determined through simulation to be approximately  $6.4 \text{ kg/mm}^3$  in order to achieve a reasonable balance between compression and weight. This inertia is achieved using .63 kg of water contained within a tube 1.524 long and 1.9 cm in diameter with nozzles on either end that expand from a diameter of 1.9 cm to 5.1 cm over a length of 7.62 cm. For comparison, if a straight pipe was used with the current initial piston surface area, the piston would need to be 10.9 meters long and weigh 21.7 kg. It would be impractical to simply use a small pipe with no reduction because there needs to be space for the injectors, spark plug, etc on the combustion head.

While imbalance is often an unavoidable problem for single cylinder engines, the unique properties of the liquid piston provided a mechanism for partially neutralizing engine vibration. By routing the liquid piston in various geometries, the inertia of the piston's movement can be made to mostly cancel itself out. The reduced vibration means that the engine can be mounted with less external bracing than is typically necessary for single-cylinder engines. This is especially important on a mobile platform such as the rescue crawler because strong shocks from the engine could cause the crawler to fall. The three configurations shown below are the ones used by Riofrio (2007), Wilhite (2010), and the figure-8 is the configuration described in this paper.

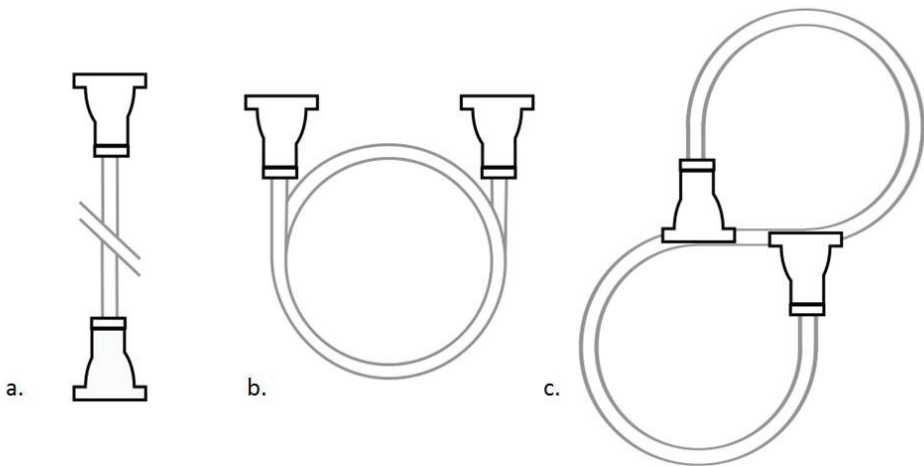


**Figure 4: a) Straight Configuration b) Loop Configuration c) Figure-8 Configuration**

This canceling effect can be understood from Newton’s second law: if two equal masses are traveling in the opposite direction at identical accelerations there is no net force. The water inside the piston is incompressible, and therefore the water has the same acceleration at every point inside the tube. Therefore if a pipe doubles back on itself, there is no net force to external bracing. This concept is shown in Equation 2. The “ $\sum F$ ” represents the sum of forces in a giving dimension, “ $\rho$ ” represents the density of the liquid, “ $\dot{V}$ ” represents the volumetric flow rate, and “ $\sum l$ ” represents the sum of lengths of tube in a given direction.

$$\sum F = \sum ma = \rho \dot{V} \sum l \tag{2}$$

For example, the configuration shown in figure 4.b exerts no force on external bracing along the axis of symmetry because the liquid inside of the tube travels equally positively and negatively in this direction. The critical distance is the length of pipe that is not “canceled”, and therefore exerts external forces. These forces not delivered to external bracing must be withstood by pipe itself.

In the current setup, it was not possible to directly measure the flow of the water inside the piston, so the model from Wilhite (2010) was used to find the volumetric acceleration inside of the piston. This data is shown below in Figure 5.

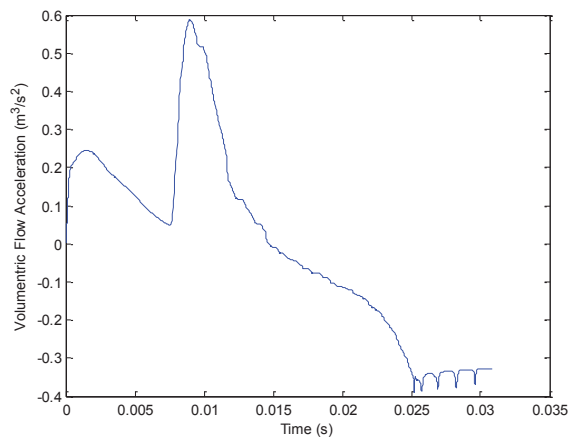


**Figure 5: Volumetric Flow Rate Inside Liquid Piston**

The model was tuned to only inject the minimum amount of fuel/air mixture to where the piston makes contact with the surface of the pressure head with a velocity of zero. A collision with the compressor head would change the acceleration profile considerably, but this is non-ideal practically because collisions indicated that fuel is being wasted and there was therefore an error with injection timing. With this flow rate shown in Figure 5, the force, moment, impulse, and angular impulse were calculated for each of the three geometries shown in Figure 4. The results are shown in Table 1 below.



**Table 1: External Effects for Various Liquid Piston Configurations**

	Straight	Loop	Figure 8
Maximum Force (N)	915	156	67.0
Maximum Moment (N*m)	0	122	8.50
Maximum Impulse (N*s)	2.65	0.452	0.194
Maximum Angular Impulse (N*m*s)	0	0.353	0.025

#### 4 COMPRESSOR HEAD

Utilizing the model described by Wilhite (2010), it was determined that a major factor limiting the maximum pressure of the free piston engine compressor was the dynamics of the compressor head check valve. A picture of the check valve and spring used in the previous compressor is shown below beside the new check valve with the accompanying o-ring. The new check valve consists of a thin metal cantilevered beam.



**Figure 6: (a) Previous Compressor Head Check Valve (b) Current Compressor Head Check Valve**

To understand this selection, it is important to understand how an ideal check valve would operate in the context of the free piston compressor. An ideal check valve would allow a large mass flow rate as soon as the pressure inside the compressor head exceeded the pressure inside of the reservoir. This valve would then immediately close as soon as the compressor pressure dropped below that of the reservoir to prevent the loss of compressed air.

Additionally, the unswept volume between the compressor head and the resevoir should be minimized as this space constitutes dead volume. Viewing a check valve as a mass-spring, it is clear that there are conflicting goals. The spring must be soft enough to open wide with small pressure differences yet fast enough to close immediately during the return stroke. These two goals are helped by reducing the mass of the check valve.



The response of the check valve was approximated as a cantilever beam. Accordingly, the stiffness of the beam is a function of the length of the beam, the stiffness of the material, and the modulus of the cross section.

The diameter of the plate could not be reduced significantly because the desired flow rate dictated the size of the check valve opening that the plate had to cover. Thus the adjustable parameters became the thickness of the plate, and the length and width of the beam, connecting the area covering the o-ring to the rigid base. A plate thickness of .2032 mm, a beam length of 9.3 mm, and a beam width of 4.1 mm was chosen. Approximating this structure as a cantilevered beam, a stiffness of 4,140 N/m was calculated. The effective mass of the beam was calculated to be .5 grams giving the valve a natural frequency of 537 Hz. On two of the three metrics of interest for the check valve (low stiffness, low mass, high speed of response), this design has advantages over the previous design. The previous check valve had a mass of 18.4 grams, a spring constant of 583,000 N/m, and a natural frequency of 895.87 Hz. Although the new valve has a lower natural frequency, it improves performance in simulation because it is more responsive to changes in pressure. Both valves have similar amounts of surface area, but because the new valve is less stiff it is able to “open” earlier in the cycle and open wider when there are small pressure variations. The model of this engine (Wilhite, 2010) predicts that by implementing the new valve, the maximum pumping pressure of the engine should increase from 552 kPa (80 psi) to 2170 kPa (315 psi).

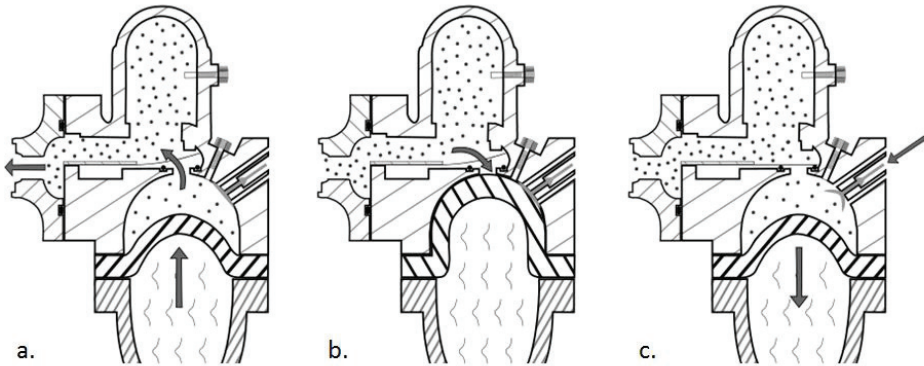


**Figure 7: (a) Compressor Head While Pumping (b) Compressor Head at BDC (c) Compressor Head During Breathe In**

To incorporate the complex geometries required for this check flap, the compressor head was constructed using stereolithography (SLA) as seen in Figure 7 (d). To protect against fracture in the likely event of a collision with the piston, a tough, impact resistant, ABS-like material known as Somos NeXt was used. Of additional benefit, the lower density of the SLA material allows for a compressor head that weighs approximately half that of the previous compressor head (270g vs. 505g).



**Figure 7: (d) Picture of Compressor Head**

The old breath-in valve was replaced with a silicon rubber umbrella-type check valve to breathe in atmospheric air during the return stroke. The new valve is soft enough to allow mass flow at low pressure differences to ensure that there is not a significant partial vacuum during breathe in. When the membrane collides with the valve during combustion, the valve does not damage the membrane because it is significantly softer than the piston membrane. While the softness of the valve reduces its ability to respond quickly to pressure, the breathe-in period is long enough that engine performance is not limited by the valve response speed.

It is critical to minimize the flow restriction immediately after the check valve because this space sees a large mass flow rate. To ensure that freshly pumped air was not being restricted by the tubing connecting the compressor head to the reservoir, an intermediate reservoir was incorporated directly into the compressor head. Small pressure sensors were mounted into this reservoir as well as the compressor head so that real-time pressure variations could be utilized for control.

## **5 ONBOARD COMPONENTS**

The previous free piston engine compressor required many external components to operate. To be a functional power source for the rescue crawler, the engine compressor must be self-contained. This section describes the steps taken to move all components on-board to while minimizing weight and electrical power consumption.

### **5.1 Electronics**

A Diamond Systems Athena single board computer with onboard data acquisition was mounted on the compressor to monitor pressures, execute the controller, and output signals to the injectors, exhaust solenoid, propane buffer valve, and spark plug. On the previous compressor, these duties were handled remotely by a desktop computer equipped with a data acquisition card.

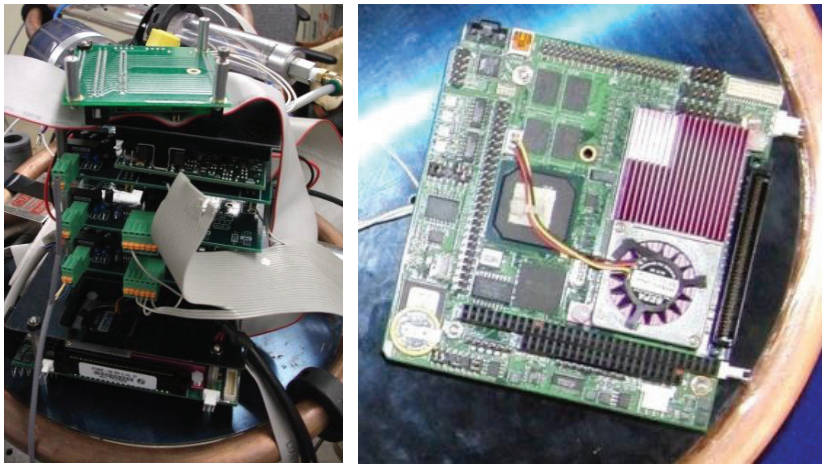


**Figure 8: a) On Board Electronics b) Athena Single Board Microprocessor**

To adjust for cycle to cycle variations, Yong (2011) developed a virtual cam controller to modify injection and exhaust timings based on operating conditions. On the previous compressor, this controller had a sampling rate of 10 kHz. In the engine described in this paper, a variation of this controller will be utilized, yet due to the lower power microprocessor, the sampling rate must be reduced to 1 kHz.

All of the electronics were mounted on printed circuit boards to reduce noise. The twelve volt battery carried on the rescue crawler provides all the electrical power that the compressor uses. Energy efficient switching DC/DC regulators were used to supply the electronics with  $\pm$ twelve volts and five volts. The specific components used for the voltage regulation are the Murata SKA1212SC and the LM2576T-005G, respectively.

## **5.2 Sensors and Actuators**

Pressures in the compressor head, propane buffer tank, and reservoir are measured using Kulite miniaturized XTL-190 and XTL-140 pressure transducers. Their signals are amplified using instrumentation amplifiers and filtered digitally inside the controller.

The exhaust valve is made by O.S. Engine and meant for use in remote control air planes. It is motivated by a Ledex 124911-028 solenoid. Power is supplied to the solenoid via an AMC servoamp model AZ20A8.

A small spark plug is powered using a RCEXL ignition box. The ignition box provides high voltage to the spark plug and allows precise control of the spark. The spark plug used is an NGK ME8 and the ignition box is a RCEXL Model A-01.

## **5.2 Fuel/Air Injection**

Air and fuel was injected independently by two Bosch fuel injectors (Part # 0280150842). To increase the speed of response of the fuel injector and decrease power consumption, an injector drive controller from Texas Instruments (LM1949) was used.



**Figure 9: Fuel Injector Used for Air and Propane Injection**

The injectors have no fittings for connecting and instead rely on an external manifold. To save weight and increase compactness, this manifold was integrated with an actively regulated propane buffer tank. High injection pressure decreases the injection duration and with with a vapor 100psi and the comparatively large fuel injectors make it impractical to accurately inject without lowering the pressure. By regulating with a solenoid as opposed to a passive regulator, it is possible for the controller to change the injection pressure. The buffer tank was constructed out of Accura 60 using an SLA process. This material has a low density which allows the tank to be light weight and the tank's complex geometry accomodates compact valving via a Clippard ET-2M 2-way valve.

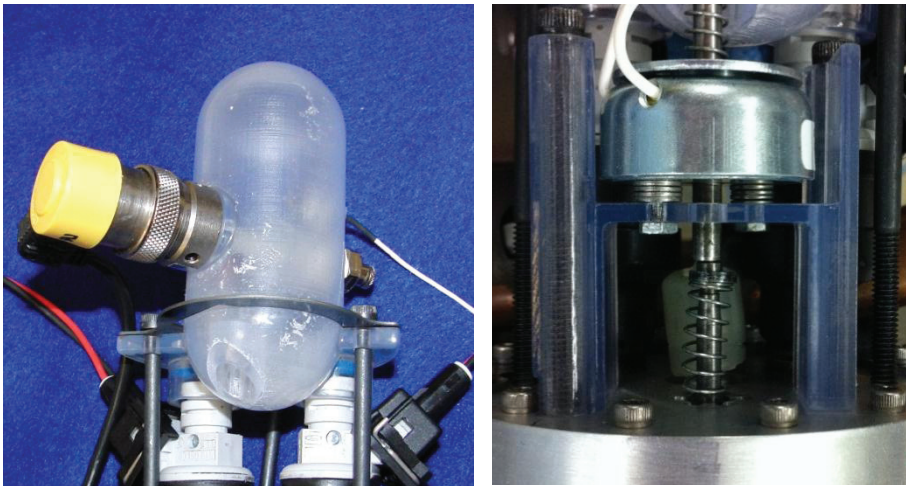


**Figure 10: a) Injector Manifold with Integrated Actively Regulated Propane Buffer Tank b) Exhaust Solenoid**

6 SIMULATION RESULTS

A simulation based upon a previously validated model (Riofrio 2007, Riofrio 2008, Wilhite 2010, Yong 2011)) was used to calculate the maximum reservoir pressure that the compressor could acheive. This simulation predicts that the engine compressor is capable of pressurizing the reservoir up to 2,140 kPa (310 psi).

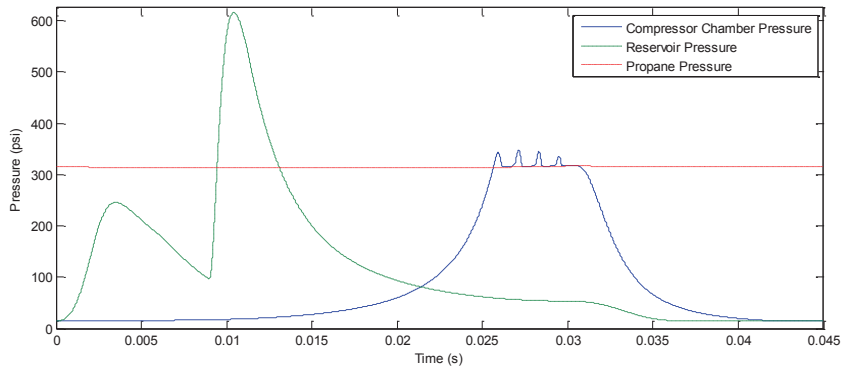


Figure 11: Simulated Results Showing Compressor Chamber, Reservoir, and Propane Pressure During Operation

7 EXPERIMENTAL RESULTS

Figure 12 a shows the reservoir, compressor head, and propane buffer tank pressure during a single cycle. Figure 12 b shows the compressor filling a one liter bottle with compressed air. The compressor is operating at four Hz, and misfires every other cycle. It is thought that the misfires are due to the use of open-loop, set timings for the injection, spark, and exhaust. In the future, Yong’s controller will be applied to adjust timings in real time. Currently, a constant pressure, 80 psi external air is connected to the reservoir to simplify the control, whereas in the final device the controller must vary the injection timings to compensate for variations in reservoir pressure.

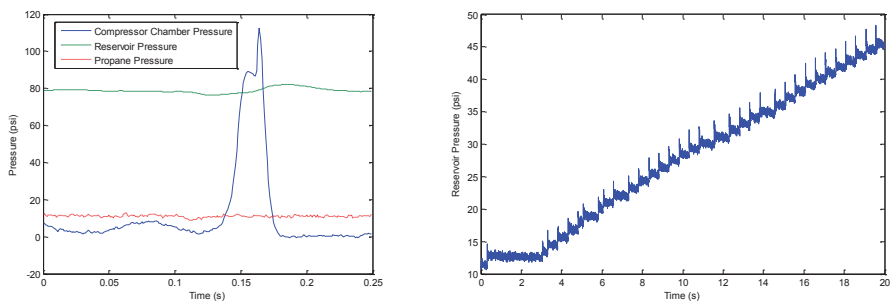


Figure 12: Experimental Results Showing Measured Pressures During Operation



The device weighs 5.9 kg and fits in an envelope of 60 cm x 30 cm x 18 cm. It consumes a peak of 75 Watts and an average of 35 Watts from a 12 volts source.

## 8 CONCLUSIONS

The free piston engine compressor described in this paper is an evolution of an engine developed by Riofrio (2007), Willhite (2010), and Yong (2011). The changes included moving all electronics onboard and attempting to make the engine pump to a higher pressure while exerting less force on external supports. Although consistent combustion has not been achieved, the controller will continue to be developed in hopes of achieving the results shown in simulation.

## 9 REFERENCES

- Aichlmayr, H. T., Kittelson, D. B., & Zachariah, M. R. (2002). *Design Considerations , Modeling , and Analysis of Micro-Homogeneous Charge Compression Ignition Combustion Free-Piston Engines. Techniques*. University of Minnesota.
- Barth, E. J. and Willhite, J. A. 2010. "High Inertance Liquid Piston Engine-Compressor and Method of use Thereof". U.S. patent application: 12/753,990, filed April 5, 2010.
- Dunn-Rankin, D., Martins, E., and Walther, D., 2005. "Personal Power Systems". *Progress in Energy and Combustion Science*, 31, August, pp. 422-465.
- Howell, L. (2001). *Compliant Mechanisms* (p. 407). New York: John Wiley and Sons.
- Riofrio, J. A., and Barth, E. J., 2007b. "Design and Analysis of a resonating Free Liquid-Piston Engine Compressor". *2007 ASME International Mechanical Engineering Congress and Exposition (IMECE)*, IMECE2007-42369, November 11-15, Seattle WA, USA.
- Riofrio, J. A. (2008). *Design, Modeling and Experimental Characterization of a Free Liquid-Piston Engine Compressor with Separated Combustion Chamber*. Dissertation, Vanderbilt University. Retrieved from Vanderbilt University Electronic Theses and Dissertations (etd - 12102010-11502)
- Willhite, J. A. (2010). *Dynamic Model-Based Design, Validation, and Characterization of a Compact, High-Inertance Free Liquid Piston Engine Compressor*. Dissertation, Vanderbilt University. Retrieved from Vanderbilt University Electronic Theses and Dissertations (etd -12102010-11502)
- Yong, C. (2011). *A Virtual-Cam Based Control Methodology for Free-Piston Engines*. Dissertation, Vanderbilt University. Retrieved from Vanderbilt University Electronic Theses and Dissertations (etd – 07282011-114037)



# Test rig and Simulation Software for Performance Comparison of Pneumatic Servo Controllers Given three Actuator Setups and five Circuit Configurations of Control Valve

**Ramhuzaini Abd. Rahman and Nariman Sepehri**

Department of Mechanical and Manufacturing Engineering, University of Manitoba,  
Winnipeg, Manitoba, Canada, R3T 5N5  
Contact: nariman@cc.umanitoba.ca

## ABSTRACT

This paper describes the development of a pneumatic test rig and the accompanied simulation software for testing various pneumatic position control algorithms under the same controlled environment. The test rig has been developed using modular design approach in order to be adaptable for operation of different circuit configurations of control valve and actuator setups. The test rig comprises of five main modules: air service, control valve, actuator, sensing and information processing. The actuating and control valve modules consist of three types of pneumatic actuators and five circuit configurations of control valve, respectively. The simulation software, having an interactive graphic user interface, has been developed to offer users with results similar to the ones from experiments conducted on the test rig. The validity of the results obtained from the simulation software, is confirmed by comparing the open-loop responses with those of the experiments. The motivation of this development is that, a considerable amount of research works claim to have successfully improved the performance of their pneumatic position control systems, yet, only a handful of studies made efforts to compare performances of those proposed control algorithms, using the same test bench, as to determine which one is more effective under similar circumstances.

**Keywords:** Pneumatic test rig, pneumatic servo position controller, pneumatic simulation software, pneumatic actuator, pneumatic control valve, performance comparison.

## 1 INTRODUCTION

Pneumatics is a technology that utilizes pressurized air as its fluid medium to perform mechanical work. Flexibility in routing the flow of pressurized air, safe and environmental friendly fluid medium, easy to install and maintain system components, high force output to weight ratio as well as fast output response of its actuators are amongst the significant factors contributing to the utilization of this technology in numerous industrial applications ranging from a simple point-to-point positioning to a high-accuracy servo positioning/force control. Nevertheless, the non-idealities associated with the pneumatic system components (e.g.,



friction between the moving parts in pneumatic cylinders, dead zone and slow response time of the control valve) as well as the natural characteristics of the pressurized air (e.g., the compressibility of air and highly nonlinear flow characteristic through the pneumatic system components) have degraded the performance and cause an accurate servo control of the pneumatic actuators difficult to achieve. As a result, research related to servo control of the pneumatic actuators has become one of the active research areas in fluid power and one of the main research focuses is to achieve a high accuracy position control. Fig. 1 shows a schematic diagram of a typical pneumatic servo position control system. The system generally consists of an actuator (e.g., pneumatic cylinder), a control valve (e.g., one 5-way, 3-position, 5/3-way proportional directional control valve), connecting tubes and different sensors such as position and pressure sensors. The actuator is often subject to an external load either by mass of an external mechanical element attached to it, or via interaction with environment.

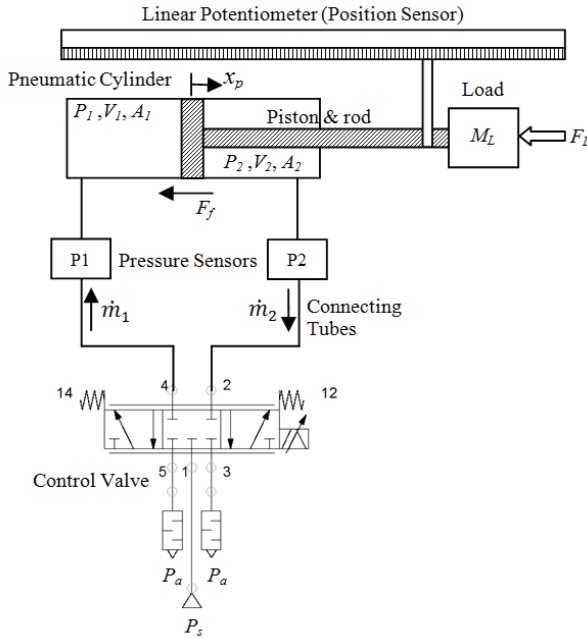


**Figure 1: Schematic Diagram of a Typical Pneumatic Position Control System.**

A considerable amount of research works has been devoted in order to improve the performance of pneumatic servo position control systems. Although these research works are widely diverged in their approaches, the overwhelming majority have focused on the utilization of different control techniques as to attain better performance and accuracy. This is proven by the number of publications that can be found in which a variety of control techniques such as PID-based (1-3), sliding mode-based (4-7), adaptive-based (8-10), Fuzzy-based (11,12) and neural network-based (13-15) controllers have been proposed. While many claimed that the proposed control technique have successfully improved the performance, including accuracy, of their pneumatic servo position control systems, only a handful of literatures (16-17) compared the existing proposed control techniques under the same controlled environment as to determine which one is more effective than the others.

This has motivated the authors to develop a pneumatic test rig and a simulation software that can be used to facilitate performance comparison of various pneumatic servo position controllers under the same controlled environment.

In this paper, we describe the development of the pneumatic test rig and the accompanied simulation software. In order to make the pneumatic test rig adaptable for operation of different circuit configurations of control valve and actuator setups, modular design approach has been used. As a result, the test rig can be generally divided into five main modules: air service unit, control valve, actuating, sensing and information processing modules. Each module possesses a specific function. The air service unit is utilized to remove all the contaminants and moisture from the pressurized air. Besides, it also keeps the operating pressure of pneumatic lines nearly constant. The control valve module plays a crucial role in controlling and regulating the flow of pressurized air to and from the actuating module. Meanwhile the actuating module is used to transfer energy which is in the form of pressurized air into a motion. The sensing module senses chamber pressures and actuator position from the test rig and converts it to the corresponding electrical signal. The information processing module which is the command center of the entire pneumatic test rig, receives the input signal coming from the sensing module, processes it according to the implemented pneumatic servo position controller and sending an appropriate output control signal to the control valve module via a data acquisition board. The information processing module for the pneumatic test rig was also developed with the capability to function as a prototype remote laboratory (PRL) station that can be operated in real-time fashion from distance. By having the PRL function, access to the test rig from anywhere can be made possible through the application of internet as communication channel in the future. On the other hand, the pneumatic simulation software which was developed for the purpose to offer users with the simulation results similar to the one from experiments conducted on the developed pneumatic test rig, is consisted of two main components: the graphic user interface (GUI) and the pneumatic system model. The GUI was developed using MATLAB GUI in order to create a user-friendly environment while the pneumatic system model which was written in C language is used to simulate the pneumatic position control system. The communication between the GUI and pneumatic system model are established through a MATLAB MEX-function. An example of typical simulation result of an open-loop system response obtained from the simulation software is also presented in this paper. The result is compared with the one from experiment in order to validate the pneumatic system model employed, and thus to justify the used of the simulation software for future works of performance comparison of pneumatic servo position controllers. The main benefit of having this simulation software is that, one is allowed to conduct performance analysis on the pneumatic system dynamic subjected to different control techniques easily before embarking to experimental evaluation on the developed pneumatic test rig for results confirmation. Besides, the simulation software would also enable others who do not have accessed to the developed pneumatic test rig to conduct the performance comparison works.

The rest of the paper is organized as follows. The developed pneumatic test rig will be described in Section II. Section III presents the proposed pneumatic simulation software in which the main graphic user interfaces (GUI) window and employed pneumatic system model will be briefly described. The model validation of the employed pneumatic system model will be addressed in Section IV and Section V provides conclusion of the paper.

2 PNEUMATIC TEST RIG

The test rig comprises of five main modules: air service unit, control valve, actuating, sensing and information processing modules. A picture of the developed pneumatic test rig as well as a diagram of all system components employed is shown in Fig. 2 and 3, respectively. With reference to Fig. 3, the functions including employed system components of each system module will be briefly described in this section.

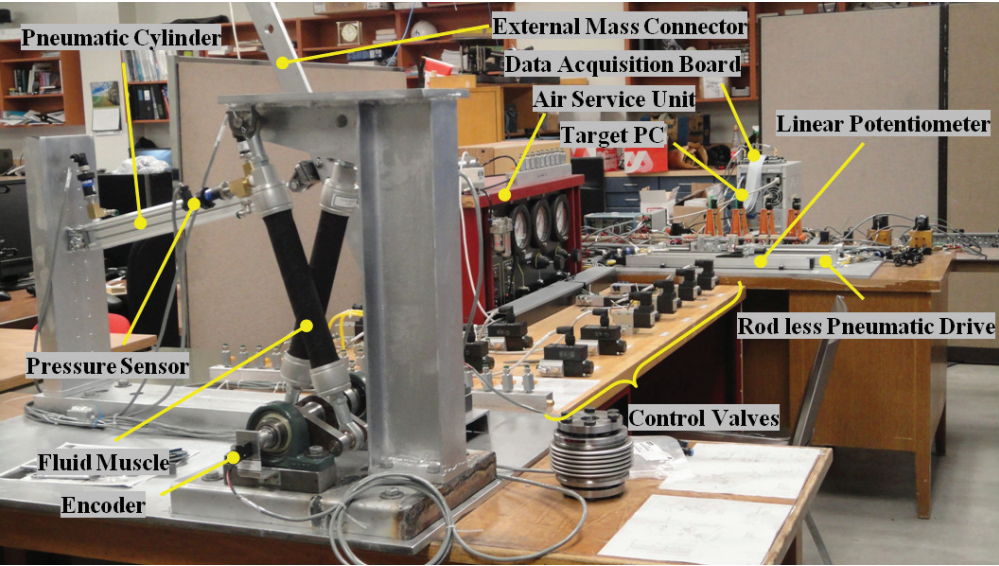


Figure 2: Developed Pneumatic Test Rig.

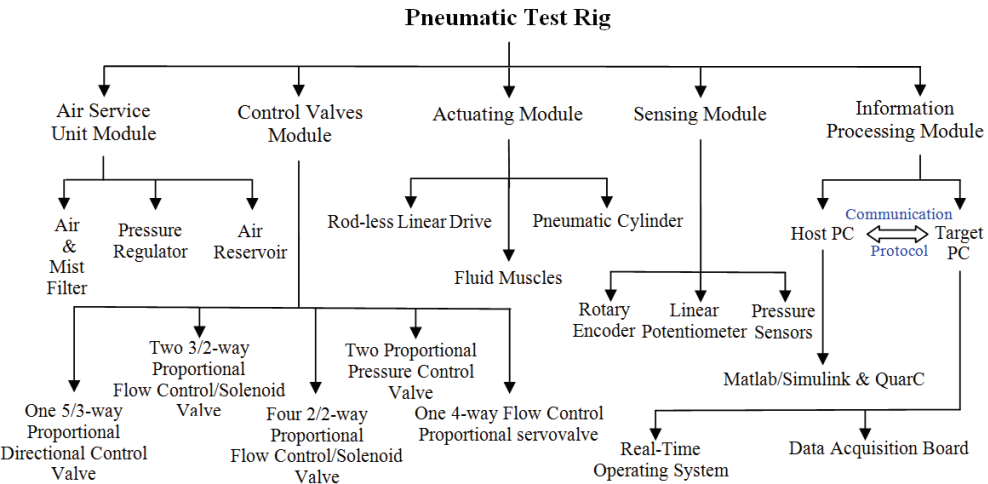


Figure 3: Components of the Developed Pneumatic Test Rig.

### 2.1 Air Service Unit Module

The air service unit module consists of three components: air and mist filter, pressure regulator and air reservoir. It has two basic functions which are to remove all the contaminants and moisture from the pressurized air, and to keep the operating pressure of the pneumatic line nearly constant. The first function is realized when the pressurized air flows through the air and mist filter while the second one is achieved through the utilization of pressure regulator and air reservoir.

### 2.2 Control Valve Module

Control valve is one of the vital components in pneumatic systems. It is responsible for controlling the pressure rate, amount of air flow as well as the direction of pressurized air as it moves through the pneumatic system. Control valves are generally divided into three main categories: servovalves, proportional valves and solenoid valves. The control valve module of the developed pneumatic test rig employs all the three categories of control valve. These control valves are arranged in five different circuit configurations: one 5/3-way proportional directional control valve (configuration 1), two 3/2-way proportional flow control/solenoid (configuration 2), four 2/2-way proportional flow control/solenoid (configuration 3), two proportional pressure control valve (configuration 4) and one 4/3-way flow control proportional servovalve (configuration 5). These circuit configurations are selected since they represent the most commonly used circuit configurations for servo position control systems as can be found in the literatures. Fig. 4 shows the arrangement of the control valves with respect to its circuit configuration.

### 2.3 Actuating Module

Pneumatic actuator converts energy into a motion. The energy is in the form of pressurized air while the motion can be either linear or rotary, depending on the types of actuator and its setups. There are three types of actuators employed in the developed test rig: pneumatic cylinder, fluid muscle and rod-less linear drive. As depicted in Fig. 5, the actuators are arranged to allow users to study performance of pneumatic servo position controllers with respect to different types of motion, under the influence of varying or fixed external load. The effect of varying external load to the performances of the pneumatic servo position controller needs to be studied since it is often accounted in the practical applications of pneumatic system especially for robot manipulator. By arranging the actuators as shown in the setups of Fig. 5(a) and 5(b), four different modes of varying external load with respect to actuator motion can be realized. Referring to Fig. 5(a) as an example, those modes can be explained as follows: the external load opposes the motion during piston's extension (mode 1), the external load assists the motion during piston's extension (mode 2), the external load opposes the motion during piston's retraction (mode 3), and the external load assists the motion during piston's retraction (mode 4). On the other hand, as depicted in Fig. 5(c) the rod-less linear drive which is available in two sets will be used to study the performance of pneumatic servo position controllers with respect to linear motion under the influence of fixed external load or for research related to cooperative motion control. The former will use only one set of the rod-less linear drive while the latter uses both.

### 2.4 Sensing Module

There are three types of sensors employed: rotary encoder, linear potentiometer, and pressure sensors. To acquire the actuators position of the pneumatic cylinder and fluid muscles, the rotary encoder is attached to the rotating shaft of external mass connector as

depicted in Fig. 5(a). The linear potentiometers which are arranged in parallel to the rod-less linear drive as shown in Fig. 5(c) are used to sense the position of mass carrier. Meanwhile, the pressure sensors are attached to each chamber of pneumatic cylinder/rod-less linear drive and fluid muscles in order to measure the pressures.

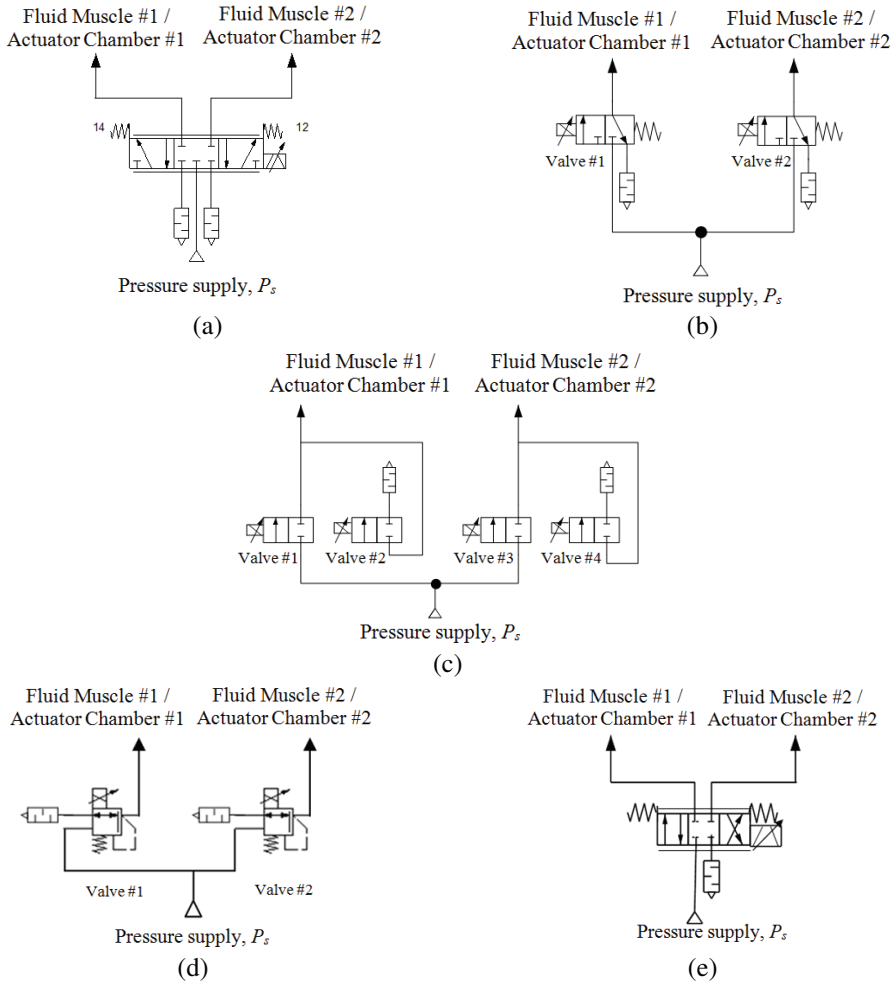


**Figure 4: Control Valve Circuit Configurations (a) Configuration 1 (b) Configuration 2 (c) Configuration 3 (d) Configuration 4 and (e) Configuration 5.**

## 2.5 Information Processing Module

The information processing module which is the command center of the developed test rig is responsible for monitoring as well as controlling all the activities that are taken place in the actuating and control valve modules, respectively. In order to equip the module with the capability to function as a prototype remote laboratory (PRL) station, a setup as depicted in Fig. 6 is employed. The setup consists of two computers where one of them acts as a host while the other as a target. These two computers are connected together via a local area

network (LAN) and use standard TCP/IP (Transmission Control Protocol/Internet Protocol) for data exchange. The host computer is employed as a platform where the development/implementation of pneumatic servo position controller is taken place. The development/implementation is carried out through the Matlab Simulink development environment integrated with QuarC software package. The QuarC software package is needed in order to convert the implemented controller which is in the form of Matlab Simulink model to a corresponding executable C-file that later will be uploaded onto the

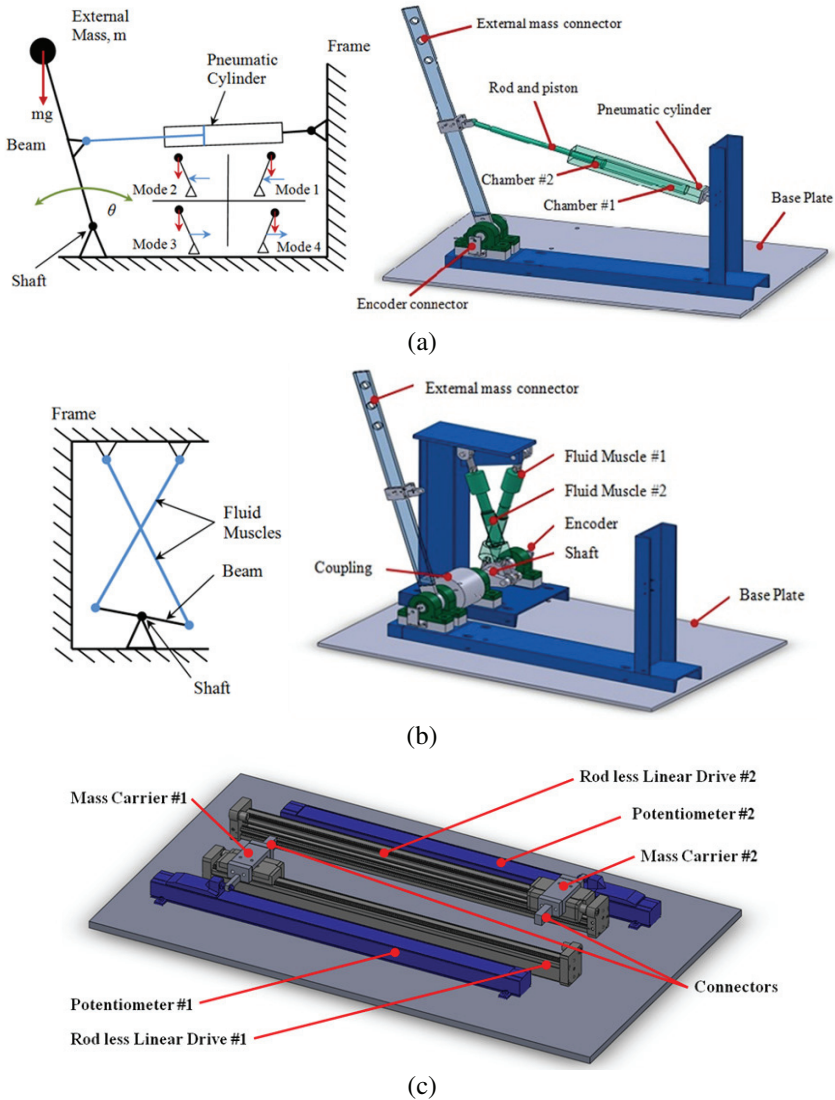


**Figure 5: Actuator Setups (a) Pneumatic Cylinder (b) Fluid Muscles and (c) Rod-less Linear Drive.**



target computer. At the same time, the host computer is also the place where all the information related to the actuating and control valves modules such as the actuator position, velocity, chamber pressures as well as the control signal are displayed during the experiment. The target computer installed with a real-time operating system on the other hand, is the place where the executable C-file from the host computer will be executed in a real-time fashion. Besides, it is also the place where interfacing between the information processing and other modules occurs. The exchange of signals between the target computer and other system modules of the developed test rig are carried out through a data acquisition board known as Q8 from Quanser. Note that at this moment, access to the target computer and ultimately to the test rig from the host computer is limited within the university area where LAN is available. However, in the future the access will be made possible from anywhere else through the utilization of internet as a communication channel.

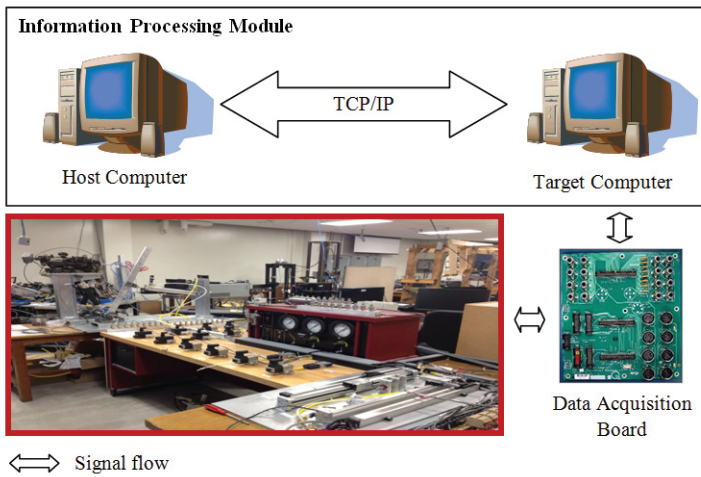


**Figure 6: Setup of the Information Processing Module**

### 3 PNEUMATIC SIMULATION SOFTWARE

The pneumatic simulation software was developed in order to offer users with the simulation results similar to the one obtained from the experimental works conducted on the developed pneumatic test rig. In this section, the two components that made up the pneumatic simulation software namely, the graphic user interface (GUI) and pneumatic system model will be presented.

#### 3.1 The Graphic User Interface (GUI)

A graphic user interface (GUI) technique has been applied to the simulation software in order to create a user-friendly environment. Fig. 7 shows a picture of the main window of the proposed pneumatic simulation software GUI. The GUI is made up of eight main sections: the system type, actuator type, valve type and configuration, compressed air properties, mass flow rate model, friction model, controller and input signal selection.

Currently there are only two types of actuator and three circuit configurations of control valve offered as depicted in Fig. 7. However in the near future, more actuators as well as circuit configurations of control valve will be made available as to fully emulate the function of the developed pneumatic test rig. To start the simulation process, users need to provide the simulation software with the necessary parameters in each section and then click on the “Run Simulation” button located at the central bottom of the GUI. The entered parameters will be passed to the pneumatic system model through MATLAB MEX-function for the simulation process. Also, note that in the mass flow rate model, friction model, controller and input signal selection sections, users can either use the standard model provided or implement a custom one. To implement a custom model in the simulation software, click on the check box of “use custom model” and a pop-up window will appear. User can then insert a corresponding file containing the custom model written in C language.

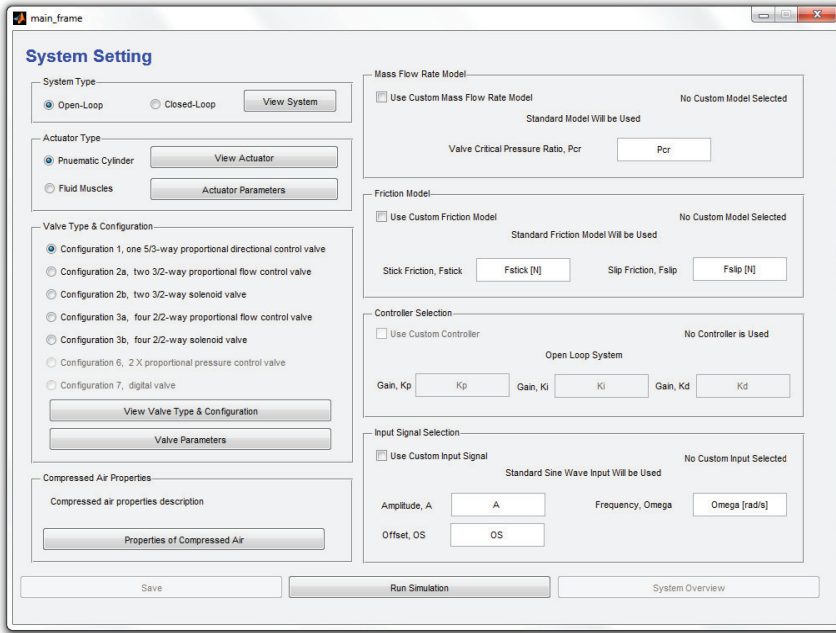


**Figure 7: Main Window of the Pneumatic Simulation Software GUI**

### 3.2 Pneumatic System Model

The second component of the proposed pneumatic simulation software which is the pneumatic system model will be briefly presented here. There are two types of actuator offered in the simulation software which are the pneumatic cylinder and fluid muscles. The equation of motion for the pneumatic cylinder can be written as follow.

$$M\ddot{x}_p + D\dot{x}_p = (P_1A_1 - P_2A_2) - (F_f + F_L) \quad (1)$$

where  $x_p$  denotes the position of the actuator.  $M$  is the combined mass of the piston-rod assembly and the external load.  $A$  is the annulus area of the piston,  $D$  is the viscous friction



coefficient,  $F_f$  represents the dry friction force and  $F_L$  signifies the external load. The dry friction force is modeled as the following equations.

$$F_f = \begin{cases} P_1 A_1 - P_2 A_2 - F_L & \text{if } \dot{x}_p = 0 \text{ and } F_f < F_{stick} \\ F_{stick} \text{sign}(\dot{x}_p) & \text{if } \dot{x}_p = 0 \text{ and } F_f \geq F_{stick} \\ F_{slip} \text{sign}(\dot{x}_p) & \text{if } \dot{x}_p \neq 0 \end{cases} \quad (2)$$

where  $F_{stick}$  and  $F_{slip}$  is the stick and slip friction and

$$\text{sign}(\dot{x}_p) = \begin{cases} -1 & \text{if } \dot{x}_p \leq 0 \\ 1 & \text{if } \dot{x}_p > 0 \end{cases} \quad (3)$$

As for the fluid muscles, the equation of motion can be represented as follows:

$$I\ddot{\theta}_s + D\dot{\theta}_s = (F_2 - F_1)r - T_L \quad (4)$$

where  $I$  is the combined inertia of the shaft and the external load,  $\theta_s$  is the shaft angular position and  $r$  represents the radius of beam connecting the shaft and the fluid muscles.  $D$  and  $T_L$  denote the angular viscous friction coefficient and the external load torque, respectively.  $F_2$  and  $F_1$  are the actual forces from the two fluid muscles. Note that the dry friction force for the fluid muscles actuator is negligible since there is no movement between the piston and rod with the cylinder wall as in the case of pneumatic cylinder. Furthermore the rotating shaft connected at the end of fluid muscles is in contact with the bearings. Thus, in the simulation software, the dry friction force is only applied to the pneumatic cylinder. From the literature, the relationship between the input voltage,  $u$ , and the valve spool position,  $x_v$ , is often modeled as a simple gain (18,19). However, according to the relevant manufacturer's literatures, the spool type control valve can be more appropriately represented by a first-order lag (3) equation. Since the proportional and solenoid control valve offered in the simulation software are of spool type which is similar to the one employed in the developed pneumatic test rig, all the control valves are modeled using the following equation.

$$\dot{x}_v = -\frac{x_v}{\tau} + \frac{k_v}{\tau} u_v \quad (5)$$

where  $k_v$  is the valve spool position gain and  $\tau_v$  represents the first order time constant of the control valve. Also, note that the input signal,  $u_v$ , of the proportional valve is equivalent to the control signal,  $u$ . However for the solenoid valve, the control signal,  $u$ , is converted to a pulse width modulation (PWM) signal,  $u_{PWM}$ , before it is subjected to the control valve. The PWM signal is realized by comparing the continuous control signal,  $u$ , with the high frequency carrier wave,  $V_d$  which can be described by the following mathematical expression:

$$u_{PWM}(t) = \begin{cases} u_p & u(t) \geq V_d(t) \\ 0 & u(t) < V_d(t) \end{cases} \quad (6)$$

with

$$V_d(t) = [t - (j-1)T] \cdot \frac{V_p}{T} \quad \text{for } (j-1)T \leq t \leq jT \quad (7)$$

where  $j = 1, 2, \dots, n$  is the  $j$ -th modulation period,  $T$ , and  $V_p$  denotes the amplitude of carrier wave. The mass flow rate model provided in the simulation software was derived from the standard orifice theory (20) which can be represented by the following equation.

$$\dot{m} = \begin{cases} \frac{C_d w x_v P_u}{\sqrt{T}} \sqrt{\frac{\gamma}{R} \left( \frac{2}{\gamma+1} \right)^{(\gamma+1)/(\gamma-1)}} & , \quad \frac{P_d}{P_u} \leq P_{cr} \\ \frac{C_d w x_v P_u}{\sqrt{T}} \sqrt{\frac{\gamma}{R} \left( \frac{2}{\gamma+1} \right)^{(\gamma+1)/(\gamma-1)}} \\ \times \sqrt{1 - \left( \frac{P_d / P_u - P_{cr}}{1 - P_{cr}} \right)^{(\lambda-1)/\gamma}} & , \quad \frac{P_d}{P_u} > P_{cr} \end{cases} \quad (8)$$

where  $C_d$  and  $w$  are the control valve coefficient of discharge and orifice area gradient, respectively.  $P_u$  is the absolute downstream pressure, whereas  $P_d$  denotes the absolute upstream pressure.  $P_{cr}$  is the valve critical pressure ratio which determined whether the compressed air attain sonic (choked) velocity or subsonic velocity flow. The equations relating chamber's pressures,  $P_1$  and  $P_2$  with mass flow rates of the compressed air, can be written as follows.

$$\begin{aligned} \dot{P}_1 &= \frac{\gamma R T}{V_1} \dot{m}_1 - \alpha \frac{\gamma P_1 A_1}{V_1} \dot{x}_p \\ \dot{P}_2 &= \frac{\gamma R T}{V_2} \dot{m}_2 - \alpha \frac{\gamma P_2 A_2}{V_2} \dot{x}_p \end{aligned} \quad (9)$$

$V_1$  and  $V_2$  are the instantaneous volumes of each actuator chamber, which depends on the actuator position.  $R$  is the ideal gas constant,  $\gamma$  is the ratio of specific heats and  $T$  is the temperature of the compressed air source. Parameter  $\alpha$  is a compressibility flow correction factor.

#### 4 MODEL VALIDATION

In order to validate the accuracy of the employed pneumatic system model, response of an open-loop system from the simulation software is compared with the one from the experiment conducted on the developed pneumatic test rig. Fig. 8 shows the simulation result of an open-loop system from the simulation software which was obtained using control valve circuit configuration 1 (one 5/3 proportional directional control valve), standard mass flow rate model, standard friction model and sinusoidal input signal with amplitude of 1.5 and frequency of 1 Hz. The parameters used in the simulation are obtained from the related manufacturer documents as well as the initial setup of the pneumatic test rig during experiment. Due to page limitation value of the applied parameters are not given. The

comparison of an open-loop system response between the simulation and experiment is shown in Fig. 9. As it can be observed, the results from both simulation and experimental are closely matched to each other. This is applied for all four figures: the actuator position, actuator velocity, chamber 1 and chamber 2 pressures. The slight differences between the simulation and experimental results may come from inaccurate value of the applied parameters. However, it can be concluded that the pneumatic system model employed in the proposed simulation software is sufficiently accurate to represent the developed test rig. Besides, this result has also justified the utilization of the pneumatic simulation software for future work of performance comparison of various pneumatic servo position controllers.

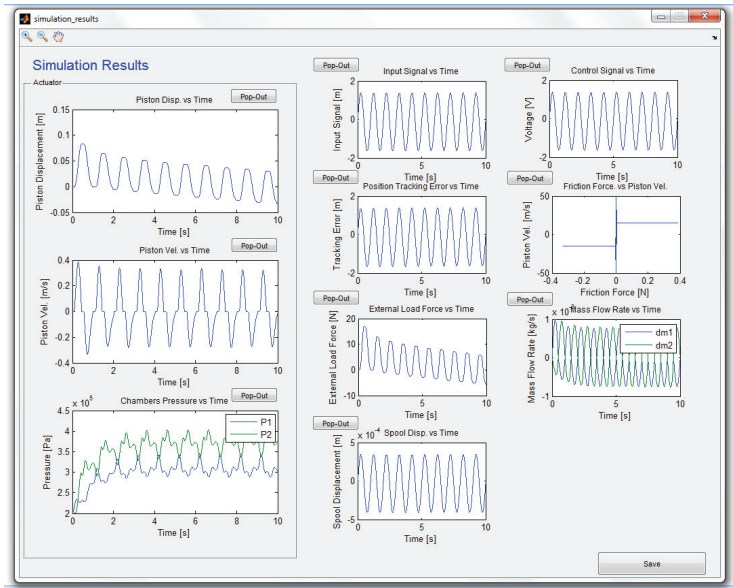


**Figure 8: A Simulation Result of an Open-loop System subjected to a Sinusoidal Input Signal**

**5 CONCLUSIONS**

A pneumatic test rig which is adaptable for operation of different circuit configurations of control valve and actuator setups has been described. The pneumatic test rig will be used to facilitate the performance comparison of various pneumatic servo position controllers under the same controlled environment. Effect of different actuator setups as well as circuit configurations of control valve towards the performance of servo position controller can also be studied. In addition, a simple, yet sufficiently accurate pneumatic simulation software with an interactive graphic user interface has also been developed. The pneumatic system model employed in the simulation software has been experimentally validated. The result confirms that the pneumatic system model is accurate enough to represent the developed pneumatic test rig as its simulation result was closely matched with the one obtained from the experiment. Thus, the objective of the development of pneumatic simulation software which is to offer users with the simulation results similar to the one

obtained from the experimental works conducted on the developed pneumatic test rig has been achieved. In the future, the results obtained from the pneumatic simulation software will be utilized as a preliminary finding before embarking to experimental evaluation on the developed pneumatic test rig for confirmation. Furthermore, the ability of the pneumatic simulation software to offer users with option either to use the provided standard model/function or to employ the custom one has made the software so flexible. The proposed pneumatic simulation software however is still subjected to future development for further improvement.

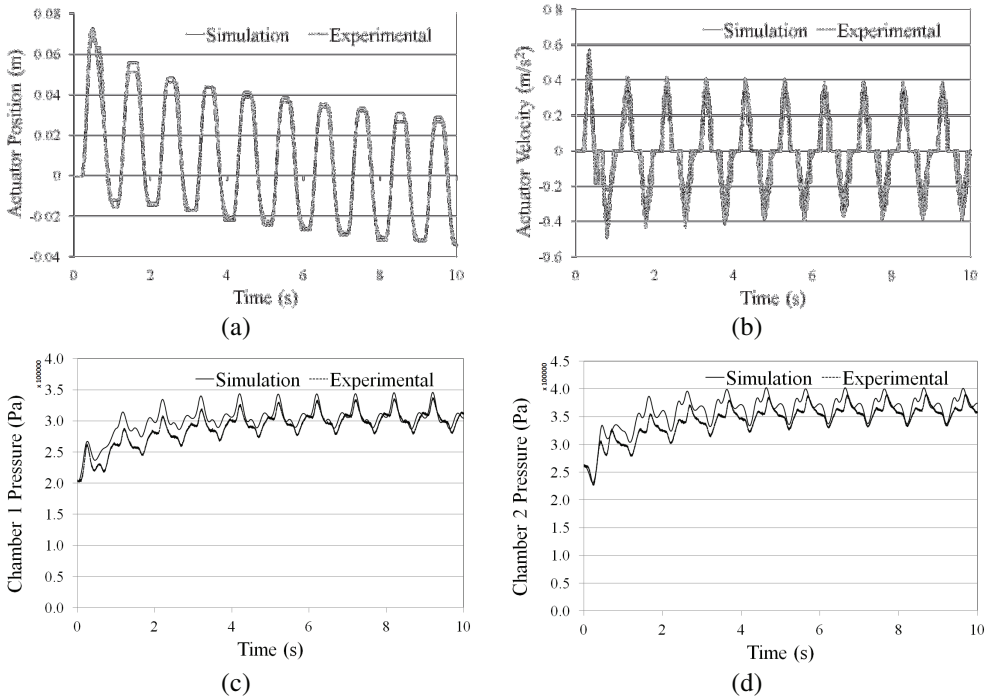


**Figure 9: Simulation and Experimental responses of an open-loop system subjected to a Sinusoidal input signal (a) Actuator Position, (b) Actuator Velocity, (c) Chamber 1 Pressure, and (d) Chamber 2 Pressure.**

## REFERENCES

1. R. B. van Varseveld and G. M. Bone, "Accurate position control of a pneumatic actuator using on/off solenoid valves," *IEEE/ASME Transactions on Mechatronics*, Vol. 2, pp. 195-204, 1997.
2. S. Aziz and G. M. Bone, "Automatic tuning of an accurate position controller for pneumatic actuators," *IEEE/RSJ International Conference on Intelligent Robots and Systems*, Vol.3, pp. 1782-1788, 1998.
3. M. Karpenko and N. Sepeshri, "Development and experimental evaluation of a fixed-gain nonlinear control for a low-cost pneumatic actuator," *IEE Proceedings on Control Theory and Applications*, Vol. 153, pp. 629-640, 2006.

4. H. M. Chen, Y. P. Shyu and C. H. Chen, "Design and realization of a sliding mode control scheme for a pneumatic cylinder X-Y axes position servo system," IET International Conference on Frontier Computing, Theory, Technologies and Applications, pp. 416-421, 2010.
5. X. Shen, "Nonlinear model-based control of pneumatic artificial muscle servo systems," Control Engineering Practice, Vol. 18, No. 3, pp. 311-317, 2010.
6. X. Shen, J. Zhang, E. J. Barth and M. Goldfarb, "Nonlinear model-based control of pulse width modulated pneumatic servo systems," Transactions of the ASME, Journal of Dynamic Systems, Measurement and Control, Vol. 128, pp. 663-669, 2006.
7. T. Nguyen, J. Leavitt, F. Jabbari and J. E. Bobrow, "Accurate Sliding-mode control of pneumatic systems using low-cost solenoid valves," IEEE/ASME Transactions on Mechatronics, Vol. 12, pp. 216-219, 2007.
8. Y. Zhu and E. J. Barth, "Accurate sub-millimeter servo-pneumatic tracking using model reference adaptive control (MRAC)," International Journal of Fluid Power, Vol. 11, pp. 43-55, 2010.
9. F. Errahimi, H. Cherrid, N. K. M'Sirdi and H. Abarkane, "Robust adaptive control and observer for a robot with pneumatic actuators," Robotica, Vol. 20, No. 2, pp. 167-173, 2002.
10. Y. C. Tsai and A. C. Huang, "FAT-based adaptive control for pneumatic servo systems with mismatched uncertainties," Mechanical System and Signal Processing, Vol. 22, No. 6, pp. 1263-1273, 2008.
11. Y. Xue, G. Peng, M. Fan and Q. Wu, "Asymmetric fuzzy PID control for pneumatic position control system," Journal of Beijing Institute of Technology (English Edition), Vol. 13, pp. 29-33, 2004.
12. J. Yu, J. Liu and X. Liu, "Intelligent Fuzzy PID Control of Pneumatic Position Servo System," Advanced Materials Research, Vol. 186, pp. 100-104, 2011.
13. S. Shibata, M. Jindai, T. Yamamoto and A. Shimizu, "A disturbance estimation type control for pneumatic servo system using neural network," JSME International Journal, Series C: Mechanical Systems, Machine Elements and Manufacturing, Vol. 49, pp. 189-196, 2006.
14. L. Lu, F. Liu and W. Shi, "Neural-network adaptive controller for nonlinear systems and its application in pneumatic servo systems," Journal of Control Theory and Applications, Vol. 6, No. 2, pp. 97-103, 2008.
15. H. K. Lee, G. S. Choi and G. H. Choi, "A study on tracking position control of pneumatic actuators," Mechatronics, Vol. 12, No. 6, pp. 813-831, 2002.
16. G. M. Bone and S. Ning, "Experimental comparison of position tracking control algorithms for pneumatic cylinder actuators," IEEE/ASME Transactions on Mechatronics, Vol. 12, No. 5, pp. 557-561, 10, 2007.
17. S. Chillari, S. Guccione and G. Muscato, "An experimental comparison between several pneumatic position control methods," Proceedings of the 40th IEEE Conference on Decision and Control, Vol. 2, pp. 1168-1173, 2002.
18. J. Wang, J. Pu, and P. Moore, "A practical control strategy for servo-pneumatic actuator systems", Control Engineering Practice, Vol. 7, No. 12, pp. 1483-1488, 1999.
19. S. Liu, and J.E. Bobrow, "An analysis of a pneumatic servo system and its application to a computer-controlled robot", Transactions of the ASME Journal of Dynamic Systems, Measurement and Control, Vol. 110, No. 3, pp. 228-235, 1988.
20. F. E. Sanville, "A new method of specifying the flow capacity of pneumatic fluid power valves," BHRA 2<sup>nd</sup> International Fluid Power Symposium, Guildford, England, 1971.

# Development of a Low Noise Pressure Reducing Valve for High Pressure Hydrogen Using a Radial Slit Structure

Chongho YOUN\*, Yoshinari Nakamura\*\*, Toshiharu KAGAWA\*

\*Tokyo Institute of Technology, Precision and Intelligence Laboratory, Japan

\*\*KYB Corporation, Mechanical Component Engineering Sect., Japan

## ABSTRACT

In the fuel cell vehicle (FCV) using hydrogen energy, there is a problem of the noise generation by fluid in a pressure reducing part because 35MPa or more high pressured hydrogen is decompressed to 1MPa or less pressure. In previous study, authors proposed the pressure reducing valve using a slit structure in the pneumatic system of supply pressure 0.6MPa, and confirmed the validity of noise reduction by experiment. Then, the noise reduction effect by using a slit structure is expected in the pressure reducing of high pressure hydrogen. In the latest study, the pressure reducing valve which set the decompression part to cone type piston was made, and it was confirmed that a noise level had become small compared with the conventional pressure reducing valve in the experiment in the flow rate 500 l/min(nor).

In this study, in order to develop a low noise pressure reducing valve for high pressure hydrogen, we propose adding radial slit structure to the downstream side of cone type piston. Six kinds of radial slit structures were made, supply pressure was set to 35MPa, and the flow rate characteristic and noise level were measured. As a result, the noise reduction effect by the addition of radial slit structure was confirmed.

**Keywords:** Noise, Pressure reducing valve, Radial slit structure, Hydrogen

## NOMENCLATURE

$A_{in}$	Total inlet area of the slit	[mm <sup>2</sup> ]
$h$	Height of slit	[mm]
$P_2$	Downstream pressure	[MPa(gage)]
$P_s$	Supply pressure	[MPa(gage)]
$Q$	Volume flow rate (273K, 1atm)	[l/min(nor)]
$SPL$	Sound pressure level	[dB(A)]

## 1 INTRODUCTION

Investigation of an alternative to fossil fuel and reduction of carbon dioxide emissions are promoted by national initiatives around the world; some also wish to reduce the dependence on nuclear power generation. Today, automobile manufacturers have decided that FCVs, which can especially extend the cruising range of pure electric vehicles, will be marketed in 2015 year. In regard to hydrogen fueling stations, fuel suppliers are aiming to construct approximately 100 throughout the country by 2015 year [1]. According to an official announcement, full commercialization of FCVs would begin in 2025 year [2]. Some research corporations, such as Fuji Keizai Co., Ltd. [3], have reported that the market for the fuel cell industry would rise to more than 1 trillion yen in Japan. For the hydrogen component market, a gradual progression of diversification in energy sources could be a good opportunity.

Therefore, assuming that the demand for hydrogen components will increase in the near future, we have begun developing technologies for the element components of fuel cell systems. One of these initiatives has been the development of a pressure-reducing valve for hydrogen gas. In addition, deployment of many core technologies, such as design and manufacturing techniques, are to be expected from the development of this valve. In a normal valve, supply pressure is depressurized with an orifice structure. When pressurized air passes through an orifice structure, considerable noise and pressure fluctuation occur at the downstream. There is a problem of the noise generation by fluid in a pressure reducing part because 35MPa or more high pressured hydrogen is decompressed to 1MPa or less pressure. Therefore, reduction of noise originating from the valve is required in industrial fields. In the gas supply system, generally, several methods such as the use of diffusers (Boger, 1971) [4], wrapping pipe with sound damping materials (Bell, 1993) [5], and the use of porous materials (N. Atalla et al., 2001) [6] have been developed to reduce noise.

In previous study, authors proposed the pressure reducing valve using a slit structure in the pneumatic system of supply pressure 0.6MPa, and confirmed the validity of noise reduction by experiment [7], [8]. Then, the noise reduction effect by using a slit structure is expected in the pressure reducing of high pressure hydrogen. In the latest study, the pressure reducing valve which set the decompression part to cone type piston was made, and it was confirmed that a noise level had become small compared with the conventional pressure reducing valve in the experiment in the flow rate 500 l/min(nor). In this study, in order to develop a low noise pressure reducing valve for high pressure hydrogen, we propose adding radial slit structure to the downstream side of cone type slit. Six kinds of radial slit structures are made. Supply pressure is set to 35MPa, and flow rate characteristic and the noise level is measured.

## 2 PRESSURE REDUCING VALVE WITH RADIAL SLIT STRUCTURE

Hydrogen is stocked as a compressed gas at high pressure in the FCV and is supplied to the fuel cell system at pressure lower than 1MPa. A pressure reducing valve is used to maintain the pressure of downstream to specific values as shown in Fig. 1. Hydrogen is supplied to a supply port from a high pressure hydrogen tank and it is depressurized at piston part. There is diaphragm on the upper part of piston. Diaphragm moves up and down with the force

balance of spring and the downstream pressure. When downstream pressure is smaller than a setting pressure, diaphragm moves downward and valve is opened. Then, Diaphragm moves until downstream pressure becomes a setting pressure.

In the latest study, we suggested the cone type piston to reduce the noise. In this study, we propose the radial slit structure in the downstream of the cone type piston to reduce the noise more. The slit height  $h$  is 0.6mm or less. Hydrogen passes through a thin slit, and the effect of noise reduction is expected.

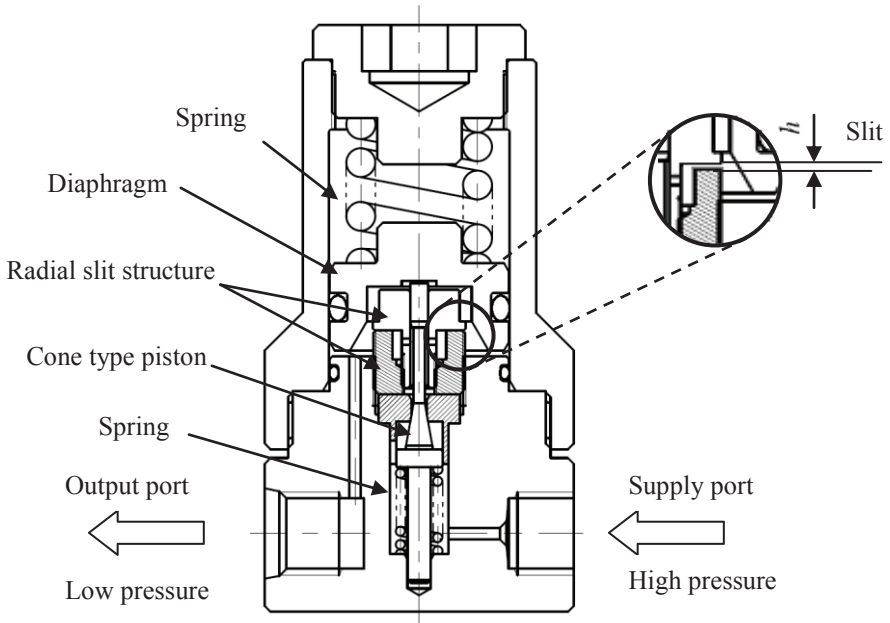


**Figure 1: Pressure reducing valve with radial slit structure**

### 3 RADIAL SLIT STRUCTURE

Figure 2 shows a schematic drawing and picture of the newly developed radial slit structure. The slit structure consists of two elements, the part 1 and the part 2. The central part of part 1 and part 2 has a hole for piston to pass. The lower part of part 1 has a screw thread and it is combined with part 2 with this screw thread. The upper part has a hexagon head in order to tighten a screw thread. The undersurface of a hexagon head has a disk shape and contacts with top face of part 2. The picture of part 1 and 2 is shown in figure 3. The outside of part 1 has a screw thread and it is combined with body of the pressure reducing valve. In order to tighten the screw thread, it has a hexagon head. Some parts of the top surface are milled about sub-millimeter order by machining and it makes the radial slit flow as shown in figure 4. The part 1 consists of upper surface of the radial slit flow. Hydrogen enters from the center of part 2 and is exhausted outward through the radial slits to the downstream. When the fluid flows through the slit, the fluid is decompressed in the slit because of viscous resistance of fluid. A sudden pressure change is reduced in the downstream.



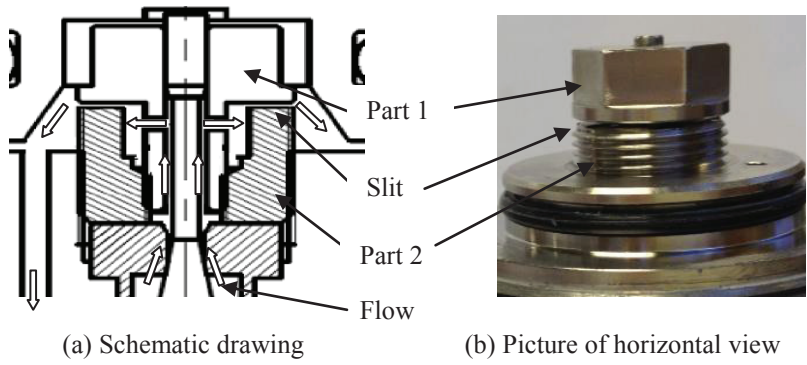


Figure 2: Radial slit structure

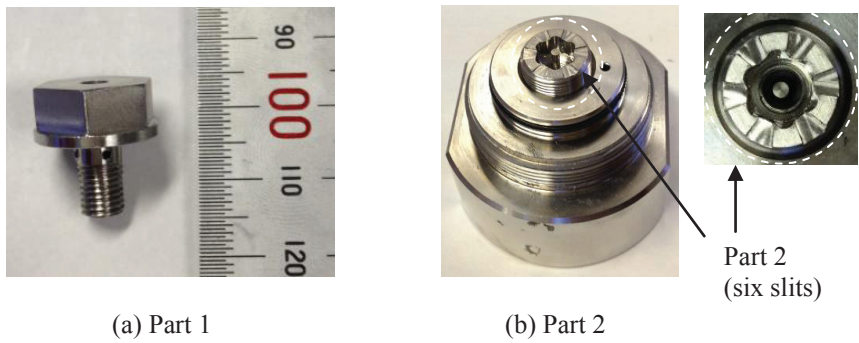


Figure 3: Radial slit structure

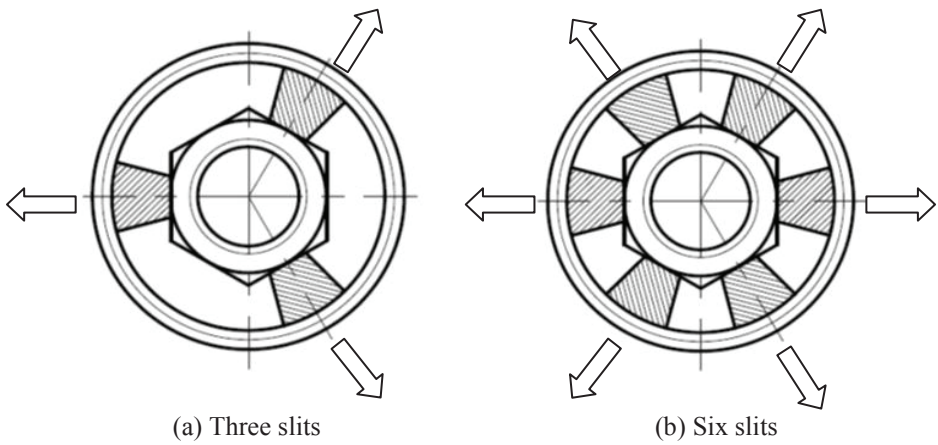


Figure 4: Radial slit structure

Six types of the radial slit structure were made as shown in table 1. Height of slit is changed from 0.1 to 0.6. The number of slits has two kinds, three slits and six slits. RSV\_01 and RSV\_02, RSV\_03 and RSV\_04, RSV\_05 and RSV\_06 have the same total inlet area respectively. CSV means the valve with only a cone type piston and the radial slit structure is not installed. It is for comparing the noise result with the radial slit structure.

**Table 1 : Specification of the slit**

Type	$h$ [mm] Height of slit	Numbers of slit [-]	$A_{in}$ [mm <sup>2</sup> ] Total inlet area
CSV (without radial slit)	-	-	-
RSV_01	0.4	3	2.57
RSV_02	0.2	6	"
RSV_03	0.2	3	1.28
RSV_04	0.1	6	"
RSV_05	0.6	3	3.85
RSV_06	0.3	6	"

#### 4 EXPERIMENTAL APPARATUS

All experimental tests were performed using the special test centre: Hydrogen Energy Test and Research Center (HyTReC, [9]) in Japan. The laboratory in HyTReC can be adapted for high-compressed hydrogen testing, which was previously unavailable. The several products in trial phases can be examined safely with the cooperation of HyTReC.

Figure 5 illustrates the experimental setup for the evaluations of test valves. Tests on the trial components have to be mounted into the explosion-resistant chamber as shown in figure 6, which is filled with nitrogen. Since oxygen is not present in the chamber, hydrogen can be easily detected and the danger of explosion is lower if hydrogen leaks from the trial valve. In addition the surroundings of the test valves are covered so that fragments do not scatter and the walls of the chamber are not damaged in the event of an explosion.

Six valves are mounted on the connecting block at one time, as illustrated in Figure 7. Each valve is measured only after a stopped valve mounted downstream is opened. However, if the delivery pressure from a test valve rises to 1MPa or more, the relief valve will operate. Furthermore, we measured using the instruments shown in Table 2, since the noise of a valve with a high flow rate sometimes becomes a problem. On the inner wall of the prevention cover, acoustic material is attached, so that sound produced by the test valve cannot echo. Two microphones are utilized at this time. One microphone is set outside of the explosion-resistant chamber, and the other is inserted near the testing valve inside the chamber.

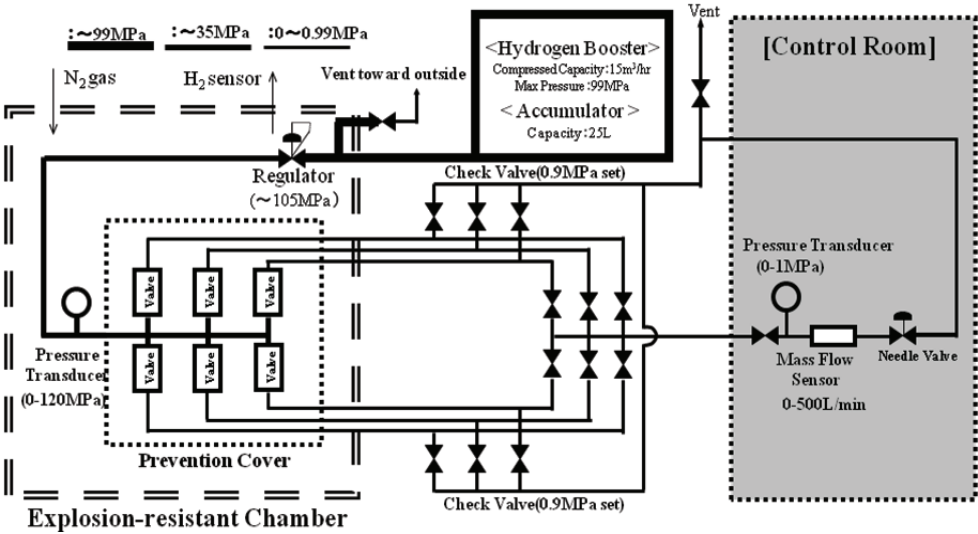


Figure 5: Experimental setup for the valve tests

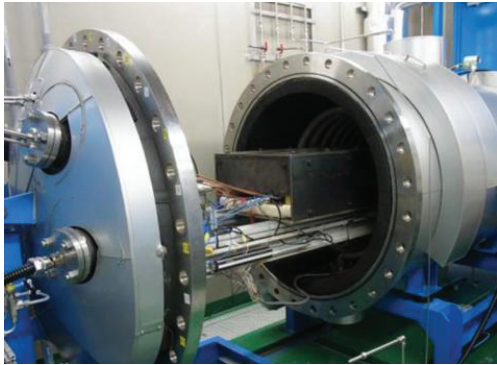


Figure 6: Picture of experimental setup

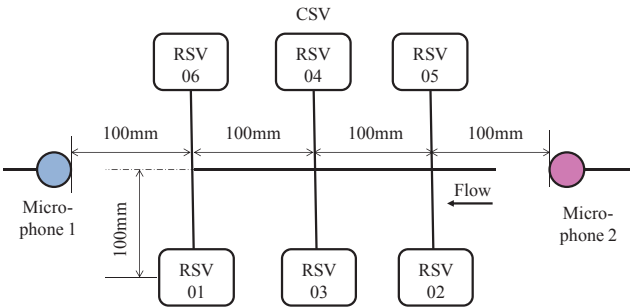


Figure 7: The position of valve

Table 2 : Sound measuring instrument

	Maker	Model No.
Logger	Bruel & Kjaer	Type7533
Software	RION	BZ5217 version 6.0
Display Unit	RION	UV-12
Sound level meter unit	RION	UN-04
Condenser microphone	RION	UC-30
Preamplifier	RION	NH-04

5 EXPERIMENTAL RESULTS

5.1 Flow rate characteristic

The pressure reducing valve was used to control downstream pressure  $P_2$  to a setting pressure. Then, the characteristic of the pressure reducing valve was investigated by experiment. Measurement of the flow rate characteristic was achieved as follows. Supply pressure is fixed with 35 MPa. The flow rate was changed by the throttle valve which was installed downstream of pressure reducing valve. The flow rate was increased from 0 l/min(nor) to 500 [l/min(nor)], and it was reduced to 0 l/min(nor).

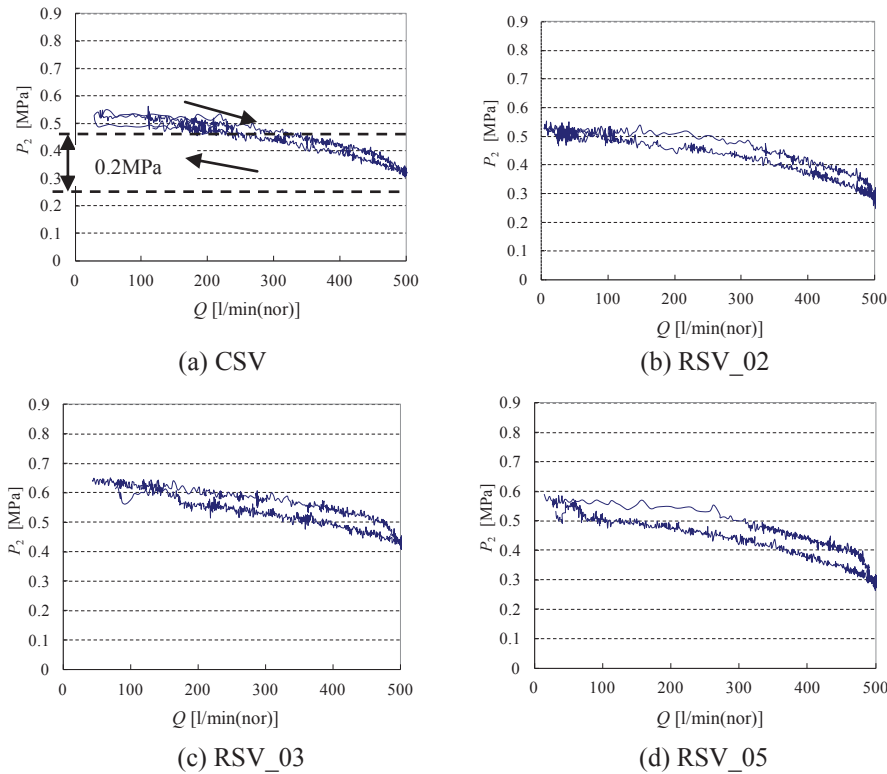


Figure 8: Flow rate characteristic

The experimental results of CSV without radial slit and three slits with different inlet area are shown in figure 8. As for two lines, phenomenon of hysteresis is seen on flow rate characteristics. However,  $P_2$  are dropping gradually as flow rate increases up to 500 l/min(nor). This pressure offsets between 0 l/min(nor) and 500 l/min(nor) become about 0.2 MPa, which is accomplished for target specification. Total inlet area of RSV\_02, RSV\_03, and RSV\_05 is  $2.57 \text{ mm}^2$ ,  $1.28 \text{ mm}^2$ , and  $3.85 \text{ mm}^2$  respectively. The maximum difference of cross-sectional area is 3 times. However, the flow rate characteristics for the four cases are almost the same. It was confirmed that radial slit structure did not affect the flow characteristic of pressure reducing valve. It means that the flow resistance by radial slit structure is small and the flow resistance by main piston is large.

5.2 Noise Level

The results of the noise level of CSV, RSV\_02, RSV\_03, and RSV\_05 are shown in Figure 9. We used the two microphones in this experiment and the position of the valves is different as shown in Figure 7. A solid line is microphone 1 and a dotted line is microphone 2. The back ground noise is about 35 dB (A). Noise level becomes large with the increase of hte flow rate. There is a difference in the noise level of the microphone 1 and the microphone 2 in RSV\_02 and RSV\_05 because the distance from the microphone is different.

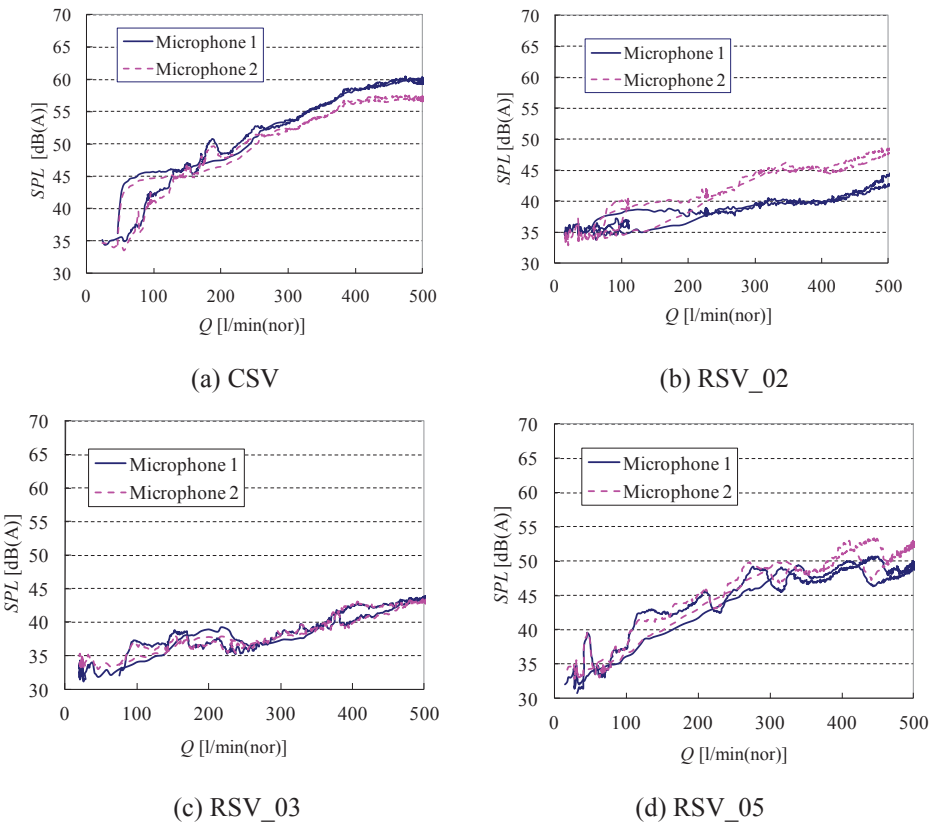


Figure 9: Sound pressure level

The noise level of each valve for the flow rate 300 l/min(nor) is shown in Figure 10. The noise levels of six types of radial slit valves are lower than CSV which has only cone type piston. Then, the noise level to the total inlet area is shown in Fig. 11. Sound pressure level is compensated by the distance from microphone 1 and microphone 2 on the basis of the center position. The noise level becomes small when the total inlet area becomes small except the RSV\_04. Then, it is considered that the effect of the number of slits is small. However, the maximum noise reduction effect of radial slit structure was about 15 dB (A) in the flow rate 300 l/min(nor) .

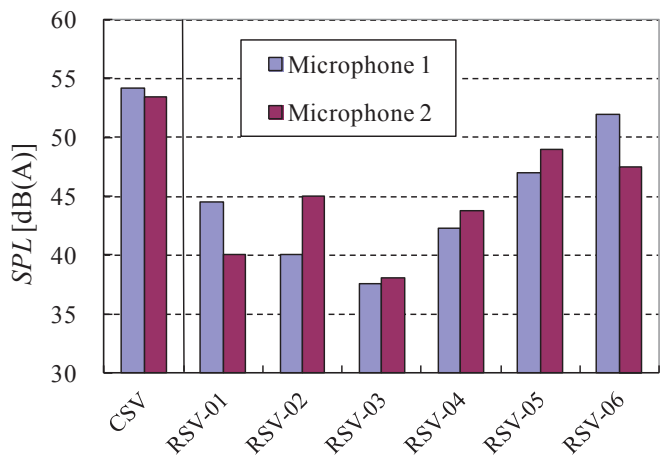


Figure 10: Sound pressure level (300 [l/min(nor)])

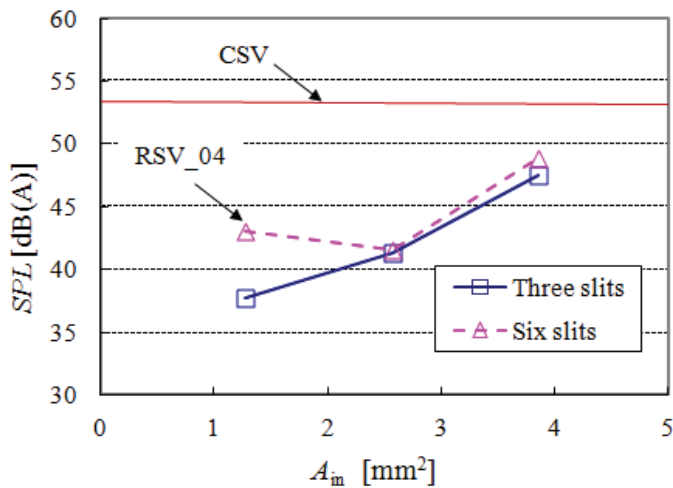


Figure 11: Sound pressure level against the total inlet area (300 [l/min(nor)])

## 6 CONCLUSIONS

In this study, in order to develop a low noise pressure reducing valve for high pressure hydrogen, we propose adding radial slit structure to the downstream side of cone type slit. Six kinds of radial slit structures were made, supply pressure was set to 35MPa, and the noise level was measured. The obtained results are as follows.

1. It was confirmed that radial slit structure did not affect the flow characteristic of pressure reducing valve.
2. The noise levels of six types of radial slit valves are lower than CSV which has only cone type piston. Then, the maximum noise reduction effect was about 15 dB (A).

## REFERENCE

- [1] Commercialization Scenario for FCVs and H2 Stations, Fuel Cell Commercialization of Japan (FCCJ), July 2010
- [2] Joint Announcement by 13 Japanese companies, January 13 2011, (In Japanese)
- [3] Future Outlook for Fuel Cell Related Technologies and Market, Vol.1, Osaka Marketing Division, Fuji Keizai Co. Ltd, January 2011, (In Japanese)
- [4] Boger, H. W. : Designing Valves and Downstream Devices as Low Noise Pack-ages, Heat./Piping/Air Cond., (1971)
- [5] Bell, L. H. : Industrial Noise Control, Mech. Eng. (Am. Soc. Mech. Eng.), No88, pp. 417-426, (1993)
- [6] N. Atalla, R. Panneton: Acoustic absorption of macro-perforated porous materials, J. Sound and Vibration, 243(4), pp.659-678, (2001)
- [7] Youn, C., Asano, S., Kawashima, K. and Kagawa, T: Development of a Nozzle-flapper Type Servo Valve using a Slit Structure, Trans. ASME Journal of Fluid Engineering, Vo.129, No.5, pp.573-578, (2007)
- [8] Kenji KAWASHIMA, Chongho YOUN, Toshiharu KAGAWA: Flow Characteristics of Pressure Reducing Valve, Journal of Visualization, Vol.11, No.4, pp.357-364, (2008)
- [9] Hydrogen Energy Test and Research Center (HyTReC), Japan, "<http://hytrec.jp>"

## Authors' Index

### A

Ramhuzaini Abd Rahman 609  
Torben O Andersen 151, 551, 565

### B

Eric J Barth 283, 595  
Michael M Bech 551  
Eric Bideaux 397  
Doug Bitner 467  
Pontus Boström 137  
Marc Budinger 537  
Richard Burton 467

### C

Maolin Cai 271  
Gianluca Carconi 59  
Diana Cardona 283  
Richard Carpenter 347  
Peter Chapple 579  
David B Comber 283

### D

Cristian D'Arcano 59  
S A El Delbari 423  
Peter Dengler 333  
Ram Sudarsan Devendran 29  
René von Dombrowski 333  
Sebastian Drumm 51  
Carsten Dunker 489

### E

Mohammed A El Sayed 181, 297  
Asko Ellman 243  
Jan Elvers 259

### F

Roger Fales 347  
Davide Ferrara 195  
Amine Fraj 537

### G

S. Andrew Gadsden 181, 423  
Marcus Geimer 333, 519  
Hossein Gholizadeh 467  
Guofang Gong 227, 411

### H

Heikki Haario 439  
Saeid Habibi 181, 297, 423  
Heikki Handroos 439  
Henri Hänninen 109  
Anders H Hansen 551  
Rico H Hansen 551, 565  
Mikko Heikkilä 137  
Stefan Heitzig 51  
Andrew Hillis 165  
Mark E Hofacker 595  
Till Homann 489  
Mikko Huova 137



## I

Monika Ivantysynova 13, 505

## J

Giovanni Jacazio 195

Per Johansen 151

Nigel Johnston 165

Ville Jouppila 243

Jyri Juhala 81

## K

Toshiharu Kagawa 271, 623

Jyrki Kajaste 81, 109, 365

Keitaro Kamata 451

Miikka Ketonen 137

## L

Xin Li 271

Matthias Liermann 213

Matti Linjama 137

Chengliang Liu 227

Junhong Liu 439

## M

Jean-Charles Mare 537

Sebastian Michel 93

Andrea Mornacchi 195

Hubertus Murrenhoff 51, 259

## N

Yoshinari Nakamura 623

Nicola Nervegna 59

Michael Niss 579

## P

Min Pan 165

Stefano Pastorelli 195

Henrik C Pedersen 151, 551, 565

Matti Pietola 81, 109, 365

Andrew R Plummer 379

## R

Daniel B Rømer 151

Massimo Rundo 59

## S

Tuomas Saarikoski 365

Guanglin Shi 321

David Schmitz 519

Greg Schoenau 467

Nariman Sepehri 609

Hu Shi 411

Lilia Sidhom 397

Mohamed Smaoui 397

Yu Song 423

Massimo Sorli 195

Michael Sprengel 505

Kim A Stelson 123

Mengze Sun 595

## T

Kazuhiro Tanaka 451

Jianfeng Tao 227

Frank Thielecke 489

Knud Erik Thomsen 579

Kouki Tomioka 451

## V

Andrea Vacca	29
--------------	----

## W

Marina Waldén	137
Feng Wang	123
Ruigang Wang	321
Jürgen Weber	93
Robert J Webster III	283
Darren T Williams	379
Peter Wilson	379
Huapeng Wu	439
Weiqiang Wu	411

## X

Yaozhong Xu	397
Zhenyin Xu	321

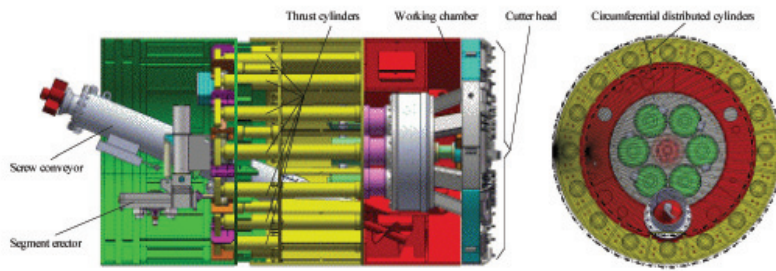
## Y

Takeshi Yamaguchi	451
Haiyan Yang	227
Chongho Youn	623

## Z

Marco Zecchi	13
--------------	----





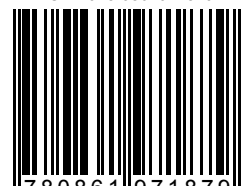
Fluid Power and Motion Control (FPMC) 2012 comprises 41 papers presented at FPMC 2012 – the latest in a long series of International Symposia held at the University of Bath. FPMC 2012 was co-organised by the American Society of Mechanical Engineers (ASME). This collection of papers reports on the latest research in the fields of hydraulic and pneumatic motion control worldwide.

Topics in FPMC 2012 include:

- Digital hydraulics;
- Energy efficiency and the environment;
- Power conversion for renewable energy generation;
- Control;
- Fluid dynamics and noise;
- Hydraulic and pneumatic components and systems;
- Modelling and simulation;
- Condition monitoring and fault diagnosis;
- Automotive and internal combustion engine applications;
- Off-road, marine and industrial applications.

This volume will be of particular interest to researchers and practitioners working in the fields of fluid power, motion control, hydraulics and pneumatics.

ISBN 978-0861971879



9 780861 971879